

UNITED KINGDOM · CHINA · MALAYSIA

Hydrodynamics and stability of Group B *Streptococcus* polysaccharides and CRM197 protein

By Thomas MacCalman

Thesis submitted to the University of Nottingham for the degree of Doctor of Philosophy

January 1, 2023

NATIONAL CENTRE FOR MOLECULAR HYDRODYNAMICS, UNIVERSITY OF NOTTINGHAM
University of Nottingham, Sutton Bonington Campus, Loughborough, LE12 5RD, U.K.

Abstract

Group B *Streptococcus* is a pathogen that chiefly infects immunocompromised individuals and neonates. To combat this infection, at-risk mothers are currently given antibiotics before birth to prevent exposure of neonates to the bacteria. A vaccine would be beneficial, as it would allow mothers to combat this infection without excessive use of antibiotics. As encapsulated bacteria, the main structure available as a target antigen is the polysaccharide capsule itself, rather than any underlying structures. For this reason, glycoconjugate vaccines are being synthesised which use surface polysaccharides conjugated to carrier proteins to improve their immunogenicity. This project studies the stability of candidate polysaccharides for use in a glycoconjugate vaccine. The polysaccharides were provided by GSK vaccines, who requested the use of specific hydrodynamic methodology. The polysaccharides were found to be generally stable, only seeing small changes in hydrodynamic properties after exposure to stress, but in many cases it is likely that the differences seen are due to minor experimental variation rather than genuine structural differences. The polysaccharides were also tested for possible association effects with blood plasma proteins: serum albumin, fibrinogen and immunoglobulin. The polysaccharides were again found to be stable in the presence of these molecules.

Together, these results suggest that these molecules are suitable for further testing and development to generate a vaccine.

Acknowledgments

I would like to thank my supervisors Stephen Harding and Gary Adams for their support throughout my studies, as well as Mary Phillips-Jones who was instrumental in the publication of a literature review from this work. I am indebted to GSK who were kind enough to sponsor this project. I am immensely grateful to my colleague Vlad Dinu for his great patience in teaching me the techniques used here, and for his excellent advice and support throughout the project. Finally, I would like to thank my family and partner Daniel, who have provided unwavering assistance throughout my studies.

Thank you.

Abstract i

Acknowledgments ii

List of Figures xiii

List of Tables xl

Publications xliv

1 Introduction 1

1.1 Group B Streptococcus 1

1.2 Glycoconjugate vaccines 11

1.2.1 Pathogens and the immune system 11

1.2.2 Vaccines 15

1.2.3 Polysaccharide and protein antigens 17

1.2.4 Production methods 19

1.2.5 Zwitterionic polysaccharides 23

1.2.6 Cancer vaccines 24

1.3 Considerations in Glycoconjugate design 24

1.3.1 Comparison of Glycoconjugate and polysaccharide vaccines 25

1.3.2 Comparison of carriers in glycoconjugate vaccines 29

1.3.3 Production methods 32

1.4 Conclusions 38

2 Aims and Objectives 39

3 Methods 40

3.1 Materials 40

3.2 Dialysis 41
3.3 Concentration measurements and dilution series 42
3.4 Density and $\bar{v}$ determination 43
3.5 Viscosity 44
3.6 Analytical Ultracentrifugation 45
3.7 Sedimentation velocity 48
3.8 Sedimentation equilibrium 51
3.9 SEC-MALS 53
4 Baseline measurements 57
4.1 Native GBS polysaccharide, serotype IA 57
4.1.1 Concentration series 57
4.1.2 Density and $\bar{v}$ determination 57
4.1.3 Viscosity 58
4.1.4 Sedimentation velocity 59
4.1.5 Sedimentation equilibrium 61
4.1.6 SEC-MALS 61
4.2 Native GBS polysaccharide, serotype IB 62
4.2.1 Concentration series 62
4.2.2 Density and $\bar{v}$ determination 62
4.2.3 Viscosity 62
4.2.4 Sedimentation velocity 63
4.2.5 Sedimentation equilibrium 64

4.2.6 SEC-MALS 65

4.3 Native GBS polysaccharide, serotype II 66

4.3.1 Concentration series 66

4.3.2 Density and $\bar{v}$ determination 66

4.3.3 Viscosity 66

4.3.4 Sedimentation velocity 67

4.3.5 Sedimentation equilibrium 68

4.3.6 SEC-MALS 69

4.4 Native GBS polysaccharide, serotype III 70

4.4.1 Concentration series 70

4.4.2 Density and $\bar{v}$ determination 70

4.4.3 Viscosity 70

4.4.4 Sedimentation velocity 71

4.4.5 Sedimentation equilibrium 72

4.4.6 SEC-MALS 73

4.5 Native GBS polysaccharide, serotype IV 74

4.5.1 Concentration series 74

4.5.2 Density and $\bar{v}$ determination 74

4.5.3 Viscosity 74

4.5.4 Sedimentation velocity 75

4.5.5 Sedimentation equilibrium 76

4.5.6 SEC-MALS 77

4.6 Native GBS polysaccharide, serotype V 78

4.6.1 Concentration series 78

4.6.2 Density and $\bar{v}$ determination 78

4.6.3 Viscosity 78

4.6.4 Sedimentation velocity 79

4.6.5 Sedimentation equilibrium 80

4.6.6 SEC-MALS 81

4.7 Sized GBS polysaccharide, serotype IA 82

4.7.1 Concentration series 82

4.7.2 Density and $\bar{v}$ determination 82

4.7.3 Viscosity 82

4.7.4 Sedimentation velocity 83

4.7.5 Sedimentation equilibrium 84

4.7.6 SEC-MALS 85

4.8 Sized GBS polysaccharide, serotype IB 86

4.8.1 Concentration series 86

4.8.2 Density and $\bar{v}$ determination 86

4.8.3 Viscosity 86

4.8.4 Sedimentation velocity 87

4.8.5 Sedimentation equilibrium 88

4.8.6 SEC-MALS 89

4.9 Sized GBS polysaccharide, serotype II 90

4.9.1 Concentration series 90
4.9.2 Density and $\bar{v}$ determination 90
4.9.3 Viscosity 90
4.9.4 Sedimentation velocity 91
4.9.5 Sedimentation equilibrium 92
4.9.6 SEC-MALS 93
4.10 CRM197 94
4.10.1 Density and $\bar{v}$ determination 94
4.10.2 Sedimentation Velocity 94
4.10.3 SEC-MALS 96
4.11 Summary 96
4.12 Discussion 97
5 Stability after repeated freeze-thaw cycles 100
5.1 Native GBS polysaccharide, serotype IA 101
5.1.1 Ten freeze-thaw cycles 101
5.1.2 One hundred freeze-thaw cycles 104
5.2 Native GBS polysaccharide, serotype IB 108
5.2.1 Ten freeze-thaw cycles 108
5.2.2 One hundred freeze-thaw cycles 110
5.3 Native GBS polysaccharide, serotype II 114
5.3.1 Ten freeze-thaw cycles 114
5.3.2 One hundred freeze-thaw cycles 116

5.4 Native GBS polysaccharide, serotype III 120
5.4.1 Ten freeze-thaw cycles 120
5.4.2 One hundred freeze-thaw cycles 122
5.5 Native GBS polysaccharide, serotype IV 126
5.5.1 Ten freeze-thaw cycles 126
5.5.2 One hundred freeze-thaw cycles 128
5.6 Native GBS polysaccharide, serotype V 132
5.6.1 Ten freeze-thaw cycles 132
5.6.2 One hundred freeze-thaw cycles 135
5.7 Sized GBS polysaccharide, serotype IA 138
5.7.1 Ten freeze-thaw cycles 138
5.7.2 One hundred freeze-thaw cycles 140
5.8 Sized GBS polysaccharide, serotype IB 144
5.8.1 Ten freeze-thaw cycles 144
5.8.2 One hundred freeze-thaw cycles 146
5.9 Sized GBS polysaccharide, serotype II 150
5.9.1 Ten freeze-thaw cycles 150
5.9.2 One hundred freeze-thaw cycles 152
5.10 Summary 156
5.11 Discussion 162
6 Stability after incubation at 20˚C 166
6.1 Native GBS polysaccharide, serotype IA 167

6.1.1 Ten day incubation 167

6.1.2 One hundred day incubation 169

6.2 Native GBS polysaccharide, serotype IB 173

6.2.1 Ten day incubation 173

6.2.2 One hundred day incubation 175

6.3 Native GBS polysaccharide, serotype II 179

6.3.1 Ten day incubation 179

6.3.2 One hundred day incubation 181

6.4 Native GBS polysaccharide, serotype III 185

6.4.1 Ten day incubation 185

6.4.2 One hundred day incubation 187

6.5 Native GBS polysaccharide, serotype IV 191

6.5.1 Ten day incubation 191

6.5.2 One hundred day incubation 193

6.6 Native GBS polysaccharide, serotype V 197

6.6.1 Ten day incubation 197

6.6.2 One hundred day incubation 199

6.7 Sized GBS polysaccharide, serotype IA 203

6.7.1 Ten day incubation 203

6.7.2 One hundred day incubation 206

6.8 Sized GBS polysaccharide, serotype IB 209

6.8.1 Ten day incubation 209

6.8.2 One hundred day incubation 211
6.9 Sized GBS polysaccharide, serotype II 215
6.9.1 Ten day incubation 215
6.9.2 One hundred day incubation 217
6.10 Summary 221
6.11 Discussion 226
7 Stability after incubation at 37˚C 229
7.1 Method 229
7.2 Native GBS polysaccharide, serotype IA 230
7.3 Native GBS polysaccharide, serotype IB 231
7.4 Native GBS polysaccharide, serotype II 232
7.5 Native GBS polysaccharide, serotype III 233
7.6 Native GBS polysaccharide, serotype IV 234
7.7 Native GBS polysaccharide, serotype V 235
7.8 Sized GBS polysaccharide, serotype IA 236
7.9 Sized GBS polysaccharide, serotype IB 237
7.10 Sized GBS polysaccharide, serotype II 238
7.11 Summary 239
7.12 Discussion 239
8 A study of potential interactions with common blood proteins 241
8.1 Protein baseline values 242
8.1.1 BSA 244

8.1.2 HSA 245
8.1.3 Fibrinogen 245
8.1.4 Immunoglobulins 246
8.1.5 Summary 247
8.2 Method 248
8.3 Native GBS polysaccharide, serotype IA 251
8.3.1 Viscosity 251
8.3.2 Sedimentation velocity 251
8.4 Native GBS polysaccharide, serotype IB 257
8.4.1 Viscosity 257
8.4.2 Sedimentation velocity 257
8.5 Native GBS polysaccharide, serotype II 263
8.5.1 Viscosity 263
8.5.2 Sedimentation velocity 263
8.6 Native GBS polysaccharide, serotype III 269
8.6.1 Viscosity 269
8.6.2 Sedimentation velocity 269
8.7 Native GBS polysaccharide, serotype IV 275
8.7.1 Viscosity 275
8.7.2 Sedimentation velocity 275
8.8 Native GBS polysaccharide, serotype V 281
8.8.1 Viscosity 281

8.8.2 Sedimentation velocity 281
8.9 Sized GBS polysaccharide, serotype IA 287
8.9.1 Viscosity 287
8.9.2 Sedimentation velocity 287
8.10 Sized GBS polysaccharide, serotype IB 293
8.10.1 Viscosity 293
8.10.2 Sedimentation velocity 293
8.11 Sized GBS polysaccharide, serotype II 299
8.11.1 Viscosity 299
8.11.2 Sedimentation velocity 299
8.12 Summary 304
8.13 Discussion 305
9 Conclusions 308
10 Bibliography 310
11 Appendix 324
11.1 Submaxillary Mucin: its Effect on Aroma Release from Acidic Drinks and New Insight into the Effect of Aroma Compounds on its Macromolecular Integrity 325
11.2 Hydrodynamic Compatibility of Hyaluronic Acid and Tamarind Seed Polysaccharide as Ocular Mucin Supplements 339
11.3 Probing the effect of aroma compounds on the hydrodynamic properties of mucin glycoproteins 351

List of Figures

Figure 1.1 - Repeating structure of GBS serotype IA. This is a class 1 capsular polysaccharide due to alternating β (1→4) linked galactose and glucose residues forming the main backbone of the repeating unit, with a β (1→3) linked side chain on the galactose. Glucose residues are shown in blue, galactose residues are shown in orange, N-Acetylglucosamine residues are shown in red, and N-Acetylneuraminic acid residues are shown in green. Redrawn from [9].. 2

Figure 1.2 - Repeating structure of GBS serotype IB. This is a class 1 capsular polysaccharide due to alternating β (1→4) linked galactose and glucose residues forming the main backbone of the repeating unit, with a β (1→3) linked side chain on the galactose. Glucose residues are shown in blue, galactose residues are shown in orange, N-Acetylglucosamine residues are shown in red, and N-Acetylneuraminic acid residues are shown in green. Redrawn from [9].. 3

Figure 1.3 - Repeating structure of GBS serotype II. This is a class 3 capsular polysaccharide due to the large backbone with no structural similarity to other serotypes. Glucose residues are shown in blue, galactose residues are shown in orange, N-Acetylglucosamine residues are shown in red, and N-Acetylneuraminic acid residues are shown in green. Redrawn from [9].. 3

Figure 1.4 - Repeating structure of GBS serotype III. This is a class 1 capsular polysaccharide due to alternating β (1→4) linked galactose and glucose residues forming the main backbone of the repeating unit, with a β (1→3) linked side chain on the galactose. Glucose residues are shown in blue, galactose residues are shown in orange, and N-Acetylneuraminic acid residues are shown in green. Redrawn from [9]. 4

Figure 1.5 - Repeating structure of GBS serotype IV. This is a class 2 capsular polysaccharide due to the trisaccharide backbone of glucose galactose and glucose in the repeating unit with a β (1→6) linked side chain. Glucose residues are shown in blue, galactose residues are shown in orange, N-Acetylglucosamine residues are shown in red, and N-Acetylneuraminic acid residues are shown in green. Redrawn from [9]. 5

Figure 1.6 - Repeating structure of GBS serotype V. This is a class 2 capsular polysaccharide due to the trisaccharide backbone of glucose galactose and glucose in the repeating unit with a β (1→6) linked side chain. Glucose residues are shown in blue, galactose residues are shown in orange, N-Acetylglucosamine residues are shown in red, and N-Acetylneuraminic acid residues are shown in green. Redrawn from [9]. 6

Figure 1.1.7 – Structure of a typical immunoglobulin of the IgG (left) and IgM (right) isotypes. 13

Figure 1.8 – Diagram showing the interaction between a glycoconjugate vaccine, antigen presenting cells and CD4+ T cells. The glycoconjugate binds to the B cell receptor, and this complex is internalised and digested. Fragments of the glycoconjugate that still contain some protein can interact with the MHCII, which is then transported to the surface of the cell where the MHCII/antigen complex can interact with the T cell receptor. This triggers to T cell to release signalling molecules, which trigger the differentiation and proliferation of the B cell. Adapted from [80]..... 19

Figure 3.1 – The centrepiece of an analytical ultracentrifuge cell is shown on the left. The two sectors are visible from above, while at the front are the holes used to inject samples and reference solvents into the assembled cells. In the middle is shown the centrepiece pressed between two transparent windows. This seals the sectors, allowing them to be filled with a sample and reference solvent, while also allowing laser light to pass through. On the right is the entire assembly placed in a metal casing, held together by a screw ring (not shown) which is tightened with a torque wrench to prevent leaks..... 46

Figure 3.2 – The analytical ultracentrifuge rotor is shown. In this case there are eight holes into which individual cells can be loaded. Light is emitted from the centrifuge through a monochromator and redirected downward through the sample cells and into a photomultiplier to detect the distribution of sample within the cell. 46

Figure 3.3 – Diagram showing the outputs of sedimentation velocity and sedimentation equilibrium experiments. The position of the cell top is shown by a blue dotted line, the meniscus by a green dashed line, and the cell base by a solid red line. A, on the left, shows an example of a sedimentation velocity experiment. The cell is almost completely filled with sample. The centrifugal force outweighs the effects of back diffusion, and so the sample sediments over time. The graph shows the readings given by the laser, appearing as an array of sigmoidal curves. The sharp increase shows the position of the boundary between the solvent region (from which sample has been depleted) and the region where solute is still present. The rate of movement of this boundary is used to give the sedimentation coefficient. B, on the right, shows an example of a sedimentation equilibrium experiment. The cell contains a much lower volume. The effects of sedimentation and back diffusion are balanced, and the system is at equilibrium. Rather than a sharp boundary between solute and solution, there is a gradual increase in concentration towards the cell base. The shape of this single curve is used to ascertain the molecular weight. 48

Figure 4.1 – Plot of density against concentration for N-IA, with a linear fit to obtain gradient. 58

Figure 4.2 – Plot of viscosity against concentration for N-IA, with linear fits to extrapolate to zero concentration. 59

Figure 4.3 – Distribution of sedimentation coefficients at a range of loading concentrations of N-IA. 60

Figure 4.4 – Plot of the reciprocal of sedimentation coefficient against loading concentration for N-IA, with a linear fit to extrapolate to zero concentration. 60

Figure 4.5 – Plot of the reciprocal of apparent molecular weight ($M_{w,app}$) values against loading concentration of N-IA, with a linear fit to extrapolate to zero concentration. 61

Figure 4.6 – Plot of density against concentration for N-IB, with a linear fit to obtain gradient. 62

Figure 4.7 – Plot of viscosity against concentration for N-IB, with a linear fit to extrapolate to zero concentration. 63

Figure 4.8 – Distribution of sedimentation coefficients at a range of loading concentrations of N-IB. 64

Figure 4.9 – Plot of the reciprocal of sedimentation coefficient against loading concentration for N-IB, with a linear fit to extrapolate to zero concentration. 64

Figure 4.10 – Plot of the reciprocal of the apparent molecular weight ($M_{w,app}$) values against loading concentration of N-IB, with linear fits to extrapolate to zero concentration.. 65

Figure 4.11 – Plot of density against concentration for N-II, with a linear fit to obtain gradient. 66

Figure 4.12 – Plot of viscosity against concentration for N-II, with linear fits to extrapolate to zero concentration. 67

Figure 4.13 – Distribution of sedimentation coefficients at a range of loading concentrations of N-II. 68

Figure 4.14 – Plot of the reciprocal of sedimentation coefficient against loading concentration for N-II, with a linear fit to extrapolate to zero concentration. 68

Figure 4.15 – Plot of the reciprocal of the apparent molecular weight ($M_{w,app}$) values against loading concentration of N-II, with linear fits to extrapolate to zero concentration..... 69

Figure 4.16 – Plot of density against concentration for N-III, with a linear fit to obtain gradient. 70

Figure 4.17 – Plot of viscosity against concentration for N-III, with linear fits to extrapolate to zero concentration 71

Figure 4.18 – Distribution of sedimentation coefficients at a range of loading concentrations of N-III. 72

Figure 4.19 – Plot of the reciprocal of sedimentation coefficient against loading concentration for N-III, with a linear fit to extrapolate to zero concentration. 72

Figure 4.20 – Plot of the reciprocal of the apparent molecular weight ($M_{w,app}$) values against loading concentration of N-III, with linear fits to extrapolate to zero concentration..... 73
Figure 4.21 – Plot of density against concentration for N-IV, with a linear fit to obtain gradient. 74
Figure 4.22 – Plot of viscosity against concentration for N-IV, with linear fits to extrapolate to zero concentration. 75
Figure 4.23 – Distribution of sedimentation coefficients at a range of loading concentrations of N-IV..... 76
Figure 4.24 – Plot of the reciprocal of sedimentation coefficient against loading concentration for N-IV, with a linear fit to extrapolate to zero concentration. 76
Figure 4.25 – Plot of the reciprocal of the apparent molecular weight ($M_{w,app}$) values against loading concentration of N-IV, with linear fits to extrapolate to zero concentration. 77
Figure 4.26 – Plot of density against concentration for N-V, with a linear fit to obtain gradient. 78
Figure 4.27 – Plot of viscosity against concentration for N-V, with linear fits to extrapolate to zero concentration. 79
Figure 4.28 – Distribution of sedimentation coefficients at a range of loading concentrations of N-V..... 80
Figure 4.29 – Plot of the reciprocal of sedimentation coefficient against loading concentration for N-V, with a linear fit to extrapolate to zero concentration. 80
Figure 4.30 – Plot of the reciprocal of the apparent molecular weight ($M_{w,app}$) values against loading concentration of N-V, with linear fits to extrapolate to zero concentration. 81
Figure 4.31 – Plot of density against concentration for S-IA, with a linear fit to obtain gradient. 82
Figure 4.32 – Plot of viscosity against concentration for S-IA, with linear fits to extrapolate to zero concentration. 83

Figure 4.33 – Distribution of sedimentation coefficients at a range of loading concentrations of S-IA. 84

Figure 4.34 – Plot of the reciprocal of sedimentation coefficient against loading concentration for S-IA, with a linear fit to extrapolate to zero concentration. 84

Figure 4.35 – Plot of the reciprocal of the apparent molecular weight ($M_{w,app}$) values against loading concentration of S-IA, with linear fits to extrapolate to zero concentration. 85

Figure 4.36 – Plot of density against concentration for S-IB, with a linear fit to obtain gradient. 86

Figure 4.37 – Plot of viscosity against concentration for S-IB, with linear fits to extrapolate to zero concentration. 87

Figure 4.38 – Distribution of sedimentation coefficients at a range of loading concentrations of S-IB..... 88

Figure 4.39 – Plot of the reciprocal of sedimentation coefficient against loading concentration for S-IB, with a linear fit to extrapolate to zero concentration. 88

Figure 4.40 – Plot of the reciprocal of the apparent molecular weight ($M_{w,app}$) values against loading concentration of S-IB, with linear fits to extrapolate to zero concentration. 89

Figure 4.41 – Plot of density against concentration for S-II, with a linear fit to obtain gradient. 90

Figure 4.42 – Plot of viscosity against concentration for S-II, with linear fits to extrapolate to zero concentration. 91

Figure 4.43 – Distribution of sedimentation coefficients at a range of loading concentrations of S-II..... 92

Figure 4.44 – Plot of the reciprocal of sedimentation coefficient against loading concentration for S-II, with a linear fit to extrapolate to zero concentration. 92

Figure 4.45 – Plot of the reciprocal of the apparent molecular weight ($M_{w,app}$) values against loading concentration of S-II, with linear fits to extrapolate to zero concentration. 93

Figure 4.46 – Plot of density against concentration for CRM197, with a linear fit to obtain gradient. 94
Figure 4.47 – Distribution of sedimentation coefficients at a range of loading concentrations of CRM197. 95
Figure 4.48 – Plot of the reciprocal of sedimentation coefficient against loading concentration for CRM197, with a linear fit to extrapolate to zero concentration. 95
Figure 5.1 – Diagram showing how the formation of ice crystals may damage dissolved polysaccharides. Following the arrows, the first square shows the freely floating polysaccharides and ions. The second shows that as ice crystals form there will be pockets of highly concentrated material which may then react, causing deviation from its usual structure. The third square shows the solution totally frozen, while the fourth shows the sample again passing through a stage in the presence of ice crystals. The last square shows the permanent change to the polysaccharide structures even after returning to ambient conditions. 100
Figure 5.2 – Plot of viscosity against concentration for N-IA after exposure to ten freeze-thaw cycles, with linear fits to extrapolate to zero concentration. 101
Figure 5.3 – Distribution of sedimentation coefficients at a range of loading concentrations of N-IA after ten freeze-thaw cycles. 102
Figure 5.4 – Plot of the reciprocal of sedimentation coefficient against loading concentration for N-IA after exposure to ten freeze-thaw cycles, with a linear fit to extrapolate to zero concentration. 103
Figure 5.5 – Plot of the reciprocal of apparent molecular weight ($M_{w,app}$) values against loading concentration of N-IA after exposure to ten freeze-thaw cycles, with a linear fit to extrapolate to zero concentration. 104
Figure 5.6 – Plot of viscosity against concentration for N-IA after exposure to 100 freeze-thaw cycles, with linear fits to extrapolate to zero concentration. 105

Figure 5.7 – Distribution of sedimentation coefficients at a range of loading concentrations of N-IA after 100 freeze-thaw cycles. 106
Figure 5.8 – Plot of the reciprocal of sedimentation coefficient against loading concentration for N-IA after exposure to 100 freeze-thaw cycles, with a linear fit to extrapolate to zero concentration. 106
Figure 5.9 – Plot of the reciprocal of apparent molecular weight ($M_{w,app}$) values against loading concentration of N-IA after exposure to 100 freeze-thaw cycles, with a linear fit to extrapolate to zero concentration. 107
Figure 5.10 – Plot of viscosity against concentration for N-IB after exposure to ten freeze-thaw cycles, with linear fits to extrapolate to zero concentration. 108
Figure 5.11 – Distribution of sedimentation coefficients at a range of loading concentrations of N-IB after ten freeze-thaw cycles. 109
Figure 5.12 – Plot of the reciprocal of sedimentation coefficient against loading concentration for N-IB after exposure to ten freeze-thaw cycles, with a linear fit to extrapolate to zero concentration. 109
Figure 5.13 – Plot of the reciprocal of apparent molecular weight ($M_{w,app}$) values against loading concentration of N-IB after exposure to ten freeze-thaw cycles, with a linear fit to extrapolate to zero concentration. 110
Figure 5.14 – Plot of viscosity against concentration for N-IB after exposure to 100 freeze-thaw cycles, with linear fits to extrapolate to zero concentration. 111
Figure 5.15 – Distribution of sedimentation coefficients at a range of loading concentrations of N-IB after 100 freeze-thaw cycles. 112
Figure 5.16 – Plot of the reciprocal of sedimentation coefficient against loading concentration for N-IB after exposure to 100 freeze-thaw cycles, with a linear fit to extrapolate to zero concentration. 112

Figure 5.17 – Plot of the reciprocal of apparent molecular weight ($M_{w,app}$) values against loading concentration of N-IB after exposure to 100 freeze-thaw cycles, with a linear fit to extrapolate to zero concentration. 113
Figure 5.18 – Plot of viscosity against concentration for N-II after exposure to ten freeze-thaw cycles, with linear fits to extrapolate to zero concentration. 114
Figure 5.19 – Distribution of sedimentation coefficients at a range of loading concentrations of N-II after ten freeze-thaw cycles. 115
Figure 5.20 – Plot of the reciprocal of sedimentation coefficient against loading concentration for N-II after exposure to ten freeze-thaw cycles, with a linear fit to extrapolate to zero concentration. 115
Figure 5.21 – Plot of the reciprocal of apparent molecular weight ($M_{w,app}$) values against loading concentration of N-II after exposure to ten freeze-thaw cycles, with a linear fit to extrapolate to zero concentration. 116
Figure 5.22 – Plot of viscosity against concentration for N-II after exposure to 100 freeze-thaw cycles, with linear fits to extrapolate to zero concentration. 117
Figure 5.23– Distribution of sedimentation coefficients at a range of loading concentrations of N-II after 100 freeze-thaw cycles. 118
Figure 5.24 – Plot of the reciprocal of sedimentation coefficient against concentration for N-II after exposure to 100 freeze-thaw cycles, with a linear fit to extrapolate to zero concentration. 118
Figure 5.25 – Plot of the reciprocal of apparent molecular weight ($M_{w,app}$)values against concentration of N-II after exposure to 100 freeze-thaw cycles, with a linear fit to extrapolate to zero concentration. 119
Figure 5.26 – Plot of viscosity against concentration for N-III after exposure to ten freeze-thaw cycles, with linear fits to extrapolate to zero concentration. 120

Figure 5.27 – Distribution of sedimentation coefficients at a range of loading concentrations of N-III after ten freeze-thaw cycles. 121
Figure 5.28 – Plot of the reciprocal of sedimentation coefficient against loading concentration for N-III after exposure to ten freeze-thaw cycles, with a linear fit to extrapolate to zero concentration. 121
Figure 5.29 – Plot of the reciprocal of apparent molecular weight ($M_{w,app}$) values against loading concentration of N-III after exposure to ten freeze-thaw cycles, with a linear fit to extrapolate to zero concentration. 122
Figure 5.30 – Plot of viscosity against concentration for N-III after exposure to 100 freeze-thaw cycles, with linear fits to extrapolate to zero concentration. 123
Figure 5.31 – Distribution of sedimentation coefficients at a range of loading concentrations of N-III after 100 freeze-thaw cycles. 124
Figure 5.32 – Plot of the reciprocal of sedimentation coefficient against loading concentration for N-III after exposure to 100 freeze-thaw cycles, with a linear fit to extrapolate to zero concentration. 124
Figure 5.33 – Plot of the reciprocal of apparent molecular weight ($M_{w,app}$) values against loading concentration of N-III after exposure to 100 freeze-thaw cycles, with a linear fit to extrapolate to zero concentration. 125
Figure 5.34 – Plot of viscosity against concentration for N-IV after exposure to ten freeze-thaw cycles, with linear fits to extrapolate to zero concentration. 126
Figure 5.35 – Distribution of sedimentation coefficients at a range of loading concentrations of N-IV after ten freeze-thaw cycles. 127
Figure 5.36 – Plot of the reciprocal of sedimentation coefficient against loading concentration for N-IV after exposure to ten freeze-thaw cycles, with a linear fit to extrapolate to zero concentration. 127

Figure 5.37 – Plot of the reciprocal of apparent molecular weight ($M_{w,app}$) values against loading concentration of N-IV after exposure to ten freeze-thaw cycles, with a linear fit to extrapolate to zero concentration. 128
Figure 5.38 – Plot of viscosity against concentration for N-IV after exposure to 100 freeze-thaw cycles, with linear fits to extrapolate to zero concentration. 129
Figure 5.39 – Distribution of sedimentation coefficients at a range of loading concentrations of N-IV after 100 freeze-thaw cycles. 130
Figure 5.40 – Plot of the reciprocal of sedimentation coefficient against loading concentration for N-IV after exposure to 100 freeze-thaw cycles, with a linear fit to extrapolate to zero concentration. 130
Figure 5.41 – Plot of the reciprocal of apparent molecular weight ($M_{w,app}$) values against loading concentration of N-IV after exposure to 100 freeze-thaw cycles, with a linear fit to extrapolate to zero concentration. 131
Figure 5.42 – Plot of viscosity against concentration for N-V after exposure to ten freeze-thaw cycles, with linear fits to extrapolate to zero concentration. 132
Figure 5.43 – Distribution of sedimentation coefficients at a range of loading concentrations of N-V after ten freeze-thaw cycles..... 133
Figure 5.44 – Plot of the reciprocal of sedimentation coefficient against loading concentration for N-V after exposure to ten freeze-thaw cycles, with a linear fit to extrapolate to zero concentration. 133
Figure 5.45 – Plot of the reciprocal of apparent molecular weight ($M_{w,app}$) values against loading concentration of N-V after exposure to ten freeze-thaw cycles, with a linear fit to extrapolate to zero concentration. 134
Figure 5.46 – Plot of viscosity against concentration for N-V after exposure to 100 freeze-thaw cycles, with linear fits to extrapolate to zero concentration. 135

Figure 5.47 – Distribution of sedimentation coefficients at a range of loading concentrations of N-V after 100 freeze-thaw cycles. 136
Figure 5.48 – Plot of the reciprocal of sedimentation coefficient against loading concentration for N-V after exposure to 100 freeze-thaw cycles, with a linear fit to extrapolate to zero concentration. 136
Figure 5.49 – Plot of the reciprocal of apparent molecular weight ($M_{w,app}$) values against loading concentration of N-V after exposure to 100 freeze-thaw cycles, with a linear fit to extrapolate to zero concentration. 137
Figure 5.50 – Plot of viscosity against concentration for S-IA after exposure to ten freeze-thaw cycles, with linear fits to extrapolate to zero concentration. 138
Figure 5.51 – Distribution of sedimentation coefficients at a range of loading concentrations of S-IA after ten freeze-thaw cycles. 139
Figure 5.52 – Plot of the reciprocal of sedimentation coefficient against loading concentration for S-IA after exposure to ten freeze-thaw cycles, with a linear fit to extrapolate to zero concentration. 139
Figure 5.53 – Plot of the reciprocal of apparent molecular weight ($M_{w,app}$) values against loading concentration of S-IA after exposure to ten freeze-thaw cycles, with a linear fit to extrapolate to zero concentration. 140
Figure 5.54 – Plot of viscosity against concentration for S-IA after exposure to 100 freeze-thaw cycles, with linear fits to extrapolate to zero concentration. 141
Figure 5.55 – Distribution of sedimentation coefficients at a range of loading concentrations of S-IA after 100 freeze-thaw cycles. 142
Figure 5.56 – Plot of the reciprocal of sedimentation coefficient against loading concentration for S-IA after exposure to 100 freeze-thaw cycles, with a linear fit to extrapolate to zero concentration. 142

Figure 5.57 – Plot of the reciprocal of apparent molecular weight ($M_{w,app}$) values against loading concentration of S-IA after exposure to 100 freeze-thaw cycles, with a linear fit to extrapolate to zero concentration. 143
Figure 5.58 – Plot of viscosity against concentration for S-IB after exposure to ten freeze-thaw cycles, with linear fits to extrapolate to zero concentration. 144
Figure 5.59 – Distribution of sedimentation coefficients at a range of loading concentrations of S-IB after ten freeze-thaw cycles..... 145
Figure 5.60 – Plot of the reciprocal of sedimentation coefficient against loading concentration for S-IB after exposure to ten freeze-thaw cycles, with a linear fit to extrapolate to zero concentration. 145
Figure 5.61 – Plot of the reciprocal of apparent molecular weight ($M_{w,app}$) values against loading concentration of S-IB after exposure to ten freeze-thaw cycles, with a linear fit to extrapolate to zero concentration. 146
Figure 5.62 – Plot of viscosity against concentration for S-IB after exposure to 100 freeze-thaw cycles, with linear fits to extrapolate to zero concentration. 147
Figure 5.63 – Distribution of sedimentation coefficients at a range of loading concentrations of S-IB after 100 freeze-thaw cycles. 148
Figure 5.64 – Plot of the reciprocal of sedimentation coefficient against loading concentration for S-IB after exposure to 100 freeze-thaw cycles, with a linear fit to extrapolate to zero concentration. 148
Figure 5.65 – Plot of the reciprocal of apparent molecular weight ($M_{w,app}$) values against loading concentration of S-IB after exposure to 100 freeze-thaw cycles, with a linear fit to extrapolate to zero concentration. 149
Figure 5.66 – Plot of viscosity against concentration for S-II after exposure to ten freeze-thaw cycles, with linear fits to extrapolate to zero concentration. 150

Figure 5.67 – Distribution of sedimentation coefficients at a range of loading concentrations of S-II after ten freeze-thaw cycles. 151
Figure 5.68 – Plot of the reciprocal of sedimentation coefficient against loading concentration for S-II after exposure to ten freeze-thaw cycles, with a linear fit to extrapolate to zero concentration. 151
Figure 5.69 – Plot of the reciprocal of apparent molecular weight ($M_{w,app}$) values against loading concentration of S-II after exposure to ten freeze-thaw cycles, with a linear fit to extrapolate to zero concentration. 152
Figure 5.70 – Plot of viscosity against concentration for S-II after exposure to 100 freeze-thaw cycles, with linear fits to extrapolate to zero concentration. 153
Figure 5.71 – Distribution of sedimentation coefficients at a range of loading concentrations of S-II after 100 freeze-thaw cycles. 154
Figure 5.72 – Plot of the reciprocal of sedimentation coefficient against loading concentration for S-II after exposure to 100 freeze-thaw cycles, with a linear fit to extrapolate to zero concentration. 154
Figure 5.73 – Plot of the reciprocal of apparent molecular weight ($M_{w,app}$) values against loading concentration of S-II after exposure to 100 freeze-thaw cycles, with a linear fit to extrapolate to zero concentration. 155
Figure 5.74 – Viscosoty of each polysaccharide as determined by U-tube viscometry, and how they altered after exposure to a series of freeze-thaw cycles. 159
Figure 5.75 – Sedimentation coefficient of each polysaccharide as determined by sedimentation velocity, and how they altered after exposure to a series of freeze-thaw cycles. 159
Figure 5.76 – Molecular weight of each polysaccharide as determined by sedimentation equilibrium, and how they altered after exposure to a series of freeze-thaw cycles. 160

Figure 5.77 – Molecular weight of each polysaccharide as determined by SEC-MALS, and how they altered after exposure to a series of freeze-thaw cycles. 160
Figure 5.78 – Viscosity of each polysaccharide as determined by SEC-MALS, and how they altered after exposure to a series of freeze-thaw cycles. 161
Figure 6.1 – Plot of viscosity against concentration for N-IA after incubation at 20˚C for ten days, with linear fits to extrapolate to zero concentration. 167
Figure 6.2 – Distribution of sedimentation coefficients at a range of loading concentrations of N-IA after incubation at 20˚C for ten days. 168
Figure 6.3 – Plot of the reciprocal of sedimentation coefficient against loading concentration for N-IA after incubation at 20˚C for ten days, with a linear fit to extrapolate to zero concentration. 168
Figure 6.4 – Plot of the reciprocal of apparent molecular weight ($M_{w,app}$) values against loading concentration of N-IA after incubation at 20˚C for ten days, with a linear fit to extrapolate to zero concentration. 169
Figure 6.5 – Plot of viscosity against concentration for N-IA after incubation at 20˚C for one hundred days, with linear fits to extrapolate to zero concentration. 170
Figure 6.6 – Distribution of sedimentation coefficients at a range of loading concentrations of N-IA after incubation at 20˚C for one hundred days. 171
Figure 6.7 – Plot of the reciprocal of sedimentation coefficient against loading concentration for N-IA after incubation at 20˚C for one hundred days, with a linear fit to extrapolate to zero concentration. 171
Figure 6.8 – Plot of the reciprocal of apparent molecular weight ($M_{w,app}$) values against loading concentration of N-IA after incubation at 20˚C for one hundred days, with a linear fit to extrapolate to zero concentration. 172
Figure 6.9 – Plot of viscosity against concentration for N-IB after incubation at 20˚C for ten days, with linear fits to extrapolate to zero concentration. 173

Figure 6.10 – Distribution of sedimentation coefficients at a range of loading concentrations of N-IB after incubation at 20˚C for ten days. 174
Figure 6.11 – Plot of the reciprocal of sedimentation coefficient against loading concentration for N-IB after incubation at 20˚C for ten days, with a linear fit to extrapolate to zero concentration. 174
Figure 6.12 – Plot of the reciprocal of apparent molecular weight ($M_{w,app}$) values against loading concentration of N-IB after incubation at 20˚C for ten days, with a linear fit to extrapolate to zero concentration. 175
Figure 6.13 – Plot of viscosity against concentration for N-IB after incubation at 20˚C for one hundred days, with linear fits to extrapolate to zero concentration. 176
Figure 6.14 – Distribution of sedimentation coefficients at a range of loading concentrations of N-IB after incubation at 20˚C for one hundred days. 177
Figure 6.15 – Plot of the reciprocal of sedimentation coefficient against loading concentration for N-IB after incubation at 20˚C for one hundred days, with a linear fit to extrapolate to zero concentration. 177
Figure 6.16 – Plot of the reciprocal of apparent molecular weight ($M_{w,app}$) values against loading concentration of N-IB after incubation at 20˚C for one hundred days, with a linear fit to extrapolate to zero concentration. 178
Figure 6.17 – Plot of viscosity against concentration for N-II after incubation at 20˚C for ten days, with linear fits to extrapolate to zero concentration. 179
Figure 6.18 – Distribution of sedimentation coefficients at a range of loading concentrations of N-II after incubation at 20˚C for ten days. 180
Figure 6.19 – Plot of the reciprocal of sedimentation coefficient against loading concentration for N-II after incubation at 20˚C for ten days, with a linear fit to extrapolate to zero concentration. 180

Figure 6.20 – Plot of the reciprocal of apparent molecular weight ($M_{w,app}$) values against loading concentration of N-II after incubation at 20˚C for ten days, with a linear fit to extrapolate to zero concentration. 181
Figure 6.21 – Plot of viscosity against concentration for N-II after incubation at 20˚C for one hundred days, with linear fits to extrapolate to zero concentration. 182
Figure 6.22 – Distribution of sedimentation coefficients at a range of loading concentrations of N-II after incubation at 20˚C for one hundred days. 183
Figure 6.23 – Plot of the reciprocal of sedimentation coefficient against loading concentration for N-II after incubation at 20˚C for one hundred days, with a linear fit to extrapolate to zero concentration. 183
Figure 6.24 – Plot of the reciprocal of apparent molecular weight ($M_{w,app}$) values against loading concentration of N-II after incubation at 20˚C for one hundred days, with a linear fit to extrapolate to zero concentration. 184
Figure 6.25 – Plot of viscosity against concentration for N-III after incubation at 20˚C for ten days, with linear fits to extrapolate to zero concentration. 185
Figure 6.26 – Distribution of sedimentation coefficients at a range of loading concentrations of N-III after incubation at 20˚C for ten days. 186
Figure 6.27 – Plot of the reciprocal of sedimentation coefficient against loading concentration for N-III after incubation at 20˚C for ten days, with a linear fit to extrapolate to zero concentration. 186
Figure 6.28 – Plot of the reciprocal of apparent molecular weight ($M_{w,app}$) values against loading concentration of N-III after incubation at 20˚C for ten days, with a linear fit to extrapolate to zero concentration. 187
Figure 6.29 – Plot of viscosity against concentration for N-III after incubation at 20˚C for one hundred days, with linear fits to extrapolate to zero concentration. 188

Figure 6.30 – Distribution of sedimentation coefficients at a range of loading concentrations of N-III after incubation at 20˚C for one hundred days. 189
Figure 6.31 – Plot of the reciprocal of sedimentation coefficient against loading concentration for N-III after incubation at 20˚C for one hundred days, with a linear fit to extrapolate to zero concentration. 189
Figure 6.32 – Plot of the reciprocal of apparent molecular weight ($M_{w,app}$) values against loading concentration of N-III after incubation at 20˚C for one hundred days, with a linear fit to extrapolate to zero concentration. 190
Figure 6.33 – Plot of viscosity against concentration for N-IV after incubation at 20˚C for ten days, with linear fits to extrapolate to zero concentration. 191
Figure 6.34 – Distribution of sedimentation coefficients at a range of loading concentrations of N-IV after incubation at 20˚C for ten days. 192
Figure 6.35 – Plot of the reciprocal of sedimentation coefficient against loading concentration for N-IV after incubation at 20˚C for ten days, with a linear fit to extrapolate to zero concentration. 192
Figure 6.36 – Plot of the reciprocal of apparent molecular weight ($M_{w,app}$) values against loading concentration of N-IV after incubation at 20˚C for ten days, with a linear fit to extrapolate to zero concentration. 193
Figure 6.37 – Plot of viscosity against concentration for N-IV after incubation at 20˚C for one hundred days, with linear fits to extrapolate to zero concentration. 194
Figure 6.38 – Distribution of sedimentation coefficients at a range of loading concentrations of N-IV after incubation at 20˚C for one hundred days 195
Figure 6.39 – Plot of the reciprocal of sedimentation coefficient against loading concentration for N-IV after incubation at 20˚C for one hundred days, with a linear fit to extrapolate to zero concentration. 195

Figure 6.40 – Plot of the reciprocal of apparent molecular weight ($M_{w,app}$) values against loading concentration of N-IV after incubation at 20˚C for one hundred days, with a linear fit to extrapolate to zero concentration. 196
Figure 6.41 – Plot of viscosity against concentration for N-V after incubation at 20˚C for ten days, with linear fits to extrapolate to zero concentration. 197
Figure 6.42 – Distribution of sedimentation coefficients at a range of loading concentrations of N-V after incubation at 20˚C for ten days. 198
Figure 6.43 – Plot of the reciprocal of sedimentation coefficient against loading concentration for N-V after incubation at 20˚C for ten days, with a linear fit to extrapolate to zero concentration. 198
Figure 6.44 – Plot of the reciprocal of apparent molecular weight ($M_{w,app}$) values against loading concentration of N-V after incubation at 20˚C for ten days, with a linear fit to extrapolate to zero concentration. 199
Figure 6.45 – Plot of viscosity against concentration for N-V after incubation at 20˚C for one hundred days, with linear fits to extrapolate to zero concentration. 200
Figure 6.46 – Distribution of sedimentation coefficients at a range of loading concentrations of N-V after incubation at 20˚C for one hundred days. 201
Figure 6.47 – Plot of the reciprocal of sedimentation coefficient against loading concentration for N-V after incubation at 20˚C for one hundred days, with a linear fit to extrapolate to zero concentration. 201
Figure 6.48 – Plot of the reciprocal of apparent molecular weight ($M_{w,app}$) values against loading concentration of N-V after incubation at 20˚C for one hundred days, with a linear fit to extrapolate to zero concentration. 202
Figure 6.49 – Plot of viscosity against concentration for S-IA after incubation at 20˚C for ten days, with linear fits to extrapolate to zero concentration. 203

Figure 6.50 – Distribution of sedimentation coefficients at a range of loading concentrations of S-IA after incubation at 20˚C for ten days. 204
Figure 6.51 – Plot of the reciprocal of sedimentation coefficient against loading concentration for S-IA after incubation at 20˚C for ten days, with a linear fit to extrapolate to zero concentration. 204
Figure 6.52 – Plot of the reciprocal of apparent molecular weight ($M_{w,app}$) values against loading concentration of S-IA after incubation at 20˚C for ten days, with a linear fit to extrapolate to zero concentration. 205
Figure 6.53 – Plot of viscosity against concentration for S-IA after incubation at 20˚C for one hundred days, with linear fits to extrapolate to zero concentration. 206
Figure 6.54 – Distribution of sedimentation coefficients at a range of loading concentrations of S-IA after incubation at 20˚C for one hundred days. 207
Figure 6.55 – Plot of the reciprocal of sedimentation coefficient against loading concentration for S-IA after incubation at 20˚C for one hundred days, with a linear fit to extrapolate to zero concentration. 207
Figure 6.56 – Plot of the reciprocal of apparent molecular weight ($M_{w,app}$) values against loading concentration of S-IA after incubation at 20˚C for one hundred days, with a linear fit to extrapolate to zero concentration. 208
Figure 6.57 – Plot of viscosity against concentration for S-IB after incubation at 20˚C for ten days, with linear fits to extrapolate to zero concentration. 209
Figure 6.58 – Distribution of sedimentation coefficients at a range of loading concentrations of S-IB after incubation at 20˚C for ten days. 210
Figure 6.59 – Plot of the reciprocal of sedimentation coefficient against loading concentration for S-IB after incubation at 20˚C for ten days, with a linear fit to extrapolate to zero concentration. 210

Figure 6.60 – Plot of the reciprocal of apparent molecular weight ($M_{w,app}$) values against loading concentration of S-IB after incubation at 20˚C for ten days, with a linear fit to extrapolate to zero concentration. 211
Figure 6.61 – Plot of viscosity against concentration for S-IB after incubation at 20˚C for one hundred days, with linear fits to extrapolate to zero concentration. 212
Figure 6.62 – Distribution of sedimentation coefficients at a range of loading concentrations of S-IB after incubation at 20˚C for one hundred days. 213
Figure 6.63 – Plot of the reciprocal of sedimentation coefficient against loading concentration for S-IB after incubation at 20˚C for one hundred days, with a linear fit to extrapolate to zero concentration. 213
Figure 6.64 – Plot of the reciprocal of apparent molecular weight ($M_{w,app}$) values against loading concentration of S-IB after incubation at 20˚C for one hundred days, with a linear fit to extrapolate to zero concentration. Hinge point analysis at the lowest concentration was an outlier and discounted, although the M* analysis is still included. 214
Figure 6.65 – Plot of viscosity against concentration for S-II after incubation at 20˚C for ten days, with linear fits to extrapolate to zero concentration. 215
Figure 6.66 – Distribution of sedimentation coefficients at a range of loading concentrations of S-II after incubation at 20˚C for ten days. 216
Figure 6.67 – Plot of the reciprocal of sedimentation coefficient against loading concentration for S-II after incubation at 20˚C for ten days, with a linear fit to extrapolate to zero concentration. 216
Figure 6.68 – Plot of the reciprocal of apparent molecular weight ($M_{w,app}$) values against loading concentration of S-II after incubation at 20˚C for ten days, with a linear fit to extrapolate to zero concentration. Two of the lower concentration did not give outlying data in hinge point analysis and were excluded, although the M* data was still acceptable. 217

Figure 6.69 – Plot of viscosity against concentration for S-II after incubation at 20˚C for one hundred days, with linear fits to extrapolate to zero concentration. 218
Figure 6.70 – Distribution of sedimentation coefficients at a range of loading concentrations of S-II after incubation at 20˚C for one hundred days. 219
Figure 6.71 – Plot of the reciprocal of sedimentation coefficient against loading concentration for S-II after incubation at 20˚C for one hundred days, with a linear fit to extrapolate to zero concentration. 219
Figure 6.72 – Plot of the reciprocal of apparent molecular weight ($M_{w,app}$) values against loading concentration of S-II after incubation at 20˚C for one hundred days, with a linear fit to extrapolate to zero concentration. 220
Figure 6.73 – Viscosity of each polysaccharide as determined by U-tube viscometry, and how they altered after incubation at 20˚C. 223
Figure 6.74 – Sedimentation coefficient of each polysaccharide as determined by sedimentation velocity, and how they altered after incubation at 20˚C. 223
Figure 6.75 – Molecular weight of each polysaccharide as determined by sedimentation equilibrium, and how they altered after incubation at 20˚C. 224
Figure 6.76 – Molecular weight of each polysaccharide as determined by SEC-MALS, and how they altered after incubation at 20˚C. 224
Figure 6.77 – Viscosity of each polysaccharide as determined by SEC-MALS, and how they altered after incubation at 20˚C. 225
Figure 7.1 – Plot of viscosity against concentration for N-IA after incubation at 37˚C, with linear fits to extrapolate to zero concentration. 230
Figure 7.2 – Plot of viscosity against concentration for N-IB after incubation at 37˚C, with linear fits to extrapolate to zero concentration. 231
Figure 7.3 – Plot of viscosity against concentration for N-II after incubation at 37˚C, with linear fits to extrapolate to zero concentration. 232

Figure 7.4 – Plot of viscosity against concentration for N-III after incubation at 37˚C, with linear fits to extrapolate to zero concentration. 233
Figure 7.5 – Plot of viscosity against concentration for N-IV after incubation at 37˚C, with linear fits to extrapolate to zero concentration. 234
Figure 7.6 – Plot of viscosity against concentration for N-V after incubation at 37˚C, with linear fits to extrapolate to zero concentration. 235
Figure 7.7 – Plot of viscosity against concentration for S-IA after incubation at 37˚C, with linear fits to extrapolate to zero concentration. 236
Figure 7.8 – Plot of viscosity against concentration for S-IB after incubation at 37˚C, with linear fits to extrapolate to zero concentration. 237
Figure 7.9 – Plot of viscosity against concentration for S-II after incubation at 37˚C, with linear fits to extrapolate to zero concentration. 238
Figure 8.1 - Plot of density against concentration for BSA, with a linear fit to obtain gradient. 244
Figure 8.2 – Plot of density against concentration for HSA, with a linear fit to obtain gradient. 245
Figure 8.3 – Plot of viscosity against concentration for fibrinogen, with linear fits to extrapolate to zero concentration. As fibrinogen is slightly more viscous than the other proteins studied it is possible to perform an extrapolation, although it was still not possible at very low concentrations (i.e. less than 0.002 $g.mL^{-1}$) and so these have not been included in the extrapolation. 246
Figure 8.4 – Distribution of sedimentation coefficients of N-IA and BSA, both alone and in combination, at 0.5 $mg.mL^{-1}$ (upper) and 1 $mg.mL^{-1}$ (lower). 252
Figure 8.5 – Distribution of sedimentation coefficients of N-IA and HSA, both alone and in combination, at 0.5 $mg.mL^{-1}$ (upper) and 1 $mg.mL^{-1}$ (lower). 253

Figure 8.6 – Distribution of sedimentation coefficients of N-IA and fibrinogen, both alone and in combination, at 0.305 mg.mL^{-1} (upper) and 0.610 mg.mL^{-1} (lower). 254
Figure 8.7 – Distribution of sedimentation coefficients of N-IA and IgG1 Cri, both alone and in combination, at 0.5 mg.mL^{-1} (upper) and 1 mg.mL^{-1} (lower). 255
Figure 8.8 – Distribution of sedimentation coefficients of N-IA and IgG1 Wid, both alone and in combination, at 0.5 mg.mL^{-1} (upper) and 1 mg.mL^{-1} (lower). 256
Figure 8.9 – Distribution of sedimentation coefficients of N-IB and BSA, both alone and in combination, at 0.5 mg.mL^{-1} (upper) and 1 mg.mL^{-1} (lower). 258
Figure 8.10 – Distribution of sedimentation coefficients of N-IB and HSA, both alone and in combination, at 0.5 mg.mL^{-1} (upper) and 1 mg.mL^{-1} (lower). 259
Figure 8.11 – Distribution of sedimentation coefficients of N-IB and fibrinogen, both alone and in combination, at 0.382 mg.mL^{-1} (upper) and 0.764 mg.mL^{-1} (lower). 260
Figure 8.12 – Distribution of sedimentation coefficients of N-IB and IgG1 Cri, both alone and in combination, at 0.5 mg.mL^{-1} (upper) and 1 mg.mL^{-1} (lower). 261
Figure 8.13 – Distribution of sedimentation coefficients of N-IB and IgG1 Wid, both alone and in combination, at 0.5 mg.mL^{-1} (upper) and 1 mg.mL^{-1} (lower). 262
Figure 8.14 – Distribution of sedimentation coefficients of N-II and BSA, both alone and in combination, at 0.5 mg.mL^{-1} (upper) and 1 mg.mL^{-1} (lower). 264
Figure 8.15 – Distribution of sedimentation coefficients of N-II and HSA, both alone and in combination, at 0.5 mg.mL^{-1} (upper) and 1 mg.mL^{-1} (lower). 265
Figure 8.16 – Distribution of sedimentation coefficients of N-II and fibrinogen, both alone and in combination, at 0.392 mg.mL^{-1} (upper) and 0.784 mg.mL^{-1} (lower). 266
Figure 8.17 – Distribution of sedimentation coefficients of N-II and IgG1 Cri, both alone and in combination, at 0.5 mg.mL^{-1} (upper) and 1 mg.mL^{-1} (lower). 267
Figure 8.18 – Distribution of sedimentation coefficients of N-II and IgG1 Wid, both alone and in combination, at 0.5 mg.mL^{-1} (upper) and 1 mg.mL^{-1} (lower). 268

Figure 8.19 – Distribution of sedimentation coefficients of N-III at 0.290 mg.mL^{-1} (upper) and 0.579 mg.mL^{-1} (lower), alone and in combination with BSA at 0.468 mg.mL^{-1} (upper) and 0.937 mg.mL^{-1} (lower). 270

Figure 8.20 – Distribution of sedimentation coefficients of N-III at 0.290 mg.mL^{-1} (upper) and 0.579 mg.mL^{-1} (lower), alone and in combination with HSA at 0.472 mg.mL^{-1} (upper) and 0.994 mg.mL^{-1} (lower). 271

Figure 8.21 – Distribution of sedimentation coefficients of N-III at 0.237 mg.mL^{-1} (upper) and 0.474 mg.mL^{-1} (lower), alone and in combination with fibrinogen at 0.386 mg.mL^{-1} (upper) and 0.772 mg.mL^{-1} (lower). 272

Figure 8.22 – Distribution of sedimentation coefficients of N-III and IgG1 Cri, both alone and in combination, at 0.5 mg.mL^{-1} (upper) and 1 mg.mL^{-1} (lower). 273

Figure 8.23 – Distribution of sedimentation coefficients of N-III and IgG1 Wid, both alone and in combination, at 0.5 mg.mL^{-1} (upper) and 1 mg.mL^{-1} (lower). 274

Figure 8.24 – Distribution of sedimentation coefficients of N-IV and BSA, both alone and in combination, at 0.5 mg.mL^{-1} (upper) and 1 mg.mL^{-1} (lower). 276

Figure 8.25 – Distribution of sedimentation coefficients of N-IV and HSA, both alone and in combination, at 0.5 mg.mL^{-1} (upper) and 1 mg.mL^{-1} (lower). 277

Figure 8.26 – Distribution of sedimentation coefficients of N-IV and fibrinogen, both alone and in combination, at 0.5 mg.mL^{-1} (upper) and 1 mg.mL^{-1} (lower). 278

Figure 8.27 – Distribution of sedimentation coefficients of N-IV and IgG1 Cri, both alone and in combination, at 0.5 mg.mL^{-1} (upper) and 1 mg.mL^{-1} (lower). 279

Figure 8.28 – Distribution of sedimentation coefficients of N-IV and IgG1 Wid, both alone and in combination, at 0.5 mg.mL^{-1} (upper) and 1 mg.mL^{-1} (lower). 280

Figure 8.29 – Distribution of sedimentation coefficients of N-V and BSA, both alone and in combination, at 0.5 mg.mL^{-1} (upper) and 1 mg.mL^{-1} (lower). 282

Figure 8.30 – Distribution of sedimentation coefficients of N-V and HSA, both alone and in combination, at 0.5 mg.mL^{-1} (upper) and 1 mg.mL^{-1} (lower). 283
Figure 8.31 – Distribution of sedimentation coefficients of N-V and fibrinogen, both alone and in combination, at 0.5 mg.mL^{-1} (upper) and 1 mg.mL^{-1} (lower). 284
Figure 8.32 – Distribution of sedimentation coefficients of N-V and IgG1 Cri, both alone and in combination, at 0.5 mg.mL^{-1} (upper) and 1 mg.mL^{-1} (lower). 285
Figure 8.33 – Distribution of sedimentation coefficients of N-V and IgG1 Wid, both alone and in combination, at 0.5 mg.mL^{-1} (upper) and 1 mg.mL^{-1} (lower). 286
Figure 8.34 – Distribution of sedimentation coefficients of S-IA and BSA, both alone and in combination, at 0.5 mg.mL^{-1} (upper) and 1 mg.mL^{-1} (lower). 288
Figure 8.35 – Distribution of sedimentation coefficients of S-IA and HSA, both alone and in combination, at 0.5 mg.mL^{-1} (upper) and 1 mg.mL^{-1} (lower). 289
Figure 8.36 – Distribution of sedimentation coefficients of S-IA and fibrinogen, both alone and in combination, at 0.5 mg.mL^{-1} (upper) and 1 mg.mL^{-1} (lower). 290
Figure 8.37 – Distribution of sedimentation coefficients of S-IA and IgG1 Cri, both alone and in combination, at 0.5 mg.mL^{-1} (upper) and 1 mg.mL^{-1} (lower). 291
Figure 8.38 – Distribution of sedimentation coefficients of S-IA and IgG1 Wid, both alone and in combination, at 0.5 mg.mL^{-1} (upper) and 1 mg.mL^{-1} (lower). 292
Figure 8.39 – Distribution of sedimentation coefficients of S-IB and BSA, both alone and in combination, at 0.5 mg.mL^{-1} (upper) and 1 mg.mL^{-1} (lower). 294
Figure 8.40 – Distribution of sedimentation coefficients of S-IB and HSA, both alone and in combination, at 0.5 mg.mL^{-1} (upper) and 1 mg.mL^{-1} (lower). 295
Figure 8.41 – Distribution of sedimentation coefficients of S-IB and fibrinogen, both alone and in combination, at 0.5 mg.mL^{-1} (upper) and 1 mg.mL^{-1} (lower). 296
Figure 8.42 – Distribution of sedimentation coefficients of S-IB and IgG1 Cri, both alone and in combination, at 0.5 mg.mL^{-1} (upper) and 1 mg.mL^{-1} (lower). 297

Figure 8.43 – Distribution of sedimentation coefficients of S-IB and IgG1 Wid, both alone and in combination, at 0.5 mg.mL^{-1} (upper) and 1 mg.mL^{-1} (lower). 298
Figure 8.44 – Distribution of sedimentation coefficients of S-II and BSA, both alone and in combination, at 0.5 mg.mL^{-1} (upper) and 1 mg.mL^{-1} (lower). 300
Figure 8.45 – Distribution of sedimentation coefficients of S-II and HSA, both alone and in combination, at 0.5 mg.mL^{-1} (upper) and 1 mg.mL^{-1} (lower). 301
Figure 8.46 – Distribution of sedimentation coefficients of S-II and fibrinogen, both alone and in combination, at 0.5 mg.mL^{-1} (upper) and 1 mg.mL^{-1} (lower). 302
Figure 8.47 – Distribution of sedimentation coefficients of S-II and IgG1 Cri, both alone and in combination, at 0.5 mg.mL^{-1} (upper) and 1 mg.mL^{-1} (lower). 303
Figure 8.48 – Distribution of sedimentation coefficients of S-II and IgG1 Wid, both alone and in combination, at 0.5 mg.mL^{-1} (upper) and 1 mg.mL^{-1} (lower). 304

List of Tables

Table 3-1 - Information relating to the samples provided upon their delivery. 40

Table 3-2 - Dilutions used in this experiment and the conversion factor to give the concentration of that dilution from the stock concentration. 43

Table 4-1 – Summary of baseline values for each sample. 96

Table 5-1 – Summary of data found after exposure of samples to ten freeze-thaw cycles. . 157

Table 5-2 – Summary of data found after exposure of samples to 100 freeze-thaw cycles.. 157

Table 5-3 – Table showing the percentage difference in parameters from baseline values due to exposure of samples to ten freeze-thaw cycles. 158

Table 5-4 – Table showing the percentage difference in parameters from baseline values due to exposure of samples to 100 freeze-thaw cycles. 158

Table 5-5 – The resulting p values when performing a student's T test on the sedimentation coefficient datasets after exposure to freeze-thaw stress. A p value < 0.05 is assumed to reflect a significant difference, and these are highlighted. 161

Table 6-1 – Summary of data found after incubation of samples at 20˚C for ten days. 221

Table 6-2 – Summary of data found after incubation of samples at 20˚C for 100 days. 221

Table 6-3 – Table showing the percentage difference in parameters from baseline values due to incubation of samples at 20˚C for ten days 222

Table 6-4 – Table showing the percentage difference in parameters from baseline values due to incubation of samples at 20˚C for 100 days. 222

Table 6-5 – The resulting p values when performing a student's T test on the sedimentation coefficient datasets after exposure to stress caused by continued incubation at 20˚C. A p value < 0.05 is assumed to reflect a significant difference, and these are highlighted. 225

Table 7-1 – Table showing which parameters changed from baseline values when samples are assessed at 37˚C. For samples which saw a statistically significant change the percentage change is given, while those which were not significantly different are marked with ✓. 239

Table 8-1 – Summary of extinction coefficients used to calculate the intrinsic viscosity and partial specific volume of each protein studied.. 243

Table 8-2 – Summary of the viscosities and partial specific volume values used in this study. 247

Table 8-3 – A summary of theoretical values for η_r and the actual values calculated using flow times for N-IA in combination with one of the proteins. 251

Table 8-4 – Summary of peak sedimentation coefficient values for N-IA and BSA. 252

Table 8-5 – Summary of peak sedimentation coefficient values for N-IA and HSA. 253

Table 8-6 – Summary of peak sedimentation coefficient values for N-IA and fibrinogen. 254

Table 8-7 – Summary of peak sedimentation coefficient values for N-IA and IgG1 Cri. 255

Table 8-8 – Summary of peak sedimentation coefficient values for N-IA and IgG1 Wid. 256

Table 8-9 – A summary of theoretical values for η_r and the actual values calculated using flow times for N-IB in combination with one of the proteins. 257

Table 8-10 – Summary of peak sedimentation coefficient values for N-IB and BSA..... 258

Table 8-11 – Summary of peak sedimentation coefficient values for N-IB and HSA. 259

Table 8-12 – Summary of peak sedimentation coefficient values for N-IB and fibrinogen. .. 260

Table 8-13 – Summary of peak sedimentation coefficient values for N-IB and IgG1 Cri. 261

Table 8-14 – Summary of peak sedimentation coefficient values for N-IB and IgG1 Wid. 262

Table 8-15 – A summary of theoretical values for η_r and the actual values calculated using flow times for N-II in combination with one of the proteins. 263

Table 8-16 – Summary of peak sedimentation coefficient values for N-II and BSA..... 264

Table 8-17 – Summary of peak sedimentation coefficient values for N-II and HSA. 265

Table 8-18 – Summary of peak sedimentation coefficient values for N-II and fibrinogen. ... 266

Table 8-19 – Summary of peak sedimentation coefficient values for N-II and IgG1 Cri. 267

Table 8-20 – Summary of peak sedimentation coefficient values for N-II and IgG1 Wid. 268

Table 8-21 – A summary of theoretical values for η_r and the actual values calculated using flow times for N-III in combination with one of the proteins. 269

Table 8-22 – Summary of peak sedimentation coefficient values for N-III and BSA. 270

Table 8-23 – Summary of peak sedimentation coefficient values for N-III and HSA. 271

Table 8-24 – Summary of peak sedimentation coefficient values for N-III and fibrinogen. .. 272

Table 8-25 – Summary of peak sedimentation coefficient values for N-III and IgG1 Cri. 273

Table 8-26 – Summary of peak sedimentation coefficient values for N-III and IgG1 Wid. 274

Table 8-27 – A summary of theoretical values for η_r and the actual values calculated using flow times for N-IV in combination with one of the proteins. 275

Table 8-28 – Summary of peak sedimentation coefficient values for N-IV and BSA. 276

Table 8-29 – Summary of peak sedimentation coefficient values for N-IV and HSA. 277

Table 8-30 – Summary of peak sedimentation coefficient values for N-IV and fibrinogen. .. 278

Table 8-31 – Summary of peak sedimentation coefficient values for N-IV and IgG1 Cri. 279

Table 8-32 – Summary of peak sedimentation coefficient values for N-IV and IgG1 Wid. 280

Table 8-33 – A summary of theoretical values for η_r and the actual values calculated using flow times for N-V in combination with one of the proteins. 281

Table 8-34 – Summary of peak sedimentation coefficient values for N-V and BSA. 282

Table 8-35 – Summary of peak sedimentation coefficient values for N-V and HSA. 283

Table 8-36 – Summary of peak sedimentation coefficient values for N-V and fibrinogen. ... 284

Table 8-37 – Summary of peak sedimentation coefficient values for N-V and IgG1 Cri. 285

Table 8-38 – Summary of peak sedimentation coefficient values for N-V and IgG1 Wid. 286

Table 8-39 – A summary of theoretical values for η_r and the actual values calculated using flow times for S-IA in combination with one of the proteins. 287

Table 8-40 – Summary of peak sedimentation coefficient values for S-IA and BSA. 288

Table 8-41 – Summary of peak sedimentation coefficient values for S-IA and HSA. 289

Table 8-42 – Summary of peak sedimentation coefficient values for S-IA and fibrinogen. ... 290

Table 8-43 – Summary of peak sedimentation coefficient values for S-IA and IgG1 Cri..... 291

Table 8-44 – Summary of peak sedimentation coefficient values for S-IA and IgG1 Wid..... 292

Table 8-45 – A summary of theoretical values for η_r and the actual values calculated using flow times for S-IB in combination with one of the proteins. 293

Table 8-46 – Summary of peak sedimentation coefficient values for S-IB and BSA. 294

Table 8-47 – Summary of peak sedimentation coefficient values for S-IB and HSA. 295

Table 8-48 – Summary of peak sedimentation coefficient values for S-IB and fibrinogen. ... 296

Table 8-49 – Summary of peak sedimentation coefficient values for S-IB and IgG1 Cri. 297

Table 8-50 – Summary of peak sedimentation coefficient values for S-IB and IgG1 Wid..... 298

Table 8-51 – A summary of theoretical values for η_r and the actual values calculated using flow times for S-II in combination with one of the proteins. 299

Table 8-52 – Summary of peak sedimentation coefficient values for S-II and BSA. 300

Table 8-53 – Summary of peak sedimentation coefficient values for S-II and HSA. 301

Table 8-54 – Summary of peak sedimentation coefficient values for S-II and fibrinogen. 302

Table 8-55 – Summary of peak sedimentation coefficient values for S-II and IgG1 Cri. 303

Table 8-56 – Summary of peak sedimentation coefficient values for S-II and IgG1 Wid. 304

Table 8-57 - Summary of data found when testing the change in viscosity after combining each polysaccharide with a blood protein. Percentage change is also given. 305

Publications

Work performed as part of this project led to the publication of a peer reviewed paper:

- MacCalman, T.E., Phillips-Jones, M.K. and Harding, S.E., 2019. *Glycoconjugate vaccines: some observations on carrier and production methods.* Biotechnology and Genetic Engineering Reviews, **35**(2), pp.93-125.

Other papers have been co-authored while this project was taking place:

- Dinu, V., Gillis, R.B., MacCalman, T., Lim, M., Adams, G.G., Harding, S.E. and Fisk, I.D., 2019. *Submaxillary mucin: its effect on aroma release from acidic drinks and new insight into the effect of aroma compounds on its macromolecular integrity*. Food biophysics, **14**(3), pp.278-286.
- Chun, T., MacCalman, T., Dinu, V., Ottino, S., Phillips-Jones, M.K. and Harding, S.E., 2020. Hydrodynamic Compatibility of Hyaluronic Acid and Tamarind Seed Polysaccharide as Ocular Mucin Supplements. Polymers, **12**(10), p.2272.
- Dinu, V., MacCalman, T., Yang, N., Adams, G.G., Yakubov, G.E., Harding, S.E. and Fisk, I.D., 2020. *Probing the effect of aroma compounds on the hydrodynamic properties of mucin glycoproteins*. European Biophysics Journal, **49**(8), pp.799-808.

A paper is also being produced from section 8 of this work studying the potential interaction of blood proteins with the vaccine candidates. A further paper is being produced studying the potential interaction of human serum albumin with immunoglobulin.

1 Introduction

1.1 Group B Streptococcus

Streptococcus agalactiae is a bacterium that causes Group B *Streptococcal* (GBS) infections. It was first categorised by Lancefield based on its reaction to serum of animals immunised with formalinized cultures [1]. Lancefield also later found that the bacterium was able to colonise the human vagina [2]. The bacterium originated in cows, where it causes bovine mastitis [3], but was then shown to infect neonates [4]. It has been suggested that this transmission from bovine hosts to humans was linked to a change in the manner in which milk was collected [5]. In the 1960s there was a sudden increase in the number of cases, which shows a temporal (but not necessarily causal) link to the beginning of bulk tank collection and large-scale organised processing of milk, rather than small batches being distributed by farms [5]. It has been suggested that, rather than this causing exposure to a novel pathogen, the improved cleanliness and reduced exposure to GBS also reduced herd immunity [6].

There are ten known serotypes of *S. agalactiae* (IA, IB, and II to IX), with serotype based on the structure of their capsular polysaccharides through a serological interaction [7, 8]. It is possible to categorise these polysaccharides into classes defined by their chemical similarities, most notably the backbone of the repeating unit [9]. Class 1 GBS have alternating β (1→4) linked galactose and glucose residues forming the main backbone of the repeating unit, with a β (1→3) linked side chain on the galactose. Class 2 GBS have trisaccharide backbone of glucose galactose and glucose in the repeating unit with a β (1→6) linked side chain. Class 3 GBS have larger backbones with no structural similarity to other serotypes. Shown in Figure 1.1, 1.2, 1.3, 1.4, 1.5 and 1.6 are the structures of serotypes IA and IB (Class 1), II (Class 3), III (Class 1), IV and V (Class 2), redrawn from previously presented structures [9]. While there are other serotypes, this PhD is chiefly concerned with these six serotypes, and so the structures of other capsular polysaccharides are not presented. It is believed that

these six serotypes are the most common disease-causing serotypes, particularly in Europe and North America, and so are the current focus for the development of a vaccine by GSK [10, 11]. Individual repeating units are synthesised and exported from the bacterial cell, where they are then polymerised into a structure covalently linked to the to the peptidoglycan cell wall. While each repeating unit is identical for a given serotype, the number of repeats, and therefore polymer length, is variable [12]. These chains are also flexible, although tend to adopt an extended conformation [13].

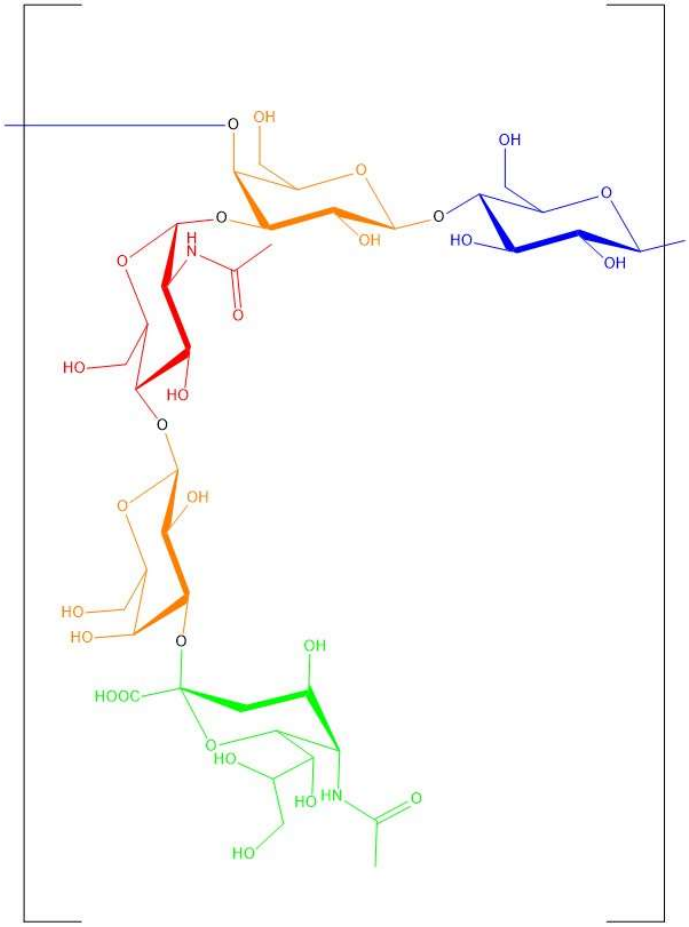


Figure 1.1 - Repeating structure of GBS serotype IA. This is a class 1 capsular polysaccharide due to alternating β (1→4) linked galactose and glucose residues forming the main backbone of the repeating unit, with a β (1→3) linked side chain on the galactose. Glucose residues are shown in blue, galactose residues are shown in orange, N-Acetylglucosamine residues are shown in red, and N-Acetylneuraminic acid residues are shown in green. Redrawn from [9].

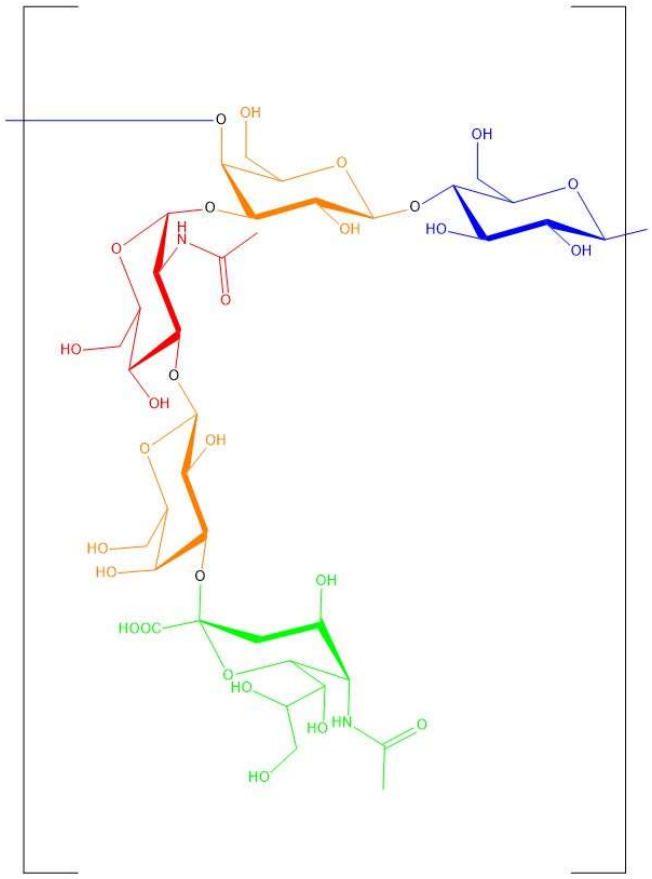


Figure 1.2 - Repeating structure of GBS serotype IB. This is a class 1 capsular polysaccharide due to alternating β (1→4) linked galactose and glucose residues forming the main backbone of the repeating unit, with a β (1→3) linked side chain on the galactose. Glucose residues are shown in blue, galactose residues are shown in orange, N-Acetylglucosamine residues are shown in red, and N-Acetylneuraminic acid residues are shown in green. Redrawn from [9].

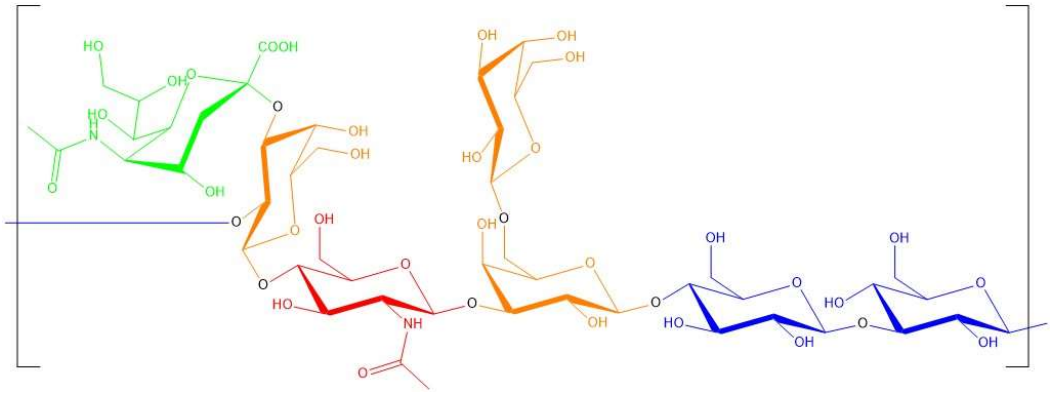


Figure 1.3 - Repeating structure of GBS serotype II. This is a class 3 capsular polysaccharide due to the large backbone with no structural similarity to other serotypes. Glucose residues are shown in blue, galactose residues are shown in orange, N-Acetylglucosamine residues are shown in red, and N-Acetylneuraminic acid residues are shown in green. Redrawn from [9].

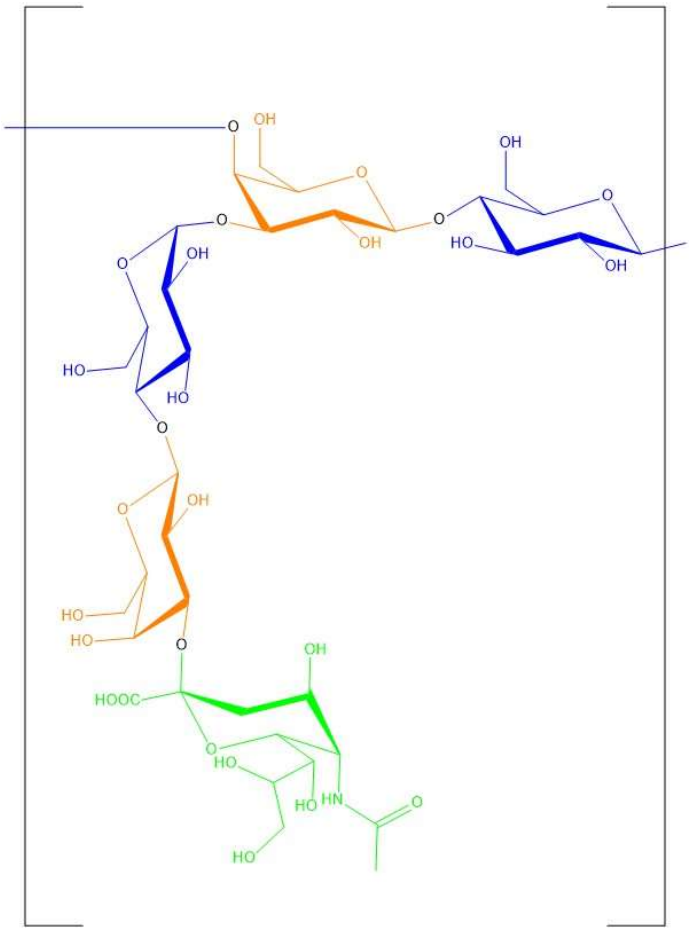


Figure 1.4 - Repeating structure of GBS serotype III. This is a class 1 capsular polysaccharide due to alternating β (1→4) linked galactose and glucose residues forming the main backbone of the repeating unit, with a β (1→3) linked side chain on the galactose. Glucose residues are shown in blue, galactose residues are shown in orange, and N-Acetylneuraminic acid residues are shown in green. Redrawn from [9].

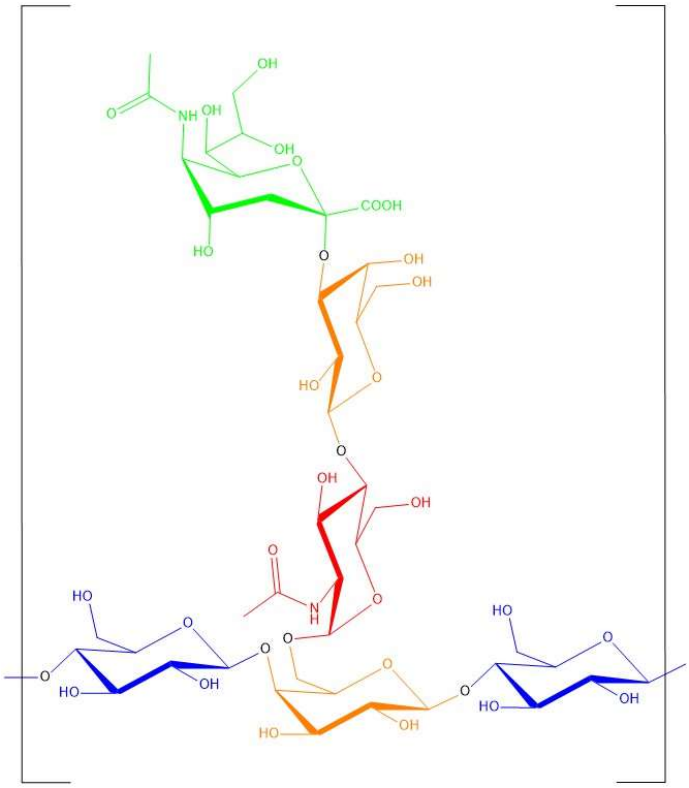


Figure 1.5 - Repeating structure of GBS serotype IV. This is a class 2 capsular polysaccharide due to the trisaccharide backbone of glucose galactose and glucose in the repeating unit with a β (1→6) linked side chain. Glucose residues are shown in blue, galactose residues are shown in orange, N-Acetylglucosamine residues are shown in red, and N-Acetylneuraminic acid residues are shown in green. Redrawn from [9].

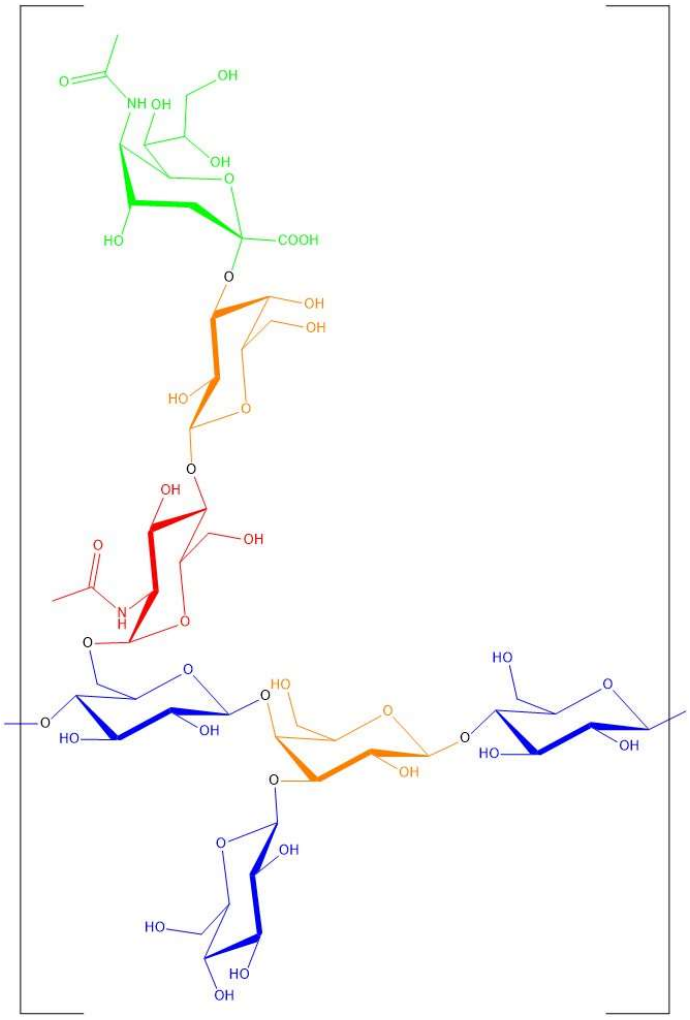


Figure 1.6 - Repeating structure of GBS serotype V. This is a class 2 capsular polysaccharide due to the trisaccharide backbone of glucose galactose and glucose in the repeating unit with a β (1→6) linked side chain. Glucose residues are shown in blue, galactose residues are shown in orange, N-Acetylglucosamine residues are shown in red, and N-Acetylneuraminic acid residues are shown in green. Redrawn from [9].

The bacterium can be carried in the gastrointestinal and genitourinary tracts of around twenty to forty percent of healthy adults, irrespective of gender [14-16]. While these carriers are usually asymptomatic, there is a risk of bacterial infection in people with underlying health issues, such as those with diabetes, the elderly, or the immunocompromised [17]. Elderly people see an increase in disease but without an increase in asymptomatic colonisation, possibly due to increased carriage of GBS serotype V, which can be more invasive [18]. This increase in disease without an increase in colonisation is similar to that in those infected with HIV [17, 19].

Outside these immunocompromised individuals, GBS is most problematic around birth. As these bacteria are present in the genitourinary tracts of pregnant women [20], it can easily be passed on to the foetus or neonate either before or during birth [21].

GBS infection in neonates can be divided into two groups depending on when the infection begins: either early (<1 week) or late (1 week to 3 months) onset. Early onset GBS is acquired vertically from mother, and is more common [22]. Late onset is less common [22] and is acquired from other environmental sources such as nurses' hands [23] and breast milk [24, 25] rather than the birth itself. Neonates may be colonised without infection, but as very young children are more likely to become infected [26] this could develop into invasive infection later. As time progresses, severity of late onset disease decreases [27].

It is also possible for the mother to develop perinatal disease (i.e. during pregnancy) [28], where it may cause inflammation of foetal membranes, (chorioamnionitis) [29]. In one study [30], 61% of cases where the mother had a serious perinatal infection led to the death of the infant, although the study did not elaborate on whether the foetus also contracted GBS, or if the maternal infection caused complications which led to the death of the infant. The study also found that the rate of transmission to live births from the seriously infected mothers was 5%, although as only 35% of births were live in this group, this represents a more

significant portion of those births. It has also been found that immunocompromised mothers are more likely to pass GBS on to a neonate [31], but this may be because of the lack of maternal antibodies making them more susceptible to the disease [32]. Associations have also been found between transmission and high degrees of colonisation or long labours [33]. While there is a link between premature birth and GBS infection, it is unclear if this is because the premature babies are more susceptible to GBS [22]. It is also possible that GBS infection causes the prematurity [34], which could be easily prevented with a suitable antibiotic treatment [35].

GBS can cause meningitis and sepsis in neonates. Sepsis occurs when the body 'overreacts' to an infection, to such an extent that the immune response becomes damaging across the entire body [36]. The increased immune response leads to increased tissue permeability, and in excess causes the loss of barrier functions, with multiple effects depending on the specific organ [37]. In the lungs it can trigger pulmonary oedema [38], which when coupled with a disruption of heart function [39] and the presence of microthrombi [40] can quickly lead to hypoxia across multiple organs. The gut epithelium is also made overly permeable [41], which can lead to injury and autodigestion [42]. The breakdown of the blood-brain barrier can lead to delirium and even coma [43, 44]. Acute kidney injury is also caused [45], although this is thought to be due to cytokine and immune-mediated tubular dysfunction rather than renal perfusion [46]. In the liver, red blood cells are normally broken down to produce bilirubin, a precursor of bile. However, during sepsis, this process is interrupted leading to cholestasis [47], a lack of bile flow, which coupled with the loss of other liver functions further stimulates systemic inflammation [48] creating a feedback loop to increase the severity of sepsis. Finally, sepsis causes a highly weakened immune system due to the almost total depletion of T cells [49], which can lead to the presence of other secondary infections [50].

Meningitis is an inflammation of the meninges, the membranes surrounding the brain [51] and is diagnosed by the growth cultures from cerebrospinal fluid. GBS is able to pass into the central nervous system due to the presence of adhesive pilus proteins [52], which allow transition across the blood-brain barrier, most likely at highly vascularized sites [53]. As with sepsis, the body's inflammatory response is thought to exacerbate some of the damage to the blood-brain barrier, particularly the release of matrix metalloproteases [54] and nitric oxide [55] by leukocytes. A combination of the inflammation and the release of bacterial toxins leads to the destruction of neurons, notably atrophy of the hippocampus [56]. The infection can prove fatal, but if the patient survives there is also the possibility of long-term neurological health implications such as blindness, deafness, problems with coordination and epilepsy. If a child patient recovers, mild sequelae such as dizziness, tiredness, mild memory deficits and gait ataxia are seen in a majority of cases [57]. They remain at a higher risk of death even after recovery, but this varies depending on the specific pathogen [58]. The degree of neurological impairment may be lower in surviving adults than children, but again this depends on the specific organism that infects the host [59].

It is estimated that in 2015, 21,734,000 live births were exposed to GBS from colonised mothers worldwide [60]. Of these, 33,000 cases of maternal GBS disease occurred [60]. It has been estimated that, given the rates of preterm births among mothers with any form of GBS carriage, up to 3,500,000 preterm births may have occurred due to maternal GBS colonisation [60]. In addition, that there were 57,000 still births from GBS disease. There were estimated to be 319,000 cases of neonatal and infant GBS, of which neonatal encephalopathy occurred in 7,000 cases, and 10,000 cases in which neurodevelopmental impairment occurred [60].

It is possible to treat GBS infection with antibiotics, usually penicillin given intravenously [61]. Penicillin is a safe antibiotic with few side effects unless the patient is allergic. As prevention

is preferable to a cure, antibiotics are also used to treat mothers who are at risk of passing on infection by intrapartum antibiotic prophylaxis [62]. By giving the mother intravenous treatment immediately before or even during labour, the bacteria is not present and so cannot be passed on [62]. It is also possible that the passage of the antibiotic to the neonate prevents their colonisation [62]. This prevents early- but not late-onset disease, and if a neonate is suspected to have GBS disease, they are treated immediately before tests for infection are completed to ensure the best possible prognosis [61].

Despite its effectiveness, the routine use of antibiotics is undesirable, particularly as issues of antimicrobial resistance become more pressing. In addition, while penicillin and ampicillin are still effective treatments and generally the first choice, they cannot be used for patients with allergies to penicillin. Erythromycin and clindamycin are the drugs of choice for patients with a penicillin allergy, but are no longer effective in all serotypes [63]. This means vancomycin must be used in cases where the patient is allergic to penicillin but GBS is resistant to other common antibiotics [64].

Extensive use of antibiotics places a strong evolutionary selective pressure for the development of antimicrobial resistance in GBS, as the bacteria most able to resist the antibiotics can survive and repopulate. If GBS did develop resistance, then an alternative antibiotic would have to be used that may incur more side effects, which could be even more problematic during the late stages of pregnancy and birth. Even if GBS itself does not develop a resistance to further antibiotics, their extensive use and the exposure of other bacteria in the environment to this antibiotic may lead to other bacteria developing resistance.

To avoid issues with antimicrobial resistance and potential side effects, it would be preferable to prevent GBS infection without using antibiotics. The best method to do this would be a vaccine. Ideally, such a vaccine would be administered to pregnant women, meaning they would no longer carry the bacteria, preventing early-onset GBS, and would also

pass antibodies to the foetus via the placenta and breast milk to prevent late-onset disease. However, there has been little impetus to develop a vaccine, in part due to the success of intrapartum antibiotic prophylaxis. It is possible to generate a vaccine, although it must target the polysaccharide capsule as it is the only available antigen on the bacterial surface. Unfortunately, such vaccines are generally insufficiently effective, unless the polysaccharide is linked to a protein carrier to improve immunogenicity, making a glycoconjugate vaccine. There are a number of vaccines currently being researched, which have already been reviewed elsewhere [65]. However, the majority of these seem to be against single serotypes [66-72]. Even those which combat multiple serotypes are mixtures of multiple monovalent vaccines [73, 74], or against relatively few serotypes [75-78]. Very few studies are performed on a single vaccine against more than three serotypes [79].

1.2 Glycoconjugate vaccines

To understand the advantages of glycoconjugate vaccines, it is imperative to understand how the immune system works, particularly concerning its interactions with protein and polysaccharide antigens. This introduction will briefly cover some general information on the immune system.

1.2.1 Pathogens and the immune system

1.2.1.1 Barrier functions

Pathogens are defined as disease-causing microorganisms [80], and the immune system protects the body from these pathogens. Human skin is hydrophobic and blocks access to the majority of pathogens, but there are regions where the skin does not provide protection, such as the stomach and eyes. In these places, chemical barriers such as stomach acid, mucus and tears provide further protection. In general, such defences occur at epithelia, more permeable regions where pathogenic entry is more likely [80]. These contain many

antimicrobial proteins, such as defensins, cathelicidins, C-type lectins, ribonucleases, S100 proteins and psoriasin [81].

However, such chemical and physical barriers are not perfect, and some pathogens are able to bypass these defences. In these cases, biological barriers provide protection. These biological defences form the immune system and are split into two categories: innate and adaptive.

1.2.1.2 Innate immunity

Innate immunity is always active and can respond immediately to threats [80]. This consists of similar molecules to the antimicrobial proteins listed above, but also enzymes such as lysozyme to digest pathogens [80]. If these fail, innate immunity also offers the complement system. Some cells have pattern recognition receptors that can interact with pathogen-associated molecular patterns, common markers of pathogens [82]. This leads to the induction of signalling pathways to trigger a number of processes. Key among these are opsonisation, where pathogens are coated to enable phagocytosis [83]; inflammation and the recruitment of further immune system cells, typically through release of cytokines [84]; and the formation of membrane attack complexes to rupture the pathogen membranes [85].

However, this innate system is not effective against all pathogens. While selective pressures have driven the evolution of the immune system, the ability to fight back also exerts a selective pressure on the pathogen community, favouring their evolution into forms that can evade or counteract the immune system. For example, the bacterial polysaccharide capsule covers the pathogen-associated molecular patterns that interact with the innate immune system, and other pathogens are able to inhibit complement activation [86]. It is most likely for this reason that the adaptive immune system has also evolved.

1.2.1.3 Adaptive immunity

The adaptive or cell-mediated immune system can be broadly considered to consist of two groups of cells: B cells and T cells. B cells mature in the bone marrow, although their name comes from the bursa, the organ in birds in which they were originally discovered [80]. These cells have receptors on their surface that can bind to complementary regions on a pathogen, and cause it to produce antibodies. As the binding causes **anti**body **gen**eration, molecules which trigger this are known as antigens, and the specific regions of the antigen that bind to a receptor are known as epitopes [80]. When activated by their antigen, B cells can differentiate into plasma cells and memory cells [80]. The plasma cells release antibodies while the memory cells persist in the body and can respond to the antigen again if it is encountered a second time [80].

Antibodies themselves vary in structure depending on their type. However, they are normally variations on the same theme: in two dimensions they are represented as Y-shaped glycoprotein, shown in Figure 1.1.7.

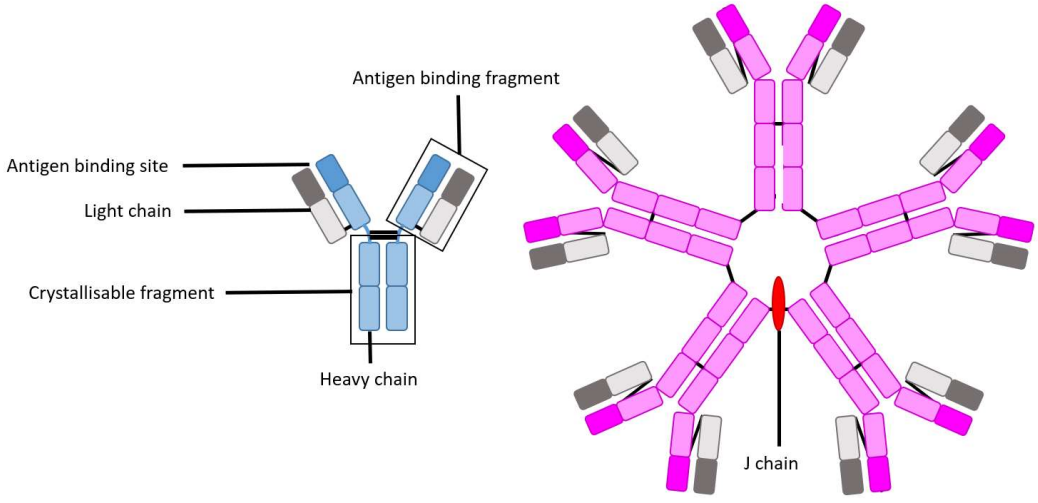


Figure 1.1.7 – Structure of a typical immunoglobulin of the IgG (left) and IgM (right) isotypes.

For a given antibody class, the central region does not vary and is not flexible. As this means it can be crystalised, it is called the crystallisable fragment (Fc). The two antigen binding

fragments (Fab) have a highly variable structure and so cannot be crystallised. There are two heavy chains, each making up half the Fc and Fab fragments; and two light chains, each completing the Fab fragments. Antigen binding occurs at the tip of the Fab fragment. In three dimensions, the structure does not necessarily form a flat "Y" structure, but can be non-coplanar.

There are five types of antibody or immunoglobulin, namely immunoglobulin A, D, E, G and M, which have α, δ, ε, γ and μ heavy chains respectively [80]. The light chains can be one of two classes, κ or λ, but these do not affect type [80]. IgG can be considered the "classic" antibody, with the "Y" shaped two-dimensional structure as previously discussed. IgM is a pentamer of IgG-style antibodies, held together in a ring by a J-chain [80]. This means that IgM has ten binding sites compared to IgG's two, giving it a higher avidity for antigens. However, this does not make IgM more effective. IgM is the first antibody produced in response to an infection, but afterwards cells undergo affinity maturation, a process of somatic hypermutation that selects for the highest-affinity antibodies to make in one of the other classes [80]. This means that other classes of antibodies should have a much stronger affinity to an antigen than its comparable IgM antibody. The specific type of antibody that is produced after IgM will depend on the function required. For example, while the IgA isotype is present in the blood it is also the predominant antibody in mucous secretions [80].

Antibodies bind antigens, but to what effect? Simply binding to the surface of a pathogen could block some vital surface protein from carrying out its function, but in general, antibodies provide an additional signal to other immune system cells, such as opsonisation to trigger phagocytosis or further signalling to the complement system.

T cells are the second group of cells in adaptive immunity. These, like all blood cells, are initially produced in the bone marrow, but after they are produced they travel to the thymus to mature, hence their name [80]. Like B cells they have surface receptors, but they may only

bind to digested antigens in the context of a Major Histocompatibility Complex (MHC), depending on the T cell type [87, 88]. Cytotoxic T cells kill any cell that displays a specific epitope by inducing apoptosis, although its target is the body's own cells. The T cell will bind to its complementary epitope, and Cluster of Differentiation (CD) 8 will bind to the MHC I complex on the surface of a cell [89], triggering a signalling pathway that kills the cell. This allows the T cell to kill cells that have become cancerous, or infected with a virus, to stop the spread of these diseases by preventing the body's own cells from multiplying [80]. Another class of T cell is the Helper T cell. These are involved in the signalling to activate B cells [80], and work in a similar way to the killer T cells. They also must bind to their complementary epitope and simultaneously contact an MHC, this time MHC II with CD4 [90]. While there are other groups of T cells, we are chiefly concerned with the helper T cells to understand glycoconjugate vaccines.

1.2.2 Vaccines

While adaptive immunity is useful, it takes time to generate a suitable immune response. The generation of complementary receptors occurs at random when the cells are made, and the extreme variation in possible structures means it takes a great deal of time to generate a suitable receptor, which must then by chance encounter the correct antigen. However, when a host is infected, this can rapidly lead to extreme discomfort, illness and death. One way to increase the speed of an immune response is to have had the infection before. A secondary infection is dealt with more rapidly and with an increased antibody titre. However, it is clear that infecting people with a harmful pathogen to protect them from that pathogen is ridiculous.

Vaccines are antigens that have been made safe enough to inoculate deliberately into a person to activate their immune system to generate an adaptive, cell-mediated immune response against a specific pathogen. In most cases, relatively little harm is caused by the

injection, and memory B cells develop that will respond rapidly if the real pathogen is encountered, preventing serious life-threatening infections. The vaccine antigens are typically attenuated pathogens, or pieces of dead pathogens, that cannot cause a disease but still retain the same antigen structures [91]. As discussed above, the primary response to the initial vaccination tends to produce a relatively slow immune response, along with a low titre of predominately IgM antibodies that have not undergone affinity maturation. However, a secondary response to the real pathogen would be much larger because, in addition to the possibility that some antibodies may remain, memory cells will be present, which are able to rapidly proliferate and antibodies which have undergone affinity maturation will be produced more rapidly. It has been estimated that vaccines annually prevent almost 6 million deaths worldwide [92], but as an individual antigen may only be specific to a single strain of a given pathogen, there is always a need for more. As people travel more, they encounter highly localised diseases they have never encountered before, for which vaccines may not exist. Similarly, pathogens can change over time, allowing them to avoid the defences generated by the immune system, driving the need for yearly vaccinations against diseases such as influenza in some at risk groups. In part, this may be avoided by targeting conserved structures which remain unchanged on the pathogen. The importance of vaccines is not just their ability to prevent disease, but that they prevent the need to treat the disease or its complications and long-term health impacts, which can prove expensive and thus particularly problematic in developing countries. Particular care must be taken due to the growing issues with antimicrobial resistance: some diseases have been known for many years but posed little risk as they are typically treated with antibiotics, but this may no longer be possible if they become resistant [93].

1.2.2.1 Antibiotics

Developing new antibiotics is difficult: it is possible to alter the structure of existing antibiotics to improve effectiveness, but this process cannot be continued indefinitely, and,

at some point, a new base chemical must be discovered. There are a number of ways this could be done. Many antibiotics were discovered through screening of soil-derived *Streptomycetes* for antimicrobial activity [94]. This system began in the 1940s and was used extensively, but within a finite group there are limits on the discoveries to be made, and after twenty years it seemed that it was no longer possible to find new classes of antibiotic [95]. Given the advances that have been made in genomics, proteomics and bioinformatics since then, it is now possible to streamline this process by screening libraries of information from a wider variety of organisms [96, 97]. However, this method is still reliant on chance. Similarly, it is possible to search libraries of structures for small molecules and perform large-scale tests to find examples which may inhibit bacterial growth [98]. Another alternative would be to use synergistic strategies by which multiple compounds are used at once to overcome the resistance to one of the antibiotics [99]. Once a new antibiotic is discovered, its use in combinational therapies would likely extend the time until resistance emerges [99]. However, when treating GBS, antibiotics would still need to be used routinely in intrapartum antibiotic prophylaxis [62]. As this would eventually lead to the development of antimicrobial resistance to these new compounds, in both GBS and other bacteria, a vaccine will be of more use for the treatment of GBS than developing a new antibiotic.

1.2.3 Polysaccharide and protein antigens

Polysaccharides should be an excellent antigen to use as a vaccine as often they make up the capsule of bacteria. While this capsule protects the bacteria from phagocytes [100], it is also readily available to interact with cells of the adaptive immune system. B cells are able to bind to polysaccharides if they possess suitable complementary binding sites. Usually, repeating patterns are recognised which then cross-link multiple binding sites on the surface [101]. This process depends on interaction with pathogen associated molecular patterns, which show that the antigen is not only non-self, but also that it is a risk to the host body [102, 103]. Once activated, the B cell releases antibodies. These are the IgM isotype [101, 103]. As stated

previously, these are pentameric by linking through a J chain, which gives it high avidity [104] but are low affinity as no affinity maturation occurs [105]. However, polysaccharides are unable to bind to MHC and be presented to T cells. There are exceptions, such as if the polysaccharide is zwitterionic [106, 107], and other mechanisms have also been found by which antigens can be presented [108]. However, in general polysaccharides cannot bind to MHC. An MHC-bound antigen can bind with T cells to activate it [109], causing isotype switching and affinity maturation in B cells, making high affinity antibodies rather than IgM [110], and memory cell development [107]. Therefore, without MHC binding, no T cells become involved and so these advantages do not occur. This means the immune response is poorer as the antibodies are less effective. In addition, as the B cells do not differentiate into memory B cells, there is a less marked improvement on re-inoculation. Polysaccharide vaccines therefore frequently need booster shots to maintain immunity.

If only the ability to successfully interact with T cells via MHC binding is considered, proteins could be considered better antigens than polysaccharides. Proteins are able to bind to the MHC after an antigen is digested; the digested fragments are then presented in the MHC on the cell surface where they can interact with CD4+ T cells to activate B cells, triggering differentiation and clonal expansion [80]. As this means the secondary response is improved due to the presence of high levels of high affinity antibodies, proteins can be seen as more effective vaccines.

In the case of pathogens such as encapsulated bacteria, the only available surface antigen is a polysaccharide [111], which can be poor molecules to use as vaccines for the reasons described above [107, 110]. Fortunately, there is a way to improve the immunogenicity of a polysaccharide antigen. Glycoconjugate vaccines are a way of giving the positive traits of a protein antigen to a polysaccharide antigen by covalently binding the two together. The conjugate molecule will be digested, and covalently linked fragments containing both

polysaccharides and proteins can interact with the MHC and be presented to T cells [108]. This triggers isotype switching and B cell differentiation into memory cells, thus acting as a good vaccine [80]. However, the target antigen will still be the polysaccharide portion, so the vaccine will allow the body to defend itself from pathogens such as encapsulated bacteria. This process is shown in .

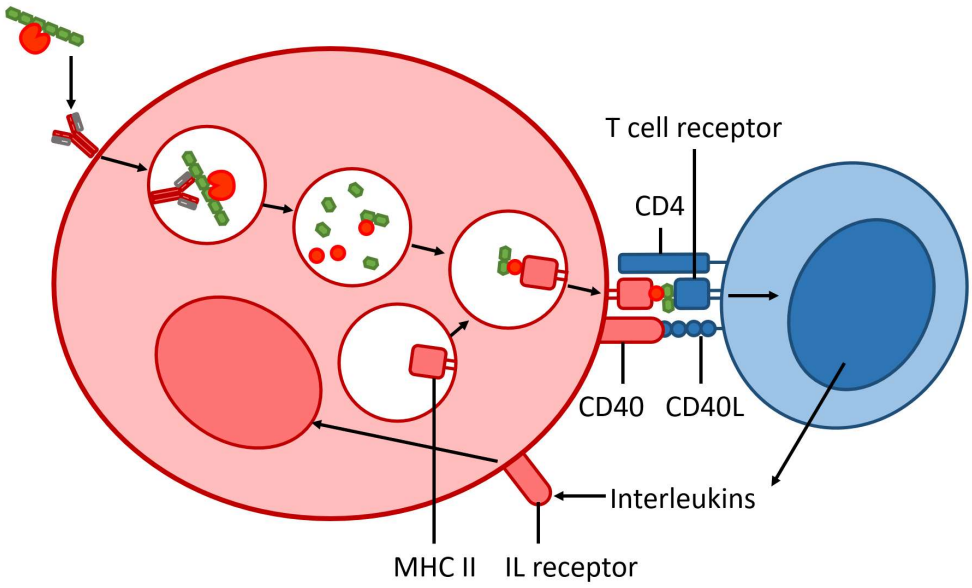


Figure 1.8 – Diagram showing the interaction between a glycoconjugate vaccine, antigen presenting cells and CD4+ T cells. The glycoconjugate binds to the B cell receptor, and this complex is internalised and digested. Fragments of the glycoconjugate that still contain some protein can interact with the MHCII, which is then transported to the surface of the cell where the MHCII/antigen complex can interact with the T cell receptor. This triggers to T cell to release signalling molecules, which trigger the differentiation and proliferation of the B cell. Adapted from [80].

1.2.4 Production methods

To produce a glycoconjugate vaccine, each element is produced individually then conjugated to form a single molecule. As the polysaccharide part contains the desired antigen, only this polysaccharide element needs to be unique for a given vaccine, usually one of a small group of proteins is used. The most commonly used protein components are toxoids, toxins that have been inactivated, usually with the use of formaldehyde [112], and have been shown historically to be strongly antigenic and safe vaccines. Toxins are produced by some pathogenic microorganisms, meaning it is possible to use these cells as bio-factories [112,

113]. For example, tetanus toxoid has been in use as a vaccine since 1924. It is also possible to use comparatively new non-toxic mutants rather than an inactivated toxin, such as Cross Reactive Material 197 (CRM197) rather than diphtheria toxoid [114, 115]. Using a non-toxic mutant rather than an inactivated toxin can be preferable as, no matter how safe the toxoid is known to be, there is still a potential risk. This could be due to a "bad batch" of toxoid that is not fully inactivated, or from which formaldehyde has not been totally removed, as well as the health and safety risks for workers during production.

Although the bulk of protein carriers are toxoids, other examples are known. As any antigen that is perceived as non-self will be sufficient to induce an immune response, there is a vast array of known proteins available for use as carriers. For example, keyhole limpet hemocyanin has been used as a carrier for glycoconjugate vaccines against *Candida albicans* [116] and even some cancers with distinct molecular markers [117]. Bovine serum albumin is a well characterised protein that has also been used, for example in a vaccine against *Aspergillus fumigatus* [118].

All these proteins could be produced by growing cell cultures to high cell density and then purifying the protein from the culture. This is particularly easy for toxoids, as the toxin is naturally secreted by pathogens [112, 113]. However, it is also possible to generate them using cloning to place a transcript of the desired gene into a different host organism [119]. This may be more attractive in the case of toxoids as it no longer requires large batches of potentially deadly bacteria to be grown.

While the protein element is relatively easy to produce, the polysaccharide portion is potentially more problematic. Unlike proteins, polysaccharides are not produced from a direct set of instructions that give an identical structure every time. Instead they are produced enzymatically, which leads to variation or polydispersity in their structure depending on the local kinetics and thermodynamics, as well as in the relative proportions of

subunits and enzymes. This means that to generate antigens that are similar to the wild type pathogen, the easiest way is to purify the polysaccharides from a bacterial culture. Similar to proteins, this is an unattractive approach, as it requires large potentially deadly cultures to be grown. If anything, this could be considered more dangerous as, unlike with the toxoids, there are less likely to be available vaccines for these pathogens. As understanding grows and the size of the epitope necessary to trigger an immune response is better understood, it is possible that smaller fragments of polysaccharides could be used which would be easier to synthesise *in vitro*.

Both the protein and polysaccharide components must be produced on an industrial scale. Ensuring that it is possible to increase production to this scale is a consideration that must be made early in the design stage to prevent potential problems later in development.

Once a protein and polysaccharide have been produced, they must be covalently linked together. However, just as the synthesis of polysaccharides results in polydispersity, this too is a step with a potential to introduce variation. On the surface of a protein or polysaccharide there will be a number of functional groups where the potential to generate a link under the right conditions may exist. One way of limiting the polydispersity from this step would be to treat the components prior to conjugation to activate or block specific functional groups to increase the probability of specific bonds occurring.

There are a number of possible pathways to glycoconjugate vaccine production [120]. In the case of protein-polysaccharide conjugation, there are generally two methods to consider. First, a large polysaccharide antigen can be broken down into smaller oligosaccharide chunks. These chunks can then be linked to a protein carrier. This linkage can be either monovalent or polyvalent, depending on the ratio of polysaccharide to protein [120]. One example of a monovalent conjugate vaccine is the Infanrix hexa vaccine. While this contains a mixture of different antigens, one of these is a *Haemophilus influenzae* type b polysaccharide

(polyribosylribitol phosphate) conjugated to tetanus toxoid as carrier protein [121]. If the vaccine is polyvalent, it is possible to attach oligosaccharides from different serotypes to give a vaccine against multiple serotypes at once, such as Menveo: a quadrivalent vaccine against meningococcal serogroups A, C, W-135 and Y [122]. The second method involves conjugating a number of protein carriers onto a high-mass polysaccharide complex [120].

Once a vaccine is made, it must be tested to ensure it is of acceptable quality. It must be proved that each part, as well as the link between them, is stable. Of the two, the most important to remain stable is the polysaccharide, as this must be able to mimic accurately the structure of the real antigen. If a certain threshold of degradation is acceptable, this will vary between the protein and polysaccharide portions. While the protein carrier's properties can have an impact on the effectiveness of a vaccine, as the protein element only needs to be recognised as non-self the vaccine can in theory still be functional even after extensive degradation, whereas the polysaccharide portion must still accurately mimic the antigens of the organism the vaccine protects against. The link between the two molecules also needs to remain intact, although similarly there must be an acceptable level of breakdown. It is possible that once memory cells have been generated using the complete glycoconjugate, any polysaccharide that has broken away will be able to act as a simultaneous booster vaccination, interacting with the memory cells to produce a secondary immune response during the immunising process.

A number of physicochemical techniques have been shown to be particularly useful as tools for monitoring macromolecular integrity of vaccines after production and processing, such as gel permeation chromatography and size exclusion chromatography. High field nuclear magnetic resonance (NMR) spectroscopy has also been shown to provide an important check on the chemical integrity of products after the industrial production of glycoconjugate vaccines, and is recommended by the World Health Organisation [123]. NMR provides a

routine release test for identity and testing conformity of polysaccharide components [123] although this can be difficult after conjugation as the protein component interferes with the polysaccharide signal. Circular dichroism spectroscopy is limited as a technique for studying polysaccharides but can monitor secondary and tertiary structural changes in the carrier protein before and after conjugation processing. Only after a vaccine has been proved to be stable and reproducible is it worth performing clinical trials to demonstrate an effective immune response and safety.

1.2.5 Zwitterionic polysaccharides

As previously stated, some glycans possess dual or zwitterionic charge motifs and can bind to the MHC-II and activate T cells without the assistance of a carrier protein [124-126]. These zwitterionic glycans possess both positive and negative centres within a repeating molecular unit [126, 127]. This shows a similarity to the repeating structure of peptides, which also contain amine and carboxylate groups, suggesting it is the interaction of these charged groups with the MHC II binding groove that allows zwitterionic polysaccharides to bind. Indeed, there is evidence that a helical structure with a specific periodicity may be required for a zwitterionic polysaccharide to bind to MHC-II, perhaps as this mimics the alpha helical structure found in many proteins [128]. A diverse range of bacteria produce zwitterionic polysaccharides including type 1 *Streptococcus pneumoniae* (the SP1 polysaccharide capsule) [129], *Staphylococcus aureus* (the CP8 polysaccharide) [130], and *Morganella morganii* (the O-chain antigen) [131]. There have been successful applications of this knowledge towards development of all-carbohydrate vaccines, especially cancer vaccines [132-135], highlighting the considerable future potential of using zwitterionic polysaccharides to control immune responses.

1.2.6 Cancer vaccines

Such a response should not be limited to combatting encapsulated bacteria. When cancerous cells develop, they alter their gene expression which can lead to the presentation of new antigens which the immune system may detect. A good target antigen could be tumour marker gangliosides, as they are expressed at high levels on cancer cells. Tumour marker gangliosides are sialic acid-containing glycosphingolipids with extracellular polysaccharide head groups, and so like encapsulated bacteria the most obvious antigen to target is polysaccharide based [136-138].

A number of possible polysaccharide-based cancer vaccines have already been explored but these generally proved to be ineffective, as they were either insufficiently immunogenic or did not provide clinical benefits [139-144]. However, in these instances, the vaccines were attempting to trigger the production of antibodies, which is not the typical method by which the body combats cancerous cells. Usually, tumours are attacked using CD8+ cytotoxic T cells, which directly trigger the death of malfunctioning body cells when they bind to tumour antigens. Therefore, a vaccine which can activate specific CD8+ T cells would be of immense importance in combatting cancer. Indeed, synthetic antigens of tumour marker gangliosides conjugated to polyamidoamine scaffolds have been produced and can illicit responses in CD8+ T cells and appear to be therapeutic [145].

1.3 Considerations in Glycoconjugate design

The author chose to review further literature that may have an impact on vaccine design and production. A search was performed on Cochrane, Web of Science, and PubMed using the key words “polysaccharide” and “vaccine” from 2013-2018. Duplicates were removed using Endnote and further searches performed for the terms “protein”, “conjugate”, “link” and “carrier”. These were then manually sorted into the following groups (where the number in parentheses is the number of papers found):

- Comparison of glycoconjugate vs unconjugated polysaccharide vaccines (20)
- Comparison of glycoconjugate vaccines using different carrier proteins (10)
- Production method (65)

Many papers referred to the same diseases, and these are highlighted in further subsections.

1.3.1 Comparison of Glycoconjugate and polysaccharide vaccines

It is known that using a glycoconjugate vaccine induces a T cell dependent B cell response onto a vaccine, which improves immunogenicity by triggering the production of memory B cells (see section 1.2) and confers immunity in people who may not respond adequately to unconjugated polysaccharides. However, the act of conjugating a polysaccharide to a protein may alter some aspects of its structure, which then has the potential to alter its effect on the immune system. For this reason, papers in which unconjugated polysaccharide vaccines were compared to glycoconjugate vaccines using the same antigenic compounds were reviewed to establish a general trend.

This has previously been reviewed in a meta-analysis [146], but the focus was more on the mechanism of action of each vaccine in terms of which immune system cells each vaccine stimulated. The results generally show that immediately after vaccination, glycoconjugate vaccines show an almost identical response to polysaccharide vaccines. However, they also found that upon a second vaccination, in the majority of cases a stronger response was seen in the groups which had received glycoconjugate vaccines, strongly suggesting memory B cells had developed.

1.3.1.1 Haemophilus influenzae type b

Two papers were found for vaccines to *Haemophilus influenzae* type b, which investigated polyribosyl ribitol phosphate as the polysaccharide antigen. This is a capsular polysaccharide, and in both studies was compared when used on its own and when conjugated to CRM197, the non-toxic diphtheria toxin mutant. In the first of these [147] different combinations of

conjugated and unconjugated vaccines were used in specific orders to establish the long-term vaccination scheme that could be used. Tests were performed on 7- to 15-month old infants and inoculation performed three times, the second two months after the first, and the third six months after the first. Their findings showed that if all three vaccinations used the conjugated vaccine, or if only the last one (six months after initial inoculation) was replaced with pure polysaccharides, the response gave similar mean antibody levels. These levels were only reduced if two of the three inoculations were replaced with polysaccharide only. This suggests that polysaccharide vaccines may be inappropriate for use as booster vaccinations. The second paper studying *Haemophilus influenzae* type b [148] looked specifically at the effect of the vaccine in HIV-infected individuals. The population studied were split into four groups: HIV-, HIV+, asymptomatic HIV+, and people with AIDS. It was found that the conjugate vaccine gave a three-fold increase in antibody titre over the pure polysaccharide vaccine unless the infection had progressed to AIDS, at which point patients responded poorly to both vaccinations. This suggests that glycoconjugate vaccines may be more suitable for use with some moderately immunocompromised patients.

1.3.1.2 Neisseria meningitidis

Commercially available *Neisseria menigitidis* vaccines typically include capsular polysaccharides from four serotypes, A, C, W and Y. In the following three papers these are conjugated to CRM197, although marketed vaccines use tetanus or diphtheria toxoids for multivalent vaccines. The first [149] studied the persistence of immunity 5 years after vaccination with polysaccharide and conjugate vaccines. It was found that whilst the all-polysaccharide vaccine gave a “less robust” response, it was still adequately protective. This suggests that while a conjugate vaccine may have increased protection, it is not always necessary, as the protection provided by a polysaccharide vaccine may still be sufficient. However, this does not take into account how the response may vary between different groups (e.g. immunocompromised) and suggests that the response may wane to unsafe

levels beyond the five years tested in immunocompromised individuals. The next study attempted to explain the differences observed in antibody titre observed after using the conjugated and unconjugated vaccine [150]. It found that some serotypes were better protected using the polysaccharide vaccine (serotype C) while others fared better with the conjugate vaccine (serotype W). It should be noted that the difference observed in serotype C may be due to the lower titre of polysaccharide C conjugated to the CRM197 protein in the conjugate vaccine. However, the mechanism by which the response to serotype W is reduced in the pure polysaccharide vaccine is unclear, although it is hypothesised that there may be some sort of negative feedback mechanism present when polysaccharide vaccines are used. This may be explained by the final paper [151], which found that as well as being less effective at eliciting a response, polysaccharide vaccines might take a role in actively depleting memory B cells when used as a booster vaccine, a mechanism that may also explain findings covered previously [147].

Two papers [152, 153] studied polysaccharides from serotypes A, C, W and Y linked to tetanus toxoid. The first [152] looked at immediate differences between the two vaccines, while the second [153] studied the difference in the persistence of immunity after 5 years. In both cases, it was found that antibody titres were higher and persisted in a greater number of patients when they were inoculated with the conjugate vaccine rather than the polysaccharide vaccine.

1.3.1.3 Streptococcus pneumoniae

All the examples found which studied conjugated vs unconjugated vaccines against S*treptococcus pneumoniae* used CRM197 as a carrier protein. In each case, a 23-valent polysaccharide vaccine was compared to a conjugate with a lower valency (up to 13-valent), with comparisons being drawn only for those serotypes present in both vaccines. Simple comparisons of the effectiveness of conjugated and unconjugated vaccines were performed

for specific populations. One [154] showed that, in people aged 60-64, increased antibody titres were seen for the majority of serotypes analysed when the conjugate vaccine was used. Similarly, in a Japanese population aged over 80, a higher titre was seen with the glycoconjugate vaccine [155]. Whilst in this latter case all vaccines were safe, there was a slight increase in swelling and redness from the conjugate vaccine. While this effect is not a significant issue, it is interesting to note that an increase in side effects seems to be linked to an increase in response. In patients with systemic lupus erythematosus, both conjugate and polysaccharide vaccines for *Streptococcus pneumoniae* were found to be safe, but neither was superior in terms of the protection they provided [156]. However, one study found that using booster vaccinations had a greater impact on vaccine efficacy than the relatively minor differences between conjugated and unconjugated vaccines [157]. It was found at first that a seven-valent conjugate vaccine had a significant increase in titre of antibodies for serotypes 5, and 23F; while a 23-valent pure polysaccharide vaccine had increased titre for serotypes 3, 19F and 19A immediately after vaccination. If a booster polysaccharide vaccination was administered to the conjugate vaccine group, antibody titre was increased for serotypes 6A, 9V, 18C and 23F, but waned in the group without booster vaccinations. No major benefit of one vaccine over the other was seen, as all vaccines were protective initially. The effect of the booster vaccination is likely to be more important. This result was corroborated by another study [158], which also found that a booster vaccination with a polysaccharide vaccine after a glycoconjugate vaccine gave a greater antibody response than polysaccharide vaccine alone. It has also been found [159] that a glycoconjugate vaccine was less able to provide a boosting effect on vaccination in patients previously inoculated with unconjugated vaccine, but at the 1-year endpoint all vaccines studied provided acceptable levels of protection. It has also been found that booster vaccination may be more effective if they are glycoconjugate, particularly in populations immunocompromised by HIV [160]. In asplenic patients, a difference is also seen depending on the order of conjugated/unconjugated

vaccinations. It is reported [161] that being inoculated by a conjugate vaccine followed by a purely polysaccharide vaccine confers greater protection than doing the reverse as there is an increased antibody titre.

1.3.1.4 Other pathogens

Two other examples of this type of comparison were found. One study examined a cholera vaccine using the O-antigen [162], and found that in a mouse model, unconjugated vaccine did not induce the production of IgG. However, IgM production was comparable between the two groups. Finally, a typhoid vaccine is being studied [163]. These initial results show that titre of antibodies is higher when using conjugate vaccines, but that both groups generated sufficient antibodies to provide protection.

1.3.2 Comparison of carriers in glycoconjugate vaccines

Assuming it is possible to produce a vaccine with the same antigen conjugated to different protein carriers, and that there is no obvious reason such as stability or ease of production which favours a specific conjugation, tests must be performed to ensure that the compound to be used in the vaccine is the best at producing an immune response. A number of papers examining this are reviewed below.

A range of vaccines were studied to establish common features in their stability, such as the effect of storage at 2-8°C, -20°C, and repeated freeze-thaw cycles [164]. It was found that while there were no significant differences in the majority of cases, storage at -20°C did have a negative impact on the stability of glycoconjugate vaccines made with CRM197.

1.3.2.1 Haemophilus influenzae type b

A number of studies have been performed on vaccines for *Haemophilus influenzae* type b. Diphtheria toxoid, CRM197 and an outer membrane protein have all been compared as potential carriers for polyribosyl ribitol phosphate [165]. While this study focused more on the interactions between the outer membrane protein conjugate with other vaccines, it did

show that all vaccine responses declined 10-15 months post inoculation but increased again following polysaccharide or outer membrane protein conjugate re-inoculation. However, different carriers were not compared in this booster, so the paper's assertion that this conjugate specifically be used as vaccination and booster for reasons of practicality is potentially flawed. It has been found [166] that CRM197 conjugates were poorly immunogenic in comparison to outer membrane protein conjugates after a single dose. The CRM197 conjugates only became effective when they were administered along with diphtheria toxoid, which acted as an adjuvant to the conjugate vaccine. However, as the vaccines being compared used different polysaccharide antigens, the comparison is not direct. The currently licensed vaccine contains tetanus toxoid, but studies have been performed to challenge its effectiveness with new vaccinations. When tetanus toxoid and CRM197 were compared as carriers for polyribosyl ribitol phosphate [167], no significant differences were found between the two carriers in terms of their immunogenicity, although the CRM197 conjugate had an increased local reaction. In contrast, it has been found [168] that CRM197 had an increased bactericidal activity compared to the tetanus toxoid.

1.3.2.2 Neisseria meningitidis

In a study on polysaccharides from *Neisseria meningitidis* serotypes A, C, W and Y conjugated to tetanus toxoid or CRM197 [169], no significant differences were found in the responses between the two vaccines, despite the fact there were subtle variations in the composition of the polysaccharide component of the vaccine in each case.

Two studies were performed which looked at both *Haemophilus influenzae* type b and *Neisseria meningitidis* simultaneously. The first [170], rather than comparing the activity of the vaccines, compared their ability to interact with aluminium-based adjuvants. It was found that aluminium phosphate was less able to interact with the vaccines than aluminium hydroxide, but it was also found that the degree of interaction varied depending on the

protein carrier. Tetanus toxoid interacted more with the adjuvants than CRM197, regardless of whether the *Haemophilus influenzae* type b or *Neisseria meningitidis* serotype C polysaccharides were bound. This information could potentially be useful when designing formulations for vaccines.

The second paper looking at both *Haemophilus influenzae* type b and *Neisseria meningitidis* serotype C sought to make a bivalent vaccine on tetanus toxoid comparing its efficacy to *Haemophilus influenzae* type b-tetanus toxoid and *Neisseria meningitidis* serotype C-CRM197 conjugates [171]. No significant differences in immunogenicity were observed between the three groups, which suggests that the bivalent vaccine may be more suitable due to the ease of application, assuming that production costs are similar.

1.3.2.3 Other pathogens

A study for a conjugate vaccine against a typhoid-causing bacterium, *Salmonella* Thyphimurium, [172] linked core O-polysaccharide to flagellin protein or CRM197 with different architecture. The flagellin protein carrier was not as effective when linked in a lattice with the O-polysaccharide antigen, but was when linked in a "sun-like" array. Polysaccharides attached to CRM197 in a similar "sun-like" array were similarly effective. However, this paper was more focused on the effect of the partial removal of O-acetyl groups than on the effect of the carrier.

Finally, a further study [173] compared the effects of the same basic carrier, diphtheria toxoid, on O-specific polysaccharide of *Salmonella* Partyphi A. However, they tested the effects of a linker (adipic acid dihydrazide) between the carrier and polysaccharide. It was found that a higher antibody titre was produced when the linker was present compared to the simple glycoconjugate.

1.3.3 Production methods

A final factor that affects the design of a vaccine is the ability to produce reliably the individual parts and the link between them. However, as the protein portion is usually easier to define and common between vaccines, there are fewer papers covering this topic. Therefore, this final section comprises of two parts: studying polysaccharide production and studying conjugation.

1.3.3.1 Polysaccharide production

Clearly, one way to produce polysaccharides for vaccines is to grow a culture of the relevant bacteria and purify the desired molecules. If this is the intent, it is first necessary to produce a culture of sufficient cell density to produce a high yield, for example controlling agitation and pH during growth [174]. One method has been described using hot phenol to extract lipopolysaccharide and core hydrolysis to extract O-antigen to produce vaccine components for *Salmonella* Typhi [175]. Another method breaks down the capsular polysaccharides of *Acinetobacter baumannii* into repeating oligosaccharide units using bacteriophage Phi AB6 tailspike protein [176]. However, the purification method of polysaccharide from a cell culture is potentially complex. One scheme [177] considers the whole process from start to finish, involving cell separation by tangential microfiltration, concentration by tangential ultrafiltration, diafiltration with sodium dodecyl-sulphate, precipitation with trichloroacetic acid, precipitation with ethanol, and finally anion exchange chromatography. This method was found to give acceptably pure polysaccharides for use as vaccines for *Streptococcus pneumoniae* serotype 14. However, as any method that involved growing a large culture of potentially deadly bacteria is understandably not ideal, alternative methods for *in vivo* production have been suggested.

One study found that it was possible to transfer the polysaccharide synthesis machinery from *Neisseria meningitidis* serotype X into *Escherichia coli* to produce polysaccharides with the

same properties as the native polysaccharide [178]. Similarly, it has been found for *Neisseria meningitidis* serotype X that it is possible to produce a trisaccharide that remains immunogenic, which could be used rather than the native pentadecasaccharide [179]. Another found a method of triggering glycosylation of lipopolysaccharides of *Raoulterra terrigena* by introducing bacteriophage lysogenic enzymes to improve the accuracy of antigen production in *E. coli* [180]. It is even possible to perform such transformation on plant cells. There has been work in which genes for *Streptococcus pneumoniae* cps3S were transformed into *Nicotiana tabacum* using pCambia2301 vector and *Agrobacterium tumefaciens* mediated gene transfer, and the resulting product was found to be immunogenic in mice [181].

Such *in vivo* production systems are not limited to single serotypes. A method has been found to produce a trisaccharide common to B and C serotypes of *Cryptococcus neoformans* [182], and capsular polysaccharides for *Streptococcus pneumoniae* serotype 6 that are sufficiently small to react with types 6A, 6B and 6D [183]. Work has also been performed to produce capsular polysaccharides from four *Streptococcus pneumoniae* serotypes *in vivo* in the same *E. coli* cells [184]. There has even been some work done to produce a live vaccine for *Salmonella* Typhi that produces the O-antigen from *Shigella* spp., and is therefore able to act as a vaccine to two diseases at once [185].

As opposed to *in vivo*, it is also possible to produce polysaccharides *in vitro*. This can be done by producing enzymes that synthesize the polysaccharides. For example, CsaA, CsaB and CsaC enzymes have all been combined *in vitro* to produce capsular polysaccharide A of *Neisseria meningitidis* that was identical to the native form [186]. A similar method has been used to produce *Neisseria meningitidis* serotype X capsular polysaccharides [187] which has even gone on to be conjugated to CRM197 [188].

Another method to produce polysaccharides *in vitro* is to do so in blocks. The exact number of monosaccharides in each block can vary, such as a di- and tetrasaccharide [189], di- and trisaccharide [190-192], three disaccharides [193] and two trisaccharides [194]. It should be noted that it is possible to compare these two assembly methods and it has been found that linear assembly may be more effective than block assembly in at least some cases [194, 195].

Other methods have been described to produce polysaccharides *in vitro* such as an automated glycan assembly [196] or solid phase synthesis using cyanopialoyl ester as a protecting group [197].

To develop a vaccine against *E. coli*, methods have been described to generate a pentasaccharide with a propyl-amino linker at one end to allow easy conjugation to CRM197 [198] or use of a heat labile p-methyloxybenzyl protecting group [199].

To develop a vaccine for *Leishmania*, glycosyl 1-phosphate was synthesised using fluoridated analogues and a solid phase phosphoramidite method to make repeating structures [200]. A repeating trisaccharide unit for *Staphylococcus aureus* has been produced, despite the difficult chemistries involved in alpha-fucosylation and beta-mannosylation, using careful choices of protecting groups [201].

A number of polysaccharides have been produced to act as vaccines to different strains of *Streptococcus pneumoniae*. For serotype 3, a tetrasaccharide [202] or glucuronic acid linked trisacharide [203] can be used. For serotype 6A, a capsular repeating unit has been produced in a "one-pot method," despite the relatively challenging chemistry needed to produce 1,2-cis glycosidic linkages. Finally, an automated glycan assembly has produced serotype 8 polysaccharides, glycan microarray-based monoclonal antibody reverse engineering and immunological evaluation *in vivo*. This uncovered the minimum epitope needed in this case to provide protection, and could be conjugated to CRM197 for effective protection in rabbits [204].

Polysaccharides can even be produced that are effective in the treatment of some cancers. Thomsen-Friedenreich tumour associated carbohydrates have been produced using 11-step synthesis using D-GalN(3) acceptor carrying pre-installed alpha-N-hydroxysuccinimidyl moiety, prepared using D-GalN(3)-thioglycoside donor with N-hydroxysuccinimide [205]

Whichever method is used to produce a polysaccharide, tests must be performed to ensure it is of sufficient quality to use in a vaccine. Methods using rapid microtiter plate tests [206] and size exclusion chromatography [207] have been described.

1.3.3.2 Conjugate production

One method of producing a glycoconjugate vaccine is to use host glycosylation enzymes to transfer polysaccharides onto protein carriers. Typically, this involves using *E.coli* as a recombinant expression vector. However, the actual glycosylation machinery used may not be native to the *E.coli*.

Campylobacter jejuni oligosaccharyltransferase PglB was transformed into *E.coli* to perform the glycosylation for *Burkholderia pseudomallei* 0 OPS II conjugated to glycoprotein AcrA [208]. It was also used to generate a vaccine for *Staphylococcus aureus* from capsular polysaccharides 5 and 8 conjugated to detoxified *Pseudomonas aeruginosa* exoprotein A, and was also shown to be protective in mice [209]. A further vaccine was made in this way for both *Salmonella* Typhi's O-antigen and *Staphylococcus aureus*'s capsular polysaccharide 5 to various proteins [210]. Another vaccine made with this scheme is that for *Shigella flexneri*, whose O-polysaccharides were linked to *Pseudomonas aeruginosa* EPA-2a [211].

Perhaps most interestingly, it has also been possible to synthesise *Streptococcus pneumoniae* polysaccharides covalently liked to CRM197 with multiple antigens, giving a 13-valent glycoconjugate produced *in vivo* [212].

E.coli is not the only possible recombinant host, and can be unsuitable in some cases as it lacks the O-linked glycosylation machinery. A glycoconjugate vaccine against *Neisseria*

meningitidis has been produced using *Shigella* spp.'s O-linked glycosylation system [213]. However, it is also possible to make a recombinant form of the original pathogen to confer O-linked glycosylating enzymes on them, as in the case with *Salmonella* Paratyphi A, where the O-polysaccharide was transferred onto an antigenic peptide (P2) [214].

Schemes have also been devised for conjugation to non-protein carriers *in vivo*. Serotype 14 polysaccharides from *Streptococcus pneumoniae* have been produced which are linked to liposomes as they are synthesised, which are highly immunogenic when administered with a suitable adjuvant [215]. Similar work has also been performed for *E.coli* vaccines using the O-antigen and outer membrane vesicles [216].

It is also possible to perform the conjugation *in vitro*. A vaccine for *Bordetella pertussis* was synthesised by linking oligosaccharides with terminal trisaccharides to aminooxylated BSA via terminal ketodeoxyoctanate residues [217]. Conjugation of *Neisseria meningitidis* serotype A capsular polysaccharides to tetanus toxoid has been performed by activating groups to make conjugation more likely [218]. Linking *Streptococcus pneumoniae* and *Salmonella* Typhi to diphtheria and tetanus toxoid respectively can be achieved using an isocyanide-based multicomponent process with a Ugi-multicomponent reaction [219].

As with the individual components, it is important to ensure that the conjugation itself has occurred successfully and the result is stable. As such, a number of analysis methods or proposals for more effective conjugations have been reported. One such result is the report that, across many glycoconjugates, the more common binding sites are at the termini of the protein, suggesting that these bonds form more easily and should be considered as first targets for conjugation [220].

A glycan-based antigen from *Candida albicans* was produced and conjugated to CRM197, using tyrosine-directed ligation to give higher anti-glycan IgG levels than if a lysine residue were used. However, a more interesting feature of this study was the improvement seen if

any directed conjugation was used rather than allowing conjugation to occur at random, which suggests that reducing the polydispersity at this stage may improve immunogenicity [221]. Conversely, it has also been found that random conjugation location on the antigen improves the bactericidal activity of antibodies produced in response to *Salmonella* Typhimurium O-antigen conjugated to CRM197. This may be logical, as if the conjugation always occurred on the same place in a polysaccharide, very little would be "seen" of the rest of the antigen after digestion and presentation on the MHC [222].

An experiment was performed to establish if ELISA was a suitable test to act as quality control in glycoconjugate synthesis. *Haemophilus influenzae* type b polyribosylribitol phosphate antigens were conjugated to tetanus toxoid, and ELISA used to assess if the polyribosyl ribitol phosphate was pure and if the two components were successfully linked. It was found that ELISA was suitably precise and cheap for use as a test by others for similar purposes [223].

For *Salmonella* Typhi, the Vi polysaccharide of different lengths were assessed as an antigen conjugated to a number of different carriers. Short chain Vi polysaccharide was less able to develop a robust immune response than long chain, but only when conjugated to diphtheria toxoid or CRM197, and only on primary infection [224]. Quantification of free Vi polysaccharide has also been used to assess the stability of conjugates [225].

The effects of a number of factors, in particular the pH, were used to find a conjugation method for lipopolysaccharide from *Vibrio cholerae* to either BSA or tetanus toxoid [226]. However, such covalent linkages may not be necessary. It has been found that simply cross-linking a polysaccharide to a protein matrix may be sufficient to trigger a T cell dependent response [227].

1.4 Conclusions

Immunity is complex, but the ability to combine different antigens together to produce beneficial effects is clearly a great advantage for pharmacologists. However, there does not appear to be a single 'best' carrier. Instead, it seems likely that the most suitable carrier in a given situation can be chosen for reasons of practicality rather than simply immunogenicity. Key elements to consider when choosing a carrier antigen are the ease with which it can be reproduced on an industrial scale, stability of the final product, and how safe it is to produce. While the methods for synthetic polysaccharide production are complex, it is clear that production *in vitro* is much safer than purification from a pathogen culture. As the repertoire of methods for polysaccharide production grows, it will become easier to produce glycoconjugate vaccines.

2 Aims and Objectives

The main aim of this study was to investigate the stability of polysaccharide extracts from the capsule of Group B *Streptococcus* to assess their suitability for developing a vaccine. For this purpose, nine samples of purified polysaccharides have been kindly provided by GSK for analysis. It was requested that this analysis was only performed using hydrodynamic methods to provide a characterisation of the properties of each molecule as they were sent in solution, and for this reason no assessment was performed the determine the purity of the samples.

In addition, the samples have been subjected to defined stresses as a means of establishing their stability. Three environmental stresses were selected: repeated freeze-thaw, incubation at room temperature (20˚C) and incubation at human body temperature (37˚C). The percentage change in the parameters measured were recorded. Additional statistical tests performed where possible to establish if these changes were significant: if $p > 0.05$, it is assumed that any changes are due to chance and therefor that the material was not significantly degraded.

As an adverse interaction of the polysaccharides with blood proteins could lead to the formation of blood clots, further tests were performed to determine if the polysaccharides interact with three of the most common blood proteins: serum albumin, fibrinogen and immunoglobulin. Finally, as the carrier for the polysaccharide antigens in the vaccine is intended to be CRM197, a sample of this protein was also kindly provided by the National Institute for Biological Standards and Control. Some initial hydrodynamic tests were performed on CRM197 to determine some baseline properties, but further work will be required that is outside the current scope of this study to understand its stability.

3 Methods

3.1 Materials

Solutions of 0.1 M phosphate buffer pH 7.0 were produced using 4.595 g $Na_2HPO_4.12H_2O$, 1.561 g KH_2PO_4 and 2.923 g NaCl, in 1L of MilliQ water. This was used to dialyse samples provided in solution or to dissolve samples provided as powders and could afterwards be used as a reference solvent in experiments.

Nine samples of polysaccharide from *Streptococcus agalactiae*, serotypes IA, IB and II to V, were kindly provided by Ghislain Delpierre of GSK, Rixensart, Belgium. These samples are potential vaccine candidates, some of which have undergone further processing after extraction ("sized"). Each sample molecule was suspended in a phosphate buffered solution, although the exact composition was not provided by GSK. Some supplementary information was provided, the which is given in full in Table 3-1. A shortened name to be used in this work is also shown here.

Table 3-1 - Information relating to the samples provided upon their delivery.

State	Serotype	Name	Concentration ($mg.mL^{-1}$)	*dn/dc* ($mL.g^{-1}$)
Native	IA	N-IA	9.5	0.147
	IB	N-IB	7.9	
	II	N-II	10.5	
	III	N-III	5.9	
	IV	N-IV	5.9	
	V	N-V	7.2	
Sized	IA	S-IA	8.4	
	IB	S-IB	7.3	
	II	S-II	5.1	

In section 4.10, the hydrodynamics of CRM197 were considered. A sample of CRM197 was provided by Barbara Bolgiano of the National Institute for Biological Standards and Control. Information was not provided on the method used to make this sample, or its storage prior to its arrival. While this sample of CRM197 was not provided by GSK, there is usually very

little variation in the structure of primary structure proteins (ie the amino acid sequence), especially as compared to polysaccharides. Proteins are produced from a defined gene sequence to give a monodisperse sample, so one sample of a proteins should be broadly comparable to another. The differences are more likely to arise between different solvents used to suspend the protein sample, or differences in the folding and glycosylation mechanisms used in the host organism producing the protein. However, if the protein were to fold incorrectly, it is likely that the resulting protein would form an insoluble aggregate Therefore, while the CRM197 used here may not be identical to that used by GSK, as it will share the same amino acid sequence and has successfully folded into a soluble protein, it should have a comparable structure and so this may not make any noticeable difference to this analysis. As only a relatively small volume of CRM197 was provided, it was only possible to perform baseline measurements.

In section 8, the interaction of these polysaccharides with blood proteins are also considered. The proteins used in these cases were Bovine Serum Albumin (Sigma, lot SLCB9433), albumin from human serum (Sigma, lot SLBT8667) and fibrinogen from human plasma (Sigma, lot SLBR592V). Each were reported to have high purity (>96%) but were also dialysed to reduce the presence of any impurities. Interactions with immunoglobulins were also considered. In these cases, samples of monoclonal antibodies isolated from human myeloma cells were used. Two samples, IgG1K m(f) Cri and IgG1K M(za) Wid, were kindly provided by Margaret Goodall of the Clinical Immunology Service at the University of Birmingham. The two have slightly different glycosylation profiles, where Wid is glycosylated on both the heavy and light chains while Cri is only glycosylated on the heavy chains [228].

3.2 Dialysis

When samples were provided in liquid form, it was necessary to produce a reference solvent with the exact same conditions and contents as the solution. This process also dilutes any

impurities present in the sample. Dialysis was performed in phosphate buffer, pH 7 and ionic strength 0.1 M using membrane BID-010-040B BioDesignDialysis Tubing™ (D006) with molecular weight cut off-of 14000 Da. Aliquots were dialysed in 500 mL of solution for at least 12 hours at 4.0°C.

3.3 Concentration measurements and dilution series

Polysaccharide concentration was measured using an Atago® Differential Refractometer DD-7 to generate six consistent Brix (%) values, of which the mean average value was converted into concentration using the formula in Equation (1), provided by the instrument manufacturer.

$$concentration = brix\ (\%) \times \frac{\frac{dn}{dc} of\ molecule}{\frac{dn}{dc} of\ sucrose} \times 10\ mg.mL^{-1} \quad (1)$$

As stated in Table 3-1, the *dn/dc* of all samples was given as 0.147 mL.g^{-1} (by G. Delpierre, private communication), and the *dn/dc* of sucrose is known to be 0.1483 mL.g^{-1}. Experimental error was calculated using the standard error of the mean for the refractometer readings, using error propagation formulae to convert into associated error for the concentration value.

A one-in-two dilution series was performed on each sample down to 2^{-7} to give a range of concentrations, allowing results to be plotted against concentration and then extrapolated to zero concentration and corrected for the effects of non-ideality. Additional dilutions were generated by combining these dilutions to give averaged concentrations. A summary of this dilution series is given in Table 3-2.

Table 3-2 - Dilutions used in this experiment and the conversion factor to give the concentration of that dilution from the stock concentration.

Dilution (2^n)	Conversion factor
0	1.000
-1	0.500
-1.415	0.375
-2	0.250
-3	0.125
-3.415	0.094
-3.678	0.078
-4	0.063
-4.415	0.047
-4.678	0.039
-5	0.031
-6	0.016
-7	0.008

The error associated with performing the dilution has been assumed to be negligible, as the same pipet was used to mix equal volumes of solution and solvent.

3.4 Density and $\bar{v}$ determination

Density of solutions was measured by an Anton Parr DMA500 to give six consistent readings. By measuring the density of the dialysate and a range of concentrations of sample, it is possible to establish the partial specific volume using Equation (2) [229].

$$\bar{v} = \frac{1}{\rho_w}\left(1 - \frac{d\rho}{dc}\right) \quad (2)$$

Where $\bar{v}$ is the partial specific volume, ρ is the density of the sample, ρ_w is the density of water, and c is the concentration. This parameter, as well as the density of solution, is used in sedimentation analysis. The density of each solution is also used in viscosity analysis.

3.5 Viscosity

Viscosity was measured by recording the flow times of dialysate (t_0) and solutions (t_s) using a semi-automated (Schott Geräte, Hofheim, Germany) U-tube Ostwald capillary viscometer held at 20 °C by immersion in a water bath. In each case six consistent measurements were made on 2 mL of solution, and this information was combined with recorded densities using Equation (3)

$$\eta_r = \frac{t}{t_0} \times \frac{\rho}{\rho_0} \quad (3)$$

where η_r is the relative viscosity. This value was then used in Equations (4) and (5) to consider the concentration of solution to find the reduced and inherent viscosities [230]:

Huggins Equation:
$$\eta_{red} = \frac{\eta_r - 1}{c} = K_H[\eta]^2 c + [\eta] \quad (4)$$

Kraemer Equation:
$$\eta_{inh} = \frac{\ln(\eta_r)}{c} = -K_K[\eta]^2 c + [\eta] \quad (5)$$

where η_{red} is the reduced viscosity, η_{inh} is the inherent viscosity, K_H and K_K are the Huggins and Kraemer constants respectively, and [η] is the intrinsic viscosity. These values were then plotted against concentration and extrapolation performed to where the concentration is zero, to correct for non-ideality effects, to give the intrinsic viscosity.

The intrinsic viscosity can also be calculated from a single point using Equation 6 [230], but in this work this value was also plotted against concentration and extrapolated to zero concentration to obtain the most accurate value possible for intrinsic viscosity.

Solomon-Ciuta Equation:
$$[\eta] \sim \frac{\sqrt{2(\eta_r - 1) - 2\ln(\eta_r)}}{c} \quad (6)$$

An average was taken of the three intrinsic viscosities. Error associated with each value was calculated using the standard error of the mean for both the flow time and concentration. The error on each point is considered by the software Origin (version 6.1) when performing a

linear fit, and a value of error for the intercept (i.e. the intrinsic viscosity) is also given. These are combined using standard error propagation formulae when taking the average.

3.6 Analytical Ultracentrifugation

Analytical ultracentrifugation can be used to characterise the shape and size of macromolecules by determining the molecular weight and sedimentation coefficient, and testing for any potential interactions. These tests can be performed in the natural state of biologically relevant molecules such as proteins and polysaccharides, under the conditions at which they are normally found [231]. As the technique does not rely on the interaction of a macromolecule with a separation matrix, there is no need to use a series of standards to analyse data, which is instead measured directly [232]. Partial specific volume and density of solution are required to analyse the data as these both impact sedimentation properties.

Samples are loaded into cells containing multiple sectors, usually two, one loaded with a reference solvent while the other is filled with the solution to be tested. The dual-sector centrepiece is pressed between two transparent windows (see Figure 3.1) which allow a laser beam to pass through the cell and optically register the sedimentation profile (see figure Figure 3.2). This can be done using different optical systems depending on the molecule to be assessed.

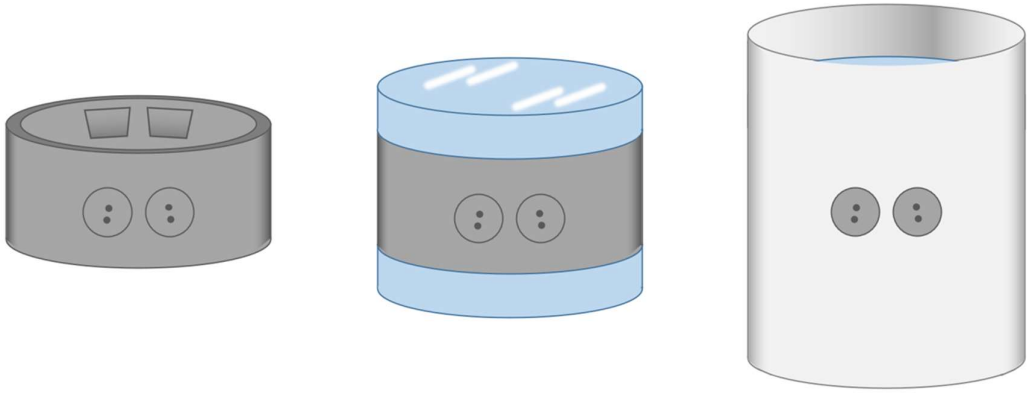


Figure 3.1 – The centrepiece of an analytical ultracentrifuge cell is shown on the left. The two sectors are visible from above, while at the front are the holes used to inject samples and reference solvents into the assembled cells. In the middle is shown the centrepiece pressed between two transparent windows. This seals the sectors, allowing them to be filled with a sample and reference solvent, while also allowing laser light to pass through. On the right is the entire assembly placed in a metal casing, held together by a screw ring (not shown) which is tightened with a torque wrench to prevent leaks.

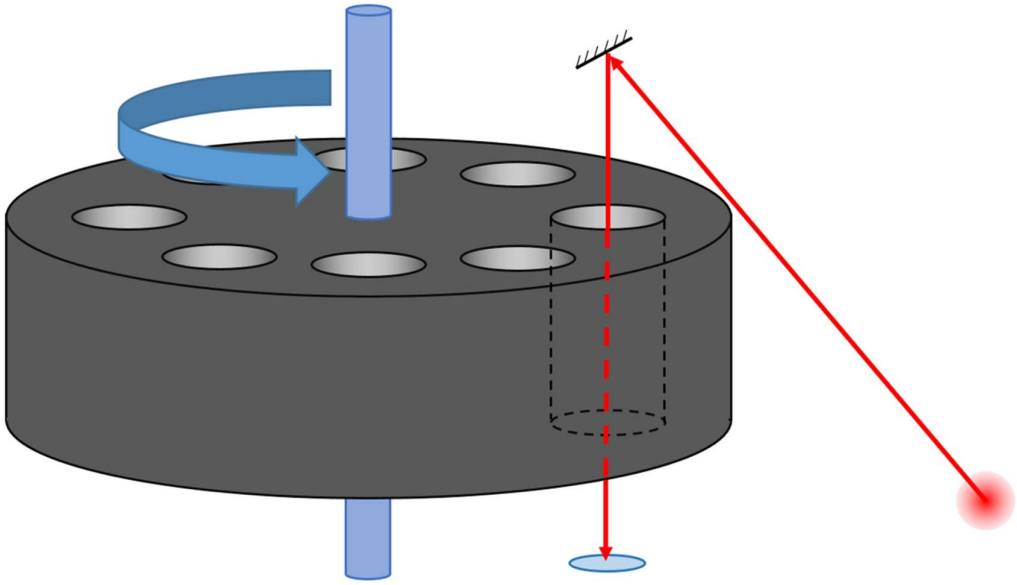


Figure 3.2 – The analytical ultracentrifuge rotor is shown. In this case there are eight holes into which individual cells can be loaded. Light is emitted from the centrifuge through a monochromator and redirected downward through the sample cells and into a photomultiplier to detect the distribution of sample within the cell.

For samples which absorb UV light, such as proteins, absorbance optics are used, and the signal registered on a photomultiplier. Absorbance optics are less suitable if proteins are heavily glycosylated, as this can interfere with the absorbance profile. As absorbance scans take a relatively long time to perform, they are also avoided if molecules sediment quickly, as

the molecule may sediment before it is possible to collect sufficient data. Absorbance data is saved as *.RA files, with a radial position relative to the centre of rotation, an absorbance value in the form of optical density, and a standard error. The Lambert-Beer law can then be used to convert the optical density to concentration.

For samples which do not absorb UV, such as polysaccharides, Rayleigh interference optics are used, and the signal registered on a charge-coupled device array. These scans are much faster than absorbance scans as monochromatic light passes through entire sector at once to produce horizontal fringes, which are bent according to the concentration profile in the solution. The fringe distribution is recorded as a *.IP file, and converted to a single line using a Fourier transformation.

Rotation in a centrifuge creates a centrifugal force, which acts as gravitational field and causes mass to redistribute. The separation of molecules depends on molecular weight, as molecules with a higher mass sediment more rapidly; and the structure, as molecules which have higher frictional ratios sediment more slowly.

There are two forms of analysis that can be performed using an analytical ultracentrifuge. Sedimentation velocity experiments are performed at high rotor speeds, which generate a high centrifugal field. This force is so great that the effects of back diffusion are small, but size and shape of molecules will both have an impact on the rate of sedimentation. As time passes and molecules are depleted from the cell closer to the centre of rotation, a boundary forms between the depleted solute region and the solution region. The rate of movement of this boundary is measured to give the sedimentation coefficient.

Sedimentation equilibrium is performed at lower rotor speeds, which generate a weaker centrifugal field. Here, an equilibrium will form between the sedimentation forces and those of back diffusion, giving an even distribution of concentrations throughout the cell. As the

two forces are balanced, friction (and therefore shape of the molecule) has no impact on the spread of concentrations, so it is possible to measure molecular weight.

These two methods are descried in Figure 3.3, and the theory given in more detail in sections 3.7 and 3.8.

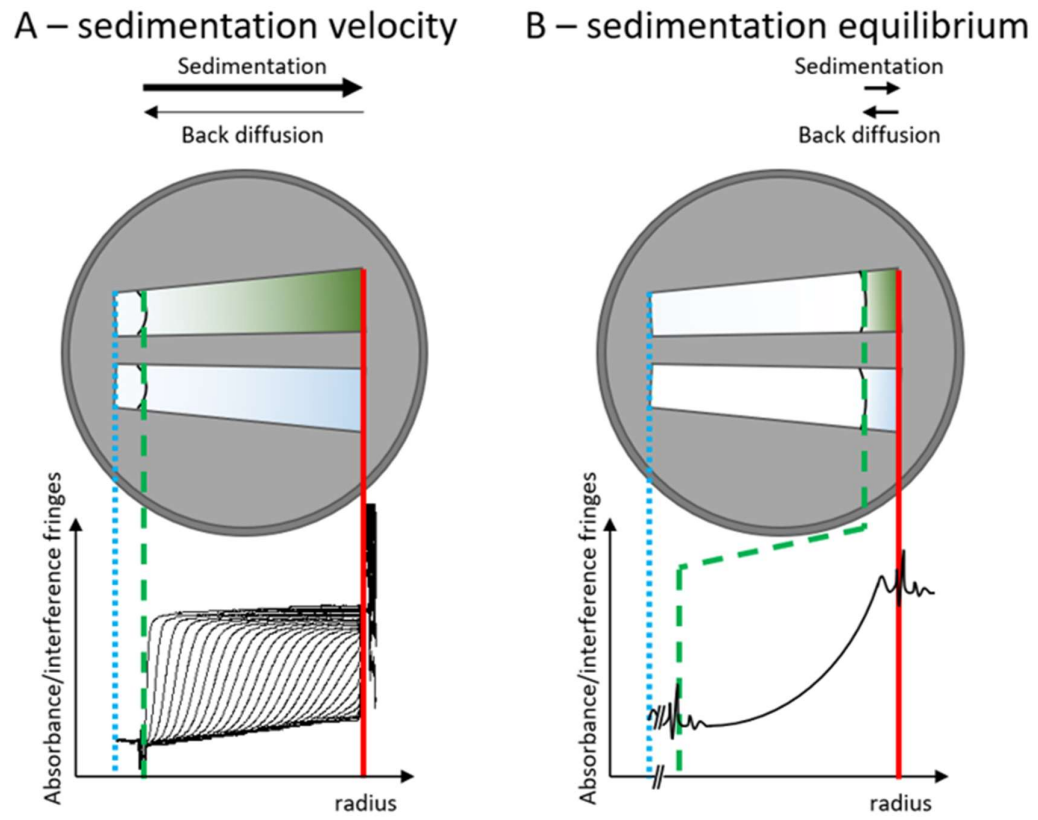


Figure 3.3 – Diagram showing the outputs of sedimentation velocity and sedimentation equilibrium experiments. The position of the cell top is shown by a blue dotted line, the meniscus by a green dashed line, and the cell base by a solid red line. A, on the left, shows an example of a sedimentation velocity experiment. The cell is almost completely filled with sample. The centrifugal force outweighs the effects of back diffusion, and so the sample sediments over time. The graph shows the readings given by the laser, appearing as an array of sigmoidal curves. The sharp increase shows the position of the boundary between the solvent region (from which sample has been depleted) and the region where solute is still present. The rate of movement of this boundary is used to give the sedimentation coefficient. B, on the right, shows an example of a sedimentation equilibrium experiment. The cell contains a much lower volume. The effects of sedimentation and back diffusion are balanced, and the system is at equilibrium. Rather than a sharp boundary between solute and solution, there is a gradual increase in concentration towards the cell base. The shape of this single curve is used to ascertain the molecular weight.

3.7 Sedimentation velocity

Sedimentation velocity establishes the sedimentation coefficient, s, using the Svedberg Equation:

$$s = \frac{v}{\omega^2 r} = \frac{M(1-\bar{v}\rho_0)}{N_A f} = \frac{M(1-\bar{v}\rho_0)D}{N_A k_B} = \frac{M(1-\bar{v}\rho_0)D}{RT} \quad (7)$$

where s is the sedimentation coefficient, v is the velocity of boundary movement, $\omega^2 r$ is the angular acceleration, M is the molar mass, $\bar{v}$ is the partial specific volume, ρ_0 is the density of the solvent, N_A is Avogadro's constant, f is the frictional coefficient, D is the diffusion coefficient, k_B is the Boltzmann constant, R is the molar gas constant, and T is the temperature.

This equation gives $s_{T,b}$, the sedimentation coefficient at an arbitrary set of temperature and buffer conditions. This must be converted to a sedimentation coefficient under a standard set of conditions to allow comparison between different experiments: $s_{20,w}$, sedimentation coefficient at 20˚C and a buffer with the density of water. This is done using the equation:

$$s_{20,w} = \frac{1-\bar{v}\rho_{20,w}}{1-\bar{v}\rho_{T,b}} . \frac{\eta_{T,b}}{\eta_{20,w}} . s_{T,b} \quad (8)$$

where s is sedimentation coefficient, ρ is the density and η is the viscosity at either experimental conditions (subscript *T,b*) or standard conditions (subscript *20,w*).

The value is heavily dependent on concentration due to the effects of non-ideality, described by the equation:

$$\frac{1}{s_{20,w}} = \frac{k_s}{s^\circ_{20,w}} c + \frac{1}{s^\circ_{20,w}} \quad (9)$$

where k_s is the concentration dependent Gralen parameter, c is concentration and the symbol ˚ indicates that the value has been corrected for non-ideality effects. Plotting the reciprocal of $s_{T,b}$ against c gives the reciprocal of $s^\circ_{20,w}$. However, if the k_s value is close to zero, meaning the gradient iss a flat line, an average of each data point can instead be taken. As this gives an average from a range of data, this allows a statistical test to be performed and compare results, which otherwise is not possible using the techniques in this thesis.

The Svedberg equation can be used to analyse monodisperse systems where only the rate of boundary movement is analysed. However, if the system is polydisperse then the boundary shape is also important due to the boundary spreading over time with diffusion. These shape effects are described by the Lamm Equation:

$$\frac{dc}{dt} = D\left[\left(\frac{d^2c}{dr^2}\right) + \frac{1}{r}\left(\frac{dc}{dr}\right)\right] - s\omega^2\left[r\left(\frac{dc}{dr}\right) + 2c\right] \quad (10)$$

where c is the concentration, t is time, D is the diffusion coefficient, r is the radius, s is the sedimentation coefficient and ω is angular velocity. The equation can be solved using an algorithm to fit the data and find an optimal solution, as in the program SEDFIT. SEDFIT was written by Schuck in 2000 [233], later updated by Dam and Schuck in 2004 [234], with the latest version, 16.1c, made in 2019. The program finds solutions to the Lamm Equation, solved in terms of apparent distribution of sedimentation coefficients. This gives a plot, the least squares Gaussian fit of sedimentation coefficient distribution ls-g*(s) vs $s_{20,w}$. The * here refers to the values not yet being corrected to account for non-ideality. SEDFIT superimposes a stepped model onto the real data which is analysed. The software also removes noise in the data, both time invariant (patterns which do not change over the course of the run) and radial invariant (artifacts of Fourier transformation).

Once analysed, the sedimentation coefficient of peaks were recorded and the reciprocals taken. These values were plotted against loading concentration and extrapolated to zero concentration to correct for the effects of non-ideality as in Equation (9). Multiple readings were not taken for these experiments. Instead the error in peak value is given by SEDFIT and incorporated by the graphing software Origin 6.1 when extrapolating the data to give an error for the y intercept, which can then be converted into an error for $s^{\circ}_{20,w}$.

In addition, as the gradient in many cases is near zero, the sedimentation coefficient can be viewed as concentration independent. Therefore, it is possible the treat the data set as a set as a series of repeated measurements. This allows a statistical test such as a student's T test

to be performed to assess whether the differences between measured sedimentation coefficient are significant.

An Optima XL-I analytical ultracentrifuge (Beckman, Palo Alto, USA) set at 20 °C with Rayleigh interference optics was used in these experiments. 395 µL of sample and 405 µL of dialysate were injected into 12 mm double sector epoxy cells with sapphire windows and analysed while spinning at 44000 rpm. Scans were taken at one-minute intervals.

3.8 Sedimentation equilibrium

These experiments are performed at lower speeds, allowing the sedimentation effects to reach an equilibrium with backflow diffusion effects [231]. In this equilibrium state, the distribution of material along the length of the sector will form an even curve, the gradient of which links to the centrifuge settings and molecular weight in the equation below:

$$\omega^2 r M(1-\bar{v}\rho_0) = \frac{RT}{c(r)}\frac{dc(r)}{dr} \qquad (11)$$

where $\omega^2 r$ is the centrifugal acceleration, M is the molar mass, $\bar{v}$ is the partial specific volume, ρ_0 is the density of the solvent, R is the molar gas constant, and T is the temperature, c is the concentration and r is the radius. This allows the shape of the curve to be used to calculate molecular weight. While the shape of a molecule can impact the time taken to reach equilibrium, no terms in Equation (11) involve the shape as forces are balanced, so shape has no effect on analysis. It is an absolute method to determine molecular weight [235]. The rotor speed is selected to provide a curve which is convenient to analyse; high enough that material is depleted from the area near the meniscus but not so high that all material sediments to the cell base. As the curve formed will be exponential, it can be described by the equation:

$$\frac{dln(c)}{dr^2} = \frac{\omega r^2 M(1-\bar{v}\rho_0)}{2RT} \qquad (12)$$

Indicating that a plot of ln(*c*) against r^2 will give a linear line, the gradient of which can be used to calculate molecular weight. However, there is an added complication. Highly polydisperse samples can form an upward curve in this graph, while non-ideality effects can cause a downward curve, both of which prevent accurate analysis. In addition, these two effects can balance out if a sample is both highly non-ideal and polydisperse, which can be misleading. For this reason, an alternative analysis is often used, particularly for polydisperse molecules such as polysaccharides.

An alternative analysis, *M** [236], uses an integral of the equilibrium distribution curve to find trends in the molecular weight throughout the distribution:

$$M^*(r) = \frac{c(r) - c(a)}{kc(a)(r^2 - a^2) + 2k\int_a^r [c(r) - c(a)]dr} \quad (13)$$

where *a* is the radial displacement at the meniscus, and *k* is a collection of constants for a given experiment:

$$k = \frac{(1 - \bar{\nu}\rho_0)\omega^2}{2RT} \quad (14)$$

where *ω* is angular velocity.

At the cell base, the value given by *M** will be the average molecular weight of the whole distribution. As this value is still impacted by non-ideality effects, it is referred to as the apparent molecular weight, $M_{w,app}$. The value of *M*(r)* approaches $M_{w,app}$ as calculations are made closer to the cell base, but the cell base itself usually has more optical distortion so it is not appropriate to calculate *M** here. Instead, *M*(r)* is calculated at a number of radial positions and then extrapolated to give the value at the cell base [237].

The M* Equation has been incorporated into SEDFIT to make the program SEDFIT-MSTAR [238]. This analyses samples as described in Equation (13), while also performing hinge point analysis. At the radial position of the inflection point of the initial distribution curve, the local

concentration will equal the cell loading concentration. Calculating the local $M_{w,app}$ at this position in Equation (12) will therefore give the apparent molecular weight across the whole distribution. The value from hinge point analysis is usually slightly less accurate because it comes from differentiation of the ln(c) vs r^2 plot, which produces inherently noisy data unless smoothing routines are applied [238]. Using both methods provides corroboration for the measurement. As with sedimentation velocity, to correct for non-ideality, the reciprocal of $M_{w,app}$ is plotted against loading concentration and extrapolated to zero concentration to give the true value of M_w.

An Optima XL-I analytical ultracentrifuge (Beckman, Palo Alto, USA) set at 20 °C with Rayleigh interference optics was used in these experiments. 95 µL of sample and 105 µL of dialysate were injected into 12 mm double-sector epoxy cells with sapphire windows and analysed while spinning at 10000 rpm. The interference system recorded changes in concentration in fringe units against radial displacement over time, and the experiment was stopped when the system had reached equilibrium. The analysis was repeated using the error of the $\bar{v}$ and density values to give maximum and minimum values. The values of $M_{w,app}$ (from the M^* function and from hinge point analysis) were plotted in Origin 6.1 and used to extrapolate to zero concentration to correct for the effects of non-ideality.

3.9 SEC-MALS

Size Exclusion Chromatography and Multi-Angle Light Scattering (SEC-MALS) is a process whereby samples are separated (by SEC), then analysed to determine molecular weight (by MALS). Size exclusion chromatography uses a column packed with a matrix of porous beads through which samples can be pumped at a constant rate. This separates molecules based on their size: smaller molecules can enter the pores and are thus retained on the column for a longer time, while larger molecules are excluded from the pores, and so are not retained in the column and pass through quickly [239]. Samples will therefore elute from the column in

order of descending molecular weight, which allows molecular weight measurement by recording elution time and comparing it to a series of standards. However, these standards must have the same conformation as the molecule under analysis, as the shape of the molecule will impact the elution time. This can be difficult when analysing polysaccharides as they tend to have a more variable conformation. To circumvent this problem, as well as to improve its utility in general, the technique can be made more powerful by incorporating a MALS detection system, an absolute method for determining molecular weight that does not rely on standards.

Particles of sufficient size will scatter light in solution, which will be of equal intensity in all directions for spherical molecules. For non-spheres, the intensity varies with scattering angle, and so measurements must be taken at multiple angles. Molar mass can then be calculated using an extrapolation of the Zimm Equation [240]:

$$\frac{Kc}{\Delta R(\Theta, c)} = \frac{1}{M}\left(1 + \frac{q^2 R_g^2}{3}\right) + 2B_2 c \qquad (15)$$

where *K* is defined in Equation (16), *c* is the concentration, *ΔR(Θ,c)* is the Rayleigh ratio at a specific wavelength as defined in Equation (17), *M* is the molecular weight, *q* is the wave vector as defined in Equation (19), R_g is the radius of gyration and B_2 is the second virial coefficient (a term relating to non-ideality).

K is a collection of constants:

$$K = \frac{4\pi^2 n_0^2 \left(\frac{dn}{dc}\right)^2}{N_A \lambda^4} \qquad (16)$$

where n_0 is the solvent refractive index, *dn/dc* is the refractive increment, N_A is the Avogadro constant and λ is the wavelength.

$$\Delta R(\Theta, c) = R_s(\Theta) - R_0(\Theta) \qquad (17)$$

The Rayleigh ratio is dependent on solution properties:

where the subscript *s* refers to solute properties and the subscript *0* refers to solvent properties. $R_s(\Theta)$ is defined by the equation:

$$R_s(\Theta) = \frac{I_s(\Theta) n_0^2 R_c}{I_c(\Theta) n_c^2 N(\Theta)} \quad (18)$$

where *I* is the intensity, *n* is the refractive index, subscript *c* refers to a calibration constant on the instrument, $N(\Theta)$ is a normalisation constant on the instrument.

The wave vector *q*, is a constant in a specific solvent at a defined wavelength and scattering angle:

$$q = \frac{4\pi n_0}{\lambda} \sin\left(\frac{\Theta}{2}\right) \quad (19)$$

Extrapolation of equation to where both angle and concentration are zero in a Zimm plot can be used to find both *M* and R_g. As these equations also rely on concentration measurements, this information is provided through refractive index measurements. Further information is also provided by viscosity measurements, which can be linked to specific molecular weights through elution time.

For this project, the SEC portion consisted of a Postnova Analysis PN7505 degassing unit, a Shimadzu LC-10 AD HPLC Pump, a Spark-Holland Marathon Basic autosampler, a Shodex™ LB-G 6B guard column and a Shodex™ LB-805 column connected in series. MALS intensities were simultaneously measured at 18 angles as a function of elution volume using a DAWN® HELEOS™ II light-scattering photometer, connected in series to a ViscoStar® II on-line differential viscometer and an Optilab® rEX refractive index detector. A 4 mW He-Ne laser was used at a wavelength of 632.8 nm, and the refractive increment for all samples was taken as 0.147 $mL.g^{-1}$ from the information supplied in Table 3-1. Samples were filtered using Whatman® Puradisc 25 syringe filters, 0.2 µm, PVDF and a 50 µL aliquot of each solution was injected onto the columns at room temperature. The eluent employed was 0.1M NaCl with

0.01% ProClin™ 150 (Sigma-Aldrich®) at a flow rate of 0.5 mL.minute^{-1}. ASTRA™ (Version 6) software was used to calculate the weight-average molecular weight (M_w) polydispersity, (M_w/M_n) and weight-average intrinsic viscosity ($[\eta]_w$). As samples are constantly diluted on the columns, concentrations are low enough that non-ideality effects are assumed to be negligible.

SEC-MALS provides a valuable orthogonal technique to the analytical ultracentrifuges and to the classical or capillary viscometry.

4 Baseline measurements

To compare the stability of a molecule to anything, the initial parameters must be measured. These are summarised in Table 4-1 on page 96, and these results will be used to make comparisons in all subsequent work.

4.1 Native GBS polysaccharide, serotype IA

4.1.1 Concentration series

After dialysis, the concentration of the stock solution was too high to measure on the refractometer. A one-in-two dilution was therefore performed and the concentration measured, and this value was doubled to give the initial stock concentration. The initial reading was (0.437 ± 0.020) Brix(%), corresponding to (4.33 ± 0.20) $mg.mL^{-1}$, and thus (8.66 ± 0.40)$mg.mL^{-1}$ of stock solution. This was diluted as previously stated in Table 3-2.

4.1.2 Density and $\bar{v}$ determination

Density was measured and the results plotted against concentration, as shown in Figure 4.1. Using the slope of this graph, $\bar{v}$ was calculated as (0.642 ± 0.018) $mL.g^{-1}$. The dialysate density was measured as (1.003861 ± 0.000003) $g.mL^{-1}$.

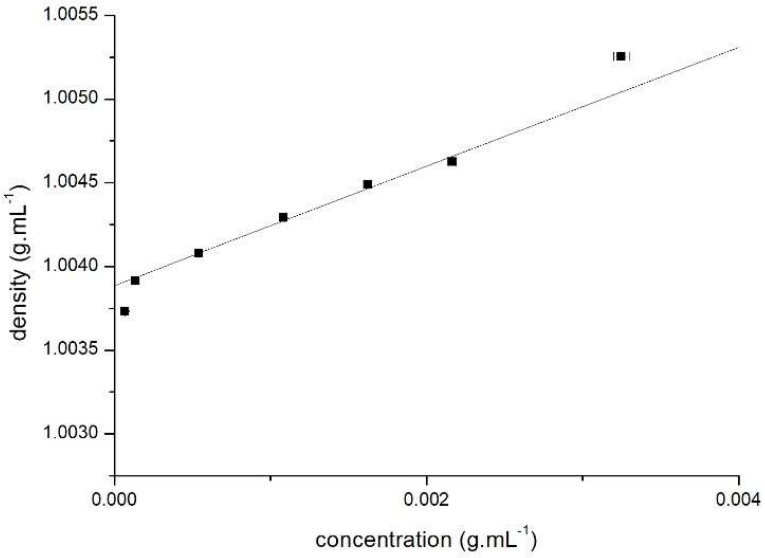


Figure 4.1 – Plot of density against concentration for N-IA, with a linear fit to obtain gradient.

4.1.3 Viscosity

Plotting the relevant viscosity functions and extrapolating back to where the concentration is zero in Figure 4.2 gives the intrinsic viscosities as (220 ± 5) $mL.g^{-1}$ (Huggins), (216 ± 2) $mL.g^{-1}$ (Kraemer) and (220 ± 3) $mL.g^{-1}$ (Solomon-Ciuta). The mean average value of these is (218 ± 2) $mL.g^{-1}$.

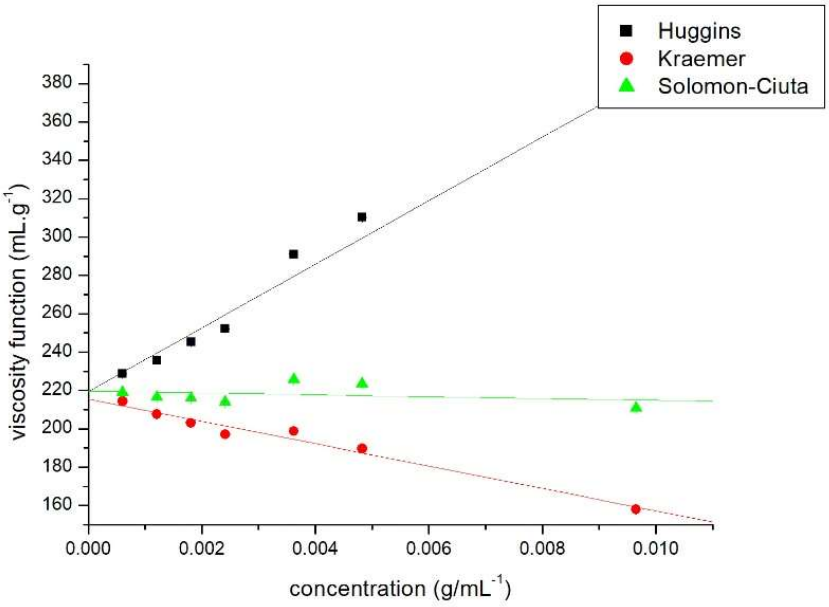


Figure 4.2 – Plot of viscosity against concentration for N-IA, with linear fits to extrapolate to zero concentration.

4.1.4 Sedimentation velocity

The distribution of sedimentation coefficients is shown in Figure 4.3. The peak data for the main component was also plotted against the loading concentration in Figure 4.4 and extrapolated back to zero concentration, giving the sedimentation coefficient as (5.02 ± 0.59) S. If instead the data set is treated as a set of repeated measurements (as discussed on page 50), then the sedimentation coefficient can instead be calculated as (4.32 ± 0.44) S. However, in this case it may not be appropriate as the gradient is relatively high.

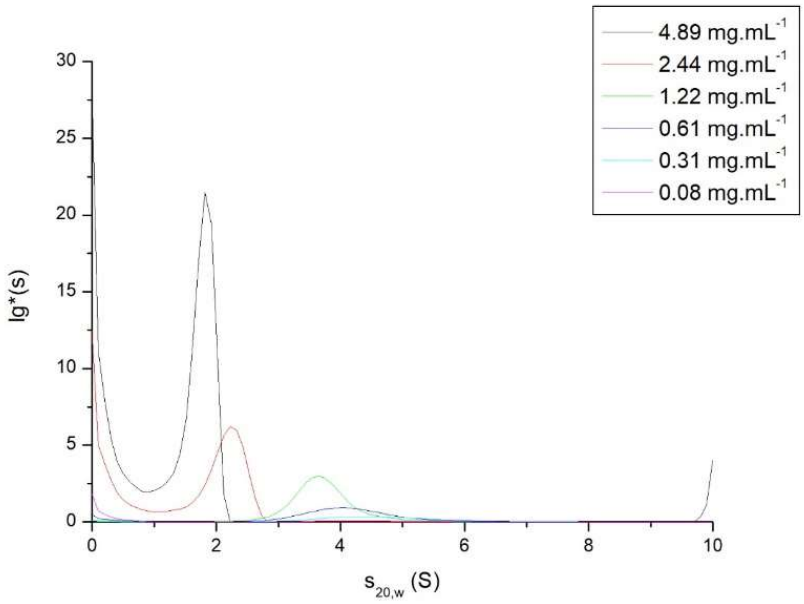


Figure 4.3 – Distribution of sedimentation coefficients at a range of loading concentrations of N-IA.

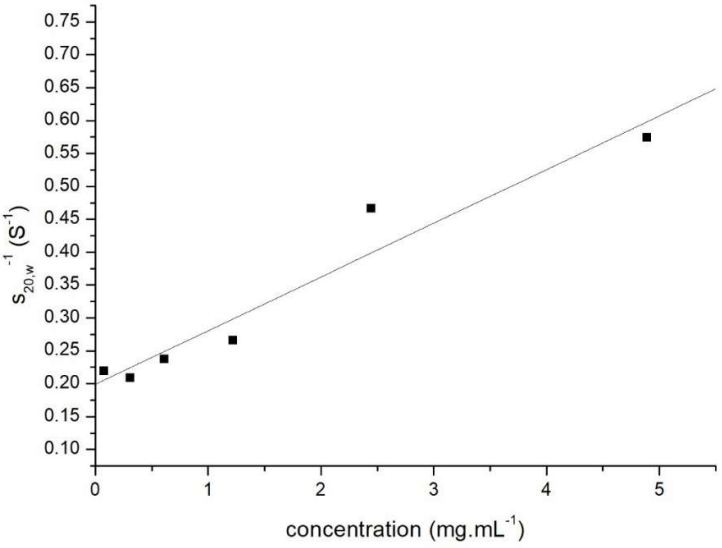


Figure 4.4 – Plot of the reciprocal of sedimentation coefficient against loading concentration for N-IA, with a linear fit to extrapolate to zero concentration.

4.1.5 Sedimentation equilibrium

SEDFIT-MSTAR provides two methods of determining apparent molecular weight, $M_{w,app}$: from the M^* function and from hinge point analysis. The values given by the program are plotted against loading concentration in Figure 4.5. Extrapolation to zero concentration gave 'thermodynamically ideal' values of M_w as (361 ± 37) kDa (from the M* method) and (329 ± 21) kDa (from the hinge method). Combining the two yields a consensus value for Mw of (345 ± 21) kDa.

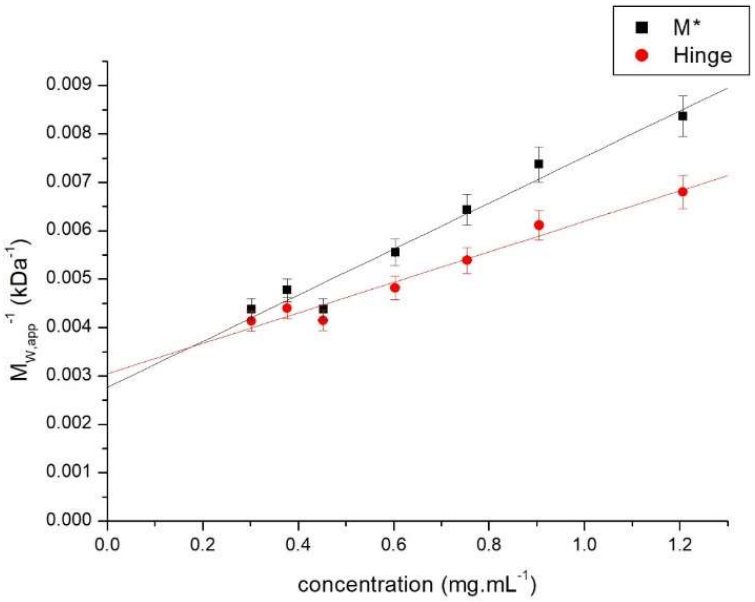


Figure 4.5 – Plot of the reciprocal of apparent molecular weight ($M_{w,app}$) values against loading concentration of N-IA, with a linear fit to extrapolate to zero concentration.

4.1.6 SEC-MALS

The M_w was determined to be (292 ± 1) kDa, with a polydispersity (M_w/M_n) of 1.077 ± 0.003. [η] was found to be 180 mL.g^{-1}, although no error is described at this level of precision.

4.2 Native GBS polysaccharide, serotype IB

4.2.1 Concentration series

After dialysis, the concentration was measured on the refractometer. The initial reading was 0.871 Brix(%), corresponding to 8.63 mg.mL^{-1}. This was diluted as previously stated in Table 3-2. Error is not reported for these values as it is too low to make an impact at three significant figures.

4.2.2 Density and $\bar{v}$ determination

Density was measured and the results plotted against concentration in Figure 4.6. Using the slope of this graph, $\bar{v}$ was calculated as (0.622 ± 0.006) mL.g^{-1}.The dialysate density was measured as (1.002544 ± 0.000002) g.mL^{-1}.

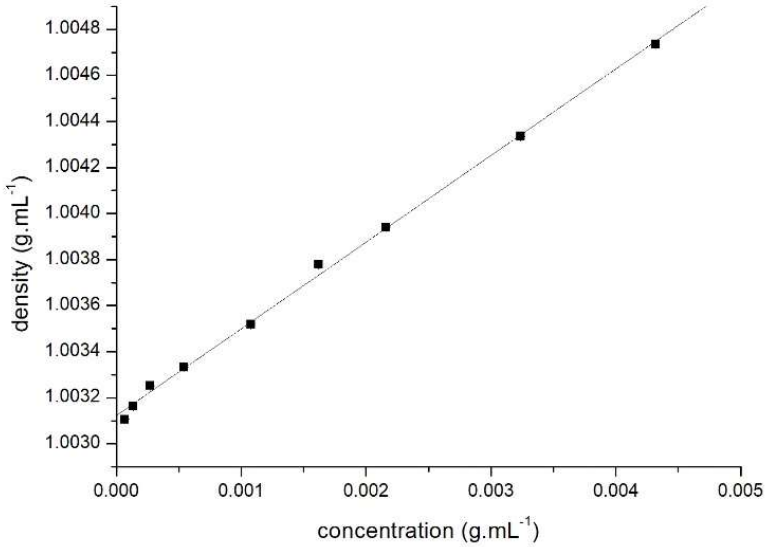


Figure 4.6 – Plot of density against concentration for N-IB, with a linear fit to obtain gradient.

4.2.3 Viscosity

Plotting the relevant viscosity functions and extrapolating back to where the concentration is zero in Figure 4.7 gives the intrinsic viscosities as (136 ± 1) mL.g^{-1} (Huggins), (136 ± 1) mL.g^{-1}

(Kraemer) and (136 ± 1) $mL.g^{-1}$ (Solomon-Ciuta). The mean average value of these is 136 $mL.g^{-1}$, although no error is described at this level of precision.

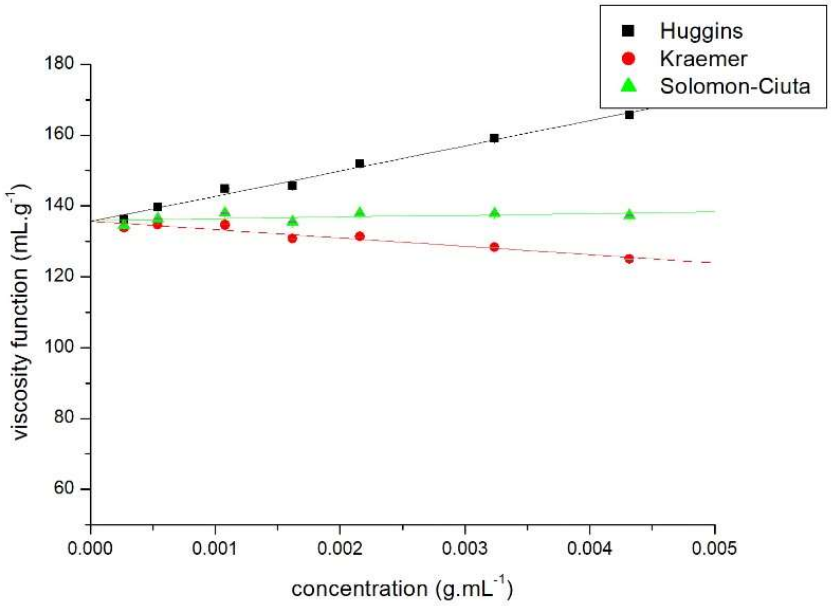


Figure 4.7 – Plot of viscosity against concentration for N-IB, with a linear fit to extrapolate to zero concentration.

4.2.4 Sedimentation velocity

The distribution of sedimentation coefficients is shown in Figure 4.8. The peak data was plotted against the loading concentration in Figure 4.9 and extrapolated back to zero concentration, giving the sedimentation coefficient as (4.05 ± 0.07) S. As the gradient is close to zero, the data can be treated as a set of repeated measurements (as discussed on page 50). The sedimentation coefficient can instead be calculated as (3.72 ± 0.16) S.

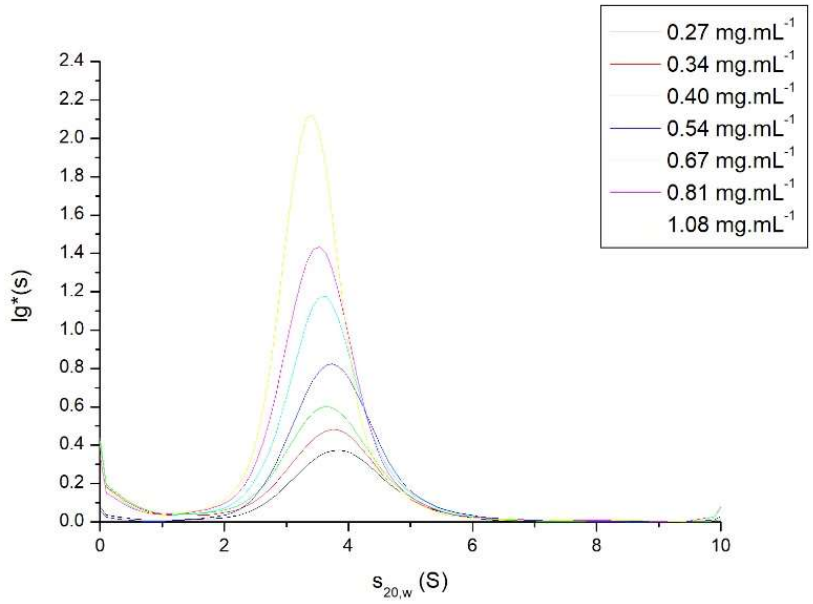


Figure 4.8 – Distribution of sedimentation coefficients at a range of loading concentrations of N-IB.

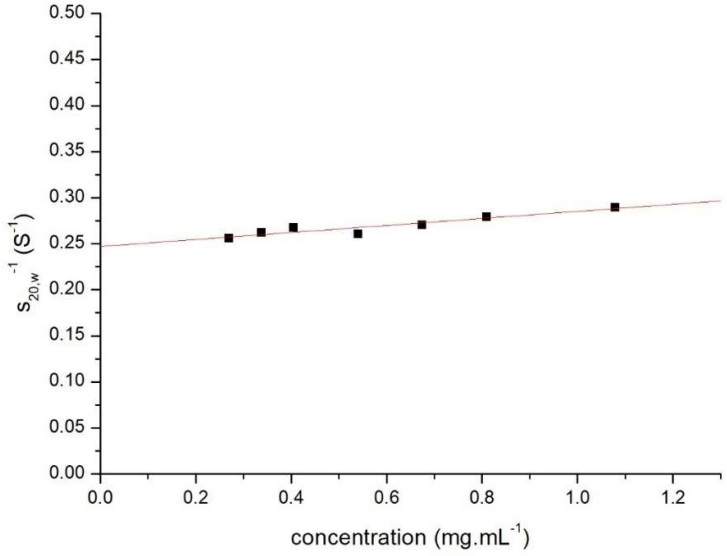


Figure 4.9 – Plot of the reciprocal of sedimentation coefficient against loading concentration for N-IB, with a linear fit to extrapolate to zero concentration.

4.2.5 Sedimentation equilibrium

SEDFIT-MSTAR provides two methods of determining apparent molecular weight, $M_{w,app}$:

from the M^* function and from hinge point analysis. The values given by the program are

plotted against loading concentration in Figure 4.10. Extrapolation to zero concentration gave 'thermodynamically ideal' values of M_w as (189 ± 15) kDa (from the M* method) and (164 ± 7) kDa (from the hinge method). Combining the two yields a consensus value for Mw of (176 ± 8) kDa.

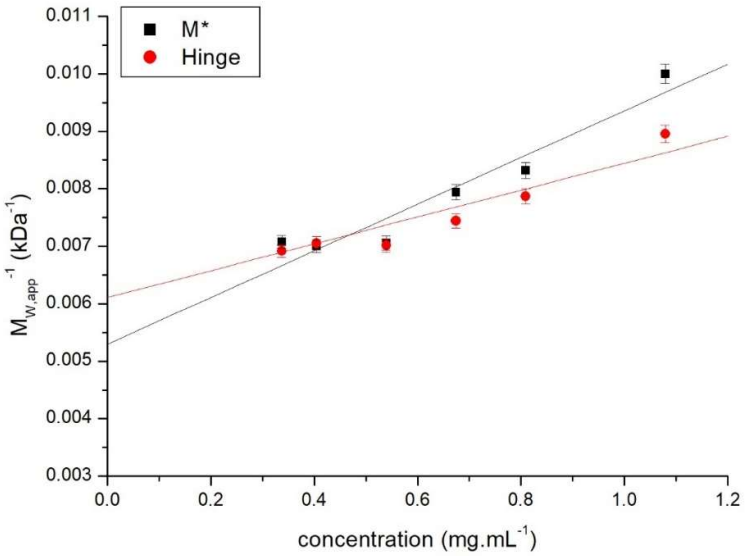


Figure 4.10 – Plot of the reciprocal of the apparent molecular weight ($M_{w,app}$) values against loading concentration of N-IB, with linear fits to extrapolate to zero concentration..

4.2.6 SEC-MALS

The M_w of the main peak was determined to be 154 kDa, (although no error is described at this level of precision), with a polydispersity (M_w/M_n) of 1.061 ± 0.004. [η] was found to be (102 ± 1) mL.g^{-1}.

4.3 Native GBS polysaccharide, serotype II

4.3.1 Concentration series

After dialysis, the concentration was measured on the refractometer. The initial reading was 0.997 Brix(%), corresponding to 9.88 mg.mL^{-1}. This was diluted as previously stated in Table 3-2. Error is not reported for these values as it is too low to make an impact at three significant figures.

4.3.2 Density and $\bar{v}$ determination

Density was measured and the results plotted against concentration, shown in Figure 4.11. Using the slope of this graph, $\bar{v}$ was calculated as (0.627 ± 0.005) mL.g^{-1}.The dialysate density was measured as 1.003083 g.mL^{-1}, although no error is described at this level of precision.

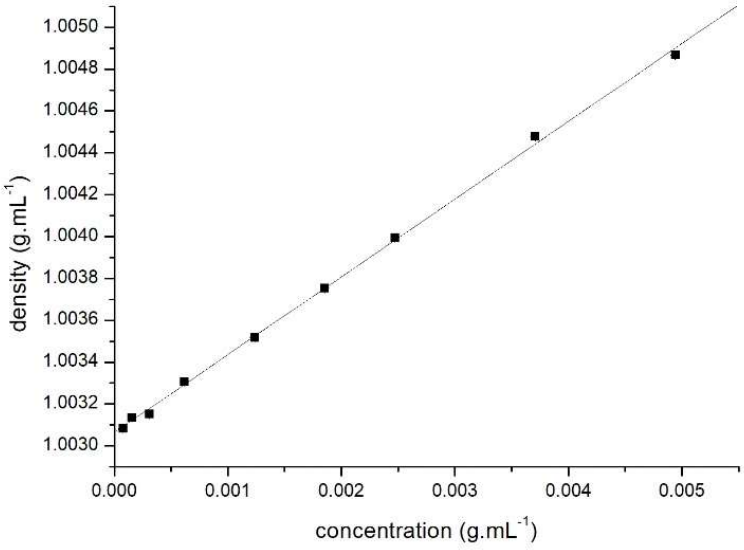


Figure 4.11 – Plot of density against concentration for N-II, with a linear fit to obtain gradient.

4.3.3 Viscosity

Plotting the relevant viscosity functions and extrapolating back to where the concentration is zero in Figure 4.12 gives the intrinsic viscosities as (126 ± 1) mL.g^{-1} (Huggins), (127 ± 1) mL.g^{-1}

(Kraemer) and (127 ± 1) mL.g^{-1} (Solomon-Ciuta). The mean average value of these is (127 ± 1) mL.g^{-1}.

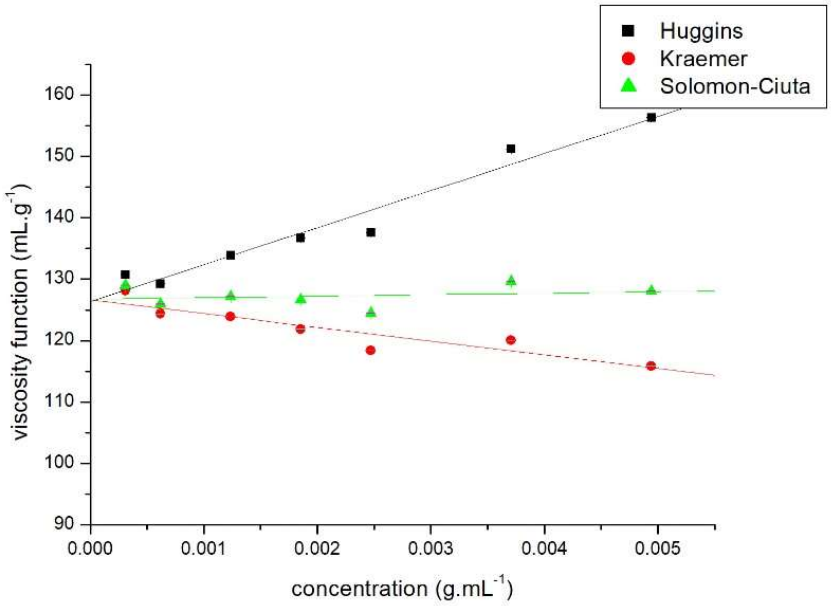


Figure 4.12 – Plot of viscosity against concentration for N-II, with linear fits to extrapolate to zero concentration.

4.3.4 Sedimentation velocity

The distribution of sedimentation coefficients is shown in Figure 4.13. The peak data for the main component was also plotted against the loading concentration in Figure 4.14 and extrapolated back to zero concentration, giving the sedimentation coefficient as (6.05 ± 0.26) S. As the gradient is close to zero, the data can be treated as a set of repeated measurements (as discussed on page 50). The sedimentation coefficient can instead be calculated as (5.85 ± 0.27) S.

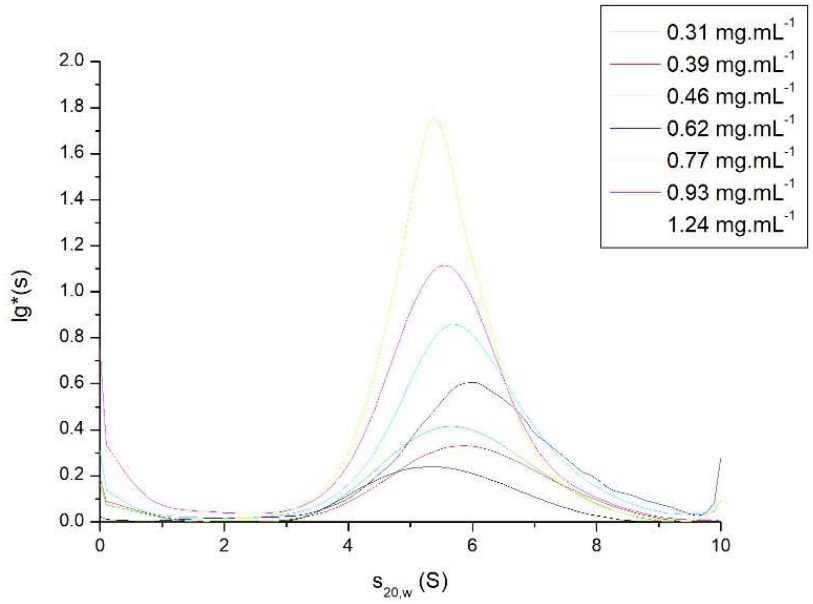


Figure 4.13 – Distribution of sedimentation coefficients at a range of loading concentrations of N-II.

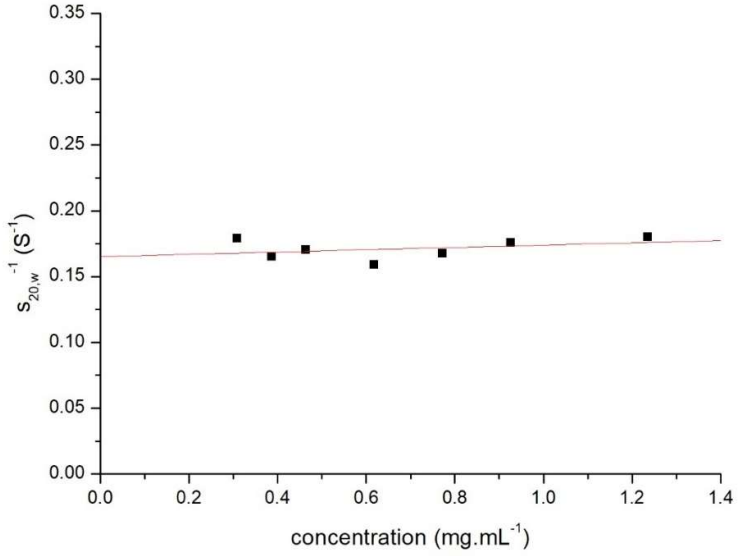


Figure 4.14 – Plot of the reciprocal of sedimentation coefficient against loading concentration for N-II, with a linear fit to extrapolate to zero concentration.

4.3.5 Sedimentation equilibrium

SEDFIT-MSTAR provides two methods of determining apparent molecular weight, $M_{w,app}$:

from the M^* function and from hinge point analysis. The values given by the program are

plotted against loading concentration in Figure 4.15. Extrapolation to zero concentration gave 'thermodynamically ideal' values of M_w as (328 ± 9) kDa (from the M* method) and (310 ± 16) kDa (from the hinge method). Combining the two yields a consensus value for Mw of (319 ± 9) kDa.

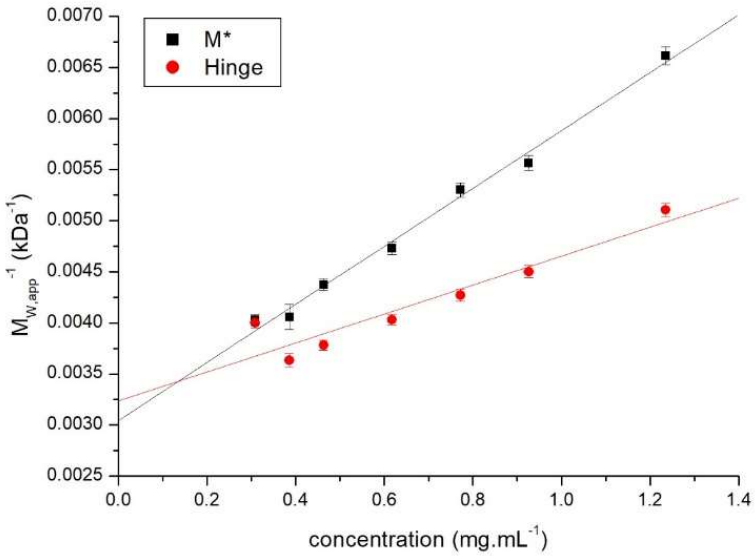


Figure 4.15 – Plot of the reciprocal of the apparent molecular weight ($M_{w,app}$) values against loading concentration of N-II, with linear fits to extrapolate to zero concentration.

4.3.6 SEC-MALS

The M_w of the main peak was determined to be (430 ± 1) kDa, with a polydispersity (M_w/M_n) of 1.125 ± 0.004. [η] was found to be (121 ± 1) mL.g^{-1}.

4.4 Native GBS polysaccharide, serotype III

4.4.1 Concentration series

After dialysis, the concentration was measured on the refractometer. The initial reading was 0.693 Brix(%), corresponding to 6.87 mg.mL^{-1}. This was diluted as previously stated in Table 3-2. Error is not reported for these values as it is too low to make an impact at three significant figures.

4.4.2 Density and $\bar{v}$ determination

Density was measured and the results plotted against concentration in Figure 4.16. Using the slope of this graph, $\bar{v}$ can be calculated as (0.661 ± 0.007) mL.g^{-1}.The dialysate density was measured as (1.002921 ± 0.000009) g.mL^{-1}.

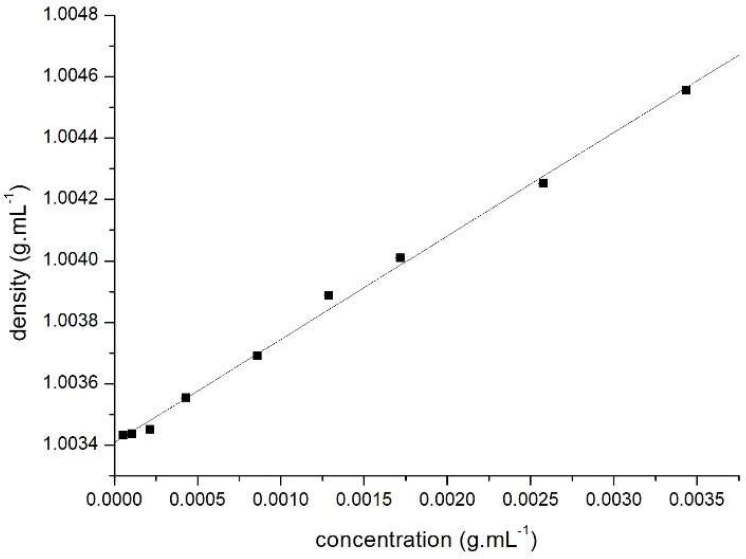


Figure 4.16 – Plot of density against concentration for N-III, with a linear fit to obtain gradient.

4.4.3 Viscosity

Plotting the relevant viscosity functions and extrapolating back to where the concentration is zero in Figure 4.17 gives the intrinsic viscosities as (45.4 ± 0.4) mL.g^{-1} (Huggins), (45.4 ± 0.4)

mL.g^{-1} (Kraemer) and (45.4 ± 0.4) mL.g^{-1} (Solomon-Ciuta). The mean average value of these is (45.4 ± 0.2) mL.g^{-1}.

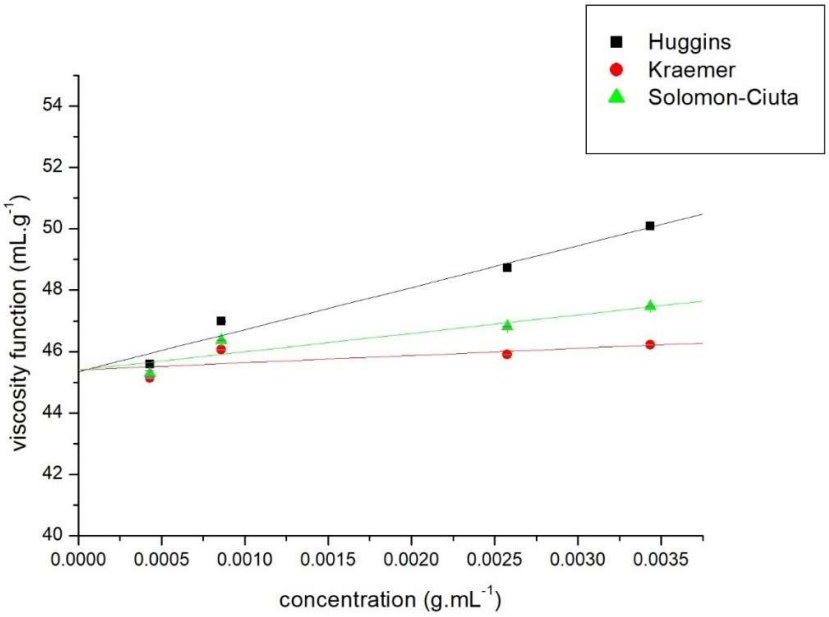


Figure 4.17 – Plot of viscosity against concentration for N-III, with linear fits to extrapolate to zero concentration

4.4.4 Sedimentation velocity

The distribution of sedimentation coefficients is shown in Figure 4.18. The peak data for the main component was also plotted against the loading concentration in Figure 4.19 and extrapolated back to zero concentration, giving the sedimentation coefficient as (3.23 ± 0.16) S. As the gradient is close to zero, the data can be treated as a set of repeated measurements (as discussed on page 50). The sedimentation coefficient can instead be calculated as (3.21 ± 0.25) S.

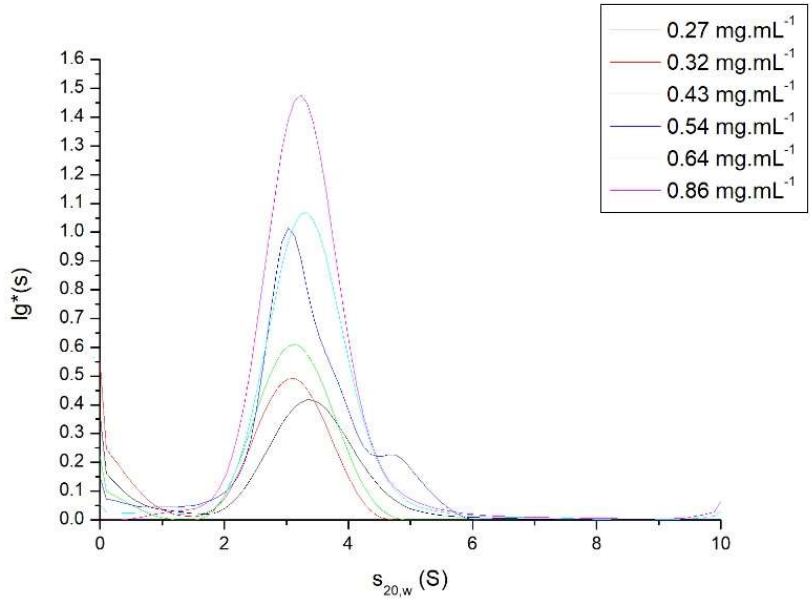


Figure 4.18 – Distribution of sedimentation coefficients at a range of loading concentrations of N-III.

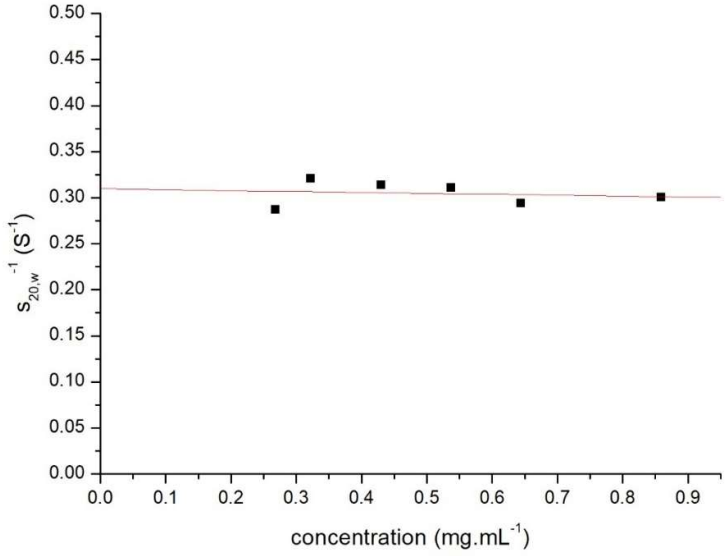


Figure 4.19 – Plot of the reciprocal of sedimentation coefficient against loading concentration for N-III, with a linear fit to extrapolate to zero concentration.

4.4.5 Sedimentation equilibrium

SEDFIT-MSTAR provides two methods of determining apparent molecular weight, $M_{w,app}$: from the M^* function and from hinge point analysis. The values given by the program are

plotted against loading concentration in Figure 4.20. Extrapolation to zero concentration gave 'thermodynamically ideal' values of M_w as (111 ± 4) kDa (from the M* method) and (116 ± 7) kDa (from the hinge method). Combining the two yields a consensus value for Mw of (13 ± 4) kDa.

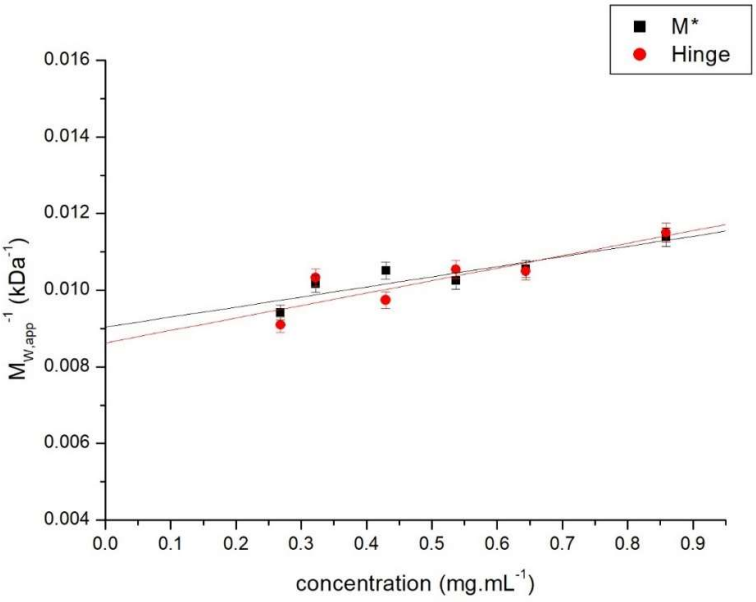


Figure 4.20 – Plot of the reciprocal of the apparent molecular weight ($M_{w,app}$) values against loading concentration of N-III, with linear fits to extrapolate to zero concentration.

4.4.6 SEC-MALS

The M_w of the main peak was determined to be (91.4 ± 0.1) kDa, with a polydispersity (M_w/M_n) of 1.006 ± 0.002. [η] was found to be (47.3 ± 0.3) mL.g^{-1}.

4.5 Native GBS polysaccharide, serotype IV

4.5.1 Concentration series

After dialysis, the concentration was measured on the refractometer. The initial reading was 0.543 Brix(%), corresponding to 5.38 mg.mL^{-1}. This was diluted as previously stated in Table 3-2. Error is not reported for these values as it is too low to make an impact at three significant figures.

4.5.2 Density and $\bar{v}$ determination

Density was measured and the results plotted against concentration in Figure 4.21. Using the slope of this graph, $\bar{v}$ can be calculated as (0.608 ± 0.005) mL.g^{-1}.The dialysate density was measured as 1.003073 g.mL^{-1}, although no error is described at this level of precision..

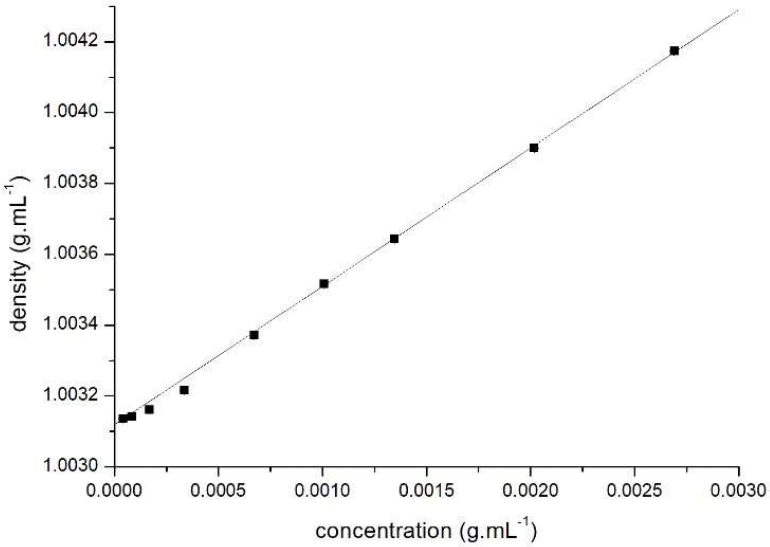


Figure 4.21 – Plot of density against concentration for N-IV, with a linear fit to obtain gradient.

4.5.3 Viscosity

Plotting the relevant viscosity functions and extrapolating back to where the concentration is zero in Figure 4.22 gives the intrinsic viscosities as (64.9 ± 1.1) mL.g^{-1} (Huggins), (65.0 ± 1.0)

mL.g^{-1} (Kraemer) and (65.0 ± 1.1) mL.g^{-1} (Solomon-Ciuta). The mean of these is (65.0 ± 0.6) mL.g^{-1}.

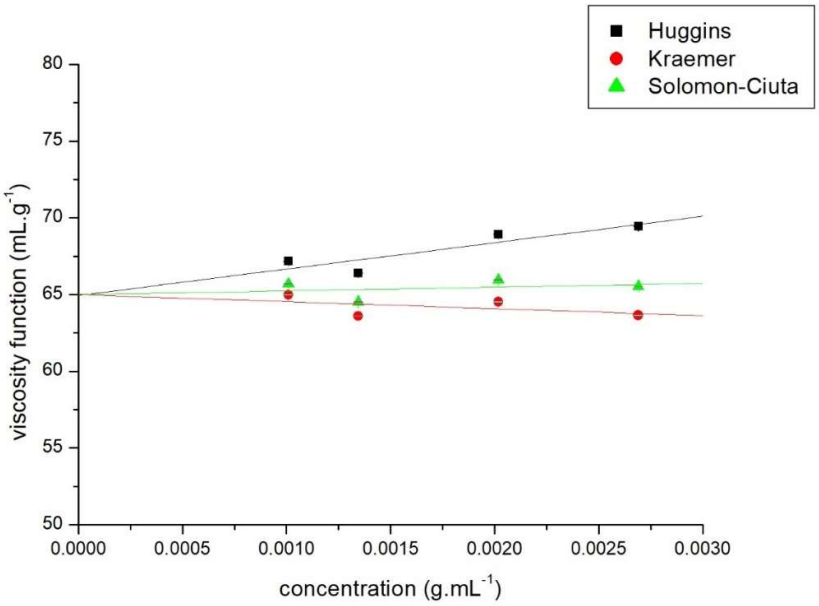


Figure 4.22 – Plot of viscosity against concentration for N-IV, with linear fits to extrapolate to zero concentration.

4.5.4 Sedimentation velocity

The distribution of sedimentation coefficients is shown in Figure 4.23. The peak data for the main component was also plotted against the loading concentration in Figure 4.24 and extrapolated back to zero concentration, giving the sedimentation coefficient as (2.56 ± 0.11) S. As the gradient is close to zero, the data can be treated as a set of repeated measurements (as discussed on page 50). The sedimentation coefficient can instead be calculated as (2.62 ± 0.12) S.

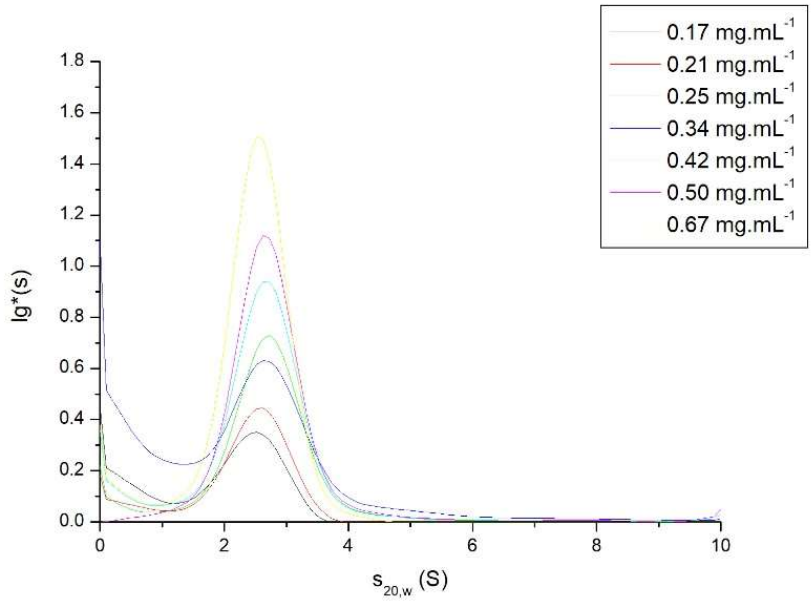


Figure 4.23 – Distribution of sedimentation coefficients at a range of loading concentrations of N-IV.

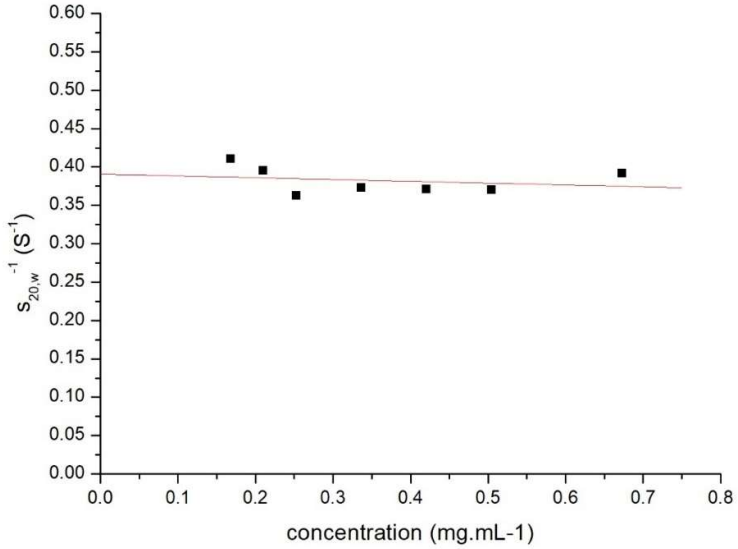


Figure 4.24 – Plot of the reciprocal of sedimentation coefficient against loading concentration for N-IV, with a linear fit to extrapolate to zero concentration.

4.5.5 Sedimentation equilibrium

SEDFIT-MSTAR provides two methods of determining apparent molecular weight, $M_{w,app}$: from the M^* function and from hinge point analysis. The values given by the program are

plotted against loading concentration in Figure 4.25. Extrapolation to zero concentration gave 'thermodynamically ideal' values of M_w as (70.8 ± 1.3) kDa (from the M* method) and (56.6 ± 1.8) kDa (from the hinge method). Combining the two yields a consensus value for Mw of (63.7 ± 1.1) kDa.

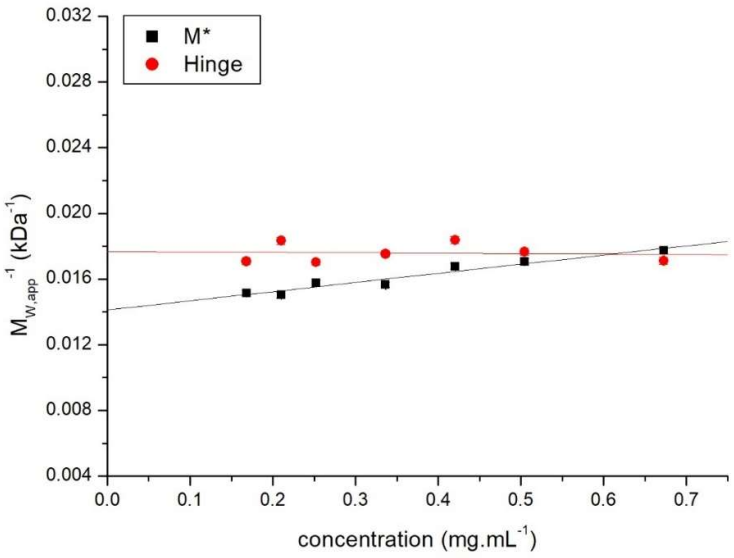


Figure 4.25 – Plot of the reciprocal of the apparent molecular weight ($M_{w,app}$) values against loading concentration of N-IV, with linear fits to extrapolate to zero concentration.

4.5.6 SEC-MALS

The M_w of the main peak was determined to be (53.4 ± 0.1) kDa, with a polydispersity (M_w/M_n) of 1.001 ± 0.003. [η] was found to be (45.9 ± 0.1) mL.g^{-1}.

4.6 Native GBS polysaccharide, serotype V

4.6.1 Concentration series

After dialysis, the concentration was measured on the refractometer. The initial reading was 0.663 Brix(%), corresponding to 6.57 mg.mL^{-1}. This was diluted as previously stated in Table 3-2. Error is not reported for these values as it is too low to make an impact at three significant figures.

4.6.2 Density and $\bar{v}$ determination

Density was measured and the results plotted against concentration in Figure 4.26. Using the slope of this graph, $\bar{v}$ can be calculated as (0.695 ± 0.005) mL.g^{-1}.The dialysate density was measured as 1.003045 g.mL^{-1}, although no error is described at this level of precision.

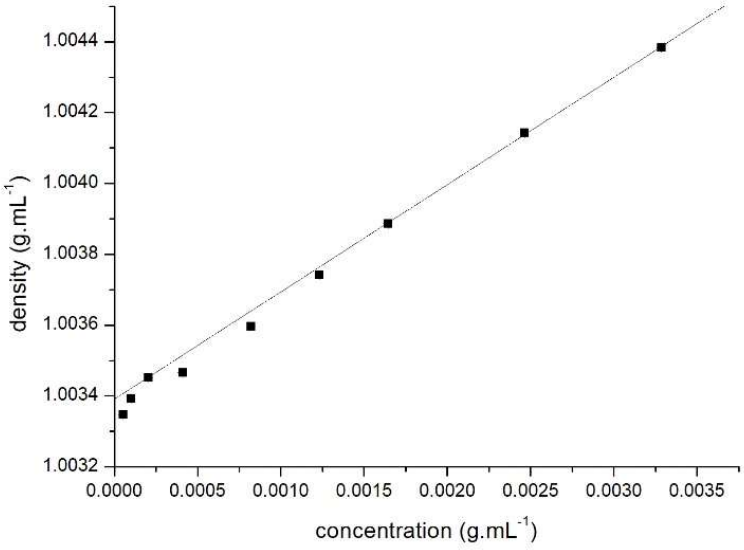


Figure 4.26 – Plot of density against concentration for N-V, with a linear fit to obtain gradient.

4.6.3 Viscosity

Plotting the relevant viscosity functions and extrapolating back to where the concentration is zero in Figure 4.27 gives the intrinsic viscosities as (81.1 ± 1.6) mL.g^{-1} (Huggins), (82.3 ± 1.6)

mL.g^{-1} (Kraemer) and (82.0 ± 1.6) mL.g^{-1} (Solomon-Ciuta). The mean average value of these is (81.8 ± 0.9) mL.g^{-1}.

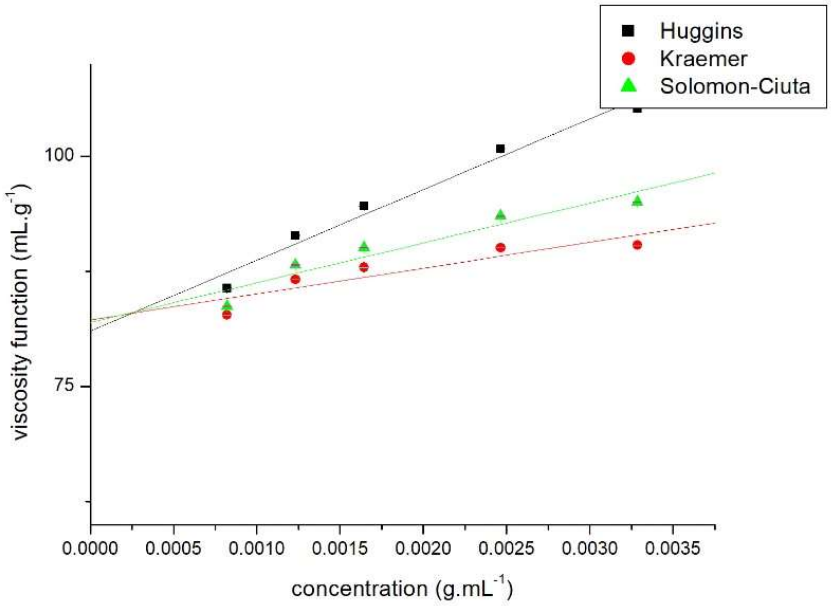


Figure 4.27 – Plot of viscosity against concentration for N-V, with linear fits to extrapolate to zero concentration.

4.6.4 Sedimentation velocity

The distribution of sedimentation coefficients is shown in Figure 4.28. The peak data for the main component was also plotted against the loading concentration in Figure 4.29 and extrapolated back to zero concentration, giving the sedimentation coefficient as (3.95 ± 0.04) S. As the gradient is close to zero, the data can be treated as a set of repeated measurements (as discussed on page 50). The sedimentation coefficient can instead be calculated as (3.71 ± 0.12) S.

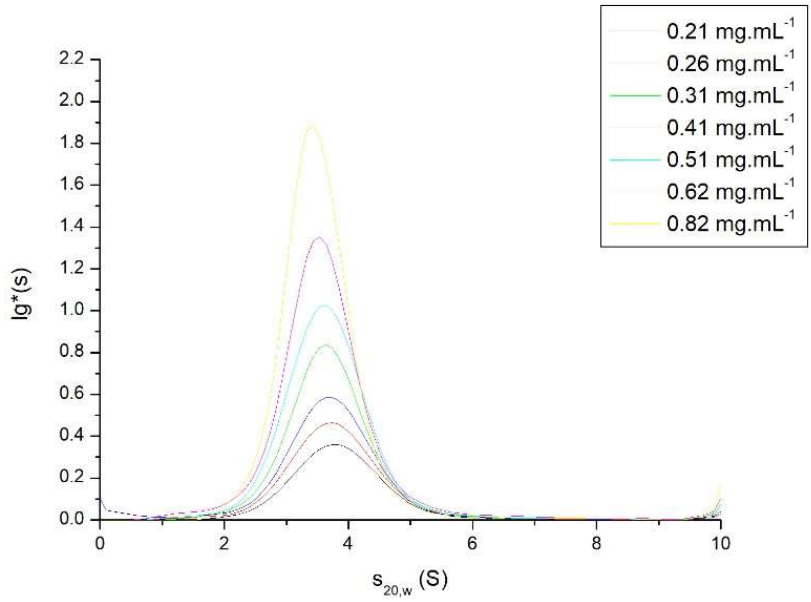


Figure 4.28 – Distribution of sedimentation coefficients at a range of loading concentrations of N-V.

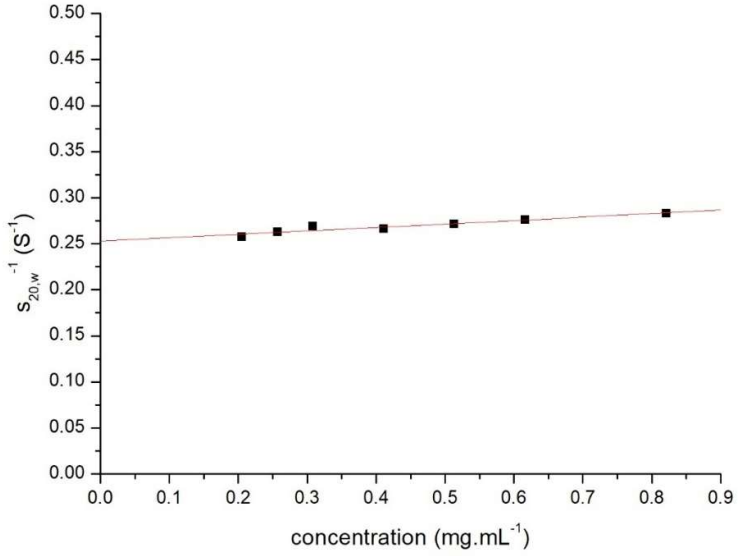


Figure 4.29 – Plot of the reciprocal of sedimentation coefficient against loading concentration for N-V, with a linear fit to extrapolate to zero concentration.

4.6.5 Sedimentation equilibrium

SEDFIT-MSTAR provides two methods of determining apparent molecular weight, $M_{w,app}$: from the M^* function and from hinge point analysis. The values given by the program are

plotted against loading concentration in Figure 4.30. Extrapolation to zero concentration gave 'thermodynamically ideal' values of M_w as (204 ± 3) kDa (from the M* method) and (201 ± 10) kDa (from the hinge method). Combining the two yields a consensus value for Mw of (202 ± 5) kDa.

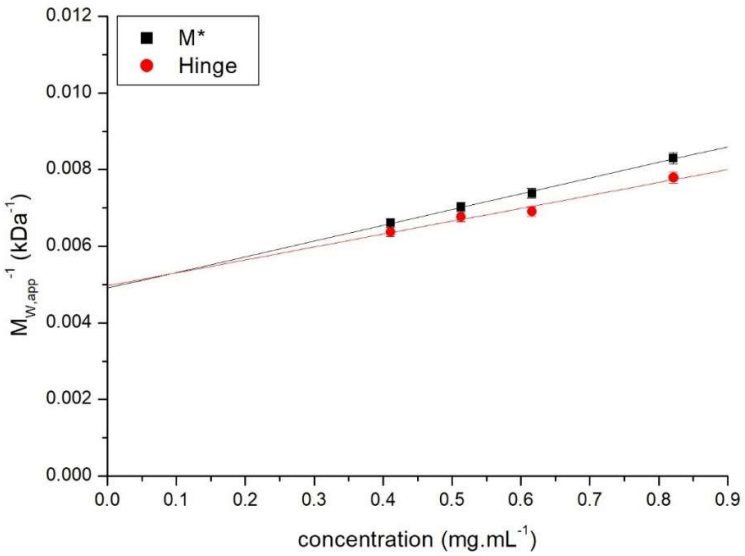


Figure 4.30 – Plot of the reciprocal of the apparent molecular weight ($M_{w,app}$) values against loading concentration of N-V, with linear fits to extrapolate to zero concentration.

4.6.6 SEC-MALS

The M_w of the main peak was determined to be 116 kDa (although no error is described at this level of precision), with a polydispersity (M_w/M_n) of 1.002 ± 0.003. [η] was found to be (71.8 ± 0.2) mL.g^{-1}.

4.7 Sized GBS polysaccharide, serotype IA

4.7.1 Concentration series

After dialysis, the concentration was measured on the refractometer. The initial reading was (1.412 ± 0.001) Brix(%), corresponding to (14.00 ± 0.001) mg.mL^{-1}. This was diluted as previously stated in Table 3-2.

4.7.2 Density and $\bar{v}$ determination

Density was measured and the results plotted against concentration in Figure 4.31. Using the slope of this graph, $\bar{v}$ can be calculated as (0.796 ± 0.004) mL.g^{-1}.The dialysate density was measured as 1.003201 g.mL^{-1}, although no error is described at this level of precision.

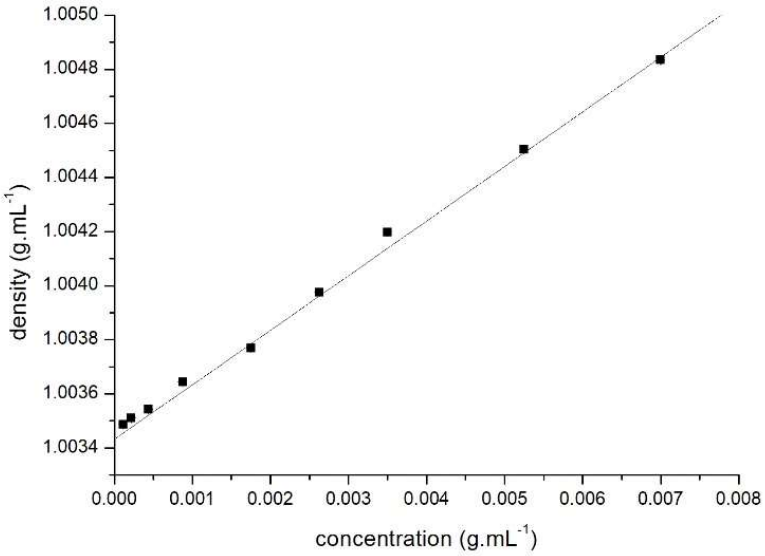


Figure 4.31 – Plot of density against concentration for S-IA, with a linear fit to obtain gradient.

4.7.3 Viscosity

Plotting the relevant viscosity functions and extrapolating back to where the concentration is zero in Figure 4.32 gives the intrinsic viscosities as (48.6 ± 0.2) mL.g^{-1} (Huggins), (48.7 ± 0.2) mL.g^{-1} (Kraemer) and (48.7 ± 0.2) mL.g^{-1} (Solomon-Ciuta). The mean average value of these is (48.7 ± 0.1) mL.g^{-1}.

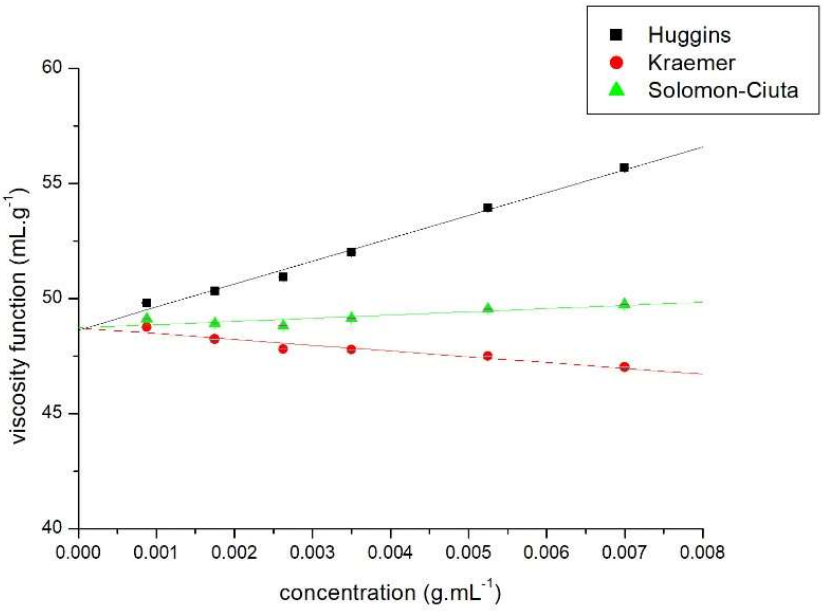


Figure 4.32 – Plot of viscosity against concentration for S-IA, with linear fits to extrapolate to zero concentration.

4.7.4 Sedimentation velocity

The distribution of sedimentation coefficients is shown in Figure 4.33. The peak data for the main component was also plotted against the loading concentration in Figure 4.34 and extrapolated back to zero concentration, giving the sedimentation coefficient as (3.31 ± 0.05) S. As the gradient is close to zero, the data can be treated as a set of repeated measurements (as discussed on page 50). The sedimentation coefficient can instead be calculated as (3.08 ± 0.11) S.

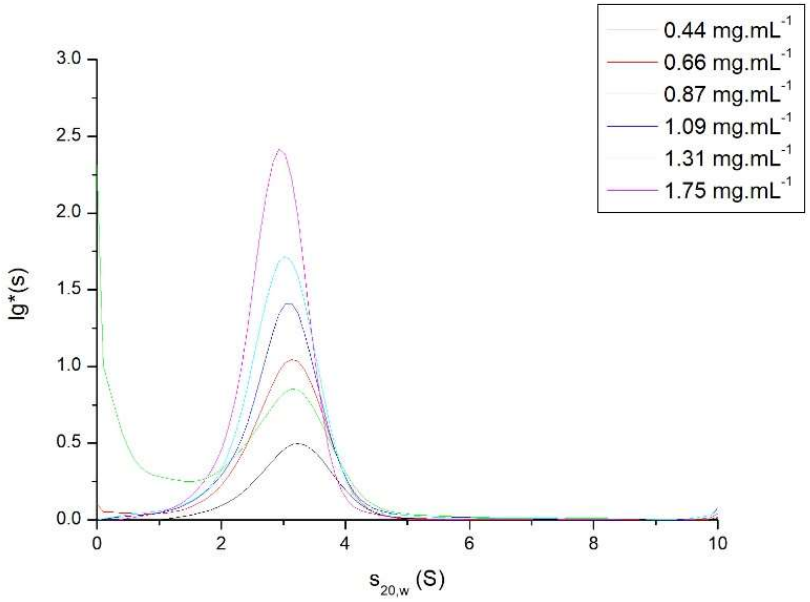


Figure 4.33 – Distribution of sedimentation coefficients at a range of loading concentrations of S-IA.

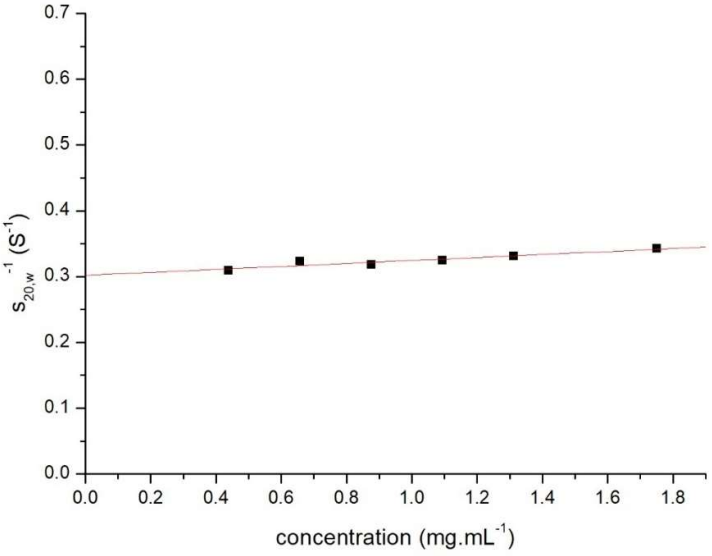


Figure 4.34 – Plot of the reciprocal of sedimentation coefficient against loading concentration for S-IA, with a linear fit to extrapolate to zero concentration.

4.7.5 Sedimentation equilibrium

SEDFIT-MSTAR provides two methods of determining apparent molecular weight, $M_{w,app}$: from the M^* function and from hinge point analysis. The values given by the program are plotted against loading concentration in Figure 4.35. Extrapolation to zero concentration

gave 'thermodynamically ideal' values of M_w as (185 ± 9) kDa (from the M* method) and (193 ± 12) kDa (from the hinge method). Combining the two yields a consensus value for Mw of (189 ± 7) kDa.

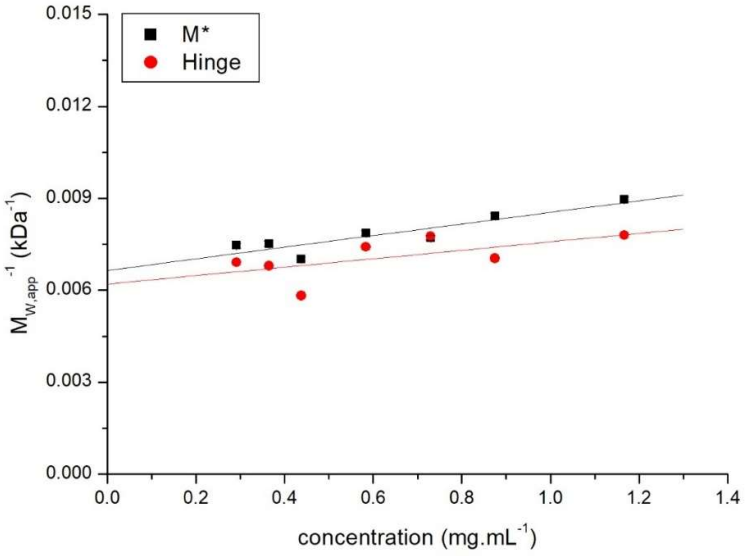


Figure 4.35 – Plot of the reciprocal of the apparent molecular weight ($M_{w,app}$) values against loading concentration of S-IA, with linear fits to extrapolate to zero concentration.

4.7.6 SEC-MALS

The M_w of the main peak was determined to be 102 kDa (although no error is described at this level of precision), with a polydispersity (M_w/M_n) of 1.006 ± 0.003. [η] was found to be (75.0 ± 0.3) mL.g^{-1}.

4.8 Sized GBS polysaccharide, serotype IB

4.8.1 Concentration series

After dialysis, the concentration was measured on the refractometer. The initial reading was 0.942 Brix(%), corresponding to 9.33 mg.mL^{-1}. This was diluted as previously stated in Table 3-2. Error is not reported for these values as it is too low to make an impact at three significant figures.

4.8.2 Density and $\bar{v}$ determination

Density was measured and the results plotted against concentration in Figure 4.36. Using the slope of this graph, $\bar{v}$ can be calculated as (0.731 ± 0.003) mL.g^{-1}.The dialysate density was measured as 1.002963 g.mL^{-1}, although no error is described at this level of precision.

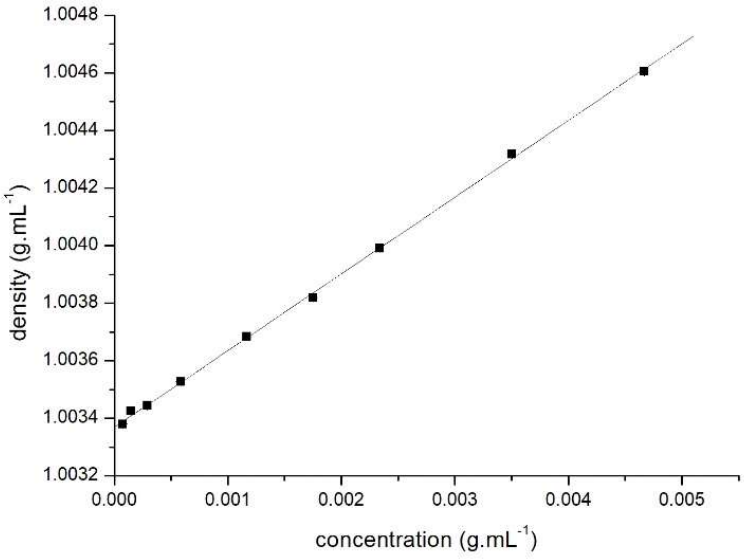


Figure 4.36 – Plot of density against concentration for S-IB, with a linear fit to obtain gradient.

4.8.3 Viscosity

Plotting the relevant viscosity functions and extrapolating back to where the concentration is zero in Figure 4.37 gives the intrinsic viscosities as (62.0 ± 0.3) mL.g^{-1} (Huggins), (62.2 ± 0.2)

mL.g^{-1} (Kraemer) and (62.1 ± 0.2) mL.g^{-1} (Solomon-Ciuta). The mean average value of these is (62.1 ± 0.1) mL.g^{-1}.

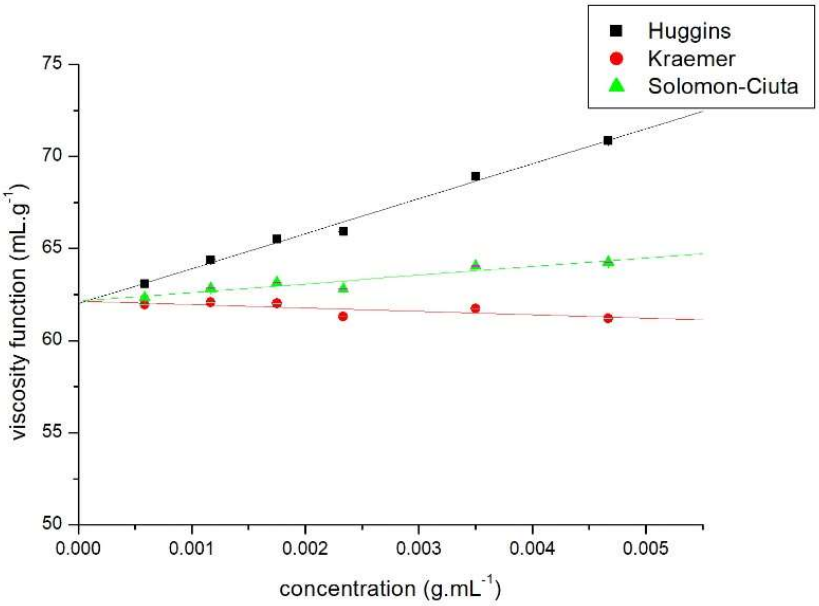


Figure 4.37 – Plot of viscosity against concentration for S-IB, with linear fits to extrapolate to zero concentration.

4.8.4 Sedimentation velocity

The distribution of sedimentation coefficients is shown in Figure 4.38. The peak data for the main component was also plotted against the loading concentration in Figure 4.39 and extrapolated back to zero concentration, giving the sedimentation coefficient as (3.28 ± 0.05) S. As the gradient is close to zero, the data can be treated as a set of repeated measurements (as discussed on page 50). The sedimentation coefficient can instead be calculated as (3.12 ± 0.09) S.

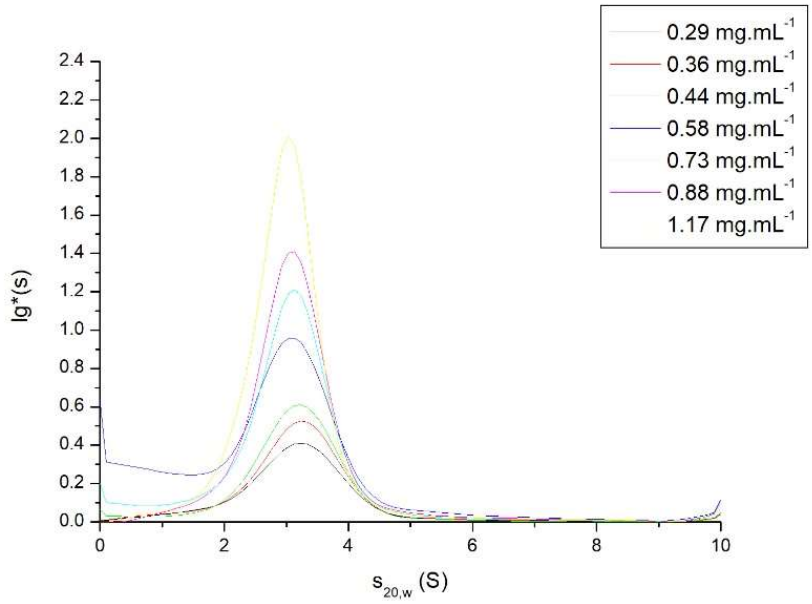


Figure 4.38 – Distribution of sedimentation coefficients at a range of loading concentrations of S-IB.

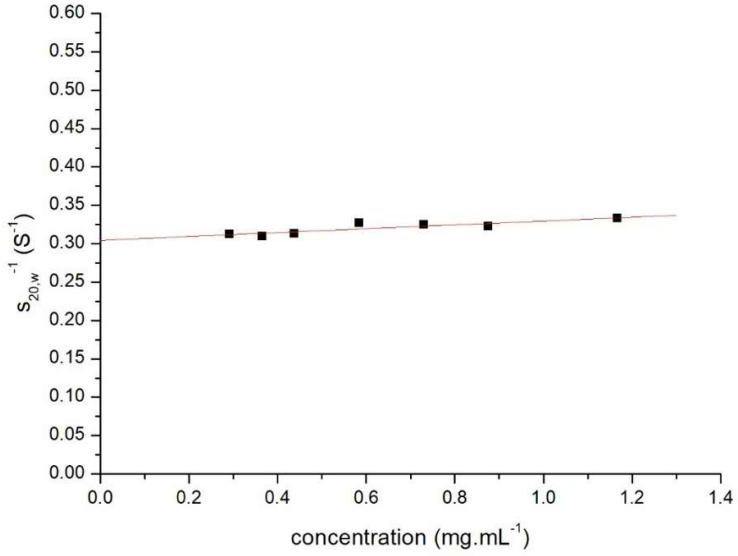


Figure 4.39 – Plot of the reciprocal of sedimentation coefficient against loading concentration for S-IB, with a linear fit to extrapolate to zero concentration.

4.8.5 Sedimentation equilibrium

SEDFIT-MSTAR provides two methods of determining apparent molecular weight, $M_{w,app}$: from the M^* function and from hinge point analysis. The values given by the program are

plotted against loading concentration in Figure 4.40. Extrapolation to zero concentration gave 'thermodynamically ideal' values of M_w as (150 ± 6) kDa (from the M* method) and (161 ± 14) kDa (from the hinge method). Combining the two yields a consensus value for Mw of (156 ± 8) kDa.

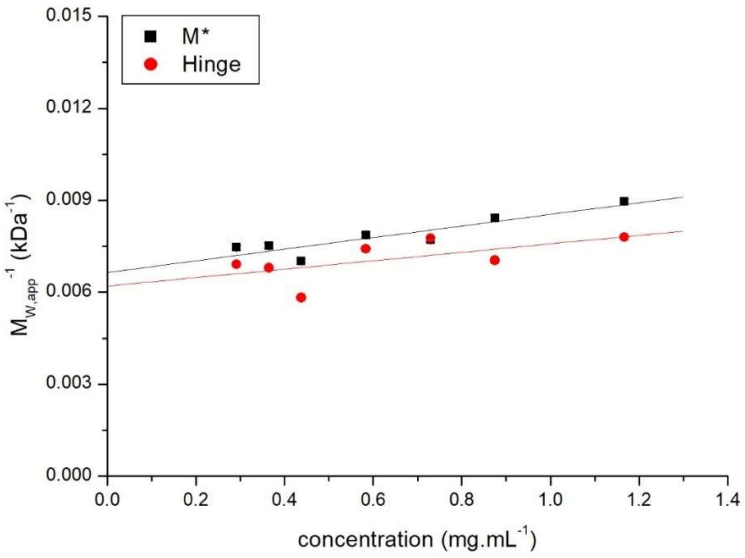


Figure 4.40 – Plot of the reciprocal of the apparent molecular weight ($M_{w,app}$) values against loading concentration of S-IB, with linear fits to extrapolate to zero concentration.

4.8.6 SEC-MALS

The M_w of the main peak was determined to be 102 kDa (although no error is described at this level of precision), with a polydispersity (M_w/M_n) of 1.006 ± 0.002. [η] was found to be (76.9 ± 0.2) mL.g^{-1}.

4.9 Sized GBS polysaccharide, serotype II

4.9.1 Concentration series

After dialysis, the concentration was measured on the refractometer. The initial reading was 0.546 Brix(%), corresponding to 5.41 mg.mL^{-1}. This was diluted as previously stated in Table 3-2. Error is not reported for these values as it is too low to make an impact at three significant figures.

4.9.2 Density and $\bar{v}$ determination

Density was measured and the results plotted against concentration in Figure 4.41. Using the slope of this graph, $\bar{v}$ can be calculated as (0.652 ± 0.007) mL.g^{-1}.The dialysate density was measured as 1.003032 g.mL^{-1}, although no error is described at this level of precision.

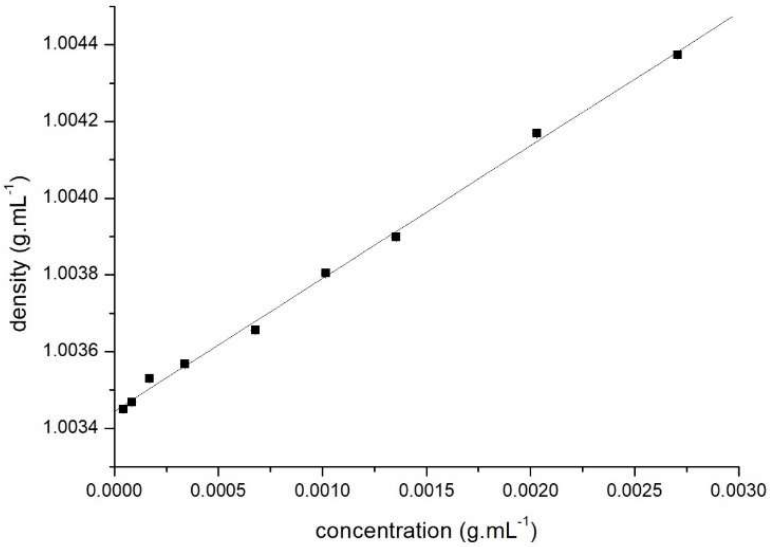


Figure 4.41 – Plot of density against concentration for S-II, with a linear fit to obtain gradient.

4.9.3 Viscosity

Plotting the relevant viscosity functions and extrapolating back to where the concentration is zero in Figure 4.42 gives the intrinsic viscosities as (54.8 ± 1.2) mL.g^{-1} (Huggins), (55.1 ± 1.1)

mL.g^{-1} (Kraemer) and (55.0 ± 1.2) mL.g^{-1} (Solomon-Ciuta). The mean average value of these is (55.0 ± 0.7) mL.g^{-1}.

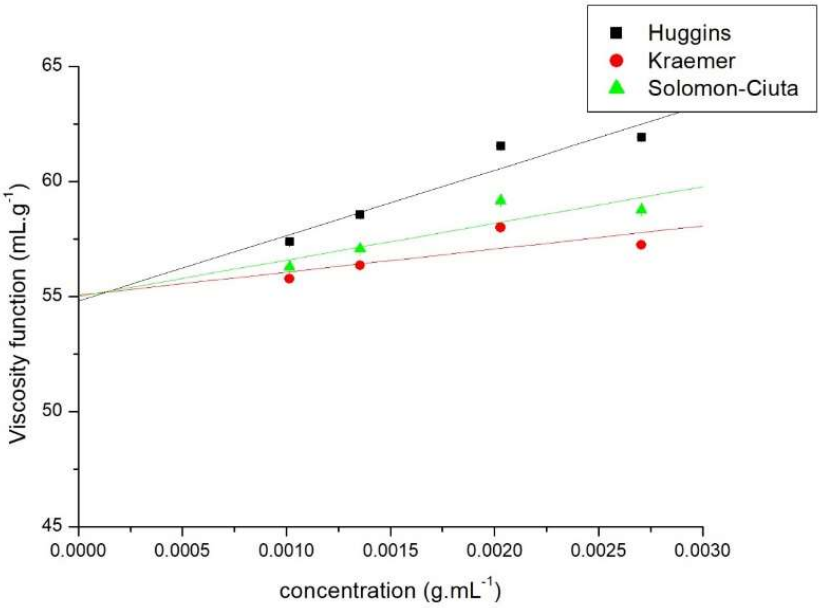


Figure 4.42 – Plot of viscosity against concentration for S-II, with linear fits to extrapolate to zero concentration.

4.9.4 Sedimentation velocity

The distribution of sedimentation coefficients is shown in Figure 4.43. The peak data for the main component was also plotted against the loading concentration in Figure 4.44 and extrapolated back to zero concentration, giving the sedimentation coefficient as (4.64 ± 0.03) S. As the gradient is close to zero, the data can be treated as a set of repeated measurements (as discussed on page 50). The sedimentation coefficient can instead be calculated as (4.3 ± 0.42) S.

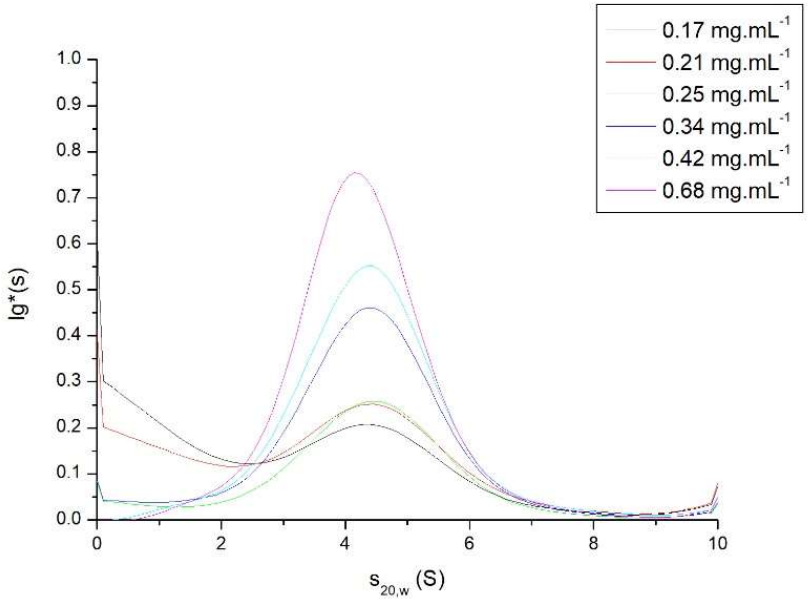


Figure 4.43 – Distribution of sedimentation coefficients at a range of loading concentrations of S-II.

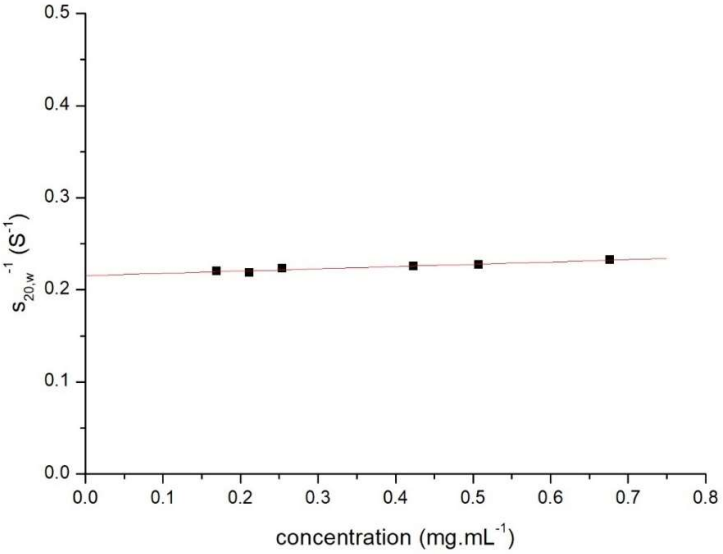


Figure 4.44 – Plot of the reciprocal of sedimentation coefficient against loading concentration for S-II, with a linear fit to extrapolate to zero concentration.

4.9.5 Sedimentation equilibrium

SEDFIT-MSTAR provides two methods of determining apparent molecular weight, $M_{w,app}$:

from the M^* function and from hinge point analysis. The values given by the program are

plotted against loading concentration in Figure 4.45. Extrapolation to zero concentration gave 'thermodynamically ideal' values of M_w as (181 ± 9) kDa (from the M* method) and (142 ± 6) kDa (from the hinge method). Combining the two yields a consensus value for Mw of (161 ± 5) kDa.

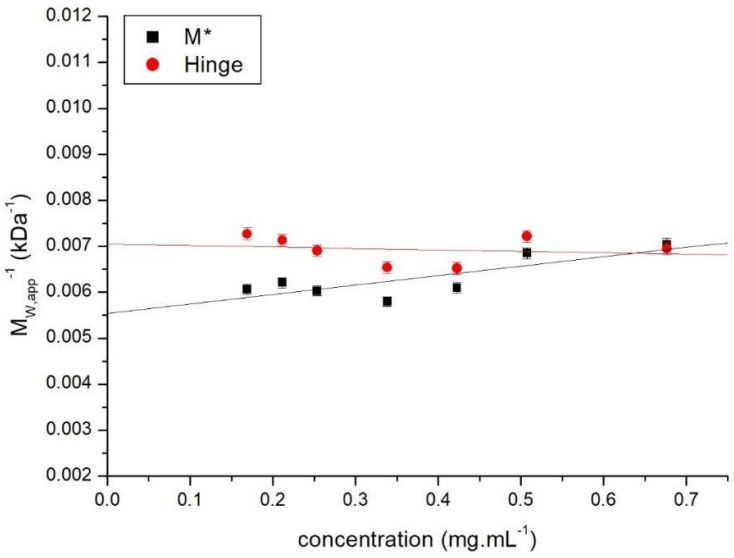


Figure 4.45 – Plot of the reciprocal of the apparent molecular weight ($M_{w,app}$) values against loading concentration of S-II, with linear fits to extrapolate to zero concentration.

4.9.6 SEC-MALS

The M_w of the main peak was determined to be 155 kDa although no error is described at this level of precision, with a polydispersity (M_w/M_n) of 1.024 ± 0.002. [η] was found to be (52.6 ± 0.1) mL.g^{-1}.

4.10 CRM197

4.10.1 Density and $\bar{\nu}$ determination

Density was measured and the results plotted against concentration, as shown in Figure 4.46. Using the slope of this graph, $\bar{\nu}$ can be calculated as (0.733 ± 0.04) mL.g^{-1}. The dialysate density was measured as (0.999579 ± 0.00006) g.mL^{-1}.

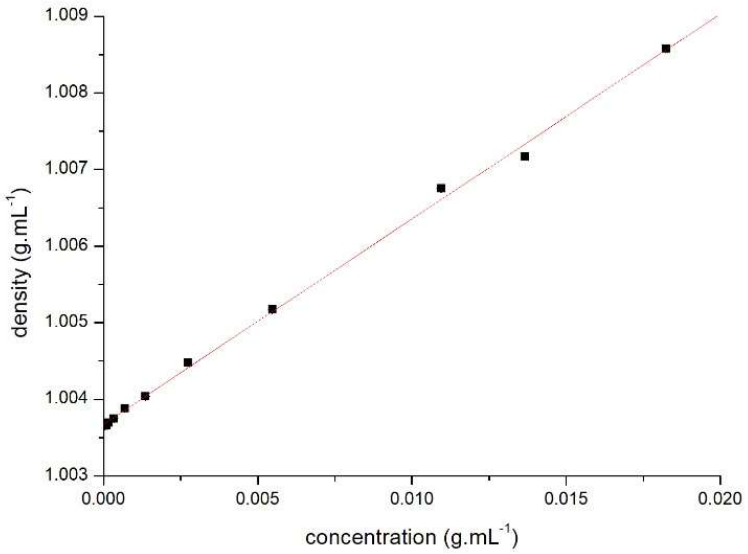


Figure 4.46 – Plot of density against concentration for CRM197, with a linear fit to obtain gradient.

4.10.2 Sedimentation Velocity

The distribution of sedimentation coefficients is shown in Figure 4.47. The peak data for the main component was also plotted against loading concentration in Figure 4.48 and extrapolated back to zero concentration, giving the sedimentation coefficient as (3.51 ± 0.14) S. If instead the data set is treated as a set of repeated measurements (as discussed on page 50), then the sedimentation coefficient can instead be calculated as (3.41 ± 0.27) S. However, in this case it may not be appropriate as the gradient is relatively high.

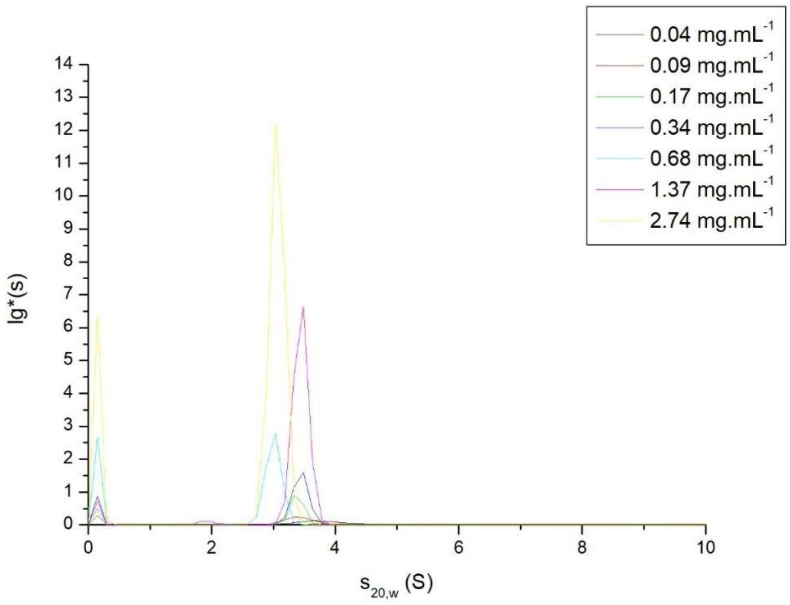


Figure 4.47 – Distribution of sedimentation coefficients at a range of loading concentrations of CRM197.

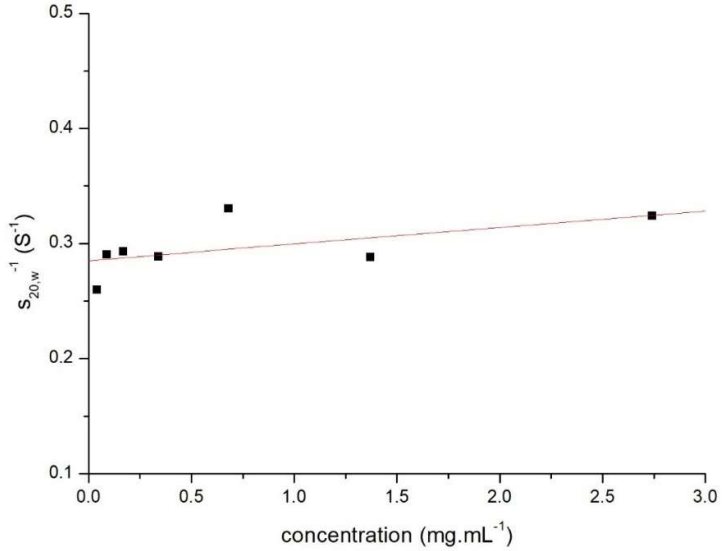


Figure 4.48 – Plot of the reciprocal of sedimentation coefficient against loading concentration for CRM197, with a linear fit to extrapolate to zero concentration.

4.10.3 SEC-MALS

The M_w was determined to be 102 kDa, although no error is described at this level of precision. The polydispersity (M_w/M_n) was 1.029 ± 0.006. [η] was found to be (4.90 ± 0.27) $mL.g^{-1}$.

4.11 Summary

The results for each serotype are summarised in Table 4-1. This table will allow a quick comparison between these baseline measurements and any changes after exposure to stress.

Table 4-1 – Summary of baseline values for each sample.

State	Serotype	$\bar{v}$ ($mL.g^{-1}$)	[η] ($mL.g^{-1}$)	Analytical ultracentrifugation			SEC-MALS		
				s˚20,w, extrapolation (S)	**s˚20,w, average (S)**	**Mw (combined, kDa)**	**Mw (kDa)**	**[η] ($mL.g^{-1}$)**	**Polydispersity ($Mw.Mn^{-1}$)**
Native	IA	0.642±0.018	218±2	5.02±0.59	4.32±0.44	345±21	292±1	180±0	1.077±0.003
	IB	0.622±0.006	136±0	4.05±0.07	3.72±0.16	176±8	154±0	102±1	1.061±0.004
	II	0.627±0.005	127±1	6.05±0.26	5.85±0.27	319±9	430±1	121±1	1.125±0.004
	III	0.661±0.007	45.4±0.2	3.23±0.16	3.21±0.25	113±4	91.4±0.1	47.3±0.3	1.006±0.002
	IV	0.608±0.005	65±0.6	2.56±0.11	2.62±0.12	63.7±1.1	53.4±0.1	45.9±0.1	1.001±0.003
	V	0.695±0.005	81.8±0.9	3.95±0.04	3.71±0.12	202±5	116±0	71.8±0.2	1.002±0.003
Sized	IA	0.796±0.004	48.7±0.1	3.31±0.05	3.08±0.11	189±7	102±0	75±0.2	1.006±0.003
	IB	0.731±0.003	62.1±0.1	3.28±0.05	3.12±0.09	156±8	102±0	76.9±0.2	1.006±0.002
	II	0.652±0.007	55.0±0.7	4.64±0.03	4.30±0.42	161±5	155±0	52.6±0.1	1.024±0.002
CRM197		0.733±0.04	-	3.51±0.14	3.41±0.27	-	102±0	4.90±0.27	1.029±0.006

4.12 Discussion

It is possible that some of the apparent small particles observed in the sedimentation velocity experiments are artefacts and not present in solution at the levels shown. However, given that these small particles are seen in sedimentation velocity and SEC-MALS experiments, it is possible that they really are present and thus of possible significance. If this were the case, sedimentation equilibrium results may be skewed by the presence of these particles to give a lower average than would be expected. However, there does appear to be good agreement between the measured values for sedimentation equilibrium and SEC-MALS, so this may not be a significant issue. A potential solution to this problem would be to perform further stages of dialysis to remove the presence of these small particles, but this would mean the sample is no longer being analysed in the state it was sent. It may be more useful to convert the sedimentation coefficient into a molecular weight, as it would then be possible to analyse the main peak on its own to establish the molecular weight. Alternatively, samples could be analysed by sedimentation velocity after one stage of dialysis, but further stages of dialysis could be performed before analysing samples by sedimentation equilibrium.

It should also be noted that some of the calculated values for $\bar{v}$ are much higher than the values to be expected for a polysaccharide. This remained the same even after measurements were repeated, which may indicate that these measurements were accurate, but it is unclear why this may have occurred. It is possible that some aspect of this process caused the increased density, as the molecules with high values of $\bar{v}$ were both sized polysaccharides, although it is unclear what this may be.

There were a number of issues with the study of CRM197. As mentioned in section 3.1, only a small volume (approximately 6 mL at 2.74 $mg.mL^{-1}$) was provided for analysis. As all these techniques rely on producing a concentration series, these experiments used the majority of the sample very quickly, and it was not possible to repeat these steps if problems occurred.

Unfortunately, some of the initially chosen concentration ranges were not appropriate, often attempting measurements at too low concentration. For example, the sedimentation velocity data (Figure 4.48) has more variation in points, each with a higher error, the lower the concentration is. The SEC-MALS data overestimates the molecular weight of CRM197 as 102 kDa, versus a literature value of 58.4 kDa. As this is close to double the molecular weight with the other technique, it is possible the CRM197 was forming a dimer due to the increased age of the sample (the EC-MALS analysis was performed almost one week after the AUC analysis). It is also possible that this is due to an interaction of the protein with the column matrix, as the Shodex™ LB-G 6B guard column and Shodex™ LB-805 column available for use are more appropriate for use with polysaccharides.

While attempts were made to analyse CRM197 using U-tube viscometry and sedimentation equilibrium analysis, the data sets produced were extremely varied and analysis was not possible. For this reason, they have not been included in this study. Part of the reason for the extreme variation in sample may be an instability in the sample, meaning that the sample was degrading while measurements were being taken. When attempts were made to repeat these experiments, it was even found that, when stored at 4 ˚C in the fridge, the samples had degraded further such that the viscosity values obtained were much lower than those previously observed. This does at least give a firm on the structure of the final glycoconjugate, even though conjugated samples were never analysed in this work: it is imperative that a conjugate vaccine is stored in the freezer, as (even if the polysaccharide portion is relatively stable) the protein portion will rapidly degrade unless kept frozen. However, as the exact age and storage conditions of the CRM197 sample prior to its arrival are unknown, this could be due to the sample age rather than a feature of the molecule itself.

This also raises a further question: how much of an impact would degradation of the protein have on the functionality of the vaccine as a whole? While glycoconjugate vaccines have improved immunogenicity over unconjugated polysaccharides, the protein portion's only function is to cause this improvement, not act as an antigen in its own right. Therefore, if only the protein portion of the vaccine were to denature, the glycoconjugate as a whole may still be able to bind to the MHCII and interact with the immune system in the same way as a correctly formed vaccine. Vaccine efficacy may be impacted if the protein instability affects the conjugation site, as this may make the bond between protein and polysaccharide less stable. In addition, if the instability in protein structure makes it likely that insoluble aggregates form, this would be a major issue for its safe use as a vaccine.

The values obtained provide a baseline value of the molecular properties of each polysaccharide, which can now be used as a baseline to assess how much deviation occurs, if any, after exposure to stress.

5 Stability after repeated freeze-thaw cycles

Repeated freezing and thawing was used as a method to deliberately expose samples to stress in a controlled manner. This stress may occur as the solvent freezes around the solute, causing pockets of extremely high concentration which may then interact in unexpected ways [241]. This process is shown in Figure 5.1. The ability of a sample to withstand controlled stress can be used as a measurement of its stability.

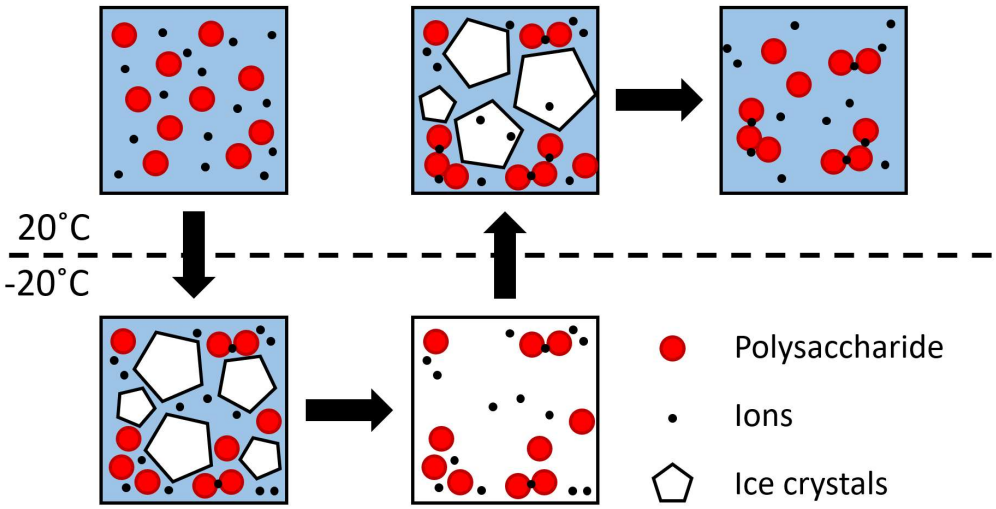


Figure 5.1 – Diagram showing how the formation of ice crystals may damage dissolved polysaccharides. Following the arrows, the first square shows the freely floating polysaccharides and ions. The second shows that as ice crystals form there will be pockets of highly concentrated material which may then react, causing deviation from its usual structure. The third square shows the solution totally frozen, while the fourth shows the sample again passing through a stage in the presence of ice crystals. The last square shows the permanent change to the polysaccharide structures even after returning to ambient conditions.

For this project, samples were dialysed overnight as previously described, then separated into aliquots to undergo different numbers of freeze-thaw cycles. As the samples tested were stored on dry ice during delivery, it was thought that the samples would so far have only undergone one freeze-thaw cycle while it was being divided into these aliquots.

Samples were thawed at room temperature (variable, average 23˚C) until no suspended frozen material could be seen on gentle agitation. The samples were then incubated at -20˚C

until no movement of fluid could be seen on gentle agitation. This process was performed on separate aliquots of each sample until they had undergone a total of 10 or 100 cycles.. Partial specific volume is unlikely to change even after the molecules are damaged. Therefore, the originally calculated values of partial specific volumes were used when analysing centrifugation data.

5.1 Native GBS polysaccharide, serotype IA

5.1.1 Ten freeze-thaw cycles

5.1.1.1 Viscosity

Plotting the relevant viscosity functions and extrapolating back to where the concentration is zero in Figure 5.2 gives the intrinsic viscosities as (234 ± 1) $mL.g^{-1}$ (Huggins), (233 ± 1) $mL.g^{-1}$ (Kraemer) and (235 ± 1) $mL.g^{-1}$ (Solomon-Ciuta). The mean average value of these is (234 ± 1) $mL.g^{-1}$.

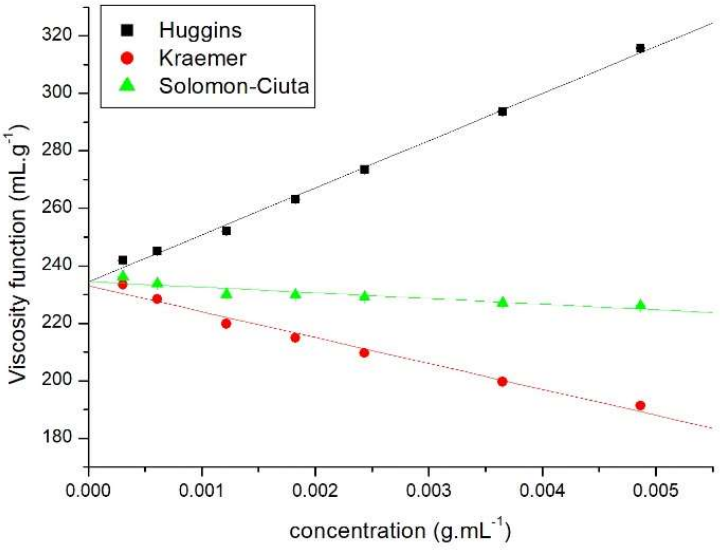


Figure 5.2 – Plot of viscosity against concentration for N-IA after exposure to ten freeze-thaw cycles, with linear fits to extrapolate to zero concentration.

5.1.1.2 Sedimentation velocity

The distribution of sedimentation coefficients is shown in Figure 5.3. The peak data for the main component was also plotted against the loading concentration in Figure 5.4 and extrapolated back to zero concentration, giving the sedimentation coefficient as (5.24 ± 0.10) S. As the gradient is close to zero, the data can be treated as a set of repeated measurements (as discussed on page 50). The sedimentation coefficient can instead be calculated as (4.29 ± 0.48) S.

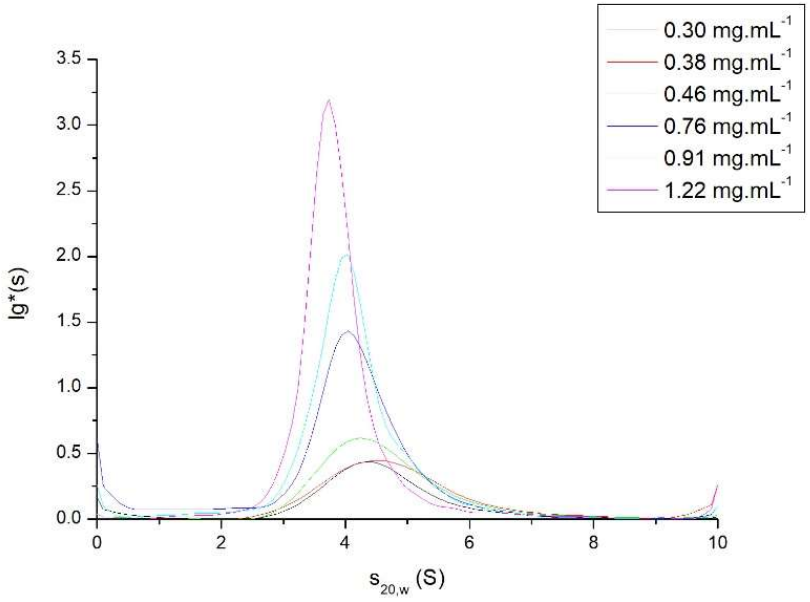


Figure 5.3 – Distribution of sedimentation coefficients at a range of loading concentrations of N-IA after ten freeze-thaw cycles.

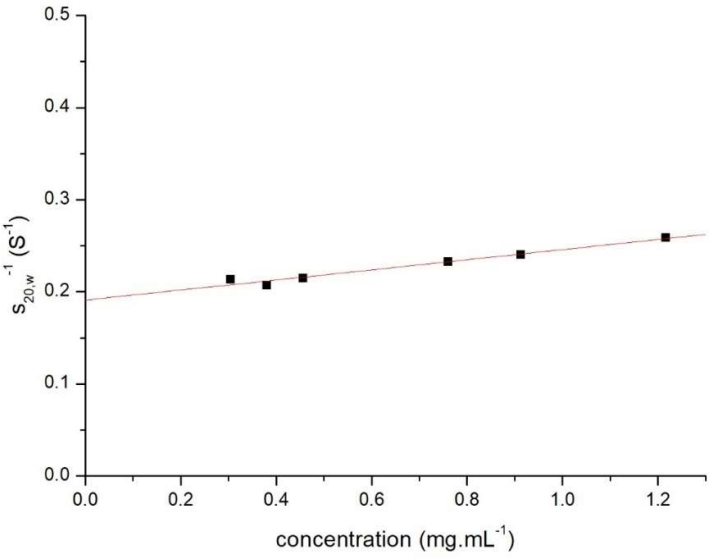


Figure 5.4 – Plot of the reciprocal of sedimentation coefficient against loading concentration for N-IA after exposure to ten freeze-thaw cycles, with a linear fit to extrapolate to zero concentration.

5.1.1.3 Sedimentation equilibrium

SEDFIT-MSTAR provides two methods of determining apparent molecular weight, $M_{w,app}$: from the M^* function and from hinge point analysis. The values given by the program are plotted against loading concentration in Figure 5.5. Extrapolation to zero concentration gave 'thermodynamically ideal' values of M_w as (364 ± 35) kDa (from the M* method) and (298 ± 21) kDa (from the hinge method). Combining the two yields a consensus value for Mw of (331 ± 20) kDa.

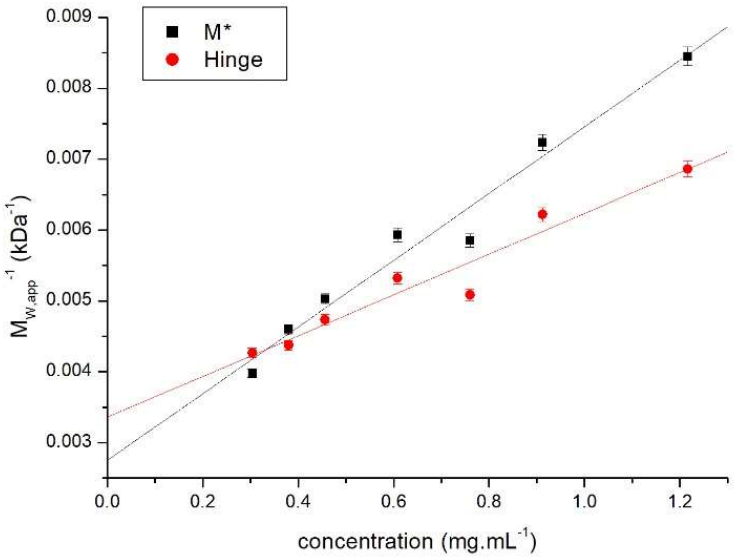


Figure 5.5 – Plot of the reciprocal of apparent molecular weight ($M_{w,app}$) values against loading concentration of N-IA after exposure to ten freeze-thaw cycles, with a linear fit to extrapolate to zero concentration.

5.1.1.4 SEC-MALS

The M_w of the main peak was determined to be (308 ± 1) kDa, with a polydispersity (M_w/M_n) of 1.147 ± 0.006. [η] was found to be 177 mL.g^{-1}, although no error is described at this level of precision.

5.1.2 One hundred freeze-thaw cycles

5.1.2.1 Viscosity

Plotting the relevant viscosity functions and extrapolating back to where the concentration is zero in Figure 5.6 gives the intrinsic viscosities as (205 ± 3) mL.g^{-1} (Huggins), (207 ± 3) mL.g^{-1} (Kraemer) and (207 ± 3) mL.g^{-1} (Solomon-Ciuta). The mean average value of these is (206 ± 2) mL.g^{-1}.

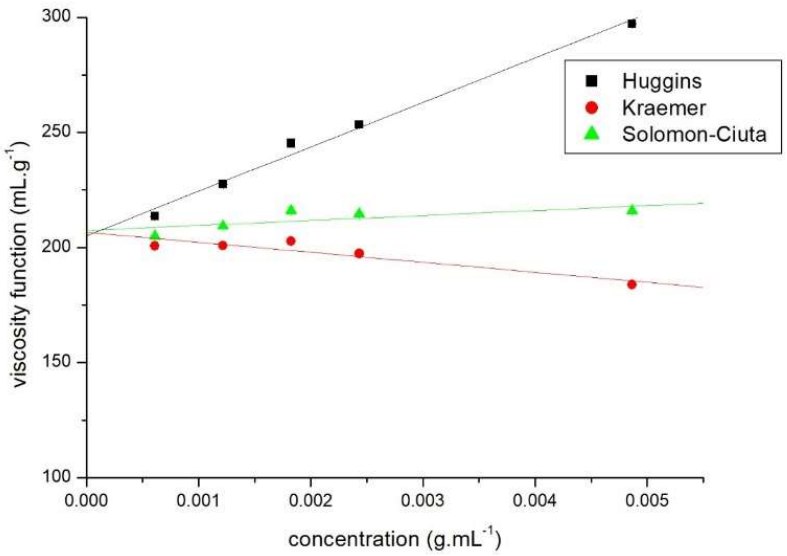


Figure 5.6 – Plot of viscosity against concentration for N-IA after exposure to 100 freeze-thaw cycles, with linear fits to extrapolate to zero concentration.

5.1.2.2 Sedimentation Velocity

The distribution of sedimentation coefficients is shown in Figure 5.7. The peak data for the main component was also plotted against the loading concentration in Figure 5.8 and extrapolated back to zero concentration, giving the sedimentation coefficient as (5.01 ± 0.05) S. As the gradient is close to zero, the data can be treated as a set of repeated measurements (as discussed on page 50). The sedimentation coefficient can instead be calculated as (4.29 ± 0.31) S.

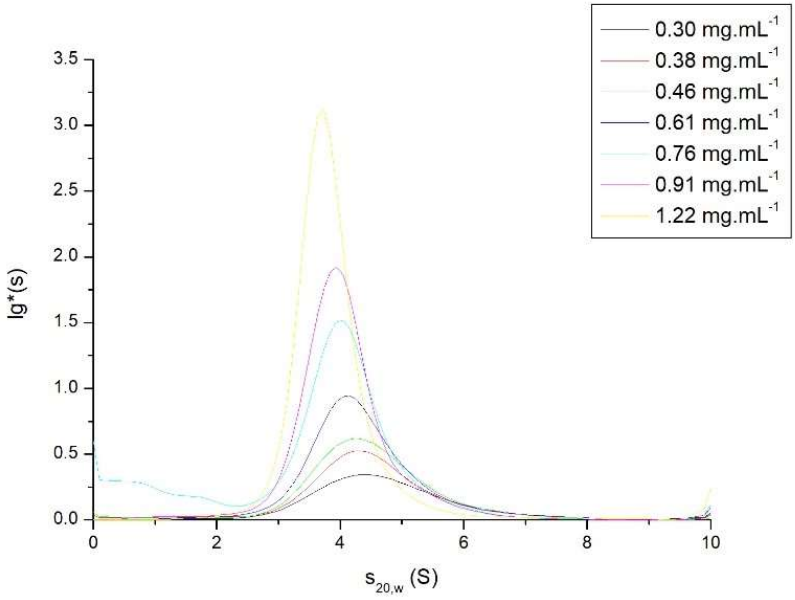


Figure 5.7 – Distribution of sedimentation coefficients at a range of loading concentrations of N-IA after 100 freeze-thaw cycles.

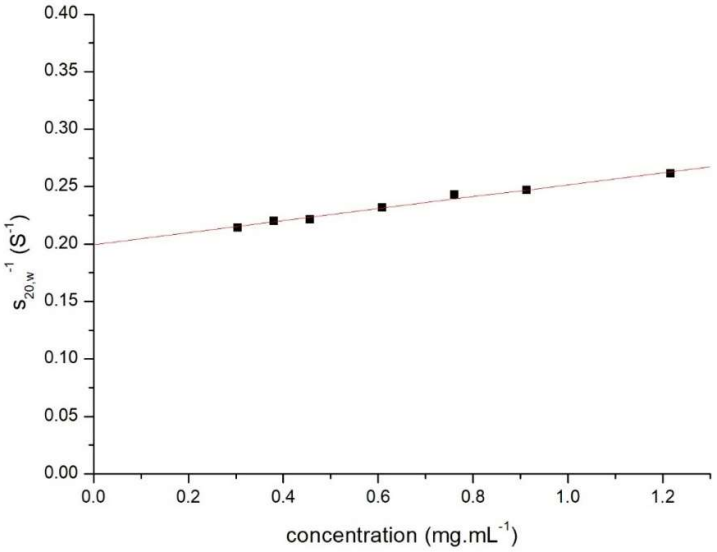


Figure 5.8 – Plot of the reciprocal of sedimentation coefficient against loading concentration for N-IA after exposure to 100 freeze-thaw cycles, with a linear fit to extrapolate to zero concentration.

5.1.2.3 Sedimentation Equilibrium

SEDFIT-MSTAR provides two methods of determining apparent molecular weight, $M_{w,app}$: from the *M** function and from hinge point analysis. The values given by the program are

plotted against loading concentration in Figure 5.9. Extrapolation to zero concentration gave 'thermodynamically ideal' values of M_w as (313 ± 9) kDa (from the M* method) and (285 ± 3) kDa (from the hinge method). Combining the two yields a consensus value for Mw of (299 ± 5) kDa.

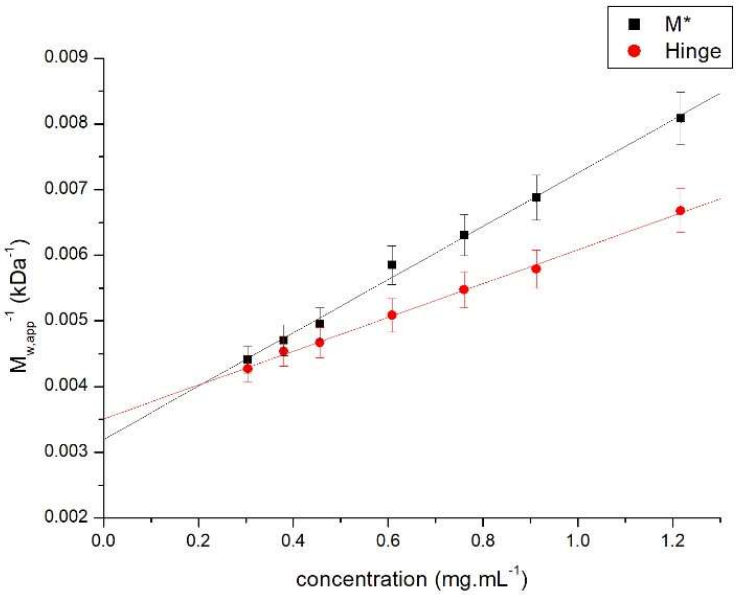


Figure 5.9 – Plot of the reciprocal of apparent molecular weight ($M_{w,app}$) values against loading concentration of N-IA after exposure to 100 freeze-thaw cycles, with a linear fit to extrapolate to zero concentration.

5.1.2.4 SEC-MALS

The M_w of the main peak was determined to be (409 ± 2) kDa, with a polydispersity (M_w/M_n) of 1.029 ± 0.005. [η] was found to be (250 ± 1) mL.g^{-1}.

5.2 Native GBS polysaccharide, serotype IB

5.2.1 Ten freeze-thaw cycles

5.2.1.1 Viscosity

Plotting the relevant viscosity functions and extrapolating back to where the concentration is zero in Figure 5.10 gives the intrinsic viscosities as (140 ± 1) mL.g^{-1} (Huggins), (140 ± 1) mL.g^{-1} (Kraemer) and (141 ± 1) mL.g^{-1} (Solomon-Ciuta). The mean average value of these is (140 ± 1) mL.g^{-1}.

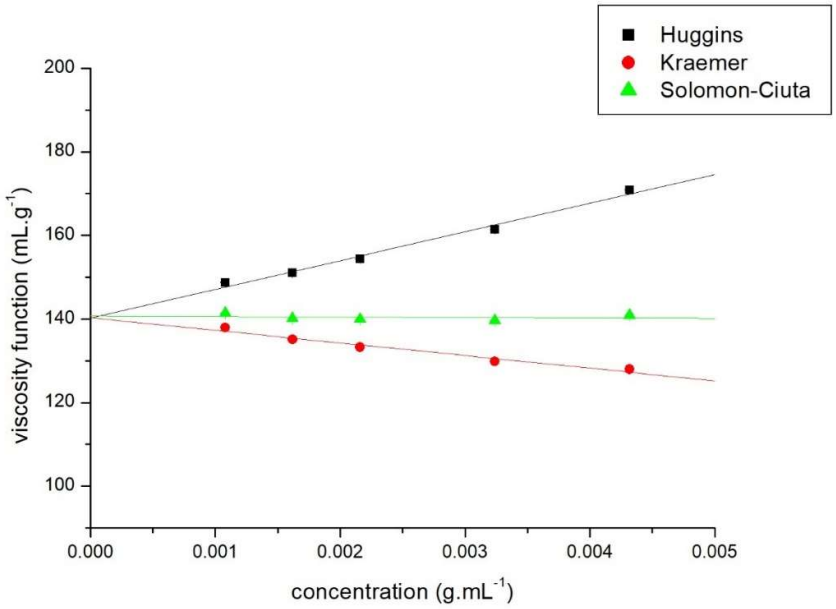


Figure 5.10 – Plot of viscosity against concentration for N-IB after exposure to ten freeze-thaw cycles, with linear fits to extrapolate to zero concentration.

5.2.1.2 Sedimentation velocity

The distribution of sedimentation coefficients is shown in Figure 5.11. The peak data for the main component was also plotted against the loading concentration in Figure 5.12 and extrapolated back to zero concentration, giving the sedimentation coefficient as (4.24 ± 0.05) S. As the gradient is close to zero, the data can be treated as a set of repeated measurements (as discussed on page 50). The sedimentation coefficient can instead be calculated as (3.65 ± 0.33) S.

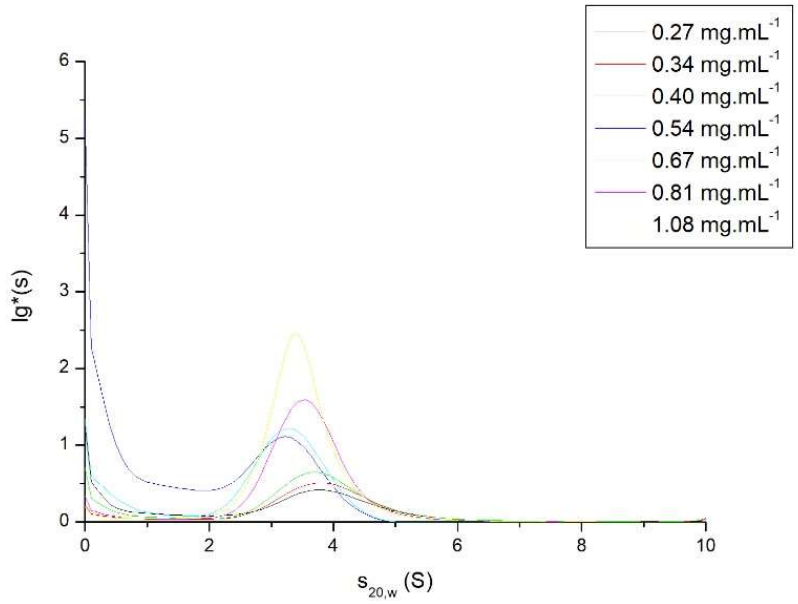


Figure 5.11 – Distribution of sedimentation coefficients at a range of loading concentrations of N-IB after ten freeze-thaw cycles.

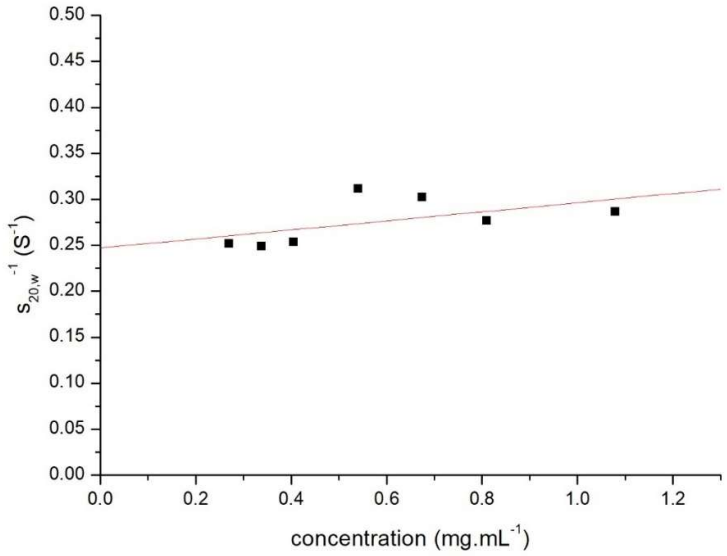


Figure 5.12 – Plot of the reciprocal of sedimentation coefficient against loading concentration for N-IB after exposure to ten freeze-thaw cycles, with a linear fit to extrapolate to zero concentration.

5.2.1.3 Sedimentation equilibrium

SEDFIT-MSTAR provides two methods of determining apparent molecular weight, $M_{w,app}$: from the M^* function and from hinge point analysis. The values given by the program are plotted against loading concentration in Figure 5.13. Extrapolation to zero concentration

gave 'thermodynamically ideal' values of M_w as (249 ± 11) kDa (from the M* method) and (230 ± 6) kDa (from the hinge method). Combining the two yields a consensus value for Mw of (240 ± 6) kDa.

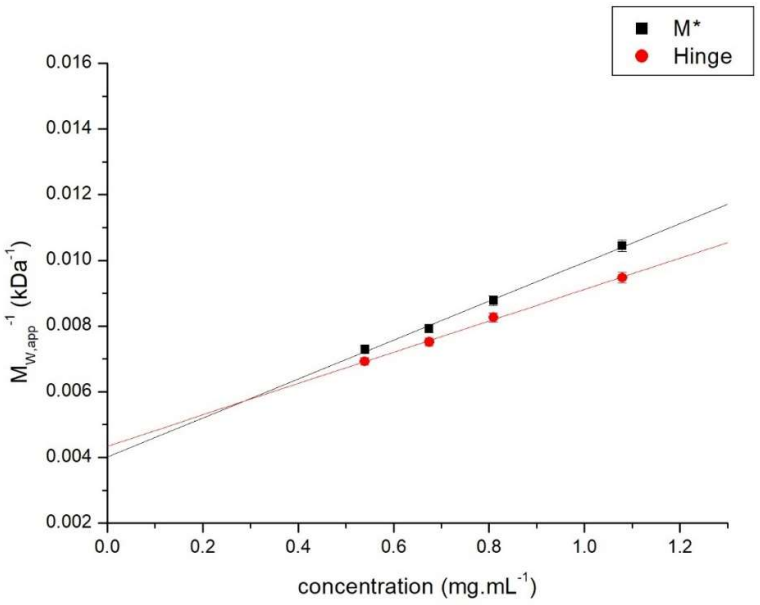


Figure 5.13 – Plot of the reciprocal of apparent molecular weight ($M_{w,app}$) values against loading concentration of N-IB after exposure to ten freeze-thaw cycles, with a linear fit to extrapolate to zero concentration.

5.2.1.4 SEC-MALS

The M_w of the main peak was determined to be (209 ± 1) kDa, with a polydispersity (M_w/M_n) of 1.082 ± 0.007. [η] was found to be 137 mL.g^{-1} although no error is described at this level of precision.

5.2.2 One hundred freeze-thaw cycles

5.2.2.1 Viscosity

Plotting the relevant viscosity functions and extrapolating back to where the concentration is zero in Figure 5.14 gives the intrinsic viscosities as (117 ± 6) mL.g^{-1} (Huggins), (119 ± 5) mL.g^{-1} (Kraemer) and (118 ± 6) mL.g^{-1} (Solomon-Ciuta). The mean average value of these is (118 ± 3) mL.g^{-1}.

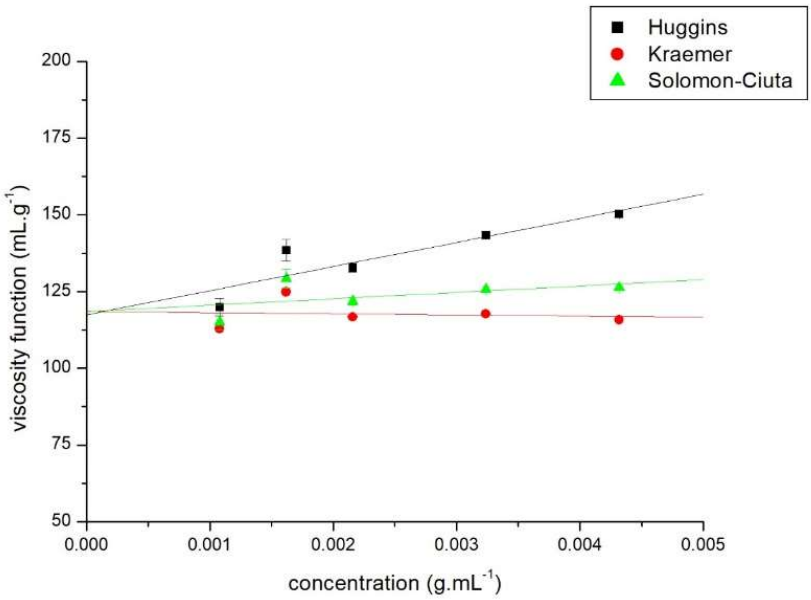


Figure 5.14 – Plot of viscosity against concentration for N-IB after exposure to 100 freeze-thaw cycles, with linear fits to extrapolate to zero concentration.

5.2.2.2 Sedimentation Velocity

The distribution of sedimentation coefficients is shown in Figure 5.15. The peak data for the main component was also plotted against the loading concentration in Figure 5.16 and extrapolated back to zero concentration, giving the sedimentation coefficient as (4.04 ± 0.04) S. As the gradient is close to zero, the data can be treated as a set of repeated measurements (as discussed on page 50). The sedimentation coefficient can instead be calculated as (3.7 ± 0.16) S.

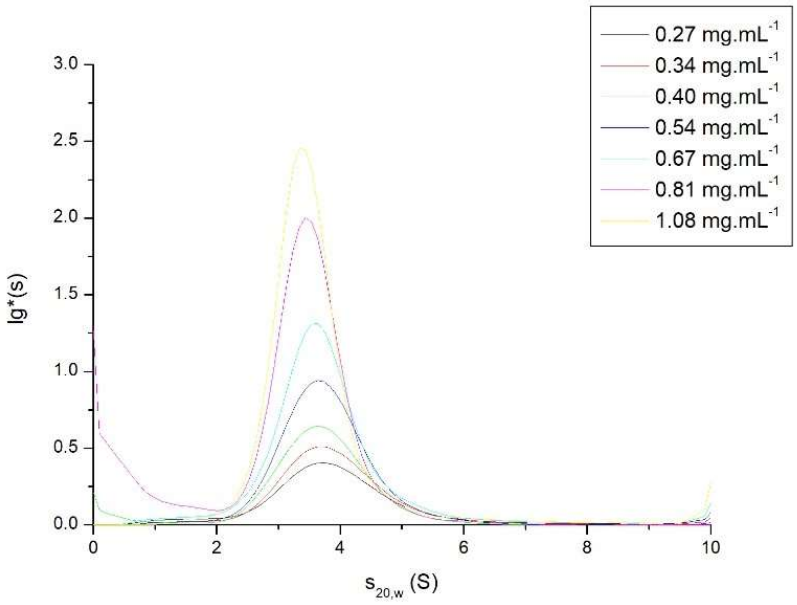


Figure 5.15 – Distribution of sedimentation coefficients at a range of loading concentrations of N-IB after 100 freeze-thaw cycles.

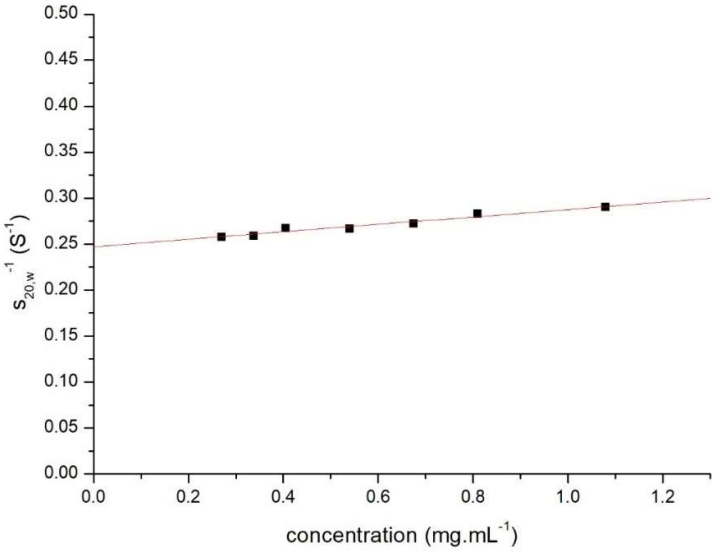


Figure 5.16 – Plot of the reciprocal of sedimentation coefficient against loading concentration for N-IB after exposure to 100 freeze-thaw cycles, with a linear fit to extrapolate to zero concentration.

5.2.2.3 Sedimentation Equilibrium

SEDFIT-MSTAR provides two methods of determining apparent molecular weight, $M_{w,app}$: from the M^* function and from hinge point analysis. The values given by the program are

plotted against loading concentration in Figure 5.17. Extrapolation to zero concentration gave 'thermodynamically ideal' values of M_w as (195 ± 7) kDa (from the M* method) and (185 ± 2) kDa (from the hinge method). Combining the two yields a consensus value for Mw of (190 ± 4) kDa.

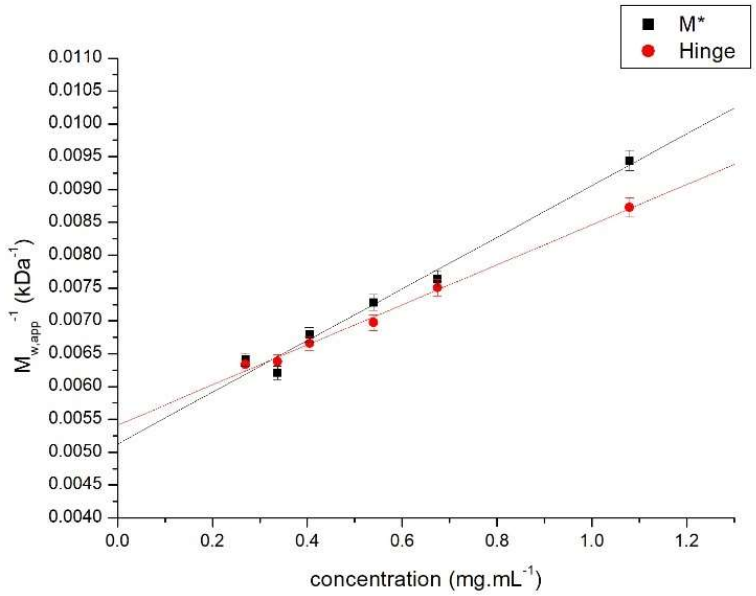


Figure 5.17 – Plot of the reciprocal of apparent molecular weight ($M_{w,app}$) values against loading concentration of N-IB after exposure to 100 freeze-thaw cycles, with a linear fit to extrapolate to zero concentration.

5.2.2.4 SEC-MALS

The M_w of the main peak was determined to be (231 ± 1) kDa, with a polydispersity (M_w/M_n) of 1.029 ± 0.005. [η] was found to be 164 mL.g^{-1}, although no error is described at this level of precision.

5.3 Native GBS polysaccharide, serotype II

5.3.1 Ten freeze-thaw cycles

5.3.1.1 Viscosity

Plotting the relevant viscosity functions and extrapolating back to where the concentration is zero in Figure 5.18 gives the intrinsic viscosities as (129 ± 1) $mL.g^{-1}$ (Huggins), (129 ± 1) $mL.g^{-1}$ (Kraemer) and (129 ± 1) $mL.g^{-1}$ (Solomon-Ciuta). The mean average value of these is (129 ± 1) $mL.g^{-1}$.

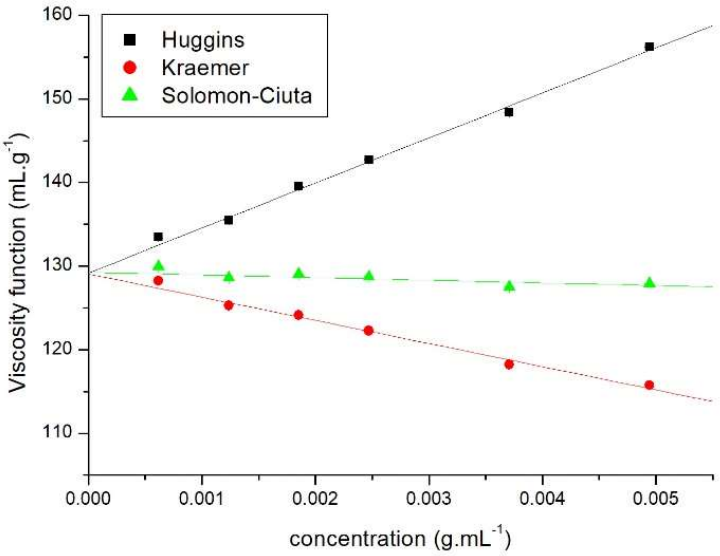


Figure 5.18 – Plot of viscosity against concentration for N-II after exposure to ten freeze-thaw cycles, with linear fits to extrapolate to zero concentration.

5.3.1.2 Sedimentation velocity

The distribution of sedimentation coefficients is shown in Figure 5.19. The peak data for the main component was also plotted against the loading concentration in Figure 5.20 and extrapolated back to zero concentration, giving the sedimentation coefficient as (6.76 ± 0.06) S. As the gradient is close to zero, the data can be treated as a set of repeated measurements (as discussed on page 50). The sedimentation coefficient can instead be calculated as (6.04 ± 0.35) S.

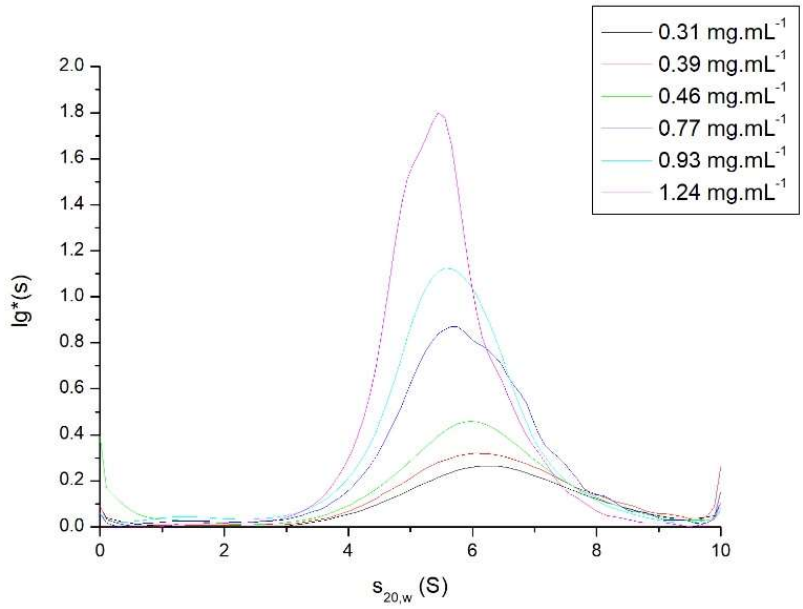


Figure 5.19 – Distribution of sedimentation coefficients at a range of loading concentrations of N-II after ten freeze-thaw cycles.

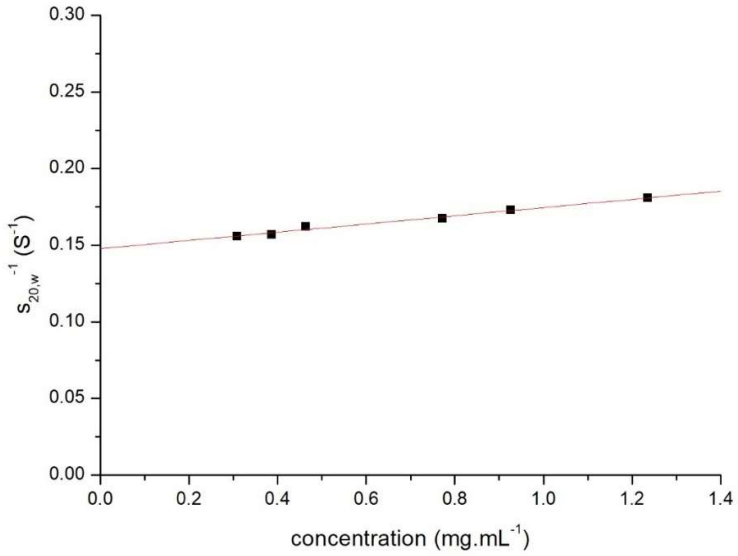


Figure 5.20 – Plot of the reciprocal of sedimentation coefficient against loading concentration for N-II after exposure to ten freeze-thaw cycles, with a linear fit to extrapolate to zero concentration.

5.3.1.3 Sedimentation equilibrium

SEDFIT-MSTAR provides two methods of determining apparent molecular weight, $M_{w,app}$: from the M^* function and from hinge point analysis. The values given by the program are plotted against loading concentration in Figure 5.21. Extrapolation to zero concentration

gave 'thermodynamically ideal' values of M_w as (330 ± 12) kDa (from the M* method) and (326 ± 4) kDa (from the hinge method). Combining the two yields a consensus value for Mw of (328 ± 7) kDa.

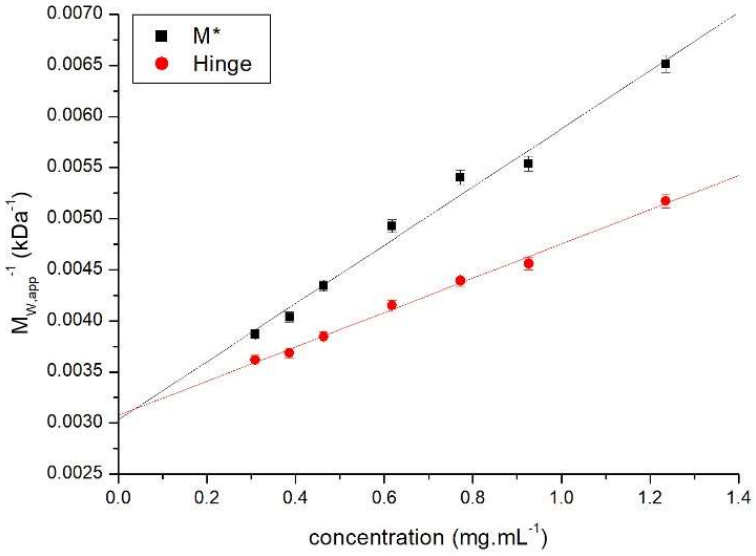


Figure 5.21 – Plot of the reciprocal of apparent molecular weight ($M_{w,app}$) values against loading concentration of N-II after exposure to ten freeze-thaw cycles, with a linear fit to extrapolate to zero concentration.

5.3.1.4 SEC-MALS

The M_w of the main peak was determined to be (466 ± 1) kDa, with a polydispersity (M_w/M_n) of 1.108 ± 0.003. [η] was found to be 126 mL.g^{-1} although no error is described at this level of precision.

5.3.2 One hundred freeze-thaw cycles

5.3.2.1 Viscosity

Plotting the relevant viscosity functions and extrapolating back to where the concentration is zero in Figure 5.22 gives the intrinsic viscosities as (136 ± 2) mL.g^{-1} (Huggins), (133 ± 1) mL.g^{-1} (Kraemer) and (134 ± 2) mL.g^{-1} (Solomon-Ciuta). The mean average value of these is (134 ± 1) mL.g^{-1}.

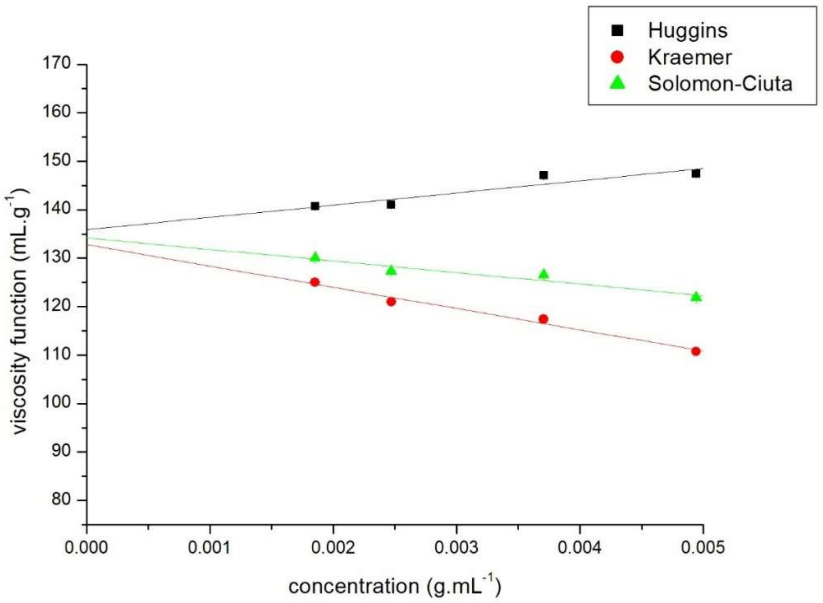


Figure 5.22 – Plot of viscosity against concentration for N-II after exposure to 100 freeze-thaw cycles, with linear fits to extrapolate to zero concentration.

5.3.2.2 Sedimentation Velocity

The distribution of sedimentation coefficients is shown in Figure 5.23. The peak data for the main component was also plotted against the loading concentration in Figure 5.24 and extrapolated back to zero concentration, giving the sedimentation coefficient as (5.86 ± 0.03) S. As the gradient is close to zero, the data can be treated as a set of repeated measurements (as discussed on page 50). The sedimentation coefficient can instead be calculated as (5.14 ± 0.31) S.

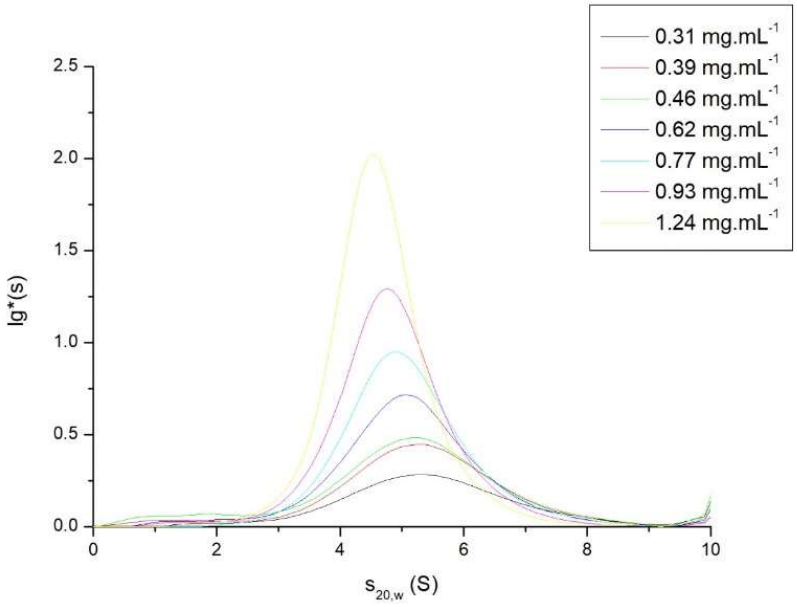


Figure 5.23– Distribution of sedimentation coefficients at a range of loading concentrations of N-II after 100 freeze-thaw cycles.

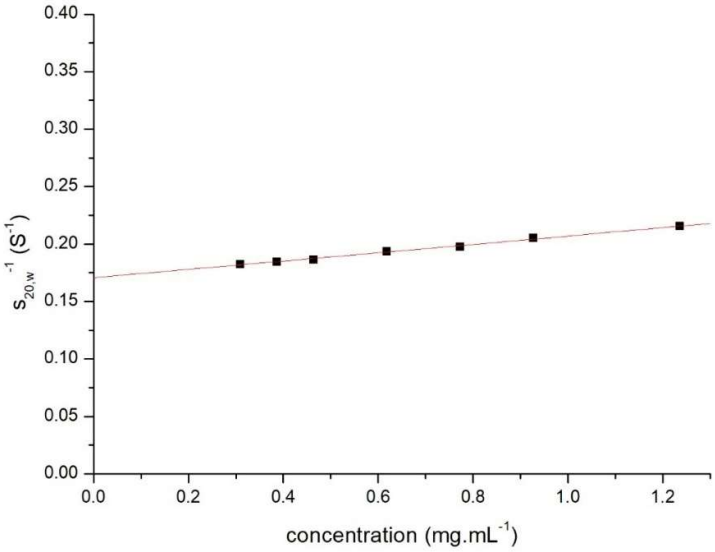


Figure 5.24 – Plot of the reciprocal of sedimentation coefficient against concentration for N-II after exposure to 100 freeze-thaw cycles, with a linear fit to extrapolate to zero concentration.

5.3.2.3 Sedimentation Equilibrium

SEDFIT-MSTAR provides two methods of determining apparent molecular weight, $M_{w,app}$: from the *M** function and from hinge point analysis. The values given by the program are

plotted against loading concentration in Figure 5.25. Extrapolation to zero concentration gave 'thermodynamically ideal' values of M_w as (446 ± 7) kDa (from the M* method) and (415 ± 3) kDa (from the hinge method). Combining the two yields a consensus value for Mw of (431 ± 4) kDa.

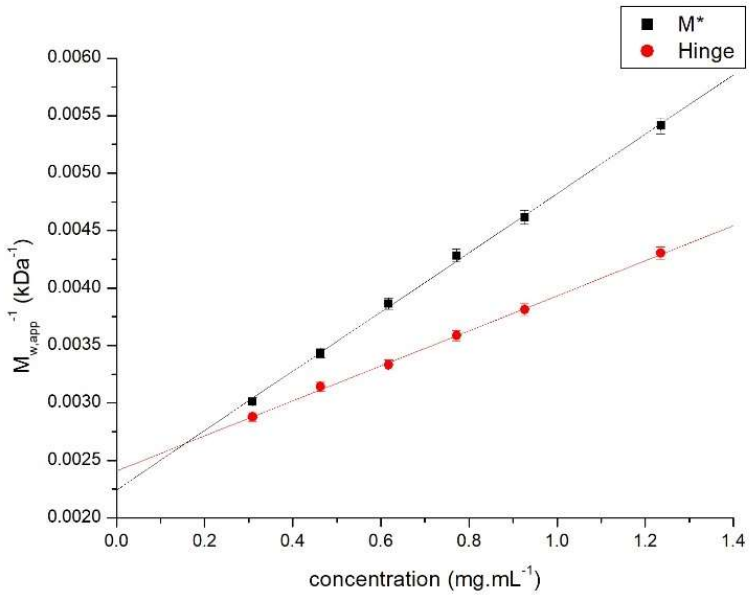


Figure 5.25 – Plot of the reciprocal of apparent molecular weight ($M_{w,app}$)values against concentration of N-II after exposure to 100 freeze-thaw cycles, with a linear fit to extrapolate to zero concentration.

5.3.2.4 SEC-MALS

The M_w of the main peak was determined to be (466 ± 1) kDa, with a polydispersity (M_w/M_n) of 1.256 ± 0.007. [η] was found to be 136 mL.g^{-1}, although no error is described at this level of precision.

5.4 Native GBS polysaccharide, serotype III

5.4.1 Ten freeze-thaw cycles

5.4.1.1 Viscosity

Plotting the relevant viscosity functions and extrapolating back to where the concentration is zero in Figure 5.26 gives the intrinsic viscosities as (47.5 ± 0.4) mL.g^{-1} (Huggins), (47.6 ± 0.3) mL.g^{-1} (Kraemer) and (47.6 ± 0.3) mL.g^{-1} (Solomon-Ciuta). The mean average value of these is (47.5 ± 0.2) mL.g^{-1}.

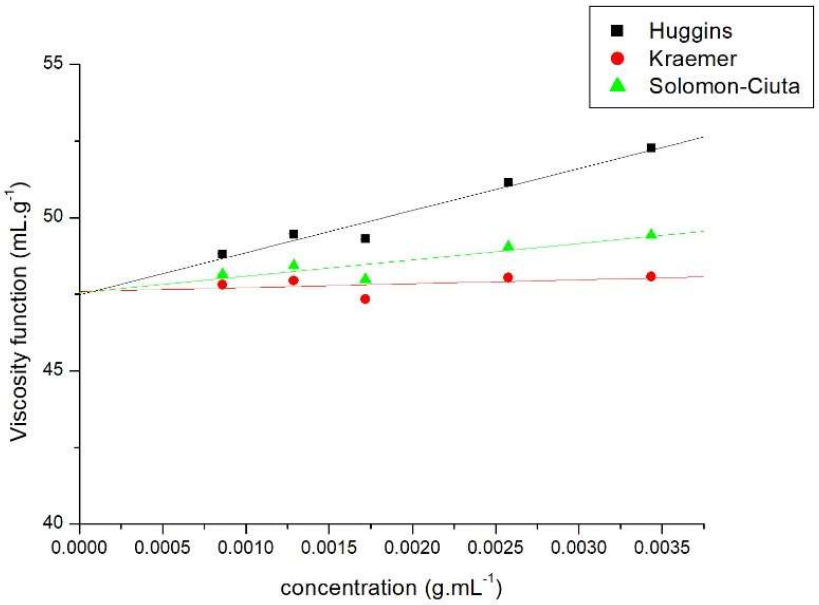


Figure 5.26 – Plot of viscosity against concentration for N-III after exposure to ten freeze-thaw cycles, with linear fits to extrapolate to zero concentration.

5.4.1.2 Sedimentation velocity

The distribution of sedimentation coefficients is shown in Figure 5.27. The peak data for the main component was also plotted against loading concentration in Figure 5.28 and extrapolated back to zero concentration, giving the sedimentation coefficient as (3.55 ± 0.02) S. As the gradient is close to zero, the data can be treated as a set of repeated measurements (as discussed on page 50). The sedimentation coefficient can instead be calculated as (3.42 ± 0.07) S.

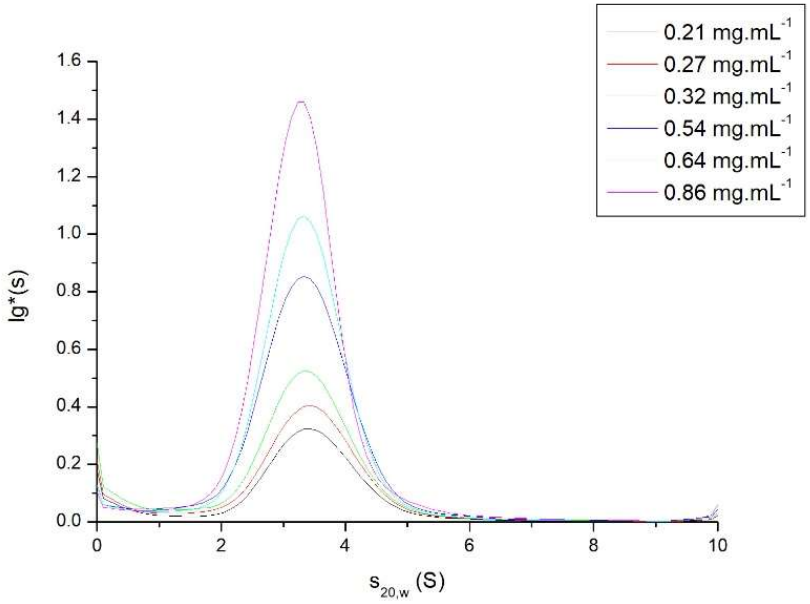


Figure 5.27 – Distribution of sedimentation coefficients at a range of loading concentrations of N-III after ten freeze-thaw cycles.

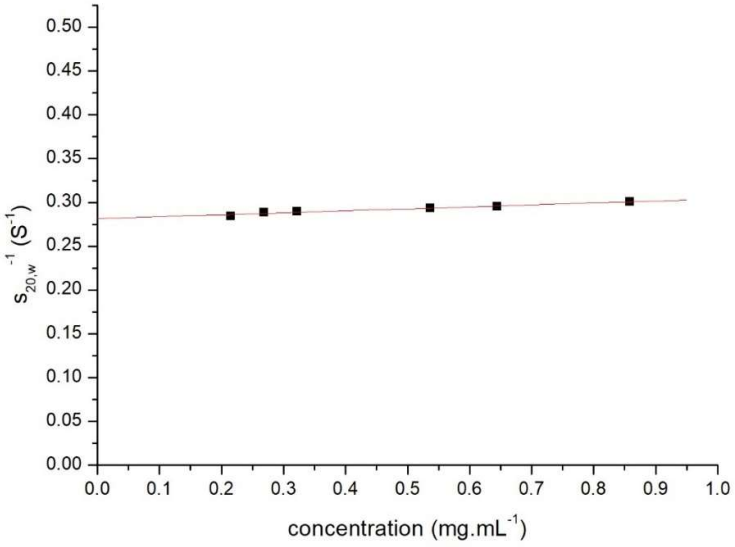


Figure 5.28 – Plot of the reciprocal of sedimentation coefficient against loading concentration for N-III after exposure to ten freeze-thaw cycles, with a linear fit to extrapolate to zero concentration.

5.4.1.3 Sedimentation equilibrium

SEDFIT-MSTAR provides two methods of determining apparent molecular weight, $M_{w,app}$: from the *M** function and from hinge point analysis. The values given by the program are plotted against loading concentration in Figure 5.29. Extrapolation to zero concentration

gave 'thermodynamically ideal' values of M_w as (116 ± 7) kDa (from the M* method) and (111 ± 10 kDa (from the hinge method). Combining the two yields a consensus value for Mw of (114 ± 6) kDa.

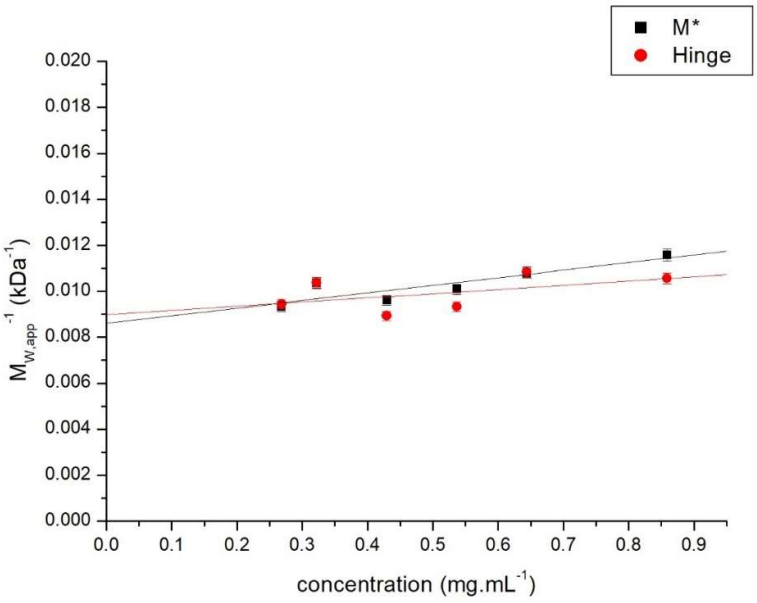


Figure 5.29 – Plot of the reciprocal of apparent molecular weight ($M_{w,app}$) values against loading concentration of N-III after exposure to ten freeze-thaw cycles, with a linear fit to extrapolate to zero concentration.

5.4.1.4 SEC-MALS

The M_w of the main peak was determined to be 107 kDa, although no error is described at this level of precision, with a polydispersity (M_w/M_n) of 1.005 ± 0.004. [η] was found to be (52.9 ± 0.1) mL.g^{-1}.

5.4.2 One hundred freeze-thaw cycles

5.4.2.1 Viscosity

Plotting the relevant viscosity functions and extrapolating back to where the concentration is zero in Figure 5.30 gives the intrinsic viscosities as (47.0 ± 0.4) mL.g^{-1} (Huggins), (47.1 ± 0.4) mL.g^{-1} (Kraemer) and (47.1 ± 0.4) mL.g^{-1} (Solomon-Ciuta). The mean average value of these is (47.1 ± 0.2) mL.g^{-1}.

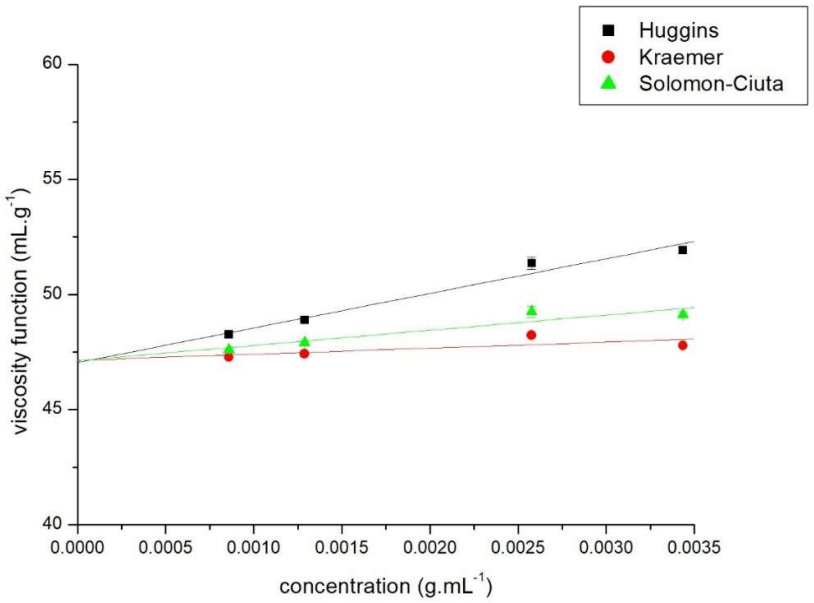


Figure 5.30 – Plot of viscosity against concentration for N-III after exposure to 100 freeze-thaw cycles, with linear fits to extrapolate to zero concentration.

5.4.2.2 Sedimentation Velocity

The distribution of sedimentation coefficients is shown in Figure 5.31. The peak data for the main component was also plotted against loading concentration in Figure 5.32 and extrapolated back to zero concentration, giving the sedimentation coefficient as (2.95 ± 0.02) S. As the gradient is close to zero, the data can be treated as a set of repeated measurements (as discussed on page 50). The sedimentation coefficient can instead be calculated as (2.86 ± 0.04) S.

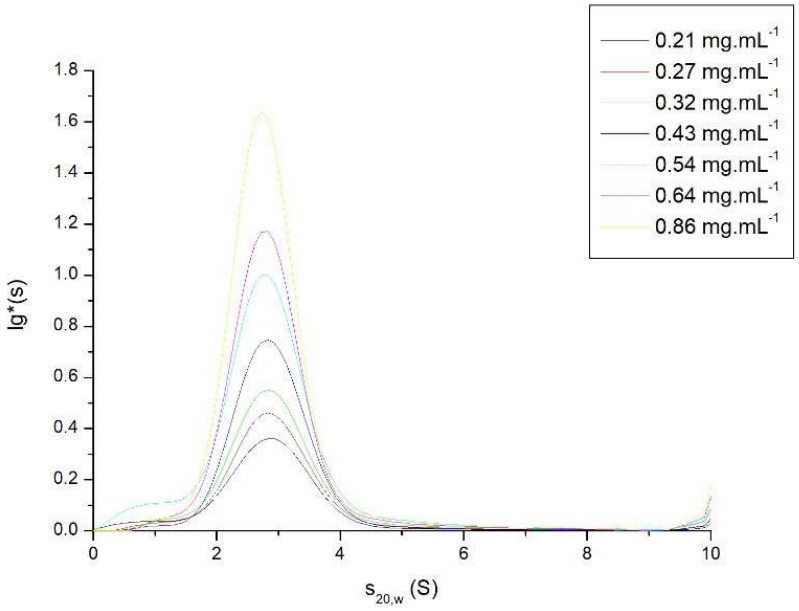


Figure 5.31 – Distribution of sedimentation coefficients at a range of loading concentrations of N-III after 100 freeze-thaw cycles.

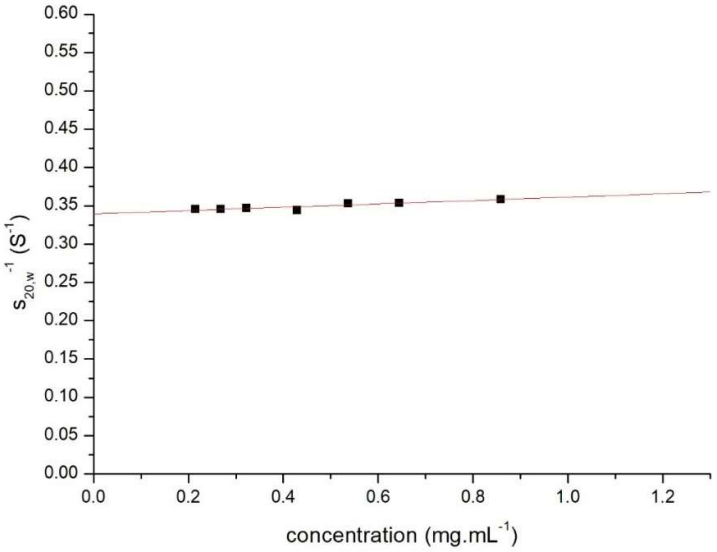


Figure 5.32 – Plot of the reciprocal of sedimentation coefficient against loading concentration for N-III after exposure to 100 freeze-thaw cycles, with a linear fit to extrapolate to zero concentration.

5.4.2.3 Sedimentation Equilibrium

SEDFIT-MSTAR provides two methods of determining apparent molecular weight, $M_{w,app}$: from the M^* function and from hinge point analysis. The values given by the program are

plotted against loading concentration in Figure 5.33. Extrapolation to zero concentration gave 'thermodynamically ideal' values of M_w as (147 ± 8) kDa (from the M* method) and (142 ± 8) kDa (from the hinge method). Combining the two yields a consensus value for Mw of (145 ± 6) kDa.

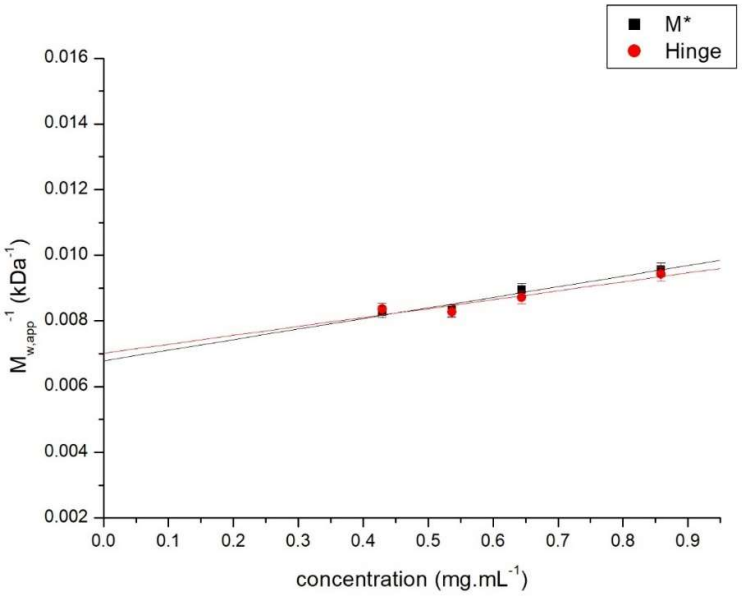


Figure 5.33 – Plot of the reciprocal of apparent molecular weight ($M_{w,app}$) values against loading concentration of N-III after exposure to 100 freeze-thaw cycles, with a linear fit to extrapolate to zero concentration.

5.4.2.4 SEC-MALS

The M_w of the main peak was determined to be 103 kDa, although no error is described at this level of precision, with a polydispersity (M_w/M_n) of 1.042 ± 0.004. [η] was found to be (54.4 ± 0.4) mL.g^{-1}.

5.5 Native GBS polysaccharide, serotype IV

5.5.1 Ten freeze-thaw cycles

5.5.1.1 Viscosity

Plotting the relevant viscosity functions and extrapolating back to where the concentration is zero in Figure 5.34 gives the intrinsic viscosities as (66.9 ± 1.2) $mL.g^{-1}$ (Huggins), (67.0 ± 1.1) $mL.g^{-1}$ (Kraemer) and (67.0 ± 1.2) $mL.g^{-1}$ (Solomon-Ciuta). The mean average value of these is (67.0 ± 0.7) $mL.g^{-1}$.

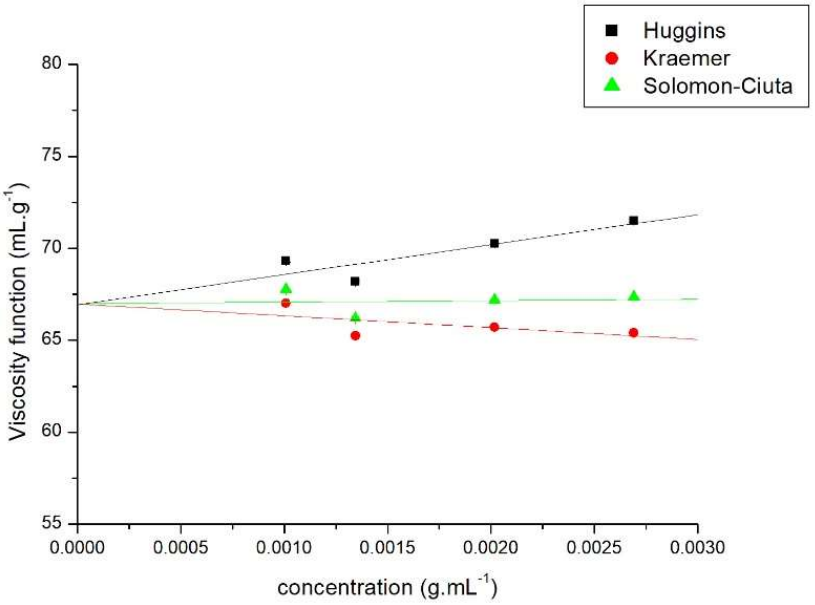


Figure 5.34 – Plot of viscosity against concentration for N-IV after exposure to ten freeze-thaw cycles, with linear fits to extrapolate to zero concentration.

5.5.1.2 Sedimentation velocity

The distribution of sedimentation coefficients is shown in Figure 5.35. The peak data for the main component was also plotted against loading concentration in Figure 5.36 and extrapolated back to zero concentration, giving the sedimentation coefficient as (2.79 ± 0.02) S. As the gradient is close to zero, the data can be treated as a set of repeated measurements (as discussed on page 50). The sedimentation coefficient can instead be calculated as (2.69 ± 0.05) S.

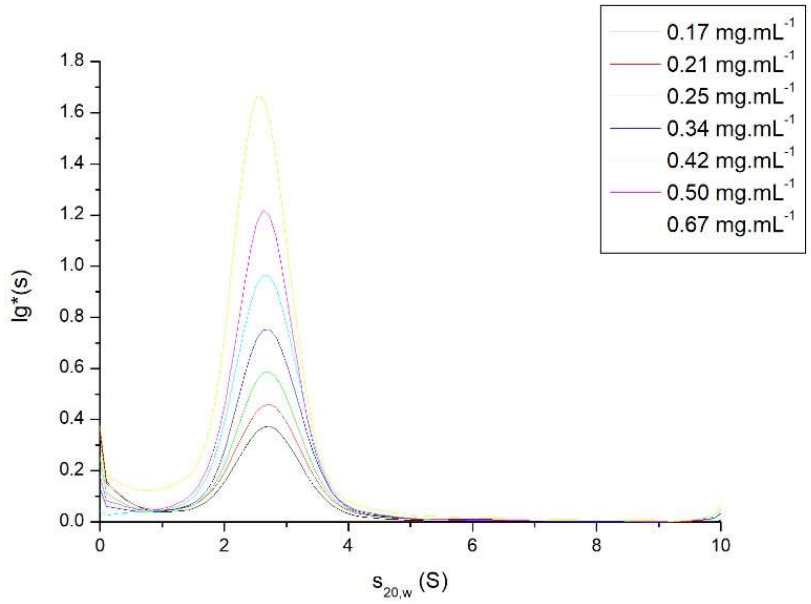


Figure 5.35 – Distribution of sedimentation coefficients at a range of loading concentrations of N-IV after ten freeze-thaw cycles.

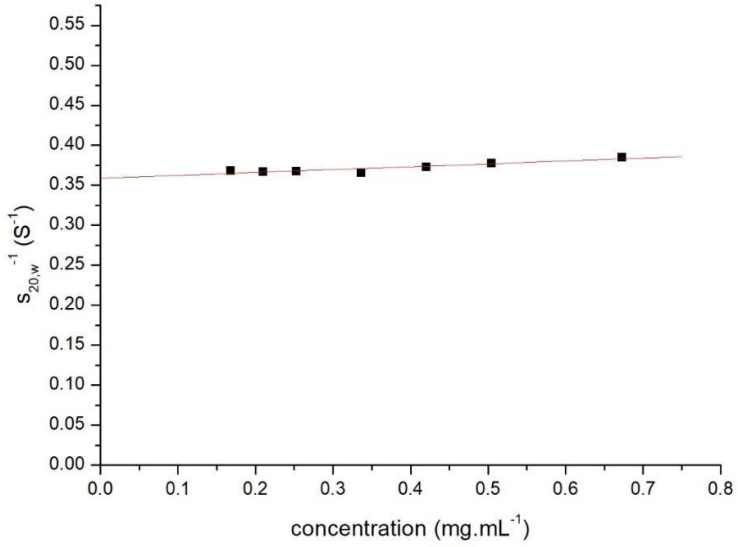


Figure 5.36 – Plot of the reciprocal of sedimentation coefficient against loading concentration for N-IV after exposure to ten freeze-thaw cycles, with a linear fit to extrapolate to zero concentration.

5.5.1.3 Sedimentation equilibrium

SEDFIT-MSTAR provides two methods of determining apparent molecular weight, $M_{w,app}$: from the M^* function and from hinge point analysis. The values given by the program are plotted against loading concentration in Figure 5.37. Extrapolation to zero concentration

gave 'thermodynamically ideal' values of M_w as (64.1 ± 3.2) kDa (from the M* method) and (64.4 ± 6.2) kDa (from the hinge method). Combining the two yields a consensus value for Mw of (64.2 ± 3.5) kDa.

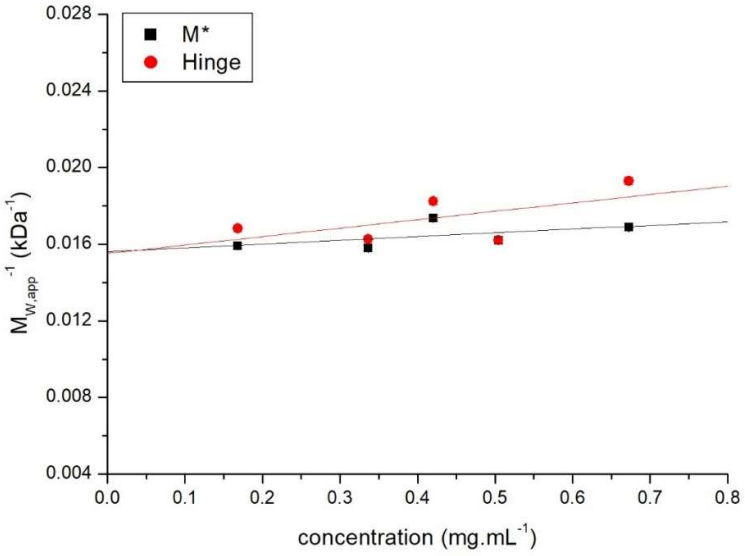


Figure 5.37 – Plot of the reciprocal of apparent molecular weight ($M_{w,app}$) values against loading concentration of N-IV after exposure to ten freeze-thaw cycles, with a linear fit to extrapolate to zero concentration.

5.5.1.4 SEC-MALS

The M_w of the main peak was determined to be (63.1 ± 0.2) kDa, with a polydispersity (M_w/M_n) of 1.003 ± 0.004. [η] was found to be (50.6 ± 0.1) mL.g^{-1}.

5.5.2 One hundred freeze-thaw cycles

5.5.2.1 Viscosity

Plotting the relevant viscosity functions and extrapolating back to where the concentration is zero in Figure 5.38 gives the intrinsic viscosities as (52.3 ± 0.6) mL.g^{-1} (Huggins), (52.8 ± 0.7) mL.g^{-1} (Kraemer) and (52.7 ± 0.7) mL.g^{-1} (Solomon-Ciuta). The mean average value of these is (52.6 ± 0.4) mL.g^{-1}.

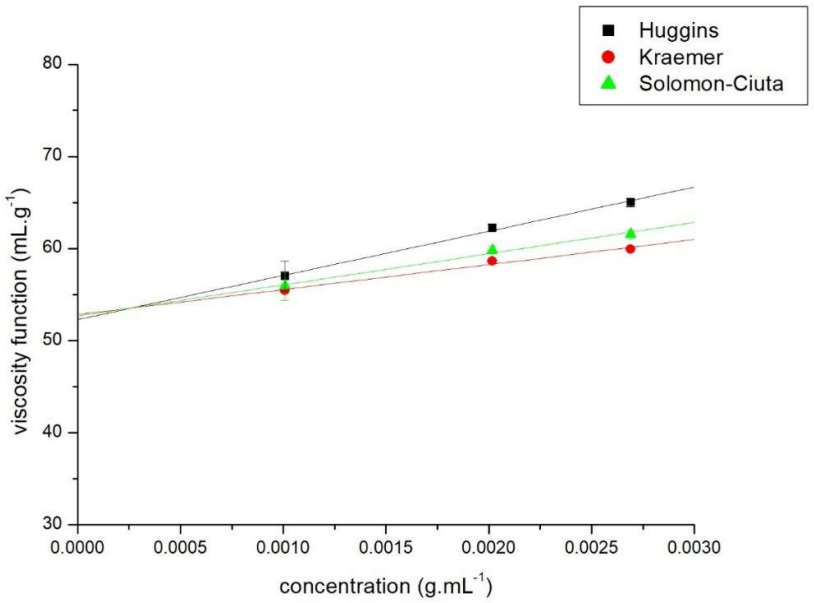


Figure 5.38 – Plot of viscosity against concentration for N-IV after exposure to 100 freeze-thaw cycles, with linear fits to extrapolate to zero concentration.

5.5.2.2 Sedimentation Velocity

The distribution of sedimentation coefficients is shown in Figure 5.39. The peak data for the main component was also plotted against loading concentration in Figure 5.40 and extrapolated back to zero concentration, giving the sedimentation coefficient as (2.37 ± 0.02) S. As the gradient is close to zero, the data can be treated as a set of repeated measurements (as discussed on page 50). The sedimentation coefficient can instead be calculated as (2.28 ± 0.04) S.

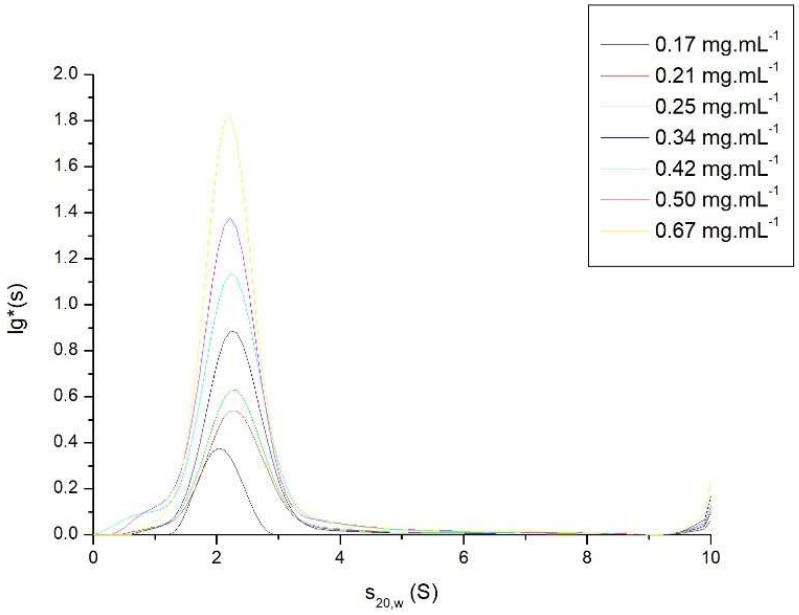


Figure 5.39 – Distribution of sedimentation coefficients at a range of loading concentrations of N-IV after 100 freeze-thaw cycles.

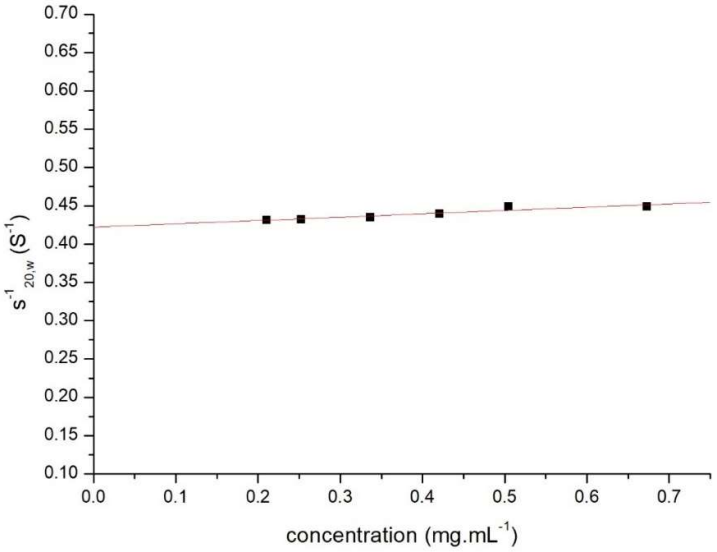


Figure 5.40 – Plot of the reciprocal of sedimentation coefficient against loading concentration for N-IV after exposure to 100 freeze-thaw cycles, with a linear fit to extrapolate to zero concentration.

5.5.2.3 Sedimentation Equilibrium

SEDFIT-MSTAR provides two methods of determining apparent molecular weight, $M_{w,app}$: from the M^* function and from hinge point analysis. The values given by the program are

plotted against loading concentration in Figure 5.41. Extrapolation to zero concentration gave 'thermodynamically ideal' values of M_w as (89.0 ± 1.8) kDa (from the M* method) and (97.3 ± 2.8) kDa (from the hinge method). Combining the two yields a consensus value for Mw of (93.2 ± 1.7) kDa.

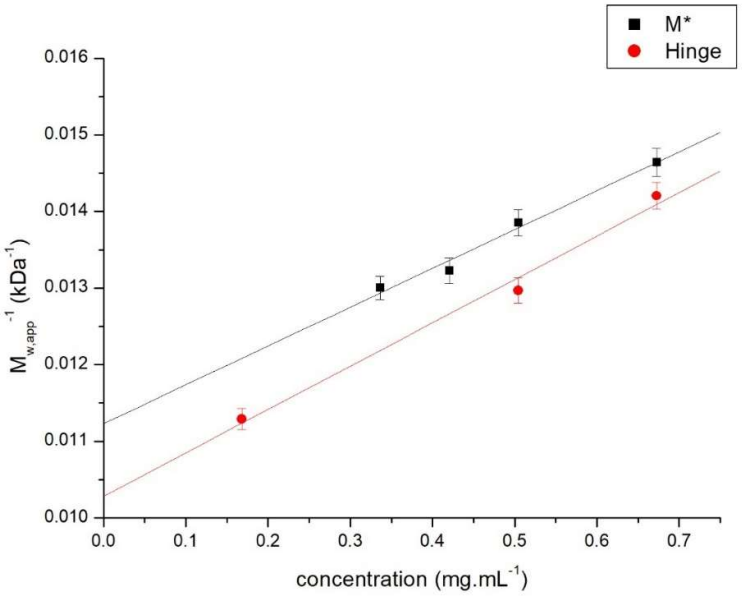


Figure 5.41 – Plot of the reciprocal of apparent molecular weight ($M_{w,app}$) values against loading concentration of N-IV after exposure to 100 freeze-thaw cycles, with a linear fit to extrapolate to zero concentration.

5.5.2.4 SEC-MALS

The M_w of the main peak was determined to be (89.1 ± 1.5) kDa, with a polydispersity (M_w/M_n) of 1.043 ± 0.028. [η] was found to be (77.7 ± 0.4) mL.g^{-1}, although no error is described at this level of precision.

5.6 Native GBS polysaccharide, serotype V

5.6.1 Ten freeze-thaw cycles

5.6.1.1 Viscosity

Plotting the relevant viscosity functions and extrapolating back to where the concentration is zero in Figure 5.42 gives the intrinsic viscosities as 106 $mL.g^{-1}$ (Huggins), 105 $mL.g^{-1}$ (Kraemer) and 105 $mL.g^{-1}$ (Solomon-Ciuta), where in each case no error is described at this level of precision. The mean average value of these is 105 $mL.g^{-1}$ although no error is described at this level of precision.

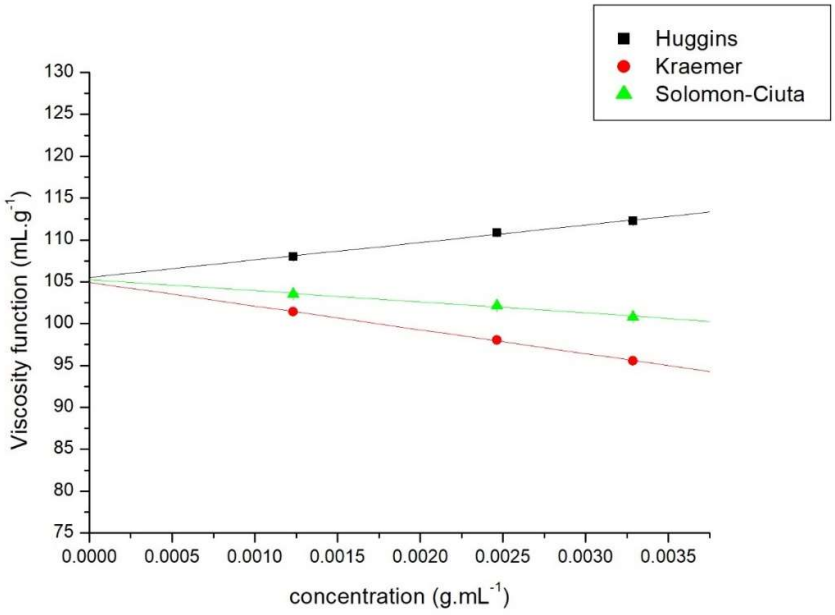


Figure 5.42 – Plot of viscosity against concentration for N-V after exposure to ten freeze-thaw cycles, with linear fits to extrapolate to zero concentration.

5.6.1.2 Sedimentation velocity

The distribution of sedimentation coefficients is shown in Figure 5.43. The peak data for the main component was also plotted against loading concentration in Figure 5.44 and extrapolated back to zero concentration, giving the sedimentation coefficient as (3.92 ± 0.01) S. As the gradient is close to zero, the data can be treated as a set of repeated measurements

(as discussed on page 50). The sedimentation coefficient can instead be calculated as (3.71 ± 0.1) S.

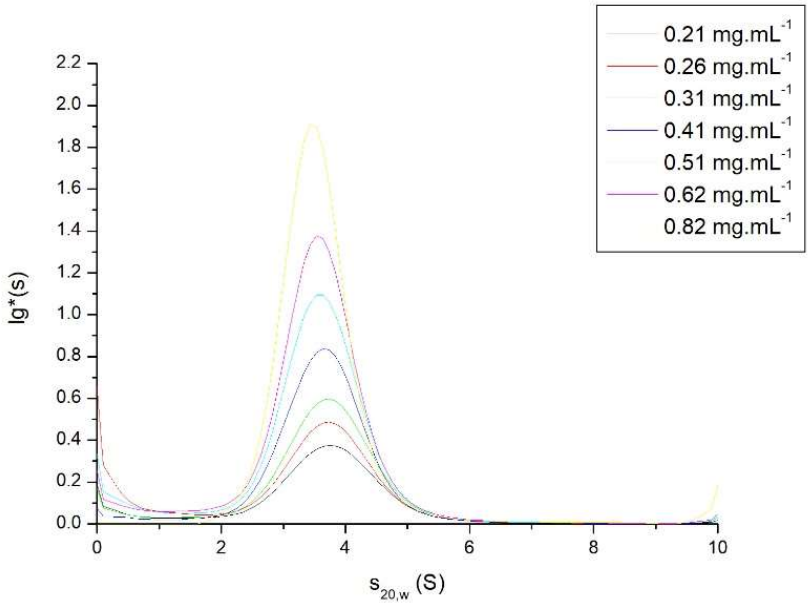


Figure 5.43 – Distribution of sedimentation coefficients at a range of loading concentrations of N-V after ten freeze-thaw cycles.

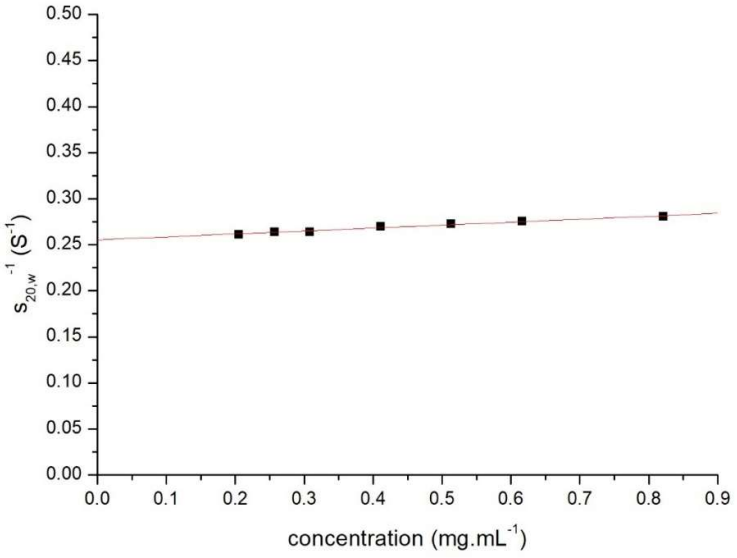


Figure 5.44 – Plot of the reciprocal of sedimentation coefficient against loading concentration for N-V after exposure to ten freeze-thaw cycles, with a linear fit to extrapolate to zero concentration.

5.6.1.3 Sedimentation equilibrium

SEDFIT-MSTAR provides two methods of determining apparent molecular weight, $M_{w,app}$: from the M^* function and from hinge point analysis. The values given by the program are plotted against loading concentration in Figure 5.45. Extrapolation to zero concentration gave 'thermodynamically ideal' values of M_w as (182 ± 10) kDa (from the M* method) and (193 ± 11) kDa (from the hinge method). Combining the two yields a consensus value for Mw of (187 ± 7) kDa.

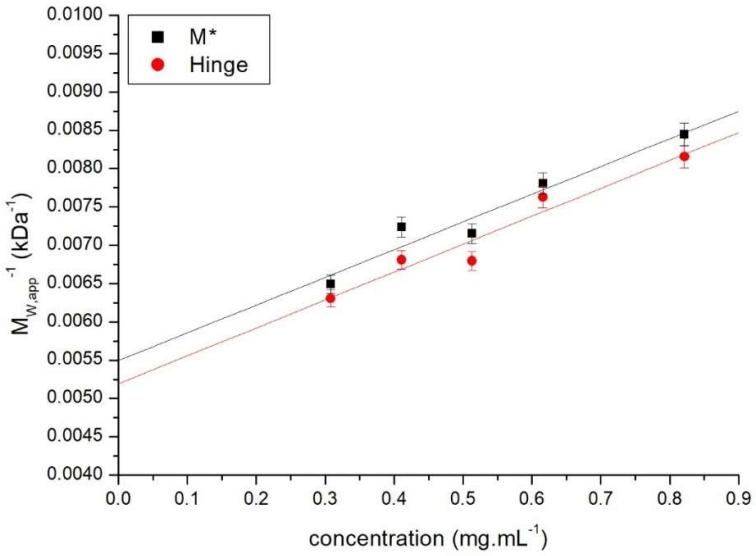


Figure 5.45 – Plot of the reciprocal of apparent molecular weight ($M_{w,app}$) values against loading concentration of N-V after exposure to ten freeze-thaw cycles, with a linear fit to extrapolate to zero concentration.

5.6.1.4 SEC-MALS

The M_w of the main peak was determined to be 126 kDa, although no error is described at this level of precision, with a polydispersity (M_w/M_n) of 1.009 ± 0.004. [η] was found to be (74.4 ± 0.1) mL.g^{-1}.

5.6.2 One hundred freeze-thaw cycles

5.6.2.1 Viscosity

Plotting the relevant viscosity functions and extrapolating back to where the concentration is zero in Figure 5.46 gives the intrinsic viscosities as (91.2 ± 0.4) $mL.g^{-1}$ (Huggins), (91.5 ± 0.4) $mL.g^{-1}$ (Kraemer) and (91.4 ± 0.4) $mL.g^{-1}$ (Solomon-Ciuta). The mean average value of these is (91.4 ± 0.2) $mL.g^{-1}$.

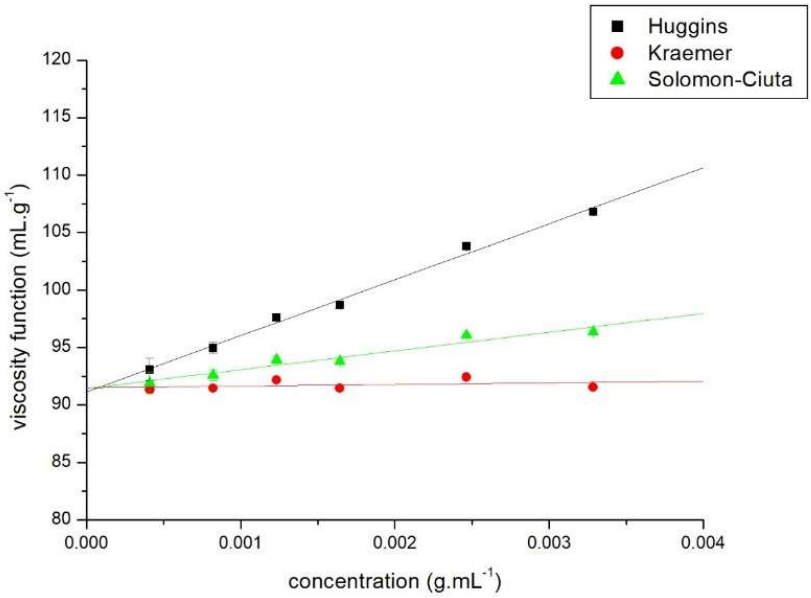


Figure 5.46 – Plot of viscosity against concentration for N-V after exposure to 100 freeze-thaw cycles, with linear fits to extrapolate to zero concentration.

5.6.2.2 Sedimentation Velocity

The distribution of sedimentation coefficients is shown in Figure 5.47. The peak data for the main component was also plotted against loading concentration in Figure 5.48 and extrapolated back to zero concentration, giving the sedimentation coefficient as (3.28 ± 0.06) S. As the gradient is close to zero, the data can be treated as a set of repeated measurements (as discussed on page 50). The sedimentation coefficient can instead be calculated as (3.71 ± 0.1) S.

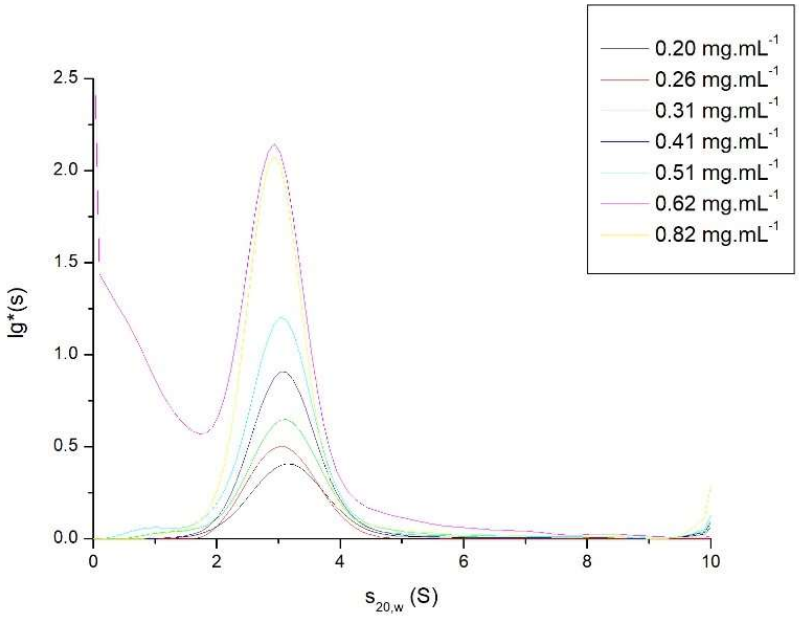
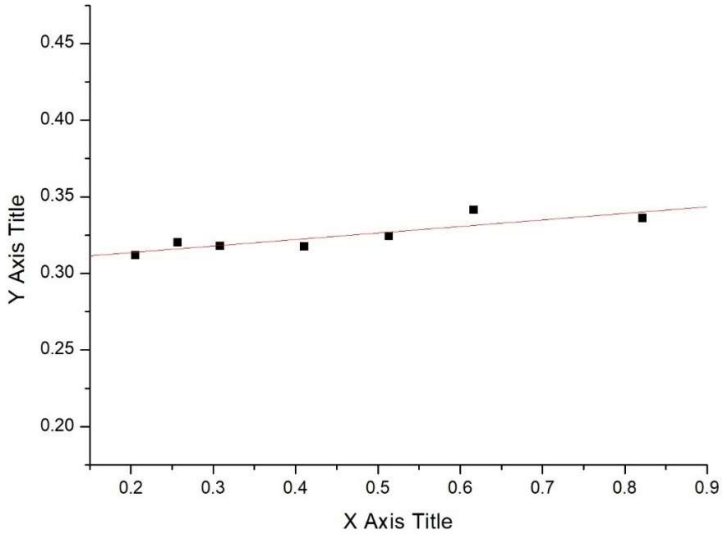


Figure 5.47 – Distribution of sedimentation coefficients at a range of loading concentrations of N-V after 100 freeze-thaw cycles.



9

Figure 5.48 – Plot of the reciprocal of sedimentation coefficient against loading concentration for N-V after exposure to 100 freeze-thaw cycles, with a linear fit to extrapolate to zero concentration.

5.6.2.3 Sedimentation Equilibrium

SEDFIT-MSTAR provides two methods of determining apparent molecular weight, $M_{w,app}$: from the *M** function and from hinge point analysis. The values given by the program are

plotted against loading concentration in Figure 5.49. Extrapolation to zero concentration gave 'thermodynamically ideal' values of M_w as (211 ± 3) kDa (from the M* method) and (193 ± 5) kDa (from the hinge method). Combining the two yields a consensus value for Mw of (202 ± 3) kDa.

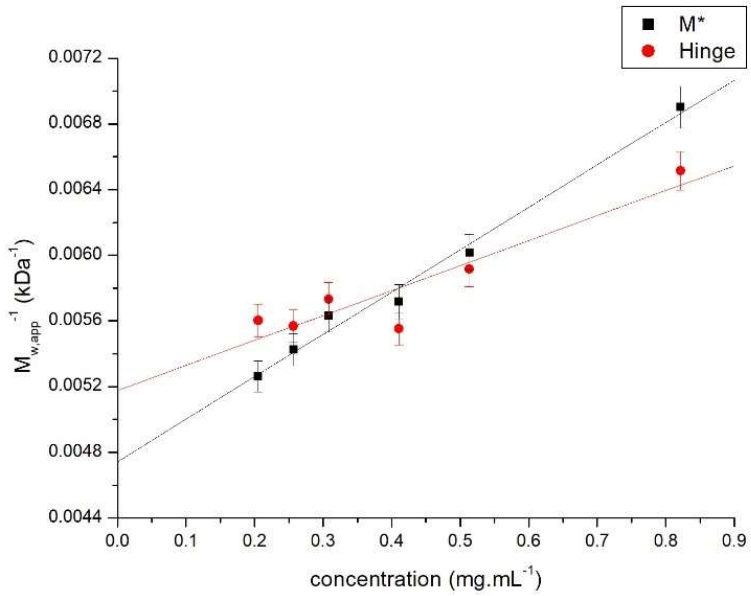


Figure 5.49 – Plot of the reciprocal of apparent molecular weight ($M_{w,app}$) values against loading concentration of N-V after exposure to 100 freeze-thaw cycles, with a linear fit to extrapolate to zero concentration.

5.6.2.4 SEC-MALS

The M_w of the main peak was determined to be (172 ± 1) kDa, with a polydispersity (M_w/M_n) of 1.100 ± 0.015. [η] was found to be 111 mL.g^{-1}, although no error is described at this level of precision.

5.7 Sized GBS polysaccharide, serotype IA

5.7.1 Ten freeze-thaw cycles

5.7.1.1 Viscosity

Plotting the relevant viscosity functions and extrapolating back to where the concentration is zero in Figure 5.50 gives the intrinsic viscosities as (52.2 ± 1.0) mL.g^{-1} (Huggins), (51.9 ± 0.9) mL.g^{-1} (Kraemer) and (52.0 ± 0.9) mL.g^{-1} (Solomon-Ciuta). The mean average value of these is (52.0 ± 0.6) mL.g^{-1}.

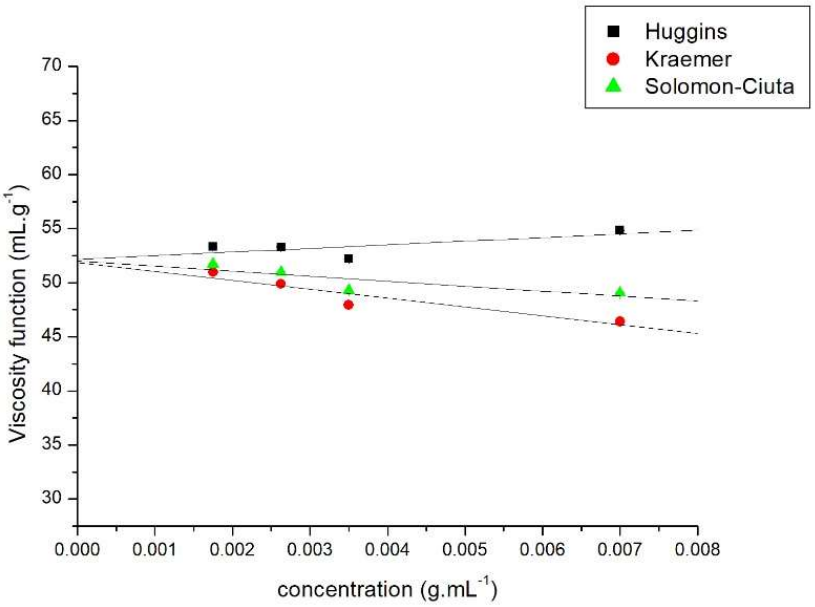


Figure 5.50 – Plot of viscosity against concentration for S-IA after exposure to ten freeze-thaw cycles, with linear fits to extrapolate to zero concentration.

5.7.1.2 Sedimentation velocity

The distribution of sedimentation coefficients is shown in Figure 5.51. The peak data for the main component was also plotted against loading concentration in Figure 5.52 and extrapolated back to zero concentration, giving the sedimentation coefficient as (3.32 ± 0.09) S. As the gradient is close to zero, the data can be treated as a set of repeated measurements (as discussed on page 50). The sedimentation coefficient can instead be calculated as (3.05 ± 0.14) S.

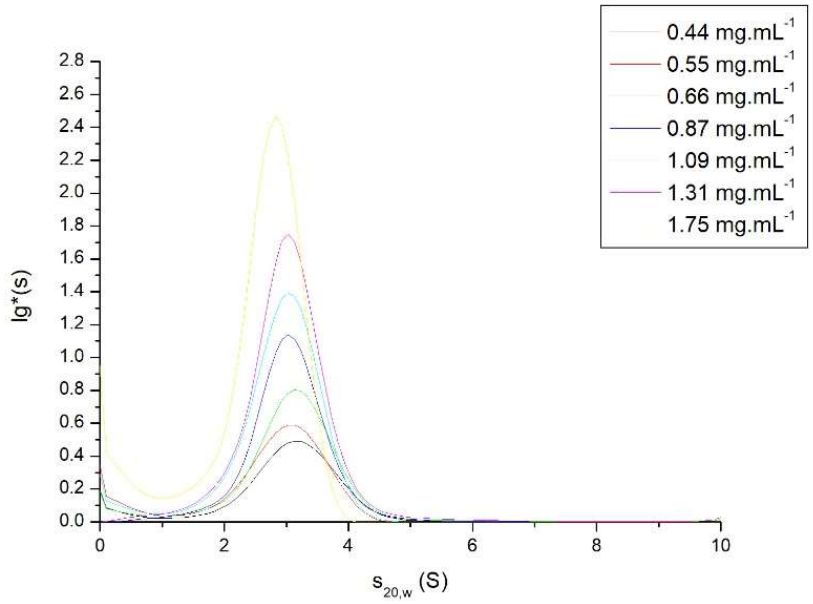


Figure 5.51 – Distribution of sedimentation coefficients at a range of loading concentrations of S-IA after ten freeze-thaw cycles.

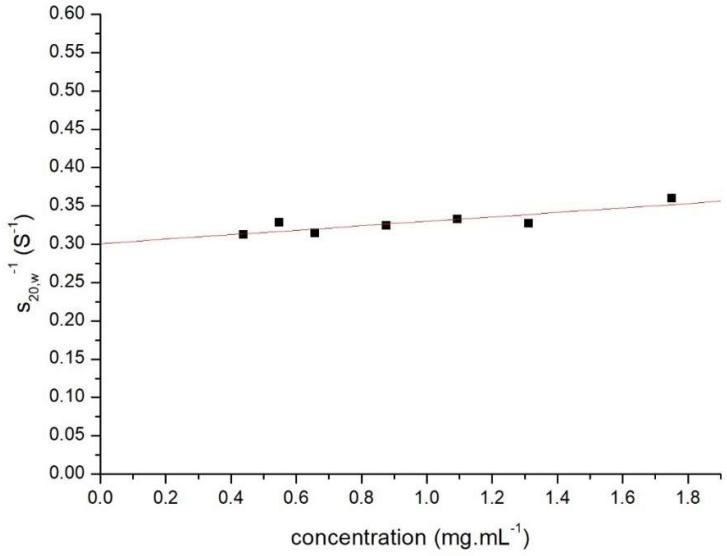


Figure 5.52 – Plot of the reciprocal of sedimentation coefficient against loading concentration for S-IA after exposure to ten freeze-thaw cycles, with a linear fit to extrapolate to zero concentration.

5.7.1.3 Sedimentation equilibrium

SEDFIT-MSTAR provides two methods of determining apparent molecular weight, $M_{w,app}$: from the *M** function and from hinge point analysis. The values given by the program are plotted against loading concentration in Figure 5.53. Extrapolation to zero concentration

gave 'thermodynamically ideal' values of M_w as (199 ± 8 kDa (from the M* method) and (201 ± 7) kDa (from the hinge method). Combining the two yields a consensus value for Mw of (200 ± 5) kDa.

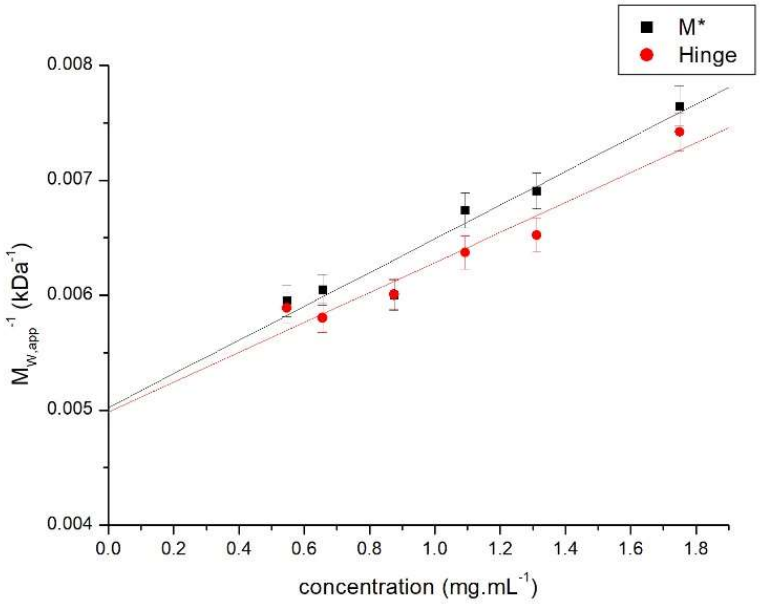


Figure 5.53 – Plot of the reciprocal of apparent molecular weight ($M_{w,app}$) values against loading concentration of S-IA after exposure to ten freeze-thaw cycles, with a linear fit to extrapolate to zero concentration.

5.7.1.4 SEC-MALS

The M_w of the main peak was determined to be 104 kDa, although no error is described at this level of precision, with a polydispersity (M_w/M_n) of 1.022 ± 0.004. [η] was found to be (71.4 ± 0.2) mL.g^{-1}.

5.7.2 One hundred freeze-thaw cycles

5.7.2.1 Viscosity

Plotting the relevant viscosity functions and extrapolating back to where the concentration is zero in Figure 5.54 gives the intrinsic viscosities as (44.3 ± 0.8) mL.g^{-1} (Huggins), (44.6 ± 0.8) mL.g^{-1} (Kraemer) and (44.6 ± 0.8) mL.g^{-1} (Solomon-Ciuta). The mean average value of these is (44.5 ± 0.4) mL.g^{-1}.

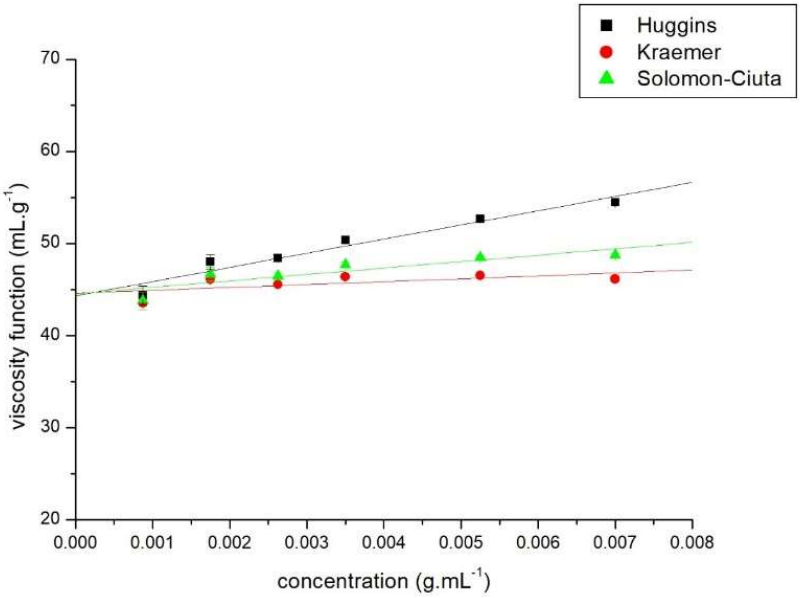


Figure 5.54 – Plot of viscosity against concentration for S-IA after exposure to 100 freeze-thaw cycles, with linear fits to extrapolate to zero concentration.

5.7.2.2 Sedimentation Velocity

The distribution of sedimentation coefficients is shown in Figure 5.55. The peak data for the main component was also plotted against loading concentration in Figure 5.56 and extrapolated back to zero concentration, giving the sedimentation coefficient as (2.82 ± 0.03) S. As the gradient is close to zero, the data can be treated as a set of repeated measurements (as discussed on page 50). The sedimentation coefficient can instead be calculated as (2.64 ± 0.09) S.

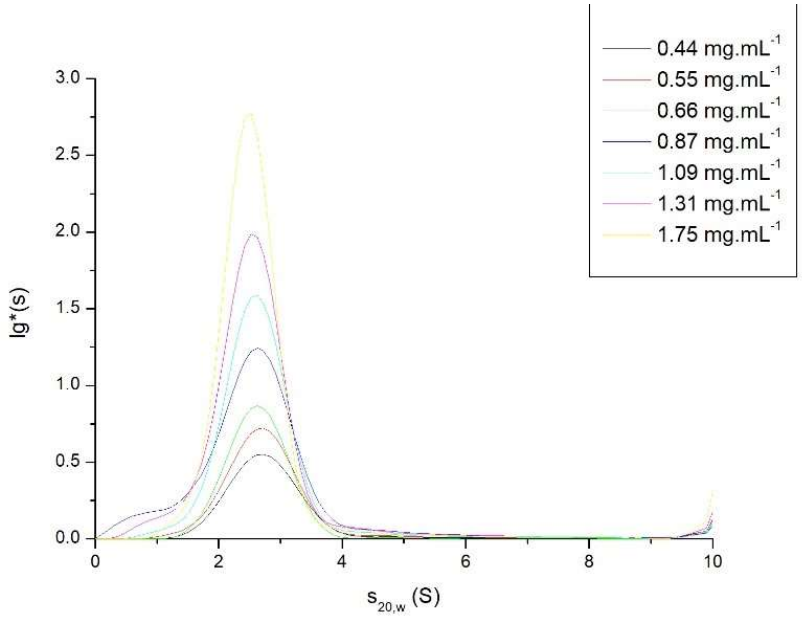


Figure 5.55 – Distribution of sedimentation coefficients at a range of loading concentrations of S-IA after 100 freeze-thaw cycles.

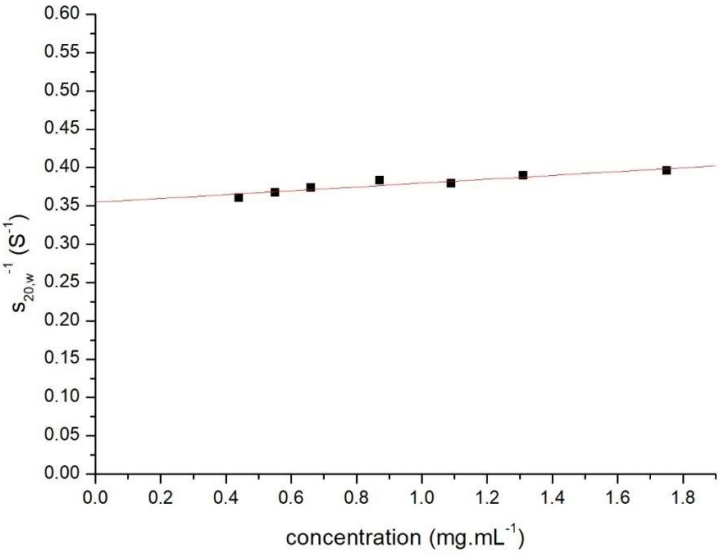


Figure 5.56 – Plot of the reciprocal of sedimentation coefficient against loading concentration for S-IA after exposure to 100 freeze-thaw cycles, with a linear fit to extrapolate to zero concentration.

5.7.2.3 Sedimentation Equilibrium

SEDFIT-MSTAR provides two methods of determining apparent molecular weight, $M_{w,app}$: from the M^* function and from hinge point analysis. The values given by the program are

plotted against loading concentration in Figure 5.57. Extrapolation to zero concentration gave 'thermodynamically ideal' values of M_w as (246 ± 3) kDa (from the M* method) and (244 ± 7) kDa (from the hinge method). Combining the two yields a consensus value for Mw of (245 ± 4) kDa.

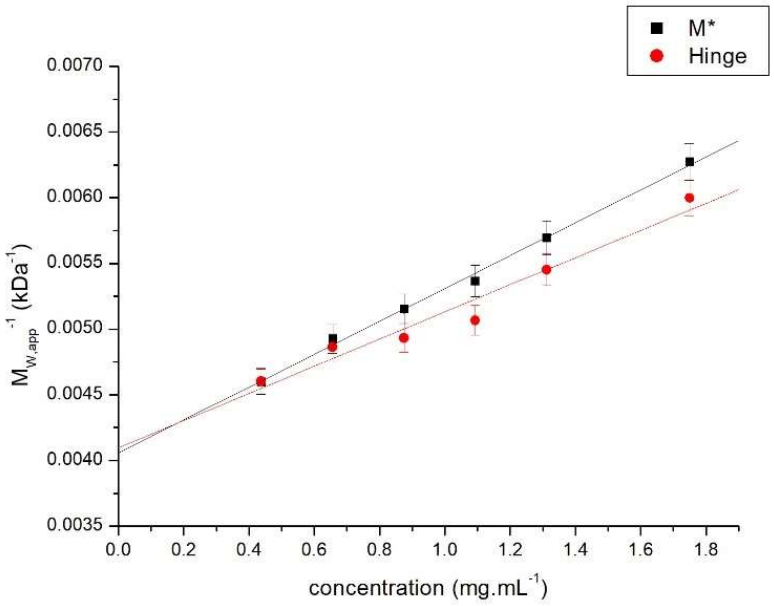


Figure 5.57 – Plot of the reciprocal of apparent molecular weight ($M_{w,app}$) values against loading concentration of S-IA after exposure to 100 freeze-thaw cycles, with a linear fit to extrapolate to zero concentration.

5.7.2.4 SEC-MALS

The M_w of the main peak was determined to be (207 ± 2) kDa, with a polydispersity (M_w/M_n) of 1.167 ± 0.218. [η] was found to be (98.7 ± 13.0) mL.g^{-1}.

5.8 Sized GBS polysaccharide, serotype IB

5.8.1 Ten freeze-thaw cycles

5.8.1.1 Viscosity

Plotting the relevant viscosity functions and extrapolating back to where the concentration is zero in Figure 5.58 gives the intrinsic viscosities as (63.9 ± 0.3) $mL.g^{-1}$ (Huggins), (64.1 ± 0.3) $mL.g^{-1}$ (Kraemer) and (64.1 ± 0.3) $mL.g^{-1}$ (Solomon-Ciuta). The mean average value of these is (64.0 ± 0.2) $mL.g^{-1}$.

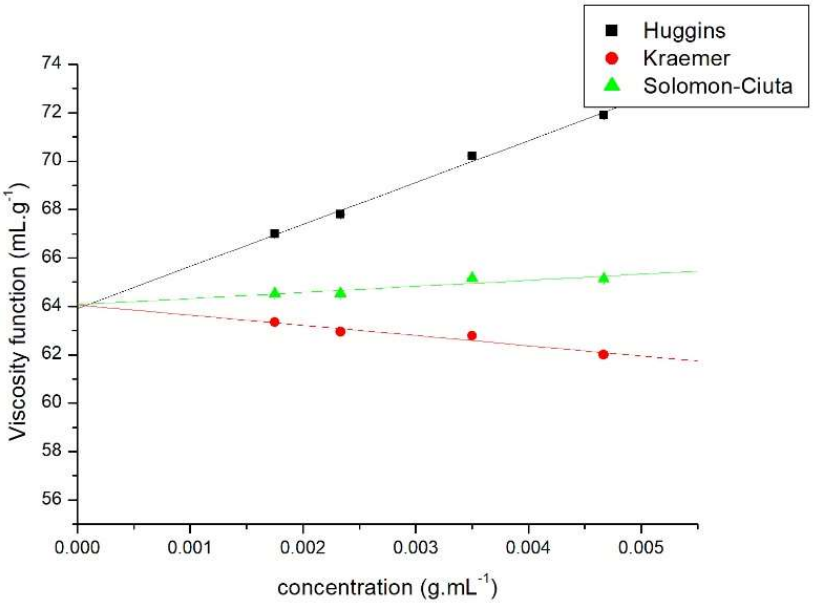


Figure 5.58 – Plot of viscosity against concentration for S-IB after exposure to ten freeze-thaw cycles, with linear fits to extrapolate to zero concentration.

5.8.1.2 Sedimentation velocity

The distribution of sedimentation coefficients is shown in Figure 5.59. The peak data for the main component was also plotted against loading concentration in Figure 5.60 and extrapolated back to zero concentration, giving the sedimentation coefficient as (3.10 ± 0.15) S. As the gradient is close to zero, the data can be treated as a set of repeated measurements (as discussed on page 50). The sedimentation coefficient can instead be calculated as (3.09 ± 0.14) S.

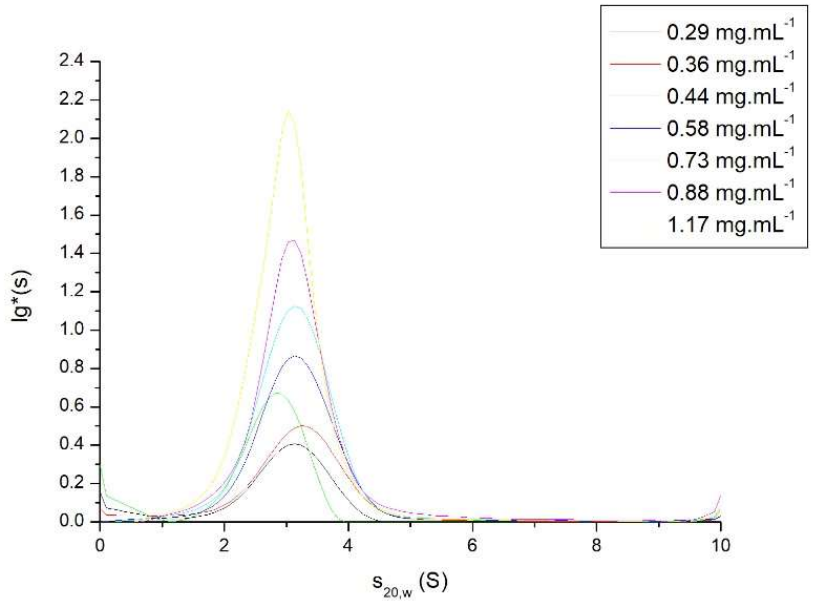


Figure 5.59 – Distribution of sedimentation coefficients at a range of loading concentrations of S-IB after ten freeze-thaw cycles.

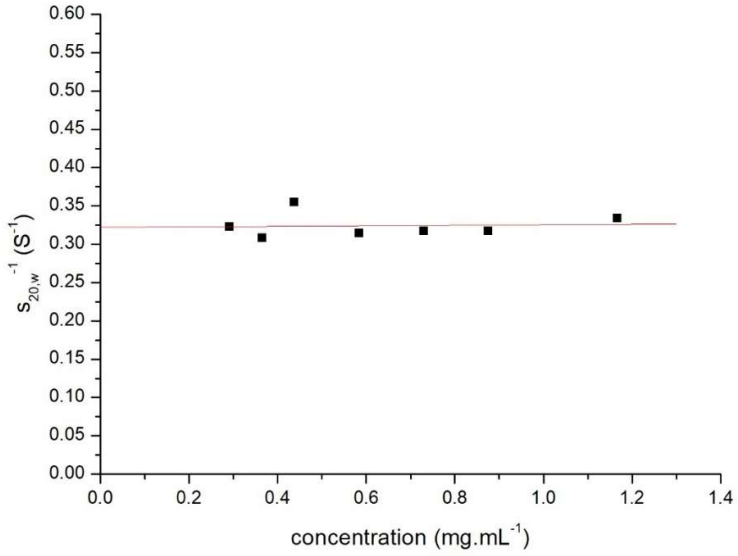


Figure 5.60 – Plot of the reciprocal of sedimentation coefficient against loading concentration for S-IB after exposure to ten freeze-thaw cycles, with a linear fit to extrapolate to zero concentration.

5.8.1.3 Sedimentation equilibrium

SEDFIT-MSTAR provides two methods of determining apparent molecular weight, $M_{w,app}$: from the M^* function and from hinge point analysis. The values given by the program are plotted against loading concentration in Figure 5.61. Extrapolation to zero concentration

gave 'thermodynamically ideal' values of M_w as (161 ± 6) kDa (from the M* method) and (177 ± 16) kDa (from the hinge method). Combining the two yields a consensus value for Mw of (169 ± 9) kDa.

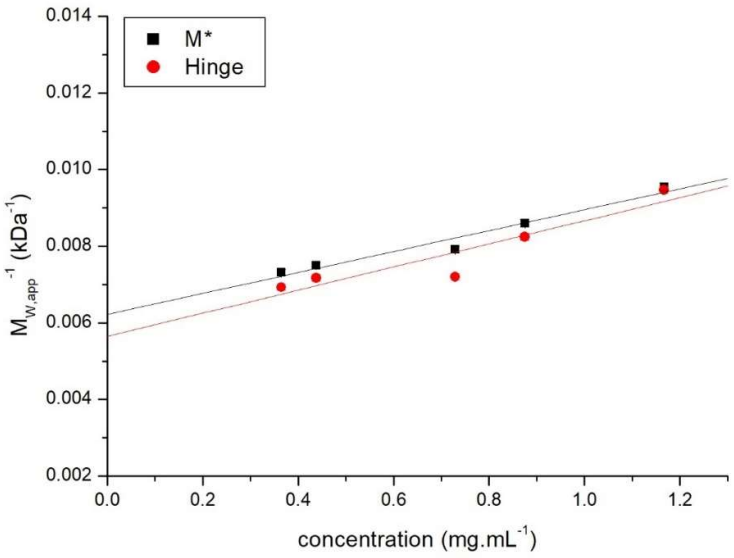


Figure 5.61 – Plot of the reciprocal of apparent molecular weight ($M_{w,app}$) values against loading concentration of S-IB after exposure to ten freeze-thaw cycles, with a linear fit to extrapolate to zero concentration.

5.8.1.4 SEC-MALS

The M_w of the main peak was determined to be (131 ± 15) kDa, with a polydispersity (M_w/M_n) of 1.006 ± 0.005. [η] was found to be (65.7 ± 0.3) mL.g^{-1}.

5.8.2 One hundred freeze-thaw cycles

5.8.2.1 Viscosity

Plotting the relevant viscosity functions and extrapolating back to where the concentration is zero in Figure 5.62 gives the intrinsic viscosities as (65.3 ± 1.0) mL.g^{-1} (Huggins), (65.3 ± 0.9) mL.g^{-1} (Kraemer) and (65.4 ± 0.9) mL.g^{-1} (Solomon-Ciuta). The mean average value of these is (65.3 ± 0.5) mL.g^{-1}.

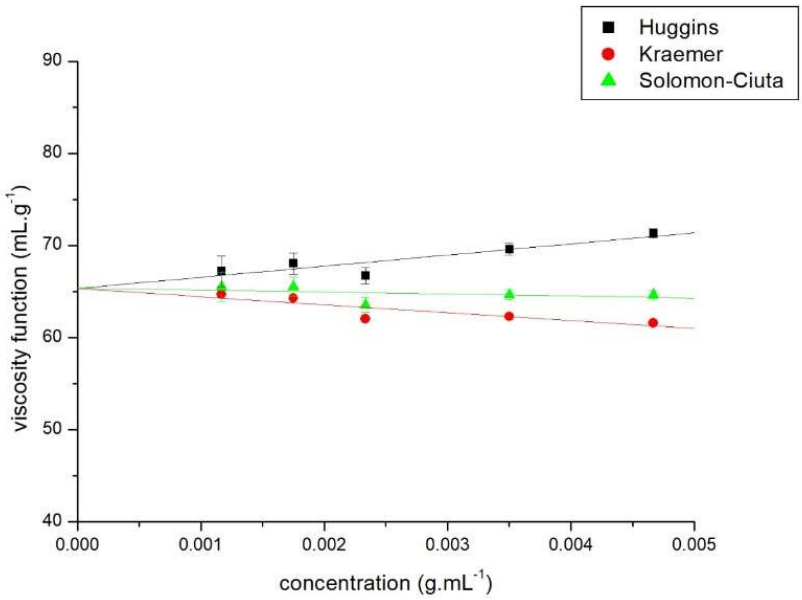


Figure 5.62 – Plot of viscosity against concentration for S-IB after exposure to 100 freeze-thaw cycles, with linear fits to extrapolate to zero concentration.

5.8.2.2 Sedimentation Velocity

The distribution of sedimentation coefficients is shown in Figure 5.63. The peak data for the main component was also plotted against loading concentration in Figure 5.64 and extrapolated back to zero concentration, giving the sedimentation coefficient as (2.84 ± 0.01) S. As the gradient is close to zero, the data can be treated as a set of repeated measurements (as discussed on page 50). The sedimentation coefficient can instead be calculated as (2.68 ± 0.08) S.

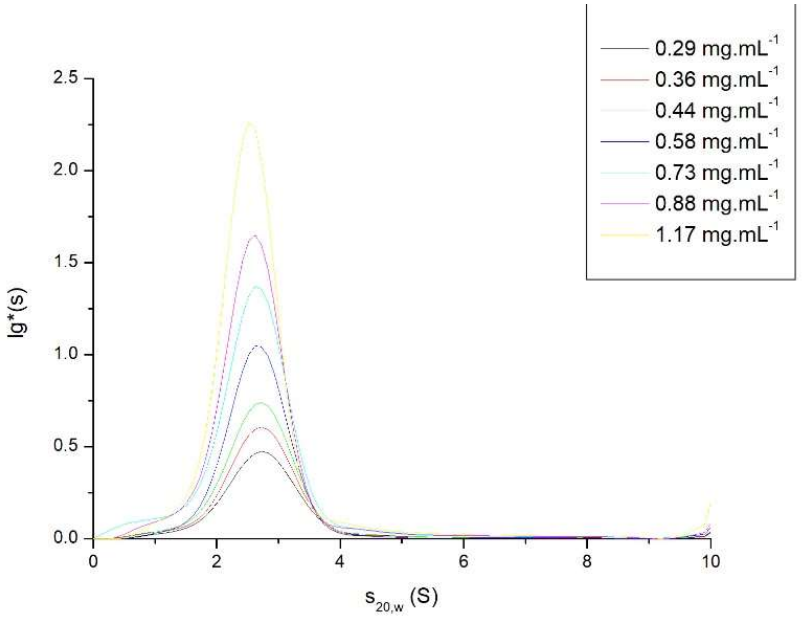


Figure 5.63 – Distribution of sedimentation coefficients at a range of loading concentrations of S-IB after 100 freeze-thaw cycles.

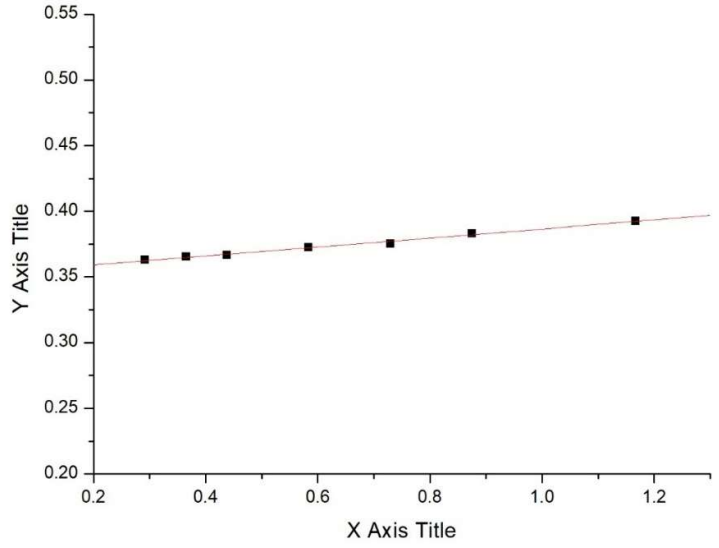


Figure 5.64 – Plot of the reciprocal of sedimentation coefficient against loading concentration for S-IB after exposure to 100 freeze-thaw cycles, with a linear fit to extrapolate to zero concentration.

5.8.2.3 Sedimentation Equilibrium

SEDFIT-MSTAR provides two methods of determining apparent molecular weight, $M_{w,app}$: from the *M** function and from hinge point analysis. The values given by the program are

plotted against loading concentration in Figure 5.65. Extrapolation to zero concentration gave 'thermodynamically ideal' values of M_w as (187 ± 5) kDa (from the M* method) and (190 ± 8) kDa (from the hinge method). Combining the two yields a consensus value for Mw of (189 ± 5) kDa.

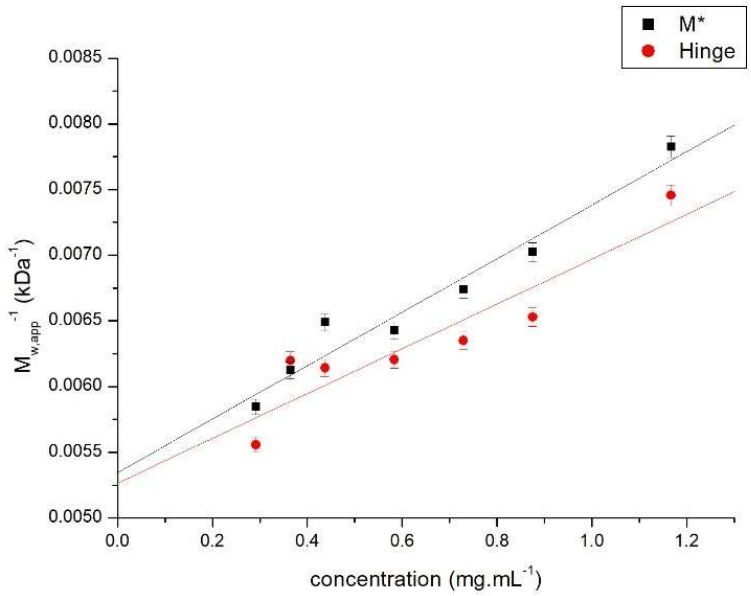


Figure 5.65 – Plot of the reciprocal of apparent molecular weight ($M_{w,app}$) values against loading concentration of S-IB after exposure to 100 freeze-thaw cycles, with a linear fit to extrapolate to zero concentration.

5.8.2.4 SEC-MALS

The M_w of the main peak was determined to be (139 ± 2) kDa, with a polydispersity (M_w/M_n) of 1.111 ± 0.023. [η] was found to be (108 ± 1) mL.g^{-1}.

5.9 Sized GBS polysaccharide, serotype II

5.9.1 Ten freeze-thaw cycles

5.9.1.1 Viscosity

Plotting the relevant viscosity functions and extrapolating back to where the concentration is zero in Figure 5.66 gives the intrinsic viscosities as (66.2 ± 0.2) mL.g^{-1} (Huggins), (66.7 ± 0.5) mL.g^{-1} (Kraemer) and (66.9 ± 0.5) mL.g^{-1} (Solomon-Ciuta). The mean average value of these is (66.6 ± 0.3) mL.g^{-1}.

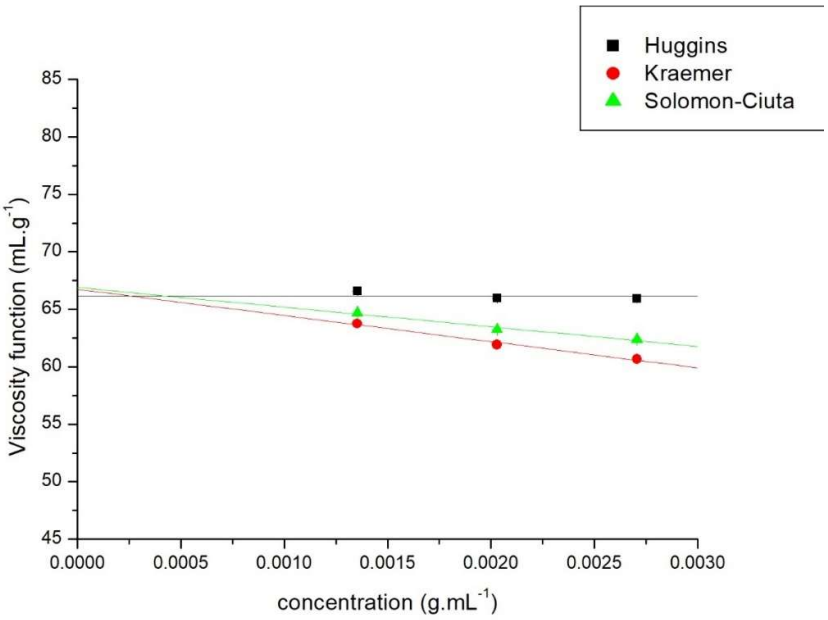


Figure 5.66 – Plot of viscosity against concentration for S-II after exposure to ten freeze-thaw cycles, with linear fits to extrapolate to zero concentration.

5.9.1.2 Sedimentation velocity

The distribution of sedimentation coefficients is shown in Figure 5.67. The peak data for the main component was also plotted against loading concentration in Figure 5.68 and extrapolated back to zero concentration, giving the sedimentation coefficient as (4.69 ± 0.11) S. As the gradient is close to zero, the data can be treated as a set of repeated measurements (as discussed on page 50). The sedimentation coefficient can instead be calculated as (4.44 ± 0.14) S.

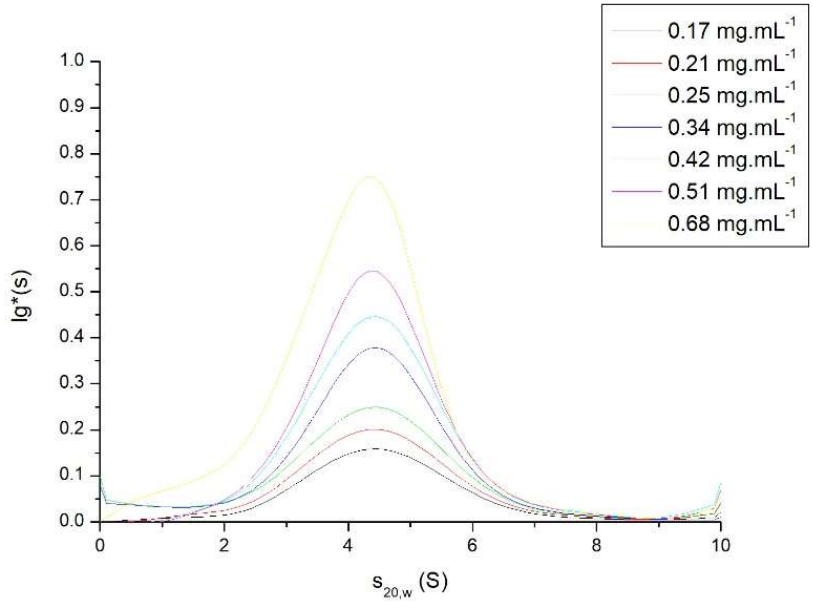


Figure 5.67 – Distribution of sedimentation coefficients at a range of loading concentrations of S-II after ten freeze-thaw cycles.

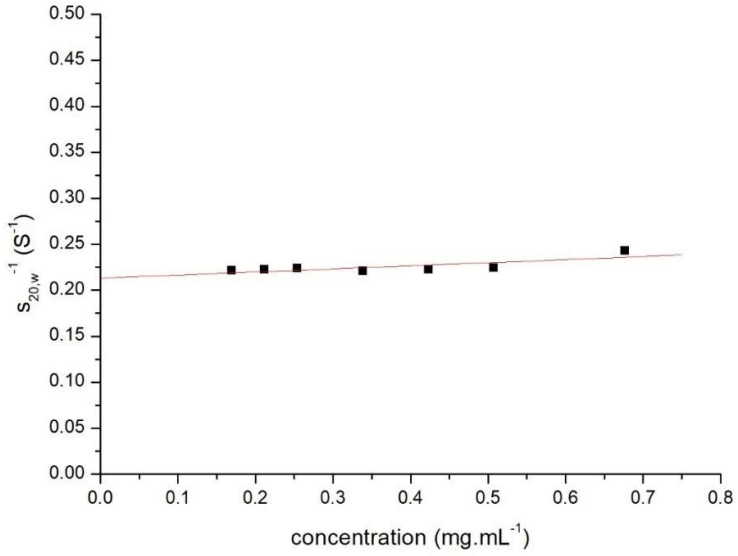


Figure 5.68 – Plot of the reciprocal of sedimentation coefficient against loading concentration for S-II after exposure to ten freeze-thaw cycles, with a linear fit to extrapolate to zero concentration.

5.9.1.3 Sedimentation equilibrium

SEDFIT-MSTAR provides two methods of determining apparent molecular weight, $M_{w,app}$: from the M^* function and from hinge point analysis. The values given by the program are

plotted against loading concentration in Figure 5.69. Extrapolation to zero concentration gave 'thermodynamically ideal' values of M_w as (160 ± 16) kDa (from the M* method) and (135 ± 11) kDa (from the hinge method). Combining the two yields a consensus value for Mw of (148 ± 14) kDa.

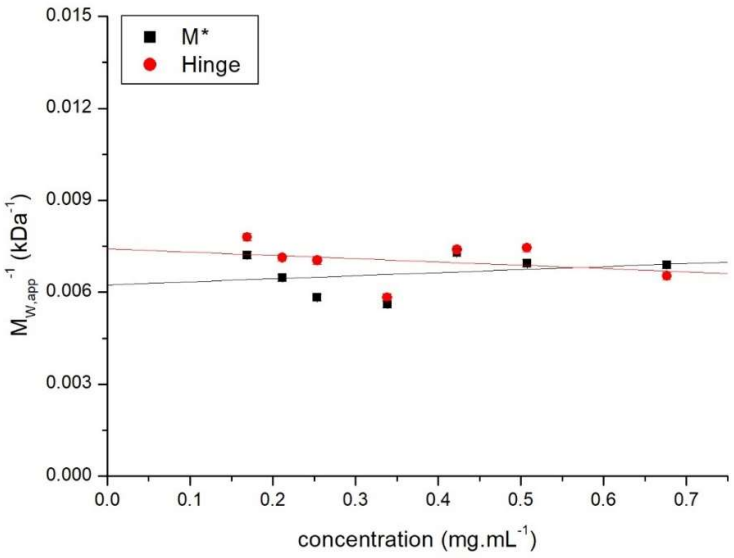


Figure 5.69 – Plot of the reciprocal of apparent molecular weight ($M_{w,app}$) values against loading concentration of S-II after exposure to ten freeze-thaw cycles, with a linear fit to extrapolate to zero concentration.

5.9.1.4 SEC-MALS

The M_w of the main peak was determined to be (154 ± 1) kDa, with a polydispersity (M_w/M_n) of 1.051 ± 0.006. [η] was found to be (52.2 ± 0.2) mL.g^{-1}.

5.9.2 One hundred freeze-thaw cycles

5.9.2.1 Viscosity

Plotting the relevant viscosity functions and extrapolating back to where the concentration is zero in Figure 5.70 gives the intrinsic viscosities as (55.3 ± 1.3) mL.g^{-1} (Huggins), (55.4 ± 1.3) mL.g^{-1} (Kraemer) and (55.3 ± 1.3) mL.g^{-1} (Solomon-Ciuta). The mean average value of these is (55.3 ± 0.7) mL.g^{-1}.

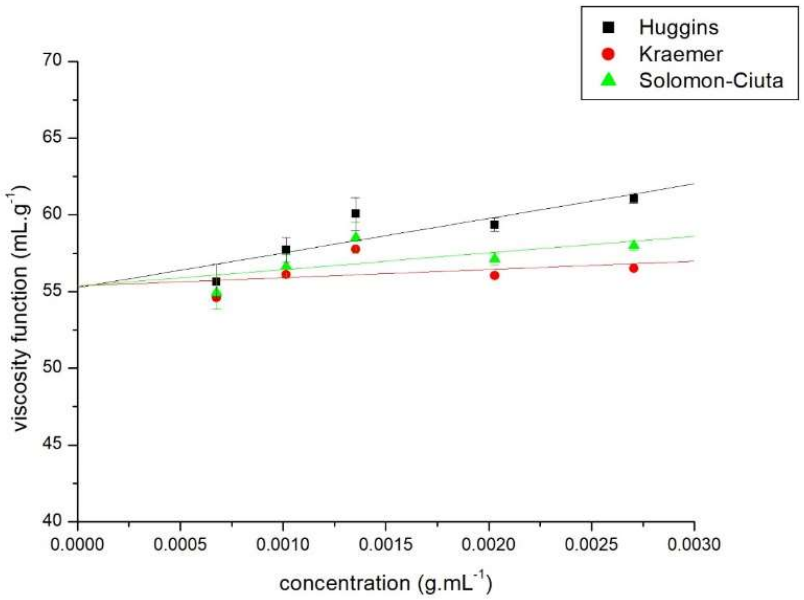


Figure 5.70 – Plot of viscosity against concentration for S-II after exposure to 100 freeze-thaw cycles, with linear fits to extrapolate to zero concentration.

5.9.2.2 Sedimentation Velocity

The distribution of sedimentation coefficients is shown in Figure 5.71. The peak data for the main component was also plotted against loading concentration in Figure 5.72 and extrapolated back to zero concentration, giving the sedimentation coefficient as (3.93 ± 0.05) S. As the gradient is close to zero, the data can be treated as a set of repeated measurements (as discussed on page 50). The sedimentation coefficient can instead be calculated as (3.79 ± 0.08) S.

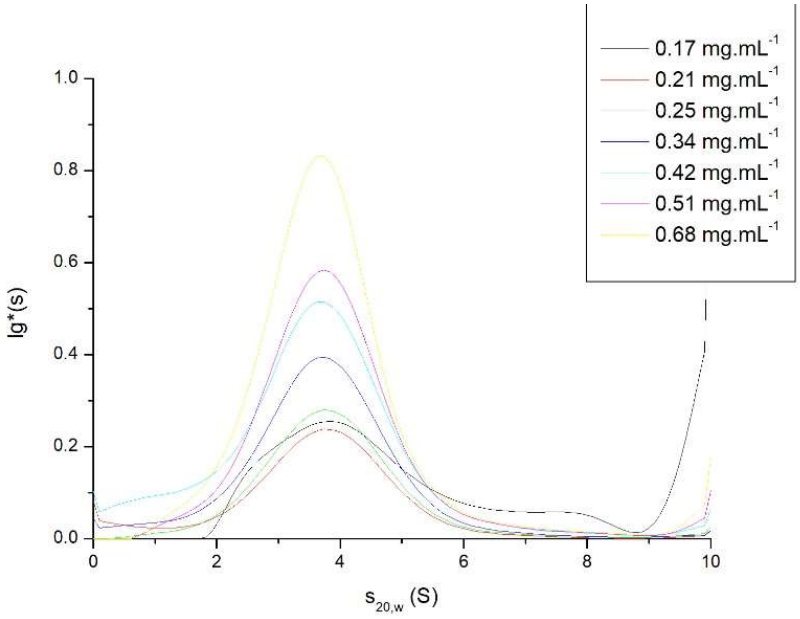


Figure 5.71 – Distribution of sedimentation coefficients at a range of loading concentrations of S-II after 100 freeze-thaw cycles.

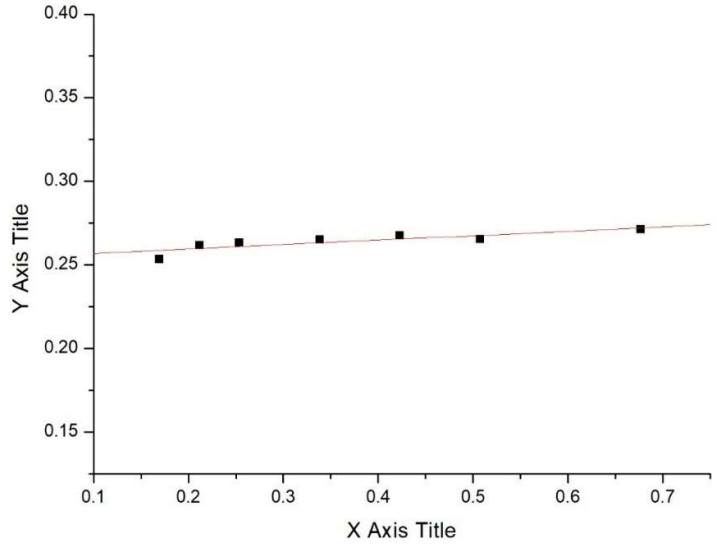


Figure 5.72 – Plot of the reciprocal of sedimentation coefficient against loading concentration for S-II after exposure to 100 freeze-thaw cycles, with a linear fit to extrapolate to zero concentration.

5.9.2.3 Sedimentation Equilibrium

SEDFIT-MSTAR provides two methods of determining apparent molecular weight, $M_{w,app}$: from the *M** function and from hinge point analysis. The values given by the program are

plotted against loading concentration in Figure 5.73. Extrapolation to zero concentration gave 'thermodynamically ideal' values of M_w as (219 ± 13) kDa (from the M* method) and (198 ± 6) kDa (from the hinge method). Combining the two yields a consensus value for Mw of (208 ± 14) kDa.

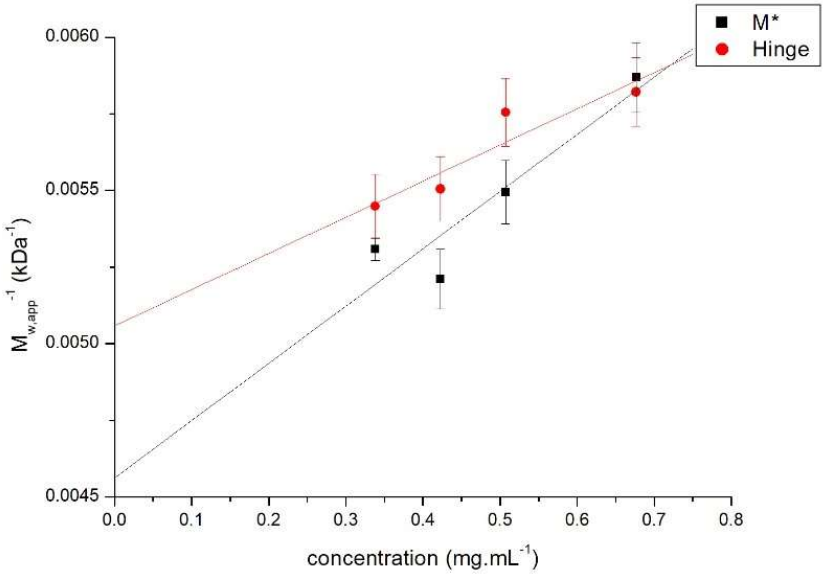


Figure 5.73 – Plot of the reciprocal of apparent molecular weight ($M_{w,app}$) values against loading concentration of S-II after exposure to 100 freeze-thaw cycles, with a linear fit to extrapolate to zero concentration.

5.9.2.4 SEC-MALS

The M_w of the main peak was determined to be (203 ± 2) kDa, with a polydispersity (M_w/M_n) of 1.222 ± 0.019. [η] was found to be (75.2 ± 0.6) mL.g^{-1}.

5.10 Summary

Table 5-1 below shows a summary of all data presented above after ten freeze-thaw cycles, while

Table 5-2 summarises the data collected after 100 freeze-thaw cycles. The percentage differences in these values are also given in

Table 5-3 (for ten cycles) and

Table 5-4 (for 100 cycles).

Table 5-1 – Summary of data found after exposure of samples to ten freeze-thaw cycles.

State	Serotype	[η] ($mL.g^{-1}$)	Analytical ultracentrifugation			SEC-MALS		
			$s^{\circ}_{20,w}$ extrapolation (S)	$s^{\circ}_{20,w}$ average (S)	M_w (combined, kDa)	M_w (kDa)	[η] ($mL.g^{-1}$)	Polydispersity ($M_w.M_n^{-1}$)
Native	IA	234±1	5.24±0.1	4.29±0.48	364±35	298±21	331±20	308±1
	IB	140±1	4.24±0.05	3.65±0.33	249±11	230±6	240±6	209±1
	II	129±1	6.76±0.06	6.04±0.35	330±12	326±4	328±7	466±1
	III	47.5±0.2	3.55±0.02	3.42±0.07	116±7	111±10	114±6	107±0
	IV	67±0.7	2.79±0.02	2.69±0.05	64.1±3.2	64.4±6.2	64.4±6.2	63.1±0.2
	V	105±0	3.92±0.01	3.71±0.10	182±10	193±11	187±7	126±0
Sized	IA	52±0.6	3.32±0.09	3.05±0.14	181±12	184±11	182±8	104±0
	IB	64±0.2	3.1±0.15	3.09±0.14	161±6	177±16	169±9	90.5±0.3
	II	66.6±0.3	4.69±0.11	4.44±0.14	160±16	135±11	148±14	154±1

Table 5-2 – Summary of data found after exposure of samples to 100 freeze-thaw cycles.

State	Serotype	[η] ($mL.g^{-1}$)	Analytical ultracentrifugation			SEC-MALS		
			$s^{\circ}_{20,w}$ extrapolation (S)	$s^{\circ}_{20,w}$ average (S)	M_w (combined, kDa)	M_w (kDa)	[η] ($mL.g^{-1}$)	Polydispersity ($M_w.M_n^{-1}$)
Native	IA	206±2	5.01±0.05	4.29±0.31	313±9	285±3	299±5	409±2
	IB	118±3	4.05±0.04	3.70±0.16	195±7	185±2	190±4	231±1
	II	134±1	5.86±0.03	5.14±0.31	446±7	415±3	431±4	466±1
	III	47.1±0.2	2.95±0.02	2.86±0.04	147±8	142±8	145±6	103±0
	IV	52.6±0.4	2.37±0.02	2.28±0.04	89±1.8	97.3±2.8	93.2±1.7	89.1±1.5
	V	91.4±0.2	3.28±0.06	3.71±0.10	211±3	193±5	202±3	172±1
Sized	IA	44.5±0.4	2.82±0.03	2.64±0.09	246±3	244±7	245±4	207±27
	IB	65.3±0.5	2.84±0.01	2.68±0.08	187±5	190±8	189±5	139±2
	II	55.3±0.7	3.93±0.05	3.79±0.08	220±6	190±4	205±3	203±2

Table 5-3 – Table showing the percentage difference in parameters from baseline values due to exposure of samples to ten freeze-thaw cycles.

State	Serotype	[η] ($mL.g^{-1}$)	Analytical ultracentrifugation		SEC-MALS		
			$s^{\circ}_{20,w}$ (S)	M_w (combined, kDa)	M_w (kDa)	[η] ($mL.g^{-1}$)	Polydispersity ($M_w.M_n^{-1}$)
Native	IA	+7%	+4%	-4%	+5%	-2%	+6%
	IB	+3%	+5%	+36%	+36%	+34%	+2%
	II	+2%	+12%	+3%	+8%	+4%	-2%
	III	+5%	+10%	0%	+17%	+12%	0%
	IV	+3%	+9%	+1%	+18%	+10%	0%
	V	+29%	-1%	-8%	+9%	+4%	+1%
Sized	IA	+7%	0%	-3%	+2%	-5%	+2%
	IB	+3%	-5%	+8%	-11%	-15%	0%
	II	+21%	+1%	-8%	-1%	-1%	+3%

Table 5-4 – Table showing the percentage difference in parameters from baseline values due to exposure of samples to 100 freeze-thaw cycles.

State	Serotype	[η] ($mL.g^{-1}$)	Analytical ultracentrifugation		SEC-MALS		
			$s^{\circ}_{20,w}$ (S)	M_w (combined, kDa)	M_w (kDa)	[η] ($mL.g^{-1}$)	Polydispersity ($M_w.M_n^{-1}$)
Native	IA	-5%	0%	-13%	+40%	+39%	-4%
	IB	-13%	0%	+1%	+50%	+60%	-3%
	II	+6%	-3%	+35%	+8%	+12%	+12%
	III	+5%	-9%	+42%	+12%	+15%	+4%
	IV	-19%	-7%	+46%	+67%	+69%	+4%
	V	+12%	-17%	+26%	+48%	+55%	+10%
Sized	IA	-9%	-15%	+30%	+103%	+32%	+16%
	IB	+5%	-14%	+21%	+37%	+41%	+10%
	II	+1%	-15%	+27%	+31%	+43%	+19%

These data sets can also be described graphically to show how each parameter changes, shown in Figure 5.74, 5.75, 5.76, 5.77 and 5.78.

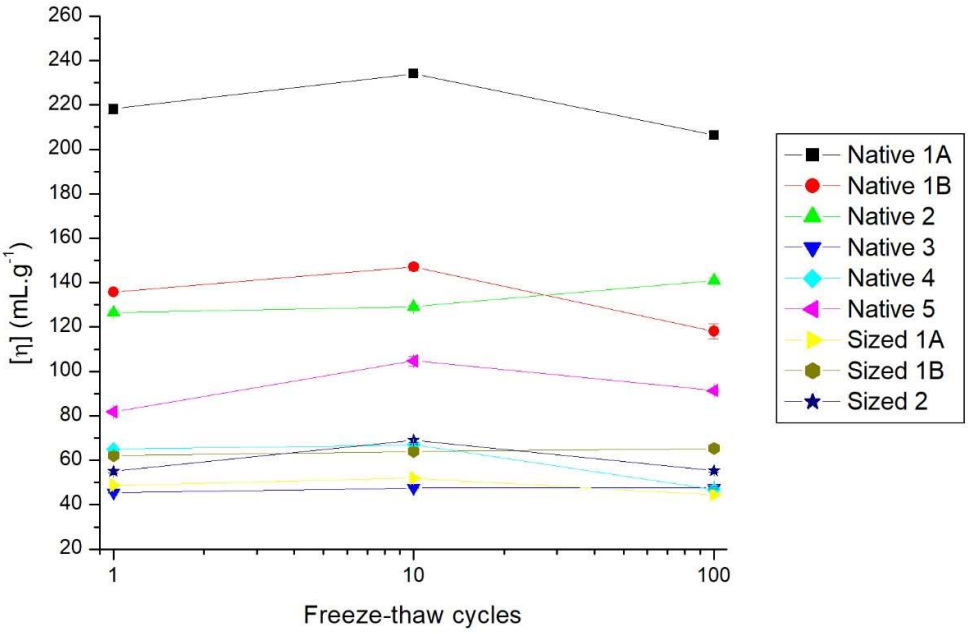


Figure 5.74 – Viscosoty of each polysaccharide as determined by U-tube viscometry, and how they altered after exposure to a series of freeze-thaw cycles.

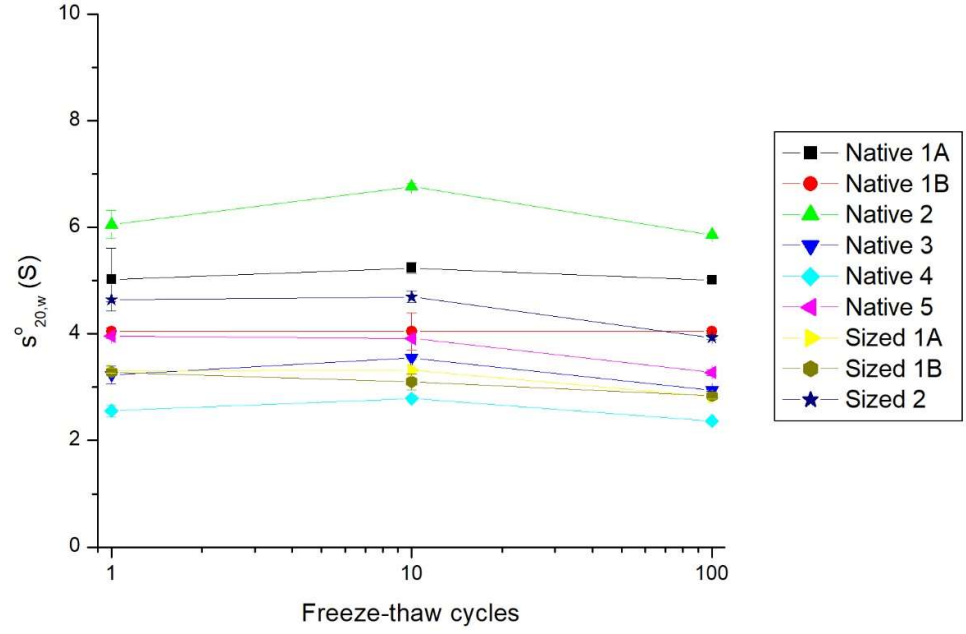


Figure 5.75 – Sedimentation coefficient of each polysaccharide as determined by sedimentation velocity, and how they altered after exposure to a series of freeze-thaw cycles.

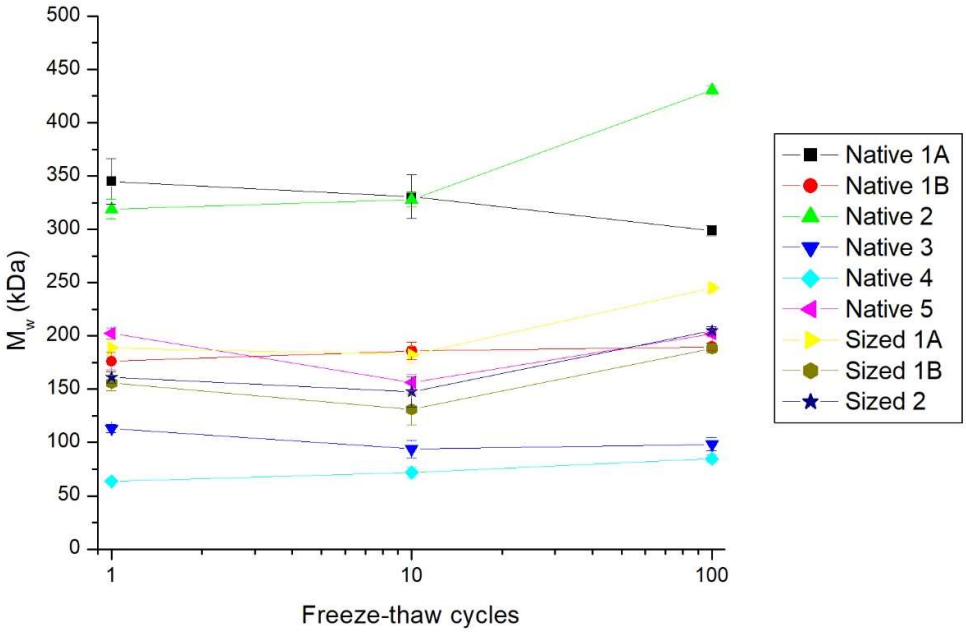


Figure 5.76 – Molecular weight of each polysaccharide as determined by sedimentation equilibrium, and how they altered after exposure to a series of freeze-thaw cycles.

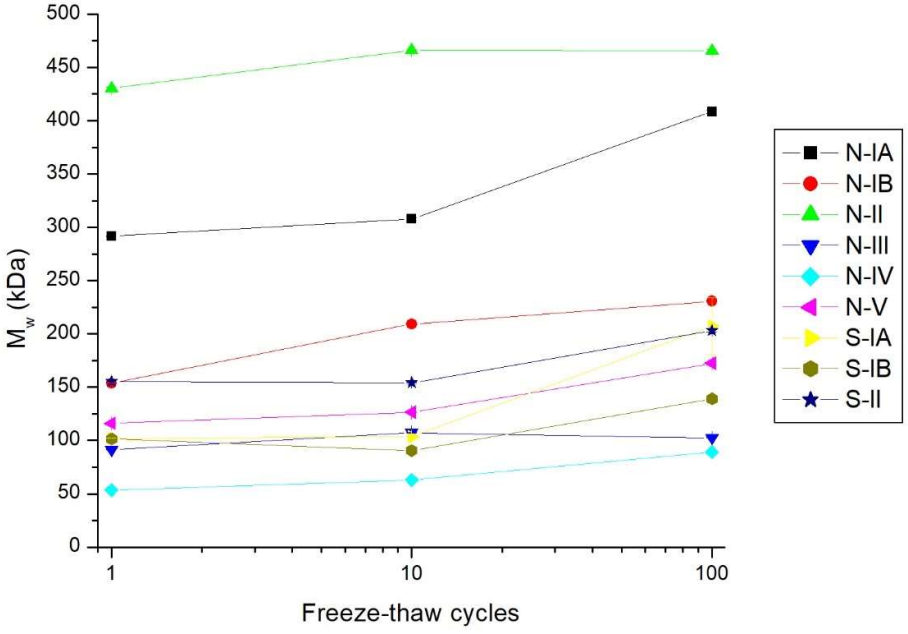


Figure 5.77 – Molecular weight of each polysaccharide as determined by SEC-MALS, and how they altered after exposure to a series of freeze-thaw cycles.

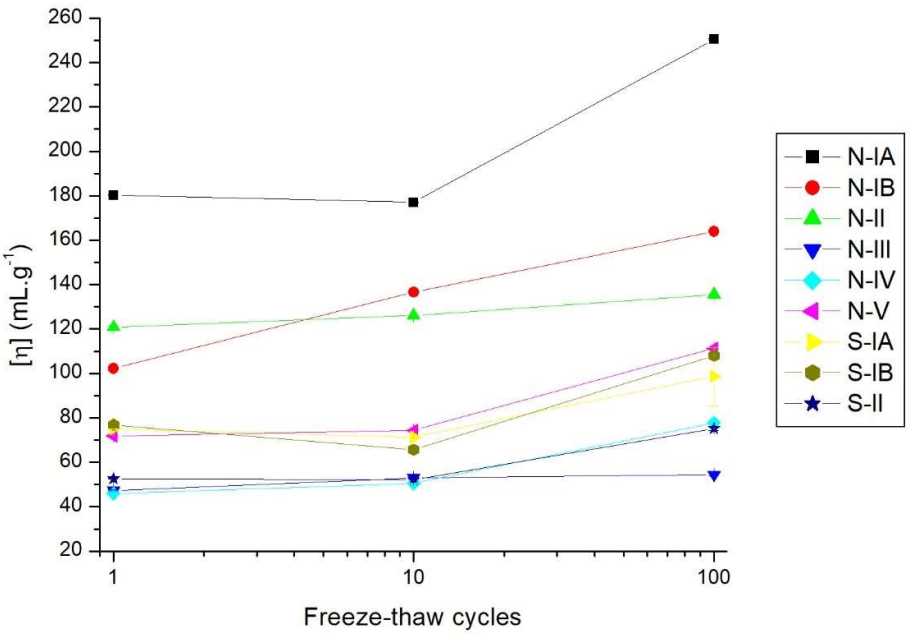


Figure 5.78 – Viscosity of each polysaccharide as determined by SEC-MALS, and how they altered after exposure to a series of freeze-thaw cycles.

For the sedimentation coefficient values, as the error ranges are large on each point and the gradient is near zero, it is possible the treat the data set as a set of repeated measurements. By doing this, it is possible to perform a statistical test to assess whether the differences between measured sedimentation coefficient are significant. These results are given in Table 5-5, by listing the P value when performing a student's T test.

Table 5-5 – The resulting p values when performing a student's T test on the sedimentation coefficient datasets after exposure to freeze-thaw stress. A p value < 0.05 is assumed to reflect a significant difference, and these are highlighted.

State	Serotype	p values	
		10 x FT	100 x FT
Native	IA	0.906	0.898
	IB	0.631	0.813
	II	0.303	**0.001**
	III	0.064	**0.004**
	IV	0.179	**0.000**
	V	0.977	0.977
Sized	IA	0.674	**0.000**
	IB	0.612	**0.000**
	II	0.421	**0.009**

5.11 Discussion

Different methods suggest different outcomes from the exposure to freeze-thaw stress, and the specific changes in values also vary between one, ten and one hundred freeze-thaw cycles.

The changes after ten freeze-thaw cycles are described in

Table 5-3. Unfortunately, as most parameters are calculated by extrapolation, it is not possible to perform a more in-depth statistical test as there are no true data ranges to compare. If only the larger differences in values (those greater than 10%) are considered, then only the native polysaccharide from serotype V and the sized polysaccharide from serotype II showed significant increases in viscosity. However, in both of these cases there was little change in molecular weight as measured by sedimentation equilibrium. It is possible that this indicates a change in shape but not molecular weight. The sedimentation coefficient does decrease for these samples, which could be due to the increased viscosity, but these changes are not statistically significant.

SEC-MALS results show in all cases that there was an increase in the molecular weight, except for sized polysaccharide from serotype IB and sized polysaccharide from serotype II which saw a reduction. The changes in viscosity were more variable, with all sized polysaccharides and native polysaccharide from serotype IA seeing a decrease in viscosity while other samples increased. Sized polysaccharide from serotype IB also saw a decrease in molecular weight observed by sedimentation equilibrium.

The changes after one hundred freeze-thaw cycles are described in

Table 5-4. Far more differences are observed, but these are not always consistent with the results after ten freeze-thaw cycles. For example, while the viscosity of sized polysaccharide from serotype V increased 29% after ten cycles, it was only 12% higher than the starting viscosity after one hundred cycles. In addition, native polysaccharides from serotypes IA, IB, IV and sized polysaccharide from serotype IA all decreased in viscosity after 100 cycles, despite increasing after ten.

All polysaccharides except native polysaccharides from serotype IA and IB saw a decrease in sedimentation coefficient after 100 freeze-thaw cycles. This would imply that either the molecular weight decreased, or the viscosity increased, or some combination of the two.

However, all these samples saw an increase in molecular weight as measured by sedimentation equilibrium, and only native polysaccharides from serotype III, V, and sized polysaccharide from serotype IB saw an increase in viscosity. The inconsistency is more likely to indicate that the techniques give more variable results than a true difference between these parameters.

All polysaccharides saw an increase in molecular weight after 100 freeze-thaw cycles as measured by SEC-MALS, which is mirrored by the results of sedimentation equilibrium except with native polysaccharides from serotype IB (which barely changed) and IA (which decreased). Sized polysaccharide from serotype IB, which previously decreased in molecular weight using sedimentation equilibrium and SEC-MALS, saw an increase after 100 freeze-thaw cycles by both techniques. Sized polysaccharide from serotype II previously saw a decrease by SEC-MALS and no change by sedimentation equilibrium, but now saw an increase using both techniques. However, most of the changes in molecular weight are too small to imply any form of self-association. Sized polysaccharide from serotype IA increases in molecular weight 103%, meaning that this sample may be forming a dimer, although the change observed by sedimentation equilibrium is much smaller (30%).

All viscosity values analysed using SEC-MALS increased after 100 freeze-thaw cycles, mirroring the changes observed in molecular weight. In each case the percentage change was of a similar proportion to the percentage change in the molecular weight, suggesting a consistency throughout the measurement process of the SEC-MALS system even if consistency was low between different techniques, as the viscosities decreased for native polysaccharides from serotypes IA, IB, IV, and sized polysaccharides from serotype IA when measured in the U-tube viscometer.

Perhaps the most useful technique used here was sedimentation velocity, as it (although unintentionally) allows a genuine statistical test to be performed. Here, there was no

statistically significant change in sedimentation coefficient after 10 freeze thaw cycles, but after 100 free-thaw cycles native polysaccharides from serotypes II, III, IV, and sized polysaccharides from all serotypes tested changed significantly. This result is more logical than the simple changes seen in Figures 6.74-6.78, as the changes are more pronounced after exposure to increased stress. This indicates there is some genuine alteration in the polysaccharide structure after exposure to pronounced stress. However, as sedimentation coefficient is affected by both molecular weight and the molecule's shape, it is not possible to infer what the alteration was. However, in those samples with a statistical difference (in all cases a decrease in sedimentation coefficient) there is a pronounced increase in molecular weight, which should also increase sedimentation coefficient. While the ability to perform a statistical test does make the sedimentation velocity analysis more powerful under these circumstances, the high variability in the techniques used leads to complications when attempted to analyse these data sets.

6 Stability after incubation at 20˚C

Exposure to room temperature for an extended period of time was used as a method to deliberately expose samples to stress in a controlled manner. While polysaccharides are generally stable in a dry environment, in solution there is a possibility that samples may degrade over time due to random interactions, and so it is important to test if this causes any observable change in the hydrodynamic properties.

To ensure that the molecular stability is tested in isolation, the chemical Proclin™ 150 was added to each sample prior to incubation. This antimicrobial agent ensures that the sample is not degraded by microorganisms, and that their presence does not alter observed results. The samples were then incubated in a water bath set to 20˚C for 10 or 100 days, after which they were placed in the freezer until they could be analysed. As in section 5, the partial specific volume is unlikely to change even after the molecules are damaged, so the originally-calculated values were used in analysing centrifugation data.

6.1 Native GBS polysaccharide, serotype IA

6.1.1 Ten day incubation

6.1.1.1 Viscosity

Plotting the relevant viscosity functions and extrapolating back to where the concentration is zero in Figure 6.1 gives the intrinsic viscosities as (211 ± 6) $mL.g^{-1}$ (Huggins), (205 ± 6) $mL.g^{-1}$ (Kraemer) and (208 ± 5) $mL.g^{-1}$ (Solomon-Ciuta). The mean average value of these is (208 ± 3) $mL.g^{-1}$.

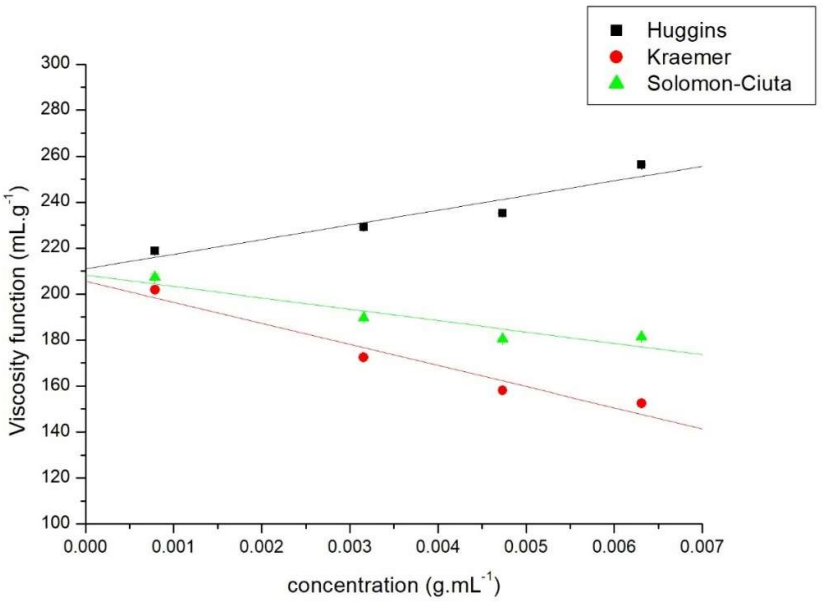


Figure 6.1 – Plot of viscosity against concentration for N-IA after incubation at 20˚C for ten days, with linear fits to extrapolate to zero concentration.

6.1.1.2 Sedimentation Velocity

The distribution of sedimentation coefficients is shown in Figure 6.2. The peak data for the main component was also plotted against loading concentration in Figure 6.3 and extrapolated back to zero concentration, giving the sedimentation coefficient as (4.35 ± 0.33) S. As the gradient is close to zero, the data can be treated as a set of repeated measurements (as discussed on page 50). The sedimentation coefficient can instead be calculated as (3.44 ± 0.4) S.

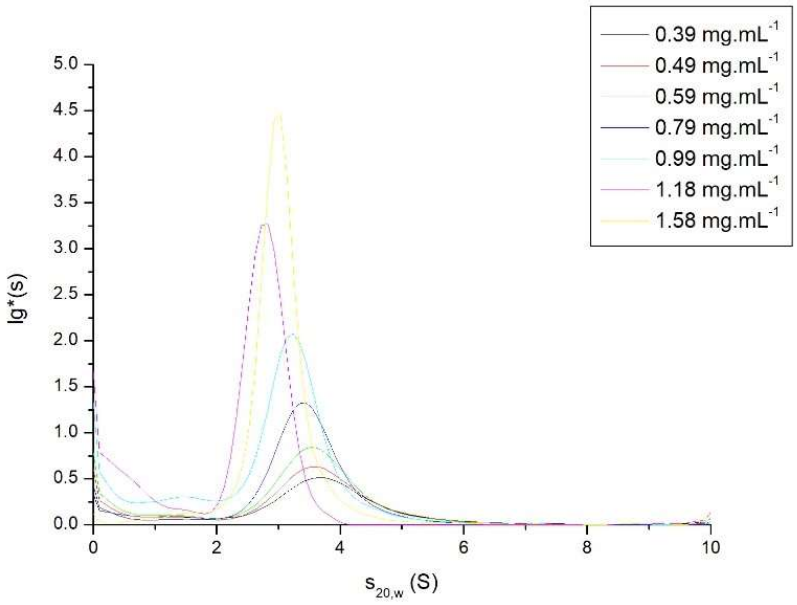


Figure 6.2 – Distribution of sedimentation coefficients at a range of loading concentrations of N-IA after incubation at 20˚C for ten days.

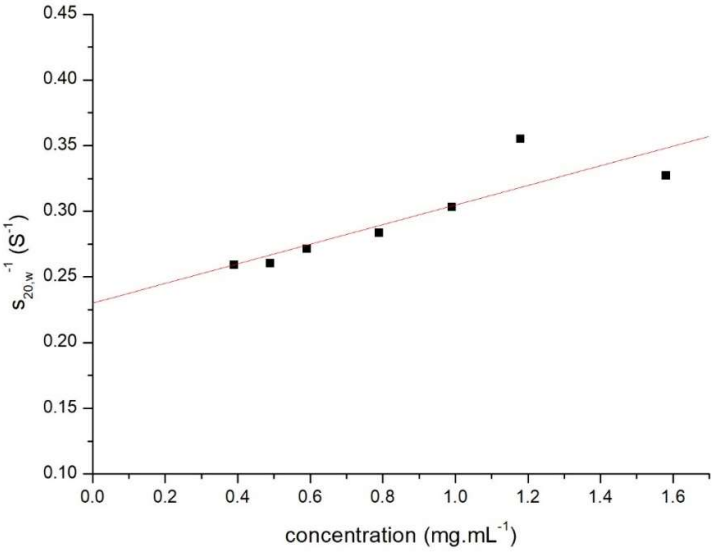


Figure 6.3 – Plot of the reciprocal of sedimentation coefficient against loading concentration for N-IA after incubation at 20˚C for ten days, with a linear fit to extrapolate to zero concentration.

6.1.1.3 Sedimentation Equilibrium

SEDFIT-MSTAR provides two methods of determining apparent molecular weight, $M_{w,app}$: from the *M** function and from hinge point analysis. The values given by the program are

plotted against loading concentration in Figure 6.4. Extrapolation to zero concentration gave 'thermodynamically ideal' values of M_w as (405 ± 5) kDa (from the M* method) and (394 ± 9) kDa (from the hinge method). Combining the two yields a consensus value for Mw of (399 ± 5) kDa.

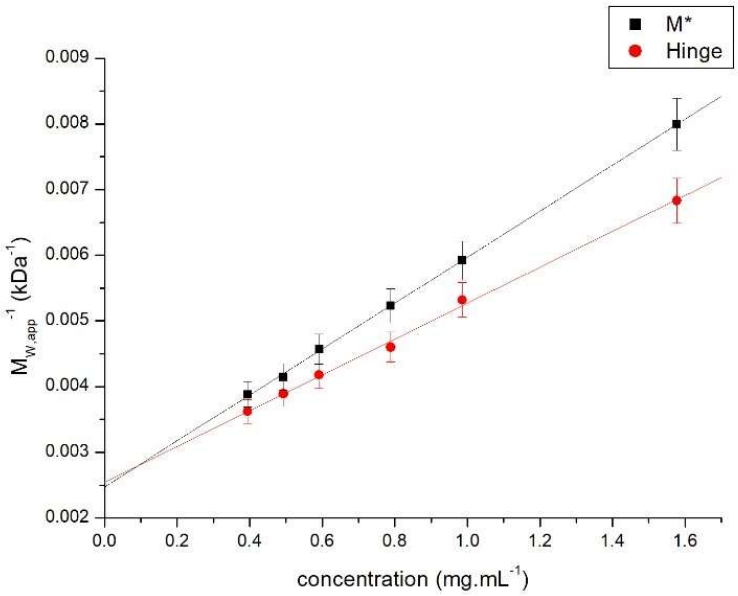


Figure 6.4 – Plot of the reciprocal of apparent molecular weight ($M_{w,app}$) values against loading concentration of N-IA after incubation at 20˚C for ten days, with a linear fit to extrapolate to zero concentration.

6.1.1.4 SEC-MALS

The M_w of the main peak was determined to be (401 ± 1) kDa, with a polydispersity (M_w/M_n) of 1.273 ± 0.005. [η] was found to be (312 ± 1) mL.g^{-1}.

6.1.2 One hundred day incubation

6.1.2.1 Viscosity

Plotting the relevant viscosity functions and extrapolating back to where the concentration is zero in Figure 6.5 gives the intrinsic viscosities as 187 mL.g^{-1} (Huggins), (186 ± 1) mL.g^{-1} (Kraemer) and 187 mL.g^{-1} (Solomon-Ciuta). The mean average value of these is 187 mL.g^{-1}, although no error is described at this level of precision, as is the case with the Huggins and Solomon-Ciuta values.

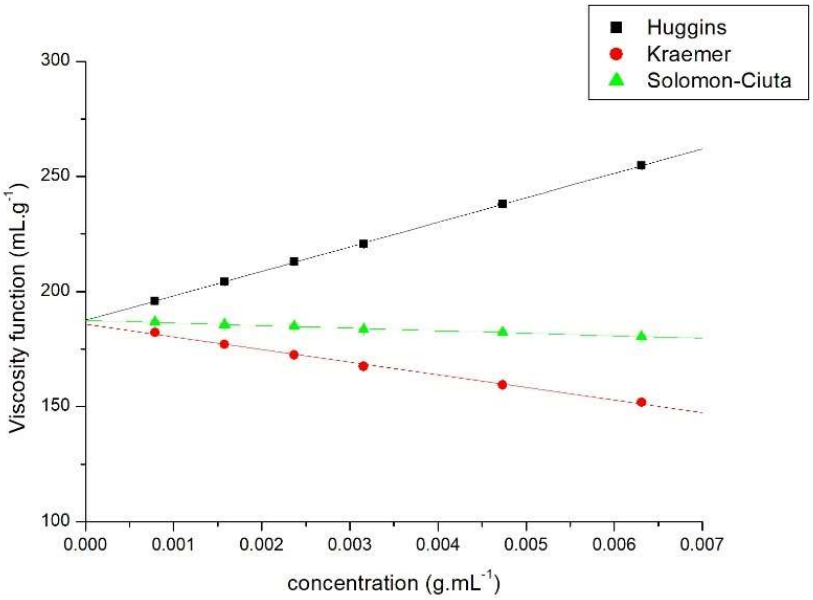


Figure 6.5 – Plot of viscosity against concentration for N-IA after incubation at 20˚C for one hundred days, with linear fits to extrapolate to zero concentration.

6.1.2.2 Sedimentation Velocity

The distribution of sedimentation coefficients is shown in Figure 6.6. The peak data for the main component was also plotted against loading concentration in Figure 6.7 and extrapolated back to zero concentration, giving the sedimentation coefficient as (5.48 ± 0.36) S. As the gradient is close to zero, the data can be treated as a set of repeated measurements (as discussed on page 50). The sedimentation coefficient can instead be calculated as (4.03 ± 0.49) S.

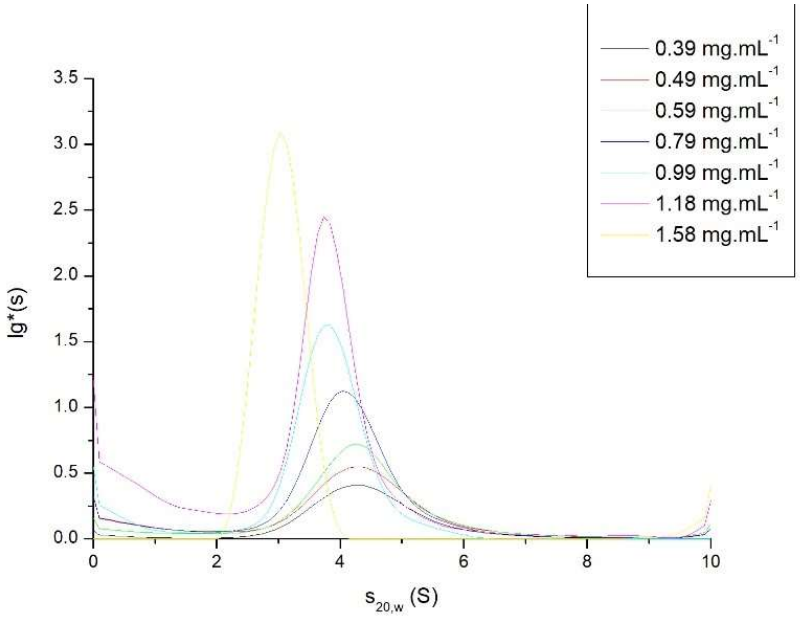


Figure 6.6 – Distribution of sedimentation coefficients at a range of loading concentrations of N-IA after incubation at 20˚C for one hundred days.

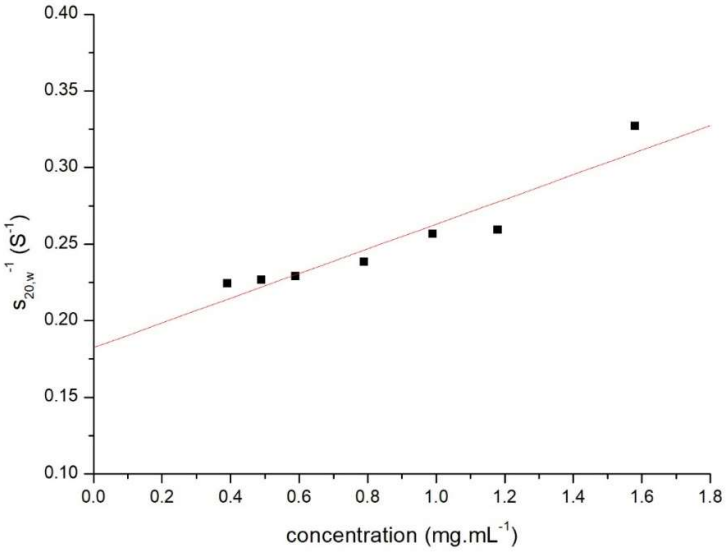


Figure 6.7 – Plot of the reciprocal of sedimentation coefficient against loading concentration for N-IA after incubation at 20˚C for one hundred days, with a linear fit to extrapolate to zero concentration.

6.1.2.3 Sedimentation Equilibrium

SEDFIT-MSTAR provides two methods of determining apparent molecular weight, $M_{w,app}$: from the *M** function and from hinge point analysis. The values given by the program are

plotted against loading concentration in Figure 6.8. Extrapolation to zero concentration gave 'thermodynamically ideal' values of M_w as (306 ± 23) kDa (from the M* method) and (310 ± 24) kDa (from the hinge method). Combining the two yields a consensus value for Mw of (308 ± 16) kDa.

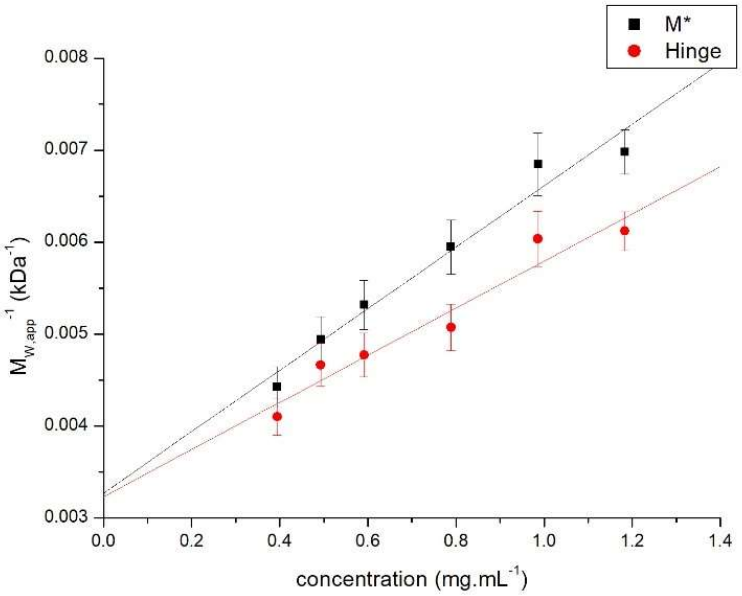


Figure 6.8 – Plot of the reciprocal of apparent molecular weight ($M_{w,app}$) values against loading concentration of N-IA after incubation at 20˚C for one hundred days, with a linear fit to extrapolate to zero concentration.

6.1.2.4 SEC-MALS

The M_w of the main peak was determined to be (291 ± 1) kDa, with a polydispersity (M_w/M_n) of 1.266 ± 0.004. [η] was found to be 180 mL.g^{-1}, although no error is described at this level of precision.

6.2 Native GBS polysaccharide, serotype IB

6.2.1 Ten day incubation

6.2.1.1 Viscosity

Plotting the relevant viscosity functions and extrapolating back to where the concentration is zero in Figure 6.9 gives the intrinsic viscosities as (114 ± 5) $mL.g^{-1}$ (Huggins), (115 ± 4) $mL.g^{-1}$ (Kraemer) and (115 ± 4) $mL.g^{-1}$ (Solomon-Ciuta). The mean average value of these is (115 ± 2) $mL.g^{-1}$.

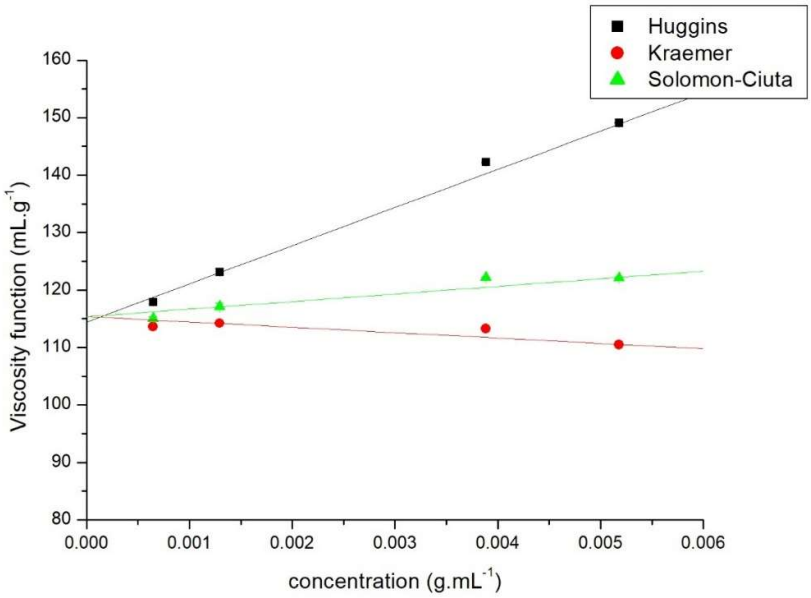


Figure 6.9 – Plot of viscosity against concentration for N-IB after incubation at 20˚C for ten days, with linear fits to extrapolate to zero concentration.

6.2.1.2 Sedimentation Velocity

The distribution of sedimentation coefficients is shown in Figure 6.10. The peak data for the main component was also plotted against loading concentration in Figure 6.11 and extrapolated back to zero concentration, giving the sedimentation coefficient as (3.22 ± 0.10) S. As the gradient is close to zero, the data can be treated as a set of repeated measurements (as discussed on page 50). The sedimentation coefficient can instead be calculated as (3.03 ± 0.13) S.

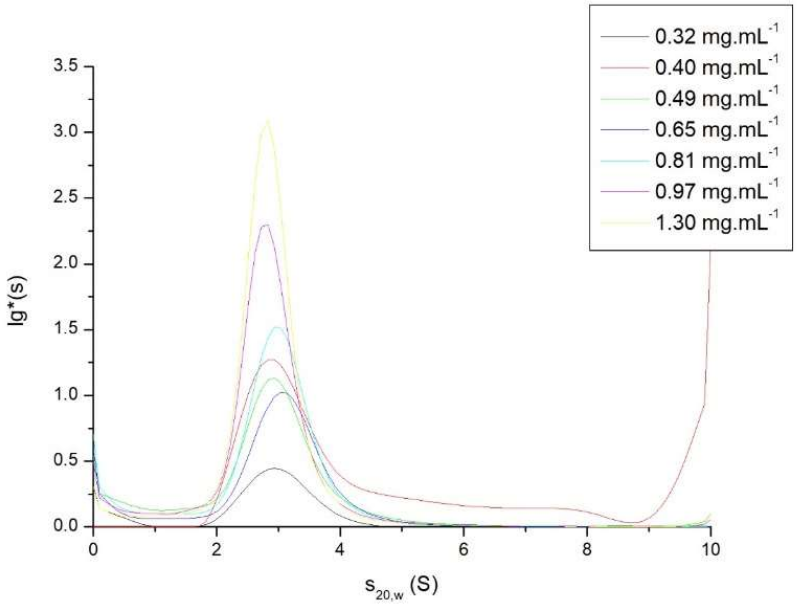


Figure 6.10 – Distribution of sedimentation coefficients at a range of loading concentrations of N-IB after incubation at 20˚C for ten days.

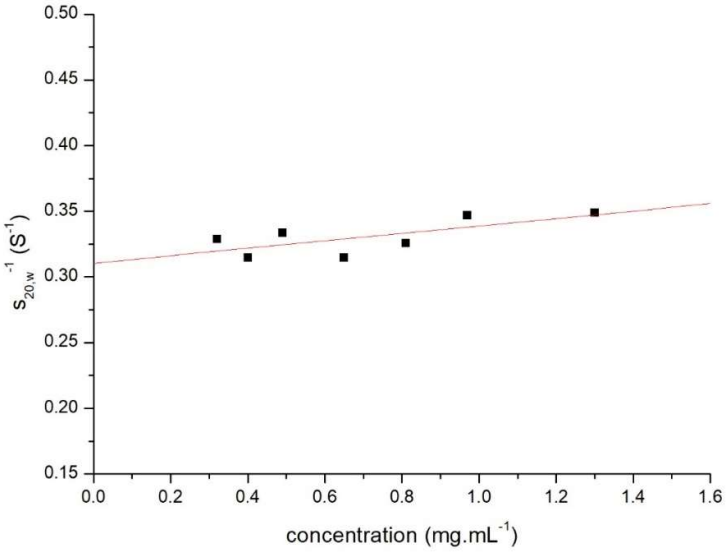


Figure 6.11 – Plot of the reciprocal of sedimentation coefficient against loading concentration for N-IB after incubation at 20˚C for ten days, with a linear fit to extrapolate to zero concentration.

6.2.1.3 Sedimentation Equilibrium

SEDFIT-MSTAR provides two methods of determining apparent molecular weight, $M_{w,app}$: from the *M** function and from hinge point analysis. The values given by the program are

plotted against loading concentration in Figure 6.12. Extrapolation to zero concentration gave 'thermodynamically ideal' values of M_w as (310 ± 58) kDa (from the M* method) and (316 ± 20) kDa (from the hinge method). Combining the two yields a consensus value for Mw of (313 ± 31) kDa.

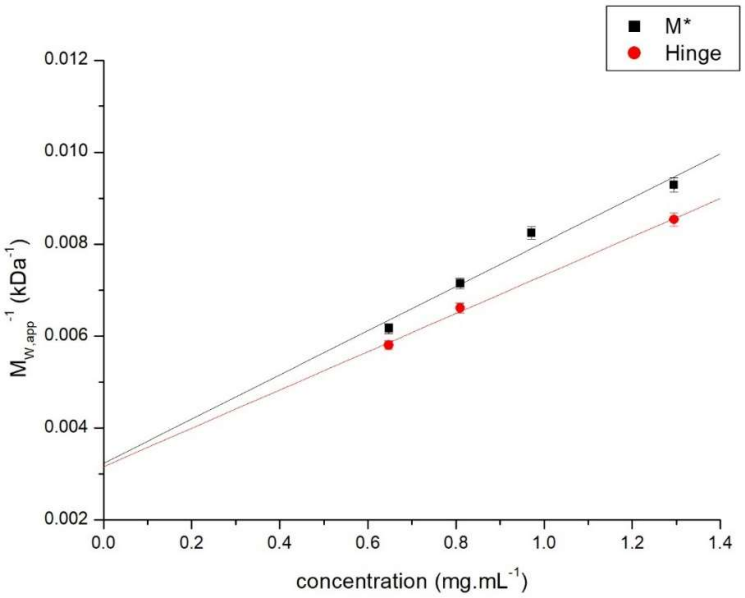


Figure 6.12 – Plot of the reciprocal of apparent molecular weight ($M_{w,app}$) values against loading concentration of N-IB after incubation at 20˚C for ten days, with a linear fit to extrapolate to zero concentration.

6.2.1.4 SEC-MALS

The M_w of the main peak was determined to be (262 ± 1) kDa, with a polydispersity (M_w/M_n) of 1.198 ± 0.007. [η] was found to be (191 ± 1) mL.g^{-1}.

6.2.2 One hundred day incubation

6.2.2.1 Viscosity

Plotting the relevant viscosity functions and extrapolating back to where the concentration is zero in Figure 6.13 gives the intrinsic viscosities as (123 ± 2) mL.g^{-1} (Huggins), (123 ± 1) mL.g^{-1} (Kraemer) and (123 ± 1) mL.g^{-1} (Solomon-Ciuta). The mean average value of these is (123 ± 1) mL.g^{-1}.

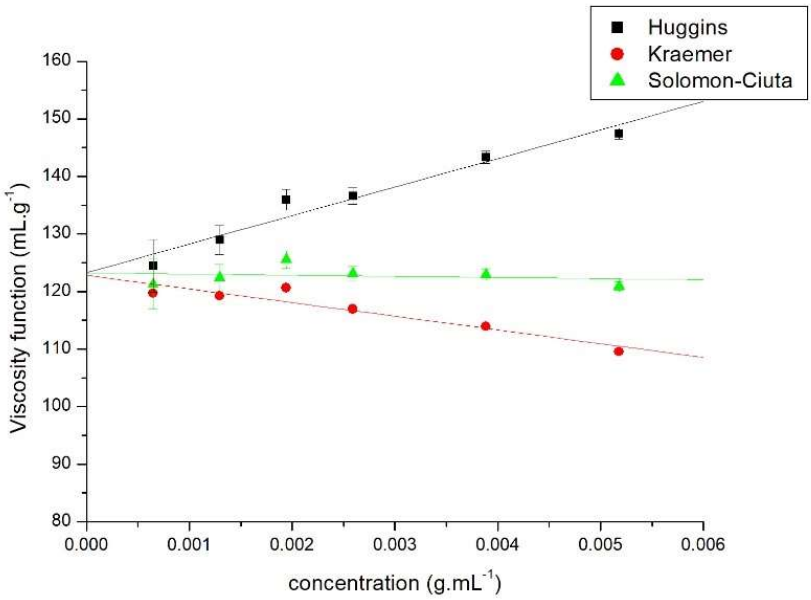


Figure 6.13 – Plot of viscosity against concentration for N-IB after incubation at 20˚C for one hundred days, with linear fits to extrapolate to zero concentration.

6.2.2.2 Sedimentation Velocity

The distribution of sedimentation coefficients is shown in Figure 6.14. The peak data for the main component was also plotted against loading concentration in Figure 6.15 and extrapolated back to zero concentration, giving the sedimentation coefficient as (4.03 ± 0.23) S. As the gradient is close to zero, the data can be treated as a set of repeated measurements (as discussed on page 50). The sedimentation coefficient can instead be calculated as (3.56 ± 0.26) S.

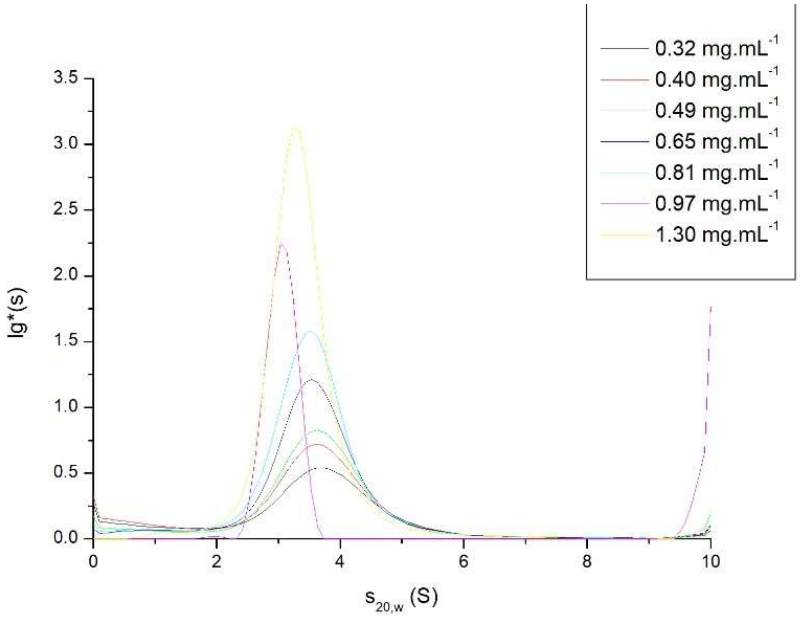


Figure 6.14 – Distribution of sedimentation coefficients at a range of loading concentrations of N-IB after incubation at 20˚C for one hundred days.

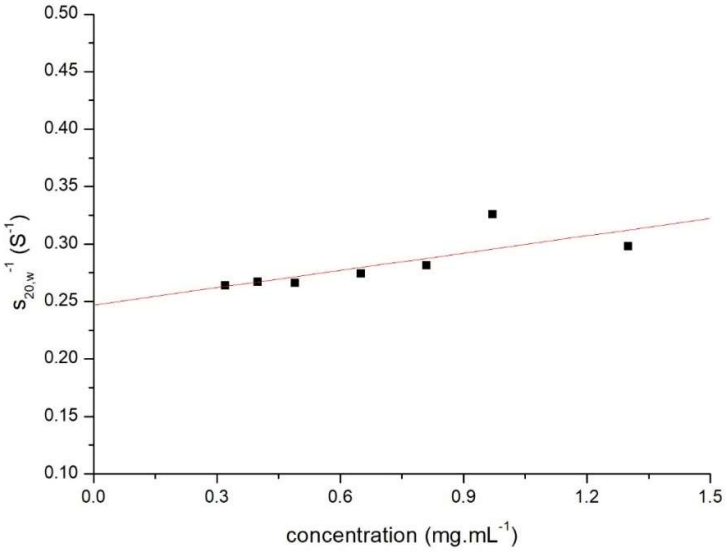


Figure 6.15 – Plot of the reciprocal of sedimentation coefficient against loading concentration for N-IB after incubation at 20˚C for one hundred days, with a linear fit to extrapolate to zero concentration.

6.2.2.3 Sedimentation Equilibrium

SEDFIT-MSTAR provides two methods of determining apparent molecular weight, $M_{w,app}$: from the *M** function and from hinge point analysis. The values given by the program are

plotted against loading concentration in Figure 6.16. Extrapolation to zero concentration gave 'thermodynamically ideal' values of M_w as (186 ± 6) kDa (from the M* method) and (176 ± 6) kDa (from the hinge method). Combining the two yields a consensus value for Mw of (181 ± 4) kDa.

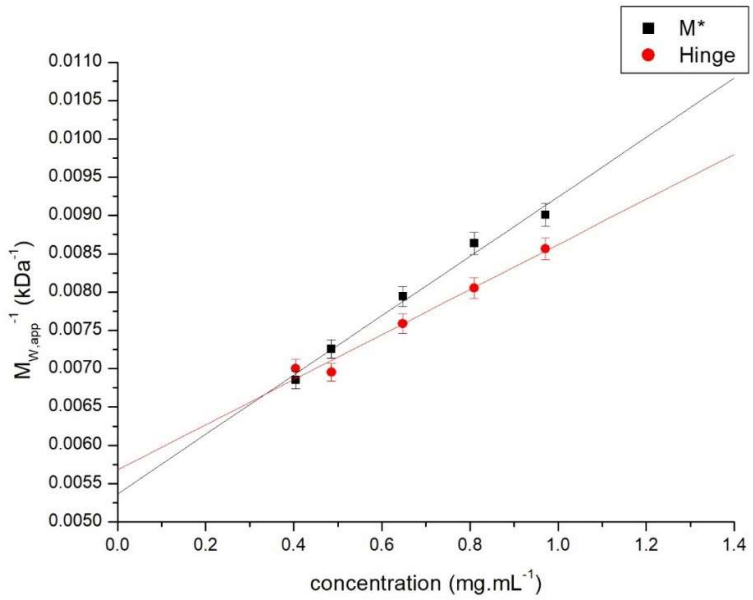


Figure 6.16 – Plot of the reciprocal of apparent molecular weight ($M_{w,app}$) values against loading concentration of N-IB after incubation at 20˚C for one hundred days, with a linear fit to extrapolate to zero concentration.

6.2.2.4 SEC-MALS

The M_w of the main peak was determined to be 159 kDa, although no error is described at this level of precision. The polydispersity (M_w/M_n) was 1.142 ± 0.003. [η] was found to be 114 mL.g^{-1}, although no error is described at this level of precision.

6.3 Native GBS polysaccharide, serotype II

6.3.1 Ten day incubation

6.3.1.1 Viscosity

Plotting the relevant viscosity functions and extrapolating back to where the concentration is zero in Figure 6.17 gives the intrinsic viscosities as (113 ± 1) $mL.g^{-1}$ (Huggins), (111 ± 1) $mL.g^{-1}$ (Kraemer) and (112 ± 1) $mL.g^{-1}$ (Solomon-Ciuta). The mean average value of these is (112 ± 1) $mL.g^{-1}$.

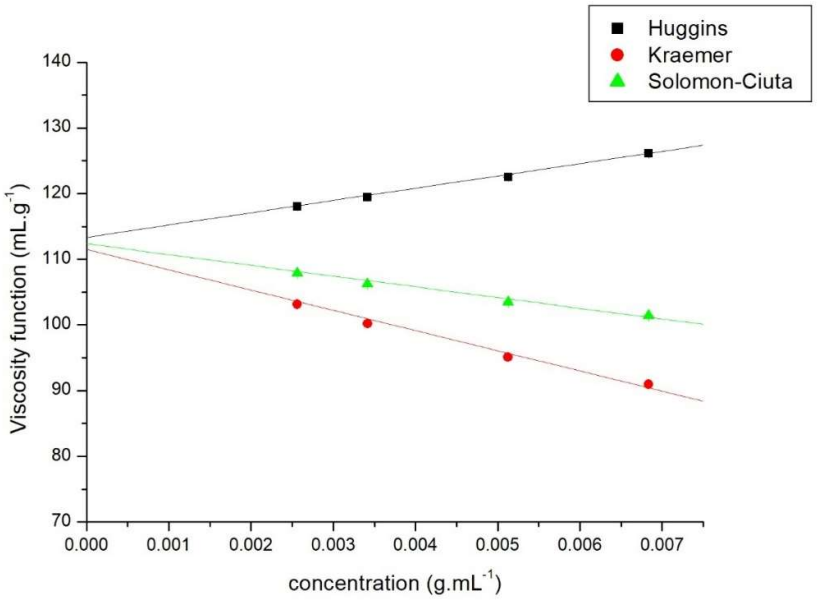


Figure 6.17 – Plot of viscosity against concentration for N-II after incubation at 20˚C for ten days, with linear fits to extrapolate to zero concentration.

6.3.1.2 Sedimentation Velocity

The distribution of sedimentation coefficients is shown in Figure 6.18. The peak data for the main component was also plotted against loading concentration in Figure 6.19 and extrapolated back to zero concentration, giving the sedimentation coefficient as (5.45 ± 0.18) S. As the gradient is close to zero, the data can be treated as a set of repeated measurements (as discussed on page 50). The sedimentation coefficient can instead be calculated as (4.77 ± 0.33) S.

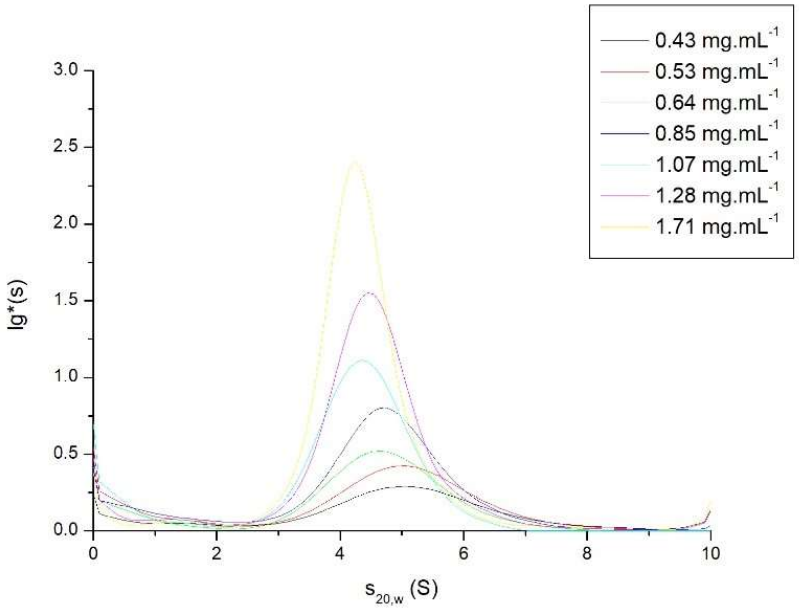


Figure 6.18 – Distribution of sedimentation coefficients at a range of loading concentrations of N-II after incubation at 20˚C for ten days.

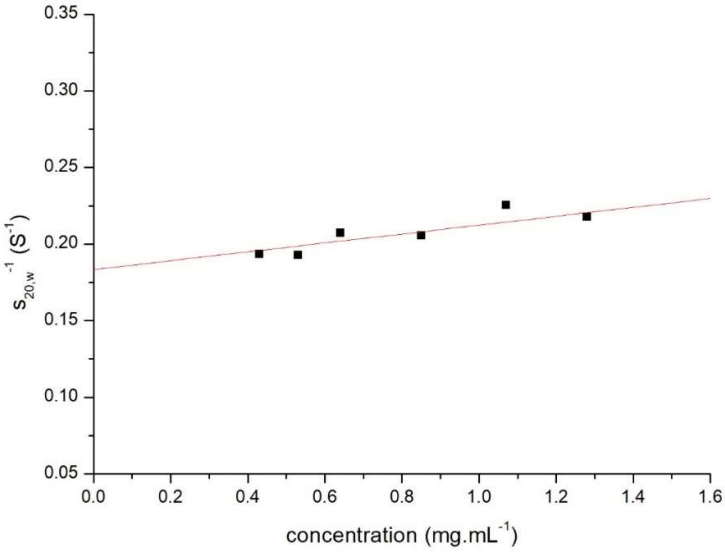


Figure 6.19 – Plot of the reciprocal of sedimentation coefficient against loading concentration for N-II after incubation at 20˚C for ten days, with a linear fit to extrapolate to zero concentration.

6.3.1.3 Sedimentation Equilibrium

SEDFIT-MSTAR provides two methods of determining apparent molecular weight, $M_{w,app}$: from the *M** function and from hinge point analysis. The values given by the program are

plotted against loading concentration in Figure 6.20. Extrapolation to zero concentration gave 'thermodynamically ideal' values of M_w as (469 ± 36) kDa (from the M* method) and (452 ± 19) kDa (from the hinge method). Combining the two yields a consensus value for Mw of (461 ± 20) kDa.

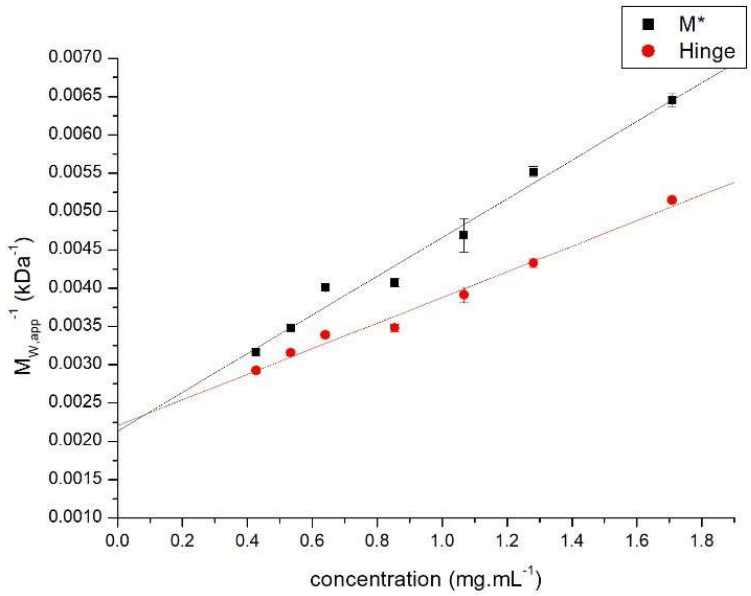


Figure 6.20 – Plot of the reciprocal of apparent molecular weight ($M_{w,app}$) values against loading concentration of N-II after incubation at 20˚C for ten days, with a linear fit to extrapolate to zero concentration.

6.3.1.4 SEC-MALS

The M_w of the main peak was determined to be (539 ± 1) kDa, with a polydispersity (M_w/M_n) of 1.193 ± 0.004. [η] was found to be (159 ± 1) mL.g^{-1}.

6.3.2 One hundred day incubation

6.3.2.1 Viscosity

Plotting the relevant viscosity functions and extrapolating back to where the concentration is zero in Figure 6.21 gives the intrinsic viscosities as (118 ± 1) mL.g^{-1} (Huggins), (116 ± 1) mL.g^{-1} (Kraemer) and (117 ± 1) mL.g^{-1} (Solomon-Ciuta). The mean average value of these is (117 ± 1) mL.g^{-1}.

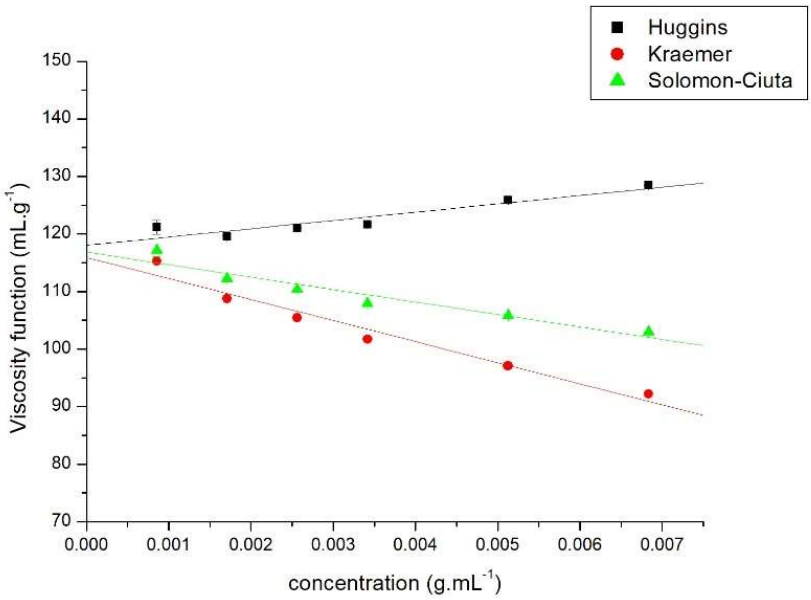


Figure 6.21 – Plot of viscosity against concentration for N-II after incubation at 20˚C for one hundred days, with linear fits to extrapolate to zero concentration.

6.3.2.2 Sedimentation Velocity

The distribution of sedimentation coefficients is shown in Figure 6.22. The peak data for the main component was also plotted against loading concentration in Figure 6.23 and extrapolated back to zero concentration, giving the sedimentation coefficient as (6.60 ± 0.06) S. As the gradient is close to zero, the data can be treated as a set of repeated measurements (as discussed on page 50). The sedimentation coefficient can instead be calculated as (5.63 ± 0.41) S.

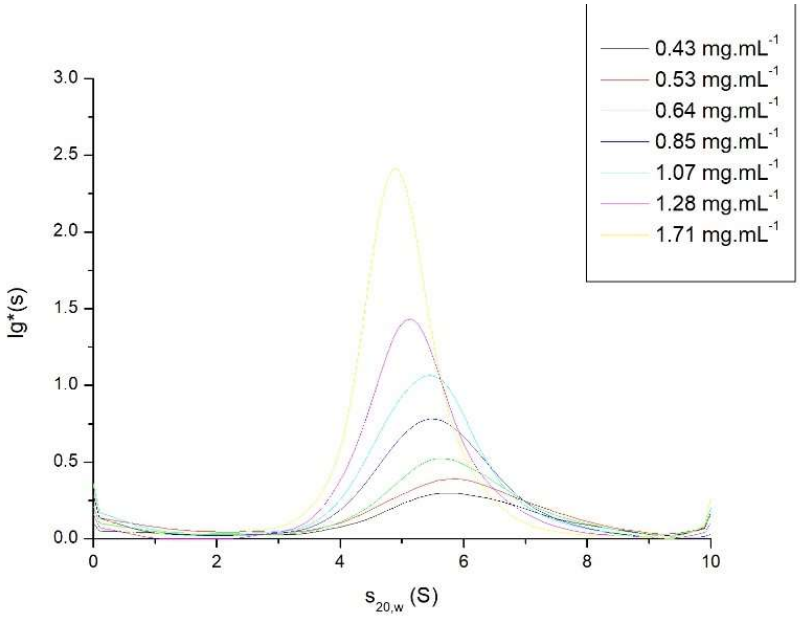


Figure 6.22 – Distribution of sedimentation coefficients at a range of loading concentrations of N-II after incubation at 20˚C for one hundred days.

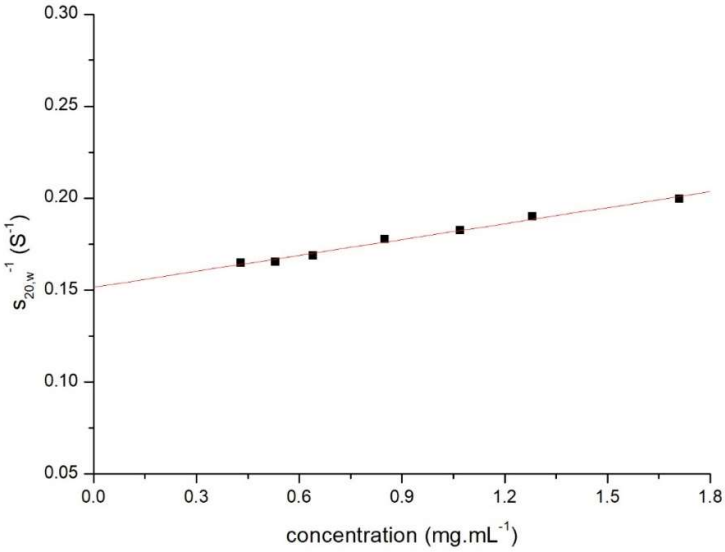


Figure 6.23 – Plot of the reciprocal of sedimentation coefficient against loading concentration for N-II after incubation at 20˚C for one hundred days, with a linear fit to extrapolate to zero concentration.

6.3.2.3 Sedimentation Equilibrium

SEDFIT-MSTAR provides two methods of determining apparent molecular weight, $M_{w,app}$: from the *M** function and from hinge point analysis. The values given by the program are

plotted against loading concentration in Figure 6.24. Extrapolation to zero concentration gave 'thermodynamically ideal' values of M_w as (433 ± 48) kDa (from the M* method) and (377 ± 40) kDa (from the hinge method). Combining the two yields a consensus value for Mw of (405 ± 31) kDa.

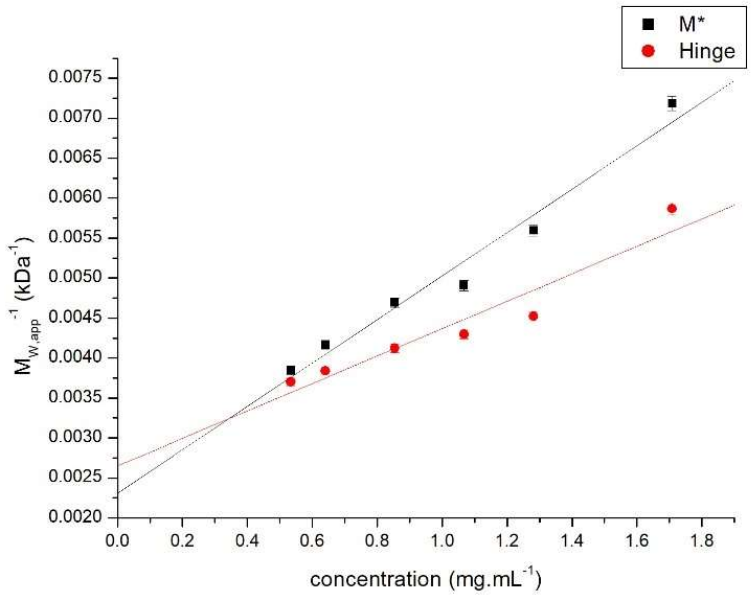


Figure 6.24 – Plot of the reciprocal of apparent molecular weight ($M_{w,app}$) values against loading concentration of N-II after incubation at 20˚C for one hundred days, with a linear fit to extrapolate to zero concentration.

6.3.2.4 SEC-MALS

The M_w of the main peak was determined to be (344 ± 1) kDa, with a polydispersity (M_w/M_n) of 1.194 ± 0.003. [η] was found to be 100 mL.g^{-1}, although no error is described at this level of precision.

6.4 Native GBS polysaccharide, serotype III

6.4.1 Ten day incubation

6.4.1.1 Viscosity

Plotting the relevant viscosity functions and extrapolating back to where the concentration is zero in Figure 6.25 gives the intrinsic viscosities as (33.0 ± 0.3) $mL.g^{-1}$ (Huggins), (33.2 ± 0.3) $mL.g^{-1}$ (Kraemer) and (33.1 ± 0.3) $mL.g^{-1}$ (Solomon-Ciuta). The mean average value of these is (33.1 ± 0.2) $mL.g^{-1}$.

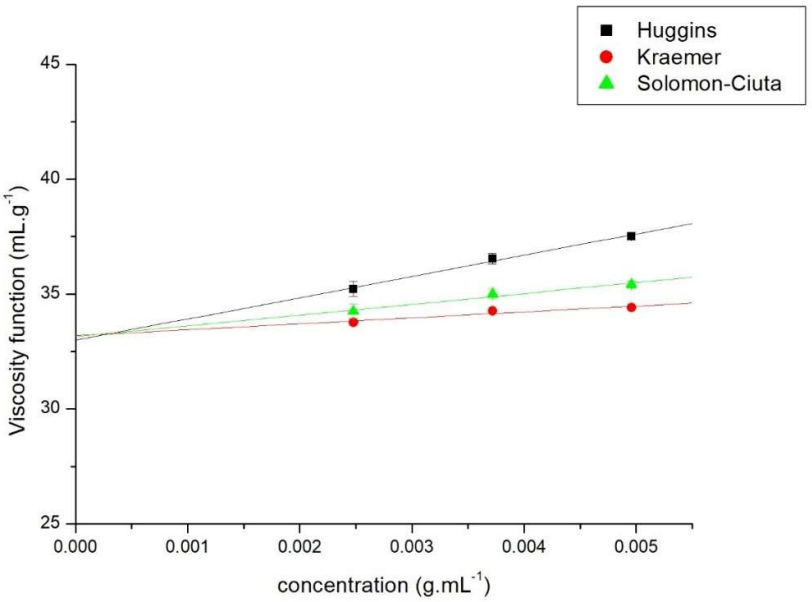


Figure 6.25 – Plot of viscosity against concentration for N-III after incubation at 20˚C for ten days, with linear fits to extrapolate to zero concentration.

6.4.1.2 Sedimentation Velocity

The distribution of sedimentation coefficients is shown in Figure 6.26. The peak data for the main component was also plotted against loading concentration in Figure 6.27 and extrapolated back to zero concentration, giving the sedimentation coefficient as (2.93 ± 0.15) S. As the gradient is close to zero, the data can be treated as a set of repeated measurements (as discussed on page 50). The sedimentation coefficient can instead be calculated as (2.74 ± 0.15) S.

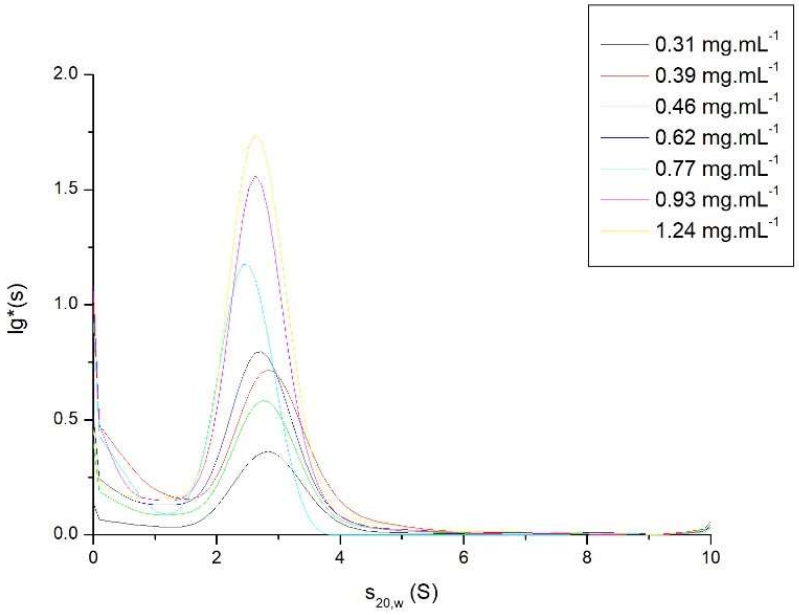


Figure 6.26 – Distribution of sedimentation coefficients at a range of loading concentrations of N-III after incubation at 20˚C for ten days.

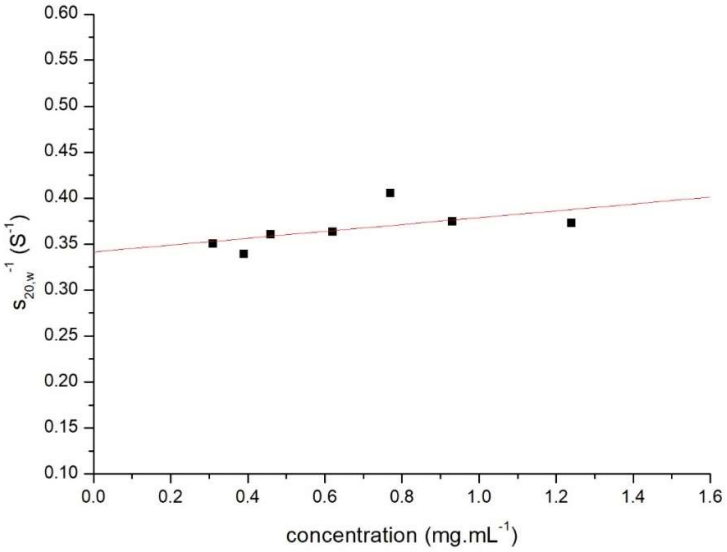


Figure 6.27 – Plot of the reciprocal of sedimentation coefficient against loading concentration for N-III after incubation at 20˚C for ten days, with a linear fit to extrapolate to zero concentration.

6.4.1.3 Sedimentation Equilibrium

SEDFIT-MSTAR provides two methods of determining apparent molecular weight, $M_{w,app}$: from the *M** function and from hinge point analysis. The values given by the program are

plotted against loading concentration in Figure 6.28. Extrapolation to zero concentration gave 'thermodynamically ideal' values of M_w as (146 ± 1) kDa (from the M* method) and (130 ± 3) kDa (from the hinge method). Combining the two yields a consensus value for Mw of (138 ± 1) kDa.

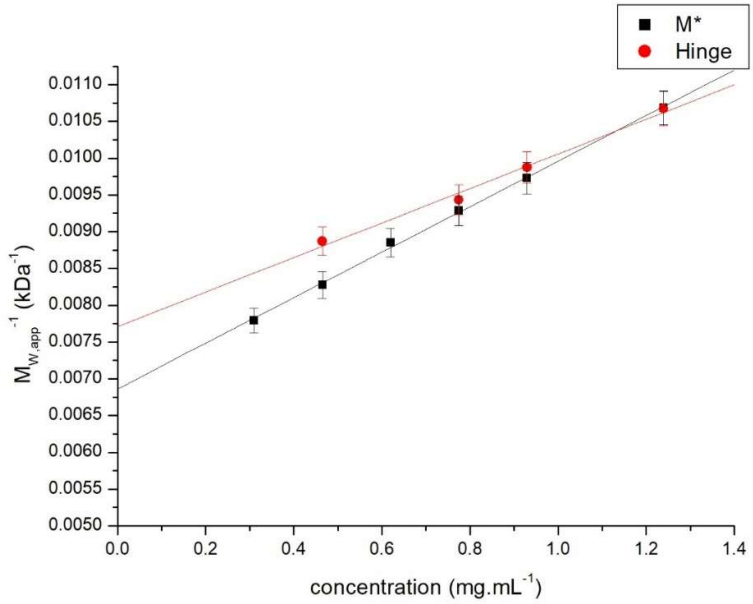


Figure 6.28 – Plot of the reciprocal of apparent molecular weight ($M_{w,app}$) values against loading concentration of N-III after incubation at 20˚C for ten days, with a linear fit to extrapolate to zero concentration.

6.4.1.4 SEC-MALS

The M_w of the main peak was determined to be 118 kDa, although no error is described at this level of precision. The polydispersity (M_w/M_n) is 1.063 ± 0.005. [η] was found to be (64.0 ± 0.7) mL.g^{-1}.

6.4.2 One hundred day incubation

6.4.2.1 Viscosity

Plotting the relevant viscosity functions and extrapolating back to where the concentration is zero in Figure 6.29 gives the intrinsic viscosities as (38.9 ± 0.3) mL.g^{-1} (Huggins), (38.7 ± 0.3) mL.g^{-1} (Kraemer) and (38.8 ± 0.3) mL.g^{-1} (Solomon-Ciuta). The mean average value of these is (38.8 ± 0.2) mL.g^{-1}.

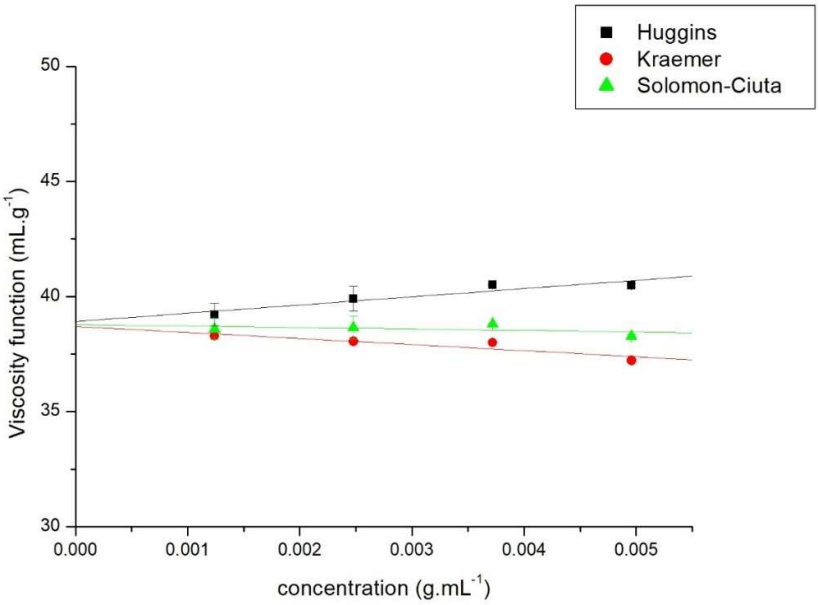


Figure 6.29 – Plot of viscosity against concentration for N-III after incubation at 20˚C for one hundred days, with linear fits to extrapolate to zero concentration.

6.4.2.2 Sedimentation Velocity

The distribution of sedimentation coefficients is shown in Figure 6.30. The peak data for the main component was also plotted against loading concentration in Figure 6.31 and extrapolated back to zero concentration, giving the sedimentation coefficient as (3.38 ± 0.08) S. As the gradient is close to zero, the data can be treated as a set of repeated measurements (as discussed on page 50). The sedimentation coefficient can instead be calculated as (3.22 ± 0.11) S.

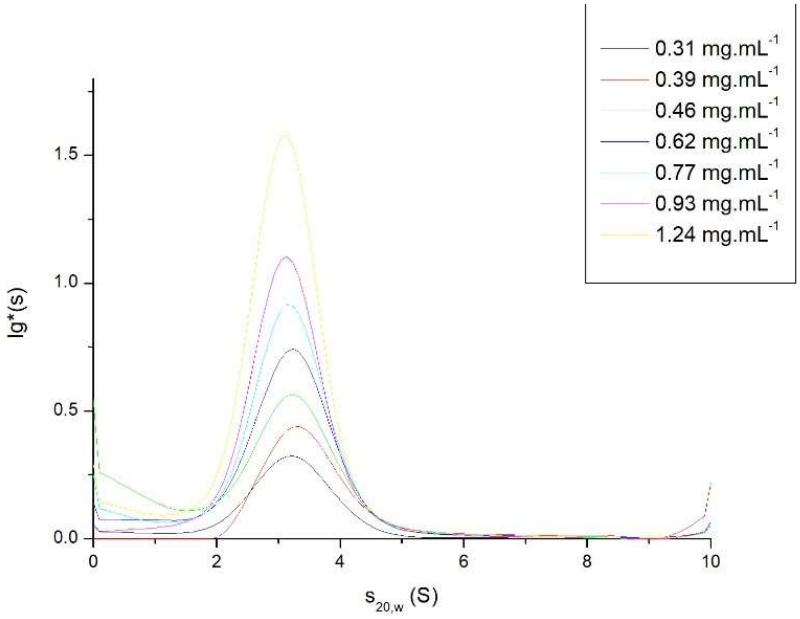


Figure 6.30 – Distribution of sedimentation coefficients at a range of loading concentrations of N-III after incubation at 20˚C for one hundred days.

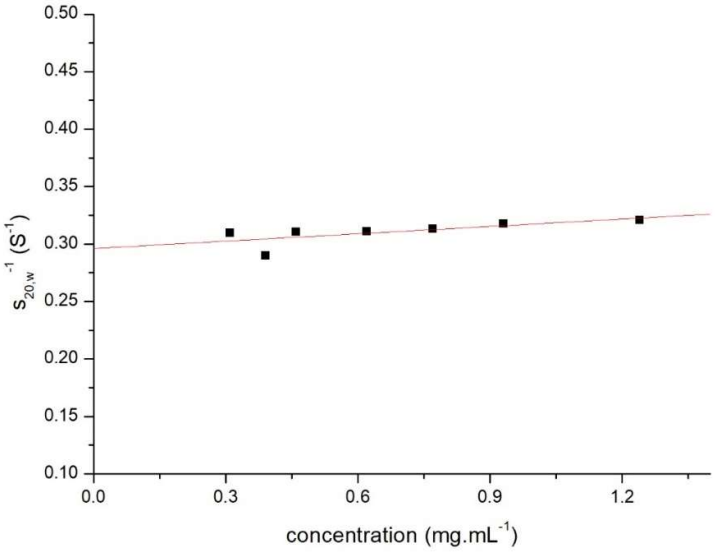


Figure 6.31 – Plot of the reciprocal of sedimentation coefficient against loading concentration for N-III after incubation at 20˚C for one hundred days, with a linear fit to extrapolate to zero concentration.

6.4.2.3 Sedimentation Equilibrium

SEDFIT-MSTAR provides two methods of determining apparent molecular weight, $M_{w,app}$: from the *M** function and from hinge point analysis. The values given by the program are

plotted against loading concentration in Figure 6.32. Extrapolation to zero concentration gave 'thermodynamically ideal' values of M_w as (114 ± 5) kDa (from the M* method) and (129 ± 7) kDa (from the hinge method). Combining the two yields a consensus value for Mw of (121 ± 4) kDa.

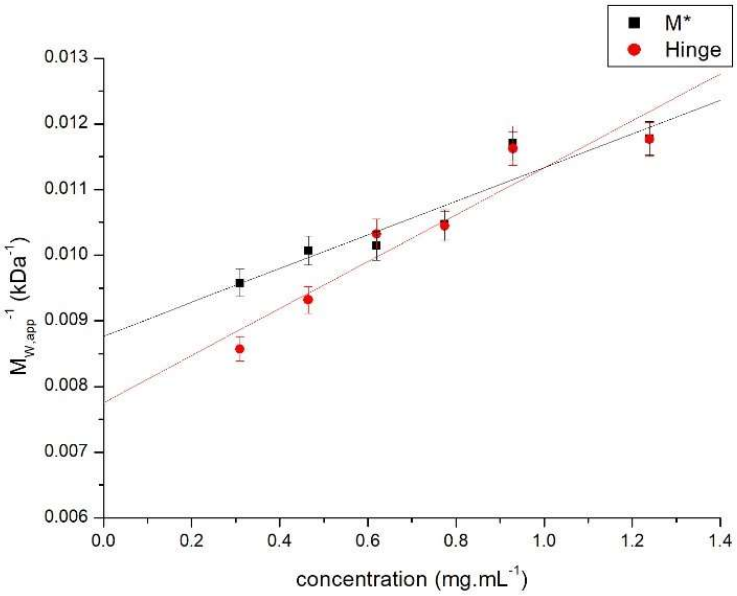


Figure 6.32 – Plot of the reciprocal of apparent molecular weight ($M_{w,app}$) values against loading concentration of N-III after incubation at 20˚C for one hundred days, with a linear fit to extrapolate to zero concentration.

6.4.2.4 SEC-MALS

The M_w of the main peak was determined to be (80.8 ± 0.1) kDa, with a polydispersity (M_w/M_n) of 1.021 ± 0.003. [η] was found to be (42.9 ± 0.4) mL.g^{-1}.

6.5 Native GBS polysaccharide, serotype IV

6.5.1 Ten day incubation

6.5.1.1 Viscosity

Plotting the relevant viscosity functions and extrapolating back to where the concentration is zero in Figure 6.33 gives the intrinsic viscosities as (37.6 ± 0.3) $mL.g^{-1}$ (Huggins), (37.7 ± 0.3) $mL.g^{-1}$ (Kraemer) and (37.6 ± 0.3) $mL.g^{-1}$ (Solomon-Ciuta). The mean average value of these is (37.6 ± 0.2) $mL.g^{-1}$.

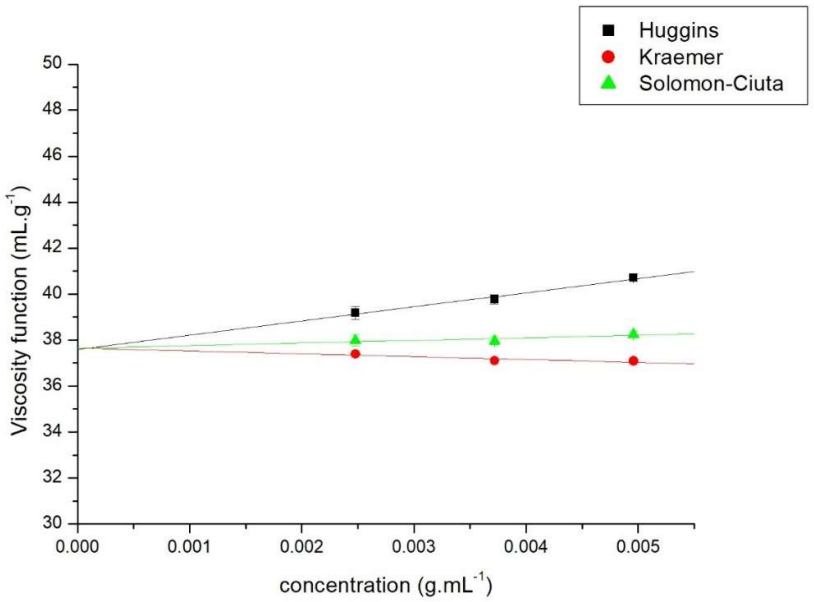


Figure 6.33 – Plot of viscosity against concentration for N-IV after incubation at 20˚C for ten days, with linear fits to extrapolate to zero concentration.

6.5.1.2 Sedimentation Velocity

The distribution of sedimentation coefficients is shown in Figure 6.34. The peak data for the main component was also plotted against loading concentration in Figure 6.35 and extrapolated back to zero concentration, giving the sedimentation coefficient as (2.67 ± 0.05) S. As the gradient is close to zero, the data can be treated as a set of repeated measurements (as discussed on page 50). The sedimentation coefficient can instead be calculated as (2.57 ± 0.07) S.

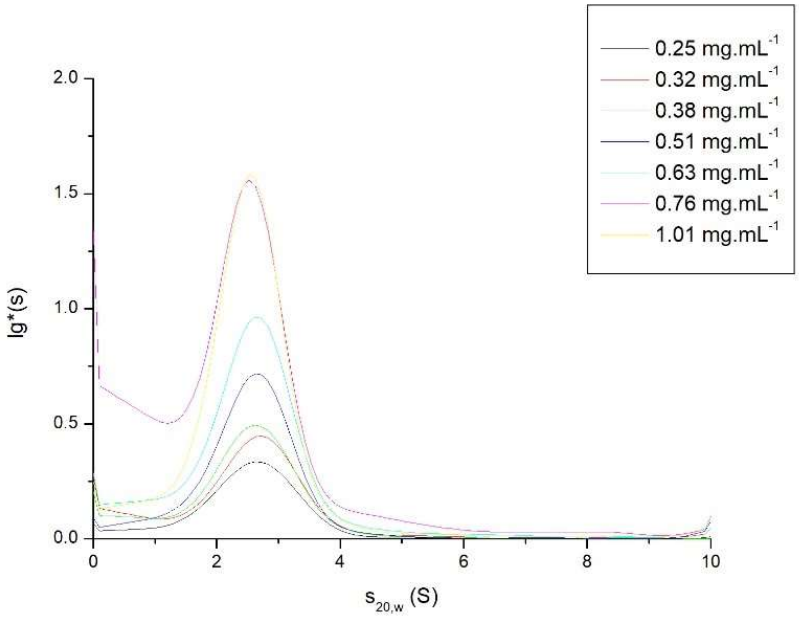


Figure 6.34 – Distribution of sedimentation coefficients at a range of loading concentrations of N-IV after incubation at 20˚C for ten days.

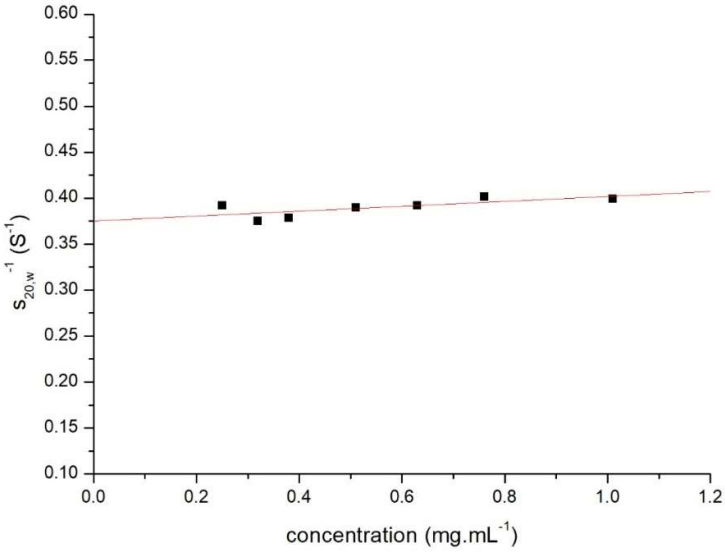


Figure 6.35 – Plot of the reciprocal of sedimentation coefficient against loading concentration for N-IV after incubation at 20˚C for ten days, with a linear fit to extrapolate to zero concentration.

6.5.1.3 Sedimentation Equilibrium

SEDFIT-MSTAR provides two methods of determining apparent molecular weight, $M_{w,app}$: from the *M** function and from hinge point analysis. The values given by the program are

plotted against loading concentration in Figure 6.36. Extrapolation to zero concentration gave 'thermodynamically ideal' values of M_w as (63.3 ± 1.7) kDa (from the M* method) and (72.5 ± 2.0) kDa (from the hinge method). Combining the two yields a consensus value for Mw of (67.9 ± 1.3) kDa.

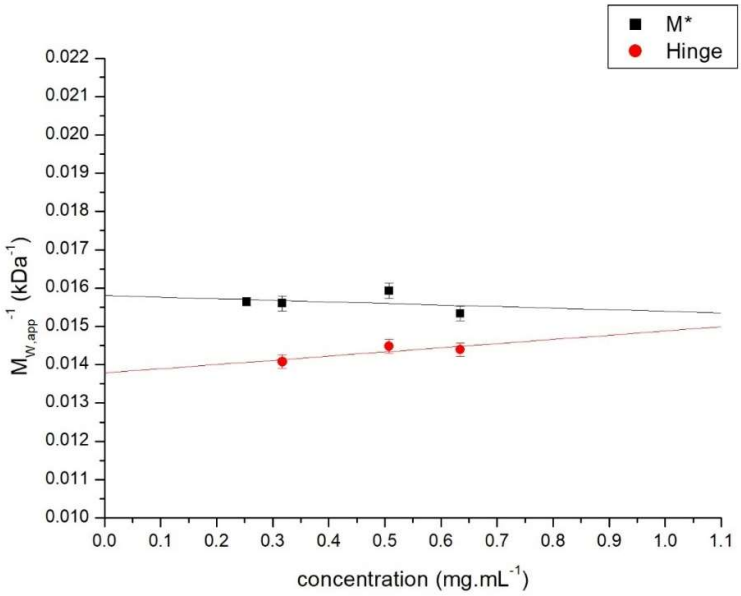


Figure 6.36 – Plot of the reciprocal of apparent molecular weight ($M_{w,app}$) values against loading concentration of N-IV after incubation at 20˚C for ten days, with a linear fit to extrapolate to zero concentration.

6.5.1.4 SEC-MALS

The M_w of the main peak was determined to be (83.3 ± 0.1) kDa, with a polydispersity (M_w/M_n) of 1.055 ± 0.002. [η] was found to be (73.9 ± 0.7) mL.g^{-1}.

6.5.2 One hundred day incubation

6.5.2.1 Viscosity

Plotting the relevant viscosity functions and extrapolating back to where the concentration is zero in Figure 6.37 gives the intrinsic viscosities as (39.7 ± 0.4) mL.g^{-1} (Huggins), (39.8 ± 0.3) mL.g^{-1} (Kraemer) and (39.8 ± 0.3) mL.g^{-1} (Solomon-Ciuta). The mean average value of these is (39.8 ± 0.2) mL.g^{-1}.

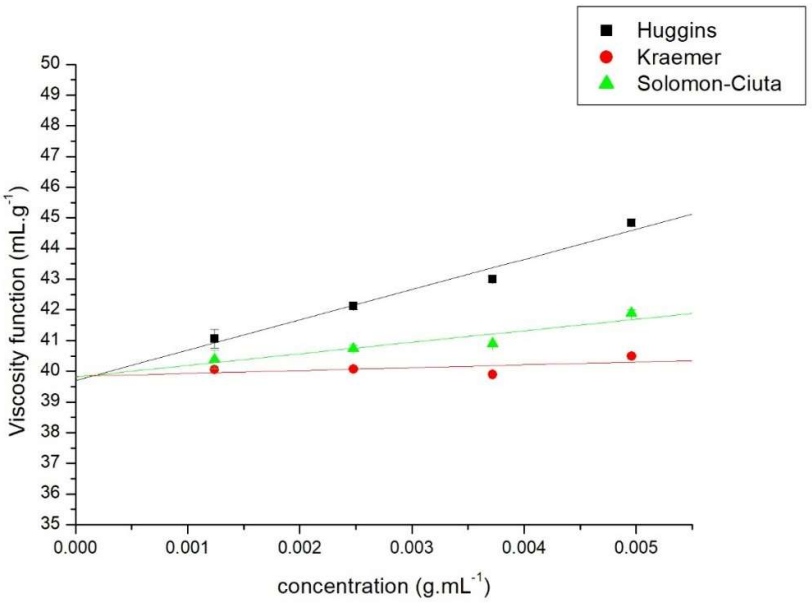


Figure 6.37 – Plot of viscosity against concentration for N-IV after incubation at 20˚C for one hundred days, with linear fits to extrapolate to zero concentration.

6.5.2.2 Sedimentation Velocity

The distribution of sedimentation coefficients is shown in Figure 6.38. The peak data for the main component was also plotted against loading concentration in Figure 6.39 and extrapolated back to zero concentration, giving the sedimentation coefficient as (2.68 ± 0.02) S. As the gradient is close to zero, the data can be treated as a set of repeated measurements (as discussed on page 50). The sedimentation coefficient can instead be calculated as (2.59 ± 0.05) S.

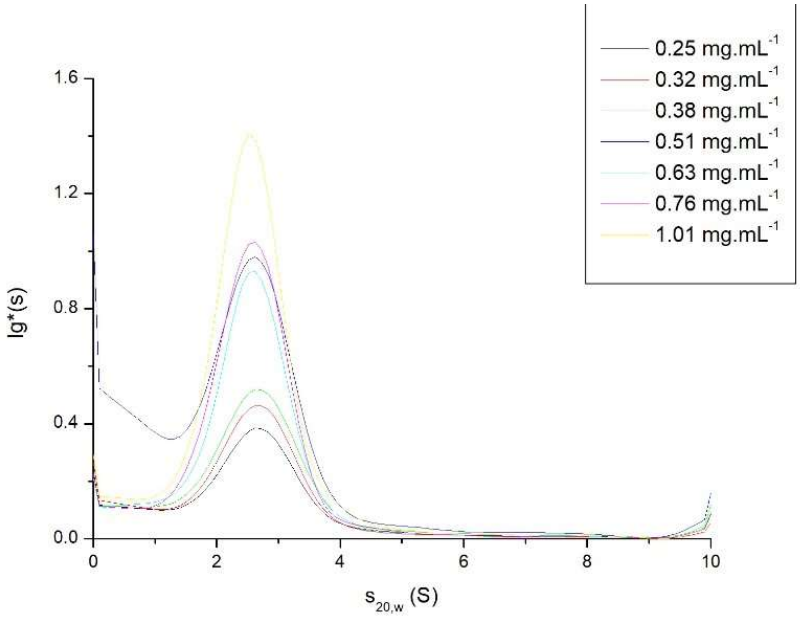


Figure 6.38 – Distribution of sedimentation coefficients at a range of loading concentrations of N-IV after incubation at 20˚C for one hundred days.

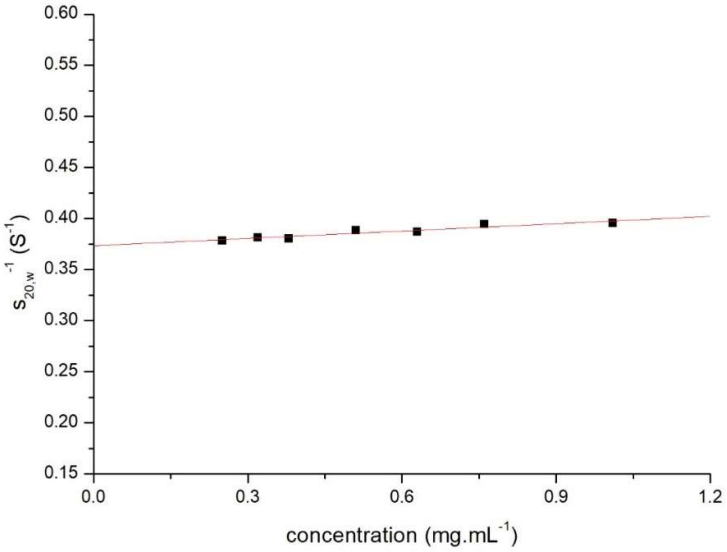


Figure 6.39 – Plot of the reciprocal of sedimentation coefficient against loading concentration for N-IV after incubation at 20˚C for one hundred days, with a linear fit to extrapolate to zero concentration.

6.5.2.3 Sedimentation Equilibrium

SEDFIT-MSTAR provides two methods of determining apparent molecular weight, $M_{w,app}$: from the *M** function and from hinge point analysis. The values given by the program are

plotted against loading concentration in Figure 6.40. Extrapolation to zero concentration gave 'thermodynamically ideal' values of M_w as (80.1± 2.1) kDa (from the M* method) and (76.1 ± 6.5) kDa (from the hinge method). Combining the two yields a consensus value for Mw of (78.1 ± 3.4) kDa.

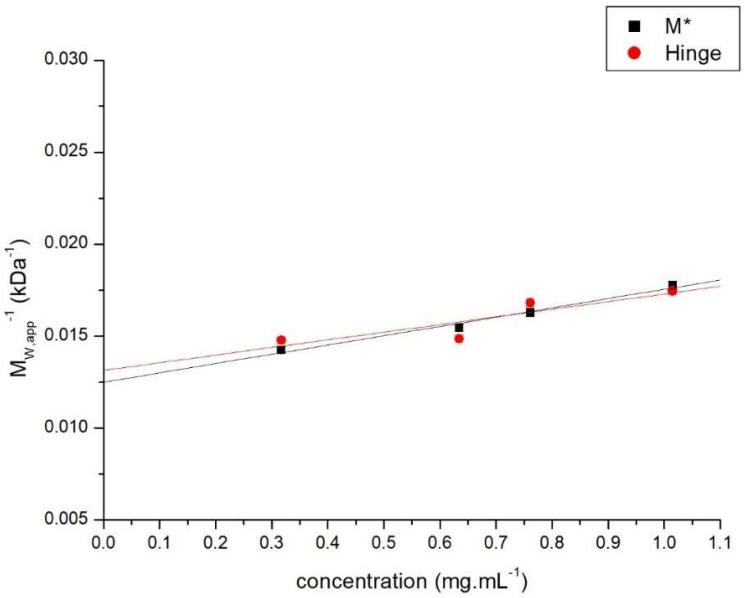


Figure 6.40 – Plot of the reciprocal of apparent molecular weight ($M_{w,app}$) values against loading concentration of N-IV after incubation at 20˚C for one hundred days, with a linear fit to extrapolate to zero concentration.

6.5.2.4 SEC-MALS

The M_w of the main peak was determined to be (59.0 ± 0.2) kDa, with a polydispersity (M_w/M_n) of 1.007 ± 0.005. [η] was found to be (51.7 ± 0.2) mL.g^{-1}.

6.6 Native GBS polysaccharide, serotype V

6.6.1 Ten day incubation

6.6.1.1 Viscosity

Plotting the relevant viscosity functions and extrapolating back to where the concentration is zero in Figure 6.41 gives the intrinsic viscosities as (62.4 ± 0.5) $mL.g^{-1}$ (Huggins), (62.5 ± 0.5) $mL.g^{-1}$ (Kraemer) and (62.5 ± 0.5) $mL.g^{-1}$ (Solomon-Ciuta). The mean average value of these is (62.5 ± 0.3) $mL.g^{-1}$.

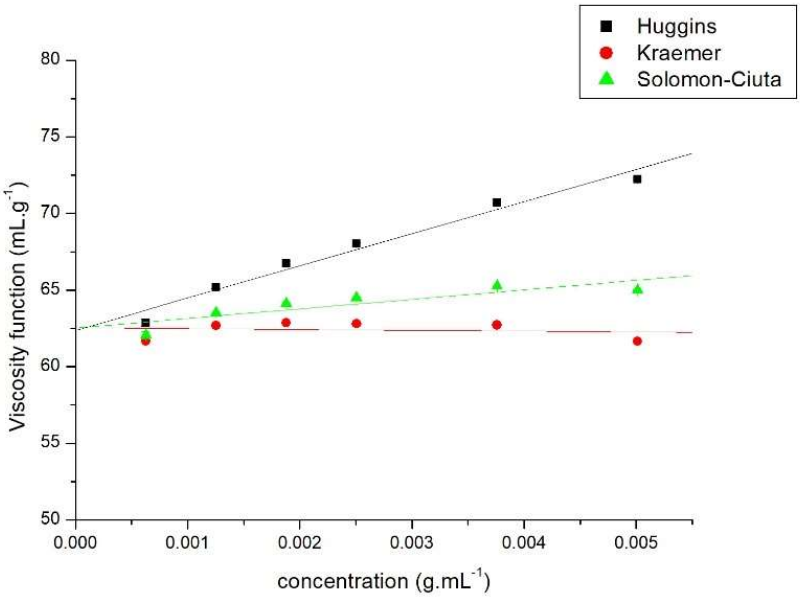


Figure 6.41 – Plot of viscosity against concentration for N-V after incubation at 20˚C for ten days, with linear fits to extrapolate to zero concentration.

6.6.1.2 Sedimentation Velocity

The distribution of sedimentation coefficients is shown in Figure 6.42. The peak data for the main component was also plotted against loading concentration in Figure 6.43 and extrapolated back to zero concentration, giving the sedimentation coefficient as (3.78 ± 0.02) S. As the gradient is close to zero, the data can be treated as a set of repeated measurements (as discussed on page 50). The sedimentation coefficient can instead be calculated as (3.56 ± 0.1) S.

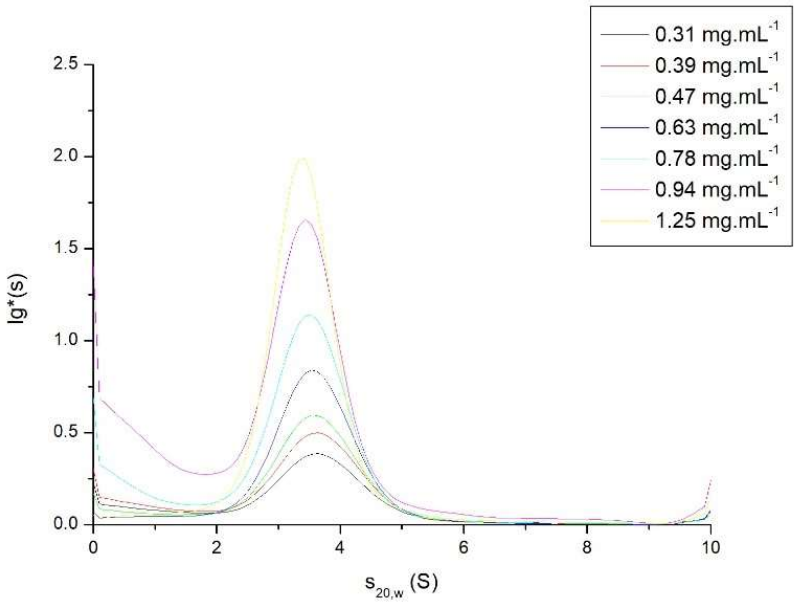


Figure 6.42 – Distribution of sedimentation coefficients at a range of loading concentrations of N-V after incubation at 20˚C for ten days.

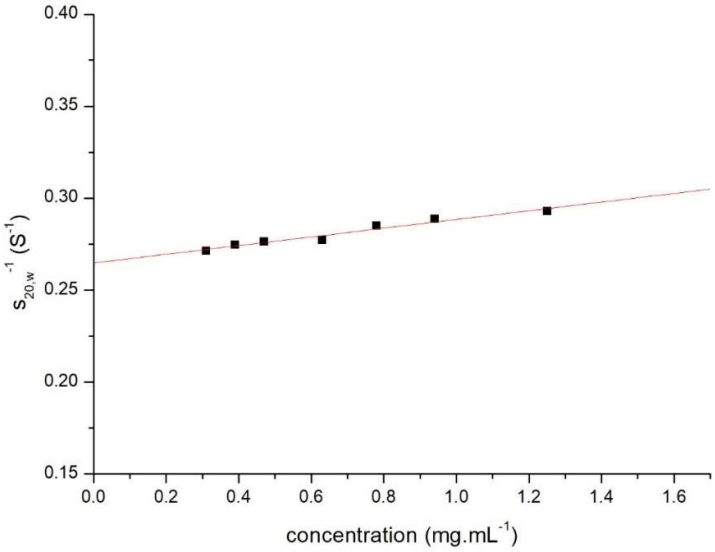


Figure 6.43 – Plot of the reciprocal of sedimentation coefficient against loading concentration for N-V after incubation at 20˚C for ten days, with a linear fit to extrapolate to zero concentration.

6.6.1.3 Sedimentation Equilibrium

SEDFIT-MSTAR provides two methods of determining apparent molecular weight, $M_{w,app}$: from the *M** function and from hinge point analysis. The values given by the program are

plotted against loading concentration in Figure 6.44. Extrapolation to zero concentration gave 'thermodynamically ideal' values of M_w as (181 ± 3) kDa (from the M* method) and (172 ± 7) kDa (from the hinge method). Combining the two yields a consensus value for Mw of (176 ± 4) kDa.

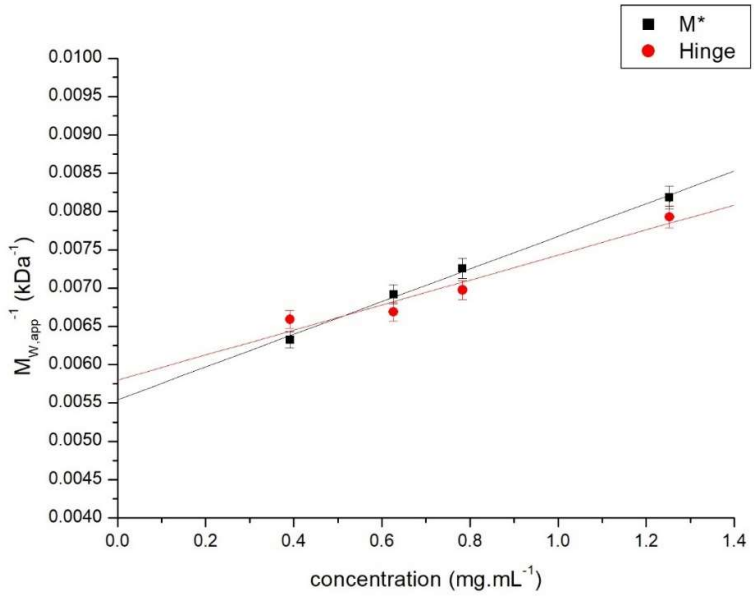


Figure 6.44 – Plot of the reciprocal of apparent molecular weight ($M_{w,app}$) values against loading concentration of N-V after incubation at 20˚C for ten days, with a linear fit to extrapolate to zero concentration.

6.6.1.4 SEC-MALS

The M_w of the main peak was determined to be 180 kDa, although no error is described at this level of precision. The polydispersity (M_w/M_n) was 1.144 ± 0.002. [η] was found to be (131 ± 1) mL.g^{-1}.

6.6.2 One hundred day incubation

6.6.2.1 Viscosity

Plotting the relevant viscosity functions and extrapolating back to where the concentration is zero in Figure 6.45 gives the intrinsic viscosities as (65.6 ± 0.4) mL.g^{-1} (Huggins), (65.6 ± 0.4) mL.g^{-1} (Kraemer) and (65.6 ± 0.4) mL.g^{-1} (Solomon-Ciuta). The mean average value of these is (65.6 ± 0.2) mL.g^{-1}.

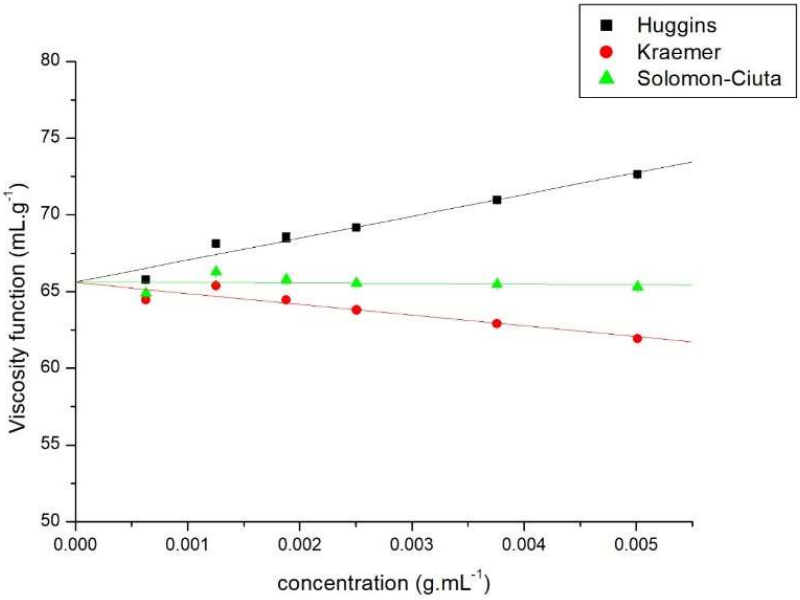


Figure 6.45 – Plot of viscosity against concentration for N-V after incubation at 20˚C for one hundred days, with linear fits to extrapolate to zero concentration.

6.6.2.2 Sedimentation Velocity

The distribution of sedimentation coefficients is shown in Figure 6.46. The peak data for the main component was also plotted against loading concentration in Figure 6.47 and extrapolated back to zero concentration, giving the sedimentation coefficient as (3.73 ± 0.03) S. As the gradient is close to zero, the data can be treated as a set of repeated measurements (as discussed on page 50). The sedimentation coefficient can instead be calculated as (3.54 ± 0.09) S.

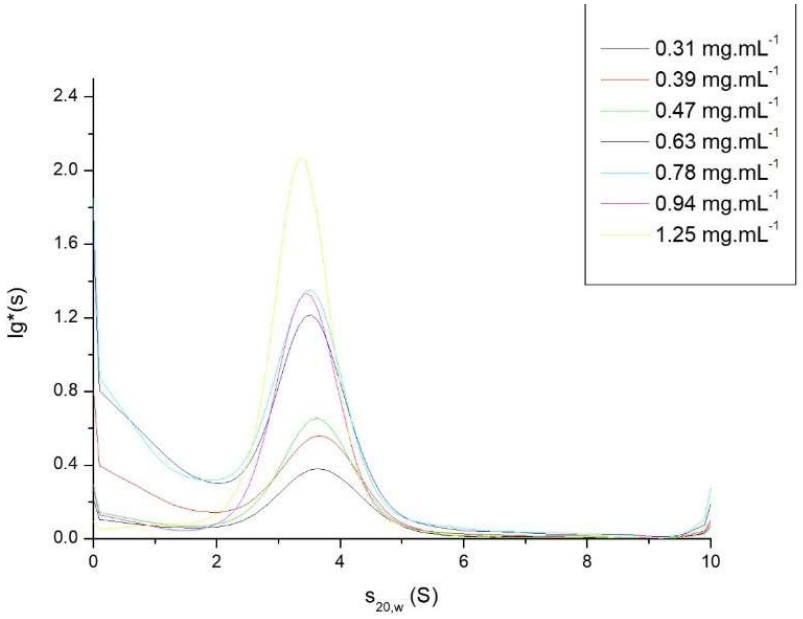


Figure 6.46 – Distribution of sedimentation coefficients at a range of loading concentrations of N-V after incubation at 20˚C for one hundred days.

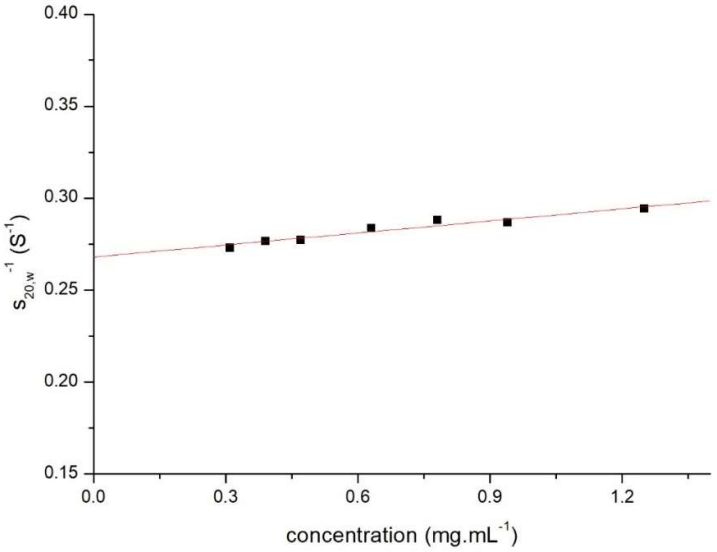


Figure 6.47 – Plot of the reciprocal of sedimentation coefficient against loading concentration for N-V after incubation at 20˚C for one hundred days, with a linear fit to extrapolate to zero concentration.

6.6.2.3 Sedimentation Equilibrium

SEDFIT-MSTAR provides two methods of determining apparent molecular weight, $M_{w,app}$: from the *M** function and from hinge point analysis. The values given by the program are

plotted against loading concentration in Figure 6.48. Extrapolation to zero concentration gave 'thermodynamically ideal' values of M_w as (191 ± 16) kDa (from the M* method) and (199 ± 14) kDa (from the hinge method). Combining the two yields a consensus value for Mw of (195 ± 10) kDa.

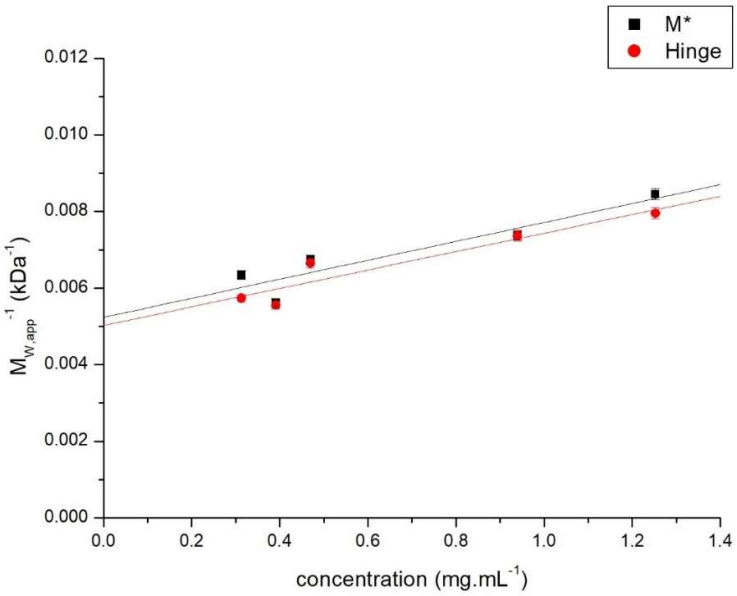


Figure 6.48 – Plot of the reciprocal of apparent molecular weight ($M_{w,app}$) values against loading concentration of N-V after incubation at 20˚C for one hundred days, with a linear fit to extrapolate to zero concentration.

6.6.2.4 SEC-MALS

The M_w of the main peak was determined to be 113 kDa, although no error is described at this level of precision. The polydispersity (M_w/M_n) was 1.036 ± 0.003. [η] was found to be (71.0 ± 0.3) mL.g^{-1}.

6.7 Sized GBS polysaccharide, serotype IA

6.7.1 Ten day incubation

6.7.1.1 Viscosity

Plotting the relevant viscosity functions and extrapolating back to where the concentration is zero in Figure 6.49 gives the intrinsic viscosities as (56.7 ± 0.9) $mL.g^{-1}$ (Huggins), (57.0 ± 0.8) $mL.g^{-1}$ (Kraemer) and (57.0 ± 0.8) $mL.g^{-1}$ (Solomon-Ciuta). The mean average value of these is (56.9 ± 0.5) $mL.g^{-1}$.

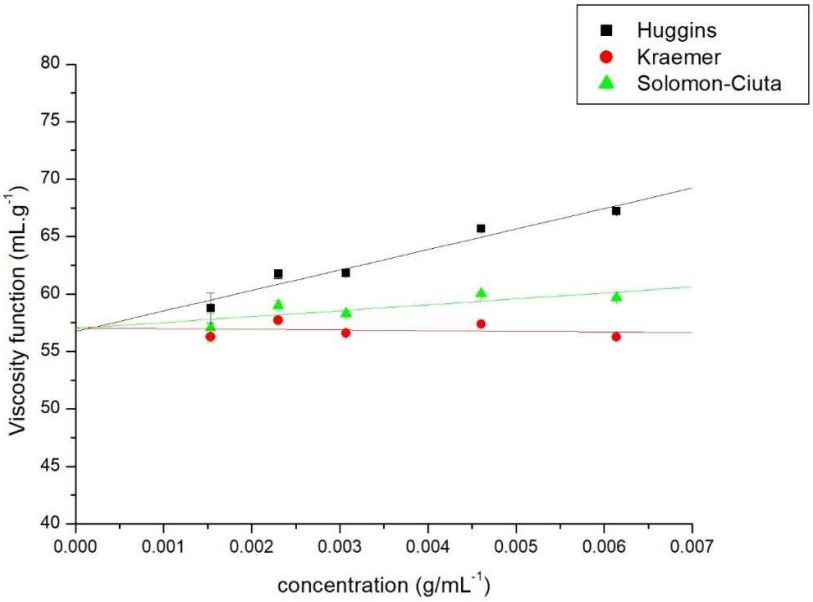


Figure 6.49 – Plot of viscosity against concentration for S-IA after incubation at 20˚C for ten days, with linear fits to extrapolate to zero concentration.

6.7.1.2 Sedimentation Velocity

The distribution of sedimentation coefficients is shown in Figure 6.50. The peak data for the main component was also plotted against loading concentration in Figure 6.51 and extrapolated back to zero concentration, giving the sedimentation coefficient as (3.30 ± 0.14) S. As the gradient is close to zero, the data can be treated as a set of repeated measurements (as discussed on page 50). The sedimentation coefficient can instead be calculated as (2.96 ± 0.18) S.

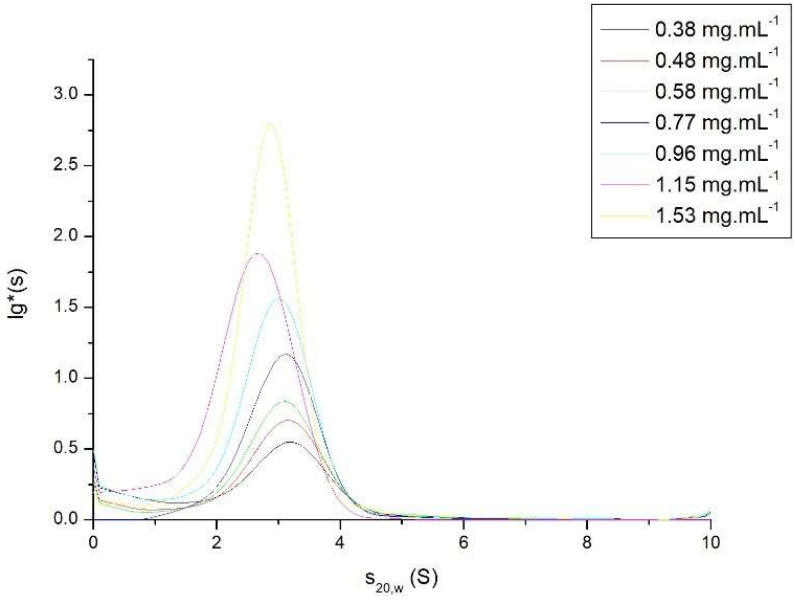


Figure 6.50 – Distribution of sedimentation coefficients at a range of loading concentrations of S-IA after incubation at 20˚C for ten days.

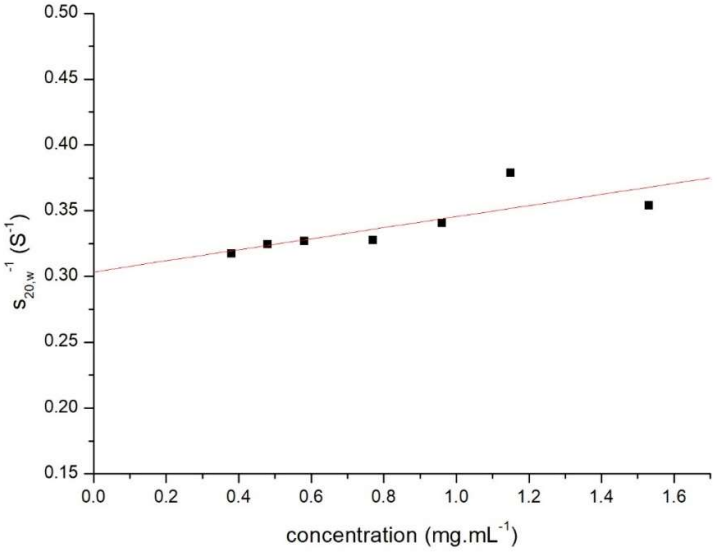


Figure 6.51 – Plot of the reciprocal of sedimentation coefficient against loading concentration for S-IA after incubation at 20˚C for ten days, with a linear fit to extrapolate to zero concentration.

6.7.1.3 Sedimentation Equilibrium

SEDFIT-MSTAR provides two methods of determining apparent molecular weight, $M_{w,app}$: from the *M** function and from hinge point analysis. The values given by the program are plotted against loading concentration in Figure 6.52. Extrapolation to zero concentration gave 'thermodynamically ideal' values of M_w as (198 ± 5) kDa (from the M* method) and (164 ± 9) kDa (from the hinge method). Combining the two yields a consensus value for Mw of (181 ± 5) kDa.

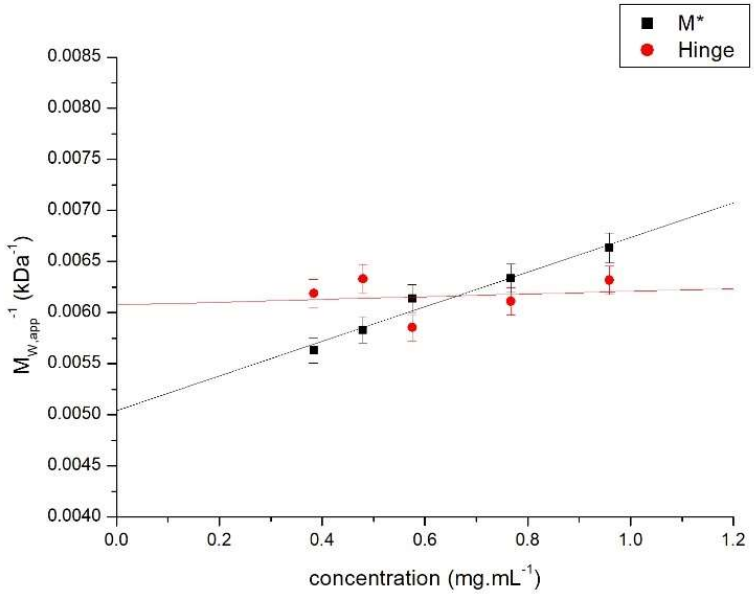


Figure 6.52 – Plot of the reciprocal of apparent molecular weight ($M_{w,app}$) values against loading concentration of S-IA after incubation at 20˚C for ten days, with a linear fit to extrapolate to zero concentration.

6.7.1.4 SEC-MALS

The M_w of the main peak was determined to be 121 kDa, although no error is described at this level of precision. The polydispersity (M_w/M_n) was 1.154 ± 0.003. [η] was found to be (92.8 ± 0.6) mL.g^{-1}.

6.7.2 One hundred day incubation

6.7.2.1 Viscosity

Plotting the relevant viscosity functions and extrapolating back to where the concentration is zero in Figure 6.53 gives the intrinsic viscosities as (64.6 ± 2.3) $mL.g^{-1}$ (Huggins), (64.2 ± 2.0) $mL.g^{-1}$ (Kraemer) and (64.4 ± 2.1) $mL.g^{-1}$ (Solomon-Ciuta). The mean average value of these is (64.4± 1.2) $mL.g^{-1}$.

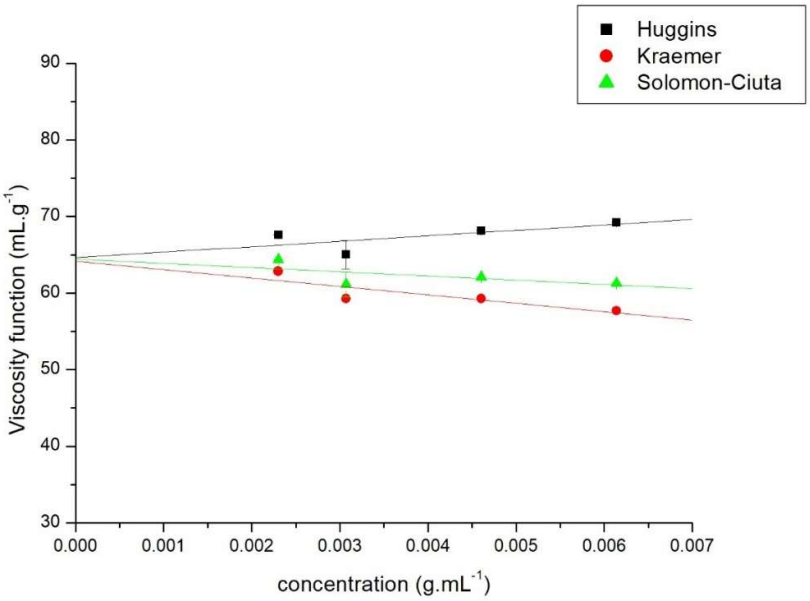


Figure 6.53 – Plot of viscosity against concentration for S-IA after incubation at 20˚C for one hundred days, with linear fits to extrapolate to zero concentration.

6.7.2.2 Sedimentation Velocity

The distribution of sedimentation coefficients is shown in Figure 6.54. The peak data for the main component was also plotted against loading concentration in Figure 6.55 and extrapolated back to zero concentration, giving the sedimentation coefficient as (3.28 ± 0.05) S. As the gradient is close to zero, the data can be treated as a set of repeated measurements (as discussed on page 50). The sedimentation coefficient can instead be calculated as (2.94 ± 0.16) S.

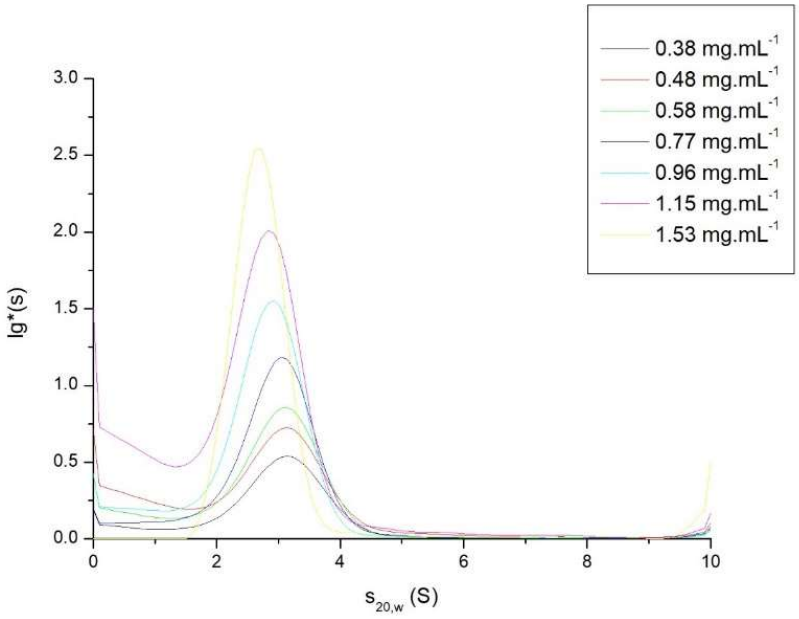


Figure 6.54 – Distribution of sedimentation coefficients at a range of loading concentrations of S-IA after incubation at 20˚C for one hundred days.

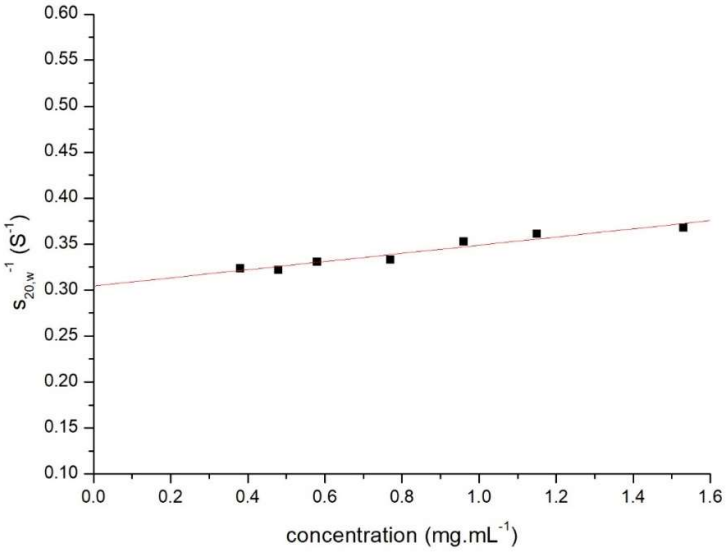


Figure 6.55 – Plot of the reciprocal of sedimentation coefficient against loading concentration for S-IA after incubation at 20˚C for one hundred days, with a linear fit to extrapolate to zero concentration.

6.7.2.3 Sedimentation Equilibrium

SEDFIT-MSTAR provides two methods of determining apparent molecular weight, $M_{w,app}$: from the *M** function and from hinge point analysis. The values given by the program are

plotted against loading concentration in Figure 6.56. Extrapolation to zero concentration gave 'thermodynamically ideal' values of M_w as (189 ± 8) kDa (from the M* method) and (195 ± 10) kDa (from the hinge method). Combining the two yields a consensus value for Mw of (192 ± 6) kDa.

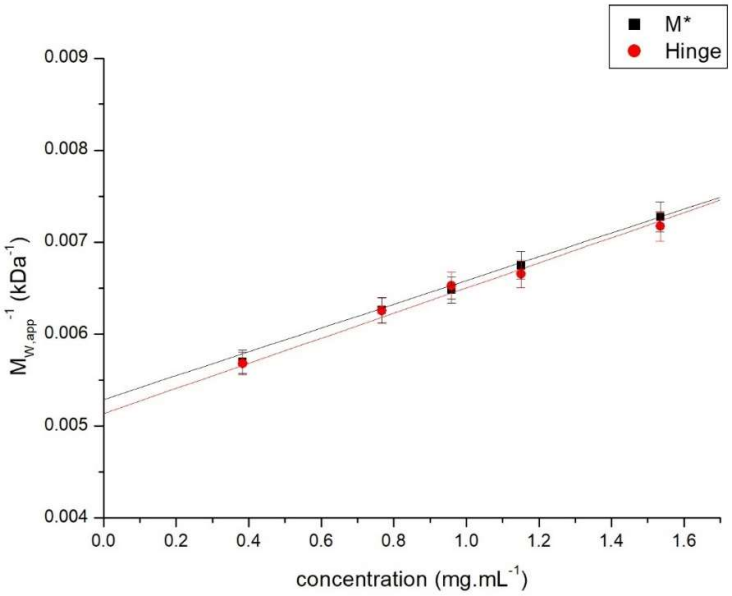


Figure 6.56 – Plot of the reciprocal of apparent molecular weight ($M_{w,app}$) values against loading concentration of S-IA after incubation at 20˚C for one hundred days, with a linear fit to extrapolate to zero concentration.

6.7.2.4 SEC-MALS

The M_w of the main peak was determined to be (84.8 ± 0.2) kDa, with a polydispersity (M_w/M_n) of 1.063 ± 0.004. [η] was found to be (64.2 ± 0.2) mL.g^{-1}.

6.8 Sized GBS polysaccharide, serotype IB

6.8.1 Ten day incubation

6.8.1.1 Viscosity

Plotting the relevant viscosity functions and extrapolating back to where the concentration is zero in Figure 6.57 gives the intrinsic viscosities as (59.7 ± 0.8) $mL.g^{-1}$ (Huggins), (59.9 ± 0.7) $mL.g^{-1}$ (Kraemer) and (59.9 ± 0.7) $mL.g^{-1}$ (Solomon-Ciuta). The mean average value of these is (59.8 ± 0.4) $mL.g^{-1}$.

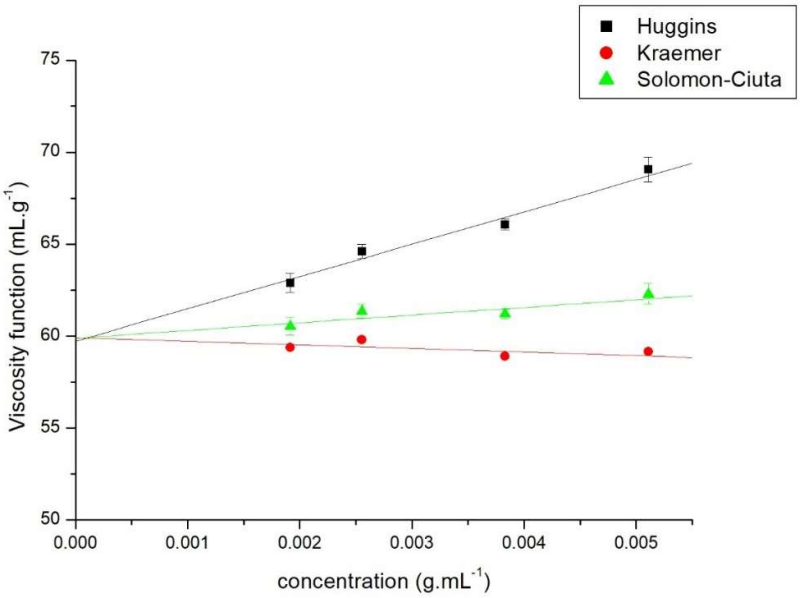


Figure 6.57 – Plot of viscosity against concentration for S-IB after incubation at 20˚C for ten days, with linear fits to extrapolate to zero concentration.

6.8.1.2 Sedimentation Velocity

The distribution of sedimentation coefficients is shown in Figure 6.58. The peak data for the main component was also plotted against loading concentration in Figure 6.59 and extrapolated back to zero concentration, giving the sedimentation coefficient as (3.22 ± 0.01) S. As the gradient is close to zero, the data can be treated as a set of repeated measurements (as discussed on page 50). The sedimentation coefficient can instead be calculated as (3.05 ± 0.09) S.

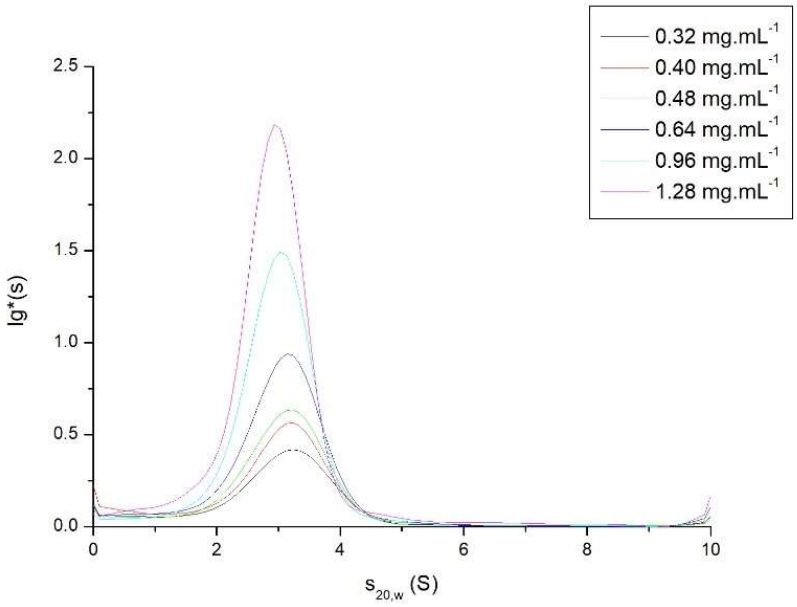


Figure 6.58 – Distribution of sedimentation coefficients at a range of loading concentrations of S-IB after incubation at 20˚C for ten days.

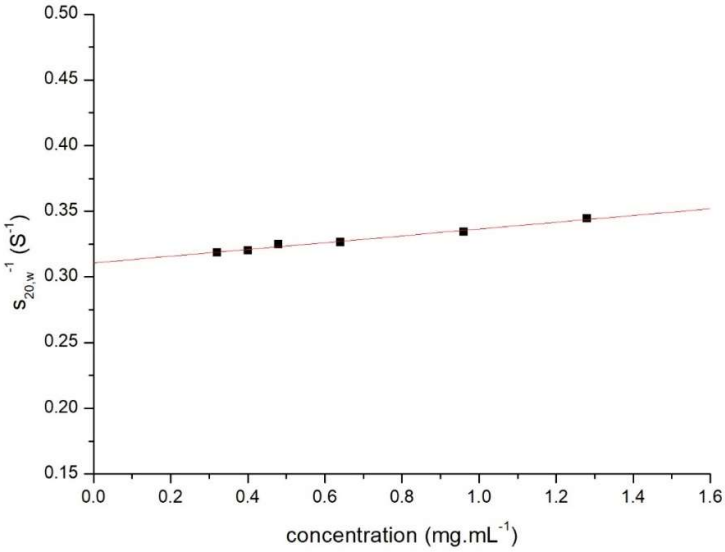


Figure 6.59 – Plot of the reciprocal of sedimentation coefficient against loading concentration for S-IB after incubation at 20˚C for ten days, with a linear fit to extrapolate to zero concentration.

6.8.1.3 Sedimentation Equilibrium

SEDFIT-MSTAR provides two methods of determining apparent molecular weight, $M_{w,app}$: from the *M** function and from hinge point analysis. The values given by the program are

plotted against loading concentration in Figure 6.60. Extrapolation to zero concentration gave 'thermodynamically ideal' values of M_w as (159 ± 6) kDa (from the M* method) and (153 ± 10) kDa (from the hinge method). Combining the two yields a consensus value for Mw of (156 ± 6) kDa.

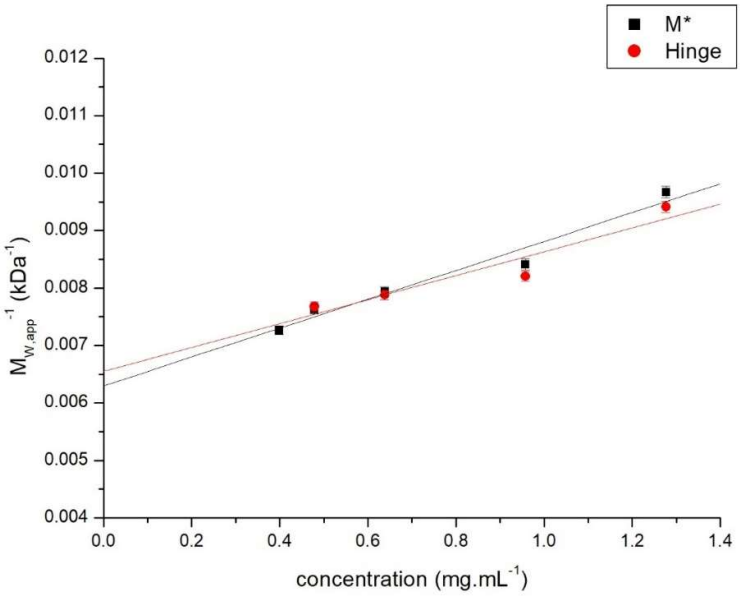


Figure 6.60 – Plot of the reciprocal of apparent molecular weight ($M_{w,app}$) values against loading concentration of S-IB after incubation at 20˚C for ten days, with a linear fit to extrapolate to zero concentration.

6.8.1.4 SEC-MALS

The M_w of the main peak was determined to be 122 kDa, although no error is described at this level of precision. The polydispersity (M_w/M_n) was 1.149 ± 0.003. [η] was found to be (96.5 ± 0.9) mL.g^{-1}.

6.8.2 One hundred day incubation

6.8.2.1 Viscosity

Plotting the relevant viscosity functions and extrapolating back to where the concentration is zero in Figure 6.61 gives the intrinsic viscosities as (63.6 ± 0.5) mL.g^{-1} (Huggins), (63.4 ± 0.4) mL.g^{-1} (Kraemer) and (63.5 ± 0.4) mL.g^{-1} (Solomon-Ciuta). The mean average value of these is (63.5 ± 0.2) mL.g^{-1}.

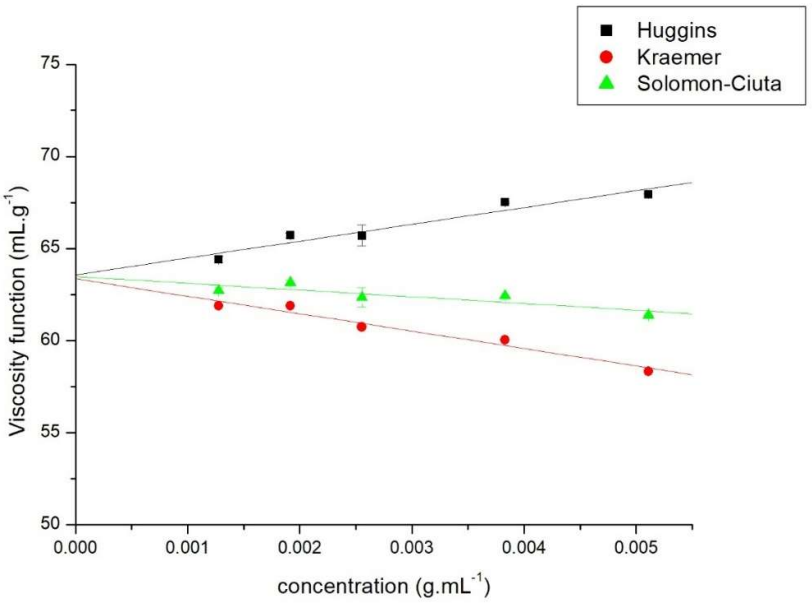


Figure 6.61 – Plot of viscosity against concentration for S-IB after incubation at 20˚C for one hundred days, with linear fits to extrapolate to zero concentration.

6.8.2.2 Sedimentation Velocity

The distribution of sedimentation coefficients is shown in Figure 6.62. The peak data for the main component was also plotted against loading concentration in Figure 6.63 and extrapolated back to zero concentration, giving the sedimentation coefficient as (3.22 ± 0.04) S. As the gradient is close to zero, the data can be treated as a set of repeated measurements (as discussed on page 50). The sedimentation coefficient can instead be calculated as (2.98 ± 0.1) S.

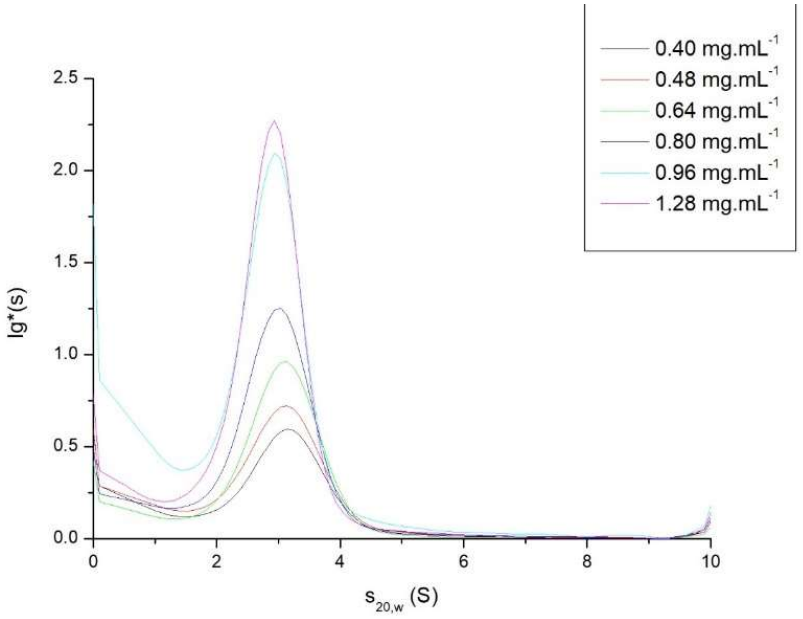


Figure 6.62 – Distribution of sedimentation coefficients at a range of loading concentrations of S-IB after incubation at 20˚C for one hundred days.

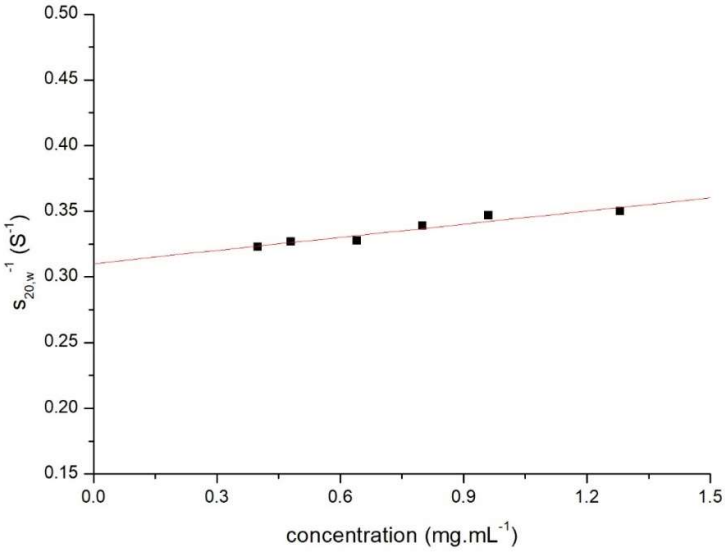


Figure 6.63 – Plot of the reciprocal of sedimentation coefficient against loading concentration for S-IB after incubation at 20˚C for one hundred days, with a linear fit to extrapolate to zero concentration.

6.8.2.3 Sedimentation Equilibrium

SEDFIT-MSTAR provides two methods of determining apparent molecular weight, $M_{w,app}$: from the *M** function and from hinge point analysis. The values given by the program are

plotted against loading concentration in Figure 6.64. Extrapolation to zero concentration gave 'thermodynamically ideal' values of M_w as (153 ± 8) kDa (from the M* method) and (147 ± 6) kDa (from the hinge method). Combining the two yields a consensus value for Mw of (150 ± 5) kDa.

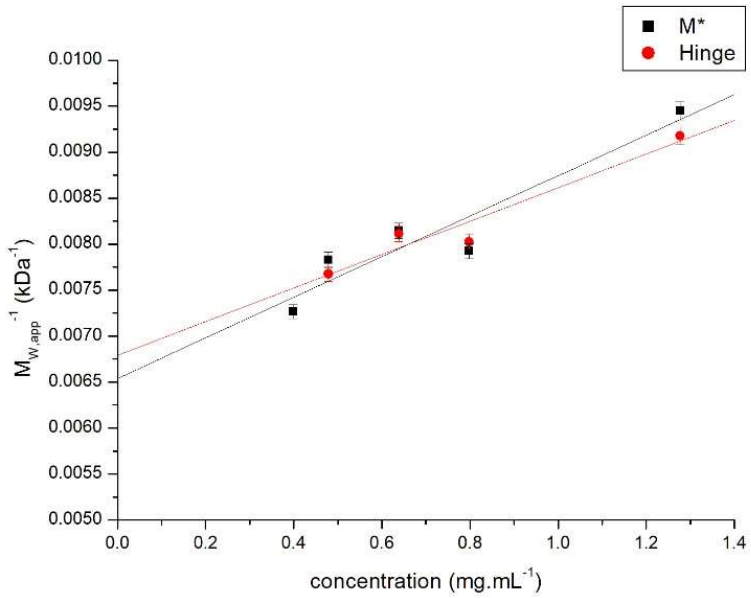


Figure 6.64 – Plot of the reciprocal of apparent molecular weight ($M_{w,app}$) values against loading concentration of S-IB after incubation at 20˚C for one hundred days, with a linear fit to extrapolate to zero concentration. Hinge point analysis at the lowest concentration was an outlier and discounted, although the M analysis is still included.*

6.8.2.4 SEC-MALS

The M_w of the main peak was determined to be (87.2 ± 0.2) kDa, with a polydispersity (M_w/M_n) of 1.045 ± 0.003. [η] was found to be (67.4 ± 0.2) mL.g^{-1}.

6.9 Sized GBS polysaccharide, serotype II

6.9.1 Ten day incubation

6.9.1.1 Viscosity

Plotting the relevant viscosity functions and extrapolating back to where the concentration is zero in Figure 6.65 gives the intrinsic viscosities as (28.1 ± 1.3) $mL.g^{-1}$ (Huggins), (29.0 ± 1.4) $mL.g^{-1}$ (Kraemer) and (28.7 ± 1.4) $mL.g^{-1}$ (Solomon-Ciuta). The mean average value of these is (28.6 ± 0.8) $mL.g^{-1}$.

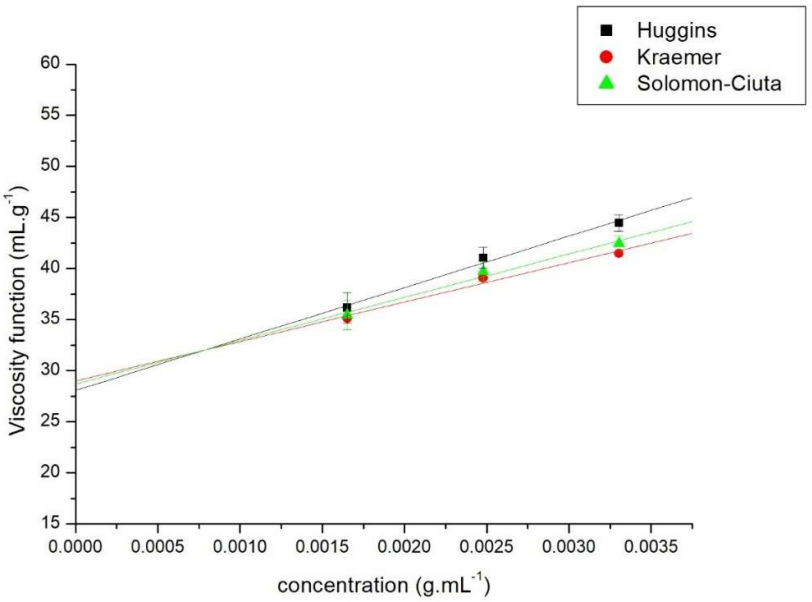


Figure 6.65 – Plot of viscosity against concentration for S-II after incubation at 20˚C for ten days, with linear fits to extrapolate to zero concentration.

6.9.1.2 Sedimentation Velocity

The distribution of sedimentation coefficients is shown in Figure 6.66. The peak data for the main component was also plotted against loading concentration in Figure 6.67 and extrapolated back to zero concentration, giving the sedimentation coefficient as (3.82 ± 0.07) S. As the gradient is close to zero, the data can be treated as a set of repeated measurements (as discussed on page 50). The sedimentation coefficient can instead be calculated as (3.68 ± 0.1) S.

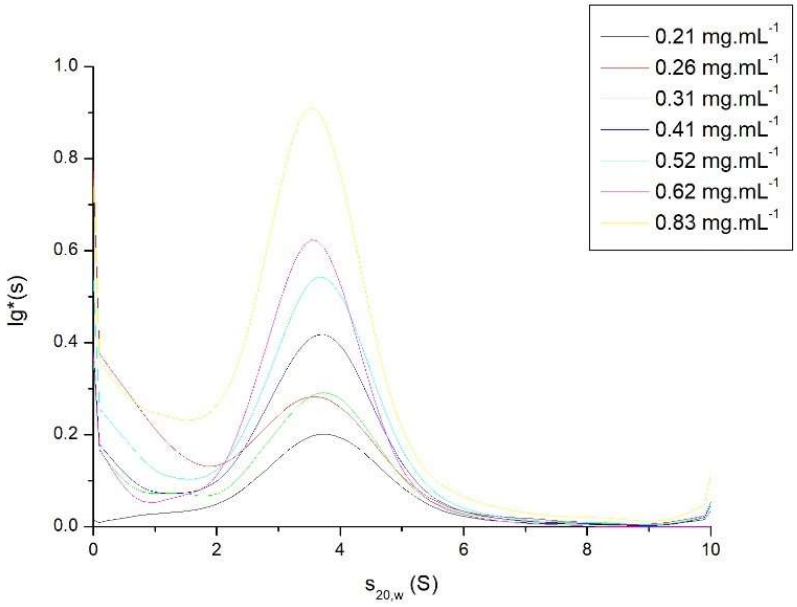


Figure 6.66 – Distribution of sedimentation coefficients at a range of loading concentrations of S-II after incubation at 20˚C for ten days.

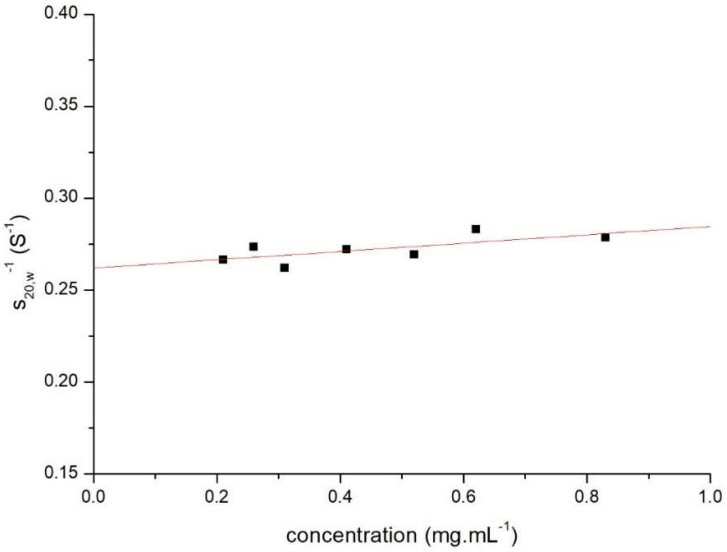


Figure 6.67 – Plot of the reciprocal of sedimentation coefficient against loading concentration for S-II after incubation at 20˚C for ten days, with a linear fit to extrapolate to zero concentration.

6.9.1.3 Sedimentation Equilibrium

SEDFIT-MSTAR provides two methods of determining apparent molecular weight, $M_{w,app}$: from the *M** function and from hinge point analysis. The values given by the program are

plotted against loading concentration in Figure 6.68. Extrapolation to zero concentration gave 'thermodynamically ideal' values of M_w as (187 ± 8) kDa (from the M* method) and (183 ± 5) kDa (from the hinge method). Combining the two yields a consensus value for Mw of (185 ± 5) kDa.

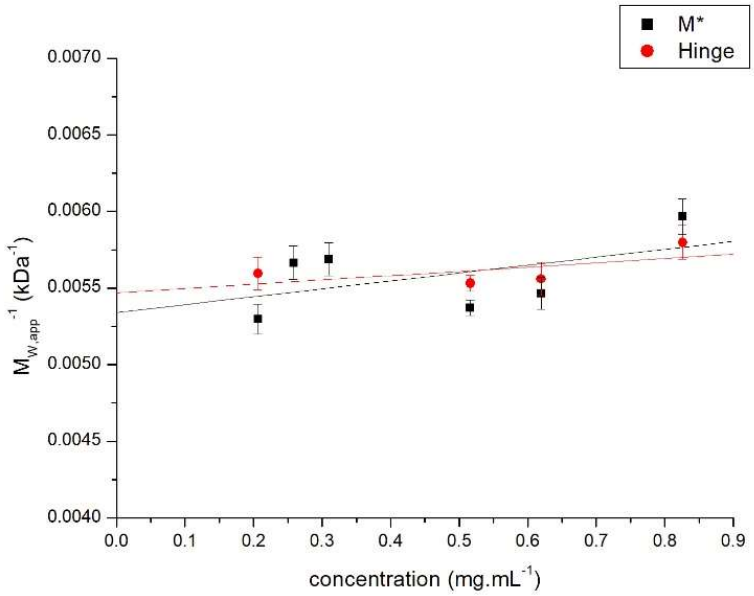


Figure 6.68 – Plot of the reciprocal of apparent molecular weight ($M_{w,app}$) values against loading concentration of S-II after incubation at 20˚C for ten days, with a linear fit to extrapolate to zero concentration. Two of the lower concentration did not give outlying data in hinge point analysis and were excluded, although the M data was still acceptable.*

6.9.1.4 SEC-MALS

The M_w of the main peak was determined to be 185 kDa, although no error is described at this level of precision. The polydispersity (M_w/M_n) was 1.320 ± 0.003. [η] was found to be (68.4 ± 0.8) mL.g^{-1}.

6.9.2 One hundred day incubation

6.9.2.1 Viscosity

Plotting the relevant viscosity functions and extrapolating back to where the concentration is zero in Figure 6.69 gives the intrinsic viscosities as (51.8 ± 0.1) mL.g^{-1} (Huggins), (51.8 ± 0.1)

mL.g^{-1} (Kraemer) and (51.8 ± 0.1) mL.g^{-1} (Solomon-Ciuta). The mean average value of these is 51.8 mL.g^{-1}, although no error is reported at this level of precision.

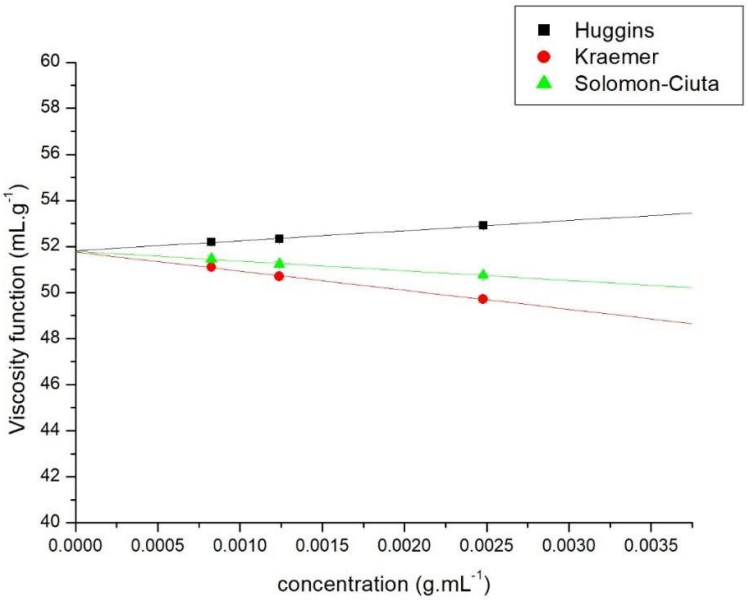


Figure 6.69 – Plot of viscosity against concentration for S-II after incubation at 20˚C for one hundred days, with linear fits to extrapolate to zero concentration.

6.9.2.2 Sedimentation Velocity

The distribution of sedimentation coefficients is shown in Figure 6.70. The peak data for the main component was also plotted against loading concentration in Figure 6.71 and extrapolated back to zero concentration, giving the sedimentation coefficient as (4.43 ± 0.04) S. As the gradient is close to zero, the data can be treated as a set of repeated measurements (as discussed on page 50). The sedimentation coefficient can instead be calculated as (4.3 ± 0.08) S.

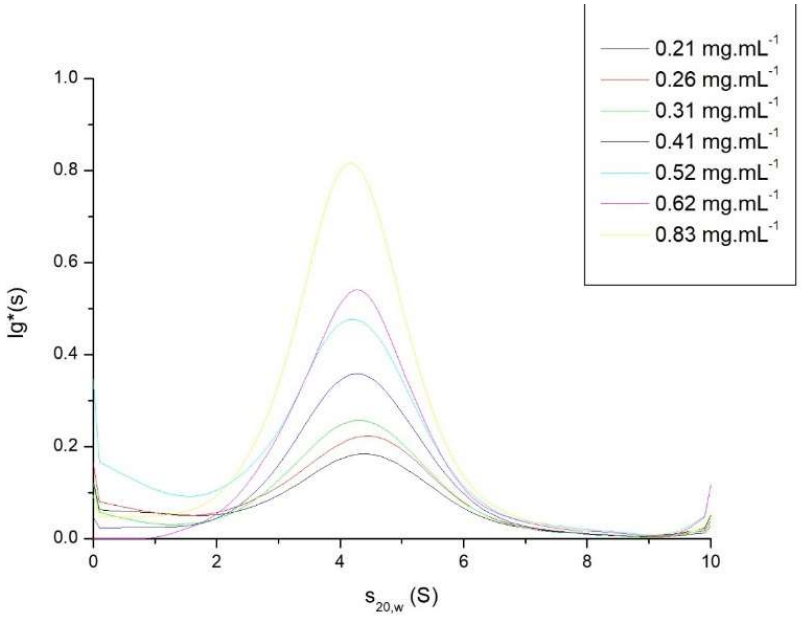


Figure 6.70 – Distribution of sedimentation coefficients at a range of loading concentrations of S-II after incubation at 20˚C for one hundred days.

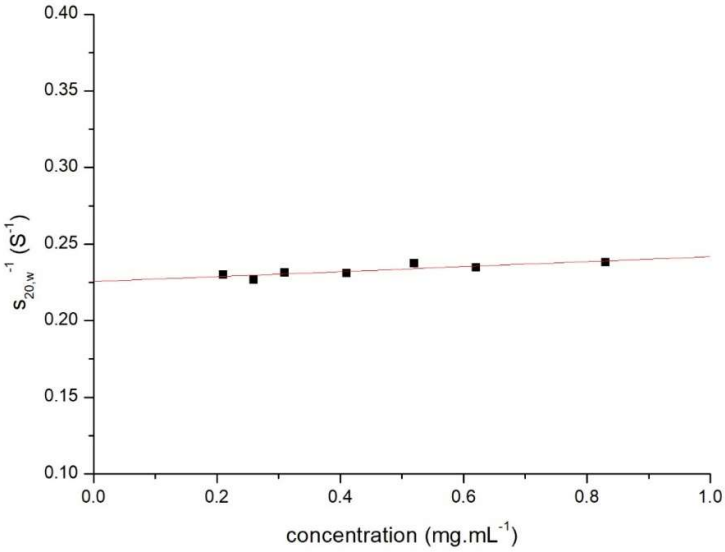


Figure 6.71 – Plot of the reciprocal of sedimentation coefficient against loading concentration for S-II after incubation at 20˚C for one hundred days, with a linear fit to extrapolate to zero concentration.

6.9.2.3 Sedimentation Equilibrium

SEDFIT-MSTAR provides two methods of determining apparent molecular weight, $M_{w,app}$: from the *M** function and from hinge point analysis. The values given by the program are

plotted against loading concentration in Figure 6.72. Extrapolation to zero concentration gave 'thermodynamically ideal' values of M_w as (188 ± 1) kDa (from the M* method) and (159 ± 4) kDa (from the hinge method). Combining the two yields a consensus value for Mw of (173 ± 2) kDa.

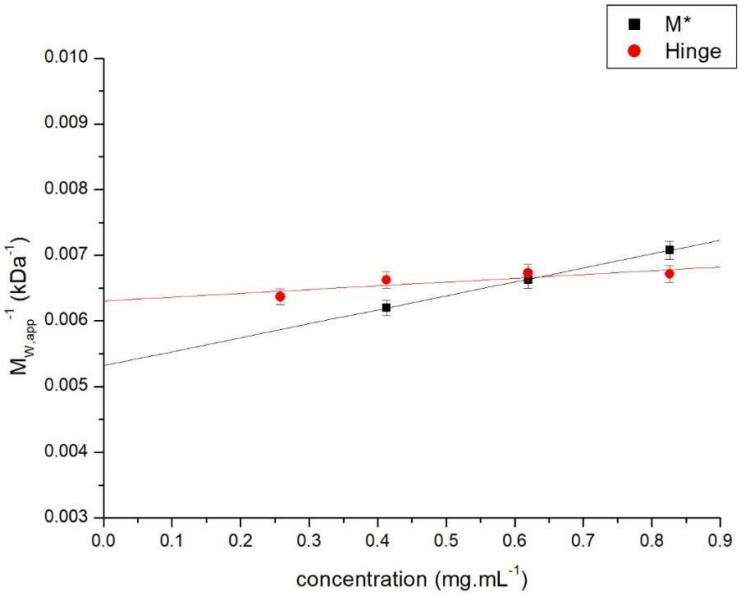


Figure 6.72 – Plot of the reciprocal of apparent molecular weight ($M_{w,app}$) values against loading concentration of S-II after incubation at 20˚C for one hundred days, with a linear fit to extrapolate to zero concentration.

6.9.2.4 SEC-MALS

The M_w of the main peak was determined to be 133 kDa, although no error is described at this level of precision. The polydispersity (M_w/M_n) was 1.152 ± 0.003. [η] was found to be (48.3 ± 0.3) mL.g^{-1}.

6.10 Summary

Table 6-1 below shows a summary of all data presented above after incubation at 20˚C for ten days, while Table 6-2 summarises the data collected after 100 days. A comparison to Table 4-1 allows a rudimentary form of a student's t-test by establishing whether the data ranges, as defined by the values and their errors, overlap in each sample. These comparisons are shown in Table 6-3 (for ten days) and Table 6-4 (for 100 days), where any samples which do not change after incubation are marked with "✓" while percentage changes are given for any samples with a statistically significant difference.

Table 6-1 – Summary of data found after incubation of samples at 20˚C for ten days.

State	Serotype	[η] (mL.g^{-1})	Analytical ultracentrifugation		SEC-MALS		
			$s^{\circ}_{20,w}$ (S)	M_w (combined, kDa)	M_w (kDa)	[η] (mL.g^{-1})	Polydispersity ($M_w.M_n^{-1}$)
Native	IA	208±3	4.35±0.33	405±5	394±9	399±5	401±1
	IB	115±2	3.22±0.1	310±58	316±20	313±31	262±1
	II	112±1	5.45±0.18	469±36	452±19	461±20	539±1
	III	33.1±0.2	2.93±0.15	146±1	130±3	138±1	118±0
	IV	37.6±0.2	2.67±0.05	63.3±1.7	72.5±2	67.9±1.3	83.3±0.1
	V	62.5±0.3	3.78±0.02	181±3	172±7	176±4	180±0
Sized	IA	56.9±0.5	3.3±0.14	198±5	164±9	181±5	121±0
	IB	59.8±0.4	3.22±0.01	159±6	153±10	156±6	122±0
	II	28.6±0.8	3.82±0.07	187±8	183±5	185±5	185±0

Table 6-2 – Summary of data found after incubation of samples at 20˚C for 100 days.

State	Serotype	[η] (mL.g^{-1})	Analytical ultracentrifugation		SEC-MALS		
			$s^{\circ}_{20,w}$ (S)	M_w (combined, kDa)	M_w (kDa)	[η] (mL.g^{-1})	Polydispersity ($M_w.M_n^{-1}$)
Native	IA	187±0	5.48±0.36	306±23	310±24	308±16	291±1
	IB	123±1	4.05±0.23	186±6	176±6	181±4	159±0
	II	117±1	6.6±0.06	433±48	377±40	405±31	344±1
	III	38.8±0.2	3.38±0.08	114±5	129±7	121±4	80.8±0.1
	IV	39.8±0.2	2.68±0.02	80.1±2.1	76.1±6.5	78.1±3.4	59±0.2
	V	65.6±0.2	3.73±0.03	191±16	199±14	195±10	113±0
Sized	IA	64.4±1.2	3.28±0.05	189±8	195±10	192±6	84.8±0.2
	IB	63.5±0.2	3.22±0.04	153±8	165±15	159±9	87.2±0.2
	II	51.8±0	4.43±0.04	188±1	159±4	173±2	133±0

Table 6-3 – Table showing the percentage difference in parameters from baseline values due to incubation of samples at 20˚C for ten days

State	Serotype	[η] ($mL.g^{-1}$)	Analytical ultracentrifugation		SEC-MALS		
			$s^{\circ}_{20,w}$ (S)	M_w (combined, kDa)	M_w (kDa)	[η] ($mL.g^{-1}$)	Polydispersity ($M_w.M_n^{-1}$)
Native	IA	-5%	-13%	12%	20%	16%	37%
	IB	-15%	-20%	64%	93%	78%	70%
	II	-11%	-10%	43%	46%	45%	25%
	III	-27%	-9%	32%	12%	22%	29%
	IV	-42%	4%	-11%	28%	7%	56%
	V	-24%	-4%	-11%	-14%	-13%	55%
Sized	IA	17%	-1%	8%	-15%	-4%	18%
	IB	-4%	-2%	6%	-5%	0%	20%
	II	-48%	-18%	4%	29%	15%	19%

Table 6-4 – Table showing the percentage difference in parameters from baseline values due to incubation of samples at 20˚C for 100 days.

State	Serotype	[η] ($mL.g^{-1}$)	Analytical ultracentrifugation		SEC-MALS		
			$s^{\circ}_{20,w}$ (S)	M_w (combined, kDa)	M_w (kDa)	[η] ($mL.g^{-1}$)	Polydispersity ($M_w.M_n^{-1}$)
Native	IA	-14%	9%	-15%	-6%	-11%	0%
	IB	-9%	0%	-1%	8%	3%	3%
	II	-8%	9%	32%	22%	27%	-20%
	III	-15%	5%	3%	11%	7%	-12%
	IV	-39%	5%	13%	35%	23%	11%
	V	-20%	-6%	-6%	-1%	-4%	-3%
Sized	IA	32%	-1%	2%	1%	2%	-17%
	IB	2%	-2%	2%	2%	2%	-14%
	II	-6%	-4%	4%	12%	8%	-15%

This data can also be described graphically to show how each parameter changes, shown in Figure 6.73, 6.74, 6.75, 6.76 and 6.77.

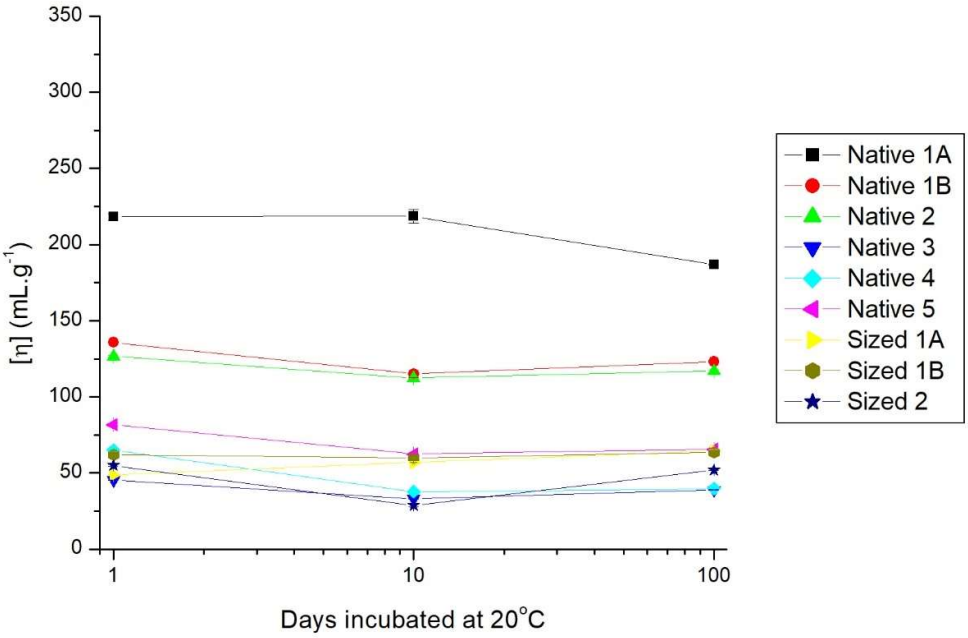


Figure 6.73 – Viscosity of each polysaccharide as determined by U-tube viscometry, and how they altered after incubation at 20˚C.

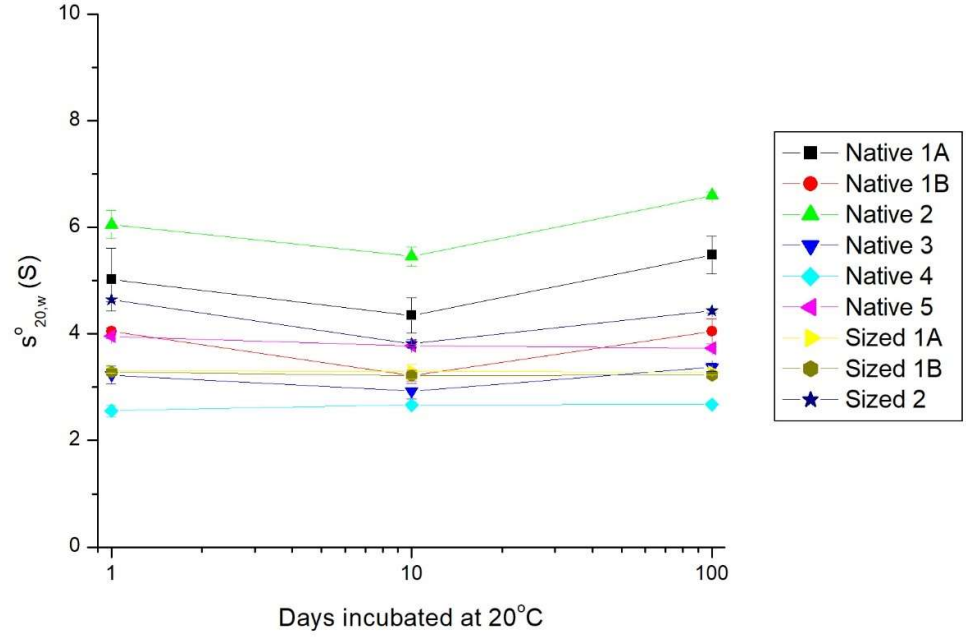


Figure 6.74 – Sedimentation coefficient of each polysaccharide as determined by sedimentation velocity, and how they altered after incubation at 20˚C.

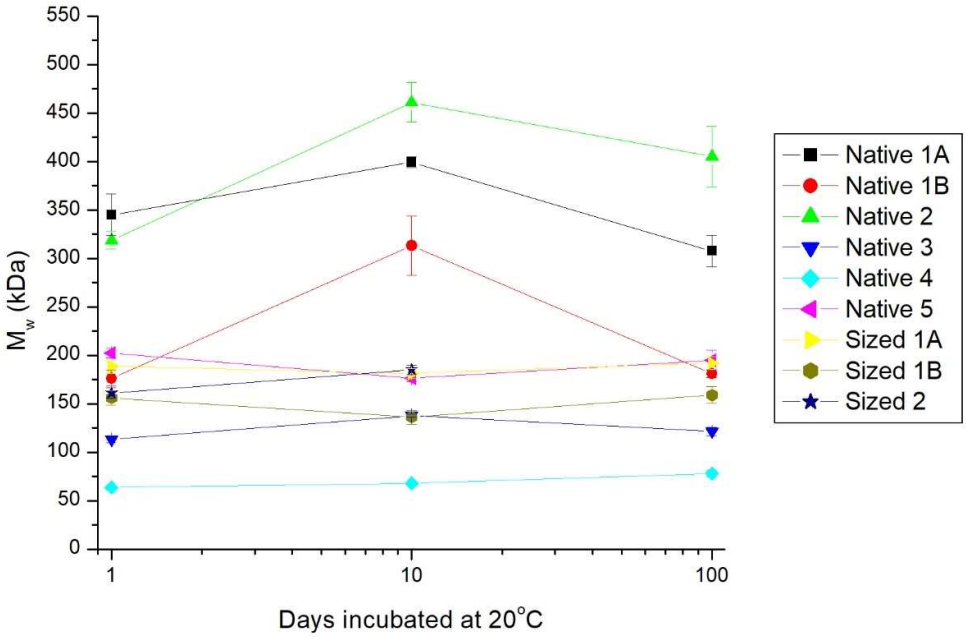


Figure 6.75 – Molecular weight of each polysaccharide as determined by sedimentation equilibrium, and how they altered after incubation at 20˚C.

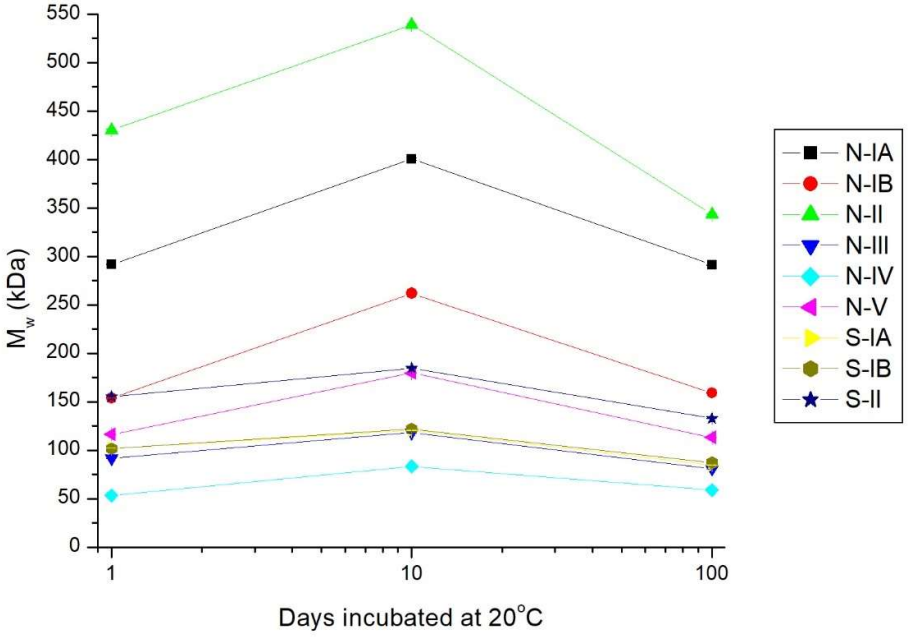


Figure 6.76 – Molecular weight of each polysaccharide as determined by SEC-MALS, and how they altered after incubation at 20˚C.

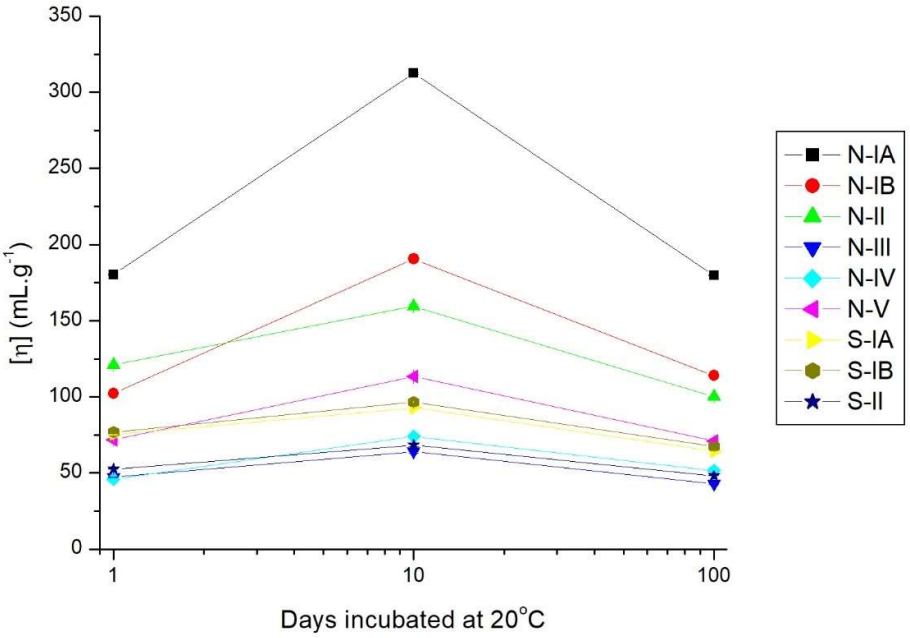


Figure 6.77 – Viscosity of each polysaccharide as determined by SEC-MALS, and how they altered after incubation at 20˚C.

For the sedimentation coefficient values, as the error ranges are large on each point and the gradient is near zero, it is possible the treat the data set as a set of repeated measurements. By doing this, it is possible to perform a statistical test to assess whether the differences between measured sedimentation coefficient are significant. These results are given in Table 6-5, by listing the P value when performing a student's T test.

Table 6-5 – The resulting p values when performing a student's T test on the sedimentation coefficient datasets after exposure to stress caused by continued incubation at 20˚C. A p value < 0.05 is assumed to reflect a significant difference, and these are highlighted.

State	Serotype	p values	
		10 days	100 days
Native	IA	**0.008**	0.364
	IB	**0.000**	0.194
	II	**0.000**	0.252
	III	**0.001**	0.871
	IV	0.311	0.497
	V	**0.025**	**0.010**
Sized	IA	0.192	0.087
	IB	**0.160**	**0.021**
	II	**0.003**	0.992

6.11 Discussion

As in section 5, different methods here suggest different outcomes. After incubation for ten days, most viscosity values fell except sized polysaccharide from serotypes IA, which increased. The possibility that some of the samples may have degraded is supported by the sedimentation velocity data, which showed a decrease in sedimentation coefficient for all samples except native polysaccharide from serotype II. As both the viscosity and sedimentation coefficient fell in most cases, it is more likely that the molecular weight has fallen rather than the samples undergoing a conformational change. However, this was only corroborated by sedimentation equilibrium data in polysaccharides from serotypes IV and V. Much of the viscometry data measured using SEC-MALS was inconsistent with that measured by U-tube viscometry, as most samples increase rather than decrease, and five of the molecular weights as measured by sedimentation equilibrium, which saw either no change or decreases. This may suggest that some feature of incubation made the samples less appropriate for analysis by SEC-MALS, although it is unclear what this may be. As native polysaccharide from serotype IB molecular weight almost doubles (increasing by 93%) this sample could be dimerising, althlugh this may be occurring only suring the SEC-MALS analysis as it was not corroborated by sedimentation equilibrium.

After incubation for one hundred days, many of the results seen by viscometry became inconsistent. Only polysaccharides from serotype IA (both native and sized) and native polysaccharide from serotype IV gave consistent results (with either a plateau or a consistent change) while all others saw an increase from the data seen after incubation for ten days. However, overall, there was still a decrease in viscosity in the majority of cases compared to the baseline values.

After combining molecular weight readings taken by sedimentation equilibrium, five samples saw changes after incubation for one hundred days. Polysaccharides from native serotypes

Ib, II, III and V all increased, while native polysaccharide from serotype IV decreased. While serotypes IV and V had not previously changed very much, serotypes II and III had increased previously, and had now decreased from the values after incubation for ten days. Further inconsistencies were seen in native polysaccharide from serotype IA, sized polysaccharide from serotype IB, and sized polysaccharide from serotype II all returned to values unchanged from the baseline, despite having changed after a ten-day incubation.

While many changes were still seen in the SEC-MALS data, they were not as great as previously found after incubation for ten days, with many of the molecular weights now decreasing. This suggests that the previous suggestion – that the incubation altered the samples in such a way that it was no longer appropriate to analyse them by SEC-MALS – was not correct, and that these results are anomalous for another reason. Most serotypes saw a decrease in molecular weight, except native polysaccharide from serotype IA which remained unchanged, and native polysaccharides from serotypes IB and IV which increased. These changes (or lack of change) in molecular weight all matched the changes seen in viscosity, suggesting an internal consistency seen in SEC-MALS results at this time point. However, there was no consensus between SEC-MALS and the previously discussed sedimentation and viscosity data, providing further evidence of the highly variable nature of the results.

Unlike with section 5, there was no obvious increase in differences seen between the two levels of stress, which may suggest that the samples are more susceptible to freeze-thaw stress than they are to degradation at room temperature. However, it is also possible that the changes seen are due to the natura variation between measurements rather than genuine changes. It is for this reason that the statistical tetst possible using sedimentation velocity analysis are so important.

In this analysis, there was statistically significant change in sedimentation coefficient for all samples except native polysaccharide from serotype IV, and sized polysaccharide from

serotype IA. However, after 100 days many of these values return to no longer being significantly different from the baseline. This means one of two things must be occurring here. Either the changes that occur after 10 days are genuine, but a further change after 100 day incubation causes a further alteration that masks the structural changes that have occurred. Alternatively, the measurements must be affected by some factor other than the stress to which the samples have been exposed, suggesting that some further factor must be controlled to allow meaningful analysis.

As in section 5, it is not possible to determine how effective the molecules would be as a vaccine even if they are damaged. It is possible that even if the changes do reflect genuine degradation, it will not impact on the ability of the polysaccharide to act as a vaccine. It also remains unclear if the differences observed are genuine, particularly as many of the observed changes are inconsistent between techniques.

7 Stability after incubation at 37˚C

While section 6 studied the effects of incubation for long periods at room temperature on the structure of the vaccine components, the effect of incubation at 37˚C should also be studied. As samples are unlikely to be stored at such a high temperature, it did not seem necessary to analyse samples that had been incubated at this temperature for 10 or 100 days as was done in section 6. Instead, measurements were taken of the samples at this temperature. However, it is not possible to take measurements at such high temperatures with all techniques outlined in this project. For this reason, measurements are presented only from results of analysis in a U-tube viscometer.

When temperature is increased, the flow time of the solution through a U-tube will decrease due to lower solution viscosity, so it may be tempting to point to this as an explanation for any decrease seen in viscosity. However, as part of the process of calculating the intrinsic viscosity, the relative viscosity is first calculated using the flow time of the solution and the solvent, as in Equation (3). As the flow time of the solvent will also be reduced, this should eliminate the effect of increased temperature on the solution viscosity unless it also causes a change in molecular structure altering the *intrinsic* viscosity.

An increase in observed viscosity may indicate that the polysaccharides adopt a less compact conformation or even self-associate at higher temperature, while a decrease in observed viscosity may indicate the polysaccharides have broken down, or that they have formed an insoluble aggregate which significantly decreases the concentration.

7.1 Method

A dilution series was made and incubated overnight in a water bath at 37˚C. The flow time of each dilution was then measured in a U-tube viscometer submerged in a water bath at 37˚C. The density of each dilution was measured in a density meter, also set to 37˚C. These values

were then used to calculate the intrinsic viscosity as outlined in section 3.5, and comparisons drawn between these values and previous results when assessing baseline values in section 4.

7.2 Native GBS polysaccharide, serotype IA

Plotting the relevant viscosity functions and extrapolating back to where the concentration is zero in Figure 7.1 gives the intrinsic viscosities as (210 ± 12) $mL.g^{-1}$ (Huggins), (203 ± 8) $mL.g^{-1}$ (Kraemer) and (207 ± 9) $mL.g^{-1}$ (Solomon-Ciuta). The mean average value of these is (206 ± 6) $mL.g^{-1}$.

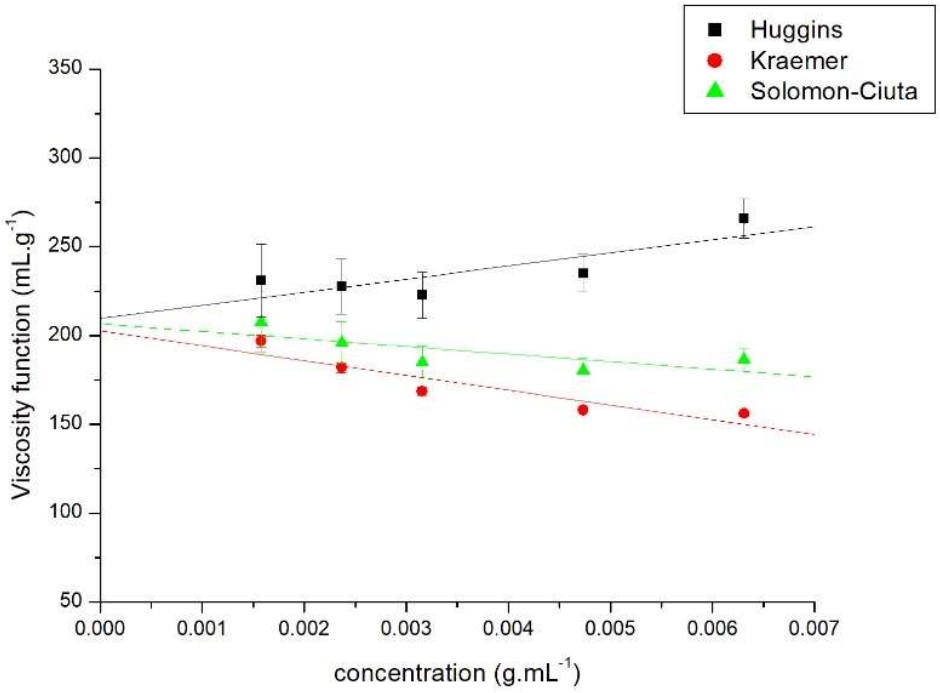


Figure 7.1 – Plot of viscosity against concentration for N-IA after incubation at 37˚C, with linear fits to extrapolate to zero concentration.

7.3 Native GBS polysaccharide, serotype IB

Plotting the relevant viscosity functions and extrapolating back to where the concentration is zero in Figure 7.2 gives the intrinsic viscosities as (111 ± 3) $mL.g^{-1}$ (Huggins), (111 ± 3) $mL.g^{-1}$ (Kraemer) and (112 ± 3) $mL.g^{-1}$ (Solomon-Ciuta). The mean average value of these is (111 ± 2) $mL.g^{-1}$.

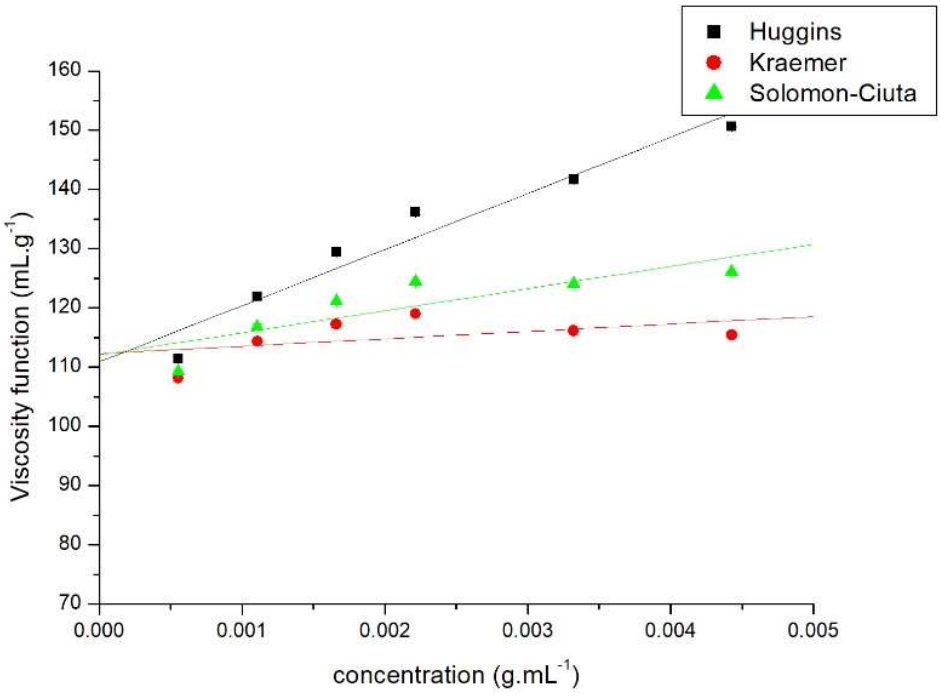


Figure 7.2 – Plot of viscosity against concentration for N-IB after incubation at 37˚C, with linear fits to extrapolate to zero concentration.

7.4 Native GBS polysaccharide, serotype II

Plotting the relevant viscosity functions and extrapolating back to where the concentration is zero in Figure 7.3 gives the intrinsic viscosities as (109 ± 2) $mL.g^{-1}$ (Huggins), (108 ± 2) $mL.g^{-1}$ (Kraemer) and (109 ± 2) $mL.g^{-1}$ (Solomon-Ciuta). The mean average value of these is (109 ± 1) $mL.g^{-1}$.

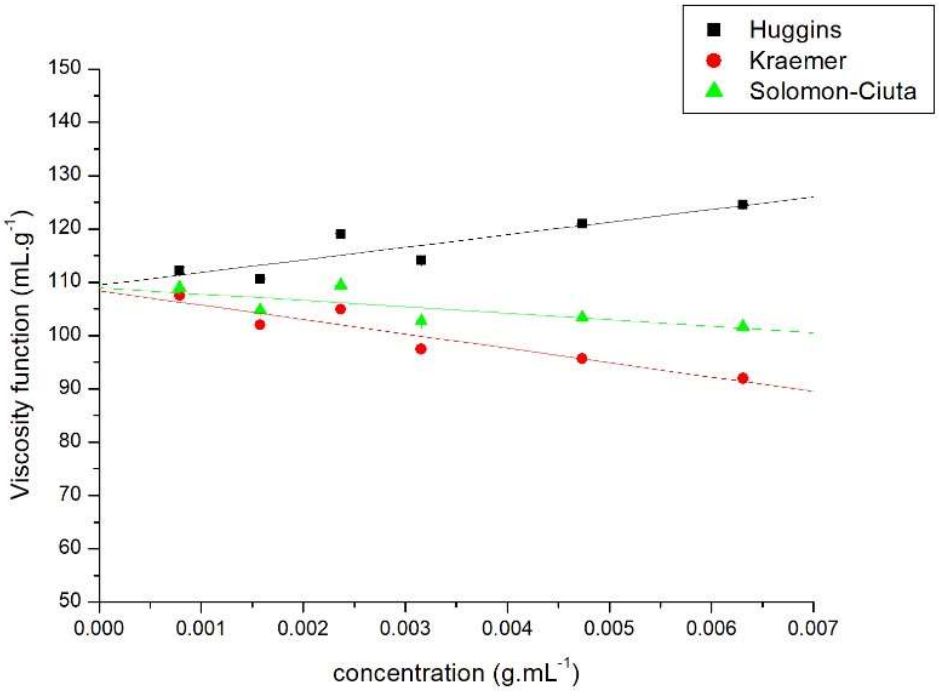


Figure 7.3 – Plot of viscosity against concentration for N-II after incubation at 37˚C, with linear fits to extrapolate to zero concentration.

7.5 Native GBS polysaccharide, serotype III

Plotting the relevant viscosity functions and extrapolating back to where the concentration is zero in Figure 7.4 gives the intrinsic viscosities as (43.5 ± 1.0) $mL.g^{-1}$ (Huggins), (43.6 ± 1.0) $mL.g^{-1}$ (Kraemer) and (43.5 ± 1.0) $mL.g^{-1}$ (Solomon-Ciuta). The mean average value of these is (43.5 ± 0.6) $mL.g^{-1}$.

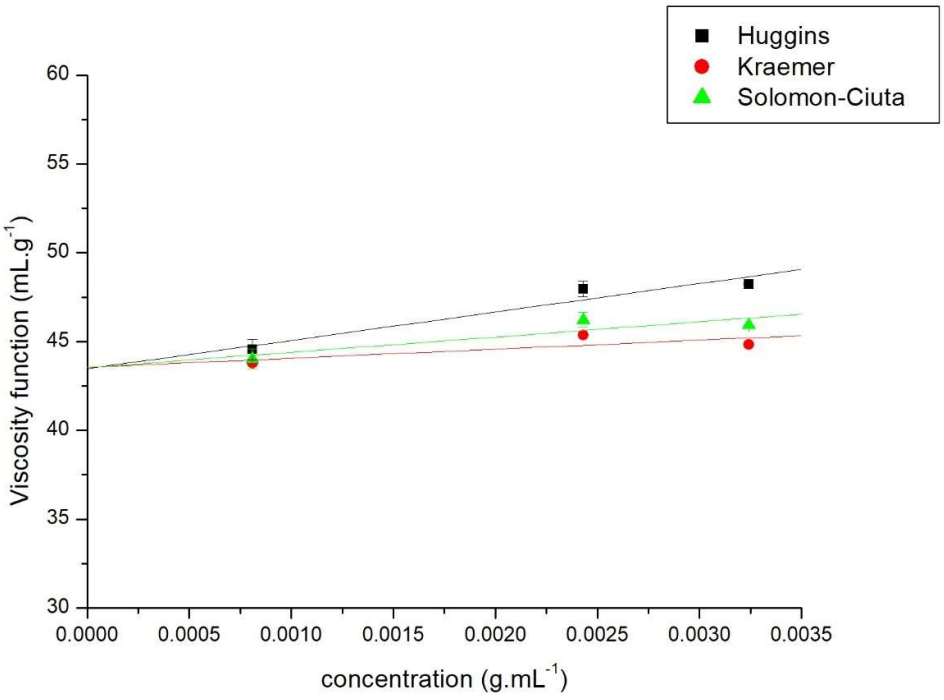


Figure 7.4 – Plot of viscosity against concentration for N-III after incubation at 37˚C, with linear fits to extrapolate to zero concentration.

7.6 Native GBS polysaccharide, serotype IV

Plotting the relevant viscosity functions and extrapolating back to where the concentration is zero in Figure 7.5 gives the intrinsic viscosities as (55.6 ± 1.3) $mL.g^{-1}$ (Huggins), (55.6 ± 1.2) $mL.g^{-1}$ (Kraemer) and (55.7 ± 1.2) $mL.g^{-1}$ (Solomon-Ciuta). The mean average value of these is (55.6 ± 0.7) $mL.g^{-1}$.

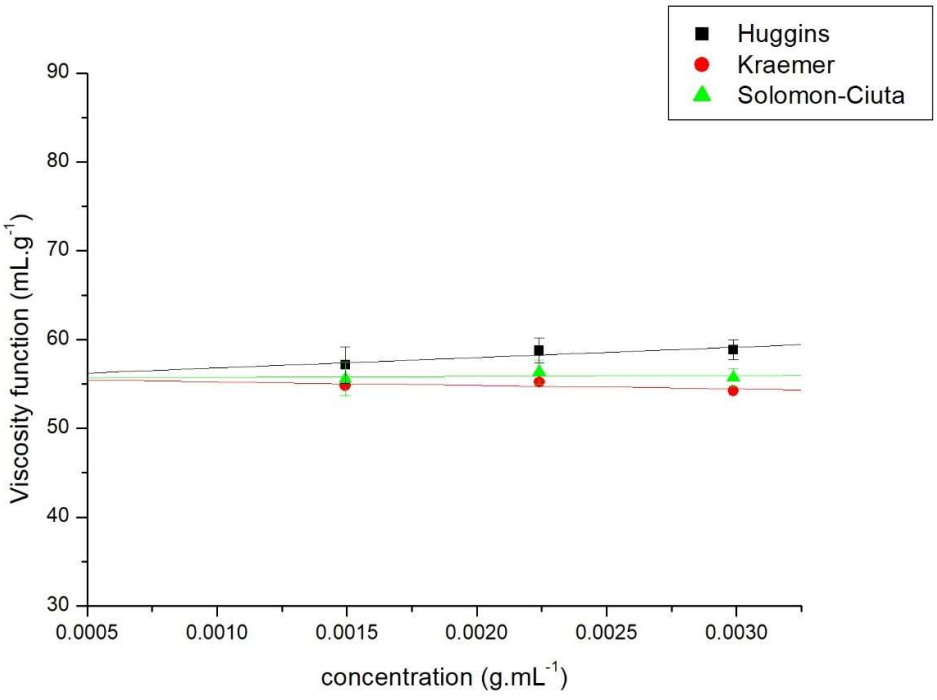


Figure 7.5 – Plot of viscosity against concentration for N-IV after incubation at 37˚C, with linear fits to extrapolate to zero concentration.

7.7 Native GBS polysaccharide, serotype V

Plotting the relevant viscosity functions and extrapolating back to where the concentration is zero in Figure 7.6 gives the intrinsic viscosities as (79.5 ± 0.1) $mL.g^{-1}$ (Huggins), (79.3 ± 0.1) $mL.g^{-1}$ (Kraemer) and (79.4 ± 0.1) $mL.g^{-1}$ (Solomon-Ciuta). The mean average value of these is (79.4 ± 0.1) $mL.g^{-1}$.

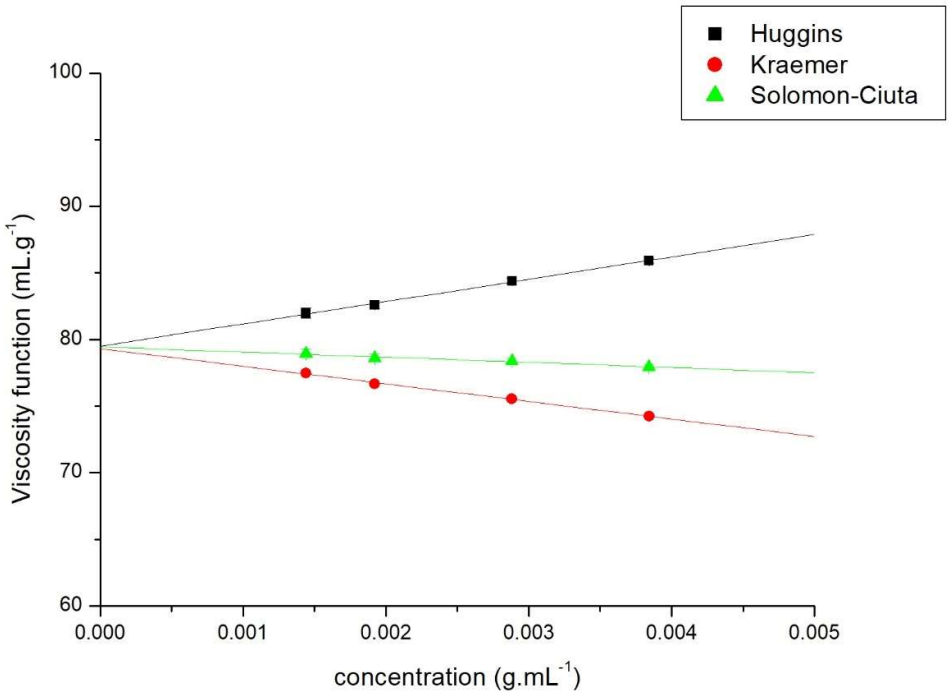


Figure 7.6 – Plot of viscosity against concentration for N-V after incubation at 37˚C, with linear fits to extrapolate to zero concentration.

7.8 Sized GBS polysaccharide, serotype IA

Plotting the relevant viscosity functions and extrapolating back to where the concentration is zero in Figure 7.7 gives the intrinsic viscosities as (70.4 ± 1.8) $mL.g^{-1}$ (Huggins), (70.6 ± 1.5) $mL.g^{-1}$ (Kraemer) and (70.6 ± 1.6) $mL.g^{-1}$ (Solomon-Ciuta). The mean average value of these is (70.5 ± 0.9) $mL.g^{-1}$.

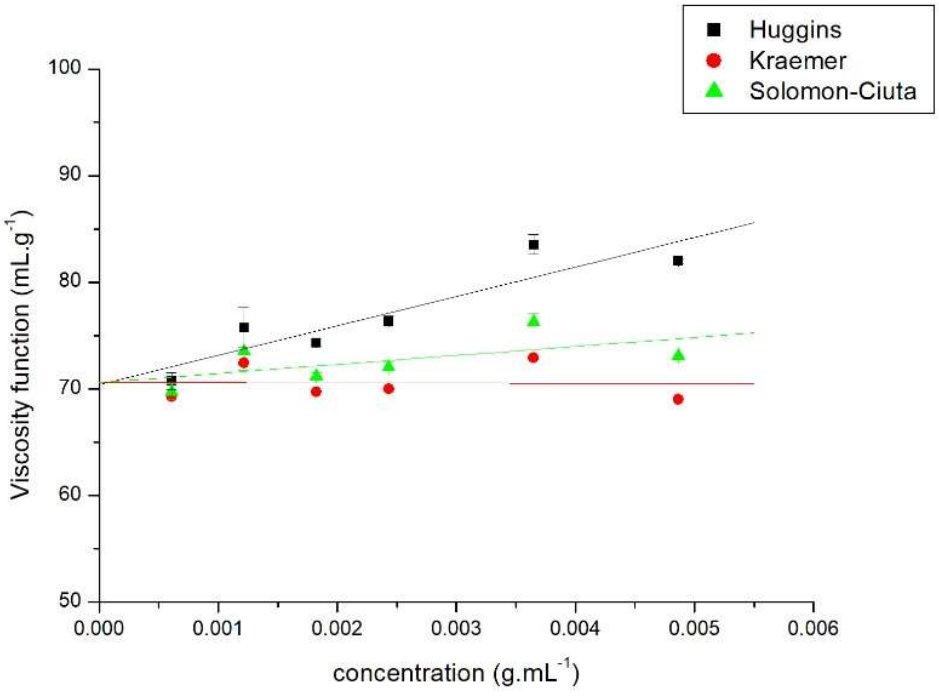


Figure 7.7 – Plot of viscosity against concentration for S-IA after incubation at 37˚C, with linear fits to extrapolate to zero concentration.

7.9 Sized GBS polysaccharide, serotype IB

Plotting the relevant viscosity functions and extrapolating back to where the concentration is zero in Figure 7.8 gives the intrinsic viscosities as (48.3 ± 0.7) $mL.g^{-1}$ (Huggins), (48.2 ± 0.6) $mL.g^{-1}$ (Kraemer) and (48.3 ± 0.6) $mL.g^{-1}$ (Solomon-Ciuta). The mean average value of these is (48.3 ± 0.4) $mL.g^{-1}$.

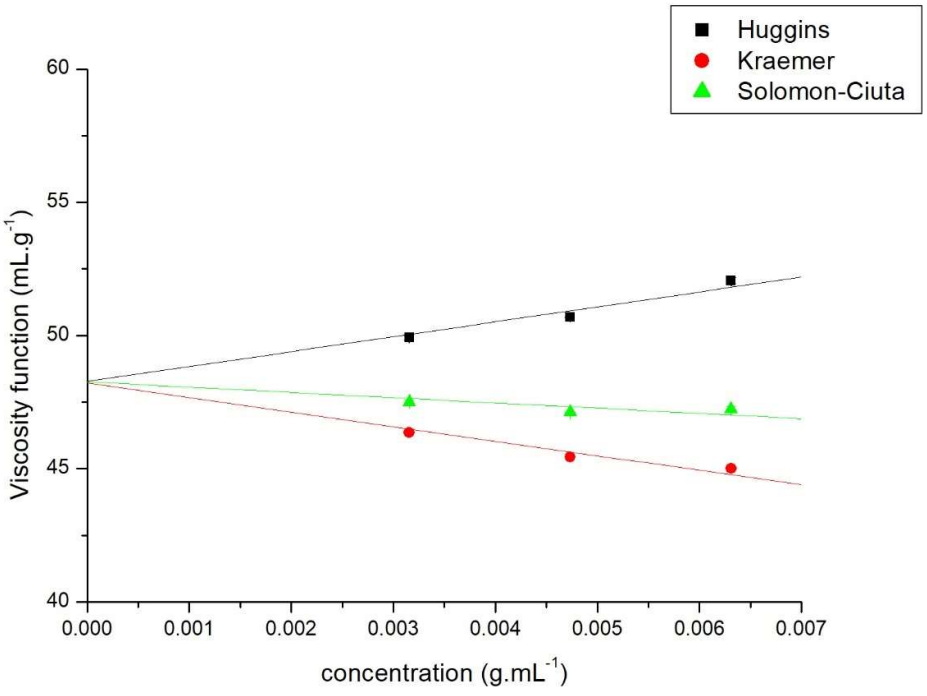


Figure 7.8 – Plot of viscosity against concentration for S-IB after incubation at 37˚C, with linear fits to extrapolate to zero concentration.

7.10 Sized GBS polysaccharide, serotype II

Plotting the relevant viscosity functions and extrapolating back to where the concentration is zero in Figure 7.9 gives the intrinsic viscosities as (53.5 ± 0.9) $mL.g^{-1}$ (Huggins), (53.6 ± 0.8) $mL.g^{-1}$ (Kraemer) and (53.6 ± 0.9) $mL.g^{-1}$ (Solomon-Ciuta). The mean average value of these is (53.6 ± 0.5) $mL.g^{-1}$.

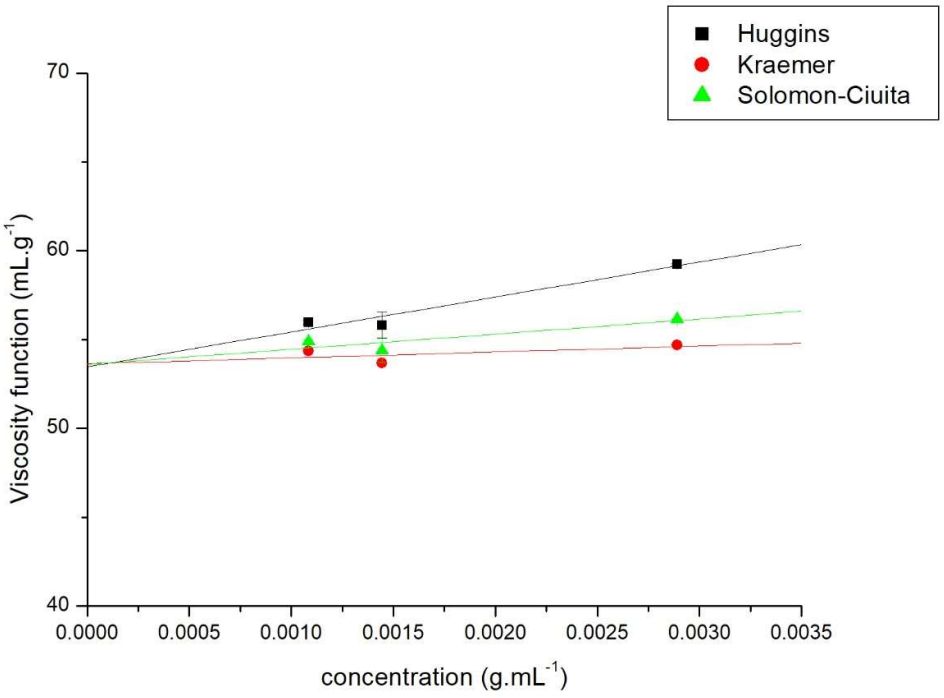


Figure 7.9 – Plot of viscosity against concentration for S-II after incubation at 37˚C, with linear fits to extrapolate to zero concentration.

7.11 Summary

Table 7-1 below shows a summary of viscosity data presented above when measured at 37˚C. A comparison to Table 4-1 allows a rudimentary form of a student's t-test by establishing whether the data ranges, as defined by the values and their errors, overlap in each sample. These comparisons are also shown in Table 7-1, where any samples which do not change after incubation are marked with "✓" while percentage changes are given for any samples with a statistically significant difference.

Table 7-1 – Table showing which parameters changed from baseline values when samples are assessed at 37˚C. For samples which saw a statistically significant change the percentage change is given, while those which were not significantly different are marked with ✓.

State	Serotype	[η] at 20˚C ($mL.g^{-1}$)	[η] at 37˚C ($mL.g^{-1}$)	Percentage difference
Native	IA	218 ± 2	206 ± 6	-5%
	IB	136 ± 0	111 ± 2	-18%
	II	127 ± 1	109 ± 9	-13%
	III	44.7 ± 0.5	43.5 ± 0.6	-1%
	IV	65.0 ± 0.6	65.4 ± 2.7	-13%
	V	81.8 ± 0.9	77.6 ± 0.6	-2%
Sized	IA	48.7 ± 0.1	70.5 ± 0.9	45%
	IB	62.1 ± 0.1	48.3 ± 0.4	-22%
	II	55.0 ± 0.7	49.5 ± 1.6	-1%

7.12 Discussion

In the majority of cases, there was a decrease in the intrinsic viscosity measured at 37˚C. This could be due to the degradation of each molecule at higher temperatures, or a decrease in concentration if an insoluble aggregate forms. No obvious aggregates were visible when analysed, which suggests that the change in viscosity is more likely to result from a breakdown in the molecular structure of each polysaccharide.

The exception to this decrease in viscosity was the sized polysaccharide from serotype IA. This molecule saw a sharp increase in measured viscosity. This could be explained by the polysaccharide adopting a less compact conformation.

Regardless of the changes that may occur due to the increase in temperature, the question remains whether this should be a concern. Does a minor change in structural integrity indicate a problem in the efficacy of the molecule as a vaccine? Where changes in viscosity have been observed they tend to be small, indicating only minor degradation, which suggests that a major portion of the molecule remains intact. Therefore, the molecule is likely to still be recognised as an antigen by the immune system. There may be an issue if the polysaccharide undergoes a degradation that causes the connection to the carrier protein to become severed, as this would remove the benefits of a glycoconjugate vaccine. The strongest conclusion that can be drawn from these results is that there is reason to be concerned that the connection to a protein may be more labile at 37˚C if the polysaccharide undergoes minor degradation, but this is something that must be tested on the final polyvalent conjugated vaccine. Testing the strength of this link should be relatively simple as if the link breaks it will cause a much more significant structural change that could be easily measured.

However, it should also be stressed that, as seen in previous sections, there is a significant variation seen between experiments even when there is no logical explanation for that change. This may indicate that unless there is a substantial change in the observed values, the change is simply due to uncontrolled variation. This is perhaps more likely as almost all samples saw a decrease in viscosity as a result of the stresses applied, suggesting that there is an additional variable at play which is not controlled by measuring the flow time of both solution and solvent at the higher temperature. In this case, the only notable result is the increased viscosity of the sized polysaccharide from serotype IA as this saw an in increase in viscosity of 45%.

8 A study of potential interactions with common blood proteins

Human blood is a complex mixture of proteins, hormones, cells, and salts. These may all be capable of interacting with a potential vaccine and can thus be considered to have an impact on its stability in the body. However, it should be noted that vaccines are usually delivered into a muscle [242] and are usually taken up by immune system cells without reaching the blood [80]. This means that interactions with the blood only become possible if the vaccine is accidentally administered directly into a blood vessel. Three proteins present at highest concentrations in the blood were selected to test for possible interactions with the vaccine candidates. The selected proteins were human serum albumin (HSA), fibrinogen and immunoglobulin, present at 80.0 $mg.mL^{-1}$, 5.33 $mg.mL^{-1}$ and 13.5 $mg.mL^{-1}$ respectively [243, 244].

Albumin is synthesized primarily by the liver [245] and has a number of functions. It contributes to maintaining the osmotic pressure of blood [245] and can bind to a variety of ions such as copper, zinc and calcium [245]. The binding properties of albumin are not limited to these extremely small particles. Albumin can bind to many endogenous molecules, such as long-chain fatty acids, L-tryptophan and steroids [245-247] as well as exogenous molecules such as chlorpromazine, ibuprofen, naproxen and warfarin [245-247]. As well as carrying these important compounds into tissues, albumin can also transport waste products, notably bilirubin, to the liver where it can be excreted [245]. By binding to these molecules, albumin prevents them from receiving oxidative damage, as the oxidation products can be harmful [245]. Oxidative damage is also prevented by the binding of metal ions to limit redox activity [247]. In addition to HSA, *bovine* serum albumin (BSA) was also used here due to its common use as a model protein, and to corroborate the HSA data.

Fibrinogen is a key protein in the formation of blood clots [248]. It is usually formed of two sets of disulphide-bridged Aα-, Bβ-, and γ-chains [249]. However, after an injury, thrombin is

released which cleaves fibrinopeptide A from the Aα-chains, forming fibrin [250]. The fibrin rapidly polymerises into double-stranded fibrils [251], which associate into a highly branched clot network after plasma protransglutaminase covalently cross links γ-chain pairs [252]. This scaffold provides a framework which can anchor to the extracellular matrix of surrounding cells through fibronectin [253] and associate with platelet $\alpha_{2b}\beta_3$ receptor to form a blood clot [254].

Immunoglobulins are also present in the blood, and their function is described briefly in section 1.2.1, page 11. When analysing interactions, immunoglobulins pose an additional challenge as they possess high polydispersity due to their variable binding site, introducing complexity and unpredictability. This issue has been circumvented by using two monoclonal antibodies in this study, IgG1 Cri and IgG1 Wid. As the chosen antibodies have not been generated in response to Group B *Streptococcus*, it can be assumed that any interaction must occur outside the binding site. As well as potentially forming aggregates, this could prevent the interaction of antibodies with the immune system and thus may weaken the immune response. For this reason, any interaction is assumed to be negative.

8.1 Protein baseline values

While baseline measurements have been taken for polysaccharides in section 4, these measurements also must be taken for the proteins to understand the nature of any potential interaction.

Proteins were dissolved in solutions of phosphate buffer at pH 7 and ionic strength 0.1 M, produced using 4.595 g $Na_2HPO_4.12H_2O$, 1.561 g KH_2PO_4 and 2.923 g NaCl, in 1L of MilliQ water. Concentration was then measured using a Unicam Thermo Helios Alpha UV/Vis Spectrophotometer. The absorbance at 280 nm was used to give the concentration using the Beer-Lambert Law:

$$A_{280} = \varepsilon . c . l \quad (20)$$

where ε is the extinction coefficient in $mL.mg^{-1}.cm^{-1}$, c is the concentration in $mg.mL^{-1}$ and l is the path length in cm. The proteins were dissolved at sufficient quantities to give a concentration of 10 $mg.mL^{-1}$, and were filtered using Whatman® Puradisc 25 syringe filters, 0.2 µm, PVDF to remove insoluble material before having their absorbance measured. The extinction coefficients used are summarised in Table 8-1. The immunoglobulins supplied were provided in solution at 7.3 $mg.mL^{-1}$ and 9.0 $mg.mL^{-1}$ for IgG1 Cri and IgG1 Wid respectively.

Table 8-1 – Summary of extinction coefficients used to calculate the intrinsic viscosity and partial specific volume of each protein studied..

Parameter	BSA	HSA	Fibrinogen
ε_{280} ($mL.mg^{-1}.cm^{-1}$)	0.655	0.538	1.510
l (cm)	0.1	0.1	0.1
Mw ($g.mol^{-1}$)	66400	66400	340000

The values of ε_{280} for BSA and HSA were taken from literature values [255, 256] while the value for fibrinogen had to be calculated using a value for $E^{1\%}$ [257], related by the formula:

$$\varepsilon_{280} = \frac{E^{1\%} . Mw}{10} \quad (21)$$

Once the concentrations were known, the samples were then diluted to give a concentration series, used to establish a baseline value for viscosity and to determine $\bar{v}$.

The viscosity and density of each protein were measured to obtain the intrinsic viscosity and partial specific volume. This was not repeated for the polysaccharides as these values were already known, provided in section 4. The values for intrinsic viscosity were then used to assess whether the mixtures of protein and polysaccharide behaved in a different manner to a mixture of each component part. The values for partial specific volume were used to calculate an average value between the protein and polysaccharide that could be used when

analysing sedimentation data. The results of these experiments on each protein are provided in the graphs and tables below.

8.1.1 BSA

Density was measured and the results plotted against concentration, shown in Figure 8.1. Using the slope of this graph, $\bar{v}$ can be calculated as 0.719 mL.g^{-1}, although no error is described at this level of precision. The buffer density was measured as (1.003472 ± 0.000001) mL.g^{-1}.

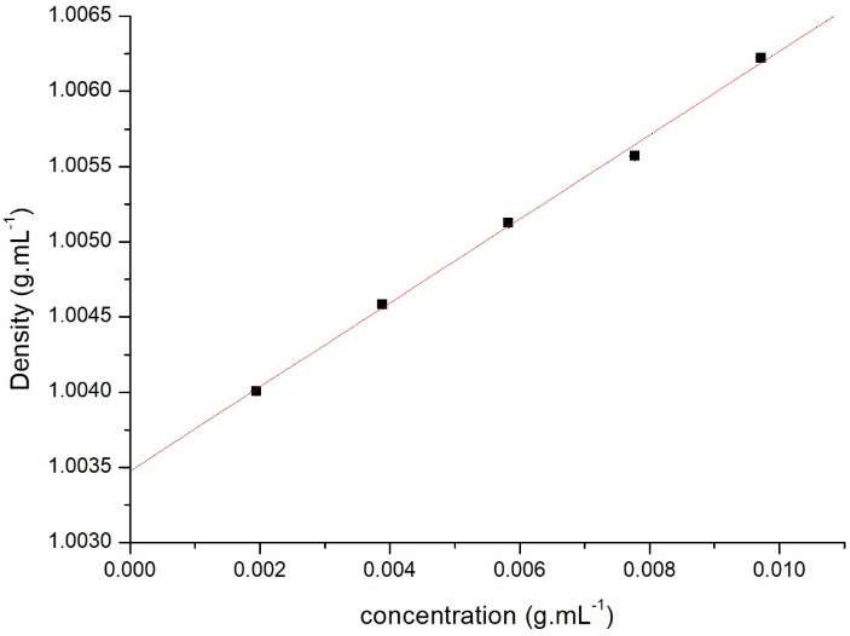


Figure 8.1 - Plot of density against concentration for BSA, with a linear fit to obtain gradient.

As the stock concentration was low, plotting the relevant viscosity functions and extrapolating back to where the concentration is zero will not give appropriate values for the intrinsic viscosity as the U-tube viscometer is not an accurate method below 5 mg.mL^{-1}. Therefore, only the value at the highest concentration (9.71 mg.mL^{-1}) is used in the Solomon-Ciuta Equation to give an intrinsic viscosity of (3.86 ± 0.01) mL.g^{-1}.

8.1.2 HSA

Density was measured and the results plotted against concentration, shown in Figure 8.2. Using the slope of this graph, $\bar{v}$ can be calculated as (0.722 ± 0.007) mL.g^{-1}. The buffer density was measured as 1.003228 mL.g^{-1}, although no error is described at this level of precision.

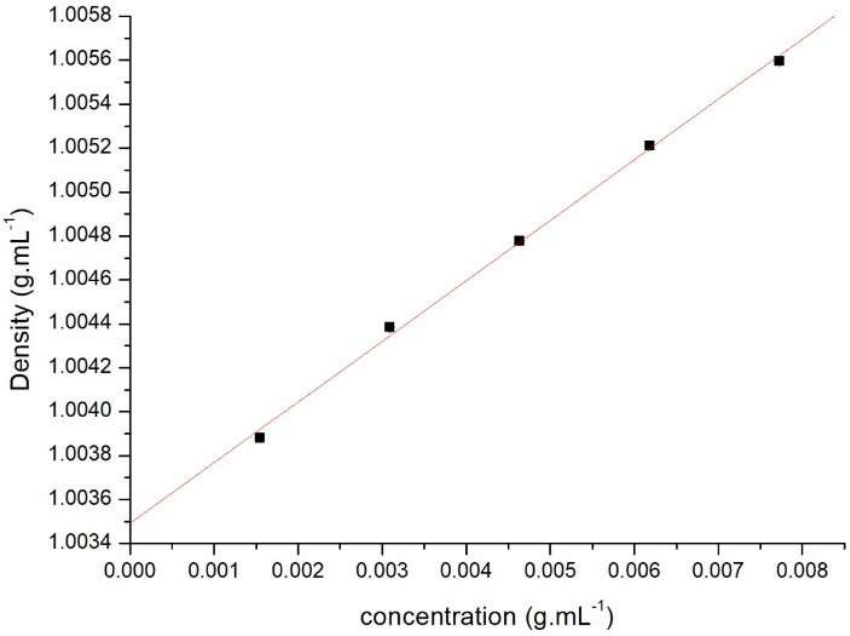


Figure 8.2 – Plot of density against concentration for HSA, with a linear fit to obtain gradient.

As with BSA, plotting the relevant viscosity functions and extrapolating back to where the concentration is zero will not give appropriate values for the intrinsic viscosity as the U-tube viscometer is not an accurate method below 5 mg.mL^{-1}. Therefore, only the value at the highest concentration (7.72 mg.mL^{-1}) is used in the Solomon-Ciuta Equation to give an intrinsic viscosity of (4.17 ± 0.02) mL.g^{-1}.

8.1.3 Fibrinogen

It was not possible to accurately measure density due to the difficulty of keeping fibrinogen in solution. This may have led to the measured concentration not being accurate as over time further molecules would have come out of solution. While attempts were made to take these

measurements, the resulting value of $\bar{v}$ was much lower than would typically be expected for a protein. Therefore, a literature value of 0.721 mL.g^{-1} for $\bar{v}$ will be used instead [258]. The buffer density was measured as 1.003228 mL.g^{-1}, although no error is described at this level of precision.

Due to the extended conformation of fibrinogen, it is possible to plot the relevant viscosity functions and extrapolate back to where the concentration is zero. This is done in Figure 8.3, which gives the intrinsic viscosities as (18.2 ± 0.03) mL.g^{-1} (Huggins), (18.6 ± 0.03) mL.g^{-1} (Kraemer) and (18.5 ± 0.03) mL.g^{-1} (Solomon-Ciuta). The mean average value of these is (18.4 ± 0.02) mL.g^{-1}.

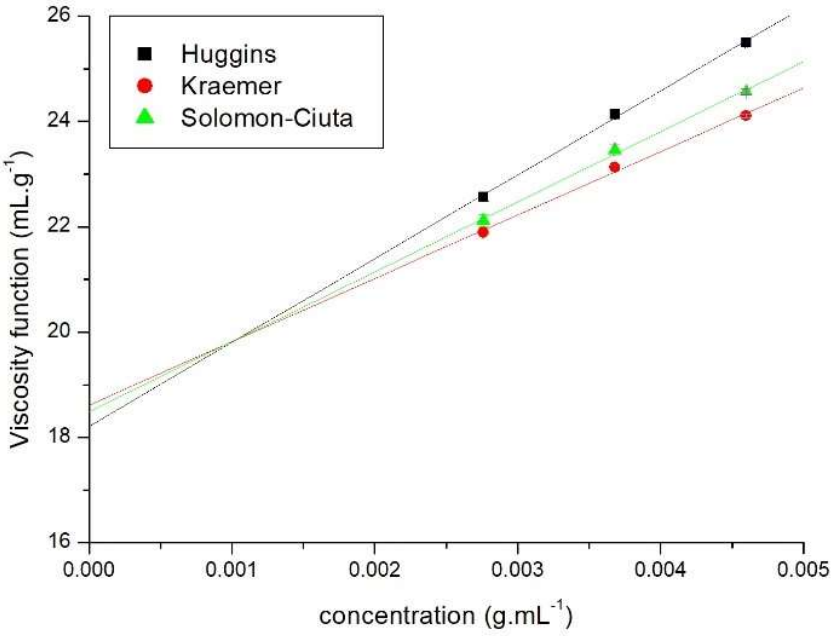


Figure 8.3 – Plot of viscosity against concentration for fibrinogen, with linear fits to extrapolate to zero concentration. As fibrinogen is slightly more viscous than the other proteins studied it is possible to perform an extrapolation, although it was still not possible at very low concentrations (i.e. less than 0.002 g.mL^{-1}) and so these have not been included in the extrapolation.

8.1.4 Immunoglobulins

As the samples of immunoglobulin were provided in solution in relatively low volume, it would have been necessary to dialyse a sample of the IgG with all nine samples of

polysaccharide simultaneously to give a suitable reference dialysate. This would have been impractical and may have led to mild cross-contamination by any small molecules unique to specific polysaccharide samples, and so was not performed. This meant it was not possible to assess the viscosity or $\bar{v}$ as there was no reference solvent to use as a comparison. The value for $\bar{v}$ had to be calculated using literature values instead.

This was done by first finding the $\bar{v}$ of an average IgG1 molecule [259]. Then, the average percentage glycosylation was also calculated [259, 260]. The $\bar{v}$ of a glycosylated molecule will be a weighted average of the $\bar{v}$ values for the individual polysaccharide and protein components, depending on their relative proportions. Reversing this can thus be used to find the $\bar{v}$ of the individual components. These values, along with the percentage glycosylation of IgG1 Cri and IgG1 Wid [228] can then be used to calculate the $\bar{v}$ of these molecules. This gives the value of $\bar{v}$ for IgG1 Cri as 0.729 $mL.g^{-1}$ and IgG1 Wid as 0.728 $mL.g^{-1}$.

8.1.5 Summary

The values for [η] and $\bar{v}$ to be used in this interaction study are summarised in Table 8-2 below.

Table 8-2 – Summary of the viscosities and partial specific volume values used in this study.

Protein	[η] ($mL.g^{-1}$)	$\bar{v}$ ($mL.g^{-1}$)
BSA	3.86 ± 0.01	0.719 ± 0.004
HSA	4.17 ± 0.02	0.732 ± 0.017
Fibrinogen	18.4 ± 0.2	0.721
IgG1 Cri	n/a	0.729
IgG1 Wid	n/a	0.728

8.2 Method

Protein samples were prepared by making an approximately 5 $mg.mL^{-1}$ solution of each protein. Three proteins (BSA, HSA and fibrinogen) and a single polysaccharide sample were then dialysed in the same dialysate, with the four dialysis tubes differentiated by their length. After this, the protein samples were filtered and an accurate reading of protein concentration found by spectrophotometry. Concentration was measured using a refractometer for the polysaccharide as before. After this, all solutions were diluted to give specific concentrations which could then be mixed at a 1:1 mass ratio when assessing their potential interactions. As previously mentioned, it was sometimes difficult to keep fibrinogen in solution and so sometimes the solutions prepared had low concentration. In these cases, the concentration of the polysaccharide was decreased to match and still give a 1:1 ratio. Assessments were performed using a viscometer and by sedimentation velocity.

The exact method was slightly different for assessing IgG interactions. As previously stated, no dialysis could be performed on the IgG samples, so it was not necessary to re-measure concentration. The samples of IgG and polysaccharide were instead diluted directly to give a 1:1 mass ratio to assess their interactions. In addition, due to time constraints when performing these experiments, sedimentation velocity experiments were not performed directly on the polysaccharide samples. Instead, averaged data from the other protein interaction experiments were used as a comparison.

Sedimentation equilibrium was not used initially as the multi-component system is more complicated to analyse, but could be incorporated later to clarify results. SEC-MALS was not used as the resolution of the columns would not allow the different components to be distinguished. The only way that SEC-MALS could provide useful information would be if it indicated that a significantly larger complex such as an aggregate formed, but as passing an

aggregate through the system would likely damage the column it was decided not to use this method.

Mixtures of protein and polysaccharide were assessed using viscosity and sedimentation velocity in an analytical ultracentrifuge. There are four possible outcomes which could be seen as a result of these two techniques. Firstly, if there were no interaction, the viscosity would act as an average of the viscosities of each component and peaks would be visible for each component of the mixture in the graph of sedimentation coefficients. Secondly, if there were an interaction which caused the components to form a complex, the viscosity would increase due to the increased size of the molecule, while the sedimentation coefficient would produce an additional peak indicating the presence of a large molecule. Third, if the interaction caused the formation of a large insoluble aggregate, the loss of this complex from the solution would cause viscosity to decrease, and would sediment almost immediately in the centrifuge, which could give either an additional peak with an extremely high sedimentation coefficient, or may even sediment too rapidly to be detected. Finally, if the interaction led to the degradation of either molecule, the overall viscosity would decrease due to the reduction in size, and additional peaks for smaller molecules would be seen in the sedimentation data.

To assess whether the viscosity was impacted by an interaction, previously calculated values of the intrinsic viscosity were used to determine a theoretical relative viscosity by rearranging the Huggins and Kraemer equations on page 44, Equations (4) and (5), in the manner shown below:

$$\eta_r = ([\eta]_{Huggins}.c) + 1 \quad (22)$$

$$\eta_r = e^{[\eta]_{Kraemer}.c} \quad (23)$$

Reversing the Solomon-Ciuta Equation is more complex as the relative viscosity is present twice as a term as shown in Equation (6), page 44. Therefore, only the Huggins and Kraemer equations are used here.

Due to the extremely low viscosities of the globular proteins studied in these experiments, their relative viscosity was found to be approximately equal to one at the concentrations studied and so only the viscosity of the polysaccharide needed to be considered in the analysis.

8.3 Native GBS polysaccharide, serotype IA

8.3.1 Viscosity

As with the comparisons in previous sections, the error ranges allow a basic statistical comparison to be made between η_r values. This is summarised in Table 8-3. For N-IA combined with each protein, there is a slight reduction in η_r, which in all cases is statistically significant except when combined with fibrinogen.

Table 8-3 – A summary of theoretical values for η_r and the actual values calculated using flow times for N-IA in combination with one of the proteins.

Components	[η] (mL.g^{-1})	c (mg.mL^{-1})	Theoretical η_r	Actual η_r
N-IA + BSA	218 ± 2	0.500	1.112 ± 0.008	1.093 ± 0.000
N-IA + BSA	218 ± 2	1.000	1.232 ± 0.009	1.215 ± 0.000
N-IA + HSA	218 ± 2	0.500	1.112 ± 0.008	1.091 ± 0.000
N-IA + HSA	218 ± 2	1.000	1.232 ± 0.009	1.212 ± 0.000
N-IA + fibrinogen	218 ± 2	0.305	1.068 ± 0.007	1.063 ± 0.001
N-IA + fibrinogen	218 ± 2	0.610	1.138 ± 0.008	1.138 ± 0.001

8.3.2 Sedimentation velocity

The values for each of the peaks in the sedimentation data are summarised in the tables below, while the distributions are given in the graphs.

Table 8-4 gives sedimentation coefficient values for N-IA and BSA, while the distributions are shown in Figure 8.4. As the sedimentation coefficients for N-IA and BSA are similar it is not possible to distinguish the distributions.

Table 8-4 – Summary of peak sedimentation coefficient values for N-IA and BSA.

Sample(s)	Concentration (mg.mL^{-1})	$s_{20,w}$ (S)
N-IA	0.5	4.56 ± 1.62
N-IA	1	4.06 ± 1.17
N-IA	2	2.89 ± 0.55
BSA	0.5	4.23 ± 1.53
BSA	1	4.41 ± 1.70
N-IA + BSA	0.5 + 0.5	3.13 ± 1.36
N-IA + BSA	1 + 1	3.88 ± 1.32

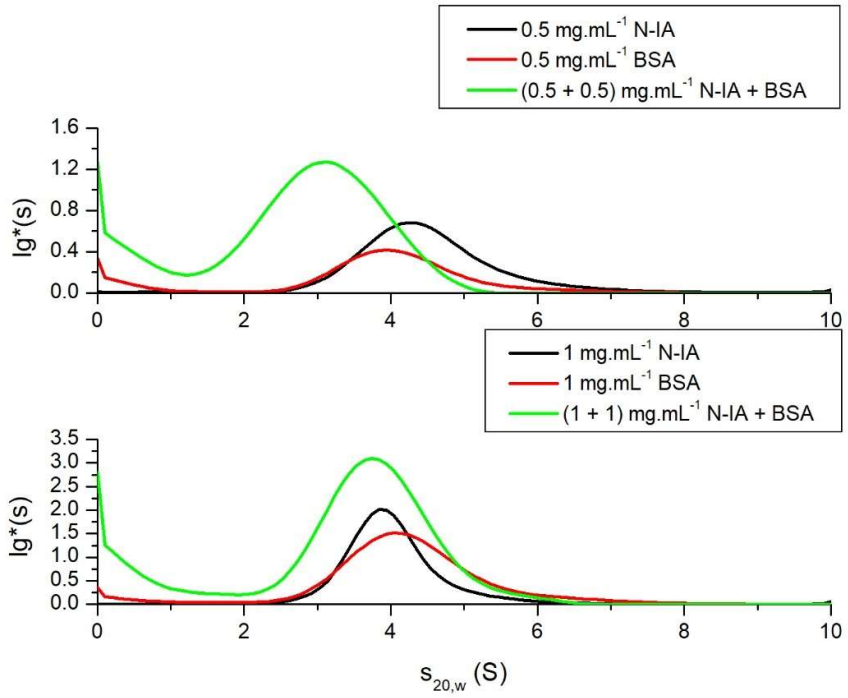


Figure 8.4 – Distribution of sedimentation coefficients of N-IA and BSA, both alone and in combination, at 0.5 mg.mL^{-1} (upper) and 1 mg.mL^{-1} (lower).

Table 8-5 gives sedimentation coefficient values for N-IA and HSA, while the distributions are shown in Figure 8.5. As the sedimentation coefficients for N-IA and BSA are similar it is not possible to distinguish the distributions.

Table 8-5 – Summary of peak sedimentation coefficient values for N-IA and HSA.

Sample(s)	Concentration (mg/mL)	$s_{20,w}$ (S)
N-IA	0.5	4.56 ± 1.64
N-IA	1	4.06 ± 1.16
N-IA	2	3.13 ± 0.59
HSA	0.5	4.58 ± 1.92
HSA	1	4.69 ± 2.02
N-IA + HSA	0.5 + 0.5	4.37 ± 1.64
N-IA + HSA	1 + 1	4.16 ± 1.49

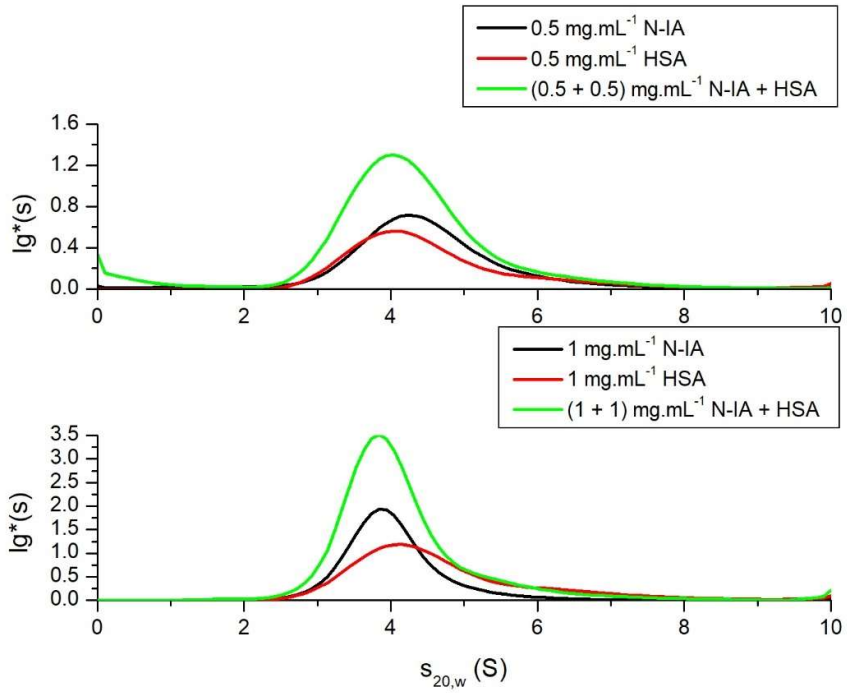


Figure 8.5 – Distribution of sedimentation coefficients of N-IA and HSA, both alone and in combination, at 0.5 mg.mL^{-1} (upper) and 1 mg.mL^{-1} (lower).

Table 8-6 gives sedimentation coefficient values for N-IA and fibrinogen, while the distributions are shown in Figure 8.6. The sedimentation coefficients for N-IA and fibrinogen are different enough that it is possible to distinguish the distributions.

Table 8-6 – Summary of peak sedimentation coefficient values for N-IA and fibrinogen.

Sample(s)	Concentration (mg.mL^{-1})	$s_{20,w}$ (S)
N-IA	0.305	4.88 ± 1.91
N-IA	0.61	4.47 ± 1.55
N-IA	1.22	3.89 ± 6.99
Fibrinogen	0.305	7.76 ± 1.20
Fibrinogen	0.61	7.77 ± 1.25
N-IA + fibrinogen peak 1	0.305 + 0.305	4.60 ± 1.31
N-IA + fibrinogen peak 2	0.305 + 0.305	7.40 ± 1.18
N-IA + fibrinogen peak 1	0.610 + 0.610	4.30 ± 1.18
N-IA + fibrinogen peak 2	0.610 + 0.610	7.20 ± 1.20

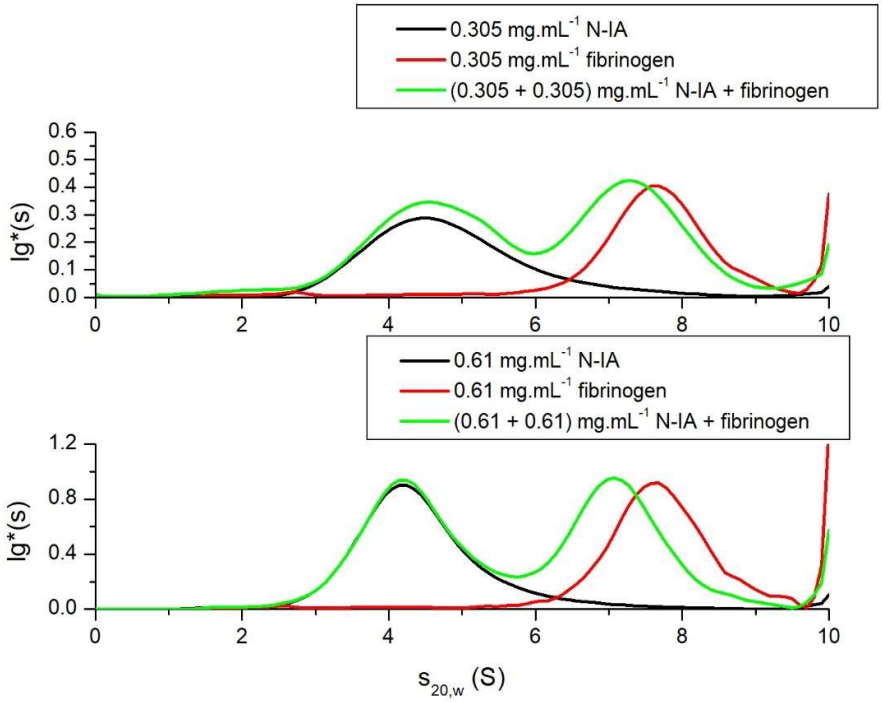


Figure 8.6 – Distribution of sedimentation coefficients of N-IA and fibrinogen, both alone and in combination, at 0.305 mg.mL^{-1} (upper) and 0.610 mg.mL^{-1} (lower).

Table 8-7 gives sedimentation coefficient values for N-IA and IgG1 Cri, while the distributions are shown in Figure 8.7. The sedimentation coefficients for N-IA and IgG1 Cri are different enough that it is possible to distinguish the distributions.

Table 8-7 – Summary of peak sedimentation coefficient values for N-IA and IgG1 Cri.

Sample(s)	Concentration (mg.mL^{-1})	$s_{20,w}$ (S)
N-IA	0.5	4.56 ± 1.34
N-IA	1	4.06 ± 0.95
IgG Cri	0.5	6.47 ± 0.79
IgG Cri	1	6.54 ± 0.89
N-IA + IgG Cri peak 1	0.5 + 0.5	4.20 ± 0.60
N-IA + IgG Cri peak 2	0.5 + 0.5	6.38 ± 0.81
N-IA + IgG Cri peak 1	1 + 1	3.91 ± 0.46
N-IA + IgG Cri peak 2	1 + 1	6.12 ± 0.75

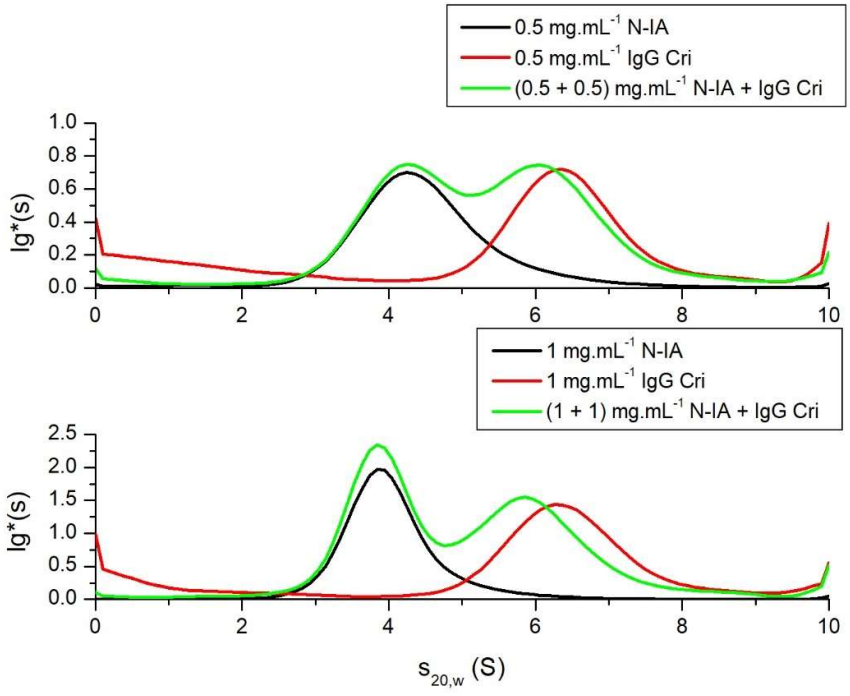


Figure 8.7 – Distribution of sedimentation coefficients of N-IA and IgG1 Cri, both alone and in combination, at 0.5 mg.mL^{-1} (upper) and 1 mg.mL^{-1} (lower).

Table 8-8 gives sedimentation coefficient values for N-IA and IgG1 Wid, while the distributions are shown in Figure 8.8. The sedimentation coefficients for N-IA and IgG1 Wid are different enough that it is possible to distinguish the distributions.

Table 8-8 – Summary of peak sedimentation coefficient values for N-IA and IgG1 Wid.

Sample(s)	Concentration (mg.mL^{-1})	$s_{20,w}$ (S)
N-IA	0.5	4.56 ± 1.34
N-IA	1	4.06 ± 0.95
IgG Wid	0.5	6.26 ± 0.75
IgG Wid	1	6.53 ± 0.86
N-IA + IgG Wid peak 1	0.5 + 0.5	4.13 ± 0.56
N-IA + IgG Wid peak 2	0.5 + 0.5	6.23 ± 0.82
N-IA + IgG Wid peak 1	1 + 1	3.90 ± 0.43
N-IA + IgG Wid peak 2	1 + 1	6.07 ± 0.78

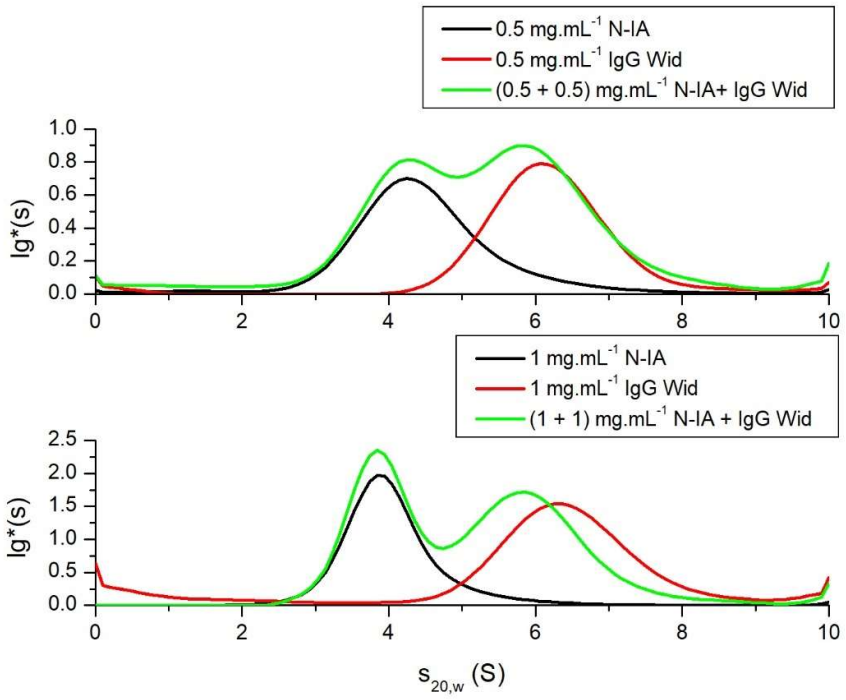


Figure 8.8 – Distribution of sedimentation coefficients of N-IA and IgG1 Wid, both alone and in combination, at 0.5 mg.mL^{-1} (upper) and 1 mg.mL^{-1} (lower).

8.4 Native GBS polysaccharide, serotype IB

8.4.1 Viscosity

As with the comparisons in previous sections, the error ranges allow a basic statistical comparison to be made between η_r values. This is summarised in Table 8-9. For N-IB combined with each protein, there is a slight reduction in η_r, which in all cases is statistically significant.

Table 8-9 – A summary of theoretical values for η_r and the actual values calculated using flow times for N-IB in combination with one of the proteins.

Components	[η] (mL.g^{-1})	c (mg.mL^{-1})	Theoretical η_r	Actual η_r
N-IB + BSA	136 ± 0	0.500	1.069 ± 0.000	1.062 ± 0.000
N-IB + BSA	136 ± 0	1.000	1.141 ± 0.000	1.135 ± 0.000
N-IB + HSA	136 ± 0	0.500	1.069 ± 0.000	1.061 ± 0.002
N-IB + HSA	136 ± 0	1.000	1.141 ± 0.000	1.134 ± 0.001
N-IB + fibrinogen	136 ± 0	0.382	1.053 ± 0.000	1.050 ± 0.002
N-IB + fibrinogen	136 ± 0	0.764	1.107 ± 0.000	1.114 ± 0.003

8.4.2 Sedimentation velocity

The values for each of the peaks in the sedimentation data are summarised in the tables below, while the distributions are given in the graphs.

Table 8-10 gives sedimentation coefficient values for N-IB and BSA, while the distributions are shown in Figure 8.9. As the sedimentation coefficients for N-IB and BSA are similar it is not possible to distinguish the distributions.

Table 8-10 – Summary of peak sedimentation coefficient values for N-IB and BSA.

Sample(s)	Concentration (mg.mL^{-1})	$s_{20,w}$ (S)
N-IB	0.5	3.83 ± 1.49
N-IB	1	3.56 ± 1.09
N-IB	2	3.12 ± 0.72
BSA	0.5	4.60 ± 1.83
BSA	1	4.58 ± 1.70
N-IB + BSA	0.5 + 0.5	4.17 ± 1.96
N-IB + BSA	1 + 1	3.94 ± 1.57

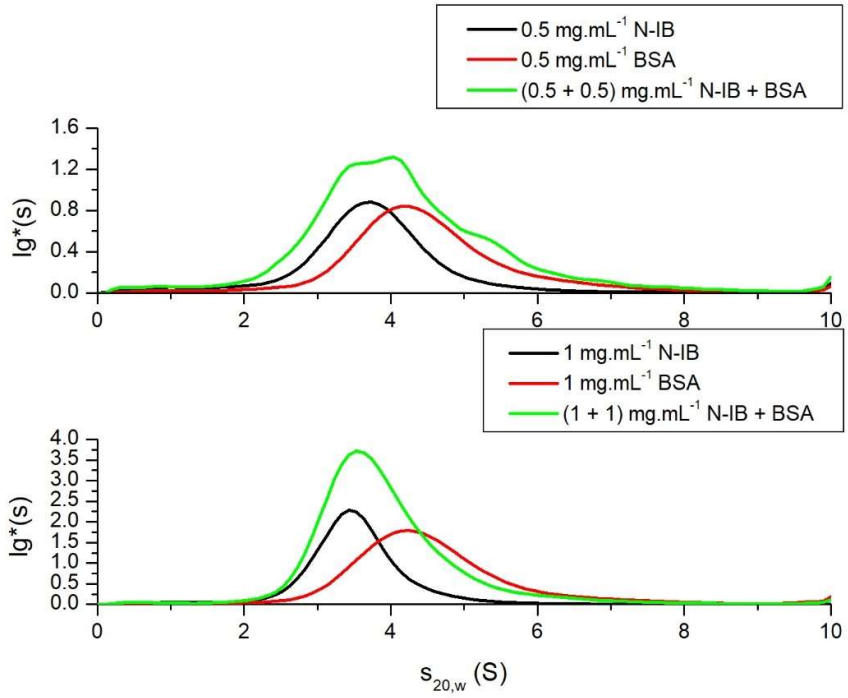


Figure 8.9 – Distribution of sedimentation coefficients of N-IB and BSA, both alone and in combination, at 0.5 mg.mL^{-1} (upper) and 1 mg.mL^{-1} (lower).

Table 8-11 gives sedimentation coefficient values for N-IB and HSA, while the distributions are shown in Figure 8.10. As the sedimentation coefficients for N-IB and BSA are similar it is not possible to distinguish the distributions.

Table 8-11 – Summary of peak sedimentation coefficient values for N-IB and HSA.

Sample(s)	Concentration (mg.mL^{-1})	$s_{20,w}$ (S)
N-IB	0.5	3.85 ± 1.30
N-IB	1	3.60 ± 1.14
N-IB	2	3.11 ± 0.71
HSA	0.5	4.50 ± 1.81
HSA	1	4.79 ± 2.07
N-IB + HSA	0.5 + 0.5	4.31 ± 1.98
N-IB + HSA	1 + 1	4.06 ± 1.82

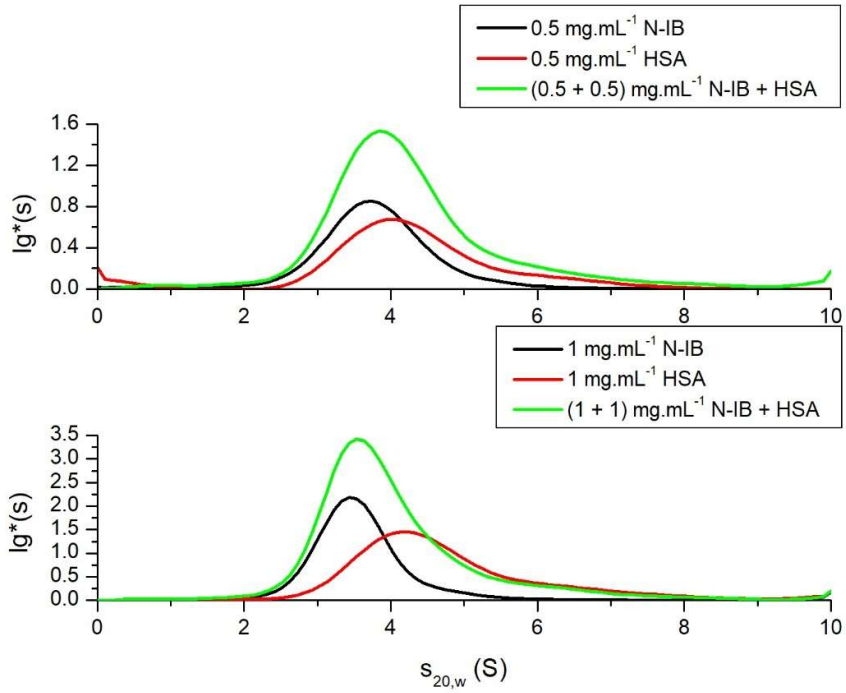


Figure 8.10 – Distribution of sedimentation coefficients of N-IB and HSA, both alone and in combination, at 0.5 mg.mL^{-1} (upper) and 1 mg.mL^{-1} (lower).

Table 8-12 gives sedimentation coefficient values for N-IB and fibrinogen, while the distributions are shown in Figure 8.11. The sedimentation coefficients for N-IB and fibrinogen are different enough that it is possible to distinguish the distributions.

Table 8-12 – Summary of peak sedimentation coefficient values for N-IB and fibrinogen.

Sample(s)	Concentration (mg.mL^{-1})	$s_{20,w}$ (S)
N-IB	0.382	3.98 ± 1.58
N-IB	0.764	3.77 ± 1.30
N-IB	1.528	3.33 ± 0.84
Fibrinogen	0.382	7.83 ± 1.22
Fibrinogen	0.764	7.79 ± 1.19
N-IB + fibrinogen peak 1	0.382 + 0.382	3.99 ± 1.36
N-IB + fibrinogen peak 2	0.382 + 0.382	7.63 ± 1.14
N-IB + fibrinogen peak 1	0.764 + 0.764	3.71 ± 1.12
N-IB + fibrinogen peak 2	0.764 + 0.764	7.29 ± 1.15

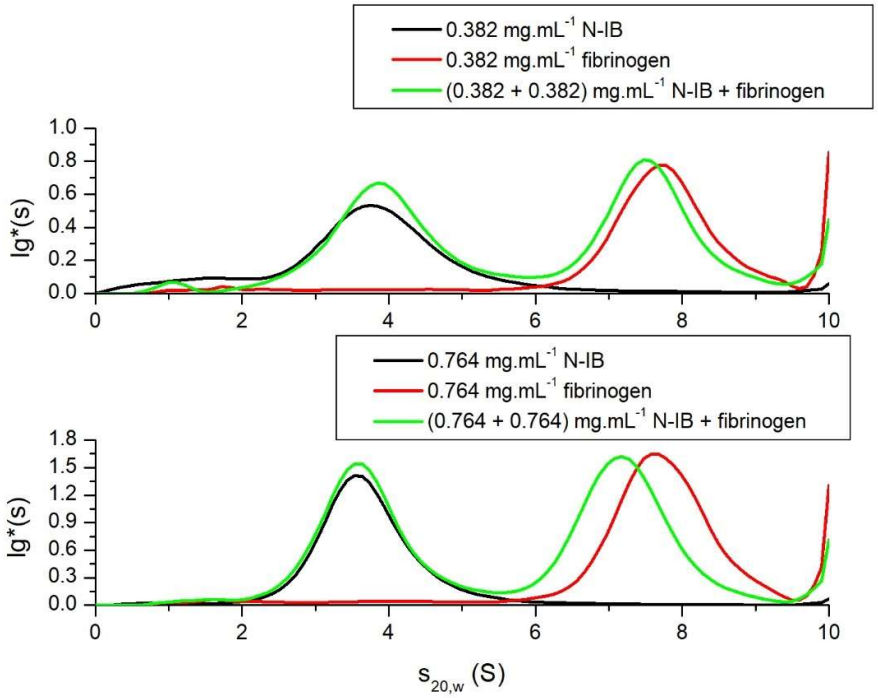


Figure 8.11 – Distribution of sedimentation coefficients of N-IB and fibrinogen, both alone and in combination, at 0.382 mg.mL^{-1} (upper) and 0.764 mg.mL^{-1} (lower).

Table 8-13 gives sedimentation coefficient values for N-IB and IgG1 Cri, while the distributions are show in Figure 8.12. The sedimentation coefficients for N-IB and IgG1 Cri are different enough that it is possible to distinguish the distributions.

Table 8-13 – Summary of peak sedimentation coefficient values for N-IB and IgG1 Cri.

Sample(s)	Concentration (mg.mL^{-1})	$s_{20,w}$ (S)
N-IB	0.5	3.84 ± 1.14
N-IB	1	3.58 ± 0.92
IgG Cri	0.5	6.47 ± 0.79
IgG Cri	1	6.54 ± 0.89
N-IB+ IgG Cri peak 1	0.5 + 0.5	3.68 ± 0.64
N-IB+ IgG Cri peak 2	0.5 + 0.5	6.42 ± 0.87
N-IB+ IgG Cri peak 1	1 + 1	3.51 ± 0.52
N-IB+ IgG Cri peak 2	1 + 1	6.24 ± 0.84

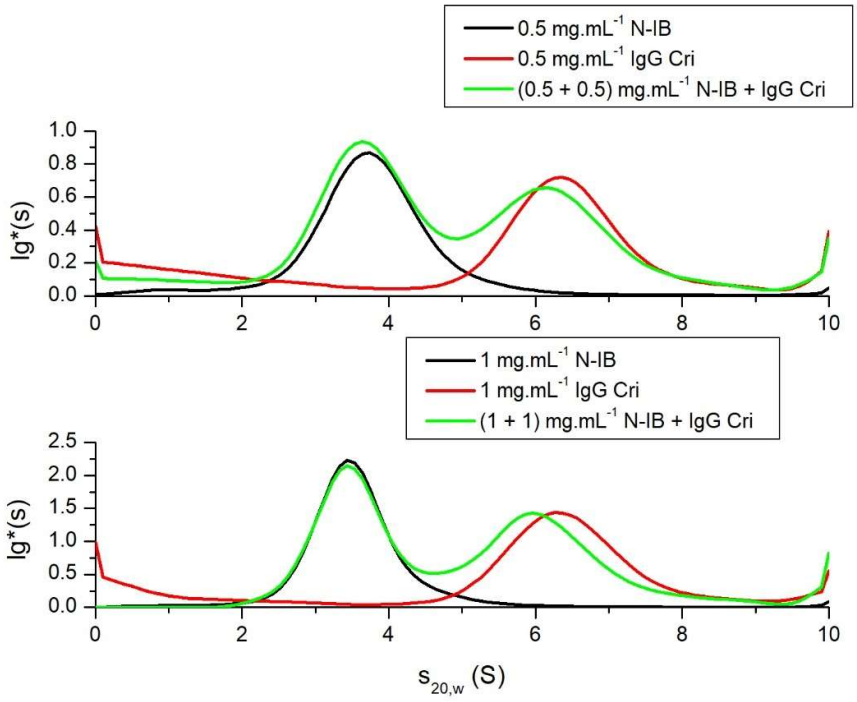


Figure 8.12 – Distribution of sedimentation coefficients of N-IB and IgG1 Cri, both alone and in combination, at 0.5 mg.mL^{-1} (upper) and 1 mg.mL^{-1} (lower).

Table 8-14 gives sedimentation coefficient values for N-IB and IgG1 Wid, while the distributions are shown in Figure 8.13. The sedimentation coefficients for N-IB and IgG1 Wid are different enough that it is possible to distinguish the distributions.

Table 8-14 – Summary of peak sedimentation coefficient values for N-IB and IgG1 Wid.

Sample(s)	Concentration (mg.mL^{-1})	$s_{20,w}$ (S)
N-IB	0.5	3.84 ± 1.14
N-IB	1	3.58 ± 0.92
IgG Wid	0.5	6.26 ± 0.75
IgG Wid	1	6.53 ± 0.86
N-IB + IgG Wid peak 1	0.5 + 0.5	3.72 ± 0.62
N-IB + IgG Wid peak 2	0.5 + 0.5	6.25 ± 0.78
N-IB + IgG Wid peak 1	1 + 1	3.38 ± 0.45
N-IB + IgG Wid peak 2	1 + 1	6.00 ± 0.78

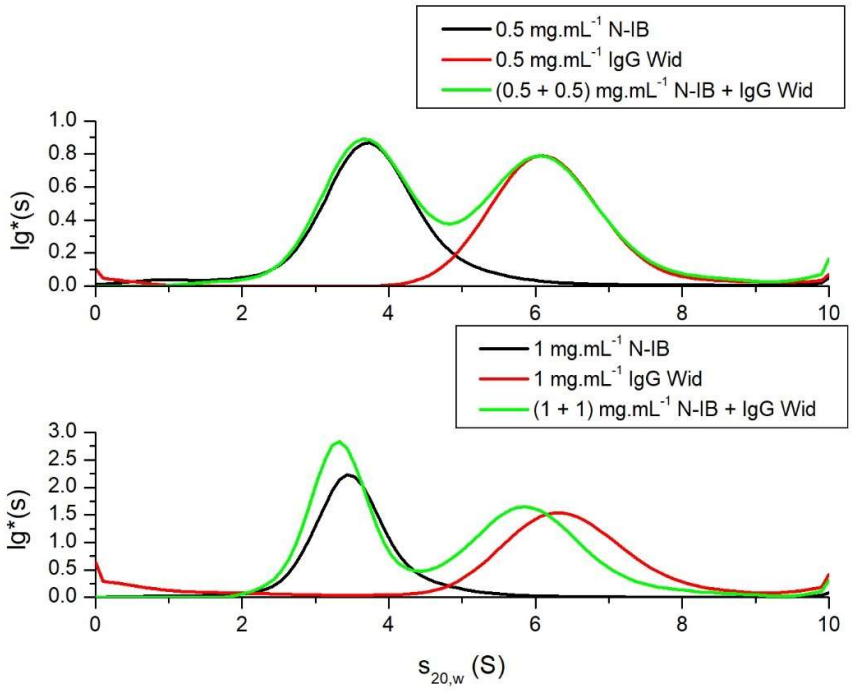


Figure 8.13 – Distribution of sedimentation coefficients of N-IB and IgG1 Wid, both alone and in combination, at 0.5 mg.mL^{-1} (upper) and 1 mg.mL^{-1} (lower).

8.5 Native GBS polysaccharide, serotype II

Here, while the concentration of fibrinogen stock produced was still low, it was possible to analyse some samples at higher concentration, although not the mixtures with polysaccharides.

8.5.1 Viscosity

As with the comparisons in previous sections, the error ranges allow a basic statistical comparison to be made between η_r values. This is summarised in Table 8-15Table 8-3. For N-II combined with each protein, there is a slight increase in η_r, which in all cases is statistically significant.

Table 8-15 – A summary of theoretical values for η_r and the actual values calculated using flow times for N-II in combination with one of the proteins.

Components	[η] (mL.g^{-1})	c (mg.mL^{-1})	Theoretical η_r	Actual η_r
N-II + BSA	127 ± 1	0.500	1.064 ± 0.005	1.093 ± 0.000
N-II + BSA	127 ± 1	1.000	1.131 ± 0.005	1.215 ± 0.000
N-II + HSA	127 ± 1	0.500	1.064 ± 0.005	1.091 ± 0.000
N-II + HSA	127 ± 1	1.000	1.131 ± 0.005	1.212 ± 0.000
N-II + fibrinogen	127 ± 1	0.392	1.050 ± 0.005	1.063 ± 0.001
N-II + fibrinogen	127 ± 1	0.785	1.102 ± 0.005	1.138 ± 0.001

8.5.2 Sedimentation velocity

The values for each of the peaks in the sedimentation data are summarised in the tables below, while the distributions are given in the graphs.

Table 8-16 gives sedimentation coefficient values for N-II and BSA, while the distributions are shown in Figure 8.14. As the sedimentation coefficients for N-II and BSA are similar it is difficult to distinguish the distributions.

Table 8-16 – Summary of peak sedimentation coefficient values for N-II and BSA.

Sample(s)	Concentration (mg.mL^{-1})	$s_{20,w}$ (S)
N-II	0.5	6.25 ± 1.26
N-II	1	5.82 ± 1.07
N-II	2	5.04 ± 0.71
BSA	0.5	4.42 ± 0.94
BSA	1	4.76 ± 0.98
N-II + BSA peak 1	0.5 + 0.5	3.60 ± 0.57
N-II + BSA peak 2	0.5 + 0.5	5.66 ± 0.59
N-II + BSA peak 1	1 + 1	4.40 ± 0.75
N-II + BSA peak 2	1 + 1	6.37 ± 0.42

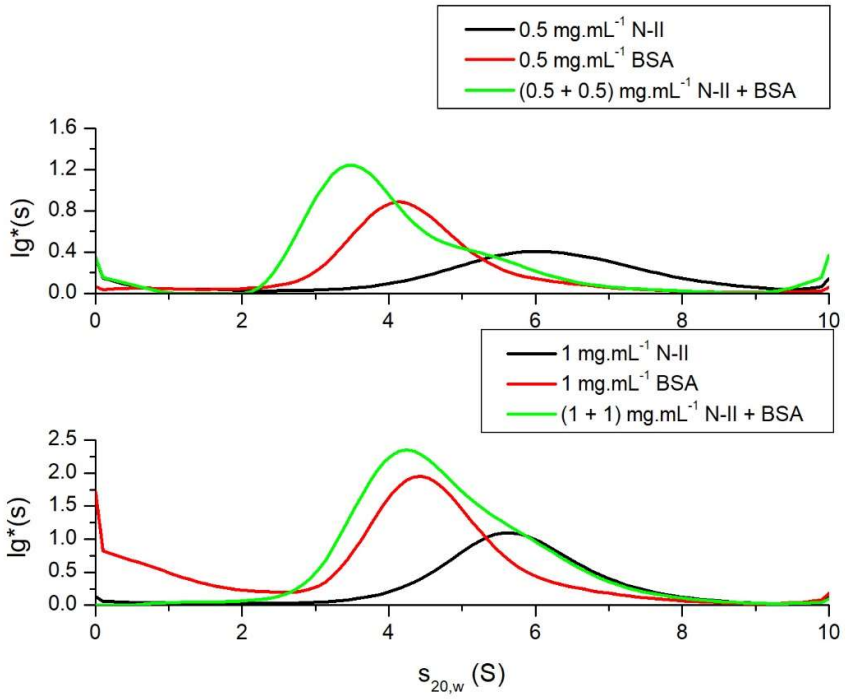


Figure 8.14 – Distribution of sedimentation coefficients of N-II and BSA, both alone and in combination, at 0.5 mg.mL^{-1} (upper) and 1 mg.mL^{-1} (lower).

Table 8-17 gives sedimentation coefficient values for N-II and HSA, while the distributions are shown in Figure 8.15. They do not show multiple peaks when the two molecules are combined at high concentrations, but two statistically different peaks are formed when the two molecules are combined at low concentration.

Table 8-17 – Summary of peak sedimentation coefficient values for N-II and HSA.

Sample(s)	Concentration (mg.mL^{-1})	$s_{20,w}$ (S)
N-II	0.5	6.27 ± 1.27
N-II	1	5.75 ± 0.98
N-II	2	4.97 ± 0.71
HSA	0.5	4.30 ± 0.72
HSA	1	4.28 ± 0.72
N-II + HSA peak 1	0.5 + 0.5	4.29 ± 0.70
N-II + HSA peak 2	0.5 + 0.5	6.69 ± 0.84
N-II + HSA	1 + 1	4.94 ± 1.14

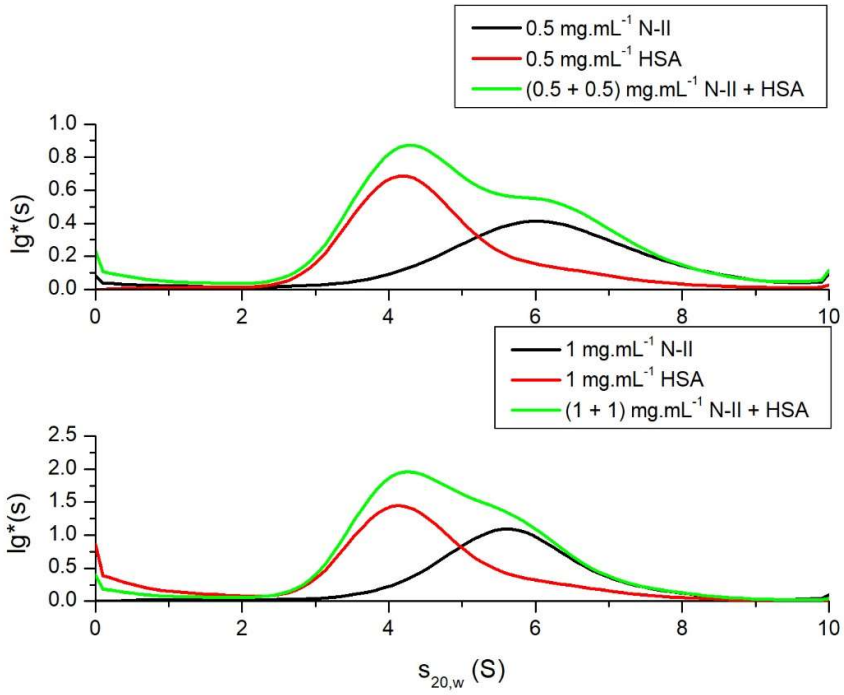


Figure 8.15 – Distribution of sedimentation coefficients of N-II and HSA, both alone and in combination, at 0.5 mg.mL^{-1} (upper) and 1 mg.mL^{-1} (lower).

Table 8-18 gives sedimentation coefficient values for N-II and fibrinogen, while the distributions are shown in Figure 8.16. The sedimentation coefficients for N-II and fibrinogen are different enough that it is possible to distinguish the distributions.

Table 8-18 – Summary of peak sedimentation coefficient values for N-II and fibrinogen.

Sample(s)	Concentration (mg.mL^{-1})	$s_{20,w}$ (S)
N-II	0.5	5.54 ± 2.20
N-II	1	5.07 ± 1.67
N-II	2	4.66 ± 1.37
Fibrinogen	0.5	6.58 ± 1.16
Fibrinogen	1	6.61 ± 1.06
N-II + fibrinogen peak 1	0.392 + 0.392	4.44 ± 1.13
N-II + fibrinogen peak 2	0.392 + 0.392	4.38 ± 0.98
N-II + fibrinogen peak 1	0.784 + 0.784	6.34 ± 1.05
N-II + fibrinogen peak 2	0.784 + 0.784	6.02 ± 0.94

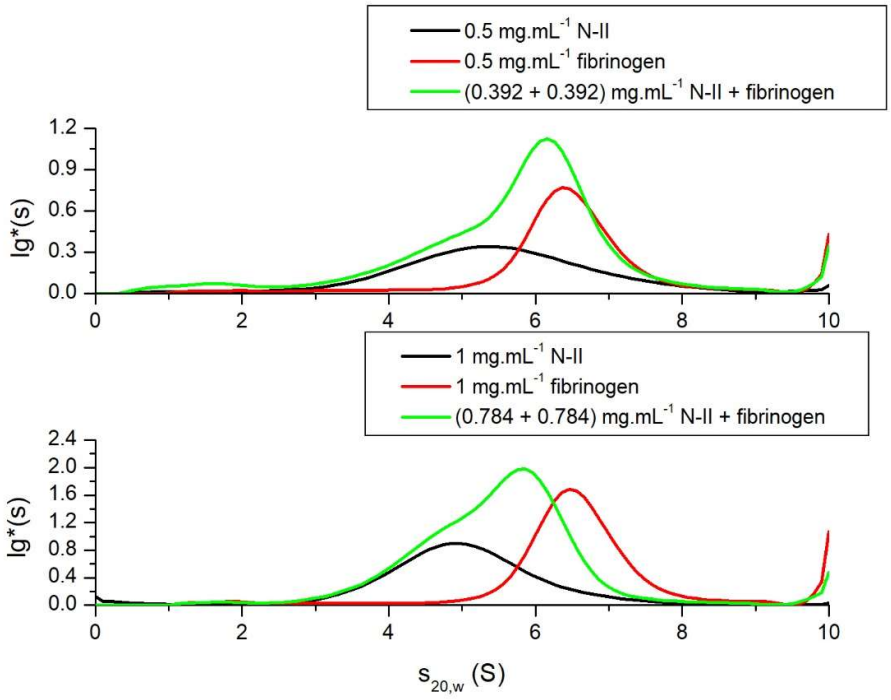


Figure 8.16 – Distribution of sedimentation coefficients of N-II and fibrinogen, both alone and in combination, at 0.392 mg.mL^{-1} (upper) and 0.784 mg.mL^{-1} (lower).

Table 8-19 gives sedimentation coefficient values for N-II and IgG1 Cri, while the distributions are shown in Figure 8.17. As the sedimentation coefficients for N-II and IgG1 Cri are similar it is difficult to distinguish the distributions.

Table 8-19 – Summary of peak sedimentation coefficient values for N-II and IgG1 Cri.

Sample(s)	Concentration (mg.mL^{-1})	$s_{20,w}$ (S)
N-II	0.5	6.26 ± 1.79
N-II	1	5.79 ± 1.45
IgG Cri	0.5	6.47 ± 0.79
IgG Cri	1	6.54 ± 0.89
N-II+ IgG Cri peak	0.5 + 0.5	6.36 ± 1.07
N-II+ IgG Cri peak	1 + 1	6.05 ± 0.93

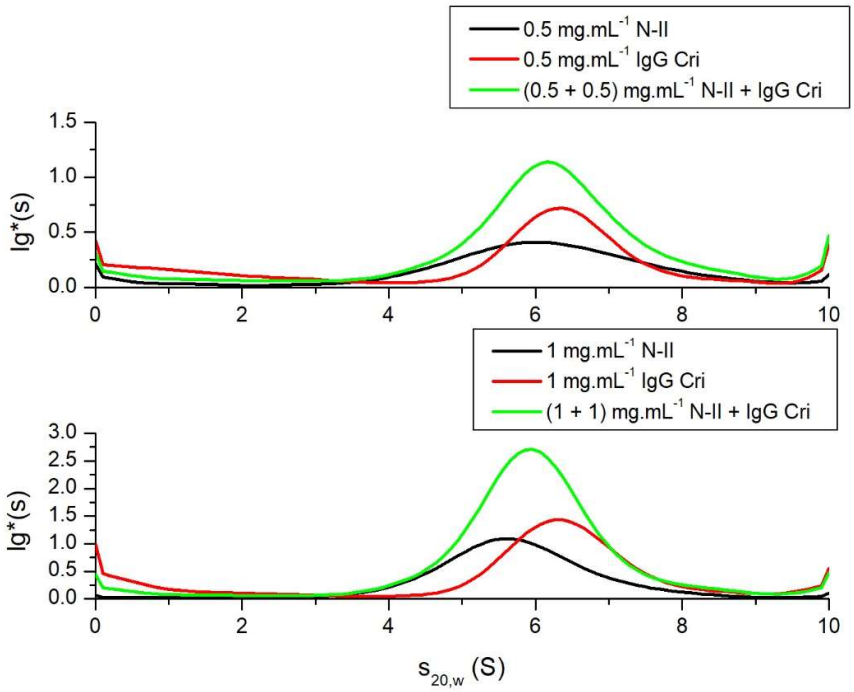


Figure 8.17 – Distribution of sedimentation coefficients of N-II and IgG1 Cri, both alone and in combination, at 0.5 mg.mL^{-1} (upper) and 1 mg.mL^{-1} (lower).

Table 8-20 gives sedimentation coefficient values for N-II and IgG1 Wid, while the distributions are shown in Figure 8.18. As the sedimentation coefficients for N-II and IgG1 Wid are similar it is difficult to distinguish the distributions.

Table 8-20 – Summary of peak sedimentation coefficient values for N-II and IgG1 Wid.

Sample(s)	Concentration ($mg.mL^{-1}$)	$s_{20,w}$ (S)
N-II	0.5	6.26 ± 1.79
N-II	1	5.79 ± 1.45
IgG Wid	0.5	6.26 ± 0.75
IgG Wid	1	6.53 ± 0.86
N-II + IgG Wid	0.5 + 0.5	6.23 ± 0.94
N-II + IgG Wid	1 + 1	5.95 ± 0.85

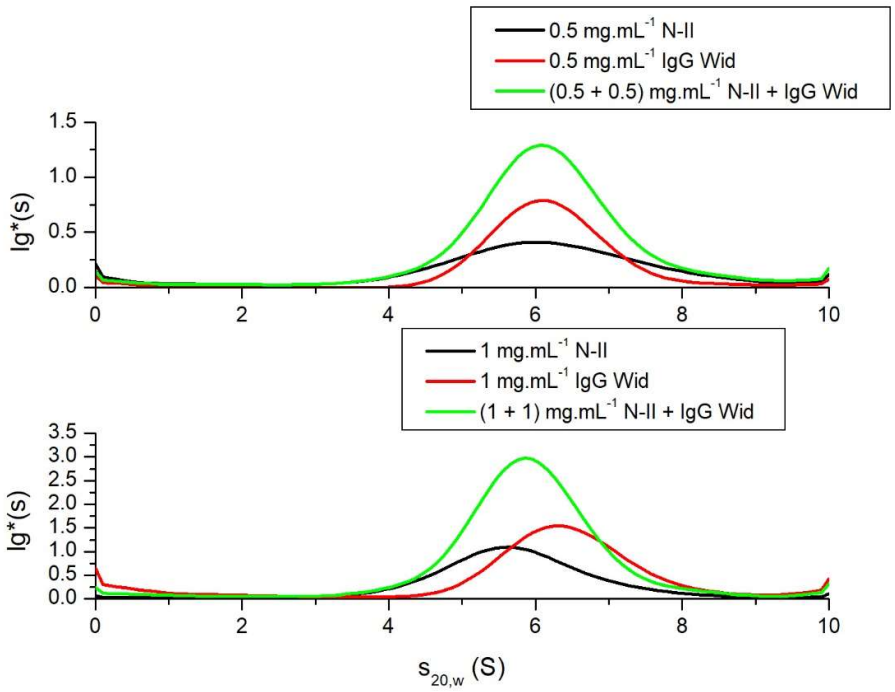


Figure 8.18 – Distribution of sedimentation coefficients of N-II and IgG1 Wid, both alone and in combination, at 0.5 $mg.mL^{-1}$ (upper) and 1 $mg.mL^{-1}$ (lower).

8.6 Native GBS polysaccharide, serotype III

With this sample there was an error in the dilution calculations, and so the desired concentrations and 1:1 ratio could not be used.

8.6.1 Viscosity

As with the comparisons in previous sections, the error ranges allow a basic statistical comparison to be made between η_r values. This is summarised in Table 8-21. For N-III combined with each protein, there is a slight increase in η_r, which is statistically significant in all cases except the lower concentrations of serum albumins.

Table 8-21 – A summary of theoretical values for η_r and the actual values calculated using flow times for N-III in combination with one of the proteins.

Components	[η] (mL.g^{-1})	c (mg.mL^{-1})	Theoretical η_r	Actual η_r
N-III + BSA	45.4 ± 0.2	0.290	1.015 ± 0.003	1.021 ± 0.000
N-III + BSA	45.4 ± 0.2	0.579	1.027 ± 0.003	1.048 ± 0.000
N-III + HSA	45.4 ± 0.2	0.290	1.015 ± 0.003	1.023 ± 0.000
N-III + HSA	45.4 ± 0.2	0.579	1.027 ± 0.003	1.047 ± 0.000
N-III + fibrinogen	45.4 ± 0.2	0.237	1.014 ± 0.003	1.025 ± 0.002
N-III + fibrinogen	45.4 ± 0.2	0.474	1.023 ± 0.003	1.035 ± 0.001

8.6.2 Sedimentation velocity

The values for each of the peaks in the sedimentation data are summarised in the tables below, while the distributions are given in the graphs.

Table 8-22 gives sedimentation coefficient values for N-III and BSA, while the distributions are shown in Figure 8.19. As the sedimentation coefficients for N-III and BSA are similar it is not possible to distinguish the distributions.

Table 8-22 – Summary of peak sedimentation coefficient values for N-III and BSA.

Sample(s)	Concentration (mg.mL^{-1})	$s_{20,w}$ (S)
N-III	0.290	2.89 ± 0.55
N-III	0.579	2.79 ± 0.53
N-III	1.158	2.51 ± 0.42
BSA	0.468	3.55 ± 0.68
BSA	0.937	3.85 ± 0.82
N-III + BSA	0.290 + 0.468	3.36 ± 0.83
N-III + BSA	0.579 + 0.937	3.25 ± 0.79

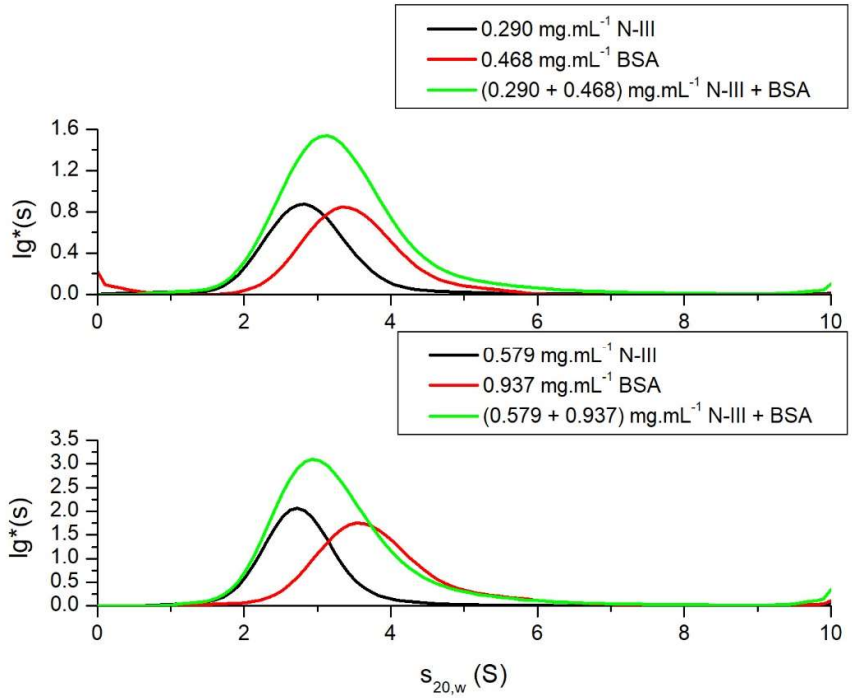


Figure 8.19 – Distribution of sedimentation coefficients of N-III at 0.290 mg.mL^{-1} (upper) and 0.579 mg.mL^{-1} (lower), alone and in combination with BSA at 0.468 mg.mL^{-1} (upper) and 0.937 mg.mL^{-1} (lower).

Table 8-23 gives sedimentation coefficient values for N-III and HSA, while the distributions are shown in Figure 8.20. As the sedimentation coefficients for N-III and HSA are similar it is not possible to distinguish the distributions.

Table 8-23 – Summary of peak sedimentation coefficient values for N-III and HSA.

Sample(s)	Concentration (mg.mL^{-1})	$s_{20,w}$ (S)
N-III	0.290	2.88 ± 0.51
N-III	0.579	2.77 ± 0.54
N-III	1.158	2.51 ± 0.43
HSA	0.472	3.46 ± 0.55
HSA	0.994	3.68 ± 0.58
N-III + HSA	0.290 + 0.472	3.22 ± 0.63
N-III + HSA	0.579 + 0.994	3.13 ± 0.65

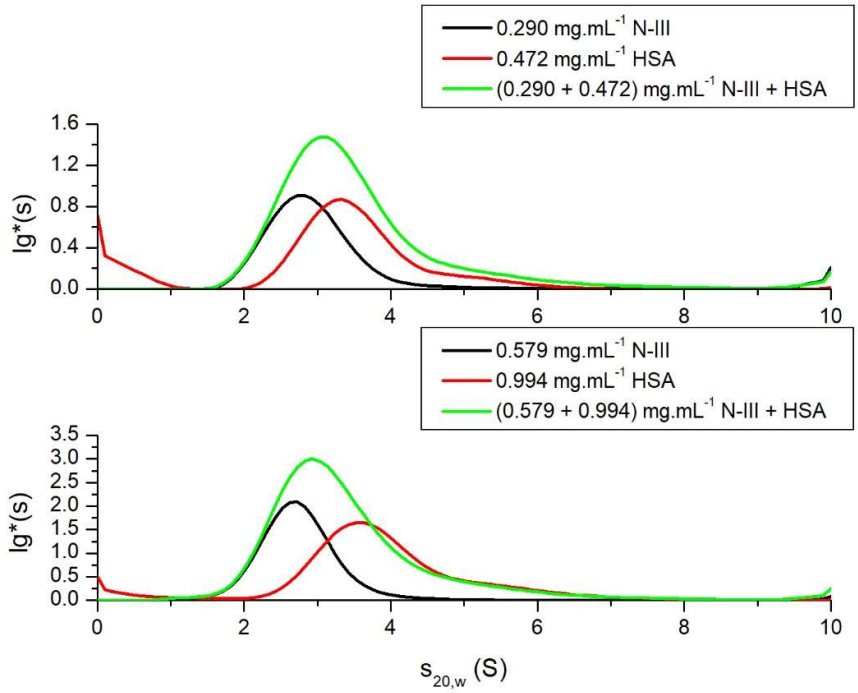


Figure 8.20 – Distribution of sedimentation coefficients of N-III at 0.290 mg.mL^{-1} (upper) and 0.579 mg.mL^{-1} (lower), alone and in combination with HSA at 0.472 mg.mL^{-1} (upper) and 0.994 mg.mL^{-1} (lower).

Table 8-24 gives sedimentation coefficient values for N-III and fibrinogen, while the distributions are shown in Figure 8.21. The sedimentation coefficients for N-III and fibrinogen are different enough that it is possible to distinguish the distributions.

Table 8-24 – Summary of peak sedimentation coefficient values for N-III and fibrinogen.

Sample(s)	Concentration (mg.mL^{-1})	$s_{20,w}$ (S)
N-III	0.237	2.98 ± 1.04
N-III	0.474	2.93 ± 1.04
N-III	0.949	2.80 ± 0.91
Fibrinogen	0.386	6.07 ± 0.90
Fibrinogen	0.772	6.65 ± 1.05
N-III + fibrinogen peak 1	0.237 + 0.386	2.96 ± 1.00
N-III + fibrinogen peak 2	0.237 + 0.386	6.56 ± 1.20
N-III + fibrinogen peak 1	0.474 + 0.772	2.95 ± 1.09
N-III + fibrinogen peak 2	0.474 + 0.772	6.57 ± 1.27

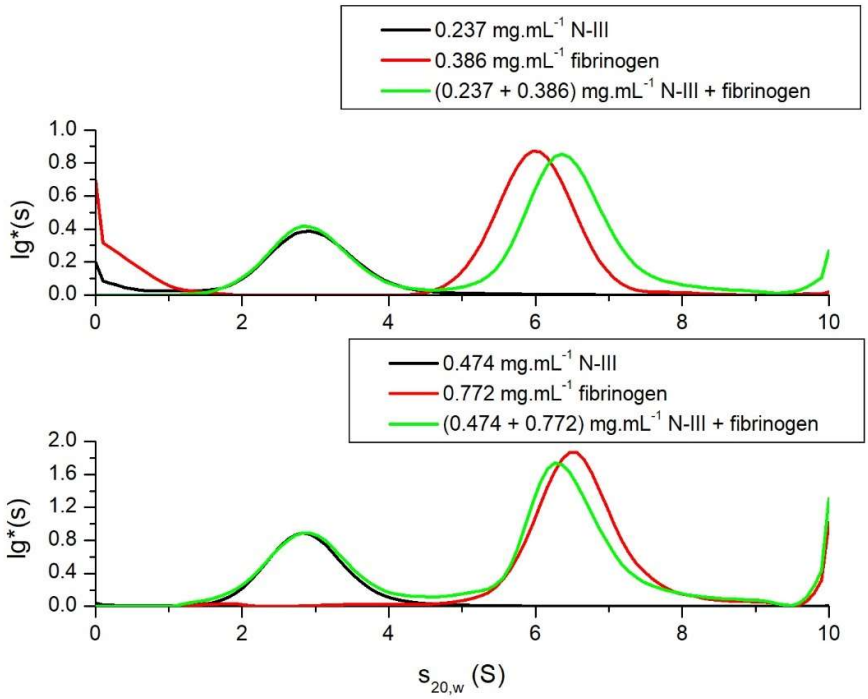


Figure 8.21 – Distribution of sedimentation coefficients of N-III at 0.237 mg.mL^{-1} (upper) and 0.474 mg.mL^{-1} (lower), alone and in combination with fibrinogen at 0.386 mg.mL^{-1} (upper) and 0.772 mg.mL^{-1} (lower).

Table 8-25 gives sedimentation coefficient values for N-III and IgG1 Cri, while the distributions are shown in Figure 8.22. The sedimentation coefficients for N-III and IgG1 Cri are different enough that it is possible to distinguish the distributions.

Table 8-25 – Summary of peak sedimentation coefficient values for N-III and IgG1 Cri.

Sample(s)	Concentration (mg.mL^{-1})	$s_{20,w}$ (S)
N-III	0.5	6.07 ± 0.52
N-III	1	6.65 ± 0.60
IgG Cri	0.5	6.47 ± 0.79
IgG Cri	1	6.54 ± 0.89
N-III+ IgG Cri peak 1	0.5 + 0.5	3.33 ± 0.66
N-III+ IgG Cri peak 2	0.5 + 0.5	6.36 ± 0.78
N-III+ IgG Cri peak 1	1 + 1	3.23 ± 0.57
N-III+ IgG Cri peak 2	1 + 1	6.23 ± 0.74

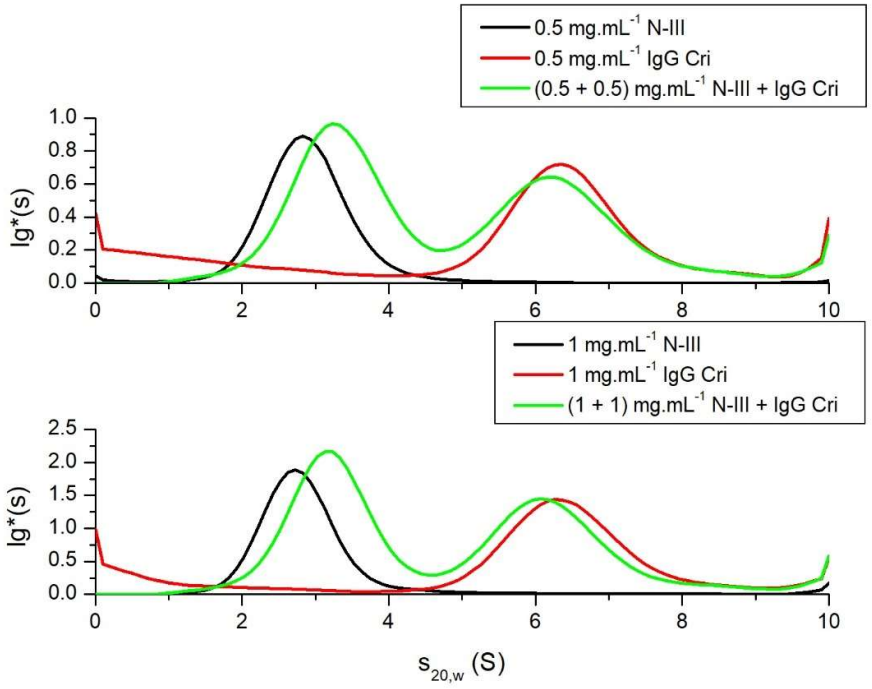


Figure 8.22 – Distribution of sedimentation coefficients of N-III and IgG1 Cri, both alone and in combination, at 0.5 mg.mL^{-1} (upper) and 1 mg.mL^{-1} (lower).

Table 8-26 gives sedimentation coefficient values for N-III and IgG1 Wid, while the distributions are shown in Figure 8.23. The sedimentation coefficients for N-III and IgG1 Wid are different enough that it is possible to distinguish the distributions.

Table 8-26 – Summary of peak sedimentation coefficient values for N-III and IgG1 Wid.

Sample(s)	Concentration (mg.mL^{-1})	$s_{20,w}$ (S)
N-III	0.5	6.07 ± 0.52
N-III	1	6.65 ± 0.60
IgG Wid	0.5	6.26 ± 0.75
IgG Wid	1	6.53 ± 0.86
N-III+ IgG Wid peak 1	0.5 + 0.5	3.35 ± 0.61
N-III+ IgG Wid peak 2	0.5 + 0.5	6.31 ± 0.80
N-III+ IgG Wid peak 1	1 + 1	3.18 ± 0.59
N-III+ IgG Wid peak 2	1 + 1	6.21 ± 0.79

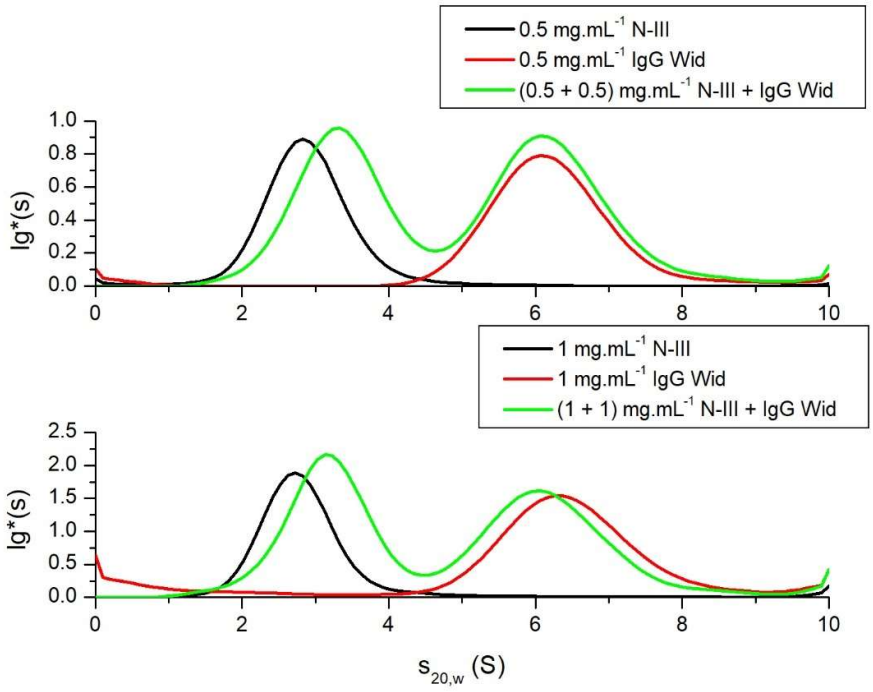


Figure 8.23 – Distribution of sedimentation coefficients of N-III and IgG1 Wid, both alone and in combination, at 0.5 mg.mL^{-1} (upper) and 1 mg.mL^{-1} (lower).

8.7 Native GBS polysaccharide, serotype IV

8.7.1 Viscosity

As with the comparisons in previous sections, the error ranges allow a basic statistical comparison to be made between η_r values. This is summarised in Table 8-27. For N-IV combined with the serum albumins there is a slight reduction in η_r, but this is not statistically significant. When combined with fibrinogen there is an increase in η_r, which is statistically significant at the higher concentration but not the lower concentration.

Table 8-27 – A summary of theoretical values for η_r and the actual values calculated using flow times for N-IV in combination with one of the proteins.

Components	[η] (mL.g^{-1})	c (mg.mL^{-1})	Theoretical η_r	Actual η_r
N-IV + BSA	65.0 ± 0.6	0.500	1.033 ± 0.008	1.028 ± 0.000
N-IV + BSA	65.0 ± 0.6	1.000	1.066 ± 0.008	1.060 ± 0.000
N-IV + HSA	65.0 ± 0.6	0.500	1.033 ± 0.008	1.026 ± 0.000
N-IV + HSA	65.0 ± 0.6	1.000	1.066 ± 0.008	1.061 ± 0.000
N-IV + fibrinogen	65.0 ± 0.6	0.500	1.033 ± 0.008	1.037 ± 0.002
N-IV + fibrinogen	65.0 ± 0.6	1.000	1.066 ± 0.008	1.087 ± 0.009

8.7.2 Sedimentation velocity

The values for each of the peaks in the sedimentation data are summarised in the tables below, while the distributions are given in the graphs.

Table 8-28 gives sedimentation coefficient values for N-IV and BSA, while the distributions are shown in Figure 8.24. The sedimentation coefficients for N-IV and BSA are different enough that it is possible to distinguish the distributions.

Table 8-28 – Summary of peak sedimentation coefficient values for N-IV and BSA.

Sample(s)	Concentration (mg.mL^{-1})	$s_{20,w}$ (S)
N-IV	0.5	2.69 ± 0.55
N-IV	1	2.59 ± 0.51
N-IV	2	2.39 ± 0.43
BSA	0.5	4.34 ± 0.73
BSA	1	4.40 ± 0.74
N-IV + BSA peak 1	0.5 + 0.5	2.75 ± 0.49
N-IV + BSA peak 2	0.5 + 0.5	4.46 ± 0.51
N-IV + BSA peak 1	1 + 1	2.61 ± 0.47
N-IV + BSA peak 2	1 + 1	4.39 ± 0.58

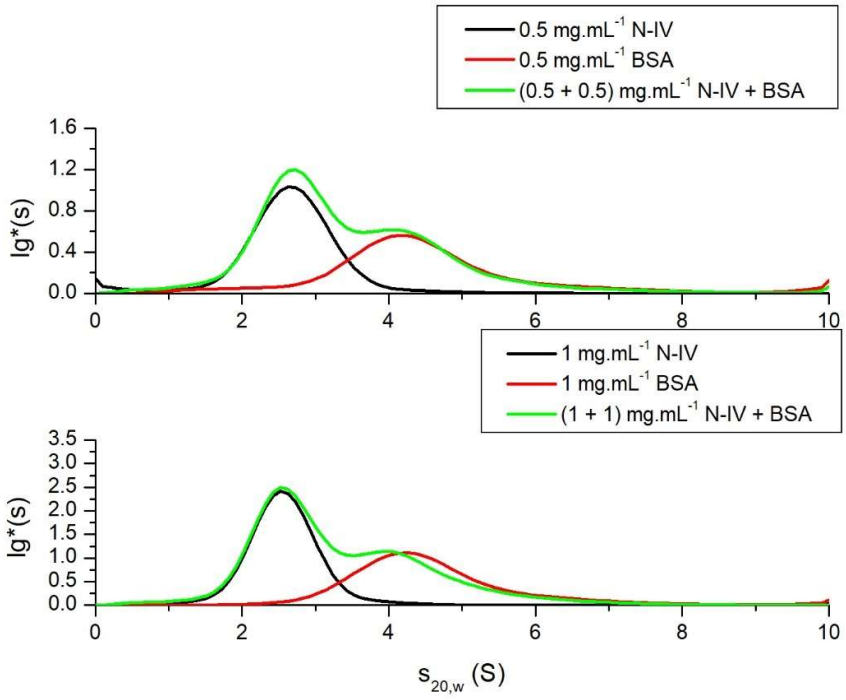


Figure 8.24 – Distribution of sedimentation coefficients of N-IV and BSA, both alone and in combination, at 0.5 mg.mL^{-1} (upper) and 1 mg.mL^{-1} (lower).

Table 8-29 gives sedimentation coefficient values for N-IV and HSA, while the distributions are shown in Figure 8.25. The sedimentation coefficients for N-IV and HSA are different enough that it is possible to distinguish the distributions.

Table 8-29 – Summary of peak sedimentation coefficient values for N-IV and HSA.

Sample(s)	Concentration (mg.mL^{-1})	$s_{20,w}$ (S)
N-IV	0.5	2.69 ± 0.51
N-IV	1	2.56 ± 0.41
N-IV	2	2.36 ± 0.35
HSA	0.5	4.33 ± 0.74
HSA	1	4.29 ± 0.71
N-IV + HSA peak 1	0.5 + 0.5	2.73 ± 0.46
N-IV + HSA peak 2	0.5 + 0.5	4.41 ± 0.49
N-IV + HSA peak 1	1 + 1	2.60 ± 0.42
N-IV + HSA peak 2	1 + 1	4.27 ± 0.53

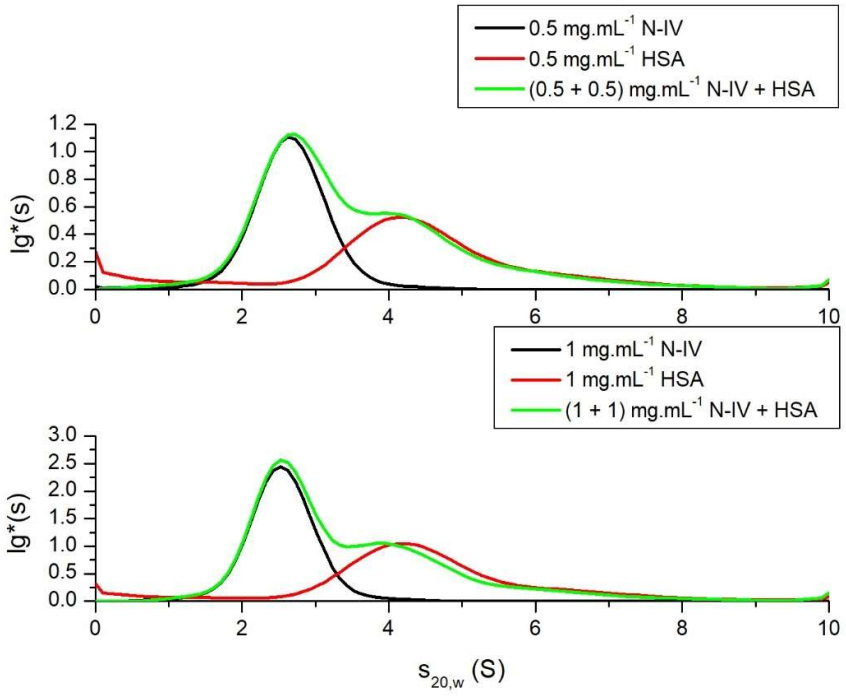


Figure 8.25 – Distribution of sedimentation coefficients of N-IV and HSA, both alone and in combination, at 0.5 mg.mL^{-1} (upper) and 1 mg.mL^{-1} (lower).

Table 8-30 gives sedimentation coefficient values for N-IV and fibrinogen while the distributions are shown in Figure 8.26. The sedimentation coefficients for N-IV and fibrinogen are different enough that it is possible to distinguish the distributions.

Table 8-30 – Summary of peak sedimentation coefficient values for N-IV and fibrinogen.

Sample(s)	Concentration (mg.mL^{-1})	$s_{20,w}$ (S)
N-IV	0.5	2.69 ± 0.90
N-IV	1	2.58 ± 0.84
N-IV	2	2.38 ± 0.71
Fibrinogen	0.5	7.76 ± 0.58
Fibrinogen	1	7.76 ± 0.60
N-IV + fibrinogen peak 1	0.5 + 0.5	2.69 ± 0.98
N-IV + fibrinogen peak 2	0.5 + 0.5	7.48 ± 1.16
N-IV + fibrinogen peak 1	1 + 1	2.56 ± 0.74
N-IV + fibrinogen peak 2	1 + 1	7.29 ± 0.91

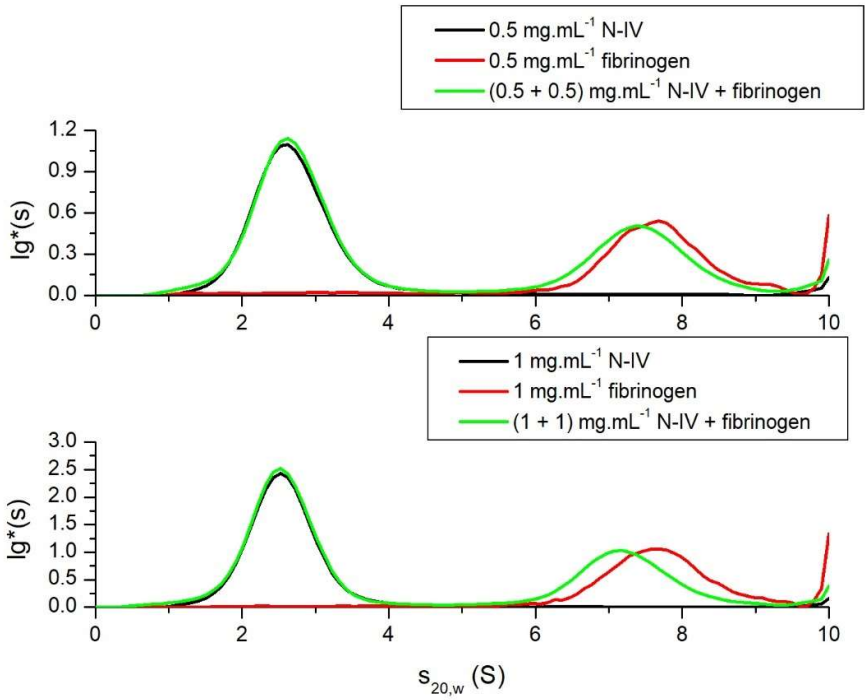


Figure 8.26 – Distribution of sedimentation coefficients of N-IV and fibrinogen, both alone and in combination, at 0.5 mg.mL^{-1} (upper) and 1 mg.mL^{-1} (lower).

Table 8-31 gives sedimentation coefficient values for N-IV and IgG1 Cri, while the distributions are shown in Figure 8.27. The sedimentation coefficients for N-IV and IgG1 Cri are different enough that it is possible to distinguish the distributions.

Table 8-31 – Summary of peak sedimentation coefficient values for N-IV and IgG1 Cri.

Sample(s)	Concentration (mg.mL^{-1})	$s_{20,w}$ (S)
N-IV	0.5	2.69 ± 0.92
N-IV	1	2.58 ± 0.81
IgG Cri	0.5	6.47 ± 0.79
IgG Cri	1	6.54 ± 0.89
N-IV+ IgG Cri peak 1	0.5 + 0.5	2.65 ± 0.55
N-IV+ IgG Cri peak 2	0.5 + 0.5	6.38 ± 0.78
N-IV+ IgG Cri peak 1	1 + 1	2.54 ± 0.48
N-IV+ IgG Cri peak 2	1 + 1	6.21 ± 0.78

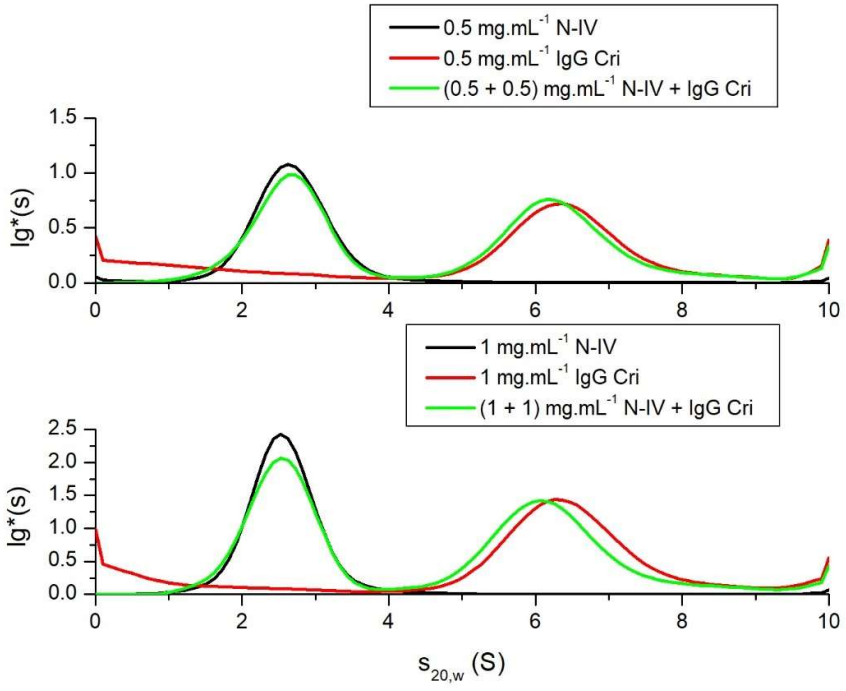


Figure 8.27 – Distribution of sedimentation coefficients of N-IV and IgG1 Cri, both alone and in combination, at 0.5 mg.mL^{-1} (upper) and 1 mg.mL^{-1} (lower).

Table 8-32 gives sedimentation coefficient values for N-IV and IgG1 Wid while the distributions are shown in Figure 8.28. The sedimentation coefficients for N-IV and IgG1 Wid are different enough that it is possible to distinguish the distributions.

Table 8-32 – Summary of peak sedimentation coefficient values for N-IV and IgG1 Wid.

Sample(s)	Concentration (mg.mL^{-1})	$s_{20,w}$ (S)
N-IV	0.5	2.69 ± 0.92
N-IV	1	2.58 ± 0.81
IgG Wid	0.5	6.26 ± 0.75
IgG Wid	1	6.53 ± 0.86
N-IV+ IgG Wid peak 1	0.5 + 0.5	2.65 ± 0.57
N-IV+ IgG Wid peak 2	0.5 + 0.5	6.32 ± 0.90
N-IV+ IgG Wid peak 1	1 + 1	2.56 ± 0.46
N-IV+ IgG Wid peak 2	1 + 1	6.21 ± 0.82

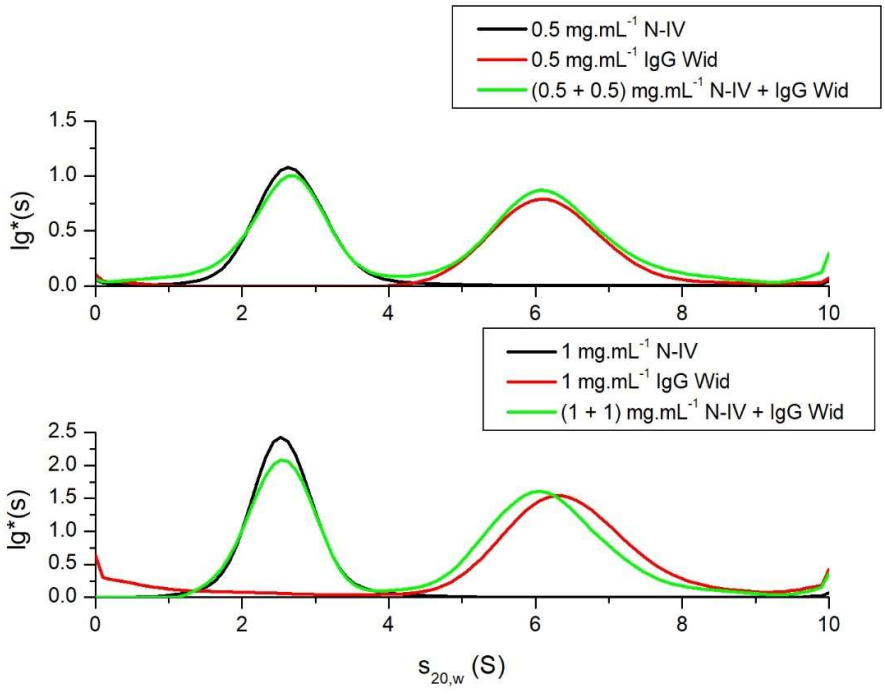


Figure 8.28 – Distribution of sedimentation coefficients of N-IV and IgG1 Wid, both alone and in combination, at 0.5 mg.mL^{-1} (upper) and 1 mg.mL^{-1} (lower).

8.8 Native GBS polysaccharide, serotype V

8.8.1 Viscosity

As with the comparisons in previous sections, the error ranges allow a basic statistical comparison to be made between η_r values. This is summarised in Table 8-33. For N-V combined with each protein there is a statistically significant increase in η_r, except for at the lower concentration of serum albumin where there is no statistically significant change.

Table 8-33 – A summary of theoretical values for η_r and the actual values calculated using flow times for N-V in combination with one of the proteins.

Components	[η] (mL.g^{-1})	c (mg.mL^{-1})	Theoretical η_r	Actual η_r
N-V + BSA	81.8 ± 0.9	0.500	1.042 ± 0.009	1.043 ± 0.001
N-V + BSA	81.8 ± 0.9	1.000	1.084 ± 0.009	1.106 ± 0.004
N-V + HSA	81.8 ± 0.9	0.500	1.042 ± 0.009	1.035 ± 0.001
N-V + HSA	81.8 ± 0.9	1.000	1.084 ± 0.009	1.111 ± 0.007
N-V + fibrinogen	81.8 ± 0.9	0.500	1.042 ± 0.009	1.056 ± 0.004
N-V + fibrinogen	81.8 ± 0.9	1.000	1.084 ± 0.009	1.103 ± 0.002

8.8.2 Sedimentation velocity

The values for each of the peaks in the sedimentation data are summarised in the tables below, while the distributions are given in the graphs.

Table 8-34 gives sedimentation coefficient values for N-V and BSA, while the distributions are shown in Figure 8.29. As the sedimentation coefficients for N-V and BSA are similar it is not possible to distinguish the distributions.

Table 8-34 – Summary of peak sedimentation coefficient values for N-V and BSA.

Sample(s)	Concentration (mg.mL^{-1})	$s_{20,w}$ (S)
N-V	0.5	3.69 ± 0.64
N-V	1	3.49 ± 0.50
N-V	2	3.19 ± 0.44
BSA	0.5	4.34 ± 0.86
BSA	1	4.52 ± 0.96
N-V + BSA	0.5 + 0.5	3.97 ± 0.80
N-V + BSA	1 + 1	3.82 ± 0.78

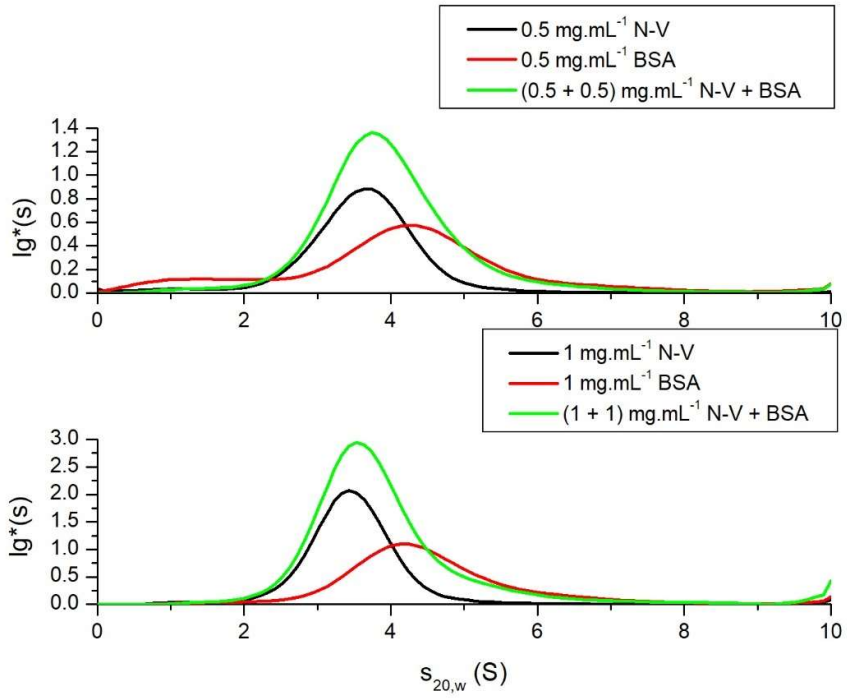


Figure 8.29 – Distribution of sedimentation coefficients of N-V and BSA, both alone and in combination, at 0.5 mg.mL^{-1} (upper) and 1 mg.mL^{-1} (lower).

Table 8-35 gives sedimentation coefficient values for N-V and HSA, while the distributions are shown in Figure 8.30. As the sedimentation coefficients for N-V and HSA are similar it is not possible to distinguish the distributions.

Table 8-35 – Summary of peak sedimentation coefficient values for N-V and HSA.

Sample(s)	Concentration (mg.mL^{-1})	$s_{20,w}$ (S)
N-V	0.5	3.66 ± 0.67
N-V	1	3.47 ± 0.55
N-V	2	3.15 ± 0.44
HSA	0.5	4.30 ± 0.68
HSA	1	4.48 ± 0.83
N-V + HSA	0.5 + 0.5	3.49 ± 0.68
N-V + HSA	1 + 1	3.62 ± 0.56

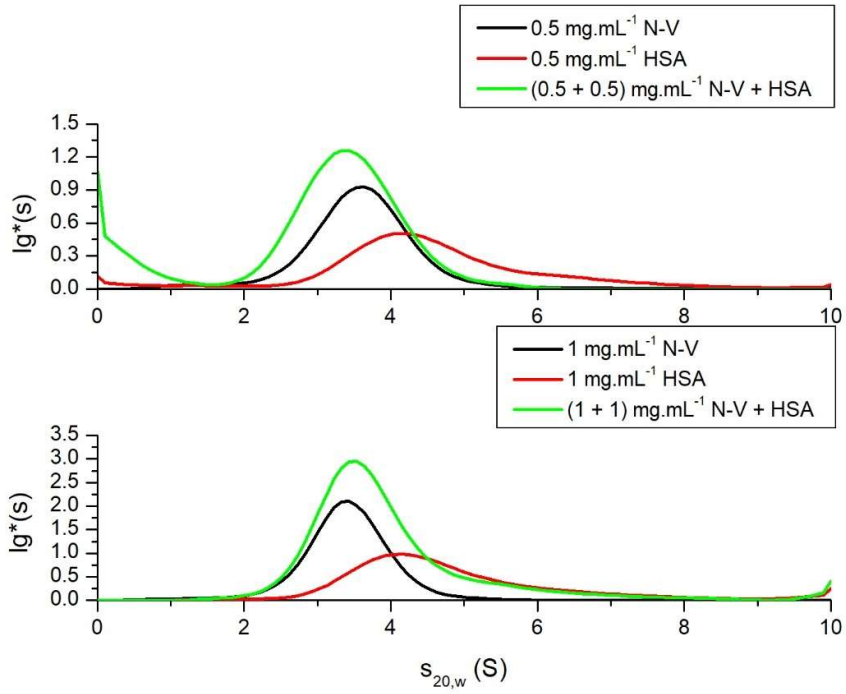


Figure 8.30 – Distribution of sedimentation coefficients of N-V and HSA, both alone and in combination, at 0.5 mg.mL^{-1} (upper) and 1 mg.mL^{-1} (lower).

Table 8-36 gives sedimentation coefficient values for N-V and fibrinogen, while the distributions are shown in Figure 8.31. The sedimentation coefficients for N-V and fibrinogen are different enough that it is possible to distinguish the distributions.

Table 8-36 – Summary of peak sedimentation coefficient values for N-V and fibrinogen.

Sample(s)	Concentration (mg.mL^{-1})	$s_{20,w}$ (S)
N-V	0.5	3.61 ± 0.65
N-V	1	3.49 ± 0.57
N-V	2	3.06 ± 0.40
Fibrinogen	0.5	7.75 ± 0.56
Fibrinogen	1	7.76 ± 0.59
N-V + fibrinogen peak 1	0.5 + 0.5	3.67 ± 0.69
N-V + fibrinogen peak 2	0.5 + 0.5	7.47 ± 0.49
N-V + fibrinogen peak 1	1 + 1	3.46 ± 0.51
N-V + fibrinogen peak 2	1 + 1	7.30 ± 0.38

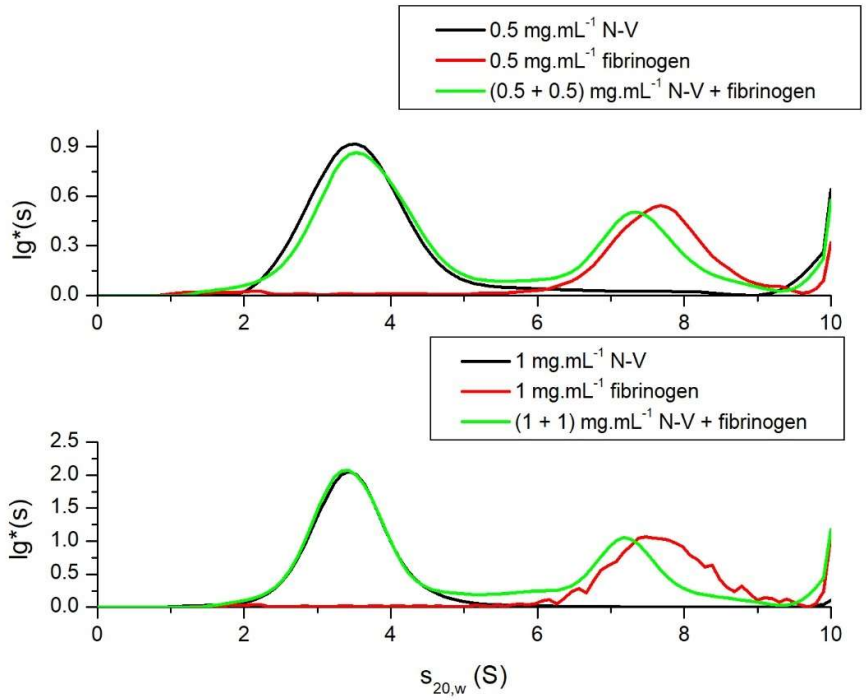


Figure 8.31 – Distribution of sedimentation coefficients of N-V and fibrinogen, both alone and in combination, at 0.5 mg.mL^{-1} (upper) and 1 mg.mL^{-1} (lower).

Table 8-37 gives sedimentation coefficient values for N-V and IgG1 Cri, while the distributions are shown in Figure 8.32. The sedimentation coefficients for N-V and IgG1 Cri are different enough that it is possible to distinguish the distributions.

Table 8-37 – Summary of peak sedimentation coefficient values for N-V and IgG1 Cri.

Sample(s)	Concentration (mg.mL^{-1})	$s_{20,w}$ (S)
N-V	0.5	3.65 ± 1.13
N-V	1	3.49 ± 0.94
IgG Cri	0.5	6.47 ± 0.79
IgG Cri	1	6.54 ± 0.89
N-V+ IgG Cri peak 1	0.5 + 0.5	3.59 ± 0.67
N-V+ IgG Cri peak 2	0.5 + 0.5	6.40 ± 0.74
N-V+ IgG Cri peak 1	1 + 1	3.46 ± 0.52
N-V+ IgG Cri peak 2	1 + 1	6.23 ± 0.76

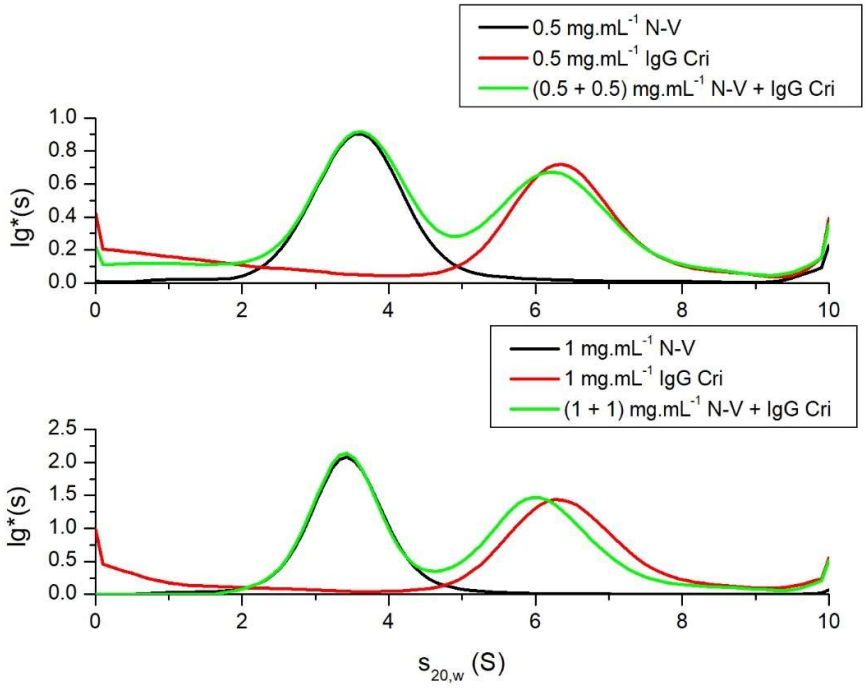


Figure 8.32 – Distribution of sedimentation coefficients of N-V and IgG1 Cri, both alone and in combination, at 0.5 mg.mL^{-1} (upper) and 1 mg.mL^{-1} (lower).

Table 8-38 gives sedimentation coefficient values for N-V and IgG1 Wid, while the distributions are shown in Figure 8.33. The sedimentation coefficients for N-V and IgG1 Wid are different enough that it is possible to distinguish the distributions.

Table 8-38 – Summary of peak sedimentation coefficient values for N-V and IgG1 Wid.

Sample(s)	Concentration (mg.mL^{-1})	$s_{20,w}$ (S)
N-V	0.5	3.65 ± 1.13
N-V	1	3.49 ± 0.94
IgG Wid	0.5	6.26 ± 0.75
IgG Wid	1	6.53 ± 0.86
N-V+ IgG Wid peak 1	0.5 + 0.5	3.59 ± 0.65
N-V+ IgG Wid peak 2	0.5 + 0.5	6.27 ± 0.74
N-V+ IgG Wid peak 1	1 + 1	3.47 ± 0.53
N-V+ IgG Wid peak 2	1 + 1	6.18 ± 0.74

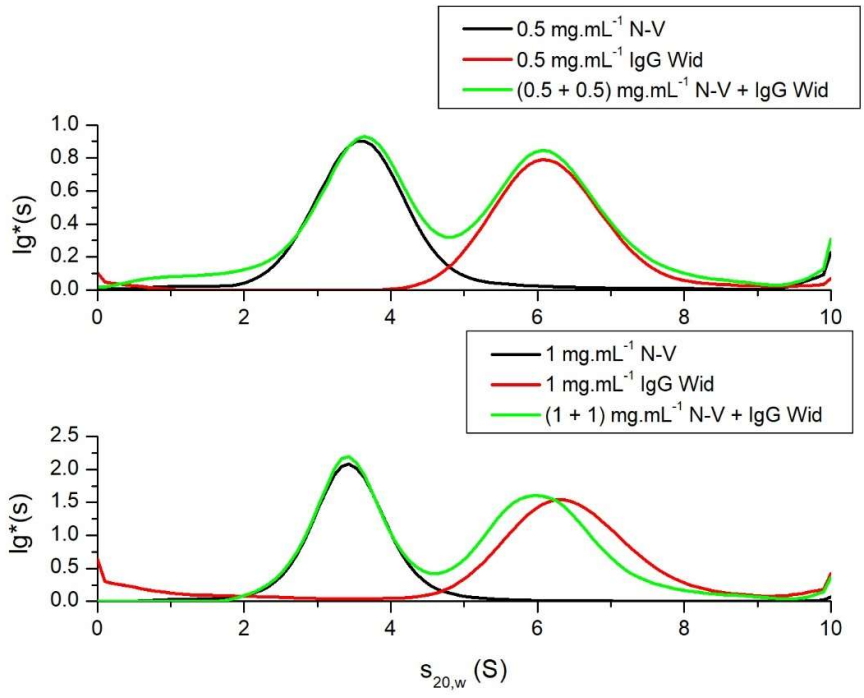


Figure 8.33 – Distribution of sedimentation coefficients of N-V and IgG1 Wid, both alone and in combination, at 0.5 mg.mL^{-1} (upper) and 1 mg.mL^{-1} (lower).

8.9 Sized GBS polysaccharide, serotype IA

8.9.1 Viscosity

As with the comparisons in previous sections, the error ranges allow a basic statistical comparison to be made between η_r values. This is summarised in Table 8-39. For S-IA combined with each protein, there is a slight increase in η_r, which in all case is statistically significant at the higher concentration but not at the lower concentration.

Table 8-39 – A summary of theoretical values for η_r and the actual values calculated using flow times for S-IA in combination with one of the proteins.

Components	[η] (mL.g^{-1})	c (mg.mL^{-1})	Theoretical η_r	Actual η_r
S-IA + BSA	48.7 ± 0.1	0.500	1.025 ± 0.001	1.029 ± 0.003
S-IA + BSA	48.7 ± 0.1	1.000	1.049 ± 0.002	1.064 ± 0.004
S-IA + HSA	48.7 ± 0.1	0.500	1.025 ± 0.001	1.027 ± 0.003
S-IA + HSA	48.7 ± 0.1	1.000	1.049 ± 0.002	1.072 ± 0.005
S-IA + fibrinogen	48.7 ± 0.1	0.500	1.025 ± 0.001	1.028 ± 0.005
S-IA + fibrinogen	48.7 ± 0.1	1.000	1.049 ± 0.002	1.075 ± 0.004

8.9.2 Sedimentation velocity

The values for each of the peaks in the sedimentation data are summarised in the tables below, while the distributions are given in the graphs.

Table 8-40 gives sedimentation coefficient values for S-IA and BSA, while the distributions are shown in Figure 8.34. As the sedimentation coefficients for S-IA and BSA are similar it is not possible to distinguish the distributions.

Table 8-40 – Summary of peak sedimentation coefficient values for S-IA and BSA.

Sample(s)	Concentration (mg.mL^{-1})	$s_{20,w}$ (S)
S-IA	0.5	2.68 ± 0.52
S-IA	1	2.56 ± 0.54
S-IA	2	1.57 ± 0.24
BSA	0.5	3.71 ± 0.77
BSA	1	3.75 ± 0.73
S-IA + BSA	0.5 + 0.5	3.06 ± 0.71
S-IA + BSA	1 + 1	2.97 ± 0.70

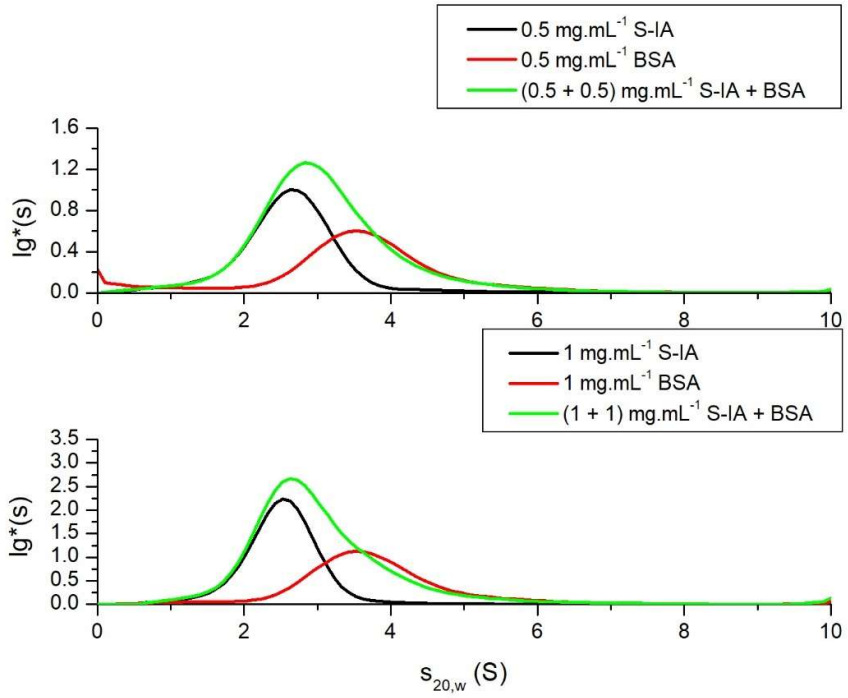


Figure 8.34 – Distribution of sedimentation coefficients of S-IA and BSA, both alone and in combination, at 0.5 mg.mL^{-1} (upper) and 1 mg.mL^{-1} (lower).

Table 8-41 gives sedimentation coefficient values for S-IA and HSA, while the distributions are shown in Figure 8.35. As the sedimentation coefficients for S-IA and HSA are similar it is not possible to distinguish the distributions.

Table 8-41 – Summary of peak sedimentation coefficient values for S-IA and HSA.

Sample(s)	Concentration (mg.mL^{-1})	$s_{20,w}$ (S)
S-IA	0.5	2.70 ± 0.53
S-IA	1	2.58 ± 0.43
S-IA	2	2.32 ± 0.39
HSA	0.5	3.71 ± 0.62
HSA	1	3.75 ± 0.65
S-IA + HSA	0.5 + 0.5	3.05 ± 0.68
S-IA + HSA	1 + 1	2.96 ± 0.67

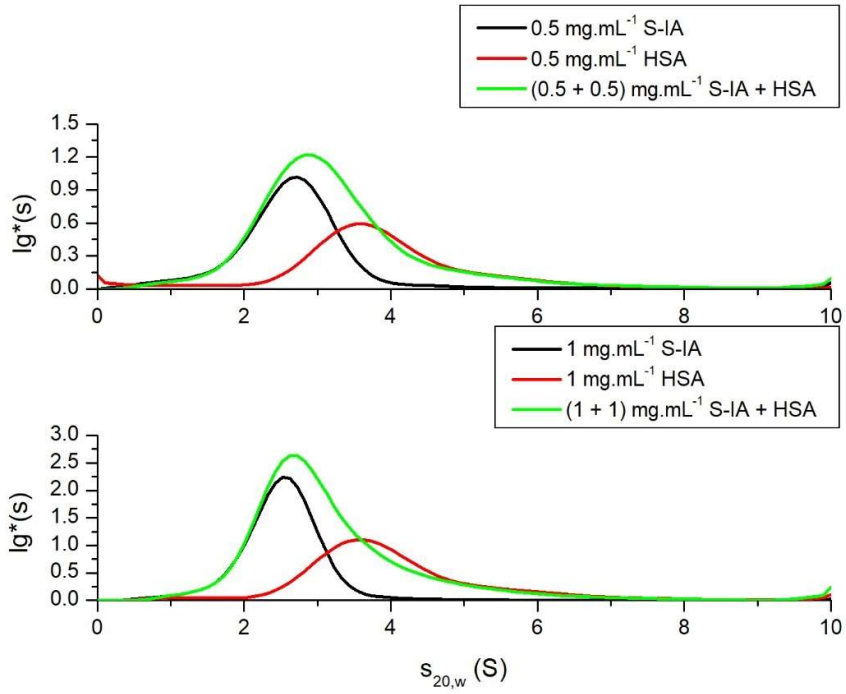


Figure 8.35 – Distribution of sedimentation coefficients of S-IA and HSA, both alone and in combination, at 0.5 mg.mL^{-1} (upper) and 1 mg.mL^{-1} (lower).

Table 8-42 gives sedimentation coefficient values for S-IA and fibrinogen, while the distributions are shown in Figure 8.36. The sedimentation coefficients for S-IA and fibrinogen are different enough that it is possible to distinguish the distributions.

Table 8-42 – Summary of peak sedimentation coefficient values for S-IA and fibrinogen.

Sample(s)	Concentration (mg.mL^{-1})	$s_{20,w}$ (S)
S-IA	0.5	2.66 ± 0.52
S-IA	1	2.55 ± 0.43
S-IA	2	2.35 ± 0.34
Fibrinogen	0.5	6.58 ± 0.58
Fibrinogen	1	6.55 ± 0.56
S-IA + fibrinogen peak 1	0.5 + 0.5	2.68 ± 0.53
S-IA + fibrinogen peak 2	0.5 + 0.5	6.39 ± 0.49
S-IA + fibrinogen peak 1	1 + 1	2.55 ± 0.47
S-IA + fibrinogen peak 2	1 + 1	6.20 ± 0.43

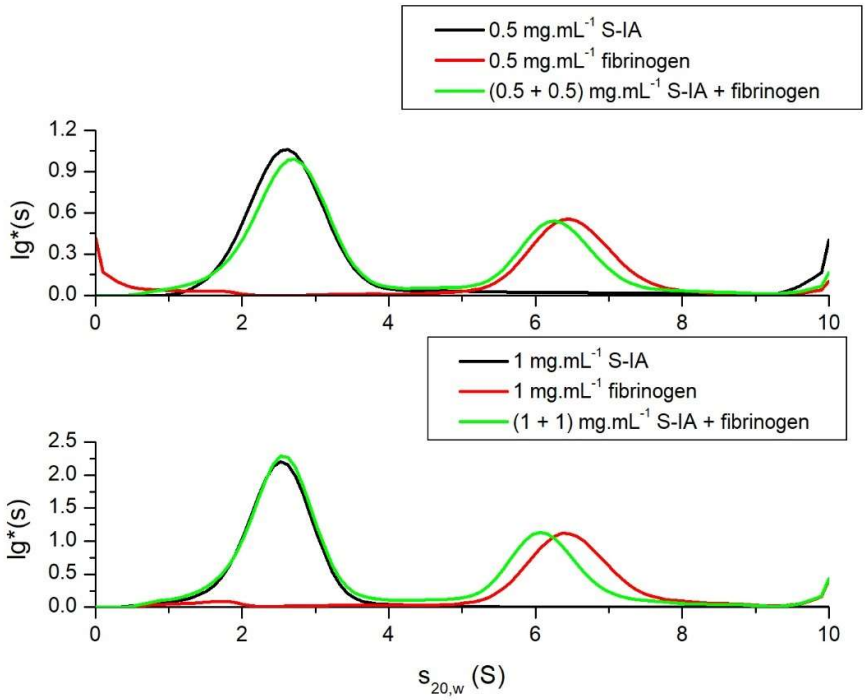


Figure 8.36 – Distribution of sedimentation coefficients of S-IA and fibrinogen, both alone and in combination, at 0.5 mg.mL^{-1} (upper) and 1 mg.mL^{-1} (lower).

Table 8-43 gives sedimentation coefficient values for S-IA and IgG1 Cri, while the distributions are shown in Figure 8.37. The sedimentation coefficients for S-IA and IgG1 Cri are different enough that it is possible to distinguish the distributions.

Table 8-43 – Summary of peak sedimentation coefficient values for S-IA and IgG1 Cri.

Sample(s)	Concentration (mg.mL^{-1})	$s_{20,w}$ (S)
S-IA	0.5	2.68 ± 0.90
S-IA	1	2.57 ± 0.81
IgG Cri	0.5	6.47 ± 0.79
IgG Cri	1	6.54 ± 0.89
S-IA+ IgG Cri peak 1	0.5 + 0.5	3.09 ± 0.62
S-IA+ IgG Cri peak 2	0.5 + 0.5	6.33 ± 0.71
S-IA+ IgG Cri peak 1	1 + 1	2.92 ± 0.60
S-IA+ IgG Cri peak 2	1 + 1	6.17 ± 0.77

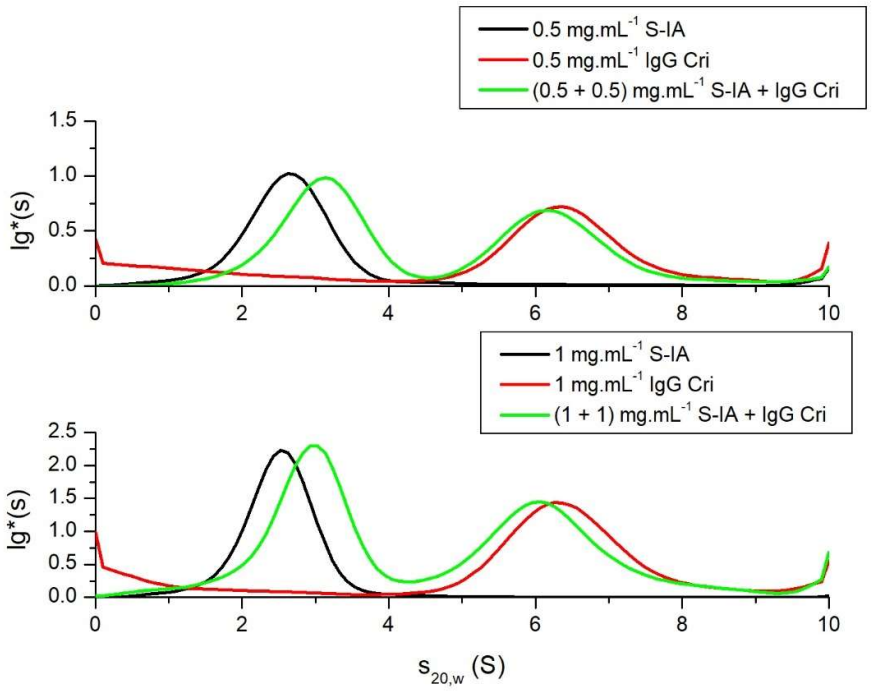


Figure 8.37 – Distribution of sedimentation coefficients of S-IA and IgG1 Cri, both alone and in combination, at 0.5 mg.mL^{-1} (upper) and 1 mg.mL^{-1} (lower).

Table 8-44 gives sedimentation coefficient values for S-IA and IgG1 Wid, while the distributions are shown in Figure 8.38. The sedimentation coefficients for S-IA and IgG1 Wid are different enough that it is possible to distinguish the distributions.

Table 8-44 – Summary of peak sedimentation coefficient values for S-IA and IgG1 Wid.

Sample(s)	Concentration (mg.mL^{-1})	$s_{20,w}$ (S)
S-IA	0.5	2.68 ± 0.90
S-IA	1	2.57 ± 0.81
IgG Wid	0.5	6.26 ± 0.75
IgG Wid	1	6.53 ± 0.86
S-IA+ IgG Wid peak 1	0.5 + 0.5	3.16 ± 0.61
S-IA+ IgG Wid peak 2	0.5 + 0.5	6.27 ± 0.75
S-IA+ IgG Wid peak 1	1 + 1	2.99 ± 0.50
S-IA+ IgG Wid peak 2	1 + 1	6.21 ± 0.82

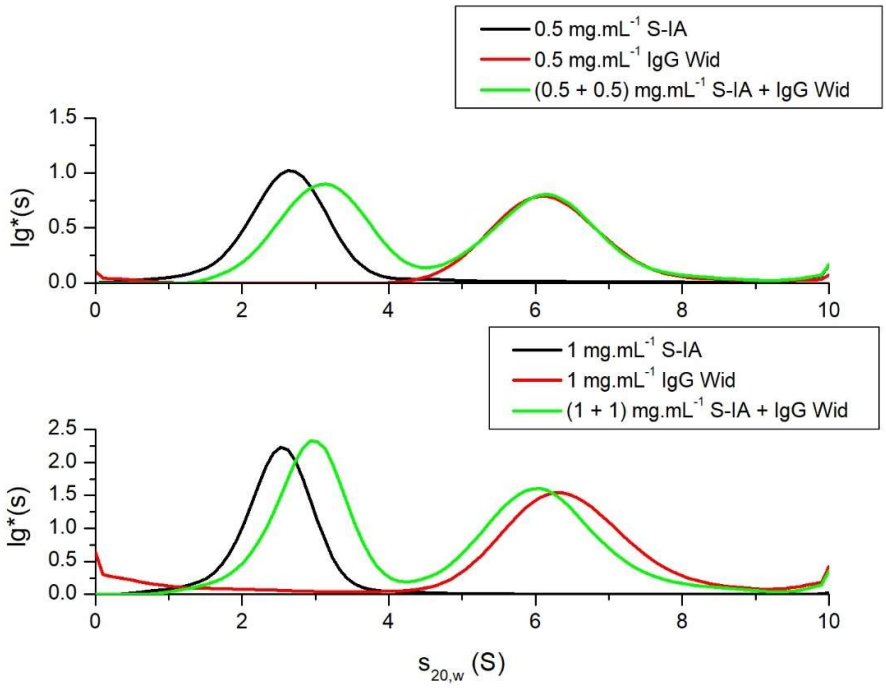


Figure 8.38 – Distribution of sedimentation coefficients of S-IA and IgG1 Wid, both alone and in combination, at 0.5 mg.mL^{-1} (upper) and 1 mg.mL^{-1} (lower).

8.10 Sized GBS polysaccharide, serotype IB

8.10.1 Viscosity

As with the comparisons in previous sections, the error ranges allow a basic statistical comparison to be made between η_r values. This is summarised in Table 8-45. For S-IB combined with each protein, there is a statistically significant increase in η_r at the higher concentration. A significant increase is also seen when combined with fibrinogen, but when combined with the serum albumins at low concentration there is a small decrease, although this is not statistically significant.

Table 8-45 – A summary of theoretical values for η_r and the actual values calculated using flow times for S-IB in combination with one of the proteins.

Components	[η] (mL.g^{-1})	c (mg.mL^{-1})	Theoretical η_r	Actual η_r
S-IB + BSA	62.1 ± 0.1	0.500	1.032 ± 0.002	1.031 ± 0.003
S-IB + BSA	62.1 ± 0.1	1.000	1.063 ± 0.002	1.084 ± 0.003
S-IB + HSA	62.1 ± 0.1	0.500	1.032 ± 0.002	1.031 ± 0.002
S-IB + HSA	62.1 ± 0.1	1.000	1.063 ± 0.002	1.078 ± 0.002
S-IB + fibrinogen	62.1 ± 0.1	0.500	1.032 ± 0.002	1.047 ± 0.006
S-IB + fibrinogen	62.1 ± 0.1	1.000	1.063 ± 0.002	1.085 ± 0.005

8.10.2 Sedimentation velocity

The values for each of the peaks in the sedimentation data are summarised in the tables below, while the distributions are given in the graphs.

Table 8-46 gives sedimentation coefficient values for S-IB and BSA, while the distributions are shown in Figure 8.39. As the sedimentation coefficients for S-IB and BSA are similar it is not possible to distinguish the distributions.

Table 8-46 – Summary of peak sedimentation coefficient values for S-IB and BSA.

Sample(s)	Concentration (mg.mL^{-1})	$s_{20,w}$ (S)
S-IB	0.5	2.72 ± 0.46
S-IB	1	2.58 ± 0.42
S-IB	2	2.34 ± 0.31
BSA	0.5	3.72 ± 0.65
BSA	1	3.72 ± 0.67
S-IB + BSA	0.5 + 0.5	3.09 ± 0.72
S-IB + BSA	1 + 1	2.94 ± 0.66

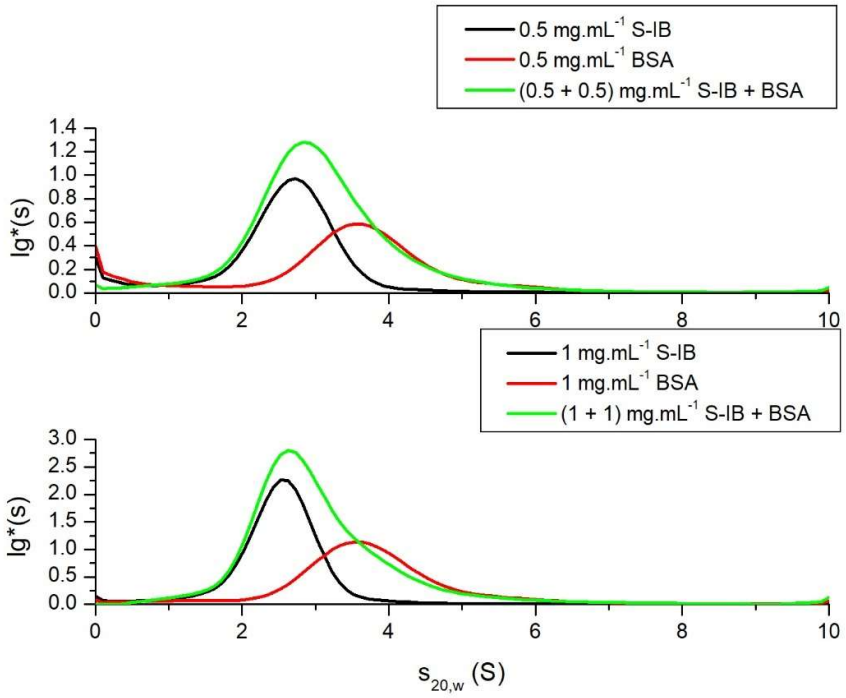


Figure 8.39 – Distribution of sedimentation coefficients of S-IB and BSA, both alone and in combination, at 0.5 mg.mL^{-1} (upper) and 1 mg.mL^{-1} (lower).

Table 8-47 gives sedimentation coefficient values for S-IB and HSA, while the distributions are shown in Figure 8.40. As the sedimentation coefficients for S-IB and HSA are similar it is not possible to distinguish the distributions.

Table 8-47 – Summary of peak sedimentation coefficient values for S-IB and HSA.

Sample(s)	Concentration (mg.mL^{-1})	$s_{20,w}$ (S)
S-IB	0.5	2.69 ± 0.49
S-IB	1	2.57 ± 0.41
S-IB	2	2.33 ± 0.31
HSA	0.5	3.77 ± 0.70
HSA	1	3.73 ± 0.65
S-IB + HSA	0.5 + 0.5	3.07 ± 0.68
S-IB + HSA	1 + 1	2.91 ± 0.64

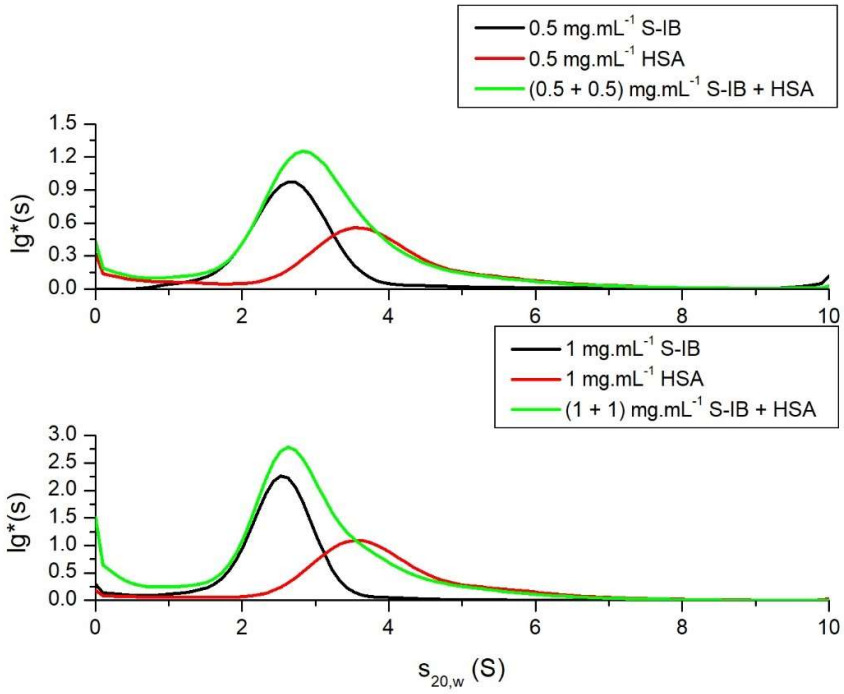


Figure 8.40 – Distribution of sedimentation coefficients of S-IB and HSA, both alone and in combination, at 0.5 mg.mL^{-1} (upper) and 1 mg.mL^{-1} (lower).

Table 8-48 gives sedimentation coefficient values for S-IB and fibrinogen, while the distributions are shown in Figure 8.41. The sedimentation coefficients for S-IB and fibrinogen are different enough that it is possible to distinguish the distributions.

Table 8-48 – Summary of peak sedimentation coefficient values for S-IB and fibrinogen.

Sample(s)	Concentration (mg.mL^{-1})	$s_{20,w}$ (S)
S-IB	0.5	2.67 ± 0.52
S-IB	1	2.57 ± 0.43
S-IB	2	2.32 ± 0.38
Fibrinogen	0.5	6.59 ± 0.63
Fibrinogen	1	6.64 ± 0.62
S-IB + fibrinogen peak 1	0.5 + 0.5	2.70 ± 0.50
S-IB + fibrinogen peak 2	0.5 + 0.5	6.46 ± 0.43
S-IB + fibrinogen peak 1	1 + 1	2.59 ± 0.45
S-IB + fibrinogen peak 2	1 + 1	6.33 ± 0.39

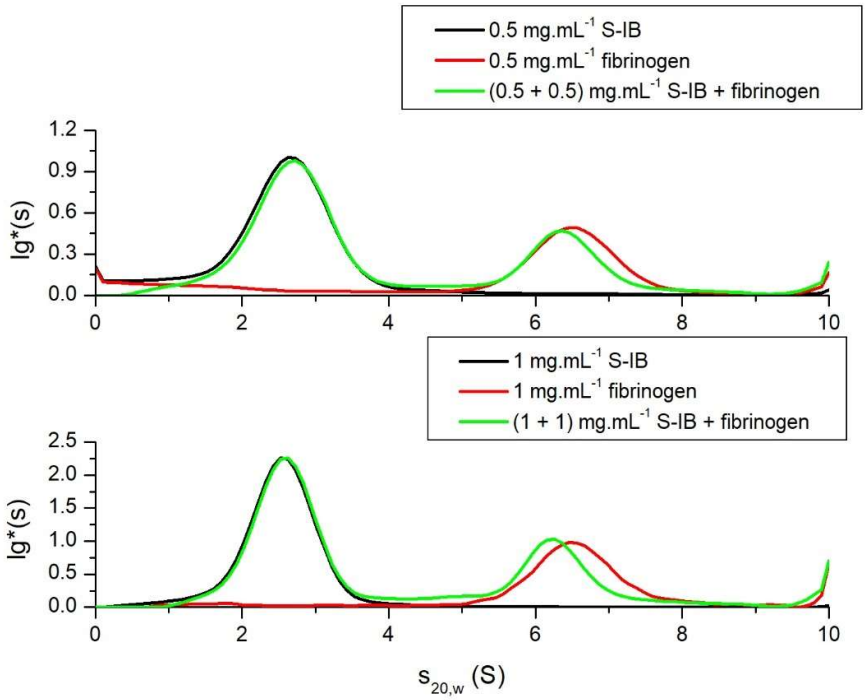


Figure 8.41 – Distribution of sedimentation coefficients of S-IB and fibrinogen, both alone and in combination, at 0.5 mg.mL^{-1} (upper) and 1 mg.mL^{-1} (lower).

Table 8-49 gives sedimentation coefficient values for S-IB and IgG1 Cri, while the distributions are shown in Figure 8.42. The sedimentation coefficients for S-IB and IgG1 Cri are different enough that it is possible to distinguish the distributions.

Table 8-49 – Summary of peak sedimentation coefficient values for S-IB and IgG1 Cri.

Sample(s)	Concentration (mg.mL^{-1})	$s_{20,w}$ (S)
S-IB	0.5	2.69 ± 0.85
S-IB	1	2.58 ± 0.73
Fibrinogen	0.5	6.47 ± 0.79
Fibrinogen	1	6.54 ± 0.89
S-IB+ IgG Cri peak 1	0.5 + 0.5	3.10 ± 0.57
S-IB+ IgG Cri peak 2	0.5 + 0.5	6.28 ± 0.77
S-IB+ IgG Cri peak 1	1 + 1	2.99 ± 0.54
S-IB+ IgG Cri peak 2	1 + 1	6.21 ± 0.74

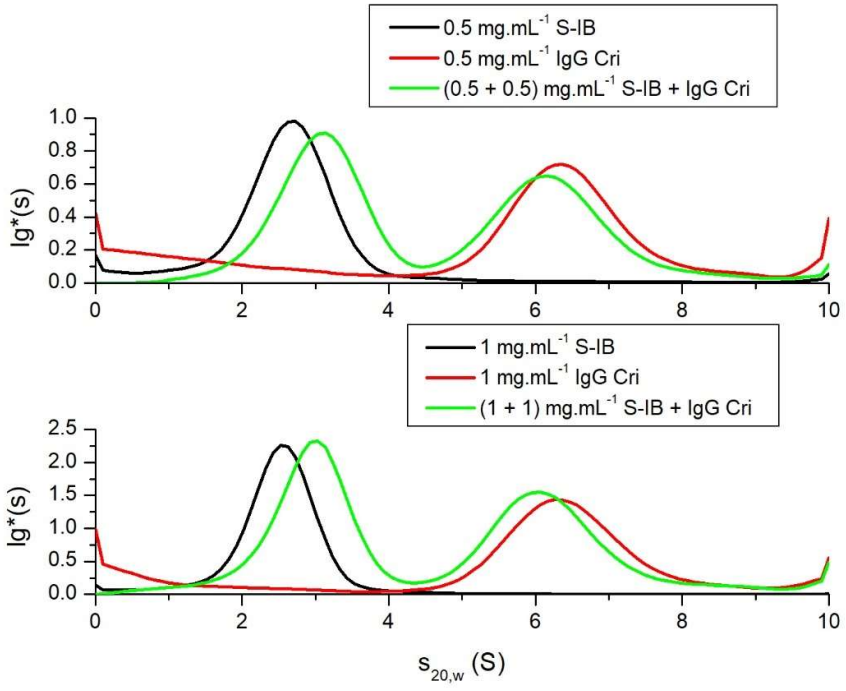


Figure 8.42 – Distribution of sedimentation coefficients of S-IB and IgG1 Cri, both alone and in combination, at 0.5 mg.mL^{-1} (upper) and 1 mg.mL^{-1} (lower).

Table 8-50 gives sedimentation coefficient values for S-IB and IgG1 Wid, while the distributions are shown in Figure 8.43. The sedimentation coefficients for S-IB and IgG1 Wid are different enough that it is possible to distinguish the distributions.

Table 8-50 – Summary of peak sedimentation coefficient values for S-IB and IgG1 Wid.

Sample(s)	Concentration (mg.mL^{-1})	$s_{20,w}$ (S)
S-IB	0.5	2.69 ± 0.85
S-IB	1	2.58 ± 0.73
IgG Wid	0.5	6.26 ± 0.75
IgG Wid	1	6.53 ± 0.86
S-IB+ IgG Wid peak 1	0.5 + 0.5	3.16 ± 0.61
S-IB+ IgG Wid peak 2	0.5 + 0.5	6.27 ± 0.75
S-IB+ IgG Wid peak 1	1 + 1	2.98 ± 0.49
S-IB+ IgG Wid peak 2	1 + 1	6.12 ± 0.73

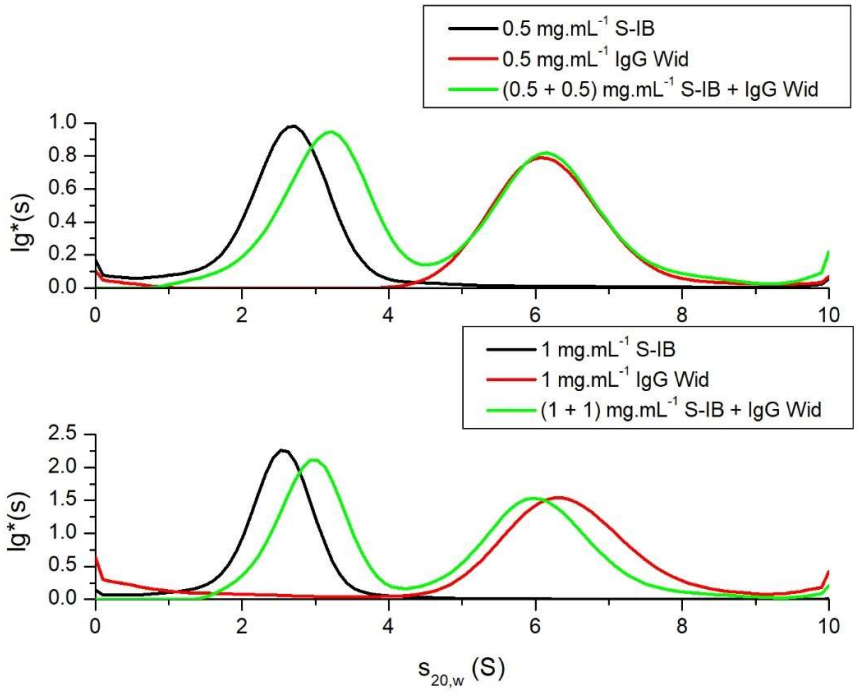


Figure 8.43 – Distribution of sedimentation coefficients of S-IB and IgG1 Wid, both alone and in combination, at 0.5 mg.mL^{-1} (upper) and 1 mg.mL^{-1} (lower).

8.11 Sized GBS polysaccharide, serotype II

8.11.1 Viscosity

As with the comparisons in previous sections, the error ranges allow a basic statistical comparison to be made between η_r values. This is summarised in Table 8-51. For S-II combined with each protein, there is a slight reduction in η_r, except when combined with fibrinogen at the higher concentration, and which in all cases is statistically significant except when combined with fibrinogen.

Table 8-51 – A summary of theoretical values for η_r and the actual values calculated using flow times for S-II in combination with one of the proteins.

Components	[η] (mL.g^{-1})	c (mg.mL^{-1})	Theoretical η_r	Actual η_r
S-II + BSA	55.0 ± 0.7	0.500	1.028 ± 0.009	1.015 ± 0.002
S-II + BSA	55.0 ± 0.7	1.000	1.056 ± 0.009	1.042 ± 0.001
S-II + HSA	55.0 ± 0.7	0.500	1.028 ± 0.009	1.017 ± 0.001
S-II + HSA	55.0 ± 0.7	1.000	1.056 ± 0.009	1.045 ± 0.002
S-II + fibrinogen	55.0 ± 0.7	0.500	1.028 ± 0.009	1.019 ± 0.003
S-II + fibrinogen	55.0 ± 0.7	1.000	1.056 ± 0.009	1.064 ± 0.005

8.11.2 Sedimentation velocity

The values for each of the peaks in the sedimentation data are summarised in the tables below, while the distributions are given in the graphs.

Table 8-52 gives sedimentation coefficient values for S-II and BSA, while the distributions are shown in Figure 8.44. The sedimentation coefficients for S-II and BSA are different enough that it is possible to distinguish the distributions.

Table 8-52 – Summary of peak sedimentation coefficient values for S-II and BSA.

Sample(s)	Concentration (mg.mL^{-1})	$s_{20,w}$ (S)
S-II	0.5	4.41 ± 1.02
S-II	1	4.23 ± 0.84
S-II	2	3.88 ± 0.69
BSA	0.5	4.30 ± 0.71
BSA	1	4.36 ± 0.78
S-II + BSA	0.5 + 0.5	4.30 ± 0.83
S-II + BSA	1 + 1	4.14 ± 0.78

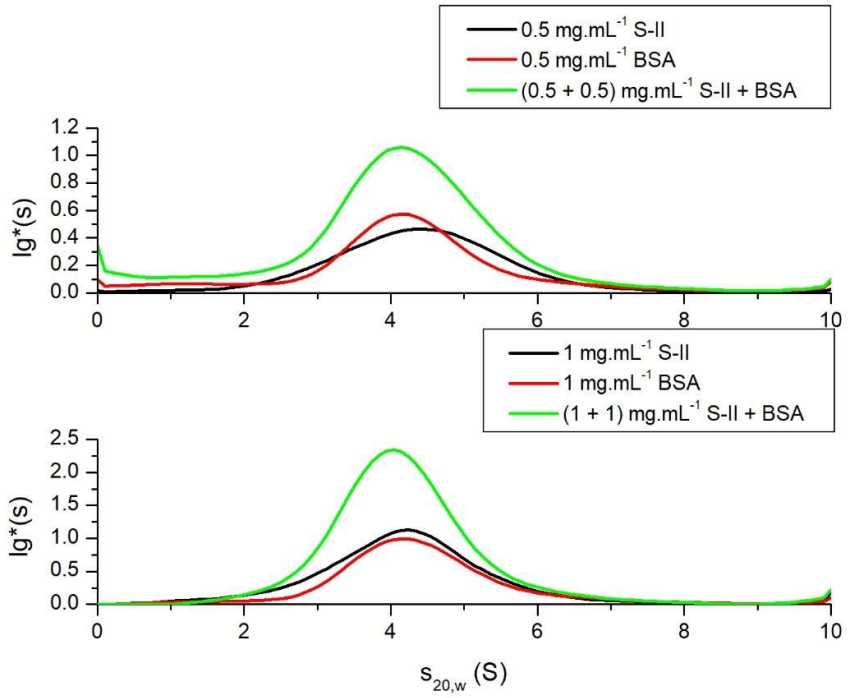


Figure 8.44 – Distribution of sedimentation coefficients of S-II and BSA, both alone and in combination, at 0.5 mg.mL^{-1} (upper) and 1 mg.mL^{-1} (lower).

Table 8-53 gives sedimentation coefficient values for S-II and HSA, while the distributions are shown in Figure 8.45. As the sedimentation coefficients for S-II and HSA are similar it is not possible to distinguish the distributions.

Table 8-53 – Summary of peak sedimentation coefficient values for S-II and HSA.

Sample(s)	Concentration (mg.mL^{-1})	$s_{20,w}$ (S)
S-II	0.5	4.41 ± 0.99
S-II	1	4.21 ± 0.88
S-II	2	3.87 ± 0.69
HSA	0.5	4.33 ± 0.67
HSA	1	4.29 ± 0.70
S-II + HSA	0.5 + 0.5	4.36 ± 0.89
S-II + HSA	1 + 1	4.29 ± 0.79

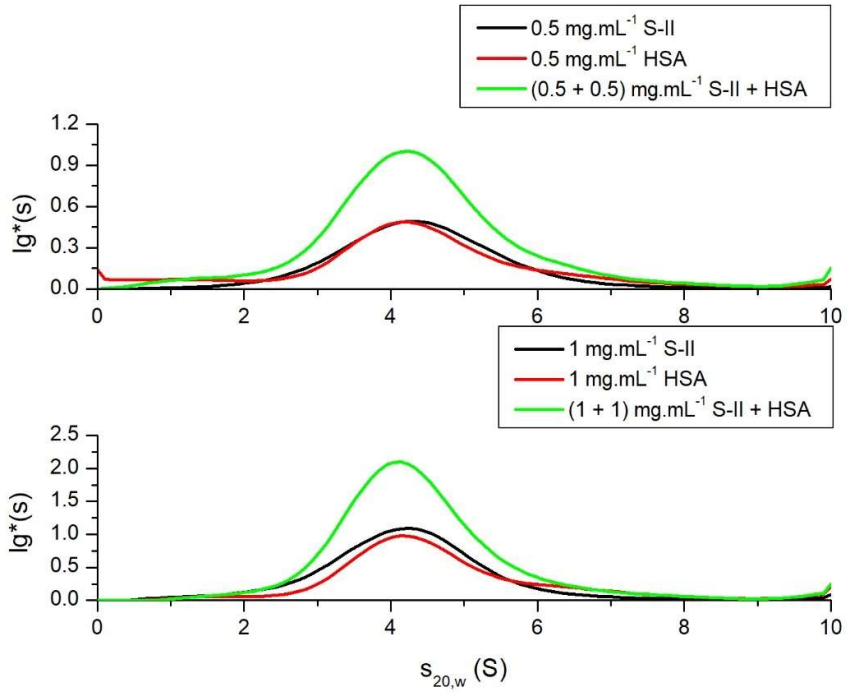


Figure 8.45 – Distribution of sedimentation coefficients of S-II and HSA, both alone and in combination, at 0.5 mg.mL^{-1} (upper) and 1 mg.mL^{-1} (lower).

Table 8-54 gives sedimentation coefficient values for S-II and fibrinogen, while the distributions are shown in Figure 8.46. The sedimentation coefficients for S-II and fibrinogen are different enough that it is possible to distinguish the distributions.

Table 8-54 – Summary of peak sedimentation coefficient values for S-II and fibrinogen.

Sample(s)	Concentration (mg.mL^{-1})	$s_{20,w}$ (S)
S-II	0.5	4.40 ± 0.97
S-II	1	4.18 ± 0.87
S-II	2	3.87 ± 0.69
Fibrinogen	0.5	7.75 ± 0.63
Fibrinogen	1	7.43 ± 0.64
S-II + fibrinogen peak 1	0.5 + 0.5	4.37 ± 0.85
S-II + fibrinogen peak 2	0.5 + 0.5	7.41 ± 0.60
S-II + fibrinogen peak 1	1 + 1	4.25 ± 0.78
S-II + fibrinogen peak 2	1 + 1	7.21 ± 0.60

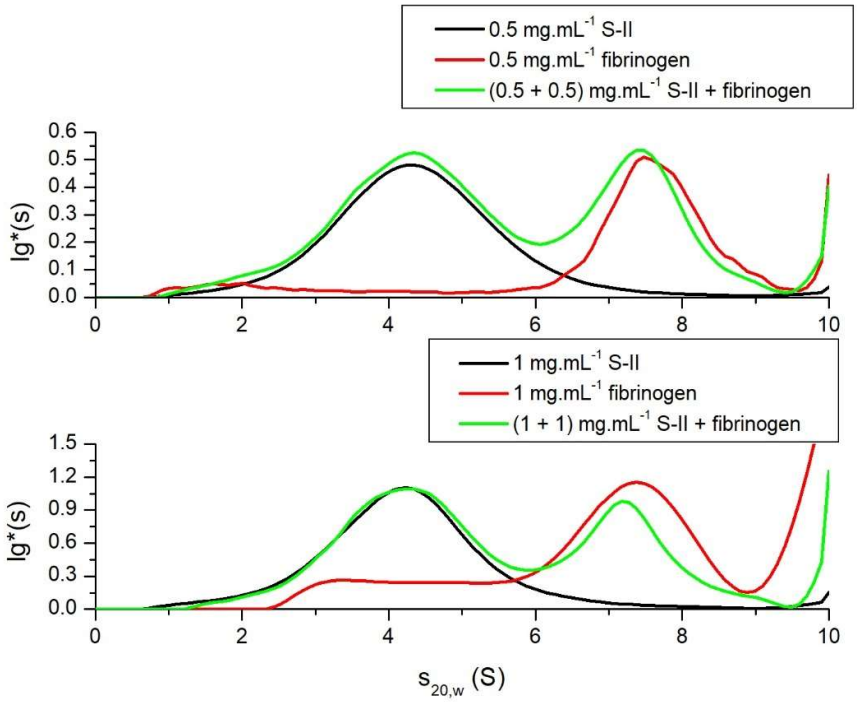


Figure 8.46 – Distribution of sedimentation coefficients of S-II and fibrinogen, both alone and in combination, at 0.5 mg.mL^{-1} (upper) and 1 mg.mL^{-1} (lower).

Table 8-55 gives sedimentation coefficient values for S-II and IgG1 Cri, while the distributions are shown in Figure 8.47. The sedimentation coefficients for S-II and IgG1 Cri are different enough that it is possible to distinguish the distributions.

Table 8-55 – Summary of peak sedimentation coefficient values for S-II and IgG1 Cri.

Sample(s)	Concentration (mg.mL^{-1})	$s_{20,w}$ (S)
S-II	0.5	4.41 ± 1.72
S-II	1	4.21 ± 1.50
IgG Cri	0.5	6.47 ± 0.79
IgG Cri	1	6.54 ± 0.89
S-II + IgG Cri peak 1	0.5 + 0.5	3.98 ± 0.78
S-II + IgG Cri peak 2	0.5 + 0.5	6.30 ± 0.70
S-II + IgG Cri peak 1	1 + 1	4.01 ± 0.66
S-II + IgG Cri peak 2	1 + 1	6.17 ± 0.70

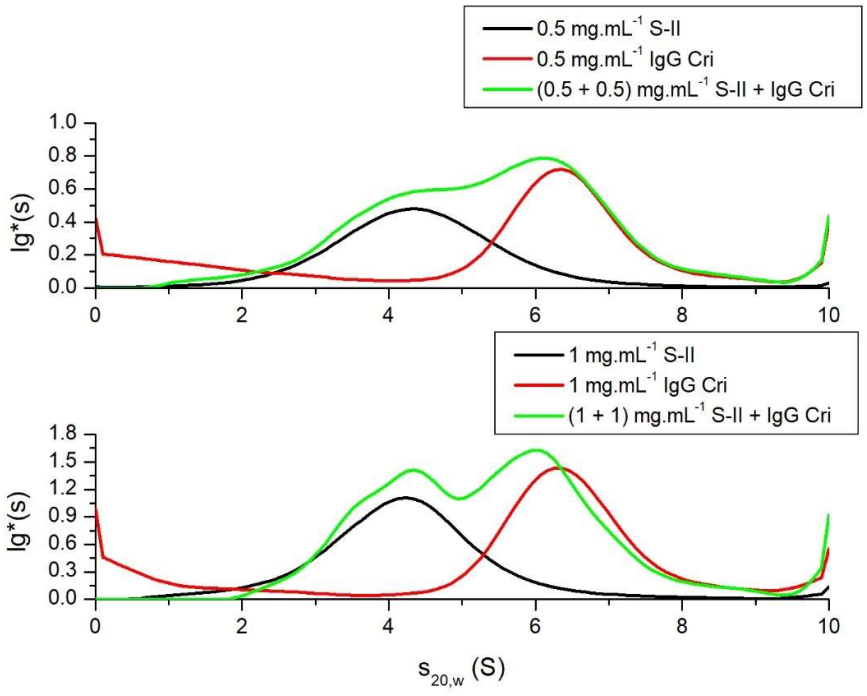


Figure 8.47 – Distribution of sedimentation coefficients of S-II and IgG1 Cri, both alone and in combination, at 0.5 mg.mL^{-1} (upper) and 1 mg.mL^{-1} (lower).

Table 8-56 gives sedimentation coefficient values for S-II and IgG1 Wid, while the distributions are shown in Figure 8.48. The sedimentation coefficients for S-II and IgG1 Wid are different enough that it is possible to distinguish the distributions.

Table 8-56 – Summary of peak sedimentation coefficient values for S-II and IgG1 Wid.

Sample(s)	Concentration (mg.mL^{-1})	$s_{20,w}$ (S)
S-II	0.5	4.41 ± 1.72
S-II	1	4.21 ± 1.50
IgG Wid	0.5	6.26 ± 0.75
IgG Wid	1	6.53 ± 0.86
S-II + IgG Wid peak 1	0.5 + 0.5	4.08 ± 0.68
S-II + IgG Wid peak 2	0.5 + 0.5	6.14 ± 0.72
S-II + IgG Wid peak 1	1 + 1	3.98 ± 0.62
S-II + IgG Wid peak 2	1 + 1	6.24 ± 0.82

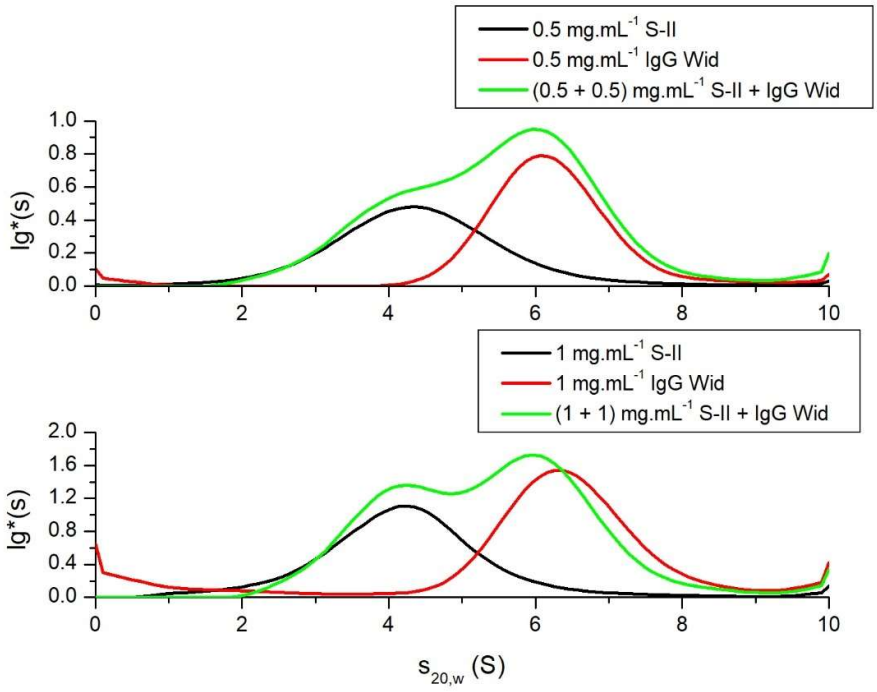


Figure 8.48 – Distribution of sedimentation coefficients of S-II and IgG1 Wid, both alone and in combination, at 0.5 mg.mL^{-1} (upper) and 1 mg.mL^{-1} (lower).

8.12 Summary

Table 8-57 summarises the data obtained from analysing viscosity, while also adding the percentage differences. No such table is presented for sedimentation velocity analysis, as in

each case the curve produced by the combination of protein and polysaccharide clearly mirrors the combination of the curves from the two constituent parts.

Table 8-57 - Summary of data found when testing the change in viscosity after combining each polysaccharide with a blood protein. Percentage change is also given.

State	Serotype	Protein	Lower concentration			Higher concentration		
			Theoretical η_r	Actual η_r	Percentage difference	Theoretical η_r	Actual η_r	Percentage difference
Native	IA	BSA	1.112 ± 0.008	1.093 ± 0.000	-1.79	1.232 ± 0.009	1.215 ± 0.000	-1.38
		HSA	1.112 ± 0.008	1.091 ± 0.000	-1.91	1.232 ± 0.009	1.212 ± 0.000	-1.59
		Fibrinogen	1.068 ± 0.007	1.063 ± 0.001	-0.40	1.138 ± 0.008	1.138 ± 0.001	+0.02
	IB	BSA	1.069 ± 0.000	1.062 ± 0.000	-0.71	1.141 ± 0.000	1.135 ± 0.000	-0.59
		HSA	1.069 ± 0.000	1.061 ± 0.002	-0.79	1.141 ± 0.000	1.134 ± 0.001	-0.62
		Fibrinogen	1.053 ± 0.000	1.05 ± 0.002	-0.24	1.107 ± 0.000	1.114 ± 0.003	+0.65
	II	BSA	1.064 ± 0.005	1.093 ± 0.000	+2.64	1.131 ± 0.005	1.215 ± 0.000	+7.41
		HSA	1.064 ± 0.005	1.091 ± 0.000	+2.50	1.131 ± 0.005	1.212 ± 0.000	+7.17
		Fibrinogen	1.050 ± 0.005	1.063 ± 0.001	+1.24	1.102 ± 0.005	1.138 ± 0.001	+3.28
	III	BSA	1.015 ± 0.003	1.021 ± 0.000	+0.56	1.027 ± 0.003	1.048 ± 0.000	+2.05
		HSA	1.015 ± 0.003	1.023 ± 0.000	+0.74	1.027 ± 0.003	1.047 ± 0.000	+1.93
		Fibrinogen	1.014 ± 0.003	1.025 ± 0.002	+1.12	1.023 ± 0.003	1.035 ± 0.001	+1.19
	IV	BSA	1.033 ± 0.008	1.028 ± 0.000	-0.53	1.066 ± 0.008	1.06 ± 0.000	-0.59
		HSA	1.033 ± 0.008	1.026 ± 0.000	-0.74	1.066 ± 0.008	1.061 ± 0.000	-0.52
		Fibrinogen	1.033 ± 0.008	1.037 ± 0.002	+0.36	1.066 ± 0.008	1.087 ± 0.009	+1.94
	V	BSA	1.042 ± 0.009	1.043 ± 0.001	+0.18	1.084 ± 0.009	1.106 ± 0.004	+2.09
		HSA	1.042 ± 0.009	1.035 ± 0.001	-0.61	1.084 ± 0.009	1.111 ± 0.007	+2.56
		Fibrinogen	1.042 ± 0.009	1.056 ± 0.004	+1.38	1.084 ± 0.009	1.103 ± 0.002	+1.83
Sized	IA	BSA	1.025 ± 0.001	1.029 ± 0.003	+0.32	1.049 ± 0.002	1.064 ± 0.004	+1.35
		HSA	1.025 ± 0.001	1.027 ± 0.003	+0.15	1.049 ± 0.002	1.072 ± 0.005	+2.14
		Fibrinogen	1.025 ± 0.001	1.028 ± 0.005	+0.20	1.049 ± 0.002	1.075 ± 0.004	+2.46
	IB	BSA	1.032 ± 0.002	1.031 ± 0.003	-0.12	1.063 ± 0.002	1.084 ± 0.003	+1.94
		HSA	1.032 ± 0.002	1.031 ± 0.002	-0.04	1.063 ± 0.002	1.078 ± 0.002	+1.42
		Fibrinogen	1.032 ± 0.002	1.047 ± 0.006	+1.52	1.063 ± 0.002	1.085 ± 0.005	+2.07
	II	BSA	1.028 ± 0.009	1.015 ± 0.002	-1.33	1.056 ± 0.009	1.042 ± 0.001	-1.27
		HSA	1.028 ± 0.009	1.017 ± 0.001	-1.06	1.056 ± 0.009	1.045 ± 0.002	-1.00
		Fibrinogen	1.028 ± 0.009	1.019 ± 0.003	-0.90	1.056 ± 0.009	1.064 ± 0.005	+0.78

8.13 Discussion

For most of the polysaccharides tested, a very slight decrease in relative viscosity is seen after mixing with the proteins. This suggests that the value seen is an average viscosity of the polysaccharide and protein molecules that has been weighted heavily towards the value for the polysaccharide rather than the protein. This is likely due to the proteins being relatively compact, globular structures, while the polysaccharides have a more extended conformation.

Similarly, there does not appear to be a major change in the sedimentation coefficient of the polysaccharides or proteins when they are mixed. There is an unfortunate difficulty that for both BSA and HSA, it was not possible to distinguish between the peaks for most molecules due to their similar behaviours when sedimenting. However, despite not seeing distinct peaks when they are mixed there is still no change in the peak position, indicating no change in sedimentation coefficient and thus no interaction.

The clearest indication that there has been no interaction comes from the sedimentation coefficient distribution graphs. When assessing the sedimentation coefficients, there are two possible outcomes. If the two molecules associate, then an additional peak would be seen when the two components are combined at a higher sedimentation coefficient. If the interaction between the two molecules causes the molecules to break down, then additional smaller peaks would be seen. If however there is no interaction then the results would appear as if the distribution for the individual components have simply been added together. In all cases, the distribution of sedimentation coefficients align almost perfectly with the addition of the distribution formed by the individual components. They give either two peaks if the sedimentation coefficients are very different, or only one if they are similar, but with a much greater intensity.

In some cases there is a slight alteration in the exact position of some peaks, notably in Figure 8.6, 8.11, 8.26, 8.31, 8.36 and 8.41. In all these cases, there is a peak for fibrinogen at a notably larger sedimentation coefficient than its respective polysaccharide, but when the two molecules are combined the sedimentation coefficient is decreased slightly. This is a good illustration of the Johnston-Ogston effect [261]. In essence, the molecule with a larger sedimentation coefficient sediments more rapidly, but does so though a more complex mixture of molecules. This mixture increases friction and so the observed sedimentation coefficient is lower than expected. The molecule with a lower sedimentation coefficient

sediments more slowly, and thus there is less material present to cause friction, and so its sedimentation coefficient is more comparable to its usual value. As the sedimentation coefficients for the polysaccharides were not measured directly and instead averages were used when assessing the interactions with immunoglobulin, these samples cannot be used to illustrate the Johnston-Ogston effect.

It should be noted that these experiments were all performed under standard conditions rather than physiological conditions. It would be beneficial for further work to assess the ability of the vaccines to interact with real human blood under laboratory conditions. However, it is not possible to do this with the techniques studied as they rely on the transmission of light (to assess meniscus position in viscosity and the refractive index in the centrifuge). An alternative analysis of viscosity could be performed with a viscometer which does not measure optically. For example, a vibrational or rotational viscometer could be used to assess the alteration in shear rates due to the addition of the polysaccharide to a blood sample. A technique such as sodium dodecyl sulphate–polyacrylamide gel electrophoresis could potentially be used to assess whether the profile of a sample of blood was altered due to the presence of the polysaccharide. However, it is likely that the sodium dodecyl sulphate used would interfere with the ability of the proteins to associate with the polysaccharide as it unfolds and negatively charges the protein. If the binding of polysaccharide and protein were irreversible then the alteration of the bands visible on the gel could be assessed, and possibly identified precisely by western blotting. While with the available equipment it was not possible to safely use human serum, there could also be a possibility of using animal serum as an alternative model, or even physiological saline rather than the phosphate buffer used here.

9 Conclusions

In general, there was good agreement between techniques for baseline measurements, suggesting the hydrodynamic properties have been accurately measured. Exposure to the stresses used here (freeze thaw cycles, incubation at 20˚C, incubation at 37˚C) appeared to cause some alterations to physical properties, although as this did not occur consistently this may be due to inherent variability in techniques. This suggests that any such changes are extremely small, indicating overall that all samples are broadly stable.

Without knowledge of the production methods, it has not been possible in this work to suggest useful conclusions regarding the future production of vaccines. It does suggest that the sizing process has little impact on stability and can be used to process antigens to bring them into a similar size range prior to conjugation.

Had time allowed, additional tests could have been performed on samples. A look at the effects of incubation at 4°C in a fridge could have been undertaken as an additional assay of shelf life. It may also be useful to perform purity analysis on the samples provided. While the dialysis of samples should have removed many trace impurities, it is possible that larger molecules may still be present, and this could be assessed using a technique such as SDS-PAGE.

A major limitation given in all this work is the variation between experiments which occurred due to factors it was not possible to control. This could be accounted for by pinpointing these sources of error and including them in the calculated error values, which would allow more accurate determination of significant differences. It is possible that this would show that, in fact, there were very few true statistically significant differences in this work. Alternatively, analysis could have been performed differently to avoid the practice of testing multiple concentrations and extrapolating data. While it is useful to find the true value of a given parameter by extrapolating to zero concentration to correct for non-ideality, to understand

the stability of a sample it is only necessary to test if a given parameter at an arbitrary concentration has changed. Therefore, if only one specific concentration of each sample were analysed, it would be possible to take repeated measurements and average them to find the error, which may give a more accurate understanding of the variability of the techniques and allow true statistical analysis based on data ranges. Perhaps the most useful technique used in this work was sedimentation velocity, as it (inadvertently) allowed a genuine statistical test to be performed. However, going forward SEC-MALS would allow much more powerful analysis as it would be possible generate much larger datasets that can be analysed statistically.

As mentioned in section 3.1, a relatively small amount of CRM197 was available, meaning it was not possible to perform a complete set of baseline measurements, or any further testing after exposure to stress. If additional samples could be obtained, further characterisation and experimentation in the same manner as the tested polysaccharides would be an excellent continuation of this work.

As mentioned in section 4.10, there is a degradation of the protein carrier, but it is unclear if this will have an impact on the immunogenicity of a glycoconjugate. The same is also true of the samples exposed to stress: it is unknown the extent to which a partially damaged polysaccharide antigen remains immunogenic. To determine this, it could be interesting to assess the immunogenicity of a completed glycoconjugate after exposure to some mild stress that degrades any component. It is possible that a mildly degraded vaccine still remains immunogenic, indicating it has a much longer useful shelf-life, which would reduce waste and increase profits of pharmaceutical companies.

10 Bibliography

1. Lancefield, R.C., *A Serological Differentiation Of Human And Other Groups Of Hemolytic Streptococci.* The Journal of Experimental Medicine, 1933. **57**(4): p. 571-595.
2. Lancefield, R.C. and R. Hare, *The Serological Differentiation Of Pathogenic And Non-Pathogenic Strains Of Hemolytic Streptococci From Parturient Women.* 1935. **61**(3): p. 335-349.
3. Nocard, M. and R.J.A.I.P. Mollereau, *Sur une mammite contagieuse des vaches laitieres.* 1887. **1**: p. 109.
4. Fry, R.J.L., *Fatal Infections by Haemolytie Streptococcus Group B.* 1938: p. 199-201.
5. Ismail, A.Q., et al., *Cow's Milk and the Emergence of Group B Streptococcal Disease in Newborn Babies.* Neonatology, 2011. **100**(4): p. 404-408.
6. Sørensen, U.B., et al., *Emergence and global dissemination of host-specific Streptococcus agalactiae clones.* mBio, 2010. **1**(3).
7. Cieslewicz, M.J., et al., *Structural and Genetic Diversity of Group B Streptococcus Capsular Polysaccharides.* Infection and Immunity, 2005. **73**(5): p. 3096-3103.
8. Slotved, H.-C., et al., *Serotype IX, a Proposed New Streptococcus agalactiae Serotype.* Journal of Clinical Microbiology, 2007. **45**(9): p. 2929-2936.
9. Lin, S.M., et al., *Status of group B streptococcal vaccine development.* Clinical and Experimental Vaccine Research, 2018. **7**(1): p. 76-81.
10. Kieran, E., et al., *Group B streptococcus (GBS) colonisation among expectant Irish mothers.* Ir Med J, 1998. **91**(1): p. 21-2.
11. Hickman, M.E., et al., *Changing Epidemiology of Group B Streptococcal Colonization.* Pediatrics, 1999. **104**(2): p. 203-209.
12. Toniolo, C., et al., *Streptococcus agalactiae Capsule Polymer Length and Attachment Is Determined by the Proteins CpsABCD.* Journal of Biological Chemistry, 2015. **290**(15): p. 9521-9532.
13. Kuttel, M.M. and N. Ravenscroft, *Conformation and Cross-Protection in Group B Streptococcus Serotype III and Streptococcus pneumoniae Serotype 14: A Molecular Modeling Study.* Pharmaceuticals, 2019. **12**(1): p. 28.
14. Bliss, S.J., et al., *Group B Streptococcus Colonization in Male and Nonpregnant Female University Students: A Cross-Sectional Prevalence Study.* Clinical Infectious Diseases, 2002. **34**(2): p. 184-190.
15. Campbell, J.R., et al., *Group B streptococcal colonization and serotype-specific immunity in pregnant women at delivery.* Obstetrics & Gynecology, 2000. **96**(4): p. 498-503.
16. Spaetgens, R., et al., *Perinatal antibiotic usage and changes in colonization and resistance rates of group B streptococcus and other pathogens.* Obstetrics & Gynecology, 2002. **100**(3): p. 525-533.
17. Farley, M.M., et al., *A Population-Based Assessment of Invasive Disease Due to Group B Streptococcus in Nonpregnant Adults.* 1993. **328**(25): p. 1807-1811.
18. Edwards, M.S., et al., *Group B Streptococcal Colonization and Serotype-Specific Immunity in Healthy Elderly Persons.* Clinical Infectious Diseases, 2005. **40**(3): p. 352-357.
19. Gray, K.J., et al., *Group B Streptococcus and HIV Infection in Pregnant Women, Malawi, 2008–2010.* Emerging Infectious Diseases, 2011. **17**(10): p. 1932-1935.
20. Dillon, J.H.C., et al., *Anorectal and Vaginal Carriage of Group B Streptococci During Pregnancy.* The Journal of Infectious Diseases, 1982. **145**(6): p. 794-799.

21. Zaleznik, D.F., et al., *Invasive Disease Due to Group B Streptococcus in Pregnant Women and Neonates from Diverse Population Groups.* Clinical Infectious Diseases, 2000. **30**(2): p. 276-281.
22. Schuchat, A., *Group B streptococcus.* The Lancet, 1999. **353**(9146): p. 51-56.
23. Noya, F.J.D., et al., *Unusual Occurrence of an Epidemic of Type Ib/c Group B Streptococcal Sepsis in a Neonatal Intensive Care Unit.* The Journal of Infectious Diseases, 1987. **155**(6): p. 1135-1144.
24. Olver, W.J., et al., *Neonatal group B streptococcal disease associated with infected breast milk.* 2000. **83**(1): p. F48-F49.
25. Dinger, J., et al., *Breast milk transmission of group B streptococcal infection.* 2002. **21**(6): p. 567-568.
26. Lawn, J.E., S. Cousens, and J. Zupan, *4 million neonatal deaths: When? Where? Why?* The Lancet, 2005. **365**(9462): p. 891-900.
27. Berardi, A., et al., *Group B Streptococcus Late-Onset Disease: 2003–2010.* 2013.
28. Krohn, M.A., S.L. Hillier, and C.J. Baker, *Maternal Peripartum Complications Associated with Vaginal Group B Streptococci Colonization.* The Journal of Infectious Diseases, 1999. **179**(6): p. 1410-1415.
29. Anderson, B.L., et al., *Untreated asymptomatic group B streptococcal bacteriuria early in pregnancy and chorioamnionitis at delivery.* American Journal of Obstetrics and Gynecology, 2007. **196**(6): p. 524.e1-524.e5.
30. Phares, C.R., et al., *Epidemiology of invasive group b streptococcal disease in the united states, 1999-2005.* JAMA, 2008. **299**(17): p. 2056-2065.
31. Schuchat, A. and J.D. Wenger, *Epidemiology of Group B Streptococcal DiseaseRisk Factors, Prevention Strategies, and Vaccine Development.* Epidemiologic Reviews, 1994. **16**(2): p. 374-402.
32. Dauby, N., et al., *Increased Risk of Group B Streptococcus Invasive Infection in HIV-Exposed but Uninfected Infants: A Review of the Evidence and Possible Mechanisms.* Frontiers in Immunology, 2016. **7**: p. 505.
33. ANCONA, R.J., P. FERRIERI, and P.P. WILLIAMS, *Maternal factors that enhance the acquisition of group-B streptococci by newborn infants.* 1980. **13**(2): p. 273-280.
34. Regan, J.A., et al., *Colonization with group B streptococci in pregnancy and adverse outcome.* American Journal of Obstetrics and Gynecology, 1996. **174**(4): p. 1354-1360.
35. Valkenburg-Van Den Berg, A.W., et al., *Association between colonization with Group B Streptococcus and preterm delivery: A systematic review.* 2009. **88**(9): p. 958-967.
36. Thompson, M.J., et al., *Clinical recognition of meningococcal disease in children and adolescents.* The Lancet, 2006. **367**(9508): p. 397-403.
37. Aird, W.C., *The role of the endothelium in severe sepsis and multiple organ dysfunction syndrome.* Blood, The Journal of the American Society of Hematology, 2003. **101**(10): p. 3765-3777.
38. Matthay, M.A., L.B. Ware, and G.A. Zimmerman, *The acute respiratory distress syndrome.* The Journal of clinical investigation, 2012. **122**(8): p. 2731-2740.
39. Rabuel, C. and A. Mebazaa, *Septic shock: a heart story since the 1960s.* Intensive care medicine, 2006. **32**(6): p. 799-807.
40. Koh, I.H., et al., *Microcirculatory evaluation in sepsis: a difficult task.* Shock, 2010. **34**(7): p. 27-33.
41. Fink, M.P., *Intestinal epithelial hyperpermeability: update on the pathogenesis of gut mucosal barrier dysfunction in critical illness.* Current opinion in critical care, 2003. **9**(2): p. 143-151.
42. Schmid-Schönbein, G.W. and M. Chang, *The autodigestion hypothesis for shock and multi-organ failure.* Annals of biomedical engineering, 2014. **42**(2): p. 405-414.

43. Stare, J., et al., *Effects of peritoneal sepsis on rat central osmoregulatory neurons mediating thirst and vasopressin release.* Journal of Neuroscience, 2015. **35**(35): p. 12188-12197.
44. Iacobone, E., et al., *Sepsis-associated encephalopathy and its differential diagnosis.* Critical care medicine, 2009. **37**(10): p. S331-S336.
45. Alobaidi, R., et al., *Sepsis-Associated Acute Kidney Injury.* Seminars in Nephrology, 2015. **35**(1): p. 2-11.
46. Prowle, J.R. and R. Bellomo. *Sepsis-associated acute kidney injury: macrohemodynamic and microhemodynamic alterations in the renal circulation*. in *Seminars in nephrology*. 2015. Elsevier.
47. Walley, K.R., et al., *The central role of proprotein convertase subtilisin/kexin type 9 in septic pathogen lipid transport and clearance.* American journal of respiratory and critical care medicine, 2015. **192**(11): p. 1275-1286.
48. Gotts, J.E. and M.A. Matthay, *Sepsis: pathophysiology and clinical management.* BMJ, 2016. **353**: p. i1585.
49. Boomer, J.S., et al., *Immunosuppression in patients who die of sepsis and multiple organ failure.* Jama, 2011. **306**(23): p. 2594-2605.
50. Cabrera-Perez, J., et al., *Impact of sepsis on CD4 T cell immunity.* Journal of leukocyte biology, 2014. **96**(5): p. 767-777.
51. Sáez-Llorens, X. and G.H. McCracken, *Bacterial meningitis in children.* The Lancet, 2003. **361**(9375): p. 2139-2148.
52. Maisey, H.C., et al., *Group B streptococcal pilus proteins contribute to adherence to and invasion of brain microvascular endothelial cells.* Journal of bacteriology, 2007. **189**(4): p. 1464-1467.
53. Hoffman, O. and J.R. Weber, *Pathophysiology and treatment of bacterial meningitis.* Therapeutic advances in neurological disorders, 2009. **2**(6): p. 401-412.
54. Kieseier, B.C., et al., *Differential expression of matrix metalloproteinases in bacterial meningitis.* Brain, 1999. **122**(8): p. 1579-1587.
55. Koedel, U., et al., *Experimental pneumococcal meningitis: cerebrovascular alterations, brain edema, and meningeal inflammation are linked to the production of nitric oxide.* Annals of Neurology: Official Journal of the American Neurological Association and the Child Neurology Society, 1995. **37**(3): p. 313-323.
56. Free, S., et al., *Bilateral hippocampal volume loss in patients with a history of encephalitis or meningitis.* Epilepsia, 1996. **37**(4): p. 400-405.
57. Bohr, V., O.B. Paulson, and N. Rasmussen, *Pneumococcal meningitis: late neurologic sequelae and features of prognostic impact.* Archives of neurology, 1984. **41**(10): p. 1045-1049.
58. Bedford, H., et al., *Meningitis in infancy in England and Wales: follow up at age 5 years.* Bmj, 2001. **323**(7312): p. 533.
59. de Beek, D.v., et al., *Cognitive impairment in adults with good recovery after bacterial meningitis.* The Journal of infectious diseases, 2002. **186**(7): p. 1047-1052.
60. Seale, A.C., et al., *Estimates of the Burden of Group B Streptococcal Disease Worldwide for Pregnant Women, Stillbirths, and Children.* Clinical Infectious Diseases, 2017. **65**(suppl_2): p. S200-S219.
61. *Prevention of Early-onset Neonatal Group B Streptococcal Disease.* BJOG: An International Journal of Obstetrics & Gynaecology, 2017. **124**(12): p. e280-e305.
62. Yow, M.D., et al., *Ampicillin prevents intrapartum transmission of group B streptococcus.* Jama, 1979. **241**(12): p. 1245-7.
63. Heelan, J.S., M.E. Hasenbein, and A.J. McAdam, *Resistance of group B streptococcus to selected antibiotics, including erythromycin and clindamycin.* Journal of clinical microbiology, 2004. **42**(3): p. 1263-1264.

64. Verani, J.R., L. McGee, and S.J. Schrag, *Prevention of perinatal group B streptococcal disease--revised guidelines from CDC, 2010.* MMWR Recomm Rep, 2010. **59**(Rr-10): p. 1-36.
65. Kwatra, G. and S.A. Madhi, *Chapter 11 - Group B Streptococcus*, in *Maternal Immunization*, E.E. Leuridan, M.C. Nunes, and C.E. Jones, Editors. 2020, Academic Press. p. 235-252.
66. Baker, C.J., et al., *Use of capsular polysaccharide-tetanus toxoid conjugate vaccine for type II group B Streptococcus in healthy women.* J Infect Dis, 2000. **182**(4): p. 1129-38.
67. Paoletti, L.C., et al., *Effects of alum adjuvant or a booster dose on immunogenicity during clinical trials of group B streptococcal type III conjugate vaccines.* Infect Immun, 2001. **69**(11): p. 6696-701.
68. Guttormsen, H.K., et al., *Type III group B streptococcal polysaccharide induces antibodies that cross-react with Streptococcus pneumoniae type 14.* Infection and Immunity, 2002. **70**(4): p. 1724-1738.
69. Palazzi, D.L., et al., *Use of type V group B streptococcal conjugate vaccine in adults 65-85 years old.* J Infect Dis, 2004. **190**(3): p. 558-64.
70. Baker, C.J., et al., *Immune response of healthy women to 2 different group B streptococcal type V capsular polysaccharide-protein conjugate vaccines.* J Infect Dis, 2004. **189**(6): p. 1103-12.
71. Baker, C.J., et al., *Dose–response to type V group B streptococcal polysaccharide–tetanus toxoid conjugate vaccine in healthy adults.* Vaccine, 2007. **25**(1): p. 55-63.
72. Hillier, S.L., et al., *A phase 2, randomized, control trial of group B streptococcus (GBS) type III capsular polysaccharide-tetanus toxoid (GBS III-TT) vaccine to prevent vaginal colonization with GBS III.* Clinical Infectious Diseases, 2019. **68**(12): p. 2079-2086.
73. Edwards, M.S., et al., *Persistence of functional antibodies to group B streptococcal capsular polysaccharides following immunization with glycoconjugate vaccines.* Vaccine, 2012. **30**(28): p. 4123-4126.
74. Pannaraj, P.S., et al., *Group B streptococcal conjugate vaccines elicit functional antibodies independent of strain O-acetylation.* Vaccine, 2009. **27**(33): p. 4452-4456.
75. Donders, G.G., et al., *Maternal Immunization With an Investigational Trivalent Group B Streptococcal Vaccine: A Randomized Controlled Trial.* Obstet Gynecol, 2016. **127**(2): p. 213-21.
76. Leroux-Roels, G., et al., *A randomized, observer-blind Phase Ib study to identify formulations and vaccine schedules of a trivalent Group B Streptococcus vaccine for use in non-pregnant and pregnant women.* Vaccine, 2016. **34**(15): p. 1786-1791.
77. Heyderman, R.S., et al., *Group B streptococcus vaccination in pregnant women with or without HIV in Africa: a non-randomised phase 2, open-label, multicentre trial.* The Lancet infectious diseases, 2016. **16**(5): p. 546-555.
78. Madhi, S.A., et al., *Safety and immunogenicity of an investigational maternal trivalent group B streptococcus vaccine in healthy women and their infants: a randomised phase 1b/2 trial.* The Lancet infectious diseases, 2016. **16**(8): p. 923-934.
79. Pfizer. *Trial to evaluate the safety, tolerability, and immunogenicity of a multivalent Group B Streptococcus vaccine in healthy nonpregnant women and pregnant women and their infants*. 2019; Available from: https://clinicaltrials.gov/ct2/show/NCT03765073.
80. Murphy, K., *Janeway's immunobiology*. 9th ed. / Kenneth Murphy, Casey Weaver ; with contributions by Allan Mowat, Leslie Berg, David Chaplin ; with acknowledgment to Charles A. Janeway Jr., Paul Travers, Mark Walport. ed, ed. C. Weaver, et al. 2017, New York: New York : Garland Science.
81. Gallo, R.L. and L.V. Hooper, *Epithelial antimicrobial defence of the skin and intestine.* Nature Reviews Immunology, 2012. **12**: p. 503.

82. Fujita, T., *Evolution of the lectin–complement pathway and its role in innate immunity.* Nature Reviews Immunology, 2002. **2**: p. 346.
83. Gasque, P., *Complement: a unique innate immune sensor for danger signals.* Molecular Immunology, 2004. **41**(11): p. 1089-1098.
84. Köhl, J., *Anaphylatoxins and infectious and non-infectious inflammatory diseases.* Molecular Immunology, 2001. **38**(2): p. 175-187.
85. Esser, A.F., *The membrane attack complex of complement. Assembly, structure and cytotoxic activity.* Toxicology, 1994. **87**(1): p. 229-247.
86. Serruto, D., et al., *Molecular mechanisms of complement evasion: learning from staphylococci and meningococci.* Nature Reviews Microbiology, 2010. **8**: p. 393.
87. Wolf, P.R. and H.L. Ploegh, *How MHC Class II Molecules Acquire Peptide Cargo: Biosynthesis and Trafficking through the Endocytic Pathway.* Annual Review of Cell and Developmental Biology, 1995. **11**(1): p. 267-306.
88. Williams, A., C.A. Peh, and T. Elliott, *The cell biology of MHC class I antigen presentation.* Tissue Antigens, 2002. **59**(1): p. 3-17.
89. Heemels, M.-T. and H. Ploegh, *Generation, Translocation, and Presentation of MHC Class I-Restricted Peptides.* Annual Review of Biochemistry, 1995. **64**(1): p. 463-491.
90. Ingulli, E., et al., *In Vivo Detection of Dendritic Cell Antigen Presentation to CD4$^+$ T Cells.* The Journal of Experimental Medicine, 1997. **185**(12): p. 2133-2141.
91. Rabinovich, N., et al., *Vaccine technologies: view to the future.* Science, 1994. **265**(5177): p. 1401-1404.
92. Ehreth, J., *The global value of vaccination.* Vaccine, 2003. **21**(7): p. 596-600.
93. Spellberg, B., J.G. Bartlett, and D.N. Gilbert, *The future of antibiotics and resistance.* New England Journal of Medicine, 2013. **368**(4): p. 299-302.
94. Schatz, A., E. Bugle, and S.A. Waksman, *Streptomycin, a Substance Exhibiting Antibiotic Activity Against Gram-Positive and Gram-Negative Bacteria.∗.* Proceedings of the Society for Experimental Biology and Medicine, 1944. **55**(1): p. 66-69.
95. Lewis, K., *Platforms for antibiotic discovery.* Nature reviews Drug discovery, 2013. **12**(5): p. 371-387.
96. Lewis, K. and F.M. Ausubel, *Prospects for plant-derived antibacterials.* Nat Biotechnol, 2006. **24**(12): p. 1504-7.
97. Shannon, E. and N. Abu-Ghannam, *Antibacterial Derivatives of Marine Algae: An Overview of Pharmacological Mechanisms and Applications.* Mar Drugs, 2016. **14**(4).
98. Payne, D.J., et al., *Drugs for bad bugs: confronting the challenges of antibacterial discovery.* Nat Rev Drug Discov, 2007. **6**(1): p. 29-40.
99. Tyers, M. and G.D. Wright, *Drug combinations: a strategy to extend the life of antibiotics in the 21st century.* Nature Reviews Microbiology, 2019. **17**(3): p. 141-155.
100. Finlay, B.B. and S. Falkow, *Common themes in microbial pathogenicity revisited.* Microbiology and molecular biology reviews, 1997. **61**(2): p. 136-169.
101. Maglione, P.J., et al., *IRAK-4- and MyD88- deficiencies impair IgM responses against T-independent bacterial antigens.* Blood, 2014.
102. Bretscher, P. and M. Cohn, *A Theory of Self-Nonself Discrimination: Paralysis and induction involve the recognition of one and two determinants on an antigen, respectively.* Science, 1970. **169**(3950): p. 1042-1049.
103. Snapper, C.M. and J.J. Mond, *A model for induction of T cell-independent humoral immunity in response to polysaccharide antigens.* The Journal of Immunology, 1996. **157**(6): p. 2229-2233.
104. Niles, M.J., L. Matsuuchi, and M.E. Koshland, *Polymer IgM assembly and secretion in lymphoid and nonlymphoid cell lines: evidence that J chain is required for pentamer IgM synthesis.* Proceedings of the National Academy of Sciences, 1995. **92**(7): p. 2884-2888.

105. Eisen, H.N. and G.W. Siskind, *Variations in affinities of antibodies during the immune response.* Biochemistry, 1964. **3**(7): p. 996-1008.
106. Brubaker, J.O., et al., *Mitogenic Activity of Purified Capsular Polysaccharide A from Bacteroides fragilis: Differential Stimulatory Effect on Mouse and Rat Lymphocytes In Vitro.* The Journal of Immunology, 1999. **162**(4): p. 2235-2242.
107. Avci, F.Y. and D.L. Kasper, *How Bacterial Carbohydrates Influence the Adaptive Immune System.* Annual Review of Immunology, 2010. **28**(1): p. 107-130.
108. Avci, F.Y., et al., *A mechanism for glycoconjugate vaccine activation of the adaptive immune system and its implications for vaccine design.* Nature Medicine, 2011. **17**(12): p. 1602-U115.
109. Janeway, C.A., *Pillars Article: Approaching the Asymptote? Evolution and Revolution in Immunology. Cold Spring Harb Symp Quant Biol. 1989. 54: 1–13.* The Journal of Immunology, 1989. **191**(9): p. 4475-4487.
110. Guttormsen, H.-K., et al., *Cognate stimulatory B-cell–T-cell interactions are critical for T-cell help recruited by glycoconjugate vaccines.* Infection and immunity, 1999. **67**(12): p. 6375-6384.
111. Kasper, D.L., *Bacterial Capsule: Old Dogmas and New Tricks.* The Journal of Infectious Diseases, 1986. **153**(3): p. 407-415.
112. Nielsen, P.A., *Large-scale production of tetanus toxoid.* Applied Microbiology, 1967. **15**(2): p. 453-454.
113. Chung, Y.-J., et al., *Optimization of diphtheria toxin production by Corynebacterium diphtheriae using a casein-based medium in a fermenter.* Biotechnology and Bioprocess Engineering, 2016. **21**(4): p. 537-543.
114. Rappuoli, R., *Isolation and characterization of Corynebacterium diphtheriae nontandem double lysogens hyperproducing CRM197.* Applied and environmental microbiology, 1983. **46**(3): p. 560-564.
115. Giannini, G., R. Rappuoli, and G. Ratti, *The amino-acid sequence of two non-toxic mutants of diphtheria toxin: CRM45 and CRM197.* Nucleic Acids Research, 1984. **12**(10): p. 4063-4069.
116. Liao, G., et al., *6-O-Branched Oligo-β-glucan-Based Antifungal Glycoconjugate Vaccines.* ACS Infectious Diseases, 2016. **2**(2): p. 123-131.
117. Song, C., et al., *A cancer vaccine based on fluorine-modified sialyl-Tn induces robust immune responses in a murine model.* Oncotarget, 2017. **8**(29): p. 47330-47343.
118. Komarova, B.S., et al., *Synthesis of a Pentasaccharide and Neoglycoconjugates Related to Fungal α-(1→3)-Glucan and Their Use in the Generation of Antibodies to Trace Aspergillus fumigatus Cell Wall.* Chemistry – A European Journal, 2015. **21**(3): p. 1029-1035.
119. Yu, R., et al., *Enhanced expression of soluble recombinant tetanus neurotoxin Hc in Escherichia coli as a tetanus vaccine candidate.* Immunobiology, 2011. **216**(4): p. 485-90.
120. Jones, C., *5: Stability and Degradation Pathways of Polysaccharide and Glycoconjugate Vaccines*, in *Stability of Complex Carbohydrate Structures*. 2012. p. 56-67.
121. Puente Gómez, I., et al., *Safety profile of Infanrix hexa – 17 years of GSK's passive post-marketing surveillance.* Expert Review of Vaccines, 2020. **19**(8): p. 771-779.
122. Cooper, B., L. DeTora, and J. Stoddard, *Menveo®: a novel quadrivalent meningococcal CRM197 conjugate vaccine against serogroups A, C, W-135 and Y.* Expert Review of Vaccines, 2011. **10**(1): p. 21-33.
123. Berti, F. and N. Ravenscroft, *Characterization of carbohydrate vaccines by NMR spectroscopy*, in *Carbohydrate-Based Vaccines*. 2015, Springer. p. 189-209.
124. Cobb, B.A., et al., *Polysaccharide processing and presentation by the MHCII pathway.* Cell, 2004. **117**(5): p. 677-687.

125. Cobb, B.A. and D.L. Kasper, *Microreview: Zwitterionic capsular polysaccharides: the new MHCII-dependent antigens.* Cellular microbiology, 2005. **7**(10): p. 1398-1403.
126. Tzianabos, A., et al., *Structural features of polysaccharides that induce intra-abdominal abscesses.* Science, 1993. **262**(5132): p. 416-419.
127. Tzianabos, A.O., J.Y. Wang, and J.C. Lee, *Structural rationale for the modulation of abscess formation by Staphylococcus aureus capsular polysaccharides.* Proceedings of the National Academy of Sciences of the United States of America, 2001. **98**(16): p. 9365-9370.
128. Kreisman, L.S.C., et al., *Structure and function relations with a T-cell-activating polysaccharide antigen using circular dichroism.* Glycobiology, 2007. **17**(1): p. 46-55.
129. Velez, C.D., et al., *Type I Streptococcus pneumoniae carbohydrate utilizes a nitric oxide and MHC II-dependent pathway for antigen presentation.* Immunology, 2009. **127**(1): p. 73-82.
130. O'Riordan, K. and J.C. Lee, *Staphylococcus aureus capsular polysaccharides.* Clinical microbiology reviews, 2004. **17**(1): p. 218-234.
131. Young, N.M., et al., *Structural characterization and MHCII-dependent immunological properties of the zwitterionic O-chain antigen of Morganella morganii.* Glycobiology, 2011. **21**(10): p. 1266-1276.
132. De Silva, R.A., et al., *The entirely carbohydrate immunogen Tn-PS A1 induces a cancer cell selective immune response and cytokine IL-17.* Cancer Immunology Immunotherapy, 2012. **61**(4): p. 581-585.
133. De Silva, R.A., et al., *Immunological response from an entirely carbohydrate antigen: Design of synthetic vaccines based on Tn− PS A1 conjugates.* Journal of the American Chemical Society, 2009. **131**(28): p. 9622-9623.
134. Nishat, S. and P.R. Andreana, *Entirely carbohydrate-based vaccines: an emerging field for specific and selective immune responses.* Vaccines, 2016. **4**(2): p. 19.
135. Trabbic, K.R., R.A. De Silva, and P.R. Andreana, *Elucidating structural features of an entirely carbohydrate cancer vaccine construct employing circular dichroism and fluorescent labeling.* Medchemcomm, 2014. **5**(8): p. 1143-1149.
136. Daniotti, J.L., et al., *Glycosylation of glycolipids in cancer: basis for development of novel therapeutic approaches.* Frontiers in oncology, 2013. **3**: p. 306.
137. Daniotti, J.L., R.D. Lardone, and A.A. Vilcaes, *Dysregulated expression of glycolipids in tumor cells: from negative modulator of anti-tumor immunity to promising targets for developing therapeutic agents.* Frontiers in oncology, 2016. **5**: p. 300.
138. Saragovi, H.U. and M. Gagnon, *Gangliosides: therapeutic agents or therapeutic targets?* Expert Opinion on Therapeutic Patents, 2002. **12**(8): p. 1215-1223.
139. Chapman, P.B., et al., *Vaccination with a Bivalent GM2 and GD2 ganglioside conjugate vaccine: a trial comparing doses of GD2-keyhole limpet hemocyanin.* Clinical cancer research, 2000. **6**(12): p. 4658-4662.
140. Kawashima, I., et al., *Expansion of natural killer cells in mice transgenic for IgM antibody to ganglioside GD2: demonstration of prolonged survival after challenge with syngeneic tumor cells.* International journal of oncology, 2003. **23**(2): p. 381-388.
141. Kim, S.-K., et al., *Impact of minimal tumor burden on antibody response to vaccination.* Cancer Immunology, Immunotherapy, 2011. **60**(5): p. 621-627.
142. Kirkwood, J.M., et al., *High-dose interferon alfa-2b significantly prolongs relapse-free and overall survival compared with the GM2-KLH/QS-21 vaccine in patients with resected stage IIB-III melanoma: results of intergroup trial E1694/S9512/C509801.* Journal of Clinical Oncology, 2001. **19**(9): p. 2370-2380.
143. Ragupathi, G., et al., *Consistent antibody response against ganglioside GD2 induced in patients with melanoma by a GD2 lactone-keyhole limpet hemocyanin conjugate vaccine plus immunological adjuvant QS-21.* Clinical Cancer Research, 2003. **9**(14): p. 5214-5220.

144. Ragupathi, G., et al., *Induction of antibodies against GD3 ganglioside in melanoma patients by vaccination with GD3-lactone-KLH conjugate plus immunological adjuvant QS-21.* International journal of cancer, 2000. **85**(5): p. 659-666.
145. Tong, W., et al., *Vaccination with Tumor-Ganglioside Glycomimetics Activates a Selective Immunity that Affords Cancer Therapy.* Cell chemical biology, 2019. **26**(7): p. 1013-1026. e4.
146. Mitchell, R., et al., *Polysaccharide-specific B cell responses to vaccination in humans.* Human Vaccines & Immunotherapeutics, 2014. **10**(6): p. 1661-1668.
147. Rothstein, E.P., et al., *Response of 7- to 15-month-old infants to sequential immunization with Haemophilus influenzae type b-CRM197 conjugate and polysaccharide vaccines.* Am J Dis Child, 1991. **145**(8): p. 898-900.
148. Steinhoff, M.C., et al., *Antibody responses to Haemophilus influenzae type B vaccines in men with human immunodeficiency virus infection.* N Engl J Med, 1991. **325**(26): p. 1837-42.
149. Jacobson, R.M., et al., *Antibody Persistence and Response to a Booster Dose of a Quadrivalent Conjugate Vaccine for Meningococcal Disease in Adolescents.* Pediatric Infectious Disease Journal, 2013. **32**(4): p. E170-E177.
150. Ramasamy, M.N., et al., *Randomized clinical trial to evaluate the immunogenicity of quadrivalent meningococcal conjugate and polysaccharide vaccines in adults in the United kingdom.* Clin Vaccine Immunol, 2014. **21**(8): p. 1164-8.
151. O'Connor, D., et al., *High-dimensional assessment of B-cell responses to quadrivalent meningococcal conjugate and plain polysaccharide vaccine.* Genome Medicine, 2017. **9**.
152. Holme, D., et al., *Neisseria meningitidis Group A IgG1 and IgG2 Subclass Immune Response in African Children Aged 12-23 Months Following Meningococcal Vaccination.* Clin Infect Dis, 2015. **61 Suppl 5**: p. S563-9.
153. Borja-Tabora, C.F., et al., *Long-term immunogenicity and safety after a single dose of the quadrivalent meningococcal serogroups A, C, W, and Y tetanus toxoid conjugate vaccine in adolescents and adults: 5-year follow-up of an open, randomized trial.* BMC Infect Dis, 2015. **15**: p. 409.
154. Jackson, L.A., et al., *Immunogenicity and safety of a 13-valent pneumococcal conjugate vaccine compared to a 23-valent pneumococcal polysaccharide vaccine in pneumococcal vaccine-naive adults.* Vaccine, 2013. **31**(35): p. 3577-84.
155. Namkoong, H., et al., *Comparison of the immunogenicity and safety of polysaccharide and protein-conjugated pneumococcal vaccines among the elderly aged 80 years or older in Japan: an open-labeled randomized study.* Vaccine, 2015. **33**(2): p. 327-32.
156. Grabar, S., et al., *Pneumococcal vaccination in patients with systemic lupus erythematosus: A multicenter placebo-controlled randomized double-blind study.* Vaccine, 2017. **35**(37): p. 4877-4885.
157. MacIntyre, C.R., et al., *A Randomized Clinical Trial of the Immunogenicity of 7-Valent Pneumococcal Conjugate Vaccine Compared to 23-Valent Polysaccharide Vaccine in Frail, Hospitalized Elderly.* Plos One, 2014. **9**(4).
158. Jackson, L.A., et al., *Influence of initial vaccination with 13-valent pneumococcal conjugate vaccine or 23-valent pneumococcal polysaccharide vaccine on anti-pneumococcal responses following subsequent pneumococcal vaccination in adults 50 years and older.* Vaccine, 2013. **31**(35): p. 3594-602.
159. Vandecasteele, S.J., et al., *Immunogenicity and safety of the 13-valent Pneumococcal Conjugate vaccine in 23-valent pneumococcal polysaccharide vaccine-naive and pre-immunized patients under treatment with chronic haemodialysis: a longitudinal quasi-experimental phase IV study.* Clin Microbiol Infect, 2018. **24**(1): p. 65-71.
160. Lu, P.J., et al., *National and State-Specific Shingles Vaccination Among Adults Aged >= 60 Years.* American Journal of Preventive Medicine, 2017. **52**(3): p. 362-372.

161. Rezai, M.S., et al., *Conjugate and 23-valent pneumococcal polysaccharide booster vaccination in asplenic patients with thalassemia major: A randomized clinical trial study.* Caspian Journal of Internal Medicine, 2017. **8**(1): p. 16-22.
162. Alam, M.M., et al., *Evaluation in Mice of a Conjugate Vaccine for Cholera Made from Vibrio cholerae O1 (Ogawa) O-Specific Polysaccharide.* Plos Neglected Tropical Diseases, 2014. **8**(2).
163. Jin, C., et al., *Efficacy and immunogenicity of a Vi-tetanus toxoid conjugate vaccine in the prevention of typhoid fever using a controlled human infection model of Salmonella Typhi: a randomised controlled, phase 2b trial.* Lancet, 2017. **390**(10111): p. 2472-2480.
164. Gao, F., et al., *A physico-chemical assessment of the thermal stability of pneumococcal conjugate vaccine components.* Human Vaccines & Immunotherapeutics, 2014. **10**(9): p. 2744-2753.
165. Dashefsky, B., et al., *Safety, tolerability, and immunogenicity of concurrent administration of Haemophilus influenzae type b conjugate vaccine (meningococcal protein conjugate) with either measles-mumps-rubella vaccine or diphtheria-tetanus-pertussis and oral poliovirus vaccines in 14- to 23-month-old infants.* Pediatrics, 1990. **85**(4 Pt 2): p. 682-9.
166. Vella, P.P. and R.W. Ellis, *Immunogenicity Of Haemophilus-Influenzae Type-B Conjugate Vaccines In Infant Rhesus-Monkeys.* Pediatric Research, 1991. **29**(1): p. 10-13.
167. Togashi, T., et al., *Immunogenicity and safety of a fully liquid aluminum phosphate adjuvanted Haemophilus influenzae type b PRP-CRM197-conjugate vaccine in healthy Japanese children: A phase III, randomized, observer-blind, multicenter, parallel-group study.* Vaccine, 2016. **34**(38): p. 4635-4641.
168. Akeda, Y., et al., *Comparison of serum bactericidal and antibody titers induced by two Haemophilus influenzae type b conjugate vaccines: A phase III randomized double-blind study.* Vaccine, 2018. **36**(12): p. 1528-1532.
169. Bona, G., et al., *Safety and immunogenicity of a CRM or TT conjugated meningococcal vaccine in healthy toddlers.* Vaccine, 2016. **34**(29): p. 3363-3370.
170. Otto, R.B.D., et al., *Patterns of binding of aluminum-containing adjuvants to Haemophilus influenzae type b and meningococcal group C conjugate vaccines and components.* Biologicals, 2015. **43**(5): p. 355-362.
171. Booy, R., et al., *Five-year Antibody Persistence and Safety After a Single Dose of Combined Haemophilus influenzae Type B Neisseria meningitidis Serogroup C-Tetanus Toxoid Conjugate Vaccine in Haemophilus influenzae Type B-primed Toddlers.* Pediatric Infectious Disease Journal, 2015. **34**(12): p. 1379-1384.
172. Baliban, S.M., et al., *Development of a glycoconjugate vaccine to prevent invasive Salmonella Typhimurium infections in sub-Saharan Africa.* Plos Neglected Tropical Diseases, 2017. **11**(4).
173. Ali, A., et al., *Synthesis and immunogenicity evaluation of Salmonella enterica serovar Paratyphi A O-specific polysaccharide conjugated to diphtheria toxoid.* Human Vaccines & Immunotherapeutics, 2014. **10**(6): p. 1494-1498.
174. Momen, S.B., et al., *Applying Central Composite Design and Response Surface Methodology to Optimize Growth and Biomass Production of Haemophilus influenzae Type b.* Jundishapur Journal of Microbiology, 2016. **9**(6).
175. Salman, M., et al., *Simplest Identification, O-Specific Polysaccharide Purification And Antigenic Evaluation Of Salmonella Enterica Serovar Typhi Vi Negative Isolate.* Excli Journal, 2015. **14**: p. 1078-1084.
176. Lee, I.M., et al., *Structural basis for fragmenting the exopolysaccharide of Acinetobacter baumannii by bacteriophage Phi AB6 tailspike protein.* Scientific Reports, 2017. **7**.

177. Zanardo, R.T., et al., *Development Of A New Process For Purification Of Capsular Polysaccharide From Streptococcus pneumoniae Serotype 14.* Brazilian Journal of Chemical Engineering, 2016. **33**(3): p. 435-443.
178. Muindi, K.M., et al., *Characterization of the meningococcal serogroup X capsule N-acetylglucosamine-1-phosphotransferase.* Glycobiology, 2014. **24**(2): p. 139-149.
179. Morelli, L., et al., *Synthesis and immunological evaluation of protein conjugates of Neisseria meningitidis X capsular polysaccharide fragments.* Beilstein Journal of Organic Chemistry, 2014. **10**: p. 2367-2376.
180. Mann, E., et al., *Bacteriophage-mediated Glucosylation Can Modify Lipopolysaccharide O-Antigens Synthesized by an ATP-binding Cassette (ABC) Transporter-dependent Assembly Mechanism.* Journal of Biological Chemistry, 2015. **290**(42): p. 25561-25570.
181. Smith, C.M., et al., *Recombinant Plants Provide a New Approach to the Production of Bacterial Polysaccharide for Vaccines.* Plos One, 2014. **9**(2): e88144.
182. Guazzelli, L., R. Ulc, and S. Oscarson, *Synthesis of a Glucuronic Acid-Containing Thioglycoside Trisaccharide Building Block and Its Use in the Assembly of Cryptococcus Neoformans Capsular Polysaccharide Fragments.* Chemistryopen, 2015. **4**(6): p. 729-739.
183. Park, I.H., et al., *Genetic, Biochemical, and Serological Characterization of a New Pneumococcal Serotype, 6H, and Generation of a Pneumococcal Strain Producing Three Different Capsular Repeat Units.* Clinical and Vaccine Immunology, 2015. **22**(3): p. 313-318.
184. Kay, E.J., et al., *Recombinant expression of Streptococcus pneumoniae capsular polysaccharides in Escherichia coli.* Open Biology, 2016. **6**(4).
185. Dharmasena, M.N., et al., *Stable expression of Shigella dysenteriae serotype 1 O-antigen genes integrated into the chromosome of live Salmonella oral vaccine vector Ty21a.* Pathogens and Disease, 2016. **74**(8).
186. Fiebig, T., et al., *Molecular Cloning and Functional Characterization of Components of the Capsule Biosynthesis Complex of Neisseria meningitidis Serogroup A Toward In Vitro Vaccine Production.* Journal of Biological Chemistry, 2014. **289**(28): p. 19395-19407.
187. Fiebig, T., et al., *Functional expression of the capsule polymerase of Neisseria meningitidis serogroup X: A new perspective for vaccine development.* Glycobiology, 2014. **24**(2): p. 150-158.
188. Fiebig, T., et al., *An efficient cell free enzyme-based total synthesis of a meningococcal vaccine candidate.* Npj Vaccines, 2016. **1**.
189. Budhadev, D. and B. Mukhopadhyay, *Convergent synthesis of the hexasaccharide related to the repeating unit of the O-antigen from E. coli O120.* Rsc Advances, 2015. **5**(119): p. 98033-98040.
190. Mondal, P.K., et al., *Chemical Synthesis of the Repeating Unit of Type Ia Group B Streptococcus Capsular Polysaccharide.* Organic Letters, 2015. **17**(5): p. 1102-1105.
191. Si, A. and A.K. Misra, *Expedient Synthesis of the Pentasaccharide Repeating Unit of the Polysaccharide O-Antigen of Escherichia coli O11.* Chemistryopen, 2016. **5**(1): p. 47-50.
192. Mandal, P.K., *Synthesis of the pentasaccharide repeating unit of the O-antigen of E-coli O117:K98:H4.* Beilstein Journal of Organic Chemistry, 2014. **10**: p. 2724-2728.
193. Scott, A.E., et al., *Protection against Experimental Melioidosis with a Synthetic manno-Heptopyranose Hexasaccharide Glycoconjugate.* Bioconjugate Chemistry, 2016. **27**(6): p. 1435-1446.
194. Seeberger, P.H., C.L. Pereira, and S. Govindan, *Total synthesis of a Streptococcus pneumoniae serotype 12F CPS repeating unit hexasaccharide.* Beilstein Journal of Organic Chemistry, 2017. **13**: p. 164-173.

195. Dhara, D. and A.K. Misra, *Convergent Synthesis of Oligosaccharide Fragments Corresponding to the Cell Wall O-Polysaccharide of Salmonella enterica O53.* Chemistryopen, 2015. **4**(6): p. 768-773.
196. Hahm, H.S., M. Hurevich, and P.H. Seeberger, *Automated assembly of oligosaccharides containing multiple cis-glycosidic linkages.* Nature Communications, 2016. **7**.
197. Volbeda, A.G., et al., *Cyanopivaloyl Ester in the Automated Solid-Phase Synthesis of Oligorhamnans.* Journal of Organic Chemistry, 2017. **82**(24): p. 12992-13002.
198. Shang, W.J., et al., *Chemical synthesis of the outer core oligosaccharide of Escherichia coli R3 and immunological evaluation.* Organic & Biomolecular Chemistry, 2015. **13**(14): p. 4321-4330.
199. Ghosh, T. and A.K. Misra, *Synthesis of the Heptasaccharide Repeating Unit of the Cell Wall O-Polysaccharide of Enterotoxigenic Escherichia coli O139.* Chemistryopen, 2016. **5**(1): p. 43-46.
200. Hara, R.I., et al., *Solid-Phase Synthesis of Fluorinated Analogues of Glycosyl 1-Phosphate Repeating Structures from Leishmania using the Phosphoramidite Method.* Chemistryopen, 2018. **7**(6): p. 439-446.
201. Gagarinov, I.A., et al., *Synthesis of Staphylococcus aureus Type 5 Trisaccharide Repeating Unit: Solving the Problem of Lactamization.* Organic Letters, 2015. **17**(4): p. 928-931.
202. Parameswarappa, S.G., et al., *A Semi-synthetic Oligosaccharide Conjugate Vaccine Candidate Confers Protection against Streptococcus pneumoniae Serotype 3 Infection.* Cell Chemical Biology, 2016. **23**(11): p. 1407-1416.
203. Weishaupt, M.W., et al., *Automated glycan assembly of a S-pneumoniae serotype 3 CPS antigen.* Beilstein Journal of Organic Chemistry, 2016. **12**: p. 1440-1446.
204. Schumann, B., et al., *A semisynthetic Streptococcus pneumoniae serotype 8 glycoconjugate vaccine.* Science Translational Medicine, 2017. **9**(380).
205. Bourgault, J.P., et al., *Synthesis of the tumor associative alpha-aminooxy disaccharide of the TF antigen and its conjugation to a polysaccharide immune stimulant.* Organic & Biomolecular Chemistry, 2014. **12**(11): p. 1699-1702.
206. Noyes, A., et al., *Quantitative high throughput analytics to support polysaccharide production process development.* Vaccine, 2014. **32**(24): p. 2819-2828.
207. Khan, I., et al., *A High-Throughput Size Exclusion Chromatography Method to Determine the Molecular Size Distribution of Meningococcal Polysaccharide Vaccine.* International Journal of Analytical Chemistry, 2016.
208. Garcia-Quintanilla, F., et al., *Production of a recombinant vaccine candidate against Burkholderia pseudomallei exploiting the bacterial N-glycosylation machinery.* Frontiers in Microbiology, 2014. **5**.
209. Wacker, M., et al., *Prevention of Staphylococcus aureus Infections by Glycoprotein Vaccines Synthesized in Escherichia coli.* Journal of Infectious Diseases, 2014. **209**(10): p. 1551-1561.
210. Ihssen, J., et al., *Increased efficiency of Campylobacter jejuni N-oligosaccharyltransferase PglB by structure-guided engineering.* Open Biology, 2015. **5**(4): 140227.
211. Kampf, M.M., et al., *In vivo production of a novel glycoconjugate vaccine against Shigella flexneri 2a in recombinant Escherichia coli: identification of stimulating factors for in vivo glycosylation.* Microbial Cell Factories, 2015. **14**.
212. Herbert, J.A., et al., *Production and efficacy of a low-cost recombinant pneumococcal protein polysaccharide conjugate vaccine.* Vaccine, 2018. **36**(26): p. 3809-3819.
213. Pan, C., et al., *Biosynthesis of Conjugate Vaccines Using an O-Linked Glycosylation System.* Mbio, 2016. **7**(2).

214. Sun, P., et al., *Design and production of conjugate vaccines against S. Paratyphi A using an O-linked glycosylation system in vivo.* Npj Vaccines, 2018. **3**.
215. Deng, S., et al., *A peptide-free, liposome-based oligosaccharide vaccine, adjuvanted with a natural killer T cell antigen, generates robust antibody responses in vivo.* Chemical Science, 2014. **5**(4): p. 1437-1441.
216. Chen, L., et al., *Outer membrane vesicles displaying engineered glycotopes elicit protective antibodies.* Proceedings of the National Academy of Sciences of the United States of America, 2016. **113**(26): p. E3609-E3618.
217. Robbins, J.B., et al., *Toward a new vaccine for pertussis.* Proceedings of the National Academy of Sciences of the United States of America, 2014. **111**(9): p. 3213-3216.
218. Frasch, C.E., et al., *Technical Development of a New Meningococcal Conjugate Vaccine.* Clinical Infectious Diseases, 2015. **61**: p. S404-S409.
219. Mendez, Y., et al., *Multicomponent polysaccharide-protein bioconjugation in the development of antibacterial glycoconjugate vaccine candidates.* Chemical Science, 2018. **9**(9): p. 2581-2588.
220. Moginger, U., et al., *Cross Reactive Material 197 glycoconjugate vaccines contain privileged conjugation sites.* Scientific Reports, 2016. **6**.
221. Adamo, R., et al., *Deciphering the structure-immunogenicity relationship of anti-Candida glycoconjugate vaccines.* Chemical Science, 2014. **5**(11): p. 4302-4311.
222. Stefanetti, G., et al., *Impact of conjugation chemistry on the immunogenicity of S. Typhimurium conjugate vaccines.* Vaccine, 2014. **32**(46): p. 6122-6129.
223. Hamidi, A. and H. Kreeftenberg, *Use of immuno assays during the development of a Hemophilus influenzae type b vaccine for technology transfer to emerging vaccine manufacturers.* Human Vaccines & Immunotherapeutics, 2014. **10**(9): p. 2697-2703.
224. Arcuri, M., et al., *The influence of conjugation variables on the design and immunogenicity of a glycoconjugate vaccine against Salmonella Typhi.* Plos One, 2017. **12**(12).
225. Giannelli, C., et al., *Determination of free polysaccharide in Vi glycoconjugate vaccine against typhoid fever.* Journal of Pharmaceutical and Biomedical Analysis, 2017. **139**: p. 143-147.
226. Xu, P., et al., *Conjugate Vaccines from Bacterial Antigens by Squaric Acid Chemistry: A Closer Look.* Chembiochem, 2017. **18**(8): p. 799-815.
227. Thanawastien, A., et al., *Conjugate-like immunogens produced as protein capsular matrix vaccines.* Proceedings of the National Academy of Sciences of the United States of America, 2015. **112**(10): p. E1143-E1151.
228. Mimura, Y., et al., *Contrasting glycosylation profiles between Fab and Fc of a human IgG protein studied by electrospray ionization mass spectrometry.* Journal of Immunological Methods, 2007. **326**(1): p. 116-126.
229. Kratky, O., H. Leopold, and H. Stabinger, *[5] The determination of the partial specific volume of proteins by the mechanical oscillator technique*, in *Methods in enzymology*. 1973, Elsevier. p. 98-110.
230. Harding, S.E., *The intrinsic viscosity of biological macromolecules. Progress in measurement, interpretation and application to structure in dilute solution.* Progress in biophysics and molecular biology, 1997. **68**(2): p. 207-262.
231. Cole, J.L., et al., *Analytical Ultracentrifugation: Sedimentation Velocity and Sedimentation Equilibrium.* Methods in cell biology, 2008. **84**: p. 143-179.
232. Harding, S.E., et al., *Recent Advances in the Analysis of Macromolecular Interactions Using the Matrix-Free Method of Sedimentation in the Analytical Ultracentrifuge.* Biology, 2015. **4**(1): p. 237-250.
233. Schuck, P., *Size-distribution analysis of macromolecules by sedimentation velocity ultracentrifugation and lamm equation modeling.* Biophysical journal, 2000. **78**(3): p. 1606-1619.

234. Dam, J. and P. Schuck, *Calculating sedimentation coefficient distributions by direct modeling of sedimentation velocity concentration profiles*, in *Methods in enzymology*. 2004, Elsevier. p. 185-212.
235. Harding, S.E., A.J. Rowe, and J.C. Horton, *Analytical ultracentrifugation in biochemistry and polymer science*. 1992: Royal Society of Chemistry.
236. Creeth, J.M. and S.H. Harding, *Some observations on a new type of point average molecular weight.* Journal of biochemical and biophysical methods, 1982. **7**(1): p. 25-34.
237. Harding, S.E., *Challenges for the modern analytical ultracentrifuge analysis of polysaccharides.* Carbohydrate Research, 2005. **340**(5): p. 811-826.
238. Schuck, P., et al., *SEDFIT–MSTAR: molecular weight and molecular weight distribution analysis of polymers by sedimentation equilibrium in the ultracentrifuge.* Analyst, 2014. **139**(1): p. 79-92.
239. Jumel, K., P. Browne, and J. Kennedy, *The use of low angle laser light scattering with gel permeation chromatography for the molecular weight determination of biomolecules*. 1992: Royal Society of Chemistry: Cambridge.
240. Burchard, W., *Static and dynamic light scattering approaches to structure determination of biopolymers.* Laser light scattering in biochemistry, 1992: p. 3-22.
241. Cao, E., et al., *Effect of freezing and thawing rates on denaturation of proteins in aqueous solutions.* Biotechnol Bioeng, 2003. **82**(6): p. 684-90.
242. Zuckerman, J.N., *The importance of injecting vaccines into muscle. Different patients need different needle sizes.* Bmj, 2000. **321**(7271): p. 1237-8.
243. Rashid, R., et al., *Novel Use for Polyvinylpyrrolidone as a Macromolecular Crowder for Enhanced Extracellular Matrix Deposition and Cell Proliferation.* Tissue engineering. Part C, Methods, 2014. **20**.
244. Jazayeri, M.H., et al., *The concentration of total serum IgG and IgM in sera of healthy individuals varies at different age intervals.* Biomedicine & Aging Pathology, 2013. **3**(4): p. 241-245.
245. Peters, T., *All about Albumin: Biochemistry, Genetics, and Medical Applications*. 1996: Academic Press.
246. Kragh-Hansen, U., *Molecular aspects of ligand binding to serum albumin.* Pharmacological Reviews, 1981. **33**(1): p. 17-53.
247. Evans, T.W., *Review article: albumin as a drug—biological effects of albumin unrelated to oncotic pressure.* Alimentary Pharmacology & Therapeutics, 2002. **16**(s5): p. 6-11.
248. MOSESSON, M.W., *Fibrinogen and fibrin structure and functions.* Journal of Thrombosis and Haemostasis, 2005. **3**(8): p. 1894-1904.
249. Huang, S., Z. Cao, and E. Davie, *The role of amino-terminal disulfide bonds in the structure and assembly of human fibrinogen.* Biochemical and biophysical research communications, 1993. **190**(2): p. 488-495.
250. Scheraga, H.A. and M. Laskowski Jr, *The fibrinogen-fibrin conversion*, in *Advances in protein chemistry*. 1957, Elsevier. p. 1-131.
251. Ferry, J.D., *The mechanism of polymerization of fibrinogen.* Proceedings of the National Academy of Sciences of the United States of America, 1952. **38**(7): p. 566.
252. Mosesson, M., et al., *The covalent structure of factor XIIIa crosslinked fibrinogen fibrils.* Journal of structural biology, 1995. **115**(1): p. 88-101.
253. Tamaki, T. and N. Aoki, *Cross-linking of α2-plasmin inhibitor and fibronectin to fibrin by fibrin-stabilizing factor.* Biochimica et Biophysica Acta (BBA)-Enzymology, 1981. **661**(2): p. 280-286.
254. Lam, S., et al., *Evidence that arginyl-glycyl-aspartate peptides and fibrinogen gamma chain peptides share a common binding site on platelets.* Journal of Biological Chemistry, 1987. **262**(3): p. 947-950.

255. Sigma-Aldrich. *Product information, albumin, human*. 1996 18/05/2020]; Available from: https://www.sigmaaldrich.com/content/dam/sigma-aldrich/docs/Sigma/Product_Information_Sheet/a9511pis.pdf.
256. Sigma-Aldrich. *Product Information, Albumin from Bovine Serum*. 2000 18/05/2020]; Available from: https://www.sigmaaldrich.com/content/dam/sigma-aldrich/docs/Sigma/Product_Information_Sheet/a2153pis.pdf.
257. Sigma-Aldrich. *Product Information, Fibrinogen from human plasma*. 2015 18/05/2020]; Available from: https://www.sigmaaldrich.com/content/dam/sigma-aldrich/docs/Sigma/Product_Information_Sheet/f3879pis.pdf.
258. Triantaphyllopoulos, E. and D.C. Triantaphyllopoulos, *Amino acid composition of human fibrinogen and anticoagulant derivatives.* Biochem J, 1967. **105**(1): p. 393-400.
259. Rayner, L.E., et al., *The Solution Structures of Two Human IgG1 Antibodies Show Conformational Stability and Accommodate Their C1q and FcγR Ligands*.* Journal of Biological Chemistry, 2015. **290**(13): p. 8420-8438.
260. IonSource. *Common N-Linked Glycan Simplified Structures and Masses*. 2016 [cited 2021 08/12/2021]; Available from: http://www.ionsource.com/Card/carbo/carbstr.htm.
261. Johnston, J. and A. Ogston, *A boundary anomaly found in the ultracentrifugal sedimentation of mixtures.* Transactions of the Faraday Society, 1946. **42**: p. 789-799.

11 Appendix

Included here are the publications in which the author was involved during the rest of this project, but which do not form a part of previously presented research.

11.1 Submaxillary Mucin: its Effect on Aroma Release from Acidic Drinks and New Insight into the Effect of Aroma Compounds on its Macromolecular Integrity

Vlad Dinu, Richard B. Gillis, Thomas MacCalman, Mui Lim, Gary G. Adams, Stephen E. Harding & Ian D. Fisk

Food Biophysics volume 14, pages278–286 (2019)

Abstract

Submaxillary mucin is a major component that defines the makeup and functionality of saliva. Understanding its structure and function during food intake is key to designing appropriate strategies for enhancing the delivery of flavour. In the present study, the hydrodynamic integrity of bovine submaxillary mucin was characterised under physiological and acidic conditions and it was shown to have a broad molecular weight distribution with species ranging from 100 kDa to over 2000 kDa, and a random coil type of conformation. A decrease in the pH of mucin appeared to result in aggregation and a broader molecular weight distribution, which was shown to correlate with a release of flavour compounds. Our study also provides indications that *p*-cresol may have an effect on the macromolecular integrity of mucin.

Introduction

Past research has generally focused on the behaviour of volatile aroma compounds in the presence of small solutes i.e. monosaccharides, salts and proteins [1, 2]. However, there is limited research on the effect of saliva and its macromolecular constituents on aroma release. During consumption of food, saliva is the first medium encountered by aroma compounds as they travel to the respiratory tract and to the olfactory receptors in the nose [3]. Saliva consists of a number of macromolecular components which protect and lubricate the lining of the oral cavity: mucins, amylases, proteins and antibodies, which play a role in regulating pH and normal functioning of the salivary film [[4, 5]. Mucin glycoproteins are the second most abundant salivary components, after salivary α-amylase, and define the structure and functionality of saliva [6]. Although the pH of the saliva is maintained between ~5.5 to 7.5, this can temporarily decrease during consumption of foods, interfering with the normal functioning of mucins and other salivary proteins [7]. These salivary changes trigger salivary glands to produce more saliva in order to compensate for the loss in functionality and to keep the oral cavity lubricated [8]. But the process is faster at replacing low molecular weight enzymes and peptides, and rather slow at replenishing viscous, higher molecular weight mucins, therefore stimulated saliva has lower mucin levels than resting saliva [5]. This effect is predicted to influence the partitioning of aroma compounds from the saliva to the olfactory receptors.

Aroma release is affected by a number of physio-chemical interactions. These effects can lower the concentrations of aroma compounds released from the bolus, resulting in a significant loss through ingestion [9, 10]. Therefore, to enhance flavour release in vivo, it is required to understand the behaviour of salivary components under different conditions i.e. pH, salt, temperature. Ultimately, these conditions are influenced by the physiochemical properties of the ingested product, such as the pH of soft drinks and other foods, which can be as low as 2.4. Recent studies on mucins have suggested that acidic environments can induce conformational changes [11]. This because mucins have a pH dependant negative charge, progressively falling as the pH decreases [12]. These pH-mucin changes are proposed to promote the release of volatile aroma compounds. In addition, some studies showed that sugars promote the degree of acid production via citrates/citric acid present in drinks interacting with the calcium present in the tooth, thus maintaining a lower pH over longer

periods of time [13, 14]. Other studies have shown that the partitioning of aroma compounds is lower in the absence of sucrose [2], and this suggests that the lack of sucrose is also responsible for the lack of flavour release in 'low calorie' drinks, despite their reformulation.

Mucins from the alimentary, reproductive and bronchial tracts are characterised as having large molecular weights of up to 20 million Daltons (Da, or in molar mass terms, g/mol), although values up to 50 million Da have also been reported [15, 16]. They adopt a branched, random coil type of conformation as described by various techniques such as AUC (analytical ultracentrifugation), SEC-MALS (size-exclusion chromatography coupled to multi-angle laser light scattering), AFM (atomic force microscopy) or electron microscopy [16, 17]. They resemble block copolymer structures, which contain a polypeptide backbone, abundant in serine, proline and threonine, which forms a bridge between the hydroxyl groups of the carbohydrate fraction. The carbohydrates can account for up to 90% of the entire molecular weight of mucin and is generally made up of galactose, sialic acid, fucose, N-acetyl galactosamine and N-acetyl glucosamine. These highly hydrophilic coated regions alternate with hydrophobic and non-glycosylated protein domains [18]. Protein domains, which are responsible for mucin polymerisation, are susceptible to proteolytic cleavage [19]. Recent studies looked at the formation of the muco-salivary film and suggested that it is formed by a monomer/dimer type of interaction in a lateral or 'layer-by-layer' approach, such that subunits are bridged together via their cysteine-rich protein domains [20].

Salivary/submaxillary mucins are different from alimentary, reproductive and tracheobronchial mucins. They have lower molecular weights, lower carbohydrate content and up to 30% more charged sialic acid residues [21]. Because human salivary/submaxillary mucin is difficult to obtain in any useful quantities, bovine submaxillary mucin (BSM) was used as a surrogate in the current study. Experiments on submaxillary mucin were amongst the first to be carried to investigate mucin's complex structural assembly [22, 23]. It appears that the glycosylated region makes up to 60% of the total mass, with abundance in acidic disaccharides such as sialic acids and N-acetyl galactosamines [24]. A detailed analysis of its oligosaccharide region has been reviewed by Chai, et al. [25].

The current study aims to investigate the molecular interactions between volatile aroma compounds and submaxillary mucin under neutral and acidic conditions. Mucin solutions were designed to mimic the physiological conditions of the saliva (buffered salts and electrolytes) and within the range of salivary concentration of mucin (0–2 mg/ml) [26, 27]. Analytical Ultracentrifugation (AUC), SEC-MALS (size-exclusion chromatography coupled to multi-angle laser light scattering), viscometry, Dynamic Light Scattering (DLS) and Raman spectroscopy were used to explore changes in mucin integrity. The hydrodynamic analysis has been linked with Atmospheric Pressure-Chemical Ionization Mass Spectrometry (APCI-MS) to explain changes in the aroma release. This strategy was further complemented by Raman spectroscopy to gain a better understanding of the interactions of an aroma active compounds- *p*-cresol with mucin.

Materials and Methods

Materials

Bovine submaxillary mucin (Type IS) and volatile aroma compounds were purchased from Sigma Aldrich (Dorset, UK). Highly purified RO (reverse osmosis) water was used for the preparation of buffer solutions. The 0.1 M phosphate buffered saline (PBS) was made according to Green (1933) [28] (Fisher Scientific, UK). The Na-citrate buffer solutions (pH 2.6–5) were made by varying the proportion of citric acid and sodium phosphate. Solutions of mucin have been dialysed with a 14,000 Da membrane (Fisher Scientific) and filtered through 0.45 µm Whatman nylon membrane filters (Millipore).

Methods

Sedimentation Velocity in the Analytical Ultracentrifugation (AUC)

Experiments were performed at 20.0 °C using the Optima XL-I analytical ultracentrifuge (Beckman, Palo Alto, USA) equipped with Rayleigh interference optics. Samples of 395 µl (and 405 µl solvent) were injected into 12 mm double sector epoxy cells with sapphire windows and centrifuged at 30000 rpm. The interference system produced data derived by recording changes in concentration (in fringe units) versus radial displacement. Data were analysed in SEDFIT using the "least squares *g*(*s*)' method of Dam & Schuck [29] by generating sedimentation coefficient distributions, g(*s*) vs *s*, where *s* is the sedimentation coefficient (in Svedberg units, S = 10^{-13} s). Weight average sedimentation coefficient values from the *g*(*s*) vs *s* distributions were normalised to standard conditions (viscosity and density of water at 20.0 °C) to give $s_{20,w}$ [30]. A partial specific volume of 0.66 ml/g was employed. To eliminate non-ideality, sedimentation coefficients are extrapolated to zero concentration, c using standard $1/s_{20,w}$ vs *c* plots.

SEC-MALS-Viscostar (Size-Exclusion Chromatography Coupled to Multi-Angle Laser Light Scattering and Viscometer)

SEC-MALS has been a powerful method for the evaluation of molecular weight distribution of mucins since the 1st application by Jumel, Fiebrig & Harding in 1996) [31], and was used for evaluation of mucin integrity at pH 7.0. The SEC set-up consisted of a Postnova Analysis PN7505 degassing unit (Landsberg am Lech Germany), Shimadzu LC-10 AD HPLC Pump (Shimadzu UK, Milton Keynes, UK.), fitted with a Spark-Holland Marathon Basic autosampler (Spark Holland, Emmen, The Netherlands) combined with a TSK Gel guard column (7.5 × 75 mm) and TSK Gel G5000, G6000 columns (7.5 × 300 mm) connected in series (Tosoh Biosciences, Tokyo, Japan), fully flushed of column debris. Light scattering intensities were simultaneously detected at 18 angles as a function of elution volume using a DAWN® HELEOS™ II, light scattering photometer connected in series to a ViscoStar® II on-line differential viscometer, an Optilab® rEX refractive index detector (Wyatt Technology Corporation, California, U.S.A.). A stock solution of 1.0 mg/ml was filtered through a 0.45 µm syringe filter (Whatman, Maidstone, England) - to remove any insoluble material or dust prior to injection - and then injected into the autosampler. A 100 µL aliquot of each solution was injected onto the columns at ambient temperature. The eluent employed was the PBS dialysate at a flow rate of 0.8 ml/min. ASTRA™ (Version 6) software (Wyatt Technology Corporation, Santa Barbara, U.S.A.) was used to estimate the weight average molecular weight, M_w, weight average intrinsic viscosity [η] and radius of gyration R_g, and also molecular weight, $M(V_e)$, intrinsic viscosity [η](V_e) and the radius of gyration $R_g(V_e)$ as a function of elution volume V_e. A 4 mW He-Ne laser was used at a wavelength of 632.8 nm, and the refractive increment for the mucin was taken as 0.181 ml/g. Because of the low solute concentrations after dilution on the columns non-ideality effects were assumed as negligible. Due to column limitations evaluations were not possible at pH 3, instead standard capillary viscometry was employed at a temperature of 20.0 °C [32].

Extended Fujita Method for Molecular Weight Distribution

Comparative molecular weight distributions *f*(*M*) vs *M* for BSM in solvents at pH 7.0 and pH 3.0 were obtained using the Extended Fujita method of Harding, Schuck and colleagues [33], which converts g(*s*) vs s plots to *f*(*M*) vs *M* and uses the scaling relationship

$$s=\kappa_s M^b s=\kappa_s M^b \quad (1)$$

where b depends on the conformation. To transform g(*s*) vs. *s* to f(*M*):

f(M)=g(s)(ds/dM)f(M)=g(s)(ds/dM) (2)

where

ds/dM=b.κs1/b.s(b−1)/bds/dM=b.κs1/b.s(b−1)/b (3)

Therefore, to perform the transformation the conformation type or *b* needs to be known under the particular solvent conditions and at least one pair of *s-M* values is needed to define the κ_s from Eq. (3). The method has been built into the SEDFIT algorithm along with the *g*(s) vs *s* procedure. To minimize non-ideality a very low loading concentration (*c* = 0.25 mg/ml) was chosen for the transformation.

Dynamic Light Scattering (DLS)

The experiments were performed using the Zetasizer Nano-ZS detector and low volume (ZEN0112) disposable sizing cuvettes (Malvern Instruments Ltd., Malvern, UK). The samples were measured at (20.0 ± 0.1) °C using the 173° scattering angle collected for 3 runs of 10 s at each mucin concentration (*c* = 0.2–1.0 mg/ml). Apparent z-average hydrodynamic radii, $r_{h,app}$ were evaluated from the apparent translational diffusion coefficient, $D_{z,app}$ via the Stokes-Einstein equation:

rh,app=(kbT)/6πηDz,apprh,app=(kbT)/6πηDz,app (4)

where k_B is the Boltzmann constant, η is the solution viscosity, T is the absolute temperature (K). We would like to stress that $D_{z,app}$ (and $r_{h,app}$) values are only apparent values as they were recorded at a scattering angle of 173° and no angular extrapolation to zero angle was possible with the instrumentation to correct for rotational/ anisotropic diffusion effects [34].

Raman Spectroscopy

Raman was performed using a RamanRXN2 optical system (Kaiser, Boston, USA) and the following conditions: laser wavelength of 785 nm, laser power at sample of ~40 mW with a spectral resolution of 7.5 cm^{-1}, fitted with a NCO-3.0-NIR system. The exposure was 30 s for the 10 mg/ml mucin sample. Raman spectra was not corrected for noise and the distribution is a result of an average of 10 scans, without smoothing. Due to the dilute state of the mucin preparation and the high proportion of carbohydrate fractions in mucin, it was difficult to obtain a higher resolution configuration [35].

Atmospheric Pressure Chemical Ionization-Mass Spectrometry (APCI-MS)

The APCI-MS (Platform II, Micromass, Manchester) was used to analyse the concentrations of volatile compounds above the headspace of the solutions under static conditions. A final concentration of ~10–50 ppm (parts per million) was sampled with an air flow adjusted to 10 ml/min. The instrument was set in Selective Ion Recording (SIR) mode to monitor the selected mass to charge ions (m/z) of the aroma compounds: 108.1, 128.13, 128.21, 156.2, 142.23 and 154.25. The ion intensity was measured at cone voltage of 50 V, source temperature of 75 °C and dwell time of 0.02 s. Sampling took place for 10 s, enough for the signal to plateau. Each peak was integrated in Mass Lynx (Waters, UK) and used to compare the maximum ion count for all samples using a similar approach used previously [36, 37].

Statistical Analysis

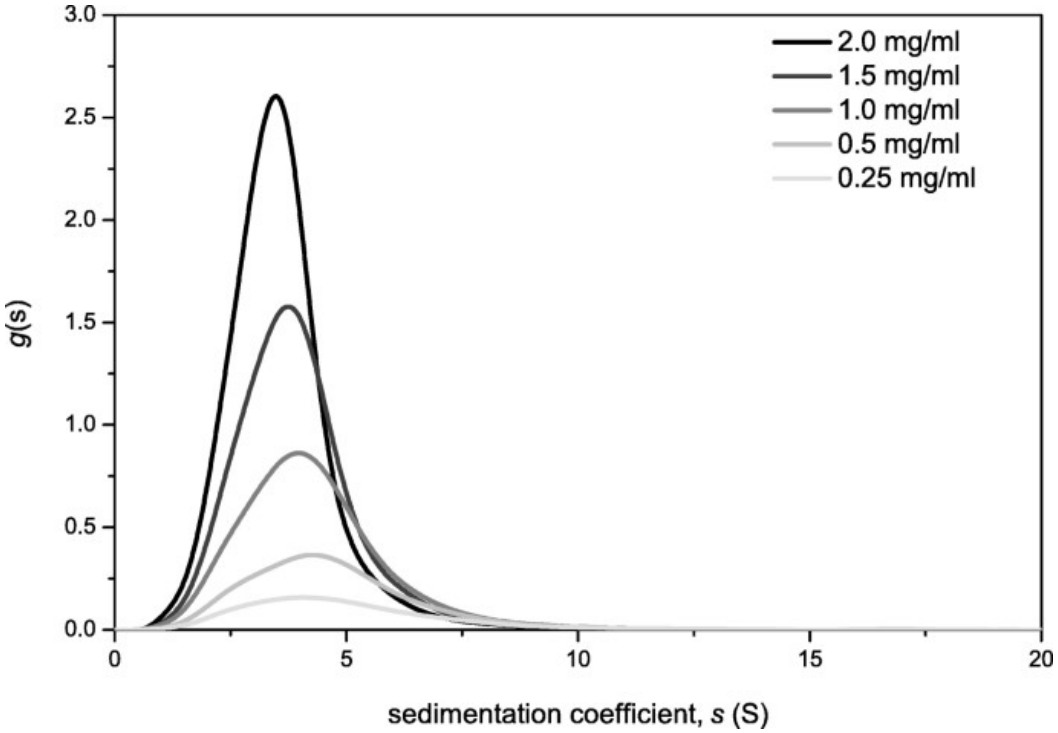
The AUC and all GC-MS samples were performed in triplicate and the analysis was prepared using Tukey's post hoc test to identify significance ($P < 0.05$). All figures were prepared in Origin 7.5 (OriginLab, Massachusetts, USA).

Results and Discussion

Characterisation of Bovine Submaxillary Mucin (BSM)

The sedimentation coefficient distribution of mucin was analysed by the *g*(s) method incorporated in SEDFIT [29, 38]. The analysis shown in Fig. 1 was used to estimate the weight average sedimentation coefficients which were corrected to standard conditions (density and viscosity of water at 20.0 °C) and then the reciprocals extrapolated to zero concentration $s^{o}_{20,w}$ (S) [38]. The experiment confirmed the presence of a polydisperse sample, similar to other mucins [39]. The $s^{o}_{20,w}$ values were commensurate with those found earlier by Payza and coworkers [39].

Fig. 1

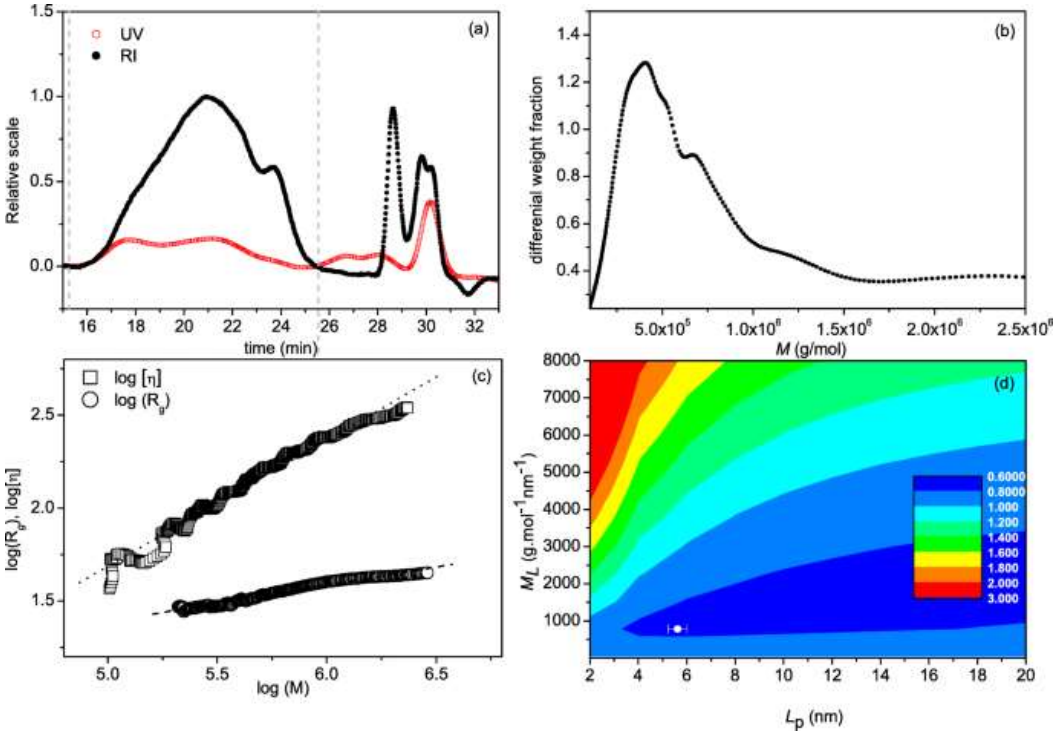


Sedimentation velocity, *g*(s) analysis of BSM showing the sedimentation coefficient distribution and the extrapolation to zero concentration. Run at 20.0 °C at 30000 rpm in PBS buffer 0.1 M (pH 7)

SEC-MALS was then applied to BSM (Fig. 2a) revealing the Rayleigh Interference (RI) and UV elution profiles of BSM in 0.1 M PBS (pH 7.0), ranging from elution times of 16 min to 25 min. The elution profiles are converted to a molecular weight distribution profile in ATRA™ software, as supplied by the manufacturer (Fig. 2b) which yielded a M_w value of ~700 kDa. The broad distribution was consistent with the multi-component nature of the sedimentation coefficient analysis. Data from SEC-MALS was also analysed for the comparison of molar mass and intrinsic viscosity, [η]. The double logarithmic plot between the two variables can be used to estimate the conformation of the macromolecule (Fig. 2d). The samples show good correlation between molar mass and intrinsic viscosity, consistent with those found for other mucins [40, 41]. A more quantitative representation comes from the measurement of the persistence length L_p, which has theoretical limits of 0 for a random coils and ∞ for a stiff rod, and mass per unit length, M_L [42]. In this study, L_p and M_L have been estimated using the MultiHYDFIT package, incorporating the Yamakawa-Fujii [43] and the Bushin–Bohdanecky [44, 45] relations into a single 'global' algorithm that can be used to estimate L_p and M_L based on a minimisation of a target function (Δ), which considers parameters including

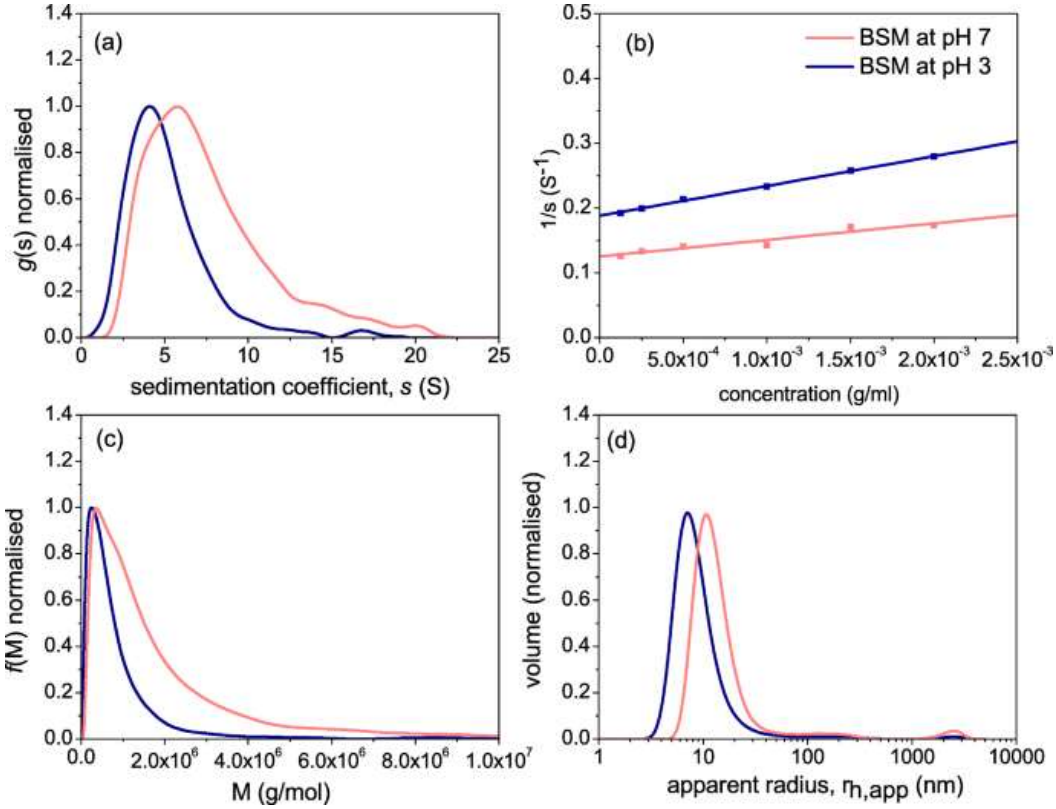
sedimentation coefficients, radius of gyration R_g, and intrinsic viscosity [η], for the entire molecular weight distribution [40, 46]. Our results yielded a persistence length value, L_p of (5.6 ± 0.5) nm and mass per unit length, M_L of ~800 g.mol^{-1}.nm^{-1}, corresponding to a random coil conformation for the BSM mucin molecules (Fig. 3d), as found for other mucins [39].

Fig. 2



SEC-MALS analysis of bovine submaxillary mucin. **a** Concentration (refractive index) and ultra-violet (UV) elution profiles; **b** molecular weight distribution; **c** Mark Houwink-Kuhn Sakurada (MHKS) plot of intrinsic viscosity [η](V_e) vs molecular weight M_w(V_e) at different elution volumes, V_e. [η](V_e), versus molecular weight M_w(V_e) and radius of gyration R_g(V_e) vs M_w(V_e). **d** Multi-HYDFIT contour plot to obtain estimates for the flexibility parameter the persistence length L_p and the mass per unit length M_L

Fig. 3



Comparative hydrodynamic properties of bovine submaxillary mucin at pH 7.0 and at pH 3.0 (**a**) sedimentation coefficient *g*(s) distribution at 0.25 mg/ml; **b** reciprocal plot of s versus concentration, fitted to $(1/s) = (1/s^{\circ})(1 + k_s c)$ where k_s is the concentration dependence 'Gralén' coefficient [47]; **c** molecular weight distribution from sedimentation velocity and Extended Fujita analysis, *f*(*M*) versus M for a loading concentration of 0.25 mg/ml. $\kappa_s = 0.007606$ and $b = 0.483$; **d** Distribution of the apparent hydrodynamic radius $r_{h,app}$. Experiments performed in PBS buffer 0.1 M (pH 7.0) and Na-citrate buffer 0.1 M (pH 3.0) at a temperature of 20.0 °C

Effect of pH on the Hydrodynamic Properties of BSM

The AUC and DLS results of Fig. 3 demonstrate how lowering the pH can affect the hydrodynamic properties of mucin. Sedimentation velocity *g*(s) analysis (Fig. 4a) revealed that the macromolecular distribution of mucin has shifted towards higher $s^{\circ}_{20,w}$ values, from 5.2S at pH 7.0 to 7.9S at pH 3. The reciprocal sedimentation coefficients were extrapolated to zero concentration to determi.0e sedimentation concentration dependence coefficient k_s, which were (238 ± 9) ml/g at pH 7.0 and (202 ± 18) ml/g at pH 3.0 (Fig. 4b and Table 1). The "Extended Fujita" *f*(*M*) vs *M* transformation from g(*s*) vs *s* was performed as according to Harding et al. [48, 49]. The procedure is employed by calculating the κ_s and *b* parameters, the latter being determined from the plot of molar mass and intrinsic viscosity, [η], first yielding the viscosity power law (scaling) coefficient *a*, which corresponds to a value of (0.565 ± 0.010), equivalent to a random coiled conformation. We then use the Tsvetkov et al relation [50] linking the sedimentation and viscosity power law coefficients

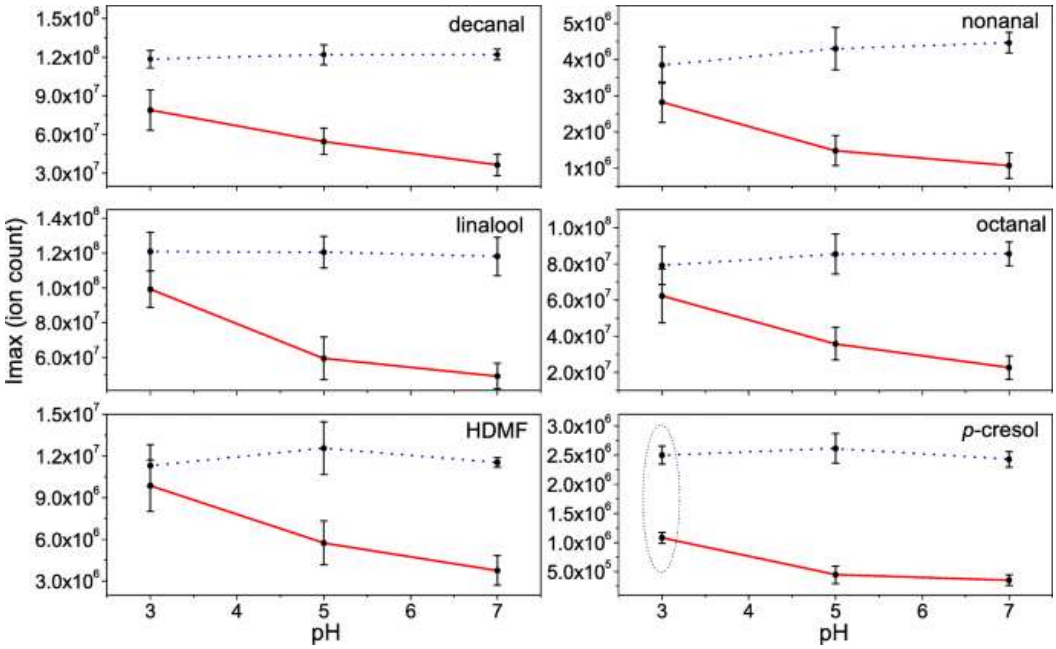
$$b=(2-a)/3 \quad (5)$$

to obtain a value of $b = (0.483 \pm 0.010)$. In order to determine κ_s, we used the weight average sedimentation coefficient $s^{o}_{20,w}$, together with the weight average M_w from SEC-MALS, and the *b* value, as follows:

κs=s/Mbκs=s/Mb (6)

and obtained a κ_s value of 0.007606. Encouragingly the molecular weight distribution from the Extended Fujita analysis in Fig. 3c is similar to that from SEC MALS (Fig. 2b) at pH 7.0. This gives us confidence that the shift to higher molecular weights at lower pH is genuine.

Fig. 4



APCI-MS results showing the impact of pH on the release of volatile aroma compounds from solutions with mucin (1 mg/ml) and from the neutral and acidic buffer solutions (dotted line). The data shown are given as mean ± standard error, number of observations, *n* = 3

Table 1 Hydrodynamic properties of bovine submaxillary mucin in 0.1 M phosphate chloride buffer (pH 7.0) and citrate buffer (pH 3.0)

	pH 7.0	**pH 3.0**
$s^o_{20,w}$ (S)	5.2 (±0.2)	7.9 (±0.7)
$M_{w,app}$ (kDa)	700 (±30)	1600 (±160)
$r_{h,app}$ (nm)	10 (±3)	15 (±3)
k_s (ml/g)	238 (±9)	202 (±18)
[η] (ml/g)	168 (±5)	127 (±2)
$R = k_s/[\eta]$	1.4 (±0.2)	1.6 (±0.3)
R_g (nm)	35.1(±1.2)	–

L_p (nm)	5.6 (±0.5)	–

Figure 3d shows the apparent hydrodynamic radius of BSM by volume, uncorrected for concentration and rotational diffusion effects [34]. The analysis produced uniform size distributions across all concentrations with an apparent hydrodynamic radius, $r_{h,app}$ of ~10 nm at neutral pH, corresponding to an apparent diffusion coefficient D_{app} of 2.2×10^{-7} cm^2/s. Conversely, the low pH fractions also reveal a shift to higher apparent hydrodynamic sizes, supporting the results from sedimentation velocity (Fig. 3d). We stress that the these values are apparent values as they are given only for comparison and are not genuine radii since there has been no angular dependence correction due to rotational diffusion effects [34].

Generally, the SEC-MALS and AUC analyses (i) confirm the low weight average molecular weight $\boldsymbol{M}_w$, of BSM at pH 7.0 is ~700 kDa, as compared to other mucins from other sources [51, 52], but with the presence of a high molecular weight tail extending to several million Da. (ii) the shift to high molecular weights (and higher apparent hydrodynamic radii) at pH 3.0 is clear from Fig. 3c and Table 1, where the distribution weight average M_w, has increased to ~1600 kDa. This behaviour is not unexpected as the lowering of pH to near the pKa of sialic acid means reduced overall negative charge and hence greater tendency to aggregate. This is somewhat similar to the behaviour observed in gastric mucus gelation, used to protect the stomach from auto-digestion, although one major difference is that salivary/submaxillary mucins have a much higher proportion of protein [53].

We can also address the question as to whether this increase in molecular weight is accompanied by a change in conformation. The simplest indicator of conformation comes from the Wales and van Holde [54] ratio '*R*', in which the ratio of the sedimentation concentration dependence coefficient k_s, to the intrinsic viscosity [η], is a direct measure (independent of assumptions of hydration) of the macromolecular gross conformation in solution. The *R* values reported in this study 1.4 ± 0.2 and 1.6 ± 0.3 at pH 7.0 and pH 3.0 respectively both corresponding to random coils, although within experimental error they are indistinguishable at the 2 pH's, the results indicate a change to a more compact conformation [55, 56]. The value at pH 7 is also consistent with a MHKS *a* coefficient value of (0.565 ± 0.010), and persistence length L_p = (5.6 ± 0.5) nm, obtained from HYDFIT analysis. The SEC-MALS-viscostar and sedimentation velocity results are all consistent with a random coil. It is worth suggesting that these mild changes in the macrostructure of mucus at low pH may also correspond the mild feeling of astringency perceived during consumption of soft drinks.

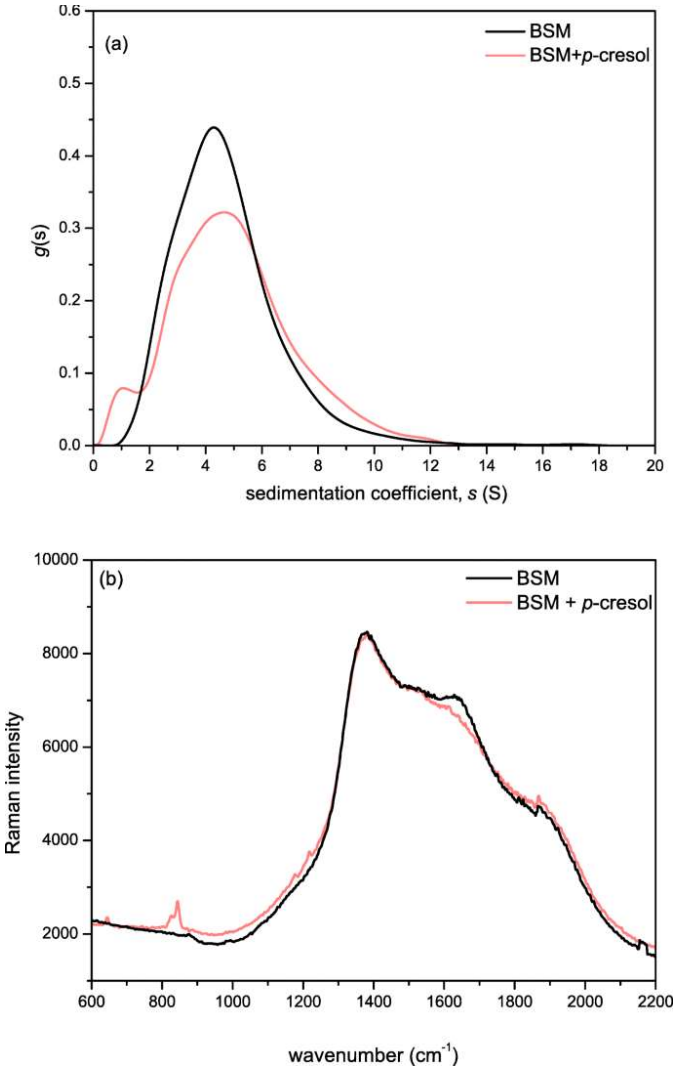
Interactions of Volatile Aroma Compounds with Mucin Solutions

Figure 4 shows the effect of pH on the partitioning of six characteristic volatile compounds found in lemon flavoured soft drinks in the presence and absence of mucin. In the absence of mucin, results indicated no significant differences ($P > 0.05$) in the release of these compounds at different pH (Fig. 4-dotted line), thus excluding the possibility of significant solvent effect. However, there was a substantial interaction effect which lowered the partitioning of aroma volatiles in the presence of mucin. For most compounds, this effect was pH dependent, with no significant differences at pH 3.0, but with significant differences ($P < 0.05$) observed for pH 5 and pH 7, indicating that pH-mucin effects lower the damping effect of mucin on the release of aroma. Interestingly, *p*-cresol showed a ~2.5 fold decrease in the relative concentration on the addition of mucin, irrespective of pH. It is known that

some proteins can bind specific aroma compounds [13, 57, 58], hence the significant reduction in the release *p*-cresol indicates a possible interaction mechanism with mucin.

Para-cresol (*p*-cresol) and its interactions with mucin has not been previously documented. This is of particular interest as it one of the main products resulting from the degradation of citral, and can be found in a wide range of citrus flavoured soft drinks and candy products [59]. We performed an SV-AUC analysis of the BSM/*p*-cresol mixture (Fig. 5a) and it was revealed that the sedimentation coefficient distribution of BSM showed a small degree of change to lower s values. Interestingly an additional Raman analysis revealed a decrease in intensity of the amide I region (~1640 cm^{-1}) upon addition of *p*-cresol, along with an increase in the ~850 cm^{-1} region, corresponding to the free *p*-cresol present in the solution [60] (Fig. 5b).

Fig. 5



a Sedimentation coefficient distribution *g*(s) vs s profiles for bovine submaxillary albumin (loading concentration *c* = 0.25 mg/ml) and the result of its interaction with *p*-cresol (*c* = 0.1 mg/ml); **b** Raman spectra of (*c* = 10 mg/ml) with and without *p*-cresol. The mucin/*p*-cresol sample was dialysed against a 14 kDa membrane prior to Raman analysis to remove unbound *p*-cresol. Performed in 0.1 M PBS pH 7 at 20.0 °C

Concluding Remarks

Our study shows that bovine submaxillary mucin has a broad molecular weight distribution with weight average (700 ± 30) kDa and adopts a randomly coiled conformation at neutral pH 7.0 – consistent with mucins from other sources [39] which is maintained under high acid conditions at pH 3.0. However there is a clear increase in aggregation at the lower pH causing a significant shift in the weight average molecular weight to (1600 ± 160) kDa. There is also a small change in the sedimentation coefficient distribution on addition of p-creosol with a concomitant small change in the Raman spectrum: this observation may also have affect in flavour release.

These effects have not been investigated previously, and it could lay grounds for new research into the health impact of commercially available flavour compounds. While the compounds used in our study are found in food or drink, they are present at very low concentrations (parts per million/billion) and are not high enough to elicit a significant effect. However, these mechanisms may have significant health implications in other products such as flavoured electronic cigarettes, where their aroma concentrations of be up to a million times higher.

References

1. S.M. Van Ruth, J.P. Roozen, J.L. Cozijnsen, Sci. Food Agric. **67**(2), 189–196 (1995)

2. E.N. Friel, A.J. Taylor, J. Agric. Food Chem. **49**(8), 3898–3905 (2001)

3. A.J. Taylor, Compr. Rev. Food Sci. Food Saf. **1**(2), 45–55 (2002)

4. R.K. Drobitch, C.K. Svensson, Clin. Pharmacokinet. **23**(5), 365–379 (1992)

5. V. Dinu, C. Liu, J. Ali, C. Ayed, P. Gershkovich, G.G. Adams, S.E. Harding, I.D. Fisk, Sci. Rep. **8**(1), 13350 (2018)

6. Z. Cheaib, A. Lussi, J. Biosci. **38**(2), 259–265 (2013)

7. R. Hans, S. Thomas, B. Garla, et al., Scicentifica, 5027283 (2016)

8. J.M. Coles, D.P. Chang, S. Zauscher, Curr. Opin. Colloid Interface Sci. **15**(6), 406–416 (2010)

9. H.A. Gremli, J. Am. Oil Chem. Soc. **51**, 95–97 (1974)

10. J.E. Kinsella, J. Am. Oil Chem. Soc. **65**(4), 506 (1998)

11. B. Barz, B.S. Turner, R. Bansil, B. Urbanc, J. Biol. Phys. **38**(4), 681–703 (2012)

12. A. Abodinar, K. Tømmeraas, E. Ronander, A.M. Smith, G.A. Morris, Int. J. Biol. Macromol. **87**, 281–286 (2016)

13. S. Lubbers, P. Landy, A. Voilley, Food Technol. **52**(5), 68 (1998)

14. M.A.R. Buzalaf, A.R. Hannas, M.T. Kat, J. Appl. Oral Sci. **20**(5), 493–502 (2012)

15. I. Carlstedt et al., Essays Biochem. **20**, 40–76 (1985)

16. S.E. Harding, Trends Food Sci. Technol. **17**(5), 255–262 (2006)

17. M.P. Deacon et al., Biochem. J. **348**(3), 557–563 (2000)

18. B.S. Turner, Dissertation, Boston University (2012)

19. H.H. Sigurdsson, J. Kirch, C.M. Lehr, Int. J. Pharm. **453**(1), 56–64 (2013)

20. S.P. Authimoolam, T.D. Dziubla, Polymers. **8**(3), 71 (2016)

21. X. Liao, D. Yuan, J. Tang, et al., J. Spectr., 9580136 (2016)

22. A. Gottschalk, Nature **186**(4729), 949–951 (1960)

23. N. Payza, M. Robert, A. Herp, Int. J. Prot. Res. **2**, 109–115 (1970)

24. T. Tsuji, T. Osawa, Carbohydr. Res. **151**, 391–402 (1986)

25. W. Chai et al., Eur. J. Biochem. **203**(1-2), 257–268 (1992)

26. S.M. Haward et al., Rheol. Acta **50**(11-12), 869–879 (2011)

27. D. Dziemianczyk, S.Z. Grabowska, R. Balicki, Rocz. Akad. Med. Bialymst. **50**, 334–338 (2015)

28. A.A. Green, J. Am. Chem. Soc. **55**, 2331–2336 (1993)

29. J. Dam, P. Schuck, *Method Enzymol*, vol 384 (2003), pp. 185–221

30. A.S. Abdelhameed, PhD Thesis, University of Nottingham (2010)

31. K. Jumel, I. Fiebrig, S.E. Harding, Int. J. Biol. Macromol. **18**(1-2), 133–139 (1996)

32. S.E. Harding, Prog. Biophys. Mol. Biol. **68**(2-3), 207–262 (1997)

33. S.E. Harding, P. Schuck, A.S. Abdelhameed, G. Adams, M.S. Kök, G.A. Morris, Methods. **54**(1), 136–144 (2011)

34. W. Burchard, in *Laser Light Scattering in Biochemistry*, ed. by S. E. Harding, D. B. Sattelle, V. A. Bloomfield. (Royal Society of Chemistry, Cambridge, UK, 1992)

35. L. Ashton et al. Adv. Colloid Interf. Sci. **199-200**, 66-77 (2013)

36. H.H. Gan, B.N. Yan, R.S.T. Linforth, I.D. Fisk, Food Chem. **190**, 442–447 (2016)

37. T. Yu, B. Macnaughtan, M. Boyer, R. Linforth, K. Dinsdale, I.D. Fisk, Food Res. Int. **48**(2), 702–709 (2012)

38. P. Schuck, in *Analytical Ultracentrifugation: Techniques and Methods*, ed. by D. J. Scott, S. E. Harding, A. J. Rowe. (The Royal Society of Chemistry, Cambridge, U.K, 2005), pp. 231–252

39. S.E. Harding, Adv. Carbohydr. Chem. Biochem. **47**, 345–381 (1989)

40. F.M. Almutairi, J.G.H. Cifre, G.G. Adams, M.S. Kök, A.R. Mackie, J.G. de la Torre, S.E. Harding, Eur. Biophys. J. **45**(1), 45–54 (2016)

41. E. Perez, J.E. Proust, J. Colloid Interf Sci. **118**(1), 182–191 (1987)

42. J. Garcia de la Torre, S.E. Harding, Biophys. Rev. **5**(2), 195–206 (2013)

43. H. Yamakawa, M. Fuji, Macromolecules. **6**(3), 407–415 (1973)

44. S. Bushin et al., Vysokomol Soedin. **23A**, 2494–2503 (1981)

45. M. Bohdanecky, Macromolecules. **16**(9), 1483–1492 (1983)

46. A. Ortega, J. Garcia de la Torre, Biomacromolecules **8**(8), 2464–2475 (2007)

47. N. Gralen, *PhD Dissertation* (Uppsala, Sweden, 1944)

48. S.E. Harding, P. Schuck, A.S. Abdelhameed, G. Adams, M.S. Kök, G.A. Morris, Methods. **54**(1), 136–144 (2011)

49. S.E. Harding et al., Sci. Rep. **8**, 11809 (2018)

50. V.N. Tsvetkov, V. Eskin, S. Frenkel, *Structure of macromolecules in solution* (Butterworths, London, 1970)

51. I. Fiebrig, S.E. Harding, A.J. Rowe, S.C. Hyman, S.S. Davis, Carbohydr. Polym. **28**(3), 239–244 (1995)

52. S. Dodd, G.A. Place, R.L. Hall, S.E. Harding, Eur. Biophys. J. **28**(1), 38–47 (1998)

53. F. Hollander, AMA Arch. Intern. Med. **93**(1), 107–120 (1954)

54. M. Wales, K.E. Van Holde, J. Polym. Sci. **14**, 8 (1954)

55. P.N. Lavrenko, K.J. Linow, E. Gornitz, in *Analytical ultracentrifugation in biochemistry and polymer science*, ed. by S. E. Harding, A. J. Rowe, J. C. Horton. (Royal Society of Chemistry, Cambridge, 1992), pp. 517–531

56. G. Berth et al., Progr. Colloid Polym. Sci. **119**, 50–57 (2002)

57. J. Solms, in *Interactions in food components. Elsevier Applied Science Publishers Ltd. Essex*, ed. by G. G. Birch, M. G. Lindley. (1986), pp. 189–210

58. E.J. Jouenne, J. Crouzet, J. Agric. Food Chem. **48**(4), 1273–1277 (2000)

59. S.J. Choi, E.A. Decker, L. Henson, L.M. Popplewell, D.J. McClements, J. Agric. Food Chem. **57**(23), 11349–11353 (2009)

60. Z. Arp, D. Autrey, J. Laane, S.A. Overman, G.J. Thomas, Biochemistry. **40**(8), 2522–2529 (2001)

Acknowledgements

This work was supported by the Biotechnology and Biological Sciences Research Council [grant number BB/N021126/1]; and the Engineering and Physical Sciences Research Council [grant number EP/L015633/1]. The work was carried out in the Flavour Research Group, Division of Food Sciences and the National Centre for Macromolecular Hydrodynamics, in the School of Biosciences, University of Nottingham. V.D. conceived the idea, performed the experiments and directed the research project. R.B.G., T.M. and M.L. assisted with data analysis and commented on the manuscript. G.G.A., S.E.H., and I.F. have supervised and co-investigated the project. We would also like to thank Dr. Rob Linforth for his technical support.

Author information

Affiliations

National Centre for Macromolecular Hydrodynamics, University of Nottingham, Sutton Bonington Campus, Leicestershire, UK

Vlad Dinu, Thomas MacCalman & Stephen E. Harding

Division of Food Sciences, School of Biosciences, University of Nottingham, Sutton Bonington Campus, Sutton Bonington, Leicestershire, UK

Vlad Dinu, Mui Lim & Ian D. Fisk

School of Health Sciences, Faculty of Medicine and Health Sciences, Queen's Medical Centre, Clifton Boulevard, Nottingham, UK

Richard B. Gillis & Gary G. Adams

Kulturhistorisk Museum, Universitetet i Oslo, Postboks 6762, St. Olavs plass, 0130, Oslo, Norway

Stephen E. Harding

Corresponding author

Correspondence to Ian D. Fisk.

Ethics declarations

Conflict of Interest

The authors declare no conflict of interest.

Additional information

Publisher's Note

Springer Nature remains neutral with regard to jurisdictional claims in published maps and institutional affiliations.

Rights and permissions

Open Access This article is distributed under the terms of the Creative Commons Attribution 4.0 International License (http://creativecommons.org/licenses/by/4.0/), which permits unrestricted use, distribution, and reproduction in any medium, provided you give appropriate credit to the original author(s) and the source, provide a link to the Creative Commons license, and indicate if changes were made.

11.2 Hydrodynamic Compatibility of Hyaluronic Acid and Tamarind Seed Polysaccharide as Ocular Mucin Supplements

Taewoo Chun , Thomas MacCalman 1, Vlad Dinu 1, Sara Ottino 2 , Mary K. Phillips-Jones 1,* and Stephen E. Harding 1,3,*

National Centre for Macromolecular Hydrodynamics (NCMH), School of Biosciences,

University of Nottingham, Sutton Bonington LE12 5RD, UK; stxtc16@exmail.nottingham.ac.uk (T.C.); stxtm22@exmail.nottingham.ac.uk (T.M.); sbavd@exmail.nottingham.ac.uk (V.D.)

Farmigea S.P.A, Via G.B. Oliva, 6/8 - 56121 Pisa, Italy; s.ottino@farmigea.it

Cultural History Museum, University of Oslo, Postboks 6762, St. Olavs plass, 0130 Oslo, Norway

* Correspondence: mary.phillips-jones@nottingham.ac.uk (M.K.P.-J.); steve.harding@nottingham.ac.uk (S.E.H.)

Received: 1 September 2020; Accepted: 28 September 2020; Published: 2 October 2020

Abstract: Hyaluronic acid (HA) has been commonly used in eyedrop formulations due to its viscous lubricating properties even at low concentration, acting as a supplement for ocular mucin (principally MUC5AC) which diminishes with aging in a condition known as Keratoconjunctivitis sicca or “dry eye”. A difficulty has been its short residence time on ocular surfaces due to ocular clearance mechanisms which remove the polysaccharide almost immediately. To prolong its retention time, tamarind seed gum polysaccharide (TSP) is mixed as a helper biopolymer with HA. Here we look at the hydrodynamic characteristics of HA and TSP (weight average molar mass Mw and viscosity [η]) and then explore the compatibility of these polymers, including the possibility of potentially harmful aggregation effects. The research is based on a novel combination of three methods: sedimentation velocity in the analytical ultracentrifuge (SV-AUC), size-exclusion chromatography coupled to multiangle light scattering (SEC-MALS) and capillary viscometry. HA and TSP were found to have Mw = (680 ± 30) kg/mol and (830 ± 30) kg/mol respectively, and [η] = (1475 ± 30) ml/g and (675 ± 20) ml/g, respectively. The structure of HA ranges from a rodlike molecule at lower molar masses changing to a random coil for Mw > 800 kg/mol, based on the Mark–Houwink–Kuhn–Sakurada (MHKS) coefficient. TSP, by contrast, is a random coil across the range of molar masses. For the mixed HA-TSP systems, SEC-MALS indicates a weak interaction. However, sedimentation coefficient (s) distributions obtained from SV-AUC measurements together with intrinsic viscosity demonstrated no evidence of any significant aggregation phenomenon, reassuring in terms of eye-drop formulation technology involving these substances.

Keywords: molar mass; heterogeneity and conformation; analytical ultracentrifugation; light scattering; viscometry

1. Introduction

As people age, their production of ocular mucin containing lacrymal fluid—with its natural protective and lubricating properties for the surface of the eye—diminishes, a term known medically as Keratoconjunctivitis sicca or “dry eye”. Solutions of polysaccharide in artificial tear drop formulations are popularly used to consolidate the mucin (of primarily type MUC5AC, also MUC2) to remove these symptoms. A problem with such formulations is how to prolong their residence time on the eye surface. The main reason for this problem is that ocular protective mechanisms (involving blinking,

both basal and reflex lachrymation, and a drainage through nasolacrimal ducts) quickly eliminates these eye drops from the precorneal region, where such drugs are absorbed and work [1]. As a result, and depending on the severity, this can lead to the need for repeated administration [2]. Therefore, various studies have investigated novel preparations to overcome such disadvantages of currently available formulations. For example, based on the viscosity enhancing effects of gelatin, the grafting of thermoresponsive polymer segments onto proteinaceous networks has led to promising results [3] and, more recently, the lectin Helix pomatia agglutinin has been considered as an ocular mucoadhesive component [4]. The properties of a promising new glutathione-dependent polymeric hydrogel with good eye drop mucoadhesive properties has also been explored [5].

Another highly significant development has been the combination of hyaluronic acid (HA) and tamarind seed gum polysaccharide (TSP), whose medical benefits were first reported by Barabino et al. [6]. Of the two components, both natural polysaccharides, HA is a linear polyanionic molecule chemically grouped in a glycosaminoglycan and comprises the repeating dimer

[→4)-β-D-glucopyranosyluronic acid-(1→3)-N-acetyl-2-amino-2-deoxy-β-d-glycopyranosyl-(1→] [7,8]. When it comes to the current market situation, it has been reported [2] that 0.1–0.5% (w/v) HA solutions are available commercially as either active or inactive ingredients to supplement ocular fluid (see also refs [9] and [10]). Hammer and Burch [11] have suggested that 0.17% HA showed superior protective effects as a coating on the eye compared to the highly viscous, more concentrated applications (1%, equivalent to 10 mg/mL) which transmit excessive shear force to endothelial cells. An alternative approach, which can also help with product stability issues is to use HA in a binary mixture with another polysaccharide. The second polysaccharide, TSP (Figure 1) is a nonionic, neutral and branched xyloglycan, which is comprised of a cellulose-like backbone, partially replaced at the O-6 position of its glucopyranosyl units with α-d-xylopyranose [6,12].

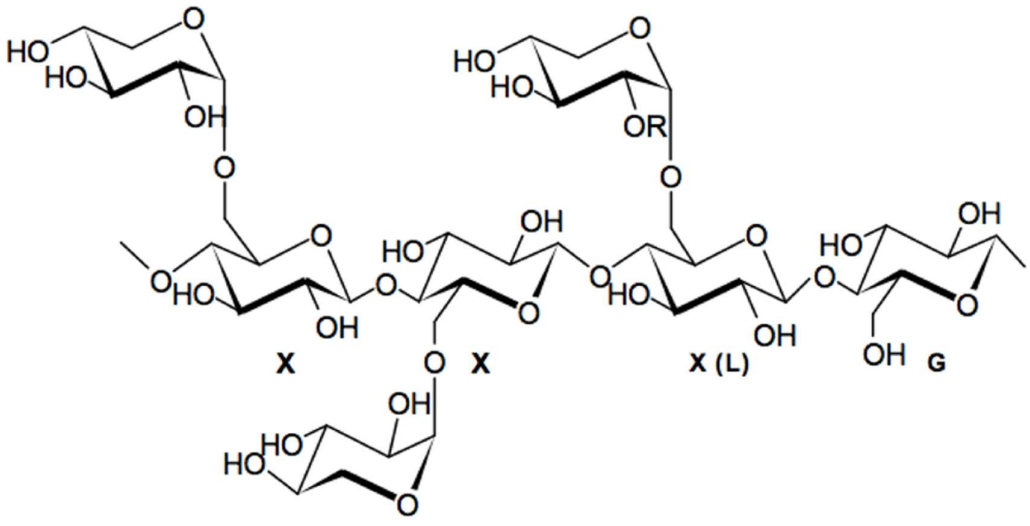


Figure 1. Chemical structure of tamarind seed xyloglucan; motif XXXG or β

A comparative study by Rolando and Valente [13] has indicated that both 0.5% and 1% solutions of TSP are comparable to 0.2% HA in terms of removing the symptoms of dry eye syndrome. Later, Barabino et al. [6] published their results with mixtures of HA and TSP, showing that this combination is effective in fixing the tear film on the cornea and repairing the endothelial damage in dry eye patients. One principal reason for these outcomes is that

the structural similarity of TSP to transmembrane mucins (MUC1) on the eye surface could lead to its longer retention time [13]. -D-galactopyranose (motif XXLG). Adapted from [14].

In addition, recent evidence using nuclear magnetic resonance spectroscopy (NMR)—a powerful method for investigating macromolecular-ligand interactions [15]—has suggested that there is an interaction between these two polysaccharides [16]. We now seek to reinforce those observations by exploring the hydrodynamic compatibility and stability of these mixtures. Specifically we examine key hydrodynamic parameters such as the molar mass and intrinsic viscosity by size exclusion chromatography coupled to multiangle (laser) light scattering SEC-MALS and capillary viscometry, together with sedimentation velocity in the analytical ultracentrifuge, SV-AUC to assess the heterogeneity and interaction strength. The matrix-free method of analytical ultracentrifugation—with its huge dynamic range (molar masses from 102–108 g/mol) is a key or "gold standard" method used to assess the molecular integrity of other biotherapeutic systems such as monoclonal antibodies (in terms of disassembly, denaturation or aggregation effects) and this is the first time that this method has been used to assess a dry-eye formulation. It has both a high separation and analysis ability without the need of columns or membranes [17,18]. We assess the change in the intrinsic viscosity with molar mass in order to estimate conformations of HA and TSP by SEC-MALS and viscometry, assess the state of self-association/aggregation of the individual components and for interaction/aggregation phenomena of the mixtures using SEC-MALS and SV-AUC, and finally investigate the stability of HA, TSP, and their mixtures.

Although polysaccharides such as cellulose acetate [19], proteins [20] and other natural polymers [21] are commonly used singly in biomedical applications, examples of the combined use of natural polymers for medicinal purposes are not so frequent but are increasing in importance. The HA-TSP system has provided a further good example [1,6,16,22], now reinforced by the present analytical ultracentrifuge-based study.

2. Materials and Methods

2.1. Materials

Hyaluronic acid and tamarind seed polysaccharide were supplied by Farmigea S.p.A., Pisa, Italy. HA or TSP samples were dissolved in a phosphate-chloride buffered saline solution (PBS, or "Paley buffer") at pH ~6.8 adjusted to an ionic strength of I = 0.1 mol/L by the addition of NaCl [23].

Stock solutions of HA and TSP were prepared by stirring gently for 30 min followed by overnight dialysis at room temperature against a two-litre volume of PBS. The concentration, c (g/mL) of the stock solution (either HA or TSP) was then measured using a differential refractometer (Atago DD7, Tokyo, Japan) set to zero with PBS, and using a refractive increment dn/dc of 0.167 mL/g for HA, and 0.152 mL/g for TSP [24]. HA/TSP was prepared by adding equal volumes with various concentrations, resulting in a range of ratios (HA:TSP = 1:3, 1:1 and 3:1) and final concentrations (4.0 mg/mL, 2.0 mg/mL and 1.0 mg/mL commensurate with concentrations used in formulations, and with materials remaining in solution (on the premise there are no significant irreversible aggregation/ complex formation interactions).

2.2. Sedimentation Velocity in the Analytical Ultracentrifuge

Sedimentation coefficients and sedimentation coefficient distributions were determined using the optimal XL-I analytical ultracentrifuge (Beckman Instruments, Palo Alto, CA, USA) with Rayleigh interference optics. Reference solvent or dialysate (420 µL) and HA, TSP or HA/TSP samples (400 µL)

with different concentrations were injected into channels of 12 mm, double-sectored cells with sapphire windows. Then these cells were loaded into an eight-hole rotor and centrifuged at a rotor speed of 45,000 rpm at a temperature of 20.0 ◦C for a run time of ∼24 h. The data was analysed using the SEDFIT algorithm [25], which gives the sedimentation coefficient distribution, g(s) versus sT,b, where s is the sedimentation coefficient, at temperature T and in buffer b. The s value was then corrected to standard solvent conditions (density and viscosity of water at 20.0 ◦C) to produce s20,w using the equation [26]:

$$s_{20,w} = \frac{1-\bar{v}\rho_{20,w}}{1-\bar{v}\rho_{T,b}} . \frac{\eta_{T,b}}{\eta_{20,w}} . s_{T,b} \text{ (1)}$$

where v is the partial specific volume of each sample. To eliminate the effect of nonideality, the Gralén equation was used for the extrapolation [27]:

$$\frac{1}{s_{20,w}} = \frac{k_s}{s^{\circ}_{20,w}} c + \frac{1}{s^{\circ}_{20,w}} \text{ (2)}$$

where ks is the Gralén coefficient (mL/g).

2.3. Size Exclusion Chromatography Coupled to Multiangle Laser Light Scattering (SEC-MALS)

Weight average molar masses (Mw) of HA, TSP and HA/TSP were estimated by SEC-MALS [7,14,28,29]. The solvent/ buffer was pumped at a steady flow rate of 0.5 mL/min through a column (Shodex LB-805 and), which was protected by a guard column (Shodex LB-G6B), coupled on-line to MALS (Dawn Heleos-11), a differential pressure viscometer (ViscoStar-11) and refractive index (Optilab rEX) detectors (Wyatt Technology, Santa Barbara, CA, USA). After being filtered through a 0.2 µm syringe filter (Whatman, Maidstone, England), the solutions of the HA, TSP, and HA/TSP sample prepared at a concentration of 1.24 mg/mL, 0.68 mg/mL, and 1.0 mg/mL (HA:TSP = 1:1) respectively, were injected into the size exclusion system using the Spark-Holland Marathon Basic autosampler to dilute on the column. ASTRATM (Version 6.2) software (Wyatt Technology, Santa Barbara, CA, USA) was used to analyse the data. Apparent weight average molar mass (Mw,app) was calculated by using a linear fit to the Zimm model [30]:

$$\frac{Kc}{\Delta R(\Theta,c)} = \frac{1}{M}\left(1 + \frac{q^2 R_g^2}{3}\right) + 2B_2 c \text{ (3)}$$

where K is an experimental constant dependent on the wavelength of the light and the refractive index increment of the polysaccharide, Rθ is the Rayleigh ratio used to determine the ratio of the integrity of light scattered by a macromolecule at an angle θ to that of the incident radiation, B is the second virial coefficient (mL·mol·g−2), Rg is the radius of gyration (cm) [31].

Mw,app is obtained from the intercept [29]. We make the reasonable assumption that correction for thermodynamic nonideality was assumed to be unnecessary due to the high dilutions on the SEC columns (see, for example ref [32]) and hence Mw the “ideal” molar mass ~Mw,app.

2.4. Capillary Viscometry

HA solutions ranging from 0.08 to 0.62 mg/mL, TSP solutions (from 0.03 to 1.91 mg/mL), and HA/TSP solutions (1 to 4 mg/mL) were analysed using a semiautomated viscosity measuring system (AVS 400, Schott Geräte, Hofheim, Germany) at a temperature of 20.00 ◦C in a 2 mL Ostwald viscometer (Table 1). Considering the fact that, because of low concentration (<2 mg/mL), a density correction is considered to be redundant [14], the relative viscosity, ηrel, was estimated to be the ratio of the flow time of the solution t (sec) to that of solvent t0:

ηrel≈t/t0=ηsp+1 (4)

where ηsp is the specific viscosity [33]. Then the reduced specific viscosity, ηred, (mL/g) and the inherent viscosity, ηinh, (mL/g) were obtained from:

$$\eta_{red}=(\eta_{rel}-1)/c \quad (5)$$

$$\eta_{inh}=(\ln \eta_{rel})/c \quad (6)$$

where c (g/mL) is the solute concentration [33].

Table 1. Hydrodynamic properties of hyaluronic acid (HA) and tamarind seed gum polysaccharide (TSP) in PBS "Paley" buffer.

Sample	HA	TSP
[η] (ml/g)	1475 ± 30	675 ± 20
$s_{020,w}$ (S)	4.7 ± 0.2	5.4 ± 0.2
a	1.1 *	0.63
$10^{-3}\times M_w$ (g/mol)	680 ± 30	830 ± 30
$10^{-3}\times M_z$ (g/mol)	730	940
$10^{-3}\times M_n$ (g/mol)	640	680
M_z/M_w	1.1	1.1
M_w/M_n	1.1	1.2

These ηred and ηinh can be extrapolated to zero concentration in order to eliminate nonideality effect, leading to the intrinsic viscosity [η]:

$$\eta_{red}=[\eta]\ (1+K_H\cdot[\eta]\cdot c) \quad (7)$$

$$\eta_{inh}=[\eta]\ (1-K_K\cdot[\eta]\cdot c) \quad (8)$$

where KH is the Huggins constant [34] and KK is the Kraemer constant [35]. Additionally, a combination of Equations (7) and (8) was used [36]:

$$[\eta]\simeq 1/c\cdot[2\eta_{sp}-2\ln(\eta_{rel})]^{1/2} \quad (9)$$

3. Results and Discussion

3.1. Comparison of Hydrodynamic Properties of HA and TSP of the Preparations

Table 1 summarizes the hydrodynamic properties of the hyaluronic acid and tamarind seed gum preparations (supplied by Farmigea AG) in the phosphate-chloride buffer. Sedimentation velocity (Figure 2a,b) and the elution profiles from SEC MALS (Figure 3a,b) show unimodal behaviour for both HA and TSP. Extrapolation of the sedimentation coefficients to zero concentration (Figure 2c,d) yield s20,wvalues of (4.7 ± 0.2)S and (5.4 ± 0.2)S, with concentration dependence or Gralén "ks" parameter values, respectively of (1171 ± 20) mL/g and (240 ± 30) mL/g. The lower value for ks for TSP is commensurate with the presence of weak self-associative effects we previously reported [14] which has an opposing effect on the concentration dependence to hydrodynamic nonideality.

SEC-MALS elution profiles for HA and TSP respectively are given inFigure3a,b, and corresponding typical Zimm extrapolations for specific elution volumes or times are given in Figure 3c,d. Weight average molar masses Mw of (680 ± 30) kg/mol and (830 ± 30) kg/mol for the HA and TSP preparations are obtained, with low polydispersities commensurate for an optical formulation. Corresponding viscosity plots obtained with the Ostwald capillary viscometer are shown in Figure 4 for HA (Figure 4a) and TSP (Figure 4b) respectively, yielding values of (1475 ± 30) mL/g and (675 ± 20) mL/g.

Values for the molar mass and intrinsic viscosity for the Farmigea hyaluronic acid preparations (Table 1) are somewhat lower than we analysed previously from a different source [7,8]. By contrast the tamarind seed gum preparations gave similar results to what we have found before [14,29]. The differential pressure Viscostar (Wyatt Technology, Santa Barbara USA) viscometer attached on-line to SEC allows relative viscosities ηrel(te) to be recorded as a function of elution volume (or elution time te), and also the corresponding molar masses Mw(te).

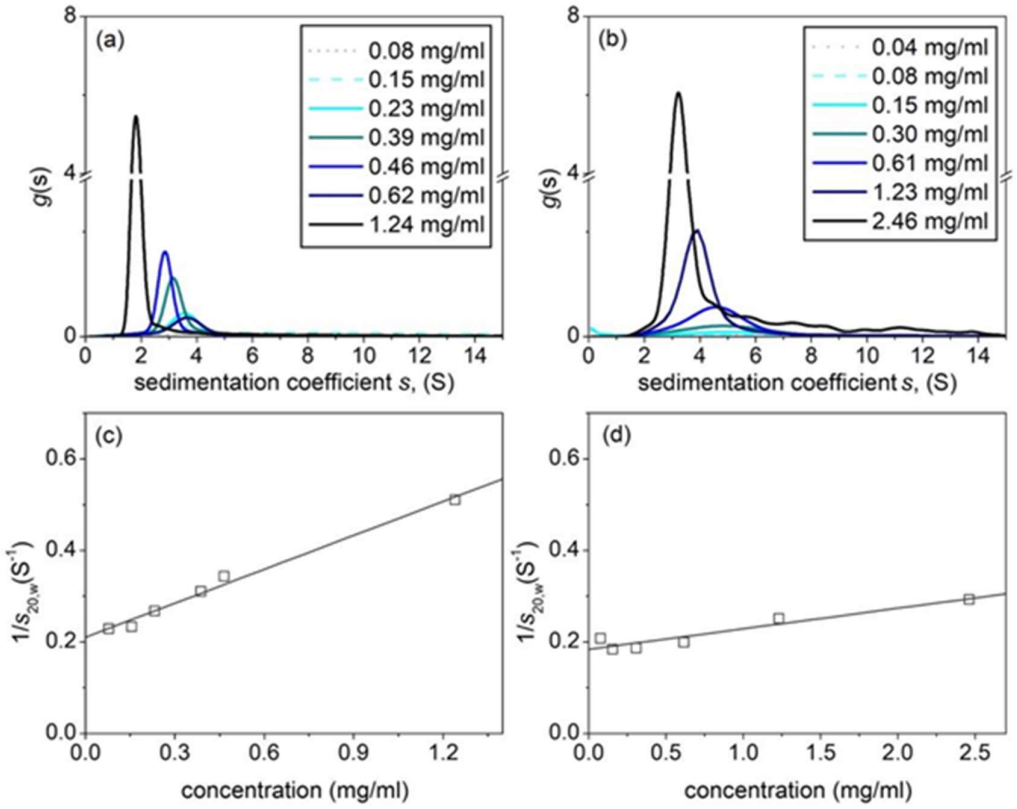


Figure 2. Sedimentation coefficient distributions. (a) Hyaluronic acid, HA. (b) Tamarind seed polysaccharide, TSP. (c) Corresponding concentration extrapolation to zero concentration to eliminate nonideality effects for HA (d) Corresponding plot for TSP. Solution pH = 6.8, I = 0.1, temperature = 20.0 ◦C.

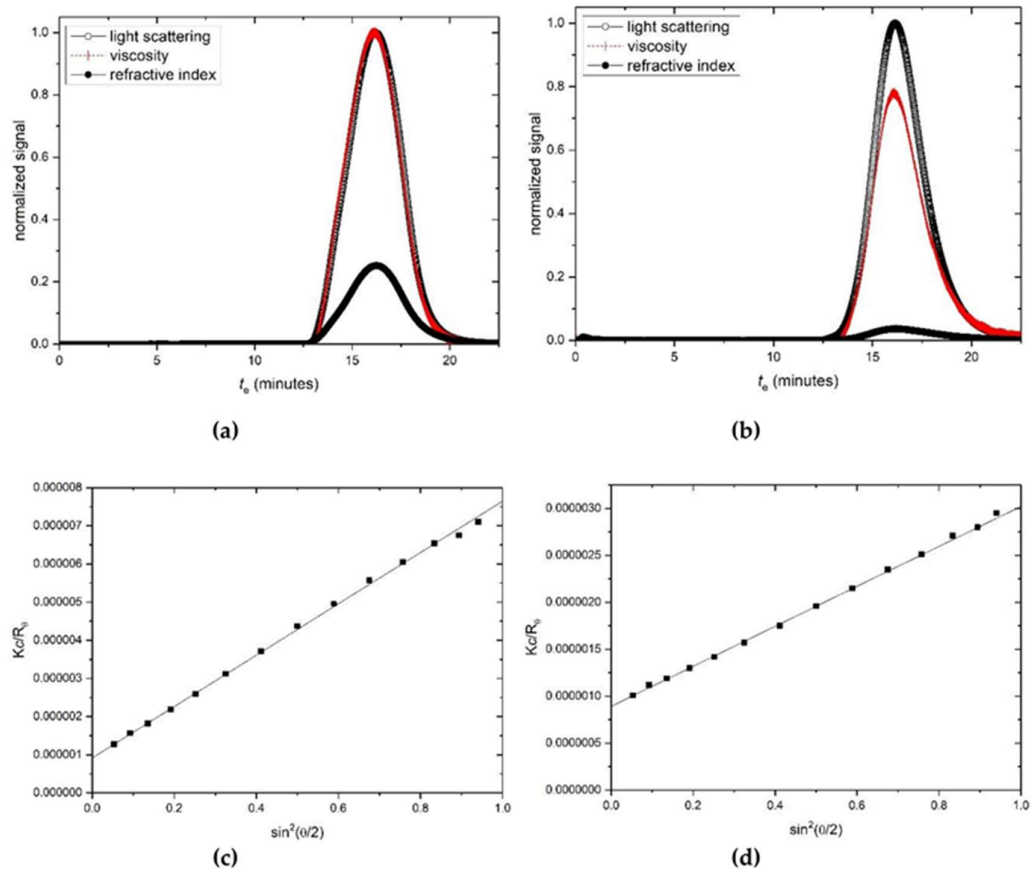
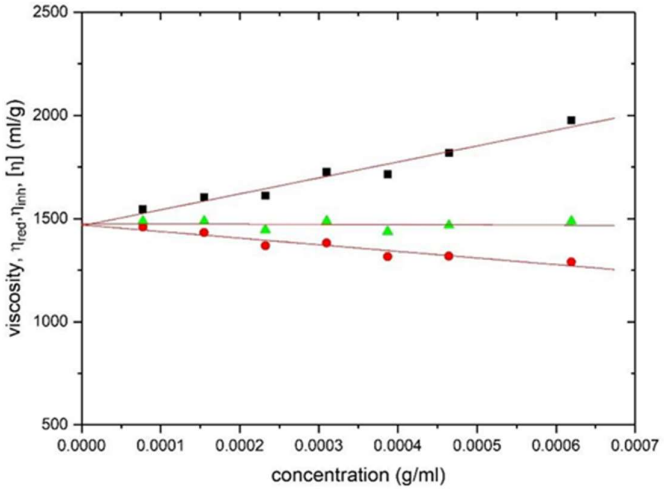
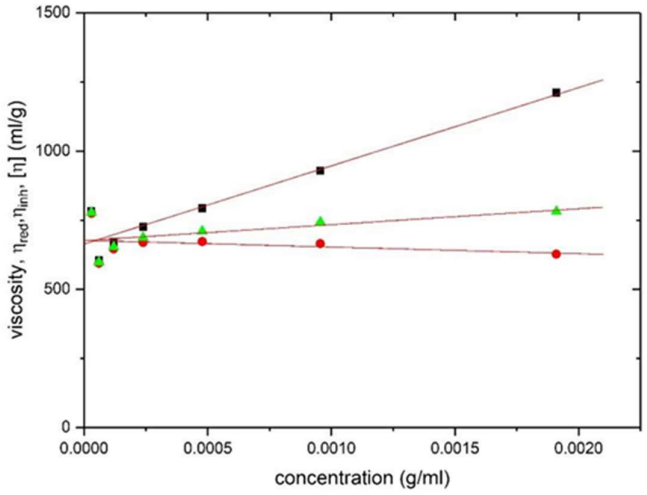


Figure 3. Size exclusion chromatography—multiangle light scattering (SEC-MALS) elution profiles for (a) hyaluronic acid, HA and (b) tamarind seed polysaccharide, TSP. Solid black circles: light scattering signal at a scattering angle θ = 90◦. Open circles: concentration (refractive index) signal; dashed line: differential pressure (viscosity) signal; te = elution time. (c) Zimm fit of Kc/Rθ (see text for definitions) vs sin2(θ/2) for HA, at a single elution time te. (d) Corresponding plot for TSP. Solution pH = 6.8, I = 0.1, temperature = 20.0 ◦C.



(a)



(b)

Figure 4. Evaluation of the intrinsic viscosity [η] from Ostwald viscometry: (a) hyaluronic acid and (b) tamarind seed polysaccharide. Squares: Huggins' extrapolation; triangles: Solomon–Ciuta; circles: Kraemer extrapolation. Solution pH = 6.8, I = 0.1, temperature = (20.00 ± 0.05) ◦C.

Since the concentration is known also for each value of te from the refractive index detection, this enables an estimate for [η](te) to be obtained from equation (9). Mark–Houwink–Kuhn–Sakurada (MHKS) plots of log [η](te) vs log Mw(te) for HA and TSP respectively are given in (Figure 4a,b), enabling evaluation of the MHKS conformation parameter a:

$[\eta](t_e) = M_w(t_e)^a$ (10)

From Figure 5a (HA) a value of a of 1.1 is obtained, corresponding to a stiff extended conformation, although >M = 800 kg/mol a lower value is obtained (a ~0.56) corresponding to a flexible random coil conformation. Figure 5b we obtain a = 0.63 for TSP, also corresponding to a flexible random coil.

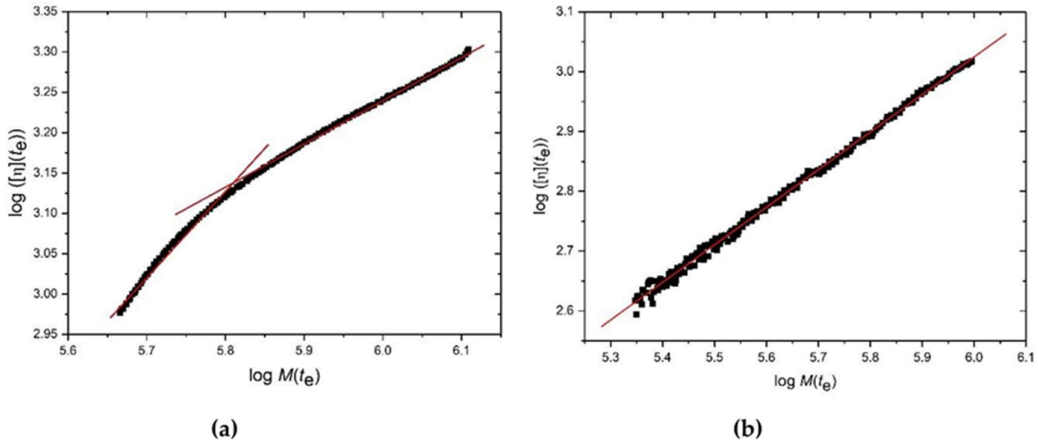


Figure 5. Mark–Houwink–Kuhn–Sakurada plots of log intrinsic viscosity vs log molecular weight M(te) at corresponding elution times te: (a) hyaluronic acid and (b) tamarind seed gum. Solution pH = 6.8, I = 0.1, temperature = (20.0 ± 0.1) ◦C.

3.2. Hydrodynamic Behaviour of Mixtures of HA and TSP

Figure 6a shows the SEC-MALS profile for a mixture of HA with TSP. One can see a slight shift to lower elution times (higher molar masses) relative to HA and TSP by themselves (Figure 3a,b)

with a shoulder at lower elution time suggestive of some degree of complexation or weak interaction. Analysis using ASTRA software shows agreement in the measured Mw (= 720 ± 30) kg/mol compared with the predicted value of 755 kg/mol.

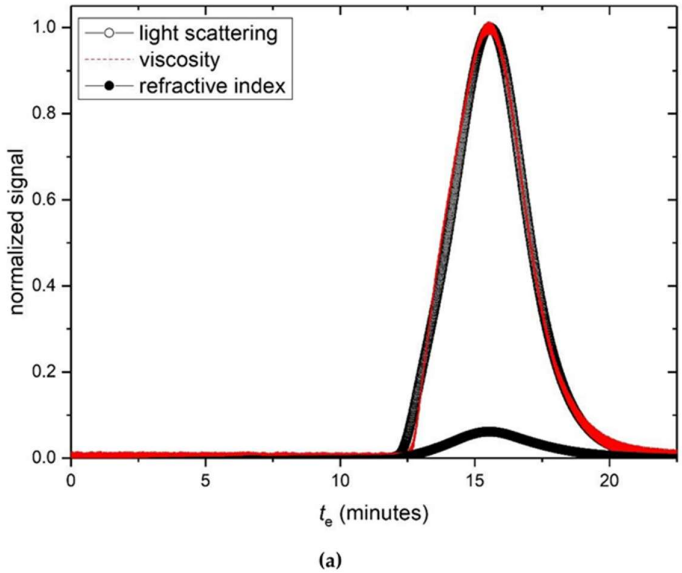


Figure6. (a) Elution profiles for a 1:1 mixture of HA to TSP in 0.1M, pH 6.8 PBS buffer. Solid circles—light scattering 90◦ signal. Open circles—concentration (refractive index) signal. Dashed line—relative viscosity signal. Concentration of HSA = 1 mg/mL, and TSP= 1 mg/mL. (b) Sedimentation coefficient distributions for HA (black), TSP (red) and HA-TSP mixture (green). Concentrations of HA, TSP 1 mg/mL. (c) As (b) but concentrations of HA, TSP = 2.0 mg/mL.

These observations are reinforced by the results from intrinsic viscosity. Table 2 shows the comparison of the theoretical intrinsic viscosity calculated from the ratio of HA to TSP in each mixture with varying ratios (the HA:TSP ratios = 3:1, 1:1 and 3:1), and the actual intrinsic viscosity obtained experimentally from the capillary viscometry. It is clear that there is no significant increase (HA:TSP = 1:1 and 1:3).

Table 2. Measured intrinsic viscosities for HA:TSP mixtures compared with the theoretically predicted (based on values from Table 1) if there was no interaction.

HA:TSP ratio	**[η]**	**[η] (theoretical)**
1:3	780 mL/g	940 mL/g
1:1	1100 mL/g	1075 mL/g
3:1	1180 mL/g	1200 mL/g

4. Conclusions

The present findings of this hydrodynamic study using mixtures of hyaluronic acid and tamarind seed polysaccharides implies there is no incompatibility in solutions of the two, at concentrations used in popular formulations to help supplement reduced lacrymal fluid/ ocular mucin in an aging population. Earlier observations using NMR spectroscopy [1] have demonstrated a synergistic interaction between the two polysaccharides. The present study complements those observations by showing that no large aggregate or supramolecular formation was evident, reassuring for formulations involving the two polymers.

Author Contributions: Conceptualization and supervision, S.E.H., M.K.P.-J.; data curation, T.C., T.M., V.D.; sample origination and application S.O. All authors have read and agreed to the published version of the manuscript.

Funding: V.D. is supported by a Research Fellowship from the United Kingdom Engineering and Physical Sciences Research Council.

Conflicts of Interest: The authors declare no conflict of interest.

References

Uccello-Barretta, G.; Nazzi, S.; Zambito, Y.; Di Colo, G.; Balzano, F.; Sanso, M. Synergistic interaction between TS-polysaccharide and hyaluronic acid: Implications in the formulation of eye drops. Int. J. Pharm. 2010, 395, 122–131.

Lee, D.; Lu, Q.; Sommerfeld, S.D.; Chan, A.; Menon, N.G.; Schmidt, T.A.; Elisseeff, J.H.; Singh, A. Targeted delivery of hyaluronic acid to the ocular surface by a polymer-peptide conjugate system for dry eye disease. Acta Biomater. 2017, 55, 163–171.

Luo, L.; Lai, J. Epigallocatechin gallate-loaded gelatin-g-poly(N-isopropylacrylamide) as a new ophthalmic pharmaceutical formulation for topical use in the treatment of dry eye syndrome. Sci. Rep. 2017, 7, 9380.

Luo, L.-J.; Nguyen, D.D.; Lai, J.-Y. Long-acting mucoadhesive thermogels for improving topical treatments of dry eye disease. Mater. Sci. Eng. C 2020, 115, 111095.

Lai, J.-Y.; Luo, L.-J.; Nguyen, D.D. Multifunctional glutathione-dependent hydrogel eye drops with enhanced drug bioavailability for glaucoma therapy. Chem. Eng. J. 2020, 402, 126190.

Barabino, S.; Rolando, M.; Nardi, M.; Bonini, S.; Aragona, P.; Traverso, C.E. The effect of an artificial tear combining hyaluronic acid and tamarind seeds polysaccharide in patients with

moderate dry eye syndrome: A new treatment for dry eye. Eur. J. Ophthalmol. 2014, 24, 173–178.

Hokputsa, S.; Jumel, K.; Alexander, C.; Harding, S.E. A comparison of molecular mass determination of hyaluronic acid using SEC/MALLS and sedimentation equilibrium. Eur. Biophys. J. 2003, 32, 450–456.

Hokputsa, S.; Jumel, K.; Alexander, C.; Harding, S.E. Hydrodynamic characterisation of chemically degraded hyaluronic acid. Carbohydr. Polym. 2003, 52, 111–117. [CrossRef]

Rah, M.J. A review of hyaluronan and its ophthalmic applications. Optom. J. Am. Optom. Assoc. 2011, 82, 38–43.

Johnson, M.E.; Murphy, P.J.; Boulton, M. Effectiveness of sodium hyaluronate eyedrops in the treatment of dry eye. Graefe's Arch. Clin. Exp. Ophthalmol. 2006, 244, 109–112.

Hammer, M.E.; Burch, T.G. Viscous corneal protection by sodium hyaluronate, chondroitin sulfate, and methylcellulose. Investig. Ophthalmol. Vis. Sci. 1984, 25, 1329–1332.

Semenzato, A.; Costantini, A.; Baratto, G. Green polymers in personal care products: Rheological properties of tamarind seed polysaccharide. Cosmetics 2015, 2, 1–10.

Rolando, M.; Valente, C. Establishing the tolerability and performance of tamarind seed polysaccharide (TSP) in treating dry eye syndrome: Results of a clinical study. BMC Ophthalmol. 2007, 7, 1–8.

Patel, T.R.; Morris, G.A.; Ebringerova, A.; Vodenicarova, M.; Velebny, V.; Ortega, A.; de la Torre, J.G.; Harding, S.E. Global conformation analysis of irradiated xyloglucans. Carbohydr. Polym. 2008, 74, 845–851.

Lian, L.-Y. NMR studies of protein-ligand interactions. In Protein-Ligand Interactions, Structure and Spectroscopy: A Practical Approach; Harding, S.E., Chowdhry, B.Z., Eds.; Oxford University Press: Oxford, UK, 2001; pp. 383–405.

Uccello-Barretta, G.; Balzano, F.; Vanni, L.; Sanso, M. Mucoadhesive properties of tamarind-seed polysaccharide/hyaluronic acid mixtures: A nuclear magnetic resonance spectroscopy investigation. Carbohydr. Polym. 2013, 91, 568–572.

Harding, S.E. The Svedberg Lecture 2017. From nano to micro: The huge dynamic range of the analytical ultracentrifuge for characterising the sizes, shapes and interactions of molecules and assemblies in Biochemistry and Polymer Science. Eur. Biophys. J. 2018, 47, 697–707.

Harding, S.E.; Adams, G.G.; Almutairi, F.; Alzahrani, Q.; Erten, T.; Kök, M.S.; Gillis, R.B. Ultracentrifuge methods for the analysis of polysaccharides, glycoconjugates, and lignins. Methods Enzymol. 2015, 562, 391–439

Yang, Y.; Chang, S.; Bai, Y.; Du, Y.; Deng-Guang, Y. Electrospun triaxial nanofibers with middle blank cellulose acetate layers for accurate dual-stage drug release. Carbohydr. Polym. 2000, 243, 116477.

Wang, M.; Hai, T.; Feng, Z.; Yu, D.-G.; Yang, Y.; Bligh, S.W.A. The relationships between the working fluids, process characteristics and products from the modified coaxial electrospinning of zein. Polymers 2019, 11, 1287.

Wang, K.; Wen, H.-F.; Yu, D.-G.; Yang, Y.; Zhang, D.-F. Electrosprayed hydrophilic nanocomposites coated with shellac for colon-specific delayed drug delivery. Mater. Des. 2018, 143, 248–255.

Yoon, W.H.; Lee, K.H. Rheological properties and efficacy of the formulation of hyaluronic acid with tamarind seed polysaccharide for arthritis. Biorheology 2019, 56, 31–38.

Green, A.A. The preparation of acetate and phosphate buffer solutions of known pH and ionic strength. Am. Chem. Soc. 1933, 55, 2331–2336.

Wang, Q.; Ellis, P.R.; Ross-Murphy, S.B.; Burchard, W. Solution characteristics of the xyloglucan extracted from Detarium senegalense Gmelin. Carbohydr. Polym. 1997, 33, 115–124.

Dam, J.; Schuck, P. Calculating sedimentation coefficient distributions by direct modeling of sedimentation velocity concentration profiles. Methods Enzymol. 2004, 384, 185–212.

Schachman, H.K. Ultracentrifugation Biochemistry; Academic Press: New York, NY, USA; London, UK, 1950.

Gralén, N. Sedimentation and Diffusion Measurements on Cellulose and Cellulose Derivatives. Ph.D. Thesis, University of Uppsala, Uppsala, Sweden, 1994.

Wyatt, P.J. Combined differential light scattering with various liquid chromatography separation techniques. In Laser Light Scatt Biochemistry; Harding, S.E., Sattelle, D.B., Bloomfield, V.A., Eds.; Royal Society of Chemistry: Cambridge, UK, 1992; pp. 35–38.

Picout, D.R.; Ross-Murphy, S.B.; Errington, N.; Harding, S.E. Pressure cell assisted solubilization of xyloglucans: Tamarind seed polysaccharide and (gum). Biomacromolecules 2003, 4, 799–807.

Zimm, B.H. The Scattering of light and the radial distribution function of high polymer Solutions. Chem. Phys. 1948, 16, 1093–1099.

Harding, S.E.; Tombs, M.P.; Adams, G.G.; Paulsen, B.S.; Inngjerdingen, K.T.; Barsett, H. An Introduction to Polysaccharide Biotechnology, 2nd ed.; CRC Press: Boca Raton, FL, USA, 2017.

Almutairi, F.M.; Erten, T.; Adams, G.G.; Hayes, M.; McLoughlin, P.; Kok, M.S.; Mackie, A.R.; Rowe, A.J.; Harding, S.E. Hydrodynamic characterization of chitosan and its interaction with two polyanions: DNA and xanthan. Carbohydr. Polym. 2015, 122, 359–366.

Harding, S.E. The intrinsic viscosity of biological macromolecules. Progress in measurement, interpretation and application to structure in dilute solution. Prog. Biophys. Mol. Biol. 1997, 68, 207–262.

Huggins, M.L. The viscosity of dilute solutions of long-chain molecules. IV. Dependence on concentration. J. Am. Chem. Soc. 1942, 64, 2716–2718.

Kraemer, E.O. Molecular weights of celluloses and cellulose derivates. Ind. Eng. Chem. 1938, 30, 1200–1203.

Solomon, O.F.; Ciuta, I.Z. Determination de la viscosite intrinseque de solutions de polymeres par une simple determination de la viscosite. J. Appl. Polym. Sci. 1962, 7, 683–686.

© 2020 by the authors. Licensee MDPI, Basel, Switzerland. This article is an open access article distributed under the terms and conditions of the Creative Commons Attribution (CC BY) license (http://creativecommons.org/licenses/by/4.0/).

11.3 Probing the effect of aroma compounds on the hydrodynamic properties of mucin glycoproteins

Vlad Dinu, Thomas MacCalman, Ni Yang, Gary G. Adams, Gleb E. Yakubov, Stephen E. Harding & Ian D. Fisk

European Biophysics Journal volume 49, pages799–808 (2020)

Abstract

Aroma compounds are diverse low molecular weight organic molecules responsible for the flavour of food, medicines or cosmetics. Natural and artificial aroma compounds are manufactured and used by the industry to enhance the flavour and fragrance of products. While the low concentrations of aroma compounds present in food may leave no effect on the structural integrity of the mucosa, the effect of concentrated aroma volatiles is not well understood. At high concentrations, like those found in some flavoured products such as e-cigarettes, some aroma compounds are suggested to elicit a certain degree of change in the mucin glycoprotein network, depending on their functional group. These effects are particularly associated with carbonyl compounds such as aldehydes and ketones, but also phenols which may interact with mucin and other glycoproteins through other interaction mechanisms. This study demonstrates the formation of such interactions in vitro through the use of molecular hydrodynamics. Sedimentation velocity studies reveal that the strength of the carbonyl compound interaction is influenced by compound hydrophobicity, in which the more reactive short chain compounds show the largest increase in mucin-aroma sedimentation coefficients. By contrast, the presence of groups that increases the steric hindrance of the carbonyl group, such as ketones, produced a milder effect. The interaction effects were further demonstrated for hexanal using size exclusion chromatography light scattering (SEC-MALS) and intrinsic viscosity. In addition, phenolic aroma compounds were identified to reduce the sedimentation coefficient of mucin, which is consistent with interactions in the non-glycosylated mucin region.

Introduction

Aroma compounds are low molecular weight compounds which are responsible for the perception of flavour. There have been over 7000 aroma compounds identified in 2014 (Parker et al. 2015). Common classes of aroma compounds include aldehydes, ketones, esters, phenols, thiols, lactones and different cyclic configurations. Fruit, vegetables, processed food and most confectionery products contain very low concentrations of aroma compounds (less than 0.01 mg/ml or 10 ppm), most of which have developed naturally during product development, such as thermal treatment or fermentation. However, some products are by design enriched with aroma compounds, to enhance their flavour. The aroma ingredients added to improve the flavour of food and other consumer products are generally recognized as safe (GRAS), and are approved for use in food, pharmaceutics and cosmetics. However, recent applications of flavour technologies led to a significant variation in the concentrations of aroma compounds in a range of products (Dinu et al. 2020). Electronic cigarettes are a prime example of a product in which the concentration of aroma compounds can exceed 5% of the entire formulation (50,000 ppm), which is approximately 10,000 times higher than the typical concentration of aroma compounds found in fruit. These concentrations are close to or even higher than it is deemed safe for consumption by the Flavor and Extract Manufacturers Association (FEMA) (FEMA FEMA, 2020a; Tierney et al. 2016; Cohen et al. 2020). Therefore, their use in e-cigarettes challenges these fundamental

GRAS assumptions, because of the high concentration of aldehyde, ketone and other classes of flavourings in direct contact with the oral and respiratory mucosa.

Irrespective of the mode of administration of flavour compounds (ingestion or inhalation), their effect on the intestinal or respiratory mucosae will be determined by a similar type of interaction mechanism, varying according to the structure and function of different mucins (Linden et al. 2008). Thermodynamic and kinetic mechanisms of interaction are influenced the physical and chemical properties of each type of aroma compound (Parker et al. 2015). Most of them are highly hydrophobic and have a low solubility in water, but the shorter chain compounds are also soluble in aqueous solvents. In addition, each molecule has a different freezing and boiling point which would have a significant effect on the properties of the mucus surface, such as density and viscosity effects, but also on the properties of other biological systems in contact with the aroma compounds.

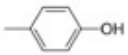
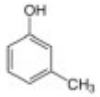
Interactions between aroma compounds and proteins have been extensively reported in the past few decades (Fares et al. 1998; Jouenne and Crouzet 2000; Paravisini and Guichard 2016; Dinu et al. 2019b). They are generally grouped into three types: (i) binding of flavour compounds, (ii) phase partitioning, i.e. air, water or lipid, or (iii) viscosity effects (Rothe 1997). Binding can either be reversible or irreversible depending on the strength of the interaction. Ketones and aldehydes were suggested to covalently bind with amino groups of proteins (Damodaran and Kinsella 1980; Weerawatanakorn et al. 2015). Others have shown that they can form weak hydrogen bonds with macromolecules containing electronegative clusters of nitrogen, sulphur or oxygen (Reineccius 2006; Tromelin et al. 2006). Although, there is no established mechanism of interaction between proteins and different classes of aroma compounds, previous studies have suggested covalent interactions between lysine and histidine residues of proteins and monounsaturated aldehydes and ketones such as hexanal, t-2-hexenal and butanone (Kikugawa et al. 1988; Meynier et al. 2004).

Mucins are the glycoprotein building blocks of the protective layer covering the mucosal membrane, lining the alimentary canal from the oral and nasal cavities through to the large intestine. They vary considerably in size, from a few thousand to several million daltons. The protein domains are rich in threonine and serine which form a bridge between their hydroxyl groups and the N-acetylgalactosamine residues of the carbohydrate region. While most mucins are heavily glycosylated (up to 90%), the ‘naked’ unglycosylated polypeptide is predominantly composed of cysteine, serine, threonine, lysine and proline which assist in the coiling of the glycoprotein which is thought to give rise to potential interaction sites with hydrophilic aroma compounds (Harding et al. 1983). These exposed amino groups are theoretically able to form several kinds of reactions with carbonyl groups, including Shiff bases or Michael addition reactions. These have also been demonstrated for more complex aldehyde compounds such as vanillin, shown to form Schiff bases with different amino acids including cysteine, lysine and phenylalanine (Kikugawa et al. 1988; Meynier et al. 2004; Ziegler 2007). In addition, reactions with cysteine were shown to be reversible under heat and acidic conditions, such as the stomach environment.

While low concentrations of aroma compounds may have negligible physical and chemical effects on the oral and intestinal mucus during oral processing, the very high concentrations of carbonyl containing flavour compounds inhaled by vaping are suggested to contribute significantly to the physical and chemical properties of the lung mucus, including viscosity effects and subsequent effects on the respiratory function. In light of this hypothesis, matrix free biophysical characterisation techniques of analytical ultracentrifugation (SV-AUC), viscometry and size exclusion chromatography multi angle laser light scattering (SEC-MALS) were employed to study some of the effects of model volatile compounds: linear aldehydes (hexanal, octanal, decanal) and linear ketones (butanone, hexanone, octanone, decanone)

(Table 1). In addition, the effects of phenolic compounds (guaiacol, p-cresol and m-cresol) on the solution properties of bovine submaxillary mucin were probed using sedimentation velocity. This work along with future investigations will provide some of the starting points on the understanding some of the effects of high concentration volatile aroma compounds on the respiratory but also on the gastro-intestinal system.

Table 1 Lipophilicity (LogP) and chemical representations of the volatile aroma compounds used in the bovine submaxillary mucin (BSM) interaction experiments

Compound	Log*P*	Structure
	Ketones	
butanone	0.37	
hexanone	1.38	
octanone	2.37	
decanone	3.73	
	Aldehydes	
hexanal	1.78	
octanal	2.54	
decanal	3.9	
	Phenols	
guaiacol	1.32	
p-cresol	1.94	
m-cresol	1.96	

Materials and methods

Sample preparation

Bovine submaxillary mucin (BSM) (type I-S, M3895) and the volatile compounds were from Sigma-Aldrich (Dorset, UK). The experiments were prepared in 0.1 M phosphate buffered saline (PBS), according to (Green 1933). Aldehydes and ketones were pre-solubilized in 70% ethanol by adding 1 mL aroma compound to 4 mL 70% ethanol to obtain a 20% (250 mg/mL stock solution). To prepare a 1 mg/mL solution of volatile compound, a 5 µL aroma compound was added to a 955 µL solution containing solubilized BSM. Phenols were added directly to their respective mucin solution.

Analytical ultracentrifugation sedimentation velocity (SV)

The experiments were performed at 20.0 °C using the Rayleigh interference optical system in the Optima XL-I analytical ultracentrifuge (Beckman, Palo Alto, USA). A volume of 395 µL sample and 405 µl solvent, respectively, were injected into 12 mm double sector epoxy cells with sapphire windows, optically aligned to 0°as described previously (Channell et al. 2018). The samples were centrifuged at 30 000 rpm for 12 h. Raw data were analysed in SEDFIT

V16.1c using the least-squares boundary modelling ls-g*(s) method, abbreviated as g(s) in this study, by generating sedimentation coefficient distributions, where s is the rate of particle sedimentation or sedimentation coefficient (in Svedberg units, S = 10–13 s). The coefficient values from the g(s) vs s distributions were normalised to standard conditions (viscosity and density of solvent at 20.0 °C) to give s20,w. A partial specific volume of 0.64 mL/g was employed for mucin (Dodd et al. 1998; Fisher et al. 2006). TI (time invariant) and RI (radial invariant) noise were removed during data fitting. The distributions were exported and plotted in Origin 7.5 (Origin Lab, MA, US).

Size exclusion chromatography: multi angle light scattering (SEC-MALS)

The SEC set-up consisted of a Postnova Analysis PN7505 degassing unit (Landsberg am Lech Germany), Shimadzu LC-10AD HPLC Pump (Shimadzu UK, Milton Keynes, UK.), fitted with a Spark-Holland Marathon Basic autosampler (Spark Holland, Emmen, The Netherlands) combined with a TSK Gel guard column (7.5 × 75 mm) and TSK Gel G5000, G6000 columns (7.5 × 300 mm) connected in series (Tosoh Biosciences, Tokyo, Japan), fully flushed of column debris. Light scattering intensities were simultaneously detected at 14 angles as a function of elution volume using a DAWN® HELEOS™ II, light scattering photometer connected in series to a ViscoStar® II on-line differential viscometer, an Optilab® rEX refractive index detector (Wyatt Technology Corporation, California, U.S.A.). A stock solution of 1.0 mg/mL BSM and BSM-hexanal was filtered through a 0.45 µm syringe filter (Whatman, Maidstone, England) to remove any insoluble material or dust prior to injection and then injected into the autosampler. A 100 µl aliquot of BSM and BSM-hexanal were injected onto the columns at ambient temperature (20 ± 3 °C) at a flow rate of 0.8 mL/min. ASTRA™ (Version 6) software (Wyatt Technology Corporation, Santa Barbara, U.S.A.) was used to estimate the weight average molecular weight, Mw and radius of gyration Rg, as a function of elution volume. The 4mW He–Ne laser was used at a wavelength of 632.8 nm, and the refractive increment used was 0.181 mL/g. Because of the low solute concentrations and column dilution, non-ideality effects were assumed negligible.

U-tube capillary (Ostwald) viscometry

Relative viscosity was measured using the semi-automated (Schott Geräte, Hofheim, Germany) U-tube Ostwald capillary viscometer immersed in a temperature-controlled water bath at 20.00 °C. A constant volume of 2.0 mL was used for sampling BSM-hexanal mixture, automatically recorded six times. BSM concentrations were constant at 1.0 mg/mL while the buffer solution was made using different concentrations of hexanal. The intrinsic viscosity, [η] was calculated according to the Solomon–Ciuta equation (Solomon and Ciuta 2019) at a constant BSM concentration “c” of 1.0 mg/mL and plotted against the concentration of the solvent in Fig. 2 using:

$$[\eta] \cong 1c(2(\eta sp) - 2\ln(\eta r))1/2.[\eta] \cong 1c(2(\eta sp) - 2\ln(\eta r))1/122. \quad (1)$$

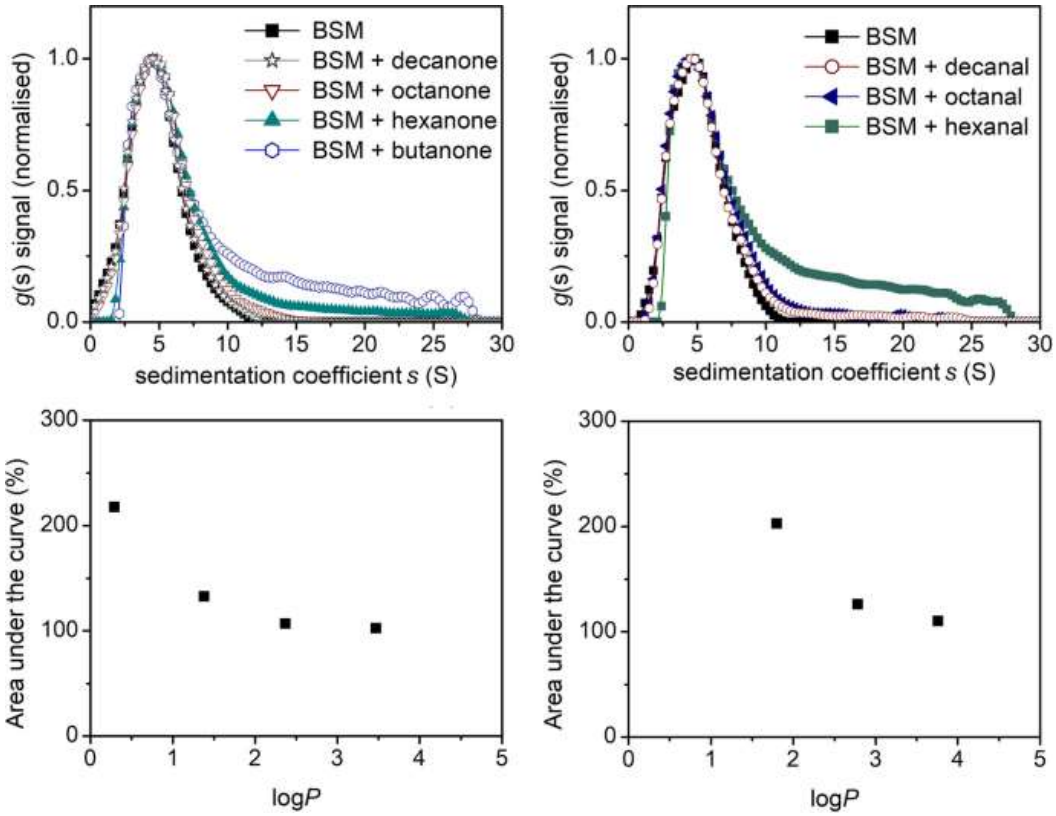
Results and discussion

Carbonyl containing compounds

The sedimentation velocity results show the distribution of sedimentation coefficients for 1.0 mg/mL BSM solution, revealing a broad polydisperse distribution ranging from 2 to 12S, as shown previously (Dinu et al. 2019a). The addition of linear aldehydes and ketone volatile compounds was shown to result in an increase in the proportion of species of high sedimentation rates, tailing up to ~ 28S for the mixtures containing more hydrophilic compounds such as butanone or hexanal (Fig. 1). The effect is negatively correlated with compound hydrophobicity, appearing milder for less soluble, longer chain aldehydes but also for ketones as a whole, possibly due to the alkyl group reducing their reactivity (see Table 1).

In other words, the SV data suggest that the mucin interaction with the aldehydes and ketones is stronger for the shorter chain compounds, given their higher solubility in water. This can also be evidenced directly from the raw data (Appendix Fig. 6) in which changes in the fringe concentration and shape correspond to species of higher sedimentation coefficient and higher diffusion. Although there is some sedimentation contribution from the aroma compounds, in particular hexanal and butanone, being the most soluble (Appendix Fig. 7), the signal and apparent sedimentation coefficient are too low to suggest the possibility of concomitant sedimentation with the much larger mucin components.

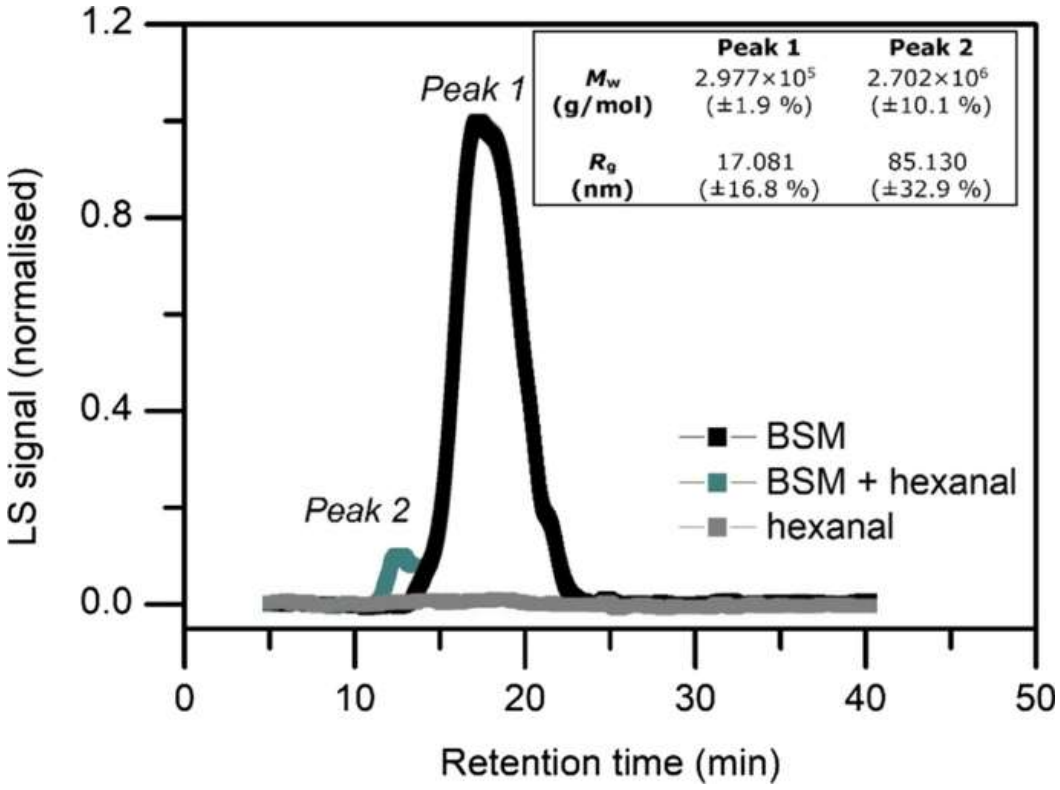
Fig. 1



Sedimentation velocity, g(s) analysis showing the sedimentation coefficient distributions of bovine submaxillary mucin (1.0 mg/mL) and the effect of aldehydes and ketones (1.0 mg/mL); and bottom: plot of hydrophobicity, logP against % change in mucin complexation as determined by the area under the normalised sedimentation coefficient curve. Rotor speed: 30,000 rpm (90,000 g), 20.0 ºC

The exact mechanism behind the increase in the higher S species remains unclear; however, AUC are indicative of non-specific mucin–solvent interactions causing either (i) partial mucin aggregation or (ii) changes in mucin conformation. In addition to the sedimentation results, an additional experiment was employed using the size exclusion chromatography coupled to a multi angle laser light scattering system (SEC-MALS) looking at the interaction of mucin with hexanal (Fig. 2).

Fig. 2



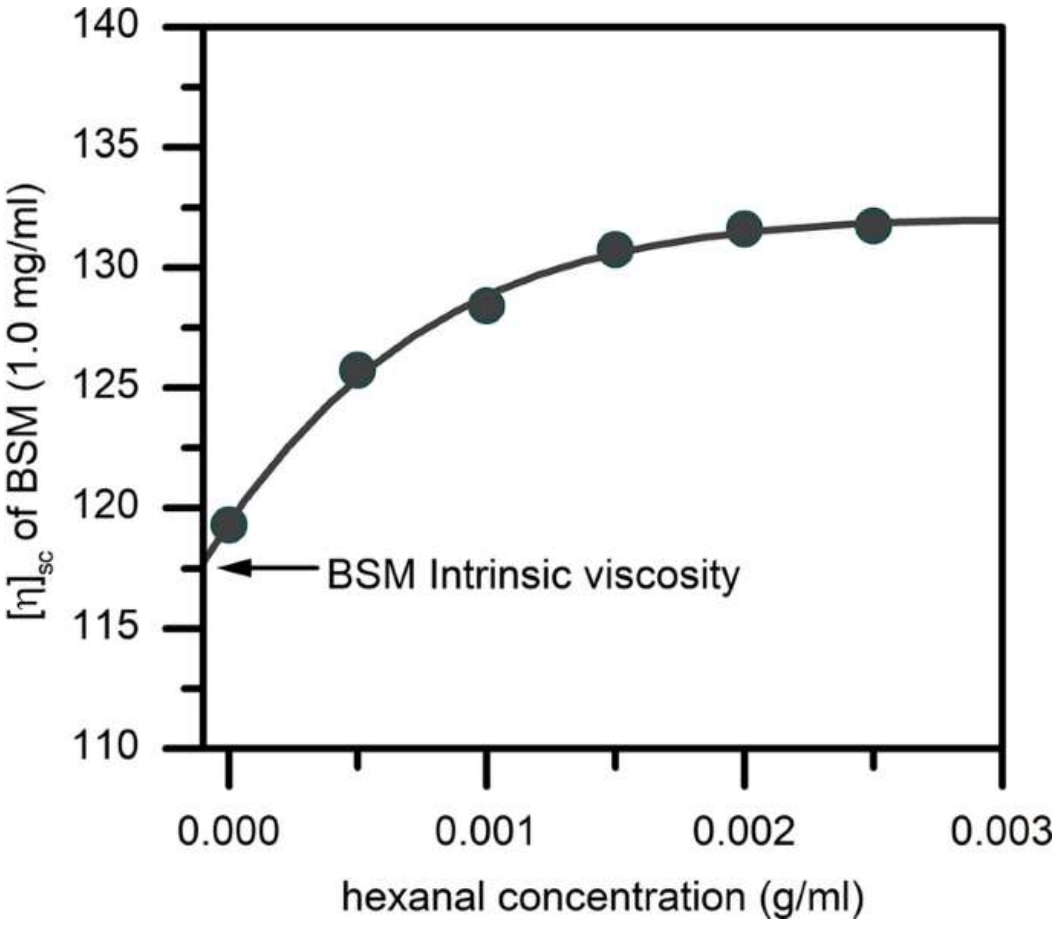
SEC-MALS results showing the light scattering (LS) elution profile of BSM, hexanal and the result of their interaction. Insert shows the summary for the hydrodynamic parameters for the main peaks, such as the apparent weight average molar mass (Mw) and radius of gyration (Rg)

During size exclusion chromatography, larger particles elute first, followed by smaller molecules. If they are too small to be detected by the column, as is the case of hexanal, they are not separated by the column and, therefore, no signal is recorded. The elution profiles (Fig. 2) reveal a broad multi-component distribution of BSM, ranging from ~ 16 to 24 min, as reported previously (Dinu et al. 2019a). However, the addition of hexanal led to the formation of larger moieties (Peak 2), which appear to be up to ten times larger than the average molecular mass for Peak 1. The apparent hydrodynamic radius Rg of the new complexes is 85 nm, which is five times larger than the average Rg values for Peak 1 although the relatively high experimental errors indicates a certain degree of size heterogeneity in addition to the limited signal resulting from its small concentration, relative to the main peak.

To further examine the effect of the aldehyde containing solvent, the intrinsic viscosity of BSM was determined in the presence of different concentrations of hexanal. They were obtained via the Solomon–Ciuta equation and plotted against concentrations of hexanal (Fig. 3). An increase in the concentrations of hexanal led to an increase in the intrinsic viscosity of mucin, gradually plateauing at higher hexanal concentrations, which is attributed to the solubility of hexanal in water (~ 2.5 mg/mL at 20.0 °C). Currently, sedimentation, size exclusion and intrinsic viscosity results confirm an interaction between volatile aldehydes/ketones and mucin. Although non-specific interactions between the glycoproteins and the solvent are suspected, due to an increase in the aggregation state of mucin, the sedimentation of the more hydrophilic aldehydes and ketones with the higher S species of

the mucin is plausible, given the increase in the solute concentration (area under the curve). But the small increase in mucins intrinsic viscosity is consistent with small changes in conformation, which is suggestion to result from the binding of the carbonyls to amino regions of mucin, rather than solvent effects. A good way of confirming the complexation with the small solutes would be the use of gel chromatography, but previous attempts on mucin glycoproteins have proved unsuccessful due to smearing and inconsistent separation due to the very high molecular weight, high polydispersity and high degree of glycosylation.

Fig. 3

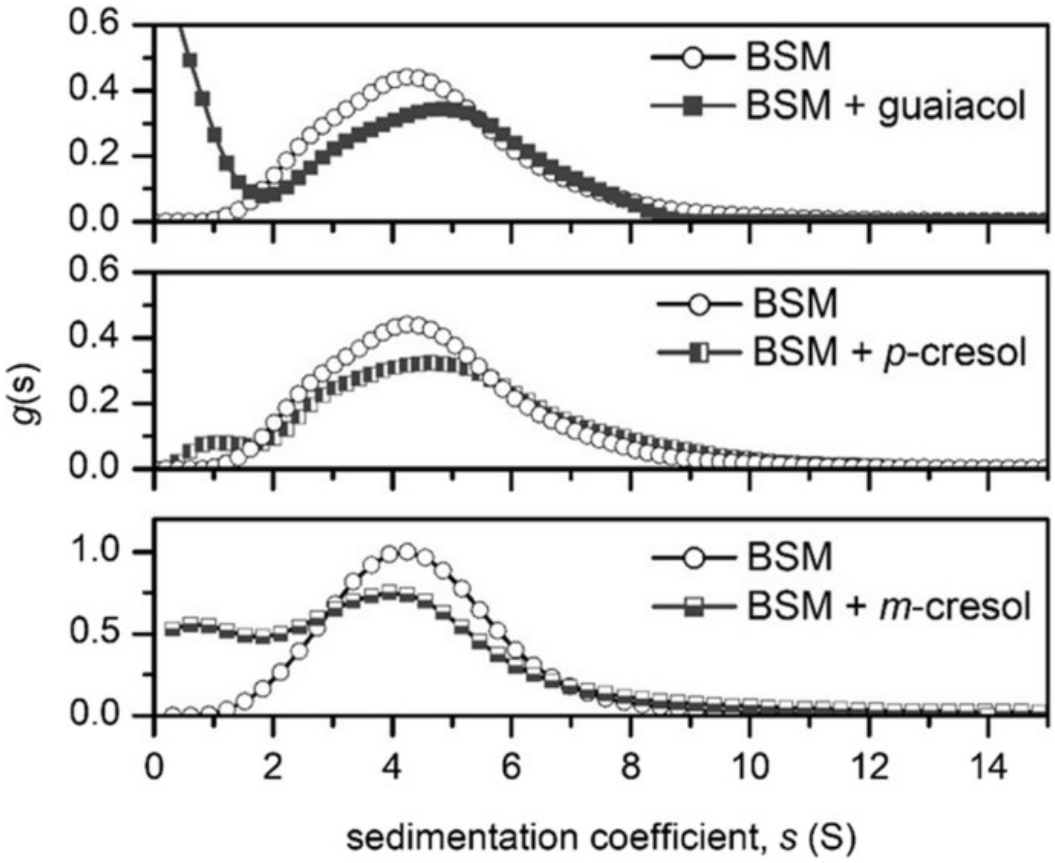


Solomon–Ciuta intrinsic viscosity [η]sc analysis showing the quantitative effect of hexanal addition to bovine submaxillary mucin (1.0 mg/mL) in 0.1 M phosphate buffer saline. The polynomial fit is based on six data points derived from the separate hexanal/BSM mixtures

Phenolic aroma compounds

Next, the sedimentation velocity analysis was applied to study the effects of another class of bioactive volatile aroma compounds—phenols, which have also been found to elicit changes in the sedimentation properties of mucin (Fig. 4). Although they are not directly used as food flavourings, they can be found in a range of medicines or as bi-products generated during heating of e-cigarette aerosol (Dinu et al. 2020). Changes in the sedimentation coefficient of BSM upon the addition of guaiacol, p-cresol and m-cresol suggest the formation of a smaller mucin components with a lower sedimentation coefficient, suggesting that phenols act as some type of molecular chaotropes.

Fig. 4



Sedimentation velocity, g(s) analysis showing the sedimentation coefficient distributions of BSM (0.5 g/mL) and the result of its interactions with different phenol volatile compounds (0.5 mg/mL). Rotor speed: 30,000 rpm (90,000 g), 20.0 ºC

These interactions were also studied by Raman spectroscopy, by examining changes in the vibrational spectrum of BSM before and after the addition of p-cresol (Appendix Fig. 8, Dinu et al. 2019a). Spectral changes were observed in the 820–850 cm−1 region, which represents a Fermi doublet, distinguished by the stronger (840 cm−1) and weaker (810 cm−1) Raman shifts. The ratio of the doublet is said to provide information on the strength of the hydrogen bonding of the phenoxy group in solution. Second, a decrease in the intensity of the 1500–1700 cm−1 Amide I and II region was observed, indicating changes in the non-glycosylated protein region of mucins (Dinu et al. 2019a).

Discussion

Protein–aroma interactions have been reported since the 1970's first study of protein-flavor binding (Arai et al. 1970). Using simple linear aldehydes and ketones, we aimed to gain some information on the reported interactions between flavourings which have a carbonyl functional group. SV-AUC was used to confirm that the interactions are dependent on the solubility of aldehyde and ketone flavours in water. Second, we have confirmed that aldehydes are more reactive than ketones, as shown by the increase in the concentrations and the rate of sedimenting boundaries (Appendix Fig. 6).

Other studies also confirmed a stronger affinity of aldehydes for binding of bovine serum albumin than ketones (Damodaran and Kinsella 1980). The mechanism of interaction is

suggestion to arise from the binding between lysine residues and the carbonyl group of the monounsaturated aroma compounds (Kikugawa et al. 1988; Meynier et al. 2004). In addition, shorter more hydrophilic molecules such as acetaldehyde were previously demonstrated to increase the risk of developing alcoholic liver disease and hepatocellular carcinoma through a similar type of protein adduct formations, leading to impairment in protein function (Donohue et al. 1983). More recently, aroma–mucin interactions have also been proposed for more complex molecules, because there is a significant reduction in the gas phase concentration of octanal, nonanal and decanal in the presence of mucin at neutral pH, reported using gas chromatography, reinforcing the hypothesis of aroma–mucin interactions (Dinu et al. 2019b). In other studies, vanillin and ethyl vanillin which also contain additional hydroxyl and ether groups were reported to interact with DNA at the A-T groove region under physiological conditions (Qais et al. 2019). Other work also found the use of vanillin as a DNA-dependent protein kinase inhibitor for use in anti-cancer therapies (Durant and Karran 2003). While the exact mechanism remains a topic of further investigation, the current SV, viscosity and size exclusion analysis suggests that the interactions induced by the small carbonyl containing compounds are inducing changes in the conformation and/or mucin aggregation.

Unlike aldehydes and ketones, some phenol molecules such as cresols and guaiacol, the latter being a phenol with a methoxy group, were found to exhibit the opposite effect. The sedimentation experiments indicate the presence of smaller components and a decrease in the mucin components. The additional Raman experiment shows a loss in the amide region, indicative of changes in the mucin region which is free of glycosylation. Previously, phenols such as m-cresol have long been used as an excipient in insulin formulations to de-aggregate insulin and keep the proteins in their active, monomeric form (Whittingham et al. 1998). Guaiacol is another related compound which is used in the synthesis of other aroma compounds but also naturally present in the flavour of whiskey. It is used as a universal substrate for peroxidase enzymes, through the interaction with glycine and isoleucine with its phenoxy group (Murphy et al. 2012). It is worth suggesting that guaifenesin, which has the same functional groups as guaiacol, has been considered for reducing the molecular weight and viscosity of mucus in medication for patients suffering from mucus congestion issues caused by common colds (Seagrave et al. 2011). Previous work suggested that the hydroxyl group of the phenol ring (phenoxy group), is primarily involved in some type of interaction with mucin glycoproteins (Seagrave et al. 2011).

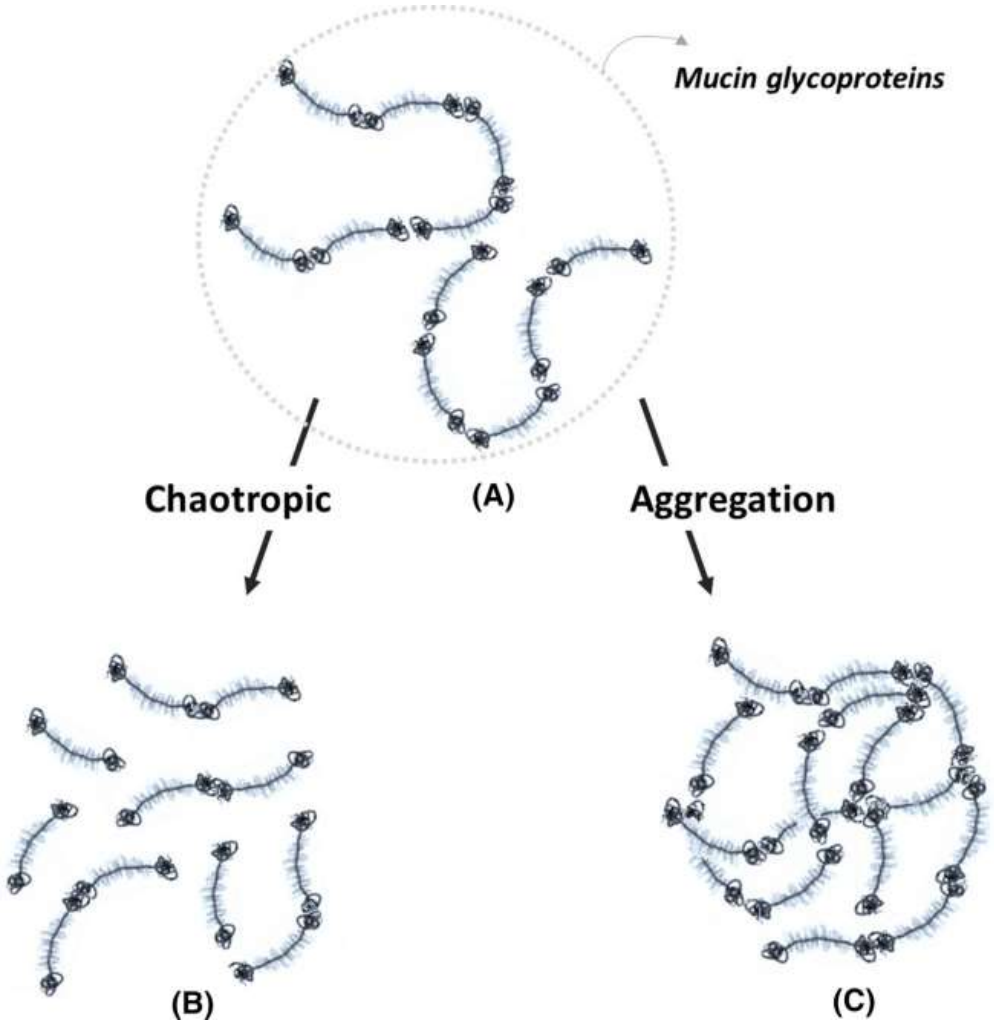
Further remarks

The exact nature by which carbonyl containing volatile compounds or the volatiles bearing a phenol group are not yet understood. Mucin glycoproteins are heavily dominated by charged oligosaccharides structures, which raise the possibility of electrostatic interactions events, such as charge shielding or charge repulsion, depending on the polarity of the volatile. Aldehydes and ketones are, therefore, suggested to have an effect on the viscoelastic properties of the mucus. In addition, volatiles bearing a phenol group are suggested to alter mucin–mucin interactions which are an important determinant in the properties of the mucus gel protecting the mucosal surfaces (Verdugo 2012). The dynamics by which the mucin stability is affected also appears to resemble that of chaotropic agents and detergents, such as urea or guanidinium hydrochloride (GuHCl), which are known to disrupt non-covalent interactions (Radicioni et al. 2016). Based on the current data and previous studies, we, therefore, suggest two possible effects on mucin–mucin interactions (Fig. 5).

While the low concentrations of volatile aroma compounds in food may not elicit a significant change on the macrostructure of mucus glycoproteins, high concentrations are, therefore, suggested to lead to a significant impairment of mucosal function. If such high

concentrations are inhaled, such as vaping products, this may also be relevant to the onset cytotoxic events reported in recent literature (Tierney et al. 2016; Omaiye 2019). Although, the components used in the current study are not desirable for use in e-cigarettes, they were used to understand the effect of more complex food flavour bearing the same types of functional groups, such as aldehydes, ketones or phenols. The two effects by which aroma compounds can affect the inherent solution properties of mucins are, therefore, proposed in the current hydrodynamic study (Fig. 5).

Fig. 5



Suggested effects on mucin–mucin interactions in solution: a Polysdisperse, random coil model of mucin in solution showing its multimeric assembly containing the glycosylated "bottlebrush" polypeptide backbone and the non-glycosylated "naked" protein region; b A proposed representation of the effect of chaotropic compounds on the solution structure of mucins; c Proposed representation of the effects of compounds causing mucin aggregation

Conclusion

This study demonstrates the evidence to suggest aroma compounds (aldehydes, ketones, and phenols) interacts with submaxillary mucin. Based on the sedimentation results, aldehydes appear to be more reactive than ketones, with shorter chain compounds leading

to species of higher sedimentation coefficients. According to size exclusion chromatography and viscosity data for hexanal, it was shown that the interactions lead to species of higher apparent molar mass, size and higher intrinsic viscosity. It is unclear whether these effects are a consequence of a direct aroma–mucin complexation induced by the interaction between carbonyls and amino groups; however, larger particle formation and conformational changes are indicated. Further investigations will continue to analyze the nature of aroma–protein interactions.

In addition, SV-AUC indicated that phenols, such as guaiacol, p-cresol, m-cresol affect the sedimentation properties of mucin as evidenced from an increase in the concentration of smaller S fractions. Complemented by Raman spectroscopy, these changes appear to be related to the observed decrease in the amide I region (~ 1640 cm−1), suggesting interactions are occurring in the non-glycosylated protein region of mucins. Future studies will focus on the analysis of proteins which have a well-defined structure to investigate the chemical and physical mechanisms of aroma-protein interactions. For instance, the use of the multi-wavelength detector capability could allow the screening of multiple aroma compounds with different optical properties at once, in the presence of heterogeneous mixtures of mucosal proteins and glycoproteins.

Data availability

Data are available upon reasonable request.

References

1. Arai S, Noguchi M, Yamashita M et al (1970) Studies on flavor components in soybean. Agric Biol Chem 34:1569–1573. https://doi.org/10.1271/bbb1961.34.1569

2. Brautigam CA (2015) Calculations and publication-quality illustrations for analytical ultracentrifugation data. Methods Enzymol 562:109–133. https://doi.org/10.1016/bs.mie.2015.05.001

3. Channell G, Dinu V, Adams GG, Harding SE (2018) A simple cell-alignment protocol for sedimentation velocity analytical ultracentrifugation to complement mechanical and optical alignment procedures. Eur Biophys J 47:809–813. https://doi.org/10.1007/s00249-018-1328-9

4. Cohen SM, Eisenbrand G, Fukushima S, et al (2020) GRAS 29 Flavoring Substances. https://www.ift.org/news-and-publications/food-technology-magazine/issues/2020/march/features/gras-29-flavoring-substances. Accessed 2 Jul 2020

5. Damodaran S, Kinsella JE (1980) Flavor protein interactions. Binding of carbonyls to bovine serum albumin: thermodynamic and conformational effects. J Agric Food Chem 28:567–571. https://doi.org/10.1021/jf60229a019

6. Dinu V, Gillis RB, MacCalman T et al (2019) Submaxillary mucin: its effect on aroma release from acidic drinks and new insight into the effect of aroma compounds on its macromolecular integrity. Food Biophys. https://doi.org/10.1007/s11483-019-09574-2

7. Dinu V, Kilic A, Wang Q et al (2020) Policy, toxicology and physicochemical considerations on the inhalation of high concentrations of food flavour. Npj Sci Food 4:15. https://doi.org/10.1038/s41538-020-00075-y

8. Dinu V, Yakubov G, Lim M et al (2019) Mucin immobilization in calcium alginate: a possible mucus mimetic tool for evaluating mucoadhesion and retention of flavour. Int J Biol Macromol. https://doi.org/10.1016/j.ijbiomac.2019.07.148

9. Dodd S, Place GA, Hall RL, Harding SE (1998) Hydrodynamic properties of mucins secreted by primary cultures of Guinea-pig tracheal epithelial cells: determination of diffusion coefficients by analytical ultracentrifugation and kinetic analysis of mucus gel hydration and dissolution. Eur Biophys J 28:38–47. https://doi.org/10.1007/s002490050181

10. Donohue TM, Tuma DJ, Sorrell MF (1983) Acetaldehyde adducts with proteins: binding of [14C]acetaldehyde to serum albumin. Arch Biochem Biophys 220:239–246

11. Durant S, Karran P (2003) Vanillins–a novel family of DNA-PK inhibitors. Nucleic Acids Res 31:5501–5512. https://doi.org/10.1093/nar/gkg753

12. Fares K, Landy P, Guilard R, Voilley A (1998) Physicochemical interactions between aroma compounds and milk proteins: effect of water and protein modification. J Dairy Sci 81:82–91. https://doi.org/10.3168/jds.S0022-0302(98)75554-7

13. FEMA (2020a) Safety and regulatory authority to use flavors—focus on vaping products | FEMA. https://www.femaflavor.org/safety-regulatory-authority-use-flavors-focus-vaping-products. Accessed 2 Jul 2020

14. Fisher SZ, Govindasamy L, Tu C et al (2006) Structure of human salivary α-amylase crystallized in a C-centered monoclinic space group. Acta Crystallograph Sect F Struct Biol Cryst Commun 62:88–93. https://doi.org/10.1107/S1744309105042491

15. Green AA (1933) The preparation of acetate and phosphate buffer solutions of known pH and ionic strength. J Am Chem Soc 55:2331–2336. https://doi.org/10.1021/ja01333a018

16. Harding SE, Rowe AJ, Creeth JM (1983) Further evidence for a flexible and highly expanded spheroidal model for mucus glycoproteins in solution. Biochem J 209:893–896. https://doi.org/10.1042/bj2090893

17. Jouenne E, Crouzet J (2000) Effect of pH on retention of aroma compounds by beta-lactoglobulin. J Agric Food Chem 48:1273–1277

18. Kikugawa K, Iwata A, Beppu M (1988) Formation of cross-links and fluorescence in polylysine, soluble proteins and membrane proteins by reaction with 1-butanal. Chem Pharm Bull (Tokyo) 36:685–692. https://doi.org/10.1248/cpb.36.685

19. Linden SK, Sutton P, Karlsson NG et al (2008) Mucins in the mucosal barrier to infection. Mucosal Immunol 1:183–197. https://doi.org/10.1038/mi.2008.5

20. Meynier A, Rampon V, Dalgalarrondo M, Genot C (2004) Hexanal and t-2-hexenal form covalent bonds with whey proteins and sodium caseinate in aqueous solution. Int Dairy J 14:681–690. https://doi.org/10.1016/j.idairyj.2004.01.003

21. Murphy EJ, Metcalfe CL, Nnamchi C et al (2012) Crystal structure of guaiacol and phenol bound to a heme peroxidase. FEBS J 279:1632–1639. https://doi.org/10.1111/j.1742-4658.2011.08425.x

22. Omaiye EE (2019) High concentrations of flavor chemicals are present in electronic cigarette refill fluids. Sci Rep 9:1–9

23. Paravisini L, Guichard E (2016) Interactions between aroma compounds and food matrix. In: Flavour. John Wiley & Sons, Ltd, pp 208–234. https://doi.org/10.1002/9781118929384

24. Parker JK, Elmore S, Methven L (2015) Flavour development, analysis and perception in food and beverages. Elsevier. https://doi.org/10.1016/C2013-0-16460-4

25. Qais FA, Husain FM, Khan MS (2019) Deciphering the interaction of food additive, vanillin with DNA: a biophysical and computational study. J Biomol Struct Dyn. https://doi.org/10.1080/07391102.2019.1692693

26. Radicioni G, Cao R, Carpenter J et al (2016) The innate immune properties of airway mucosal surfaces are regulated by dynamic interactions between mucins and interacting proteins: the mucin interactome. Mucosal Immunol 9:1442–1454. https://doi.org/10.1038/mi.2016.27

27. Reineccius G (2006) Flavor release from foods. Flavour chemistry and technology. CRC Press, Boca Raton, pp 139–159

28. Rothe M (1997) Flavor-food interactions. ACS symposium series 633. edited by R. J. McGorrin and J. V. Leland. XII and 235 pages, numerous figures and tables. American Chemical Society, Washington, DC, 1996. Price: 89.95 US $. Food Nahr 41:379–379. https://doi.org/10.1002/food.19970410618

29. Seagrave J, Albrecht H, Park YS et al (2011) Effect of guaifenesin on mucin production, rheology, and mucociliary transport in differentiated human airway epithelial cells. Exp Lung Res 37:606–614. https://doi.org/10.3109/01902148.2011.623116

30. Solomon OF, Ciuta IZ (2019) Détermination de la viscosité intrinsèque de solutions de polymères par une simple détermination de la viscosité—Solomon—1962—Journal of Applied Polymer Science—Wiley Online Library. https://onlinelibrary.wiley.com/doi/abs/https://doi.org/10.1002/app.1962.070062414. Accessed 6 May 2019

31. Tierney PA, Karpinski CD, Brown JE et al (2016) Flavour chemicals in electronic cigarette fluids. Tob Control 25:10–15

32. Tromelin A, Andriot I, Guichard E (2006) Protein-flavour interactions. In: Flavour in Food. Woodhead Publishing Limited, p 320. https://doi.org/10.1533/9781845691400.2.172

33. Verdugo P (2012) Supramolecular dynamics of mucus. Cold Spring Harb Perspect Med 2:a009597. https://doi.org/10.1101/cshperspect.a009597

34. Weerawatanakorn M, Wu J-C, Pan M-H, Ho C-T (2015) Reactivity and stability of selected flavor compounds. J Food Drug Anal 23:176–190. https://doi.org/10.1016/j.jfda.2015.02.001

35. Whittingham JL, Edwards DJ, Antson AA et al (1998) Interactions of phenol and m-cresol in the insulin hexamer, and their effect on the association properties of B28 pro—Asp insulin analogues. Biochemistry 37:11516–11523. https://doi.org/10.1021/bi980807s

36. Ziegler H (2007) Flavourings: Production, Composition, Applications, Regulations. John Wiley & Sons. https://doi.org/10.1002/9783527611454

Acknowledgements

This work was supported by the Engineering and Physical Sciences Research Council [Grant number EP/L015633/1], Biotechnology and Biological Sciences Research Council [Grant number BB/T006404/1] and the 2019 EPSRC Doctoral Prize fellowship. The work was carried out at the National Centre for Macromolecular Hydrodynamics, in the School of Biosciences, University of Nottingham.

Author information

Affiliations

1. National Centre for Macromolecular Hydrodynamics, School of Biosciences, University of Nottingham, Sutton Bonington Campus, Leicestershire, UK

Vlad Dinu, Thomas MacCalman, Gleb E. Yakubov & Stephen E. Harding

2. Division of Food, Nutrition and Dietetics, School of Biosciences, University of Nottingham, Sutton Bonington Campus, Leicestershire, UK

Vlad Dinu, Ni Yang, Gleb E. Yakubov & Ian D. Fisk

3. International Diabetes Education and Research, Faculty of Medicine and Health Sciences, University of Nottingham, Nottingham, UK

Gary G. Adams

Contributions

V.D. performed the experiments and wrote the manuscript. T.M. performed the SEC-MALS experiments and data interpretation. G.E.Y. wrote and commented on the manuscript. S.E.H. and I.F. supervised and commented on the manuscript.

Corresponding author

Correspondence to Vlad Dinu.

Ethics declarations

Competing interest

The authors declare that they have no known competing financial interests or personal relationships that could have appeared to influence the work reported in this paper.

Additional information

Publisher's Note

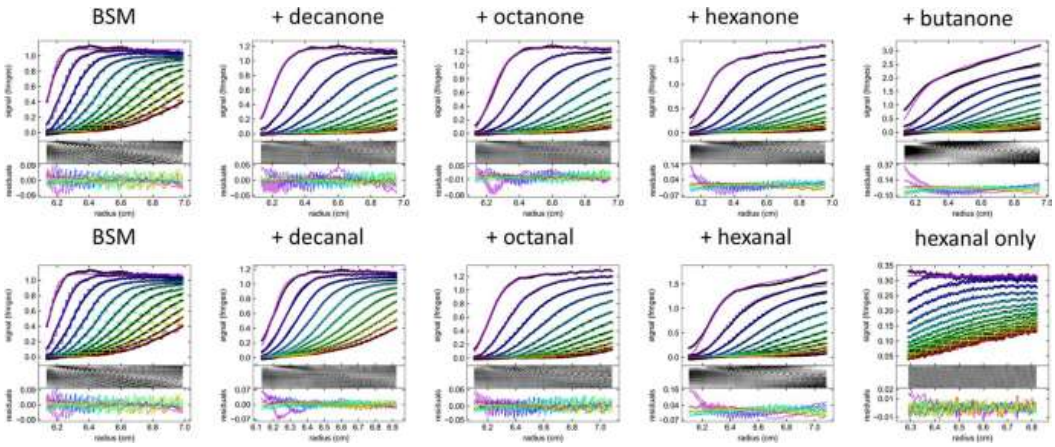
Springer Nature remains neutral with regard to jurisdictional claims in published maps and institutional affiliations.

Special Issue: Analytical Ultracentrifugation 2019.

Appendix

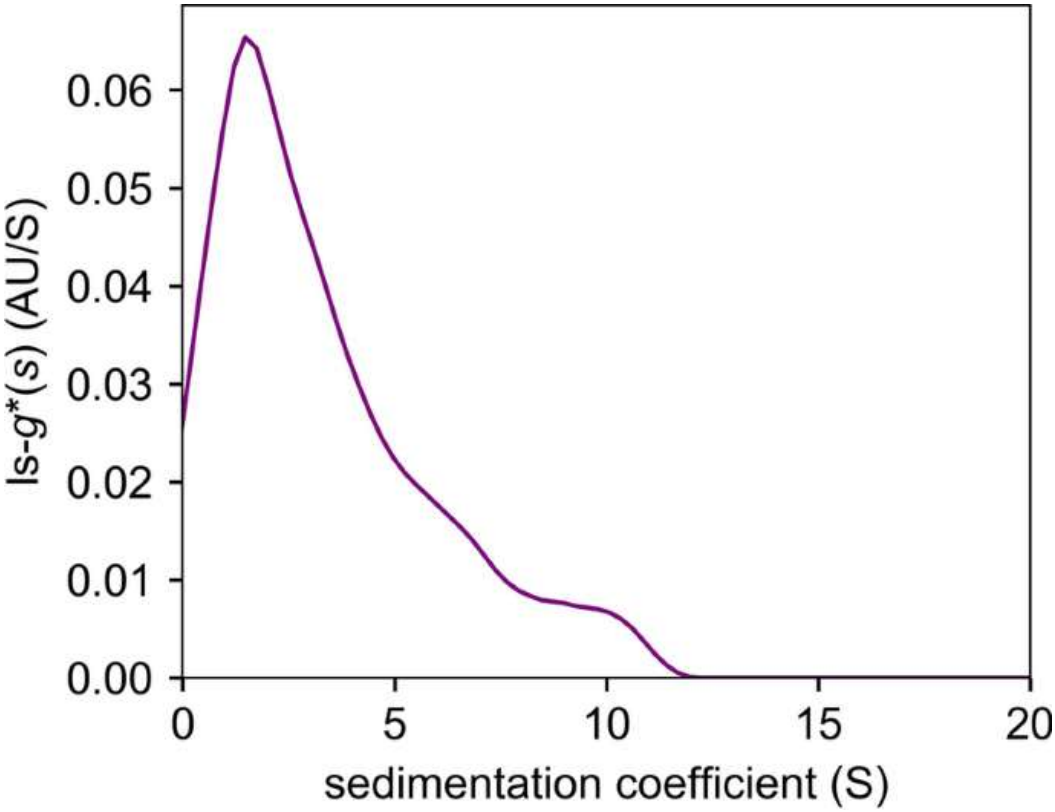
See Figs. 6, 7 and 8.

Fig. 6



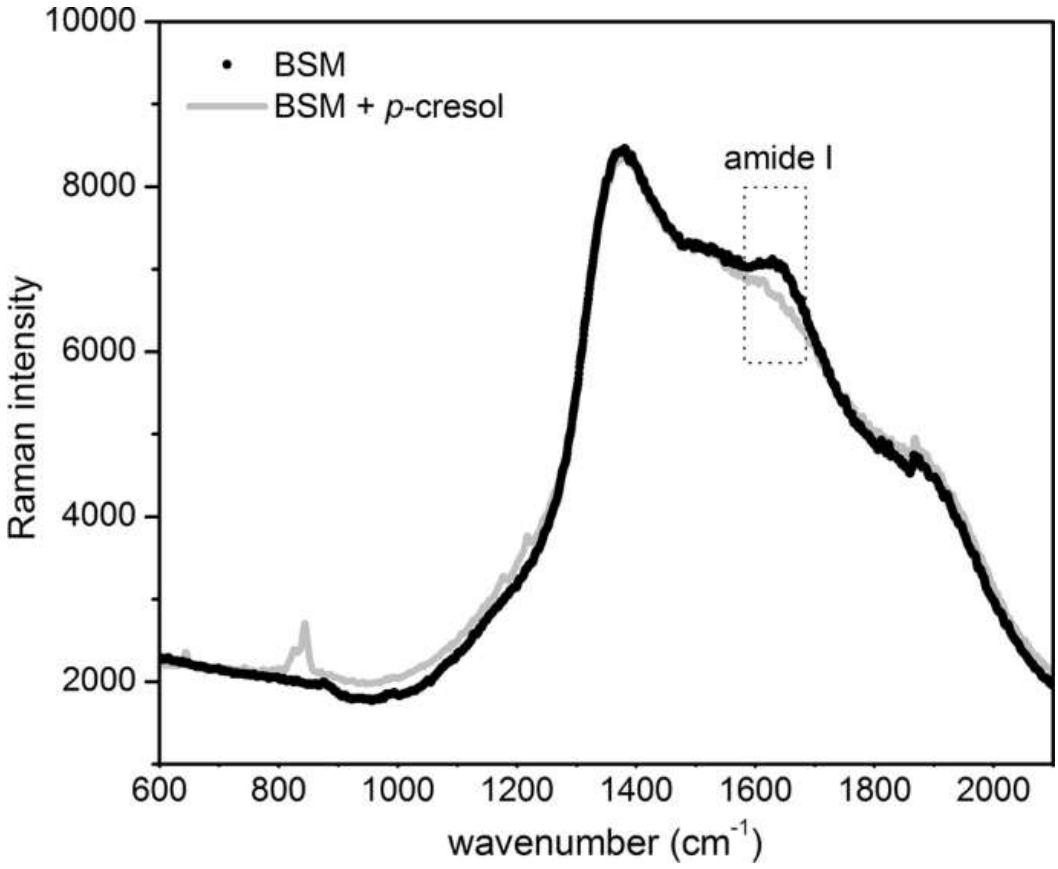
Raw data showing the changes in fringe concentration and residuals plots for BSM, BSM/aroma compounds mixtures and hexanal control, plotted using the GUSSI extension in SEDFIT (Brautigam 2015)

Fig. 7



Sedimentation coefficient distribution of hexanal control (1.0 mg/mL) in 0.1 M PBS pH 7. Rotor speed: 30,000 rpm (90,000 g), 20.0 ºC

Fig. 8



Raman spectra of BSM (c = 10 mg/mL) with and without p-cresol. The mucin/p-cresol sample was dialysed against a 14 kDa membrane prior to Raman analysis to remove excess p-cresol. Performed in 0.1 M PBS pH 7 at 20.0 °C. Adapted from (Dinu et al. 2019a)

Rights and permissions

Open Access This article is licensed under a Creative Commons Attribution 4.0 International License, which permits use, sharing, adaptation, distribution and reproduction in any medium or format, as long as you give appropriate credit to the original author(s) and the source, provide a link to the Creative Commons licence, and indicate if changes were made. The images or other third party material in this article are included in the article's Creative Commons licence, unless indicated otherwise in a credit line to the material. If material is not included in the article's Creative Commons licence and your intended use is not permitted by statutory regulation or exceeds the permitted use, you will need to obtain permission directly from the copyright holder. To view a copy of this licence, visit http://creativecommons.org/licenses/by/4.0/.

The End